Boiling Enhancement Characteristics of An Antifouling Three-Phase (vapour-liquid-solid) Circulating Fluidised Bed Heat Exchanger

by

MICHAEL ARUMEMI-IKHIDE

Submitted for the Degree

of

Doctor of Philosophy

THE UNIVERSITY OF EDINBURGH

School of Engineering and Electronics

Edinburgh, UK

February 2006

DEDICATION

This Thesis is dedicated to my beloved Grandfather:

Mr Augustine, Akhere Otoide (a.k.a A.A)

Your memory remains,

and

Continues to inspire

"Blessed is the man who finds *wisdom*, the man who gains *understanding*; for she is more profitable than silver and yields better returns than gold. Nothing you can desire can compare with her. Long life is in her right hand; and in her left are riches and honour. Her ways are pleasant ways, and all her paths lead to peace.

PROVERBS 3: v 13 - 17

ABSTRACT

Scale formation on heat transfer surfaces results in the build-up of deposits (products of heat and mass transfer processes) which act as additional thermal resistance, thereby leading to the degradation of equipment heat transfer performance. Under most conditions fouling is more severe during sub-cooled boiling heat transfer, mainly due to the mechanisms which govern the bubble formation and detachment process.

Therefore in response, the current project aims to investigate the boiling enhancement characteristics and fouling mitigation potential of a three-phase (vapour-liquid-solid) circulating fluidised bed heat exchanger (CFBHX). The design of the three-phase boiling system is predicated on a combination of multiphase fluidisation and flow boiling heat transfer. Experiments are performed at atmospheric pressure, and distilled water is used as the working fluid. The three-phase test unit consist of a glass riser column with a mini-channel of square cross sectional area 21.5 mm x 11mm, height 1000mm, fitted with an electrically heated cartridge heater rod of 8mm diameter x 730mm length. The set-up employs stainless steel particles as the solid phase.

A systematic experimental study is made to understand the influence of particles and particle size on the boiling heat transfer behaviour of the three-phase CFBHX. The effect of operating parameters such as heat flux and superficial velocity are also investigated. In the riser column, the use of transparent glass walls is of major significance as it provides a means of observing, and studying (via the use of flow visualisation techniques) the complex multiphase flow system. Results from our experimental work show that higher heat transfer coefficients are achieved in (vapour-liquid-solid) three-phase flow boiling, compared with (vapour-liquid) two-phase flow boiling. The observed enhancement becomes more pronounced for progressively larger diameter particles.

Based on both an analysis of the mechanisms governing three-phase boiling heat transfer, and the extension of existing two-phase flow boiling (and liquid-solid fluidised bed) heat transfer models, a boiling heat transfer correlation has been derived for the prediction of heat transfer in our vapour-liquid-solid circulating fluidised bed system. A favourable agreement between the derived three-phase boiling correlation and our empirically obtained results has also been duly demonstrated.

ACKNOWLEDGEMENTS

I wish to express my sincere appreciation to my supervisors Dr. Khellil Sefiane and Dr. Don Glass. Both have contributed immeasurable to my academic and personal development, and for this I am eternally grateful.

My thanks also to all the technical staff at the School of Engineering and Electronics, without whom this project would never have been realised. However, special thanks must go to Mr Ian Fowler, Mr Bobby Hogg, Mr Kenny Fee, Mr Alistair Fitchie and Mr Rab Kilgour who were all directly involved in the fabrication and maintenance of the experimental apparatus over the period of study. I am indebted to them for their guidance and assistance.

In many ways this body of work represents the combined efforts of several former undergraduate students: Alan Bruce, Daniel Chaplin, Jean Arnaud, Julie Barraud, Jacqueline Barber, Tope Bajowa, Bryony Davidson, Hery Anne-Laure, and Allan Balata. Their contributions could never be forgotten and are highly appreciated.

To my wonderful friends, I extend my deepest thanks and heartfelt gratitude for all the continued understanding, support and care provided through the years. In particular I would like to thank The McMartin and Russell families' for infusing my life with the very best of Scotland. Your kindness and generosity have always been my reliable companions. I also acknowledge Susan McMartin, Gabriel Bolu, Cosimo Buffone, Aimee Martin, Joy and Ngozi Anwuri, Marianne Amasike and Donald Chimbwete. I thank them all for their love and friendship.

Alistair McLean is singled out for special praise. Not only has Alistair been the truest of friends, offering guidance and encouragement when needed, but he has also been intricately linked with the execution of this project. His patience and dedication in helping me accomplish my goals have been truly remarkable. Thank you.

And finally to my family; indeed I have been blessed with the most wonderful parents (Joseph and Mary Arumemi-Ikhide) who through their toils and efforts have always sought to provide the very best for their children, many times to the detriment of their own personal needs. This thesis is a direct result of their exemplary love and dedication; they have set us (i.e. the children) an example that must be emulated. To my darling sister Omo, and my champion brothers Martin, Joseph and Eromosere, I extend all my love, wish you every success and happiness, and pray that we all remain on a steady incline.

The work following has been supported by both 'ExxonMobil' and 'Hansworth Ltd'; their financial contributions are here acknowledged and greatly appreciated.

TABLE OF CONTENTS

CHAPTER 3: LITERATURE REVIEW

CHAPTER 4: EXPERIMENTAL APPARATUS & METHODS

CHAPTER 5: FLOW BOILING ENHANCEMENT – EXPERIMENTAL RESULTS

CHAPTER 6: FLOW BOILING ENHANCEMENT – DISCUSSION OF MECHANISMS

CHAPTER 7: CORRELATING THE THREE-PHASE (V-L-S) FLOW BOILING EXPERIMENTAL RESULTS

CHAPTER 8: CONCLUSIONS AND FUTURE OUTLOOKS

LIST OF TABLES

CAPTIONS

PUBLICATIONS & PRESENTATIONS

The following publications and presentations have been made during the course of the present investigation:

(in chronological order)

Arumemi-Ikhide, M., Sefiane, K. and Glass, D., "Flow boiling heat transfer in a 3-Phase circulating fluidised bed," 18th HEXAG Meeting, The University of Edinburgh, UK, April 2002. *Presentation only*

Arumemi-Ikhide, M., Sefiane, K. and Glass, D., "Flow boiling heat transfer in a 3-Phase circulating fluidised bed (self-cleaning heat exchanger)," In: Proceedings of 8th UK National Heat Transfer Conference, Oxford University, UK, September 2003. *Presentation and Publication.* ' **HTFS Aspen Technology Best Paper Award**'

Arumemi-Ikhide, M., Sefiane, K. and Glass, D., "Boiling heat transfer enhancement in a three-phase circulating fluidised bed," *Submitted Jan 2005 for Publication in The International Journal of Heat and Mass Transfer.*

Arumemi-Ikhide, M. and Sefiane, K., "Boiling enhancement in a mini-channel of a three-phase circulating fluidised bed," In: Proceedings of ICMM2005, 3RD International Conference on Microchannels and Minichannels, Toronto, Ontario, Canada, June 2005. *Presentation and Publication.*

Arumemi-Ikhide, M. and Sefiane, K., "Developing correlation for three-phase flow boiling in a circulating fluidised bed," In: Proceedings of The 1st International Conference on Diffusion in Solids and Liquids, DSL-2005, University of Aveiro, Portugal, June 2005. *Publication only.*

Arumemi-Ikhide, M., Sefiane, K. and Glass, D., "Boiling enhancement in a mini-channel of a three-phase circulating fluidised bed," Presented at Institute for Materials and Processes (IMP) Seminar, The University of Edinburgh, UK, January 2006.

NOMENCLATURE

Roman

a, b, m	Coefficients and exponents in equations 3.51 and 3.52
A	Heat transfer surface area, m^2
A_{CS}	Cross-sectional area of heated flow channel, m^2
$A_{CS,1}$	Cross-sectional area of non-heated section of fluidised bed, m^2
$A_{CS,2}$	Cross-sectional area of expanded outlet chamber, m^2
A_c	Forced convective heat transfer surface area in liquid-solid fluidised flow, m^2
A_{LO}	Area of heat transfer surface affected by two-phase (vapour-liquid) forced convective boiling, m^2
A_p	Area of heat transfer surface affected by particles in liquid-solid fluidisation, m^2
A_{pds}	Pipe distributor bed occupation area, m^2
A_{nb}	Area of heat transfer surface affected by two-phase (vapour-liquid) boiling, m^2
Ar	Archimedes number ($= \{g.\rho_L(\rho_p - \rho_L).d_p^3\}/\{\mu_L^2\}$), dimensionless
A_{TOTAL}	Overall heat transfer surface area, m^2
Bo	Boiling number, dimensionless
B''	Coefficient in equation 3.60
B_α	Bias limit of experimentally determined heat transfer coefficient
B_T	Bias error of point measured local wall temperature, °C
B_{Tw}	Bias limit of measured wall temperature, °C
Be_T	Elemental bias contribution to B_T, °C
Bc_T	Conceptual bias contribution to B_T, °C

B_{Tf^*}	Bias limit of mean bulk fluid temperature, °C
$B_{Tf.i}$	Bias error of point measured inlet fluid temperature, °C
$Be_{Tf.i}$	Elemental bias contribution to $B_{Tf.i}$, °C
$Bc_{Tf.i}$	Conceptual bias contribution to $B_{Tf.i}$, °C
$B_{Tf.o}$	Bias error of point measured outlet fluid temperature, °C
$Be_{Tf.o}$	Elemental bias contribution to $B_{Tf.o}$, °C
$Bc_{Tf.o}$	Conceptual bias contribution to $B_{Tf.o}$, °C
C	Constant in equation 2.5 and equation 3.24
C''	Constant in equation 3.50
$C_{d,or}$	Orifice coefficient, dimensionless
C_D	Drag coefficient, dimensionless
$C_{D,TL}$	Drag coefficient calculated according to Turton and Levenspiel [100], dimensionless
CF	Cleanliness factor, dimensionless
C_p	Specific heat capacity, J/kg.K
Co	Convective number in Shah correlation [22]
d_b	Bubble departure diameter, m
d_p	Particle diameter, m
$d_{optimum}$	Optimum pipe diameter for design of liquid entry pipes, m
d_{or}	Orifice diameter of porous plate distributor, m
$d_{S.pipe}$	Diameter of standpipe, m
D	Tube or bed diameter, m
D_e	Equivalent (or mean hydraulic) bed diameter, m
$D_{e,1}$	The equivalent bed diameter for the non-heated entrance section of fluidised bed, m
D_{nor}	Normalised bed diameter, m
f	Particle-wall collision frequency, s^{-1}
f_i	Friction factor, dimensionless
$f(m, x)$	Correction function of mass velocity and vapour fraction

f_a and f_b	Fanning friction factors in equations 3.9-3.10 & 3.21-3.22
$f(U)$	Three-phase convective adjustment factor
F	Multiplier in equation 3.57
F_{CB}	Three-phase flow convective factor, dimensionless
$F(d)$	Tube diameter correction factor, dimensionless
F_{fb}	Two-phase flow convective factor, dimensionless
$F(M)$	Fluid molecular weight correction factor, dimensionless
F_{nbf}	Two-phase nucleate flow boiling correction factor, dimensionless
F_{NB}	Three-phase nucleate flow boiling correction factor, dimensionless
F_{pr}	Nucleate flow boiling pressure correction factor, dimensionless
$F(Ra)$	Heat transfer surface roughness correction factor, dimensionless
g	Acceleration due to gravity, $9.81 ms^{-1}$
Δh_v	Latent heat of vaporization, J/kg
H-$H5$	Coefficients and exponents in equation 3.27
I	Defined in equation 3.41
J	Number in equations 7.9 and 7.10, dimensionless
K	Total number of thermocouple probes
L	Tube length or bed height, m
L_1- L_3	Tube lengths in equation 3.8
L_{mf}	Height of bed at minimum fluidisation, m
L_{pds}	Height of particle distribution section, m
$\dot{m}$	Mass velocity, kg/s
$\dot{m}_{p,1}$	Solid mass flowrate exiting outlet chamber, kg/s
$\dot{m}_{L,1}$	Liquid mass flowrate exiting outlet chamber, kg/s
$\dot{m}_{V,1}$	Vapour mass flowrate exiting outlet chamber, kg/s

$\dot{m}_{TOTAL}$	Combined vapour, liquid and solid mass flowrate, kg/s
M	Molecular weight, kg/kmol
M_d	Mass flux of foulant deposited, kg/m^2.s
M_r	Mass flux of foulant removed, kg/m^2.s
n	Richardson and Zaki exponent
N	Number of repeated temperature measurements within a sample
N_{pipe}	Number of main liquid pipe distributors in test section
NBF	Nucleate boiling fraction as defined in equation 3.58
N_{or}	Number of orifices per unit area of porous plate distributor
Nu	Nusselt number (= $\alpha_c.D_e / \lambda_L$), dimensionless
P_α	Precision limit of experimentally determined heat transfer coefficient
P_{T*}	Precision error of mean local wall temperature, °C
P_{Tw}	Precision limit of measured wall temperature, °C
P_{Tf*}	Precision limit of mean bulk fluid temperature, °C
$P_{Tf,i}$	Precision error of inlet fluid temperature, °C
$P_{Tf,o}$	Precision error of outlet fluid temperature, °C
$P(I)$	Factor in equation 3.39 and defined in equation 3.40
Pr	Prandtl number (= $\mu_L C_{p,L} / \lambda_L$), dimensionless
P''	Pressure, Nm^{-2} or bar
P_∂''	Dynamic pressure, Nm^{-2} or bar
P_R''	Reduced pressure, dimensionless
$\Delta P''$	Pressure drop, Nm^{-2} or bar
$\Delta P_t''$	Total pressure drop across fluidised bed, Nm^{-2} or bar
$\Delta P_d''$	Pressure drop across porous plate distributor, Nm^{-2} or bar
$\Delta P''_{pds}$	Pressure drop over particle distribution section, Nm^{-2} or bar
q	Heat duty or power, Watts

q_{loss}	Heat loss to environment in equation 4.45, Watts
q_{pump}	Pumping power requirement, Watts
q''	Heat flux, kW/m^2
q''_{npb}	Nucleate pool boiling heat flux for pure liquid, kW/m^2
q''_{o}	Normalised heat flux, kW/m^2
$q''_{p,cs}$	The pool boiling convective sensible heat flux in the presence of solid particles, kW/m^2
Q	Volumetric flowrate, m^3/s
Q_{TOTAL}	Combined vapour, liquid and solid volumetric flowrate, m^3/s
R	Universal gas constant, 8.314 J/mol.K
R_a	Wall roughness parameter, μm
$R_{a,o}$	Reference or normalised wall roughness, μm
R_f	Fouling resistance, m^{2}K/W
R(I)	Factor in equation 3.39 and defined in equation 3.40
Re	Vessel Reynolds number (= $U_L.D_e / \nu_L$), dimensionless
Re_d	Vessel Reynolds number for flow approaching porous plate distributor (= $U_{AL}.D_{e,l} / \nu_L$), dimensionless
Re_{FB}	Two-phase Reynolds number in equation 3.57, dimensionless
Re_p	Particle Reynolds number (= $U_L.d_p / \nu_L$), dimensionless
$Re_{p,mf}$	Particle Reynolds number at minimum fluidising conditions (= $U_{mf}.d_p / \nu_L$), dimensionless
Re_{pt}	Particle terminal Reynolds number corrected for wall effect (= $U_t.d_p / \nu_L$), dimensionless
$Re_{p\infty}$	Particle terminal Reynolds number in the absence of wall effect (= $U_\infty.d_p / \nu_L$), dimensionless
S	Suppression factor in Chen model as presented in equation 3.57

S_M	The sampling error in the estimation of the mean local wall temperature, °C (calculated for a number of samples, each of size N)
S_T	Precision index for a sample (size N) of local wall temperature measurements, °C
S_{EFF}	Separation efficiency, %
t	Time, s
t_c	Contact time, s
T	Individual local wall temperature sampled by probe number j, °C
T^*	Mean local wall temperature measured by probe number j, °C
T_{f^*}	Mean bulk fluid temperature, °C
$T_{f.i}$	Inlet fluid temperature, °C
$T_{f.o}$	Outlet fluid temperature, °C
T_b	Bulk processing temperature, °C
T_w	Measured wall temperature, °C
ΔT	Wall superheat or temperature driving force, K
Th	Thickness, or depth, measurement, m
u, v, w	velocity vector components
U	Fluid superficial velocity, m/s
U_L	Liquid superficial velocity, m/s
U_{mf}	Minimum fluidising velocity, m/s
U_{or}	Fluid superficial velocity through orifice, m/s
U_p	Particle rise velocity, m/s
$U_{S.pipe}$	Solid velocity through standpipe, m/s
U_∞	Particle terminal velocity in the absence of wall effect, m/s
U_t	Particle terminal velocity corrected for wall effect, m/s

U_α	Uncertainty in the experimentally determined heat transfer coefficient, %
V	Volume, m^3
W	Width, or breadth, measurement, m
W_f	Wall factor
W_g	Evaporation intensity of fluidised bed heat exchanger
x, y, z	Spatial coordinates
x	Vapour quality, dimensionless
X_{tt}	Martinelli parameter
Y	Coefficient in equation 3.52
Y''	Number in equation 7.6
Y_1'' & Y_2''	Rate constants for the interchange of solids as defined in equation 4.9

Greek Letters

α	Heat transfer coefficient (also referred to as the '*k*-value'), $kW/m^2.K$
α_c	Forced convective (liquid only) heat transfer coefficient in liquid-solid fluidised flow, $kW/m^2.K$
α_{cb}	Two-phase convective flow boiling heat transfer coefficient, $kW/m^2.K$
α_{CB}	Three-phase convective flow boiling heat transfer coefficient, $kW/m^2.K$
$\alpha_{E.T}$	Heat transfer enhancement percentage, %
α_{fb}	Experimentally determined two-phase flow boiling heat transfer coefficient, $kW/m^2.K$
$\alpha_{F.B}$	Predicted two-phase flow boiling heat transfer coefficient, $kW/m^2.K$

α_{LO}	Two-phase flow boiling convective coefficient based on total mass velocity assumed as liquid only, $kW/m^2.K$
α_{LS}	Overall heat transfer coefficient in liquid-solid fluidised bed system, $kW/m^2.K$
α_{nb}	Two-phase nucleate flow boiling heat transfer coefficient, $kW/m^2.K$
α_{NB}	Three-phase nucleate flow boiling heat transfer coefficient, $kW/m^2.K$
α_{npb}	Nucleate pool boiling heat transfer of pure liquid, $kW/m^2.K$
$\alpha_{npb,p}$	Nucleate pool boiling with suspended particles, $kW/m^2.K$
$\alpha_{npb,o}$	Nucleate pool boiling heat transfer of pure liquid at normalised conditions, $kW/m^2.K$
α_p	Heat transfer coefficient of the particle controlled surface area in liquid-solid fluidised flow, $kW/m^2.K$
$\alpha_{t.f.b}$	Experimentally determined three-phase (vapour-liquid-solid) flow boiling heat transfer coefficient, $kW/m^2.K$
$\alpha_{T.F.B}$	Predicted three-phase (vapour-liquid-solid) flow boiling heat transfer coefficient, $kW/m^2.K$
α_{wl}	Heat transfer coefficient from the wall to the adjacent liquid layer (a component of α_p), $kW/m^2.K$
α_{wp}	Heat transfer coefficient from the wall to the fluidised particles (a component of α_p), $kW/m^2.K$
$f(\alpha_o)$	Film heat transfer coefficient for outer tubes, $kW/m^2.K$
$f(\alpha_i)$	Film heat transfer coefficient for inner tubes, $kW/m^2.K$
ε	Bed voidage or volume fraction of continuous fluid phase, dimensionless

ε_p	Particle volume fraction or average solid holdup, dimensionless
ε''_p	Local solid holdup within fluidised bed, dimensionless
ε_{mf}	Bed voidage at minimum fluidising conditions
ε_{pds}	Bed voidage in particle distribution section
$\varepsilon_{S.pipe}$	Accounts for bed voidage of standpipe, dimensionless
ε_1- ε_3	Bed porosities in equation 3.8
ε_{SB}	Static bed voidage, dimensionless
ε_s	Solid fraction
β	Number in equation 7.5
ν	Kinematic viscosity, m^2/s
μ	Dynamic viscosity, kg/m.s
ρ	Density, kg/m^3
λ	Thermal conductivity, W/m.K
λ_M	Thermal conductivity of solid-liquid mixture, W/m.K
σ	Surface tension, N/m
Ω	Thermal diffusivity, m^2/s
Θ	Bubble contact angle, °
η	Fin efficiency, dimensionless
ξ	Exponent in equation 7.6
Φ_{nb}	Mass flux of foulant deposited in nucleate boiling zone of heater surface, $kg/m^2.s$
Φ_{LO}	Mass flux of foulant deposited in forced convective zone of heater surface, $kg/m^2.s$
θ_{Tw}	Sensitivity coefficient of measured wall temperature, $kW/m^2.K$
θ_{Tf^*}	Sensitivity coefficient of mean bulk fluid temperature, $kW/m^2.K$

Superscripts and subscripts

*	Average
AL	Auxiliary liquid
b_E	Three-phase flow boiling enhancement exponent
cal	calculated
cl	clean or without fouling
CR	at critical conditions
d	deposit
ehd	enhanced surface
exp	experimental
f	with fouling
fin	fin
i	inner tube
L	liquid
ML	main liquid
o	outer tube
p	particle
pln	plain surface
r	nucleate flow boiling q'' exponent
sat	saturated
t_R	flow boiling transition exponent
V	vapour
Z	Fluidisation index

Abbreviations

AC	Amorphous carbon
A.R.E	Average relative error
CFB	Circulating fluidised bed

CFBHX	Circulating fluidised bed heat exchanger
CFD	Computational fluid dynamics
CMC	Carboxymethylcellulose
DLC	Diamond-like carbon
DLC-F	Diamond-like carbon and fluorine
FBHX	Fluidised bed heat exchanger
GNP	Gross national product
HTRI	Heat transfer research inc.
KE	Kinetic energy
LSFB	Liquid solid fluidised bed
MDF	Medium density fibreboard
O.F.B	Onset of nucleate flow boiling
PE	Potential energy
PTFE	Polytetrafluoroethylene
S.D	Standard deviation
TEMA	Tubular exchanger manufacturers association
UOP	Universal oil products
(v-l)	vapour and liquid
(v-l-s)	vapour, liquid and solid

CHAPTER 1: INTRODUCTION & THESIS STRUCTURE

1.1. INTRODUCTION

Fouling of heat transfer surfaces is a frequent engineering problem, which is more acute under boiling conditions due to the mechanisms connected with bubble formation and detachment. As a result, in engineering applications which require the dual combination of heat transfer enhancement and fouling prevention, most putative boiling enhancement methods are rendered non-viable due to the severity of boiler fouling. Hence, in light of these considerations, a new type of (vapour-liquid-solid) three-phase circulating fluidised bed system has been developed for the purposes of enhancing heat transfer and preventing scale deposition during the boiling process.

1.2. THESIS STRUCTURE

The thesis begins in earnest in *Chapter 2*, where the key subject areas of heat exchanger fouling and boiling heat transfer are formerly introduced. At this initial stage, the intention is simply to familiarise the reader with the main topics relevant to the present project. To this effect, the history of heat exchanger fouling is briefly discussed; basic terminologies are set-out and defined; and the fundamental principles of scale deposition are clearly explained, including the most important influencing factors and the economic impact of industrial fouling.

Similar background information is provided in respect of boiling heat transfer, beginning with a detailed description of the boiling process, where the basic concepts and mechanisms in this field of science are outlined and discussed. In addition, the most important correlations for the prediction of heat transfer in two-phase (vapour-liquid) flow boiling are also presented.

Armed with this necessary background information, we then proceed to *Chapter 3*, where an extensive and comprehensive review is performed on the subject of fouling mitigation and heat transfer enhancement. In terms of chronology, the format of the review delineates between scale deposition under boiling and non-boiling conditions. Hence starting with the basic fouling prevention, treatment, and control methods, we describe and critique the various mitigation strategies both under development and in present industrial use. The generalised discourse is followed by a more focused appraisal of heat transfer enhancement and its role in the mitigation of heat exchanger fouling. Here we identify the various heat transfer enhancement measures which are typically employed in antifouling services, and classify them according to the means by which they effect the reduction of scale deposition. From the ensuing discussion, the most advantageous techniques for non-boiling operations, including the self-cleaning liquid-solid circulating fluidised bed heat exchanger, are further expanded upon.

Following its preliminary introduction, the self-cleaning heat exchanger is then comprehensively reviewed, beginning with a detailed discussion of its developmental history; here we chronicle the evolution of the fluidised bed technology, outlining the principles of operation, and comparing the consequences and limitations of the different modifications made over the past 35 years. Reported experimental and theoretical results regarding the heat transfer enhancement and antifouling performance of the fluidised bed heat exchanger are subsequently presented and compared. With respect to the observed effects, the different opinions from the available literature are also explained. From a commercial point of view, as well as the economics of the technology, a number of successful case studies are presented in order to demonstrate the versatility and relevance of the self-cleaning fluidised bed as a dual heat transfer enhancement and fouling mitigation technique.

The focus of the narrative then turns to the problem of scale deposition under conditions of boiling heat transfer. Here we extend and modify our understanding of the fouling process, by examining the impact of the bubble formation process on the nature, rate, and degree of boiler fouling. To this effect, fundamental observations and predictive correlations from the literature are explained to some detail. Finally, some of the most state of the art boiling enhancement and antifouling techniques are presented for discussion, including the contemporary three-phase (vapour-liquid-solid) circulating fluidised bed heat exchanger and its emerging role in the promotion of two-phase (vapour-liquid) boiling heat transfer and the suppression of heater surface fouling.

Overall, in conjunction with the background information given in *Chapter 2*, the chronological course of the review should help the reader understand the impact of scale deposition in heat transfer equipment, as well as communicate the need for measures which are capable of enhancing the rate of heat transfer whilst simultaneously minimising the incidence of fouling. The liquid fluidised bed technique is an eminent example of such a device, and so by clearly identifying its important contribution to heat transfer enhancement and fouling mitigation (in both boiling and non-boiling operations) we hope to effectively communicate the relevance of this present investigation.

Chapter 4 specifies the explicit objectives of the project and describes the development of the three-phase boiling device used to obtain experimental results. The designs of various constituent parts of the test section are explained in great detail, thereby allowing the reader an appreciation of the technical performance of the test unit. The ancillary components of the test rig and the adopted experimental procedures are also discussed at length, thus affording the reader a complete insight into our experimental program.

Arranged according to the flow boiling mode of interest (i.e. two-phase flow boiling and three-phase flow boiling respectively), *Chapter 5* presents the heat transfer results obtained at the test section. Here, a comprehensive description of the results is included, in order to

explain the influence of the various investigated parameters, specifically heat flux, liquid superficial velocity and the physical properties of the employed solid-phase.

Following on from *Chapter 5*, in *Chapter 6*, the experimental effects and features which have been recognised during our boiling heat transfer investigations are discussed and related to visualised heat and mass transfer processes, thereby leading to an established explanation of the heat transfer enhancement mechanisms associated with three-phase circulating fluidised bed boiling.

In *Chapter 7*, together with adapted two-phase flow boiling and liquid-solid fluidised bed heat transfer models, the conclusions drawn from the comprehensive set of experimental results are used as a basis for formulating a correlation capable of predicting heat transfer in our particular three-phase flow boiling device.

Chapter 8 summarises the work undertaken during this study, pointing out our main conclusions concerning the mechanisms of three-phase flow boiling heat transfer and recommending topics for future possible work.

In summary, this study aims to investigate the performance of a proposed three-phase boiling device, identifying its governing heat transfer mechanisms, and contrasting its behaviour with the case of two-phase flow boiling. The results of such work, should indeed buttress our understanding of three-phase flow boiling and its associated fundamentals.

CHAPTER 2: BACKGROUND

2.1. INTRODUCTION

This chapter presents the necessary background information required for a proper appreciation of the literature review and experimental investigation which follow. Starting from the significance and consequence of heat exchanger fouling, a brief description of the fouling process is given, including the mechanisms and sequential events, governing equations and representations, as well as the influence of various operating conditions. Coupled with discussions regarding the economic penalty of fouling, the overall presentation emphasises the operational and commercial ramification of scale formation in heat transfer equipment.

As our experimental concerns pertain to the enhancement of heat transfer and reduction of fouling under flow boiling conditions, background information on boiling heat transfer is also provided, helping to put in context the boiling enhancement techniques reviewed in *Chapter 3* and implemented in this study. Distinction is made between the *pool* and *flow* boiling modes of heat transfer, after which the fundamental mechanisms and observations in two-phase flow boiling are explained. Finally, the most important boiling correlations with an impact on the present study are identified and briefly discussed.

2.2. HEAT EXCHANGER FOULING

In today's world of expensive energy, the need for proper energy management has considerably increased the importance of heat exchanger equipment over the past 2-3 decades. There is virtually no chemical, food processing or power generating facility without a whole variety of heat exchangers. In most of these practical processes, heat exchanging fluids contain certain amounts of dissolved or suspended material or provide conditions favourable for the growth of biological organisms [1]. This may lead to the accumulation of poorly conducting materials, or deposits, on the heat transfer surfaces, a phenomenon commonly known as fouling or scale deposition.

Fouling has been recognised as a nearly universal problem in heat exchanger operation. 25 years ago heat exchanger fouling was referred to as "the major unresolved problem in heat transfer". Today, despite the copious explorations into the subject, the design and operation of heat exchangers is still, to a major extent, determined by the process-related formation of deposits on the heat transfer surface, requiring substantial safety margins in equipment design, pre-treatment of hot/cold fluids and regular cleaning of equipment. Scale formation affects the operation of process equipment in three major ways:

- The fouling layer has a low thermal conductivity. This increases the resistance to heat transfer and reduces effectiveness of heat exchangers.

- The formation of deposits on the heat transfer surface causes an increase of the frictional pressure drop across the apparatus, due to increased surface roughness and restricted cross-sectional flow area. This therefore requires additional pumping or fan power to maintain the same throughput. According to Müller-Steinhagen [1], more heat exchangers are taken out of service because of excessive pressure drop than because of reduced heat transfer

- Finally, fouling can cause substrate corrosion and erosion.

2.2.1. THE FOULING RESISTANCE

In order to quantify the fouling propensity of heat transfer surfaces in heat exchanger design, it is normal to define a "fouling resistance" or "fouling factor", R_f, in the calculation of the overall heat transfer coefficient, α :

$$\frac{1}{\alpha_o.A_o} = \frac{1}{f(\alpha_o).A_o} + \frac{R_{fo}}{A_o} + R_w + \frac{R_{fi}}{A_i} + \frac{1}{f(\alpha_i).A_i} \tag{2.1}$$

here α_o is the overall heat transfer coefficient based on the outside surface area of the tubes, A_o; $f(\alpha_i)$and $f(\alpha_o)$ are the film heat transfer coefficients for the inside and outside of the tubes (based on the inside and outside heat transfer surface areas A_i and A_o), R_{fi} and R_{fo} are the fouling factors for the inside and outside of the tubes respectively, and R_w is the tube wall thermal resistance of the separating wall. The frequently used expression 'fouling factor' is incorrect, as the effect of fouling is to create an *additional* thermal resistance. The fouling resistance reduces the overall heat transfer coefficient, α_o, which in turn leads to the reduction in the heat duty of existing heat exchangers, or to additional surface requirement in the design of heat exchangers. For power station condensers, instead of the fouling resistance R_f, it is common practise to account for fouling using a cleanliness factor, *CF*, which is the fraction of the predicted clean surface heat transfer which occurs after accounting for fouling:

$$CF = \frac{\alpha_f}{\alpha_{cl}} \tag{2.2}$$

where α_f and α_{cl} are fouled and cleaned overall heat transfer coefficients respectively; a typical *CF* value for a power condenser might be 90%. The most available source of fouling resistances is the approximately 100 values suggested by the Tubular Exchanger Manufacturers Association (TEMA), which has not been significantly updated since its first publication in 1947. Since the TEMA values are only for a very limited number of fluids (mainly water and hydrocarbon processing streams) and do not have any correction for the effects of operating parameters (flow velocity, concentration of impurities, surface temperature, etc.), selection of the appropriate fouling resistance is generally experience based.

Table 2.1 shows the excess heat transfer surface required for several heat exchanger types, if a typical TEMA fouling resistance of 0.18 m^2K/kW is used for each of the two heat exchanging fluids. The table demonstrates the significance of the selected fouling resistance on the sizing of heat exchangers [1]. The increase in required surface area is related to the fouling resistance by the equation:

$$\frac{A_f}{A_{cl}} = 1 + \alpha_{cl}.R_f \tag{2.3}$$

where A_f and A_{cl} are the heat transfer surface areas with and without fouling. Clearly, the excess surface area for cases with highest heat transfer coefficients is much larger than would realistically be expected. To account for unreliable design procedures and operational problems, heat exchangers are typically over-designed by 70-80%, from which 30-50% is attributed to fouling.

Application	Clean Overall Coefficient	Excess Area
gas/gas shell & tube heat exchanger	50 W/m^2K	1.8%
liquid/gas shell & tube heat exchanger	150 W/m^2K	5.4%
liquid/liquid shell & tube heat exchanger	1000 W/m^2K	36%
liquid/liquid plate & frame heat exchanger	3000 W/m^2K	108%
water-cooled shell & tube steam condenser	4500 W/m^2K	162%

Table 2.1: Excess surface area for various heat exchanger applications, R_f = 0.36 m^2K/kW. From [1]

2.2.2. MECHANISMS AND SEQUENTIAL EVENTS OF FOULING

Because of the variety of fouling problems many classifications have been suggested; however, it is useful to divide the mechanisms of fouling into five major categories, based on the key physical/chemical processes, namely [2]:

a. *Precipitation Fouling*: This type of fouling, referred to as scaling, is related to the deposition of a solid layer on the heat transfer surface from a solution containing dissolved inorganic salts. Every salt has a solubility limit at a given temperature. If this limit is exceeded, precipitation will occur. Supersaturation may be caused by the following factors;

    1) Evaporation of solvent.
    2) Cooling below solubility limit for solution with normal solubility, e.g. increasing solubility with increasing temperature.
    3) Heating above the solubility limit for solutions with inverse solubility such as calcium carbonate ($CaCO_3$) and calcium sulphate ($CaSO_4$) in water.
    4) Mixing of streams with different composition.

b. *Particulate Fouling*: Particulate fouling is the accumulation of particles from a fluid containing suspended solids. In some installations the deposition occurs due to gravity, and is hence referred to as sedimentation fouling. The suspended particles may be pollutants (clay, silt, etc.), upstream corrosion products (iron oxide), or products from chemical reactions occurring in the bulk fluid.

c. *Chemical Reaction Fouling*: In this type of fouling a chemical reaction occurs on the heat transfer surface and the solid product remains on the surface. Cracking and polymerisation of hydrocarbons are some examples. Corrosion fouling is a specific form of chemical reaction fouling.

d. *Biological Fouling*: The uncontrolled growth and multiplication of living organisms on heat exchanger surfaces results in biofilm or biofouling formation. These organisms can be either microorganisms such as bacteria or algae, or macroorganisms such as barnacles.

e. *Solidification (Freezing) Fouling*: This type of fouling occurs as a result of the solidification of a fluid or some of its higher melting components on a sub-cooled heat transfer surface. Ice formation during cooling of water and deposition of paraffin wax from hydrocarbons are two examples.

Generally, in industrial situations, several fouling mechanisms occur simultaneously and are nearly always mutually reinforcing. A universal sequence of fouling events which may play a role in all types of fouling has been proposed by Epstein [3]:

I. *Initiation period or delay period*: When the new or cleaned heat exchanger has been taken into operation, the initially high heat transfer coefficients may remain unchanged for a certain period of time. During this time, nuclei for crystallization are formed or nutrients for biological growth are deposited. This delay period may last any time from a few seconds to several days. For precipitation fouling and for chemical reaction fouling, the initiation period decreases with increasing surface temperature, as supersaturation and/or reaction rate increases.

II. *Mass transport of foulant*: To form a deposit at the heat transfer surface it is necessary that at least one key component is transported from the fluid bulk to the heat transfer surface. In most cases, this oocurs by diffusion.

III. *Formation of deposit*: After the foulant has been transported to the heat transfer surface it should stick to the surface (for particulate fouling) or react to the deposit forming substance (for precipitation fouling).

IV. *Removal of deposit or auto-retardation*: Depending on the strength of the deposit, erosion occurs immediately after the first deposit has been laid down. Furthermore, several mechanisms exists which cause auto-retardation of the deposition process. For the thermal boundary condition of constant temperature difference between heated and cooled fluid, the growth of deposit causes a reduction of the driving temperature difference between heat transfer surface and fluid.

V. *Aging of the deposit on the surface*: Every deposit is subjected to aging. Aging may increase the strength of the deposit by polymerization, re-crystallization, de-hydration etc. Biological deposits are poisoned by metal ions and may be washed away by the bulk flow. Aging is the least investigated and understood step and is usually ignored in modelling attempts.

2.2.3. FOULING REPRESENTATIONS AND MODELS

2.2.3.1. FOULING CURVES

A fouling curve shows the relationship between the fouling thermal resistance and time. The pioneering articles by Kern-Seaton [4] and by Taborek *et al.* [5] introduced "fouling model" equations in 1968 and 1972 respectively, basically defining the rate of fouling as a difference

between a deposition and a removal rate, where both processes occur simultaneously. Equation 2.4 gives the rudimentary form of the recognised model:

$$\frac{dR_f}{dt} = \frac{dM_d}{dt} - \frac{dM_r}{dt}, \tag{2.4}$$

here M_d and M_r are the mass fluxes (kg/m^2.s) of the foulant deposited and/or removed respectively. The presented equation creates several possible fouling curves, as shown in Figure 2.1 [2].

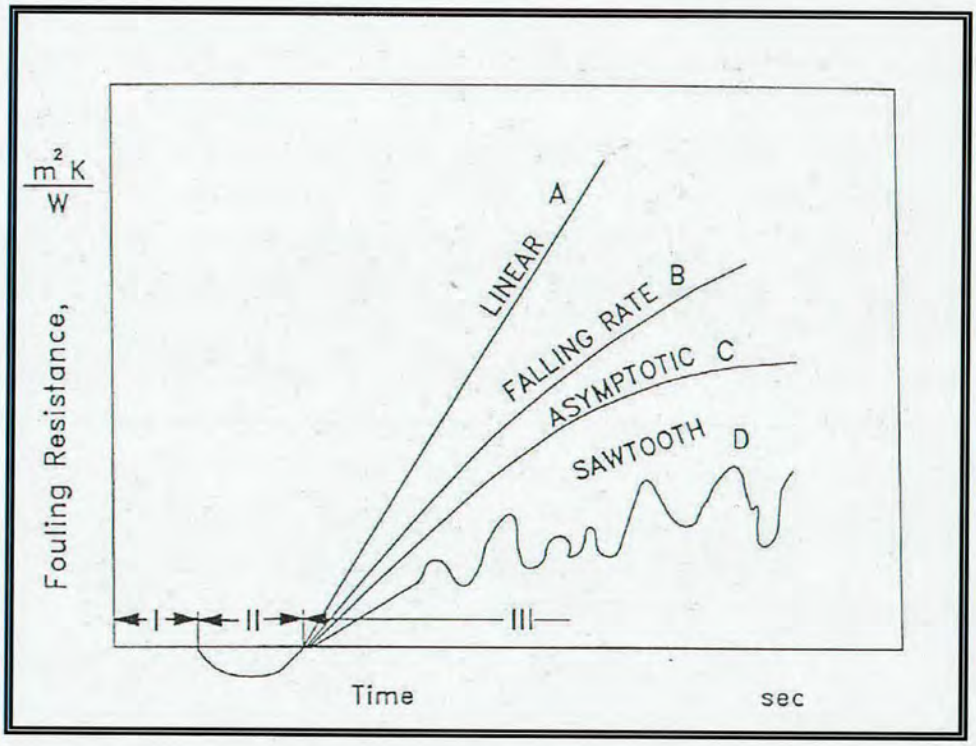

Figure 2.1: Typical fouling resistance versus time curves. Taken from Najibi [2].

The shape of each curve is indicative of the phenomena occurring during the fouling process:

A: Deposition is constant and there is no removal. Fouling is linear. Typical to pure salts deposits, which are hard and resistant to removal (e.g. $CaCO_3$).

B: A falling rate shows that the rate of solid deposition is slowing down with increasing thickness of the layer. Even with no removal, this type of fouling curve may be obtained due to the mechanism of retardation, which increases as the deposit builds up.

C: Asymptotic behaviour, typical for constant deposition rate, but removal rate increasing with deposition thickness due to increased shear forces and/or decreased resistance to removal (i.e. loosening of the upper fouling layers). This is the idealised fouling behaviour and the only value on the fouling-time curve which can be defined. In practise, however, disturbances usually cause a reversal to curve type B.

D: A saw-tooth curve brought about by periodic changes of conditions (such as temperature), and occurs when all or part of the deposit is suddenly removed. Subsequent growth of deposit results in a sawtooth pattern, occasionally observed with commercial cooling tower water.

While the fouling resistance-time curve may be of great importance to the designer, one must be careful in interpreting the curves to determine the mechanisms that occur. The fouling curve is the result of a combination of deposition and removal, which are very complex and often interrelated processes.

As shown in Figure 2.1, the curves of fouling resistances versus time can be divided into three different phases. Phase I: induction; Phase II: transition; Phase III: fouling. It must be remembered that Phases I and/or II need not necessarily occur. Occasionally, particularly with new surfaces, a delay time is observed before deposition occurs (Phase I in Figure 2.1). As detailed in subsection 2.2.2, during this time nuclei are forming on the surface and their population is expanding with time. In the transition period (Phase II in Figure 2.1) the curve shows negative values for the fouling resistance. This implies an enhancement of heat transfer which is frequently observed due to increased roughness of the surface, or, for the case of boiling heat transfer, as a result of increased number of active bubble nucleation sites attributed to the presence of the deposit. In due course, we shall return to the subject of scale formation during boiling heat transfer.

2.2.3.2. FOULING MODELS

As mentioned, the first real attempt to derive a general fouling model was provided by Kern and Seaton [4] who noted that experimentally observed fouling curves followed a pattern in which after an initial period of fast fouling build-up, the fouling resistance tended to remain constant. This behaviour could be described by the correlation given in equation 2.4. To date, a number of models have appeared in the literature for the characterisation of the different types of fouling under non-boiling heat transfer; the fundamentals of most of these proposed correlations are predicated upon Kern and Seaton's basic model, a concept which is still adopted today [2]. However, because of the difficulty involved in reproducible measurements of the fouling resistances and the complex nature of the deposit formation, accurate modelling is still not

possible. Most of the models that have been proposed are highly simplified, as they are founded on the following assumptions:

- Only one type of fouling is usually considered
- The fouling layer is assumed to be homogenous
- The deposit surface roughness is neglected
- Changes in physical properties of the streams are omitted
- The initial condition of the surface is not considered

Furthermore, models published so far only consider some of the variables such as velocity, time, concentration, and temperature, whereas other parameters, which are very difficult to evaluate, are often neglected. These include:

- Effect of simultaneous action of different fouling mechanisms
- Nature and condition of surface
- Properties of foulant stream
- Design of the equipment
- Fluctuations in operation
- Aging

For a comprehensive review on some of the more important fouling models, the reader is referred to Najibi [2]

2.2.4. Influence of Operating Conditions on Industrial Fouling

As mentioned, a prodigious number of correlations have been recommended for the prediction of individual fouling mechanisms under conditions of forced convective or non-boiling heat transfer. However, these correlations are generally not applicable to industrial conditions where a combination of fouling mechanisms and foulants occur. Comparing fouling data from a range of industries, the following approximate influence of process parameters on industrial fouling has been suggested by Müller-Steinhagen [1]:

a. Fouling usually increases linearly with increasing foulant concentration in the fluid bulk.

b. The fouling resistance nearly always decreases with increasing wall shear stress due to increased removal forces. As an average, it has been established that the fouling resistance is proportional to the flow velocity to the power of (-)1.5.

c. For almost all fouling mechanisms, the fouling resistance (i.e. the additional thermal resistance brought about by scale formation) increases exponentially with increasing surface temperature according to an Arrhenius term given as:

$$\frac{dR_f}{dt} = Ce^{-E/RT_w} \tag{2.5}$$

d. Fouling was found to increase with increasing surface roughness of the heat transfer surface

2.2.5. Cost Due to Heat Exchanger Fouling

Despite the enormous cost associated with heat exchanger fouling, only very limited research has been done to determine accurately the economic penalties due to fouling and to attribute these costs to the various aspects of heat exchanger design and operation. However, reliable knowledge of fouling economics is desirable to evaluate the cost effectiveness of various mitigation strategies. The total fouling related costs consist of [2]:

I. *Capital Expenditure:* This includes excess surface area, costs for stronger foundations, provisions for extra space, increased transport and installation costs. There are also additional capital costs for antifouling equipment, such as the installation of on-line cleaning devices, pre-treatment plants and cleaning in-place equipment

II. *Fuel Costs:* Costs for extra fuel occur if fouling leads to extra fuel burning in furnaces or boilers, or if more secondary energy such as electricity, or process steam, is necessary to overcome the effects of fouling.

III. *Maintenance Costs:* Maintenance costs are costs for removing fouling deposits and costs for chemicals or other operating costs for antifouling devices

IV. *Costs Due to Production Loss:* Because of planned and unplanned plant shut-downs due to fouling in heat exchangers, large production losses are possible. These costs are often considered to be the main cost of fouling and are extremely difficult to estimate.

Garrett-Price [7] and Pritchard [8] found that the total fouling costs for highly industrialised countries such as the U.S. and U.K. are about 0.25% of the countries' Gross National Product (GNP). The fouling related costs for New Zealand, which is less industrialised, are 0.15% of the New Zealand GNP. Using these percentages, Table 2.2 lists total fouling related costs for various countries, based on 1992 US$.

Country	Fouling Costs ($ million)	1992 GNP ($ billion)	Fouling Costs/GNP (%)
UK	2500	1000	0.25
US	14,175	5670	0.25
New Zealand	64.5	43	0.15
Australia	463	309	0.15
Germany	4875	1950	0.25
Japan	10,000	4000	0.25
Total industrialised world	45,020	22,510	0.20

Table 2.2: Total fouling costs for several countries. Adopted from Müller-Steinhagen [9]

2.3. BOILING HEAT TRANSFER

Boiling may occur when a surface in contact with a liquid is maintained at a temperature above the saturation temperature of the liquid. In boiling heat transfer the temperature difference between the surface temperature, T_w, and the saturation temperature corresponding to the liquid pressure, T_{sat}, acts as the driving potential for the heat flow from the surface to the liquid [10]. The process is characterised by the formation of vapour bubbles, which subsequently detach from the surface. Vapour bubble growth and dynamics depend, in a complicated manner, on the wall superheat (i.e. $T_w - T_{sat}$), the nature of the surface, and the thermophysical properties of the fluid, such as its surface tension. In turn, the dynamics of vapour bubble formation affects fluid motion near the surface and therefore strongly influences the heat transfer coefficient [11]. Although higher heat transfer coefficients are usually expected from boiling heat transfer, in reality this depends on ensuring that the heat transfer process is predominately that of nucleation, i.e. the formation of vapour bubbles at sites on the heat transfer surface. However, for nucleation to occur the temperature driving force must exceed a certain value; otherwise, the dominant process will be convective boiling heat transfer, where vapour bubbles are produced at the liquid/vapour interface. Heat transfer coefficients associated with convective boiling are generally considerably lower than those connected with nucleate boiling.

There are two basic types of boiling conditions or modes, namely, *Pool* and *Flow Boiling*:

I. *Pool Boiling:* This mode of boiling occurs on a heated surface submerged in a quiescent or non-agitated liquid pool.

II. *Flow Boiling:* In contrast, flow boiling occurs in a flowing stream, and the boiling surface may itself be a portion of the flow passage. The flow of liquid and vapour associated with flow boiling is an important type of two-phase flow, and, moreover, is the boiling mode of interest relevant to this particular investigation.

Boiling may also be classified according to whether it is *sub-cooled* or *saturated.* In sub-cooled boiling the temperature of the liquid is below the saturation temperature and bubbles formed at the surface may condense in the liquid. Conversely, the temperature of the liquid slightly exceeds the liquid saturation temperature in saturated boiling. Bubbles formed at the surface are then propelled through the liquid by buoyancy forces, eventually escaping from a free surface.
For the purpose of this study, all experimental investigations have been conducted under sub-cooled boiling conditions.

2.3.1. Fundamental Mechanisms and Observations in Flow Boiling

When a sub-cooled liquid flows past a heated solid surface, a rapid increase in the heat transfer rate at the solid surface is observed once boiling commences. Mosiki and Broder [12] were probably the first investigators of sub-cooled boiling; in 1926 the researchers studied heat transfer from an electrically heated vertical platinum wire submerged in water at atmospheric pressure. They found that the wire temperature at the highest obtainable heat flux was essentially independent of the water temperature. Local heat transfer coefficients were considerably greater than the values predicted for non-boiling conditions. This was also found by both McAdams *et al.* [13], and Davidson *et al.* [14]. Both investigators suggested the occurrence of sub-cooled boiling to explain the discrepancy. By 1951 Gunther [15], in an early attempt to establish the mechanism of heat transfer during sub-cooled flow boiling related to the cooling of rocket nozzle throats, showed that heat transfer coefficients of an order of 10^2 kW/m^{2}K were attainable in sub-cooled flow boiling of water in small diameter tubes at high velocities. These values are two orders of magnitude greater than those measured in ordinary convective heat transfer. He showed that the surface boiling activity in the sub-cooled flow boiling experiments consisted of small hemispherical vapour bubbles, which grew and collapsed while always remaining attached to the heating surface.

Thus far, two major mechanisms have been promulgated in an attempt at describing the sub-cooled boiling phenomenon [2]. The first mechanism is based on the additional turbulent mixing, or micro-convection, which is achieved near the surface due to the growing and collapsing bubbles. The second mechanism focuses on latent heat transport through the bubble: When a vapour bubble grows on a solid surface, a thin layer, called a microlayer, must be formed beneath

the bubble in order to satisfy the no-slip boundary condition at the solid surface. The top of the bubble quickly grows beyond the thermal boundary layer into the cooler bulk liquid. Latent heat is transported through the bubble, with the microlayer evaporating whilst condensation occurs simultaneously at the colder bubble cap. Figure 2.2, taken from [16], shows diagrammatically the various conditions encountered over the tube length when a uniform heat flux is applied to a tube charged with a sub-cooled liquid.

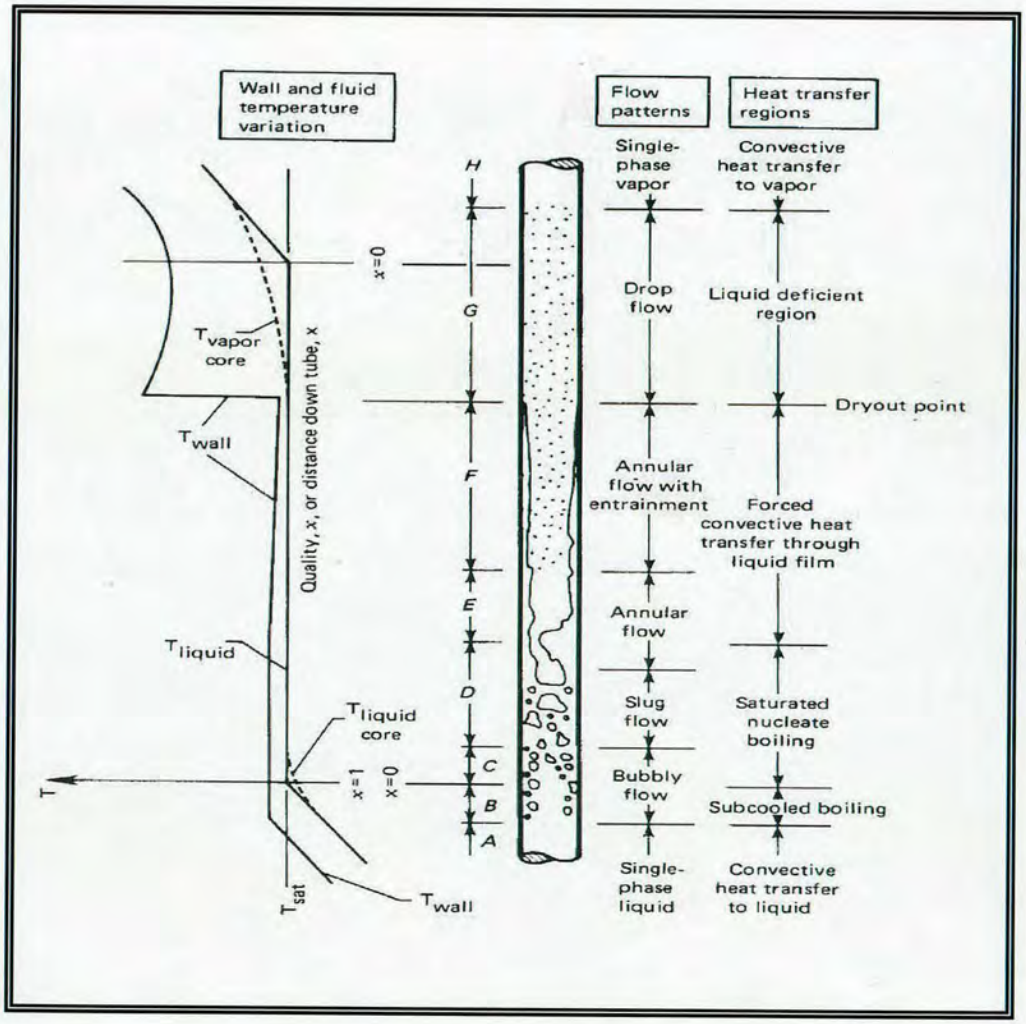

Figure 2.2: The development of two-phase (v-l) flow in a vertical tube with a uniform wall heat flux. Taken from [16].

In region A the heating surface temperature is below the temperature necessary to nucleate bubbles. This region is known as the "*single phase forced convection region*". At some point along the tube, the conditions within the vicinity of the wall allow the formation of vapour

bubbles from nucleation sites. Since the bulk fluid is still sub-cooled the vapour bubbles grow into the colder liquid and finally collapse. This region is known as "*sub-cooled nucleate boiling*" (region B). The sub-cooled nucleate boiling region comprises of two sub-regions. In the early stages of the sub-cooled region a limited number of nucleation sites are active, so a proportion of the heat will still continue to be transferred by the single phase forced convective mechanism. This region is commonly referred to as the "*partial sub-cooled boiling region*". As the surface temperature increases, the number of nucleation sites also increases, and as a consequence, the area for single phase forced convection is further reduced. Finally, when the whole surface is covered with nucleation sites "*fully developed sub-cooled boiling*" occurs. Beyond region B the bulk processing temperature gradually approaches the saturation temperature of the liquid. This denotes the start of "*saturated nucleate boiling*" (regions C and D on diagram) where vapour bubbles generated from the heater surface remain stable within the bulk liquid flow (at this point it is worth noting that even if the bulk liquid is at saturation temperature, a certain wall superheat is still necessary for the production of vapour bubbles). In the subsequent annular flow regimes (E and F on diagram) the heat transfer mechanism changes substantially; here nucleation is increasingly suppressed, and vaporisation takes place mainly at the free surface of the liquid film on the tube wall.

From extensive data sources in both vertical tubes and submerged test sections, the two fundamental characteristics of flow boiling can be noted as follows:

a. For heat fluxes below the onset of nucleate flow boiling, only the forced convective mechanism is present and the heat transfer coefficient is largely independent of heat flux over a wide range of flow velocities.

b. In fully developed nucleate boiling, the flow boiling heat transfer coefficient is virtually independent of flow velocity.

These characteristics are demonstrated in Figure 2.3, taken from Najibi [2], where flow boiling heat transfer coefficients for a NaCl solution are shown as a function of heat flux, q'', with velocity as a parameter. Note that at low heat fluxes the lines for different velocities are almost horizontal (i.e. independent of q'') but at higher q'' they converge into a single line, representing developed nucleate boiling. The onset of nucleate flow boiling is at the point where the straight lines begin to curve. Numerous other references support these observations, which have been noted inside vertical tubes, as well as outside tubes and plates [17,18]. The mechanism of the transition between the two boiling regimes can be abrupt or more gradual, but it is not yet well

understood; flow velocity, dissolved gases, and especially the distribution of nucleation cavity sizes play a significant role [2].

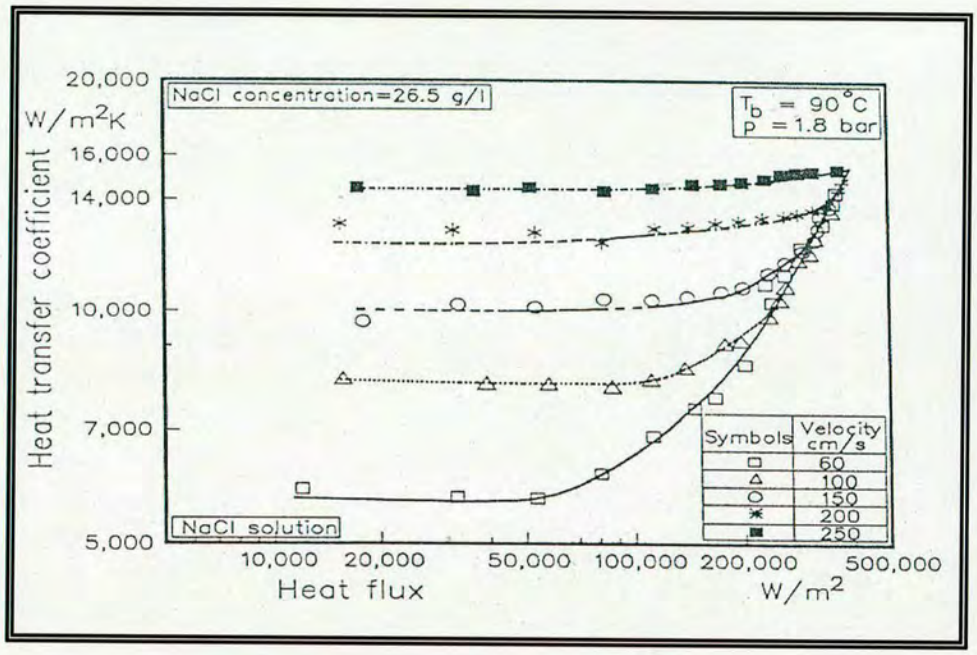

Figure 2.3: Heat transfer coefficient for NaCl solution as a function of heat flux at various flow velocities. Taken from Najibi [2].

2.3.2. Prediction of Two-Phase (v-l) Flow Boiling Heat Transfer

It was recognised in the early stages of boiling research that the heat transfer coefficient in two-phase flow boiling is a complex interaction of nucleate and convective boiling. Building a model to capture these complicated and competing trends has presented a challenge to researchers for several decades. In 1943 Davidson [14] introduced a dimensionless ratio called the boiling number,

$$Bo = \frac{q''}{\dot{m}\Delta h_v} \tag{2.6}$$

in an early attempt to relate the effects of heat flux and flow velocity in the flow boiling process; this was later utilised in numerous correlations and may be interpreted as a measure of the nucleate boiling contribution. As heat flux, q'', increases, nucleation is increased and so

is the nucleate heat transfer coefficient α_{nb}; meanwhile, increased mass velocity, $\dot{m}$, results in higher convective coefficient α_{cb}, lower wall temperature, and hence decreased activation of nucleation cavities.

The first true correlational model for predicting (vapour-liquid) two-phase flow boiling coefficient was proposed by Rohsenow [19] in 1952 as a simple addition of the nucleate and convective components:

$$\alpha_{FB} = \alpha_{nb} + \alpha_{cb} \tag{2.7}$$

This model was used in principle by Chen [20], who in 1963 formulated the first coherent and popular flow boiling method. However, Chen found it necessary to introduce a nucleate boiling "suppression" factor to the term α_{nb}, in order to account for the diminished contribution of nucleate boiling as convective boiling effects, α_{cb}, increased with higher flow velocity. In 1963 and 1965 Kutateladze proposed a "power-type" addition model for the two boiling components, which is presented below in generalised form

$$\alpha_{F.B} = \left[(\alpha_{nb})^2 + (\alpha_{cb})^2 \right]^{1/2} \tag{2.8}$$

This model is best termed asymptotic, as the value of the two-phase heat transfer coefficient, $\alpha_{F.B}$, approaches the larger of the two components. This assures a smooth transition as the mechanism of boiling changes from convective to nucleate dominated with the increase of heat flux, as observed in numerous experiments. The theory of the "power additive" correlational principle was formalised by Churchill [21], and was used successfully to represent transition between the two regimes, each dominated by different limiting phenomena, such as forced and natural convection and similar phenomena.

A different approach to flow boiling was proposed by Shah [22], where the nucleate boiling component is represented by the boiling number, see equation 2.6 , while a "convective number" *Co* (really a two-phase multiplier, a function of the vapour quality x and the ratio of liquid and vapour densities), is used for the convective boiling component. For selection between the two components, the method uses a graphical chart, later curve fitted [23] as the "greater of the two", a procedure originally proposed by Chawla in 1967 [24]. The method is easy to use because nucleate boiling is represented by the Boiling number alone, rather than appropriate correlations. However, this restricts the range of applicability and accuracy, especially for pressure effects.

Neither the Chen nor the Shah model presents a satisfactory solution, as attested by the numerous methods published since then, mostly variations on either the original Chen "additive with suppression factor" method or Shah's method with $f(Bo, Co)$. Representative of these second-generation correlations are the methods of Winterton *et al.* [25,26] and Kandlikar [27,28], all developed between 1983 and 1988. Accepting the form of the base models, a variety of correction factors were introduced, relying heavily on regression analysis rather than on functional modelling. While prediction accuracy by these methods can be fairly good for the data tested, confidence for extrapolation to other conditions and fluids is limited to the model structure itself. These methods are critically reviewed in Steiner and Taborek [29].

Based on Kutateladze's work, Steiner *et al.* [29] introduced a new two-phase flow boiling asymptotic model with appropriately adjusted nucleate and convective boiling coefficients, and defined it as shown in equation 2.9. Their main emphasis was placed on developing a sound mechanistic model, which would respect all the established principles of pool and convective boiling; clearly predictable behaviour and accurate convergence to the extreme values of all parameters was another objective. A large data bank of about 20,000 data points (all tube orientations) was assembled at the University of Karlsruhe, from which about 13,000 data points (tube-side vertical flow only), were used for development of their method.

In this rather simple mechanistic model the two boiling components are independent of each other; hence the selection of methods for the nucleate and convective components is independent of the base model itself. This is an extremely attractive property, as it readily facilitates the development, improvement, or in our particular case the 'extension' of the boiling heat transfer model (we elaborate on this subject in *Chapter 7* following).

$$\alpha_{FB} = \left[\left(\alpha_{nb}\right)^{t_R} + \left(\alpha_{cb}\right)^{t_R} \right]^{1/t_R}$$

$$\alpha_{FB} = \left[\left(\alpha_{npb,o} F_{nbf}\right)^{t_R} + \left(\alpha_{LO} F_{fb}\right)^{t_R} \right]^{1/t_R} \qquad (2.9)$$

Briefly, $\alpha_{npb,o}$ is the nucleate pool boiling coefficient, based on normalised conditions (subscript "o") of heat flux and reduced pressure. F_{nbf} is a correction factor to $\alpha_{npb,o}$, which compensates for differences between pool and flow conditions. α_{LO} is the convective heat transfer coefficient, based on the total (liquid plus vapour) mass velocity assumed as liquid only (LO). F_{fb}, is the two-phase flow multiplier to the convective α_{LO} value, accounting for enhancement of the coefficient

in the liquid-vapour mixture. Finally, t_R is an exponent that dictates the range of transition between the nucleate and convective components.

The model successfully predicts the heat transfer coefficients of vapour-liquid vertical flow boiling, demonstrating results superior to previous correlations. Central to the model's range of applicability and accuracy is its adherence to the fundamental characteristics or principles of flow boiling heat transfer:

- At heat fluxes below the onset of nucleate flow boiling, only convective boiling, α_{cb}, is a significant component, becoming rapidly more dominant with increasing flow velocity. The two-phase flow boiling coefficient, $\alpha_{F.B}$, is largely independent of heat flux over a wide range of mass velocities and other parameters. Thus, for low heat fluxes (i.e. $q'' \leq q''_{OFB}$), the nucleate boiling term in equation 2.8 is zero and the equation remains valid for convective boiling only (i.e. at $q'' \leq q''_{OFB}$, $\alpha_{F.B} \approx \alpha_{cb}$)

- Once the conditions for the onset of nucleate flow boiling have been satisfied (i.e. at $q'' = q''_{OFB}$), then the nucleate and convective boiling coefficients are superimposed, by a complex mechanism, according to their relative magnitudes. In the fully developed nucleate boiling region (where $q'' \geq q''_{OFB}$), the nucleate boiling coefficient, α_{nb}, attains pre-eminence, increasing as nucleation is increased for progressively higher wall superheats and/or heat fluxes. Conversely, in this region the flow boiling coefficient, $\alpha_{F.B}$, (calculated by the asymptotic addition of the nucleate and convective components) becomes virtually insensitive to the magnitude of imposed flow velocity.

2.4. SUMMARY

In summary, this background chapter aspired to furnish the reader with an important overview of the key subject areas pertinent to the current investigation. Hereafter, based on the *fouling* and *boiling heat transfer* background information so far described, the following literature review presents the most important publications regarding methods of fouling mitigation and heat transfer enhancement, with particular emphasis on the role of the self-cleaning fluidised bed heat exchanger within the current state of research.

3.1. FUNDAMENTAL FOULING PRECAUTIONS, TREATMENTS & CONTROLS

3.1.1. INTRODUCTION

Not all heat exchangers have serious problems with fouling; many of them operate satisfactorily for long periods of time without being cleaned. However, if fouling is anticipated, then it is important to bear in mind that heat exchanger scale formation can be effectively mitigated at the design stage of the heat exchanger. Regardless of the approach, the selection of appropriate values still relies more on engineering judgement from past experience than on the application of results from experimental and theoretical research. To design for reliable operation:

- Select a suitable heat exchanger type. If fouling will be significant, it may very well control the selection of the type of heat exchanger and its size. This is clearly demonstrated in Table 3.1, which recommends different re-boiler types depending on the severity of fouling [1].

- Avoid plant conditions which promote fouling. This includes operation at the appropriate velocities and temperatures.

- Attempt an optimum design which avoids hot spots, by-pass flow or dead zones. From Chenoweth [30], Figure 3.1 shows results from HTRI (Heat Transfer Research Inc.) investigations, indicating the importance of avoiding zones with low flow velocity by the depiction of deposit formation in two shell and tube heat exchangers for identical heat duty. The smaller heat exchanger is designed with appropriate baffle spacing and baffle cut, and hence has higher heat transfer coefficients and less fouling.

Anticipated fouling	kettle/internal boiler	horizontal shell side thermosyphon	vertical tube side thermosyphon	forced flow
no fouling	good	good	good	expensive
moderate	risky	good	best	expensive
heavy	poor	risky	best	good
very heavy	poor	poor	risky	best

Table 3.1: Re-boiler selection guide. Taken from Müller-Steinhagen [1]

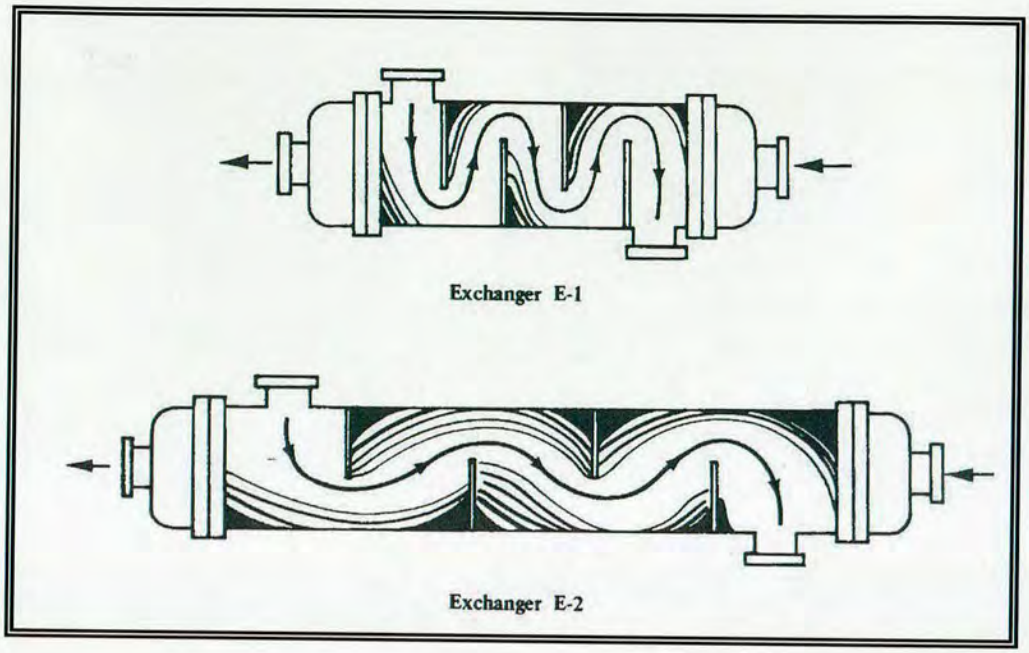

Figure 3.1: Sketch of heat exchanger geometry and observed deposit formation. Taken from Chenoweth [30].

However, even when all these factors are properly addressed, fouling may still occur, thereby making it necessary to seek mitigation, control and cleaning methodologies which allow for scale deposition to be maintained at acceptable levels.

To this regard, typical cleaning treatments are briefly examined in subsection 3.1.2 following; meanwhile, subsection 3.1.3 places emphasis on fundamental fouling mitigation and control strategies, which are essentially "on-line" processes, carried out either continuously or intermittently.

3.1.2. "OFF-LINE" CLEANING OF HEAT EXCHANGERS

Periodical cleaning of heat exchangers will be necessary, even if the heat exchanger is well designed and the fluid treatment is effective. Additionally, conditions may deviate from the design conditions due to changes in flow rates and temperatures, plant failures, ingress of air and bacteria, changes in the fluid composition or up-stream corrosion, which all may promote fouling. If a heat exchanger or pipe-line develops deposit formation, this can be start of a whole series of problems. It is, therefore, advantageous to remove non-protective deposits soon after the onset of their formation. Heat exchangers may be cleaned by chemical or mechanical methods, or by a combination of both.

3.1.2.1. CHEMICAL CLEANING METHODS

Chemical cleaning methods have a number of advantages over mechanical methods, namely:

a. They are relatively quick; typically a chemical clean would take one day, whereas a mechanical clean might extend up to three days, principally because most mechanical methods require the unit to be isolated and removed for cleaning.

b. Surfaces do not experience mechanical damage

c. Chemical solutions reach normally inaccessible areas

d. They are less labour intensive than mechanical cleaning

e. Cleaning may be performed in situ

Some of the many possible choices available for cleaning procedures are: ambient temperature treatments, high temperature treatments, fill-and-soak techniques, circulating techniques, on-stream techniques, vapour phase techniques, foam techniques and emulsion techniques. Soaking treatments are effective in many instances. Their application generally reduces equipment costs while increasing chemical costs and downtime costs. Obviously, it is advantageous to circulate the cleaning agent in order to improve the even mixing of the chemicals and to reduce concentration gradients near the fouled surfaces. Circulation also increases physical disintegration of the deposit by mechanical scouring. As chemical reaction rates increase exponentially with temperature, the cleaning process may be more efficient if the cleaning agent is heated. Foaming reduces the cleaning agent requirements and increases the effectiveness of cleaning. Also, the foaming treatment may be faster in some cases, and it allows for good contact in large shell and tube heat exchangers.

Sulphuric acid and hydrochloric acid are the most widely used chemical cleaning agents. When used properly, they are safe and relatively low cost materials. However, these mineral acids are highly ionized and strong, which may cause rapid corrosion if the solution is insufficiently inhibited. Therefore, weaker organic acids and chelating agents are coming into wider use. Table 3.2 lists a number of chemicals used for cleaning. Generally, a mixture of several chemicals is used to attack complex deposits. The type of cleaning agent to be chosen has a major effect on the economics of the cleaning job. The selection of cleaning chemicals is not only dependent on the type of deposit, but also on the exchanger material and the cleaning conditions. As many cases of chemical cleaning of heat exchangers involves the use of acids, personal danger (i.e. burns and toxicity) as well as environmental issues, such as waste disposal, have to also be considered. Acids and alkalis must be neutralized, organic materials may be burned and fluorides must be reacted to inactive solid residues. Some of the organic acids such as citric acid and gluconic acid are biodegradable.

Acids	Alkalis	Complexing Agents
Hydrochloric Nitric Sulphuric Hydrofluoric Citric Formic Sulphamic	Caustic Soda Ammonia Trisodium phosphate Sodium metasilicate Soda ash	EDTA Gluconates
Oxidants	**Solvents**	**Others**
Potassium permangangate Sodium Bromate Sodium nitrite Sodium hypochlorite Ammonium persulphate	Aromatic Aliphatic Chlorinated Emulsifiers Dewatering formulations	Biocides Surfactants Inhibitors Antifoams Dispersants Hydrazine bifluoride

Table 3.2: Common types of Chemicals utilized for in-situ chemical cleaning. From [31]

3.1.2.2. MECHANICAL CLEANING METHODS

For virtually all mechanical cleaning methods, the heat exchanger has to be taken off-line and dismantled. Some of the deposits may then be removed manually. Steam-blasting and hydro-blasting (up to 600 bar) are probably the most common mechanical cleaning methods. Hydro-blasting is used in cases where chemical cleaning is unsatisfactory. The advantage of hydro-blasting is that the equipment can be easily inspected after the cleaning operation is completed to verify that the deposits have indeed been removed. The main disadvantage of both steam and hydro-blasting is the time, cost, and labour intensiveness of pulling and reinstalling the exchanger bundles. For hydro-blasting, high pressure water is often effective. If deposits are very tenacious, sand can be added to the pressurized water to increase the cleaning efficiency [7]. Another popular mechanical cleaning method is brush cleaning. As with steam and hydro-blasting, simple brush cleaning of heat exchanger surfaces is effective in many cases but has to be done off-line. Studies of brush cleaning are reported by Lewis [32] and by Sasscer [33].

While blasting (or brushing for soft deposits) is the only available alternative for the shell side of the tube bundle, several cleaning methods can be used for the inside of straight tubes including the use of rubber plugs or metal scrapers shot through the tubes. Rubber plugs fail for hard deposits but shooting metal scrapers through the tubes at a water pressure of 35 bar and a scraper velocity of 3 m/s to 6 m/s results in the removal of most deposits. Biofilms in pipelines can be removed by a process known as "pigging" [34]. The pig, a hard sponge bullet or ball fitted to the diameter of the pipe, is placed inside the pipe and propelled through the system in the direction of flow. Due to the high water pressure building up behind it, it rotates whilst moving, scrubbing off the attached material on its way. Pigging requires launching of the pig into the pipe and its retrieval at the end of the pipe; a number of systems

are available to achieve this. A major disadvantage of pigging is that the pig can sometimes jam in the pipe. Nevertheless, pigging systems are widely used in seawater cooling facilities.

3.1.3. "ON-LINE" FOULING MITIGATION AND CONTROL METHODS

Since about 1920, a number of companies have specialised in the mitigation of fouling and corrosion, mainly for the flow of cooling water and hydrocarbons. These companies have gained considerable expertise and have developed a wide range of strategies and equipment [1]. In what follows a small selection of methods to reduce fouling by "on-line" chemical, mechanical, and alternative means are discussed.

3.1.3.1. CHEMICAL MITIGATION STRATEGIES

The most obvious method of mitigating fouling is to reduce the foulant concentration in the fluid bulk. Scaling species may be removed by ion exchange and by chemical treatment. The solubility of scale-forming constituents increases with decreasing pH. Therefore many treatment programs involve the addition of acid (usually H_2SO_4) to the system to maintain a pH in the region of 6.5 to 7.5. Scale inhibitors (for example polyphosphates) inhibit the growth and nucleation of crystals or reduce the driving concentration difference between fluid bulk and fluid/solid interface. Particulate fouling is usually mitigated by the addition of surfactants or dispersants. If the surface tension is reduced, large particle agglomerates can break down into smaller particles, which tend to less sedimentation. Dispersants impart like charges to both the heat transfer surface and the particles and reduce deposition.

For oil refining processes a number of chemical additives to reduce reaction fouling have been developed. Most antifoulants have several functions. Generally they are oxygen scavengers, metal deactivators and dispersants [35]. For autoxidation induced fouling, anti-oxidants can be added to consume oxygen or react with oxidation products in a way as to prevent the chain reaction of the autoxidation process, or metal-deactivators are added to chelate metal ions thereby preventing their catalytic effect on the autoxidation process. Dispersants can be added to minimise either the agglomeration of small insoluble polymeric/coke-like particles into larger particles/deposit, or the sticking of particles to the tube wall.

Biological growth is usually controlled by addition of biocides. In recent years, chlorine has most widely been used, which reacts with water to hydrochloric and hypochlorous acid:

$$Cl_2 + H_2O \rightarrow HCl + HOCl \tag{3.1}$$

Hypochlorous acid is an extremely powerful oxidant that easily diffuses through the cellular walls of micro-organisms. Birchall [36], Miller & Bott [37], and Novak [38], assume that

HOCl oxidises the active sites of certain enzyme sulfhydryl groups, which constitute intermediate steps in the production of adenosine triphosphate (ATP). The system ATP-ADP allows conversion of carbohydrates and hence the energy supply for living things.

3.1.3.2. MECHANICAL MITIGATION STRATEGIES

For most liquid-side applications, it is difficult to design mechanical on-line fouling mitigation methods. Nevertheless, a number of mitigation techniques have been developed for the tube-side liquid. Some of these techniques are considered below. Generally, all existing methods are based on one of the following mechanisms:

a. Short-time overheating of the heat transfer surfaces. The different thermal expansions of tubes and tube deposits may cause cracking of the deposit.

b. Mechanical vibration of heat transfer surfaces.

c. Acoustical vibration of heat transfer surfaces.

d. Increased shear stress at fluid deposit interface.

e. Reduced adhesion of deposits

Regular reversal of the flow direction in conjunction with a short-time increase of the flow velocity is sometimes used as a method to mitigate the formation of weak deposits. Deposits with moderate stickability to the heat transfer surfaces (e.g. particulate and some biological deposits) can be dislocated and washed out by increasing the fluid shear forces for a short time, in regular time intervals. If enough pump capacity is available, this can be achieved by increasing the flow velocity. However, more effective is to introduce compressed air or nitrogen into the liquid system thus increasing the turbulence level; this is known as gas rumbling. The resulting highly turbulent gas-liquid two-phase flow can provide shear forces and pressure fluctuations, which are substantially higher than for single-phase flow [1]. In both instances (i.e. reversal of flow direction and gas rumbling) additional pressure drop is the pay-off for the reduction of fouling and for the increase in heat transfer coefficient.

A number of companies (Water Services of America, KALVO [39]) have developed a continuous tube cleaning system using small nylon brushes which are inserted into each tube, see Figure 3.2. These brushes are pushed through the tubes by the fluid flow. For continuous operation and optimum cleaning efficiency, the flow direction has to be reversed about every 8 hours. Life expectancy of the brushes is about 5 years. Typical applications for the nylon brush system are cooling water duties in condensers or chillers. Although there are many examples of the successful application of the brush tube cleaning system, nevertheless, a comparison of the performance of 52 power stations in Germany, equipped with continuous

tube cleaning systems, shows that the brush cleaning system may fail for very tenacious deposits [1].

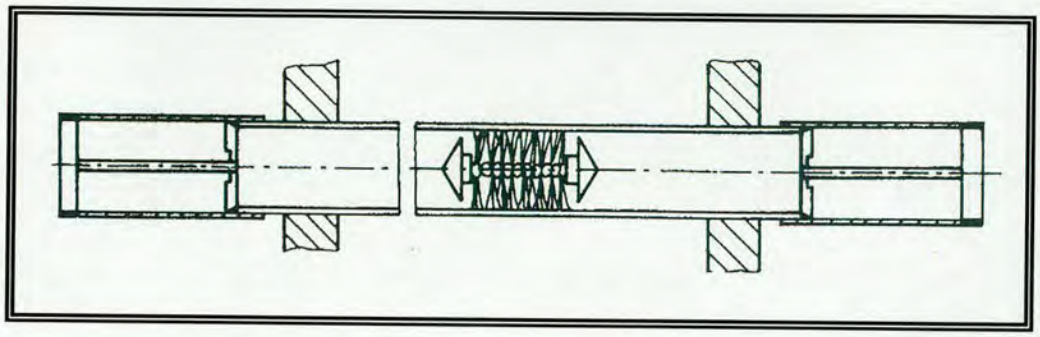

Figure 3.2: Continuous cleaning with a KALVO wire brush system. Taken from Müller-Steinhagen [1].

3.1.3.3. OTHER MITIGATION STRATEGIES

When it comes to commercial mitigation of scale formation, one of the most frequently and emotionally discussed topics are devices which claim to reduce scaling by magnetic, electronic or catalytic means. Such devices have been on the market for several decades, demonstrating limited success. For example, on the laboratory scale some success has been achieved in removing or inhibiting deposits by ultrasonic vibrations. However, to-date, no conclusive scientific proof or theory for the mechanisms which may be responsible for the beneficial effects of such technologies has been identified, thus preventing the extrapolation of these results into industrial practise.

According to Troup and Richardson [40], extensive experimental and field work is required to evaluate the efficiency of all such magnetic, electrical and ultrasonic devices. Until this is done and any limitations which these apparatus may have are clearly established, no generalised statement can be made about their economic evaluation with respect to other available scale prevention methods.

3.2. FOULING MITIGATION & THE ROLE OF HEAT TRANSFER ENHANCEMENT

3.2.1. INTRODUCTION

As previously stated in *Chapter 2*, the fouling of heat exchangers is a much researched subject and many attempts have been made to minimise its impact on processing plants. However, as evidenced by some of the fundamental fouling precaution, treatment and control methods outlined in the preceding section 3.1, the phenomenon is resistant to attempts to arrive at a generalised solution. Indeed, it could be said that energy or production losses due to fouling

may become more widespread, as increased confidence in the prediction of heat transfer coefficients leads to reductions in design margins, giving rise to the occurrence of fouling having a potentially greater practical impact on the ability of the heat exchanger to perform the required duty [1].

From the information available in the literature, it has been clearly established that many fouling mechanisms are strongly affected by local heat transfer conditions. The increase in fouling with increasing heat transfer surface temperature depends on an Arrhenius term given in equation 2.5, and is caused by increased reaction rates, increased stickability or increased biological growth [41]. Therefore, a logical conclusion to be drawn from such an observation is that decreasing heat transfer surface temperature can result in a dramatic reduction of fouling. Hence, greater understanding of heat transfer processes, and the ability to make them more efficient through the use of heat transfer enhancement, gives rise to the possibility of reducing the incidence and impact of fouling. If these heat transfer conditions can be accurately predicted and manipulated, the tendency to foul can be controlled in a systematic manner [1].

In process heat exchangers, a finite difference between the bulk fluid temperature and the heat transfer surface temperature must exist, or no heat transfer will take place. Equation 3.2 depicts the basic heat exchanger design equation:

$$q = \alpha.A.\Delta T \tag{3.2}$$

here q is the heat duty or power, α is the overall heat transfer coefficient, A is the available heat transfer surface area, and ΔT is the overall temperature driving force. ΔT can be expressed as:

$$\Delta T = T_{\mathrm{w}} - T_{\mathrm{b}} \tag{3.3}$$

here T_{w} is the temperature found at the heat transfer surface, whilst T_{b} is the bulk processing temperature. Equation 3.2 illustrates the possibilities for the use of heat transfer enhancement to reduce overall temperature driving forces. Quite simply, any increase in the overall heat transfer coefficient, achieved via the use of heat transfer enhancement, allows a corresponding decrease in the required overall temperature driving force without the need to increase the size of the heat exchanger. At a local level this reduction in ΔT will affect the wall temperature through the relationship established in equation 3.3 [1].

A variety of heat transfer enhancement techniques are available and may be applied to new designs, or in some cases to existing equipment by retrofit. However, it is commonplace in discussions relating to the application of heat transfer enhancement techniques that concerns

about their performance under fouling conditions are raised. The wide variety of existing heat transfer enhancement techniques means that how one method behaves under fouling conditions is no indicator of how another might behave. The conventional wisdom is that heat transfer enhancement techniques experience a decline in performance when they are exposed to fouling conditions. Furthermore, it is felt that the devices used to enhance heat transfer promote fouling by, for example, trapping foulant on the heat transfer surface. In 1985, the author Bergles [42] developed a scheme to classify heat transfer enhancement techniques. The main headings of this classification are as follows,

- Roughened surfaces
- Extended surfaces
- Displaced enhancement devices
- Surface tension devices
- Surface or fluid vibration
- Additives
- Treated and Structured surfaces (for boiling conditions)
- Electric and electromagnetic fields
- Compound enhancement (to combine two or more of the above measures, such as the use of roughened surfaces combined with liquid additives)

From the fouling point of view, it is important to further distinguish between those techniques of heat transfer enhancement that *intensify* the heat transfer at a plain surface, and those that represent an *enlargement* of a plain surface, where the heat transfer area is usually increased by means of fins.

Heat Transfer Intensification

With respect to heat transfer intensification, it can be anticipated that the average surface temperature on an enhanced heat transfer surface, will be lower than on a plain surface exposed to the same operating conditions. The suppression of surface temperature can be expected to affect scale deposition processes that are dependent on this parameter. As previously stated, a reduction in the rate of these processes would mitigate the overall effects of fouling. From the list above, a few heat transfer enhancement techniques that function by intensifying the heat transfer relative to that at a comparable plain surface are: rough surfaces, displaced enhancement devices, surface tension devices, additives, vibration, electric and electromagnetic fields, and vibration [43]. The combination of rough surfaces and additives (i.e. compound enhancement) can be classified as heat transfer intensification.

Heat Transfer Area Enlargement

According to Somerscales and Bergles [43], to investigate the effect of an enlarged heat transfer area on fouling mitigation, it is appropriate to compare the heat transfer (expressed in terms of watts) from a fouled surface, q_f, with that from the same surface when it is clean, q_{cl}:

$$q_{cl} = \alpha \left[A_{TOTAL} - A_{fin}(1-\eta_{cl})\right](T_w - T_b) \tag{3.4}$$

$$q_f = \frac{\left[A_{TOTAL} - A_{fin}(1-\eta_f)\right]}{(1/\alpha)+R_f}(T_w - T_b) \tag{3.5}$$

A_{fin} is the fin heat transfer area, η is the fin efficiency and A_{TOTAL} represents the overall heat transfer surface area (i.e. finned + unfinned). If an enlarged heat transfer surface mitigates the effect of fouling, it is expected that the ratio q_{cl}/q_f would be less for an enlarged surface than for a plain surface carrying the same thickness of fouling deposit. Therefore the enlarged heat transfer surface mitigates fouling if:

$$\left.\frac{q_{cl}}{q_f}\right|_{ehd} < \left.\frac{q_{cl}}{q_f}\right|_{pln} \tag{3.6}$$

here the enhanced and plain surfaces are denoted by subscripts 'ehd' and 'pln' respectively. Extended surfaces appear to be the only method of heat transfer enhancement that makes use of heat transfer area enlargement to achieve its purpose.

3.2.2. Heat Transfer Enhancement And Antifouling Devices

It is important to note, that the possibility that the aforementioned heat transfer enhancement devices might also mitigate fouling, has only recently been realised among engineers concerned with heat transfer equipment. This recognition has come as a consequence of experimental studies, which have been undertaken in order to establish the fouling behaviour of such heat transfer enhancement devices. Even though the manufacture and application of many such heat transfer enhancement devices could involve substantial expenses over those incurred by the application of un-enhanced heat transfer equipment under similar conditions, as fouling plays an important part in the economics of operating heat transfer equipment, its occurrence must be included in the economic considerations of any program intending to develop design methods for enhanced heat transfer devices with minimum fouling. Furthermore, pragmatic constraints on our energy and material expenditure necessitate the development of methods that both enhance heat transfer and mitigate fouling. Somerscales and Bergles [43] excellent review demonstrates that, contrary to popular theory as stated

above, the application of certain types of heat transfer enhancement can result in less fouling than is experienced with un-enhanced heat transfer surfaces, under the same general conditions of heat exchange, fluid flow, and fluid composition. In concluding, the authors state that for non-boiling conditions, the following enhanced heat transfer devices may also be antifouling devices:

3.2.2.1. ROUGH SURFACES

A roughened heat transfer surface's ability to mitigate the effects of fouling depends particularly on category of fouling, type of roughness, and mean fluid velocity. In themselves, rough surfaces can range from random and grain-type roughness to discrete structures. In the latter case, machining and forging operations can be used to obtain protrusions or depressions in the surface. Protuberances also can be produced by inserts in a tube, such as wire coils that are maintained by their elasticity in close contact with the inner surface of the tube. Enhancement by rough surfaces is intended to promote fluid turbulence rather than increase the heat transfer area. They are used primarily on single-phase (liquid only) flow. From reports in the literature two types of in-tube heat transfer enhancements are commonly used in laboratory tests, namely, *corrugated* or *roped* type enhancement, and *rib roughness* type enhancement.

In the opinon of Somerscales and Bergles [43], from the conclusions of laboratory testing, it can generally be said that roped-type enhancement mitigates both precipitation and particulate fouling at all flow velocities; conversely, the rib-type roughness does not mitigate particulate fouling at low fluid velocities, though it is not affected by fouling at higher fluid velocities. In their referenced work, the researchers also comment on the important effects of fluid velocity as observed in the published literature. According to Somerscales and Bergles [43], higher fluid velocities are typically associated with lower R_f values; in fact, the authors report that at sufficiently high velocities, the fouling thermal resistance proves negligible for both plain and enhanced roughened heat transfer surfaces.

Field tests involving biofouling and corrosion fouling from seawater have been reported by Panchal [44] and by Panchal and Sasscer [45]. The authors' results strongly suggest that for the particular circumstances of their test, the enhanced roughened surface exhibits a superior fouling performance compared with the plain heat transfer surface, thus demonstrating an ability to mitigate fouling of the types encountered in freshwater rivers and ocean environments. Of course, tests involving a wide variety of natural waters would have to be conducted in order to corroborate such a conclusion.

For a comprehensive summary of the various laboratory and field tests conducted on the fouling performance of rough surfaces, the reader is referred to Somerscales and Bergles [43].

3.2.2.2. EXTENDED SURFACES

Increased rates of heat transfer can be attained by fins which provide additional heat transfer area. The fins can be specially shaped, or interrupted, so that the heat transfer coefficient at the surface can be increased.

Although theoretical analysis, admittedly under the unrealistic conditions of uniform fouling deposition, suggests that enhanced heat transfer surfaces employing fins have the intrinsic property of mitigating fouling, the experimental data is not so clear. Using an electrically heated test section, tests by Somerscales *et al.* [46] studied the effects of particulate fouling on tubes with inside fins. The results of the tests are inconclusive, but suggest that perhaps for certain geometries finned surfaces exposed to particulate fouling may mitigate the effects of fouling. However, available experimental data does suggest that finned surfaces mitigate fouling for both precipitation and chemical reaction fouling conditions.

3.2.2.3. DISPLACED ENHANCEMENT DEVICES

Bodies of various forms can be inserted into a fouling stream, so as to augment heat transfer by the increase of mixing between the fluid at the wall and the fluid in the free stream or bulk flow. Devices of this type enhance heat transfer by intensification. Discussed below are some test data supporting the above expectation.

Hi-Tran® radial mixing elements are patented inserts made from wire loops spaced radially and axially within a tube, and supported by a central core [47]. The dimensions of the insert are chosen such that the wire loops are in contact with the tube wall. Hi-Tran® elements are claimed to produce complete radial mixing of the fluid stream. This not only improves heat transfer by increasing the convective coefficient on the inner surface of the tube, but reduces the residence time of the fluid at the heat transfer surface. Gough and Rogers [48] provide data on the performance of these elements in tubes when handling a fluid described as "tar" in a steam heated shell-and-tube heat exchanger. According to Gough and Rogers, the use of inserts in the heat exchanger tubes successfully attenuates the effects of fouling.

3.2.2.4. ADDITIVES

Additives for liquids include solid particles and gas bubbles for single-phase flows, as well as liquid trace additives, example surfactants, for boiling systems. Additives for gases include liquid droplets or solid particles; either dilute phase (gas-solid suspensions) or dense phase (fluidised beds). The subject of 'additives in boiling systems' is revisited in proceeding subsection 3.4.3.2.

Meanwhile, under conditions of forced convective heat transfer, the 'Fluidised Bed Heat Exchanger' (FBHX) is an eminent paradigm of the additive technique, as utilised in the enhancement of heat transfer and prevention of scale deposition. Originally developed in the

1970's for sea water desalination service [49], the fluid bed heat exchanger consists of a number of parallel heat exchanger tubes in which small solid particles are kept in a fluidised condition by the liquid flowing through the tubes. The exchanger must be operated in the vertical position, in order for particles to be uniformly distributed in the section normal to the mean flow. According to Klaren [50], the fluid bed heat exchanger enhances heat transfer as a result of solid particles breaking through the boundary layer at the tube wall, causing higher heat transfer coefficients than would usually be the case for the employed liquid velocities. In fact, in the presence of fluidised inert particles, reports of heat transfer increases by up to a factor of eight are not uncommon within the literature [51]. The other notable advantage of the fluid bed exchanger is the removal of formed deposits, emanating from the continual contact of the particles with the walls of the heat exchanger tubes.

Hence, over the past 35 years, the self-cleaning liquid-solid fluidised bed heat exchanger (a device central to the undertakings of this present investigation) has been successfully developed, exhibiting buoyant performance in many severe fouling applications [49,52-56] across the globe. Further more, their potential in the utilisation of geothermal energy was tested between 1975 and 1980 [52] Presently, several generations of technological advancements have made the modern self-cleaning heat exchanger inimitable when employed in the enhancement of heat transfer and mitigation of scale formation for most severely fouling liquids [57-59]. Additionally, due to the excellent mixing of the bulk fluid, liquid-solid fluidised bed heat exchangers are today also used throughout the process industry for hydrometallurigal operations, catalytic cracking, crystallisation and sedimentation.

As a project keystone, a presentation outlining the course of development, as well as heat transfer and fouling mitigation characteristics, of the self-cleaning heat exchanger is certainly justified and subsequently presented in section 3.3 proceeding.

3.3. THE SELF-CLEANING FLUIDISED BED HEAT EXCHANGER

3.3.1. INTRODUCTION: DEVELOPMENT HISTORY

Self-cleaning heat exchange technology, applying a fluidised bed of cleaning particles in the tubes of a vertical shell and tube exchanger, has been studied in the USA [49,52,60], the Netherlands [53-55,57-59,61,70-82], and the Federal Republic of Germany [56,62,63]. The experiences gained with this technology can be briefly summarised as follows;

a. The fluidised bed will in many cases maintain totally clean surfaces and neither scaling nor fouling will occur [49,51-59,70-75].

b. Owing to increased turbulence, ascribed to the presence of the fluidised inert particles, values of heat transfer coefficient in liquid fluidised beds can be up to eight times higher

than for single phase forced convection [50,81]. Furthermore, there are always excellent heat transfer coefficients at low superficial velocities of less than $U < 0.5$ m/s [53,56,62,63].

c. Fluidised bed pressure losses are comparable to normal forced convection tube bundle heat exchangers, since normal heat exchangers are operated at much higher superficial velocities (approximately 2-3 m/s) thus achieving higher pressure drop ($\Delta P^{"}$) values [56,62,63].

d. Heat transfer enhancement is largely dependent on the characteristics of the solid particles, primarily size, density, thermal conductivity and shape. Particles for use in fluidised bed heat exchangers can be manufactured from a wide range of chemically and mechanically resistant materials such as sand, glass, ceramics and metals [63].

e. Erosion of tubes is negligible [49,53,60].

More will be said regarding these observations.

3.3.1.1. THE STATIONARY FLUIDISED BED HEAT EXCHANGER

In 1971, development of the self-cleaning fluidised bed heat exchanger for seawater desalination plants started at the Technical University of Delft in the Netherlands [1]. Then, only stationary fluidised beds were considered. This early fluidised bed heat exchanger consisted of a large number of parallel heat exchanger tubes, in which small solid particles were kept in a fluidised condition by the liquid passing up the tubes. The solid particles would regularly break through the boundary layer in the tubes, resulting in the achievement of good heat transfer, despite comparatively low liquid velocities in the tubes. Further still, the solid particles exerted an abrasive effect on the wall of the heat exchanger tubes, removing any deposits from the tube wall at an early stage. It was at once apparent that this continuous cleaning of the wall by the action of the suspended particles was an exceedingly valuable attribute, as periodic cleaning by chemical or mechanical means could be dispensed with or at least done less frequently. The principle of the stationary fluidised bed heat exchanger is shown in Figure 3.3. The heat exchanger consisted of the tube bundle, an inlet section and the outlet channel. The inlet section is divided into two chambers by a distribution plate, namely the liquid inlet chamber, and the particle distribution chamber from where particles are equally distributed over all the tube plates. The particle inlet chamber also contained the tube extensions, which were provided with a side hole.

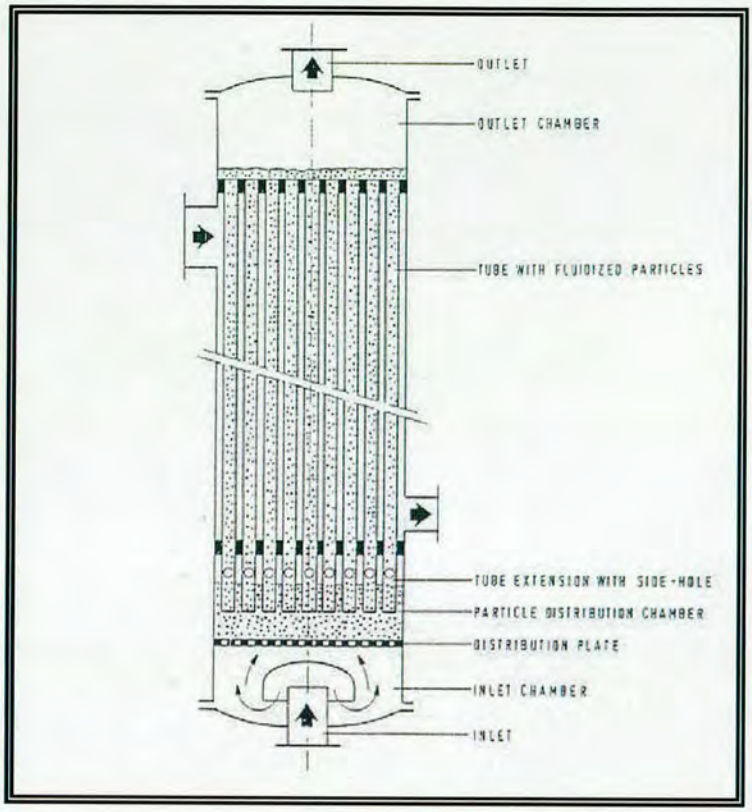

Figure 3.3: Self-cleaning heat exchanger with stationary fluidised bed of cleaning particles. Taken from Klaren [55].

As well as the tube extensions, design of the distribution plate, and the pressure drop across the distribution plate, were of the utmost importance in achieving satisfactory operation with equal distribution of liquid and particles inside all the tubes. According to Klaren [55], for stable operation, the pressure drop across the distribution plate should satisfy the condition:

$$\Delta P_{\mathrm{d}}^{"} > 0.1\Delta P_{\mathrm{t}}^{"} \tag{3.7}$$

where $\Delta P_{\mathrm{d}}^{"}$ is the pressure drop across the distribution plate and $\Delta P_{\mathrm{t}}^{"}$ is the total pressure drop over the heat exchanger due to the weight of the solid particles. The latter pressure drop follows from the equation:

$$\Delta P_{\mathrm{t}}^{"} = g(\rho_{\mathrm{p}} - \rho_{\mathrm{L}})\{L_1(1-\varepsilon_1) + L_2(1-\varepsilon_2) + L_3(1-\varepsilon_3)\} \tag{3.8}$$

here L_1, and L_3 are the bed height in particle inlet and outlet chamber respectively, whilst L_2 symbolises the tube length. $\varepsilon_1, \varepsilon_2, \varepsilon_3$ represent the porosity of the bed, i.e. volume fraction of the continuous phase, in the particle distribution chamber, the length of tube and the outlet chamber respectively. The distribution plate itself was typically designed as a perforated plate, with the diameter and number of perforations satisfying the pressure drop required for

stable operation of the bundle. In practical applications, the diameter of the perforations in the distribution plate may approach half of the inner diameter of the heat exchanger tube plates, thus resulting in fairly large holes with 1.5" and 2" tubes often used in severe fouling heat transfer. Minimum flow through the heat exchanger mostly corresponds to a nearly fixed bed in the particle distribution chamber, with an associated bed porosity of approximately 0.4; minimum flow also required the fluidised beds in the tubes to be extended over the full tube length. Increasing the flow through the heat exchanger implied higher bed porosities, and the accommodation of a large fraction of the particles in the outlet channel; such operating conditions would require an outlet chamber of sufficient volume. Higher density and/or larger sized particles were used to overcome such constraints, making it possible to operate the stationary fluidised bed heat exchanger at slightly elevated flows. The diameter of the side-hole in the tube extension(s) is approximately 40% of the internal diameter of the heat exchanger tubes.

Consequences and Limitations of the fluid bed heat exchanger with a stationary bed

In 1978, the Dutch government subsidised the design and construction of a multi-stage flash distillation plant for demonstrational purposes. The heat exchanger in this plant, with a surface of 1,000 m^2, comprised a stationary fluidised bed in 1,600 parallel tubes with a diameter of 20 mm and a tube length of 12.5 m. More than 4,000 kg of cleaning particles were used which consisted of glass balls with a diameter of 2 mm. Over an operating period of more than 15,000 hours, the installation proved - very convincingly - that the fluidised bed heat exchanger could easily operate on chemically untreated high temperature seawater without any indication of fouling caused by the familiar hard scales (see also references [53] and [55]). The fluidised bed heat exchanger also demonstrated the possibility of obtaining heat transfer coefficients of equivalent magnitude as normally obtained in conventional heat exchangers, but at much lower superficial liquid velocities in the tubes, typically 0.1 to 0.2 m/s (depending on the particles, the density of the particle material and the porosity of the bed) as compared to 1.8 m/s for conventional exchangers [55].

However, the type of liquid-solid fluid bed heat exchanger discussed so far possessed a number of limiting disadvantages. Firstly, because of the low liquid velocities in the tubes, stationary fluidised bed heat exchangers required a large number of parallel tubes. The accommodation of a large number of parallel tubes increases the diameter of the shell and tube plates of the exchanger. Secondly, a fluidised bed heat exchanger should always contain particles fluidised over the total tube length in order to assure maximum heat transfer performance; this made it necessary to maintain a minimum velocity in the tubes, as elevated flow would require quite a voluminous outlet chamber for the accommodation of a considerable amount of particles. These limitations precipitated industrial exchangers that were economically and structurally untenable [1, 55]

3.3.1.2. THE SELF-CLEANING CIRCULATING FLUIDISED BED HEAT EXCHANGER

Stimulated by the success in desalination, in the early 1980's an alternative design of the fluid bed concept, applying internal circulation of the cleaning particles through multiple parallel downcomers, was developed to concentrate on applications in the process industry, where fouling can be more severe and the liquids often contain large quantities of undissolved solids [61]. This version of the self-cleaning liquid-solid fluidised bed, the design of which is shown in Figure 3.4, significantly reduced the aforementioned stationary fluidised bed disadvantages.

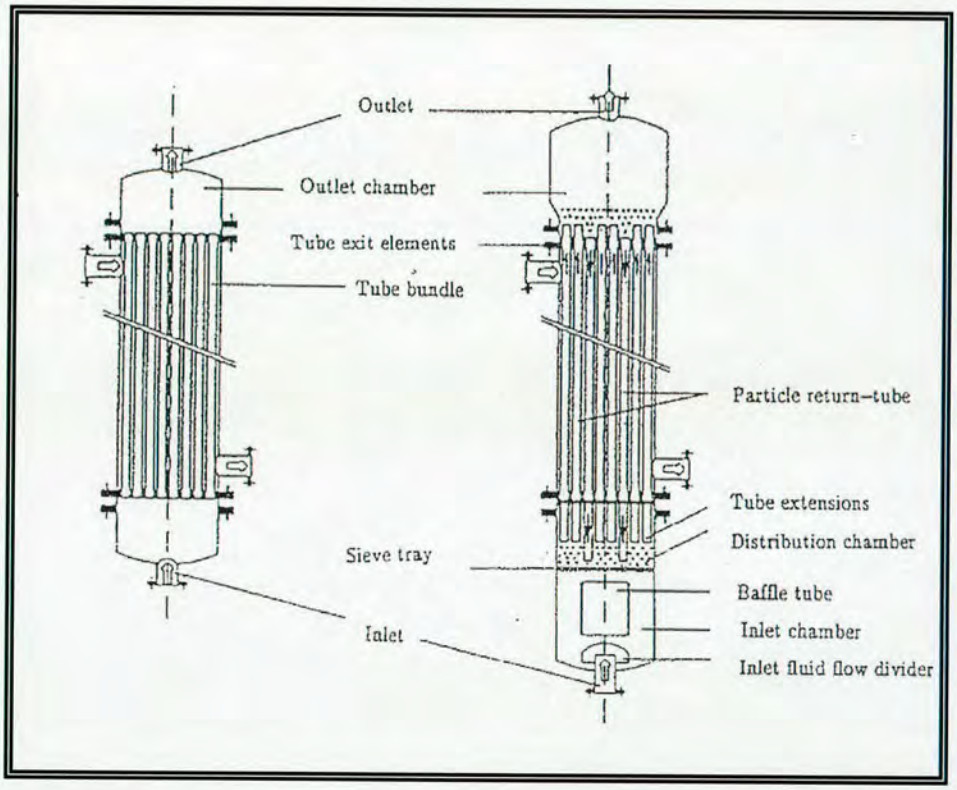

Figure 3.4: Conventional heat exchanger and modified heat exchanger with circulating fluidised bed. Taken from Rautenbach *et al.* [56].

In this heat exchanger the particles are not kept in a stationary fluidised condition, but are moved by the upward flow of liquid from the inlet section up into the riser tubes and further into the outlet channel. From the outlet chamber, particles enter the particle recycle tube(s)/downcomer(s), and are returned to the particle distribution chamber by the downward flow of liquid. As far as stable operation is concerned, the hydraulics of this particular exchanger does not differ from those of the stationary fluidised bed. Here, equal distribution of liquid and particles over all parallel tubes is again achieved by the same distribution system (consisting of distribution plate, particle distribution chamber and tube extensions with side hole) as applied for the stationary fluid bed heat exchanger [55]. However, the transport of

particles greatly improves operational stability. According to Fig 3.4, almost any conventional single pass shell and tube heat exchanger can be converted into a circulating fluidised bed heat exchanger by a few relatively simple modifications [62, 63]:

— Tube exit nozzles for stable upward flow
— A large outlet chamber for the separation of the particles
— Tube extensions at the lower end (short extensions for the upward flow and longer ones for the downcomers)

For the design of the circulating fluidised bed, a short baffle tube is included above the fluid inlet. The device induces a lift effect on the particles, resulting in a significant reduction in the required amount of cleaning particles (per m^2 of heat transfer surface) than is necessary for stationary fluidised beds.

In 1995, Tianqing [64] reported on the mechanism of circulating flow of particles within the fluid bed heat exchanger. In order to explain why the particles could circulate, the author firstly analysed the flow of pure liquid without particles. For single phase steady state flows, the author simplified the Navier Stokes equation as follows:

$$\frac{1}{2}f_a \rho_L U_a^2 \pi D_{i,a} L_a = \frac{1}{4}\pi D_{i,a}^2 \left(P_a'' - P_c''\right) - \frac{1}{4}\pi D_{i,a}^2 \rho_L g L_a \quad \text{-long tubes in Fig. 3.5} \qquad (3.9)$$

$$\frac{1}{2}f_b \rho_L U_b^2 \pi D_{i,b} L_b = \frac{1}{4}\pi D_{i,b}^2 \left(P_b'' - P_c''\right) - \frac{1}{4}\pi D_{i,b}^2 \rho_L g L_b \text{ - short tubes in Fig 3.5} \qquad (3.10)$$

here, in relation to the schematic of the circulating fluidised bed exchanger depicted in Fig 3.5, $D_{i,a}$ and $D_{i,b}$ are the inner diameter for the downward and upward flow tubes respectively, whilst L_a and L_b are the downward and upward tube lengths. P_a'', P_b'', and P_c'' are the total pressure at exit(s) of downward flow tubes, at inlet(s) of upward flow tubes, and at upside of the tube bundle respectively. Finally, f_a and f_b are the fanning friction factors.

Start Note:

At this stage, before going any further, we intend to examine the Navier Stokes equations in greater detail, and by such means, to offer a rudimentary justification for the simplifications presented in equations 3.9 and 3.10 above…

The Navier Stokes equations are a set of equations that describe the motion of fluid substances such as liquids and gases. These equations establish that changes in momentum (acceleration) of 'fluid particles' (here the terminology stems from the fact that sometimes it is necessary to consider a finite arbitrary volume, i.e. a control volume, over which certain fluid dynamic principles can be easily understood) are simply the product of changes in pressure and dissipative viscous forces (similar to friction) acting inside the fluid. These viscous forces originate in molecular interactions and dictate how sticky a fluid is (we revisit the definition of viscosity in subsection 3.3.4.1 following). Hence, the Navier Stokes equations are a dynamical statement regarding the balance of forces acting at any given region of the fluid. They are undoubtedly one of the central sets of equations in fluid mechanics, as they describe the physics of a wide range of phenomena of both academic and economic interest. For instance, Navier Stokes equations are used to model weather, ocean currents, water flow in a pipe, motion of stars around a galaxy, and flow around an air foil. Their use also extends to the design of aircrafts and motor vehicles, the study of blood flow and the design of power stations [220].

In terms of their mathematical structure, the equations are set of coupled differential equations, which, unlike algebraic equations, do not seek to establish a relation among the variables of interest (i.e. velocity, pressure, temperature, and density), but instead seek to construct relations amongst the rates of change or fluxes of these quantities (i.e. their derivatives) in a moving fluid. In expanded syntax, the three-dimensional unsteady form of the equations can be written as follows:

Continuity equation

$$\frac{\partial \rho}{\partial t} + \frac{\partial \rho.\mathrm{u}}{\partial x} + \frac{\partial \rho.\mathrm{v}}{\partial y} + \frac{\partial \rho.\mathrm{w}}{\partial z} = 0 \qquad (3.11)$$

X-momentum equation

$$\frac{\partial \rho.\mathrm{u}}{\partial t} + \frac{\partial \rho.\mathrm{u}^2}{\partial x} + \frac{\partial \rho.\mathrm{uv}}{\partial y} + \frac{\partial \rho.\mathrm{uw}}{\partial z} = -\frac{\partial P^{''}}{\partial x} + \frac{1}{Re}\left[\frac{\partial \tau_{xx}}{\partial x} + \frac{\partial \tau_{xy}}{\partial y} + \frac{\partial \tau_{xz}}{\partial z}\right] \qquad (3.12)$$

Y-momentum equation

$$\frac{\partial \rho.\mathrm{v}}{\partial t}+\frac{\partial \rho.\mathrm{uv}}{\partial x}+\frac{\partial \rho.\mathrm{v}^2}{\partial y}+\frac{\partial \rho.\mathrm{vw}}{\partial z}=-\frac{\partial P^{"}}{\partial y}+\frac{1}{Re}\left[\frac{\partial \tau_{xy}}{\partial x}+\frac{\partial \tau_{yy}}{\partial y}+\frac{\partial \tau_{yz}}{\partial z}\right] \qquad (3.13)$$

Z-momentum equation

$$\frac{\partial \rho.\mathrm{w}}{\partial t}+\frac{\partial \rho.\mathrm{uw}}{\partial x}+\frac{\partial \rho.\mathrm{vw}}{\partial y}+\frac{\partial \rho.\mathrm{w}^2}{\partial z}=-\frac{\partial P^{"}}{\partial z}+\frac{1}{Re}\left[\frac{\partial \tau_{xz}}{\partial x}+\frac{\partial \tau_{yz}}{\partial y}+\frac{\partial \tau_{zz}}{\partial z}\right] \qquad (3.14)$$

Energy equation

$$\frac{\partial E}{\partial t}+\frac{\partial \mathrm{u}.E}{\partial x}+\frac{\partial \mathrm{v}.E}{\partial y}+\frac{\partial \mathrm{w}.E}{\partial z}=-\frac{\partial \mathrm{u}.P^{"}}{\partial x}-\frac{\partial \mathrm{v}.P^{"}}{\partial y}-\frac{\partial \mathrm{w}.P^{"}}{\partial z} \qquad (3.15)$$

$$-\frac{1}{Re.Pr}\left[\frac{\partial q^{"}_{x}}{\partial x}+\frac{\partial q^{"}_{y}}{\partial y}+\frac{\partial q^{"}_{z}}{\partial z}\right]+$$

$$\frac{1}{Re}\left[\frac{\partial}{\partial x}\left(\mathrm{u}\tau_{xx}+\mathrm{v}\tau_{xy}+\mathrm{w}\tau_{xz}\right)+\frac{\partial}{\partial y}\left(\mathrm{u}\tau_{xy}+\mathrm{v}\tau_{yy}+\mathrm{w}\tau_{yz}\right)+\frac{\partial}{\partial x}\left(\mathrm{u}\tau_{xz}+\mathrm{v}\tau_{yz}+\mathrm{w}\tau_{zz}\right)\right]$$

As shown in equations 3.11 to 3.15, the Navier Stokes equations consist of a time-dependent continuity equation for conservation of mass, three time-dependent conservation of momentum equations and a time-dependent conservation of energy equation. There are four independent variables in the problem, the *x*, *y*, and *z* spatial coordinates and the time *t*. There are six dependent variables: the pressure $P^{"}$, density ρ, and temperature *T* (which is contained in energy equation 3.15 through the total energy *E*) and three components of the velocity vector (the 'u' component is in the *x* direction, the 'v' component is in the *y* direction, and the 'w' component is in the z direction). In general, all of the dependent variables are functions of all four independent variables. Also, Reynolds number (*Re*) appears here as a similarity parameter, i.e. the ratio of the scaling of the inertia of the flow to the viscous forces in the flow. The $q^{"}$ variables are the heat flux components, whilst *Pr* (Prandtl number) is also a similarity parameter, i.e. the ratio of the viscous stresses to the thermal stresses. The tau (τ) variables are components of the stress tensor. A tensor is generated when you multiply two vectors in a particular way. Whereas the velocity vector has three components, the stress tensor has nine components. Each component of the stress tensor is itself a second derivative of the velocity components.

The terms on the left hand side of the momentum equations (i.e. equations 3.12 to 3.14) are called the *convection* terms of the equation; whilst the terms on the right hand side of the momentum equations, which are multiplied by the inverse Reynolds number, are called the

diffusion terms (recall that convection is a physical process that occurs in a fluid flow, in which some property is transported by the ordered motion of the flow. Meanwhile, diffusion is a physical process that occurs in fluid flow, in which some property is transported by the random motion of the fluid molecules).

In theory for a given flow problem, the set of differential equations can be solved using methods from calculus. In practise, however, the Navier Stokes equations are far too difficult to be solved analytically. For complex situations, such as global weather systems, solutions of the Navier Stokes equations must be found with the aid of high speed computers. This is a particular field of science, referred to as computational fluid dynamics (CFD). Nevertheless, in many instances, the equations can be simplified by various means, a few of which are discussed below. All of the simplifications make the equations easier to solve. Some of them may admit analytical solutions, thereby allowing engineers to solve appropriate fluid dynamic problems in a closed form [220,221].

The Navier Stokes equations and the assumption of inviscid, and steady, flow

Viscous problems are those in which fluid friction has a significant effect on the final solution. Problems for which friction can safely be neglected are called *inviscid.* The Reynolds number can be used to evaluate whether viscous or inviscid equations are appropriate to the problem. Stokes flow is flow at very low Reynolds number, where inertial forces can be neglected compared to viscous forces. On the contrary, high Reynolds numbers indicate that the inertial forces are more significant than the viscous (friction) forces. Therefore, at high Reynolds number (Re > 2000) we may assume the flow to be an inviscid flow, an approximation (or simplification) in which we neglect viscosity compared to inertial terms.

The standard equations of inviscid flow are the Euler equations; they effectively correspond to the Navier Stokes equations with zero viscosity. In general, the Euler equations have a time dependent continuity equation for conservation of mass, and three time dependent conservation of momentum equations (unlike the Navier Stokes equations, the Euler momentum equations contain only convection terms). In equations 3.16 to 3.18, we present a simplified two-dimensional, *steady* form of the Euler equations, which show how the derivatives of velocity, pressure and density of a moving fluid are related - *steady flow* is another simplification of fluid dynamic equations, where all changes of fluid properties with time are set to zero. Steady forms of the Navier Stokes and Euler equations are applicable to a large class of problems, including flow through a pipe or channel [222,223].

Continuity equation

$$\frac{\partial \rho.\mathrm{u}}{\partial x} + \frac{\partial \rho.\mathrm{v}}{\partial y} = 0 \qquad (3.16)$$

X-momentum equation

$$\frac{\partial \rho.\mathrm{u}^2}{\partial x} + \frac{\partial \rho.\mathrm{uv}}{\partial y} = -\frac{\partial P''}{\partial x} \qquad (3.17)$$

Y-momentum equation

$$\frac{\partial \rho.\mathrm{uv}}{\partial x} + \frac{\partial \rho.\mathrm{v}^2}{\partial y} = -\frac{\partial P''}{\partial y} \qquad (3.18)$$

here the independent variables = x, y coordinates; and the dependent variables = the pressure P'', density ρ, and two components of the velocity vector (the 'u' component in the x direction and the 'v' component in the y direction).

The Navier Stokes – Euler equations and the assumption of steady incompressible flow

Like the Navier Stokes expressions of equations 3.11 to 3.15, generalised solutions to the Euler equations stated above are difficult to obtain, requiring the utilisation of either CFD techniques or further viable simplifications.

A special form of the Euler equations, derived along a fluid flow streamline. is often called the Bernoulli equation. Bernoulli's principle (named after Daniel Bernoulli, who in the 1700's investigated the forces present in a moving fluid) states that in fluid flow, an increase in velocity occurs simultaneously with decrease in pressure. This principle is a simplification of Bernoulli's equation, which is unquestionably one of the most recognisable equations in fluid mechanics and states that the sum of all forms of energy in a fluid flowing along an enclosed path (a streamline) is the same at any two points in that path. In other words, the Bernoulli equation is a statement derived from the conservation of energy principle. Conservation of energy states that within a system, energy is neither created nor destroyed, but may be converted from one form to another. This basic energy principle may be written as follows [224]:

$$KE + \sum PE = \text{constant} \qquad (3.19)$$

or,

$$KE = \text{constant} - \left(\sum PE\right) = \text{constant} - \left(PE_{P''} + PE_g\right) \qquad (3.19a)$$

where KE refers to the kinetic energy of the system, and $PE_{P''}, PE_g$ are the potential energies due to the pressure and gravity forces respectively. The derivation of Bernoulli's equation from the Euler equations, or the above thermodynamic principle, does not feature in

this work, but can be readily obtained from a wide range of textbooks on physics, fluid mechanics and aerodynamics.

To summarise, the best way to think about the Bernoulli equation, is that it is an exact first integral of the *inviscid*, and *steady*, Navier Stokes-Euler equations. As in the case of many first integrals, it reduces the problem of solving a fluid mechanic problem from one of calculus to one of algebra. The most commonly encountered form of the Bernoulli equation, given in equations 3.20 and 3.20a below, is that corresponding to *incompressible flow* – a fluid problem is called *compressible* if changes in density of the fluid have a significant effect on the final solution. If density changes have a negligible effect on the solution, the problem is called *incompressible* and changes in density are ignored. In order to determine whether to use compressible or incompressible fluid dynamics, the Mach number of the problem is evaluated. As a rough guide, compressible effects (i.e. density effects) can be ignored at Mach numbers below approximately 0.3. Nearly all problems involving liquids are in this regime, and are therefore modelled as incompressible [225,226].

$$\frac{1}{2}\rho.U^2 + P'' + \rho.g.h = \text{constant} \tag{3.20}$$

or,

$$\frac{1}{2}\rho.U^2 = \text{constant} - \left(P'' + \rho.g.h\right) \tag{3.20a}$$

where U is the fluid velocity along the streamline and h is the height/elevation from an arbitrary point in the direction of gravity (i.e. the z coordinate). With reference to the conservation of energy principle as expressed above, the left hand side of equation 3.20a originates from the kinetic energy terms of equation 3.19a, whilst the right hand side of equation 3.20a originates from the potential energy terms of equation 3.19a. Now although the restrictions (or assumptions) governing the application of Bernoulli's equation might appear severe (i.e. valid for *inviscid*, *steady*, and *incompressible* flows), in actuality the Bernoulli equation is very useful, partly due to the fact that it is much easier to use, i.e. compared to the full and more general Navier Stokes equations, and partly due to the fact that it offers great insight into the balance between pressure, velocity and elevation.

Hence, in attempting to describe the circulation of particles in FBHXs', it is for the above reasons that the author Tianqing [64] chose to present his/her simplified Navier Stokes equations in the 'Bernoulli like' expressions of equations 3.9 and 3.10. Although for Tianqing's purposes, elevation h has been replaced with tube length, or bed height, L.

End Note

We now return to the main text, taking up the narrative from Tianqing's Navier Stoke simplifications as given in equations 3.9 and 3.10 above...

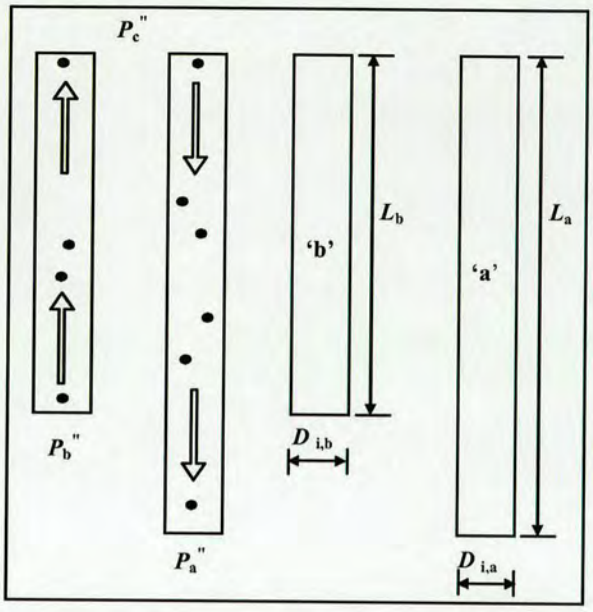

Figure 3.5: Schematic of the fluid bed heat exchanger, illustrating the circulating flow of particles. Adapted from Tianqing [64].

Dividing total pressure into dynamic and static pressures, and noting that static pressure is the same as the gravity borne by the fluid, equations (3.9) and (3.10) then become:

$$\frac{1}{2} f_a \rho_L U_a^2 \pi D_{i,a} L_a = \frac{1}{4} \pi D_{i,a}^2 \left(P_{\partial,a}'' - P_{\partial,c}'' \right) \tag{3.21}$$

$$\frac{1}{2} f_b \rho_L U_b^2 \pi D_{i,b} L_b = \frac{1}{4} \pi D_{i,b}^2 \left(P_{\partial,b}'' - P_{\partial,c}'' \right) \tag{3.22}$$

Furthermore, assuming $P_{\partial,a}'' = P_{\partial,b}''$ Tianqing [64] demonstrated that the ratio of velocities in the two kinds of tubes should be:

$$U_a / U_b = \left[L_b / L_a \left(D_{i,a} / D_{i,b} \right)^{1+e} \right]^{\frac{1}{2-e}} \qquad 0 \le e \text{ (constant)} \le 1 \tag{3.23}$$

From equation 3.23 above, we see that the velocity in shorter tubes will be greater than that in longer tubes. As a result, during start up operation of the exchanger type shown in Figure 3.5, the minimum transport/fluidisation velocity would first be is achieved in the short tubes, subsequently resulting in the upward flow of liquid and cleaning particles to the fluidised bed heat exchanger. Thereafter, an apparent density difference between the two kinds of tubes is built up, causing particles in long tubes to flow downwards, thereby setting the circulation of particles between the long and short tubes.

Consequences and Limitations of fluid bed heat exchanger with internal circulation

During the period 1980 till 1995, the Dutch research group designed and commissioned about 60 self-cleaning heat exchangers of various stationary and circulating fluidised bed designs. Meanwhile in Germany, the Institut für Verfahrenstechnik of the RWTH Aachen, in collaboration with industry, designed and commissioned over 40 stationary and circulating fluidised bed units [62]. Typically, in both instances, installed fluidised bed heat exchangers (FBHXs) were employed for operations in industries such as pulp and paper, chemical and petrochemical processing, geothermal energy, and waste water processing. From the experiences gained, aside from the continuous maintenance of clean tube walls for the heating or cooling of severe fouling liquid systems, operational stability over a wide range of superficial velocities has been recognised as one of the greatest advantages of the self-cleaning exchanger with internal circulation [56,62,63].

However, such experiences have also revealed the disadvantages of the internal circulation fluidised bed technique [1], namely:

- The internal circulation of particles through multiple parallel downcomers cannot be seen, hardly be measured and also not controlled or influenced. This is often referred to as the "black box" effect; as a consequence, operators of these devices are often unaware of any malfunctioning of the internal circulation system, which might immediately or eventually impede the proper operation of the heat exchanger.

- Internal circulation applies to the particles and the liquid. The circulating liquid can be as much as 10 to 60% of the flow supplied to the exchanger. This causes a mixing temperature at the inlet section and in case of a saturated feed flow, this could produce heavy deposits on parts of the inlet section and distribution system not in contact with the fluidised bed. During operation such deposits might break loose and cause plugging of parts of the distribution system (i.e. distribution plate, particle distribution chamber and tube extensions with side hole). Strong internal circulation may also cause serious wear of parts of the inlet section.

- Another weak point of the system is the separation of the particles from the liquid in the outlet channel. With internal circulation, the efficiency of particle separation from the upward flowing liquid is somewhat limited.

3.3.1.3. SELF-CLEANING CIRCULATING FBHX - WTH EXTERNAL DOWNCOMER

In 1990, Shell, DuPont de Nemours and Pechiney started discussions with the original developers of the fluidised bed heat exchangers to replace internal circulation of the cleaning particles by external circulation. In particular, Shell expressed their interest in the wider

application of the technology, but insisted on better controllability of the cleaning particles, which, according to Shell, could only be realised by external circulation [1].

Further to this, interest in new processes involving the utilisation of liquid fluidised units in the fields of food technology, biochemical processing, water treatment, etc, [65] also lent incentive to the development of the liquid-solid circulating fluidised bed technique. A common characteristic of the listed processes is that employed particles are light and small; as such, having rather low terminal velocities, particles are easily entrained from their fluidisation units [66]. Thus, in order to operate these processes with high feedstock, it is necessary to feed new particles into the bottom of the bed, or to separate the entrained particles at the top of the bed and recirculate them back to the bottom of the bed; hence, particle circulation between the fluidised bed and a particle return vessel becomes of essence. Progress in the petrochemical and metallurgical industries also fostered the need for new types of liquid-solid contacting equipment, where utilised solid particles would be circulated between two separated reactors or vessels [67]. For example, in the production of linear alkylbenzene – an intermediate for detergent – continuous regeneration of the solid catalyst is necessary due to rapid catalyst deactivation [68,69]. For this kind of application, involving solid catalysts, the liquid-solid circulating fluidised bed system appeared a naturally good candidate. The system envisaged contains a reactor for the catalytic alkylation reaction and a separate catalyst regenerator which allows the spent and regenerated catalyst particles to circulate easily between the reactor and the regenerator [67].

Hence, after numerous studies and a large and costly development program, self-cleaning fluidised bed technology with a single external downcomer has been successfully developed.

Operating principle and advantage(s) of self-cleaning FBHX with external circulation

Taken from the work of Klaren [57-59,70-72], the operating principle of the self-cleaning heat exchanger with external downcomer is shown in Figure 3.6a and is described as follows: Fouling liquid is supplied to the inlet channel. Solid particles are also fed at the inlet, where an internal flow distribution system (including particle distribution chamber and distribution plate) provides a uniform distribution of the liquid and suspended particles throughout the internal surface of the bundle. As in earlier designs, the particles are carried by the upward flow of the liquid through the tubes, where they impart a mild scraping effect on the wall of the heat exchanger tubes, thereby removing any deposits at an early stage of formation. The particles can be cut metal wire, glass or ceramic balls with diameters varying from 1 to 4 mm. At the top, within the cyclone separator connected to the outlet channel, the particles disengage from the liquid and are returned to the inlet channel through a single external downcomer; thereafter the cycle is continuously repeated as outlined above. Figure 3.6b shows an alternative configuration in which particles disengage from the liquid in a widened outlet channel before subsequently being returned to the inlet channel via an external

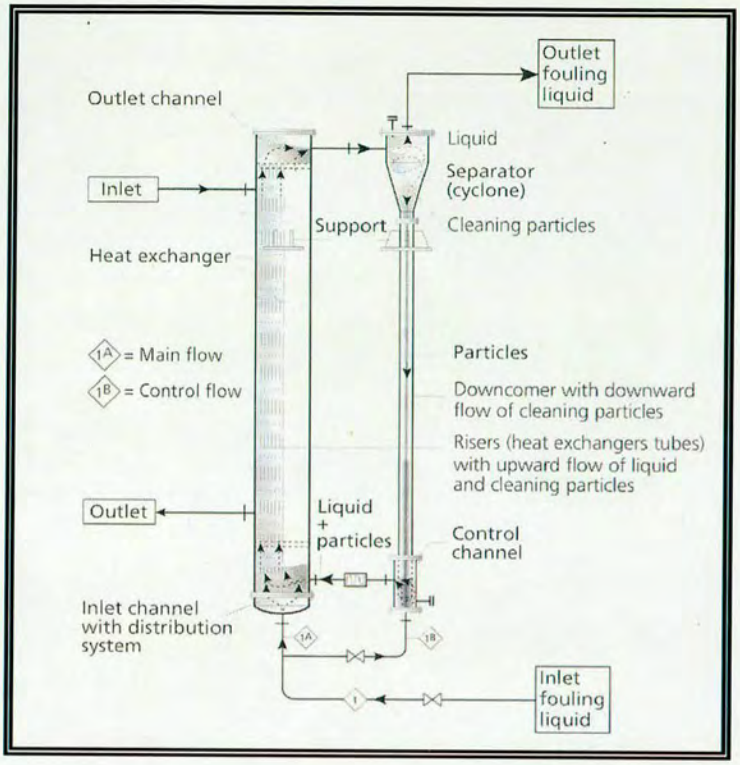

(a)

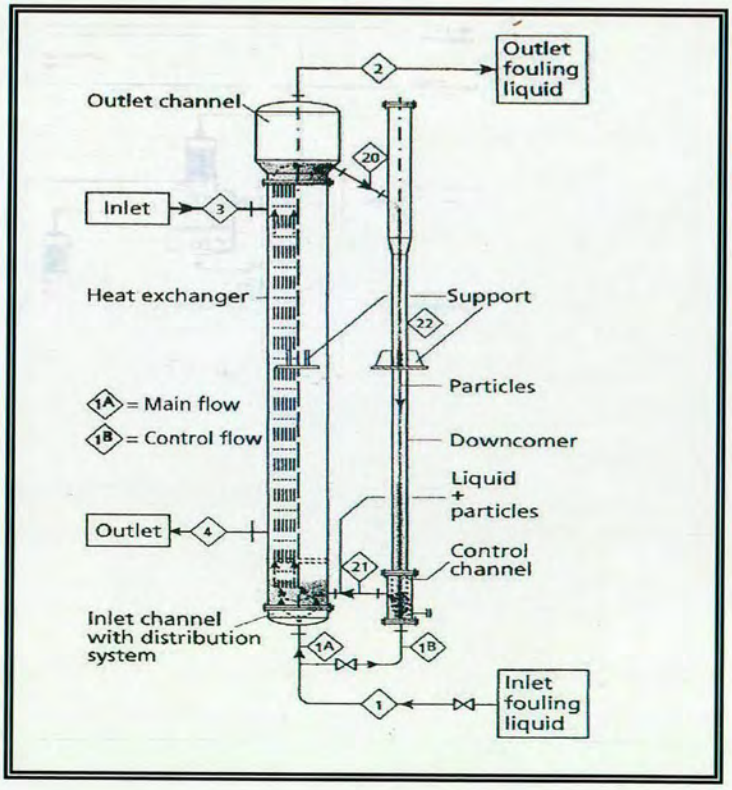

(b)

Figure 3.6: (a) Principle of external circulation self-cleaning heat exchanger with cyclone, (b) Principle of external circulation self-cleaning heat exchanger with widened outlet channel. Taken from Klaren [72].

downcomer. In both configurations, the process liquid fed to the exchanger is divided into a main flow and a secondary, or auxiliary, flow that sweeps the solid particles into the exchanger. By varying the secondary flow, it is possible to control the particle inventory in the tubes and even apply continuous or intermittent cleaning action by the particles. The particle flow supplied to the exchanger (i.e. the particle circulation rate) can be measured through the wall of the downcomer by Doppler shift measuring technique

Obviously the unique advantage of heat transfer enhancement and scaling prevention associated with stationary and internally circulating fluidised beds, also applies to the self-cleaning liquid-solid circulating fluidised bed heat exchanger with external downcomer. However, the aforementioned disadvantages of the exchanger with internal circulation (see subsection 3.3.1.2.) do not apply to the exchanger with external circulation. Moreover, the self-cleaning heat exchanger with external circulation of the cleaning particles allows for excellent measurement and controllability of the particle inventory active in the fluidisation process. The system with a singular external downcomer also accommodates the possibility of retrofitting some existing conventional exchangers into a self-cleaning configuration [1]. Such observations seem to justify the conclusion that the self-cleaning heat exchange technology with external circulation of solids through a single external downcomer, is preferable to the system with internal circulation through multiple parallel downcomers. This is also supported by the fact that over a period of only 3 years from the point of its introduction, more than 8,000 m^2 of self-cleaning surface with external circulation were installed and put into operation. That is more than three times more heat transfer surface with external circulation than all surfaces with internal circulation installed since the early 1980s [1].

3.3.2. Performance Of The Self-Cleaning Liquid-Solid Fluidised Bed Heat Exchanger

3.3.2.1. Heat Transfer Enhancement in Liquid-Solid Fluidised Beds

Heat transfer coefficients from a heated surface of liquid-solid fluidised beds have been measured by several investigators under non-boiling conditions [50-53,55,56,62,63,73-75,78-81]. Rautenbach *et al.* [56,62,63] demonstrated the heat transfer enhancement and fouling mitigation potential of a circulating fluidised bed heat exchanger for severe fouling/scaling cases. With respect to heat transfer improvement, Figure 3.7 shows the results of the authors' experiments for particles of different material (stainless steel cylinders, glass and aluminium oxide spheres) compared with heat transfer in tubes for single phase flow; in the presence of the fluidised particles, the overall increase of heat transfer between fluid and tube walls is clearly demonstrated, with excellent heat transfer coefficients being obtained even at low

superficial velocities of 0.3 – 0.5 m/s. In single phase flow, comparable heat transfer coefficients require fluid velocities of 2 – 3 m/s.

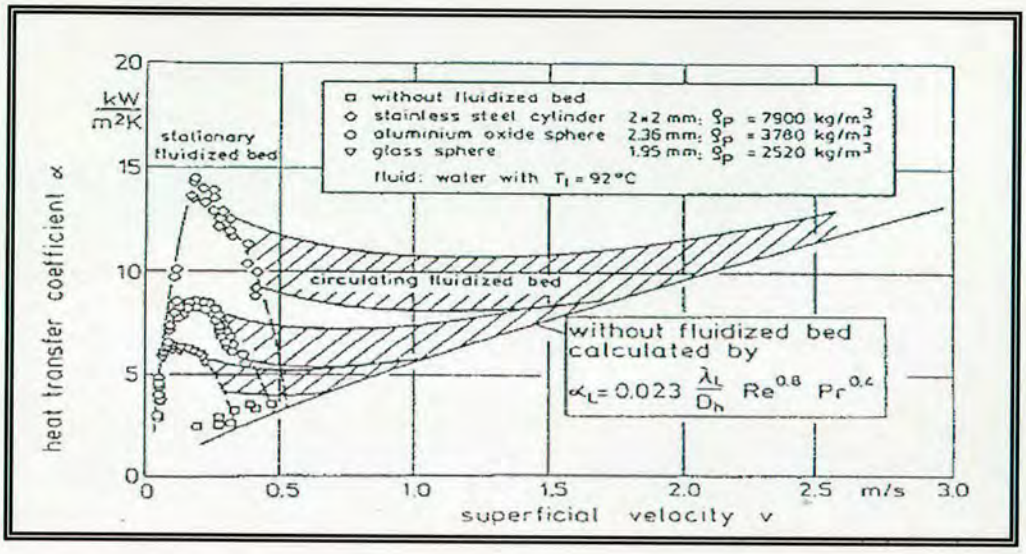

Figure 3.7: Influence of superficial velocity and particle material on the heat transfer performance in a FBHX. Adopted from Rautenbach *et al.* [56].

Lee *et al.* [73,74] studied the pressure loss, heat transfer and fouling characteristics of a particulate/slurry flow in a circulating fluidised bed heat exchanger. Particles used were glass beads of 3.0 mm diameter. Experiments were conducted across a velocity range of 0.5 m/s to 1.7 m/s and a glass bead volume fraction ranging from 0.04 to 0.21. For each volume fraction, the flow rate was varied to determine the impact on heat transfer. Figure 3.8 depicts the heat transfer coefficient of the slurry flow plotted against the flow velocity. The solid line in the figure denotes the heat transfer coefficient of pure water.

Figure 3.8 shows that above 1.0 m/s, the heat transfer coefficient of the slurry flow is approximately the same as that of pure water. However, below 1.0 m/s the heat transfer coefficient of the slurry flow is higher. It is shown to increase slightly as the particle volume fraction/average solid hold-up (i.e. the ratio of the initial volume of added particles to the total volume of the system) increases from 0.04 to 0.21, being almost constant and independent of flow velocity. In reasonable agreement with Lee *et al.* [73,74] data from Rautenbach *et al.* [56], also for 3.0 mm glass beads, are themselves shown in the figure. By way of explanation, Lee *et al.* suggest that glass beads moving within the water flow field periodically strike the heat exchanger tube wall, thus precipitating thermal boundary layer disruption and a concomitant increase in heat transfer coefficient. The investigators' also performed flow visualisation studies, which suggest that the particle-wall impact frequency is closely related to the heat transfer enhancement. The authors observed that as water flow velocity decreased,

the frequency with which the particles contacted the wall seemed to increase, thereby augmenting the heat transfer [73,74].

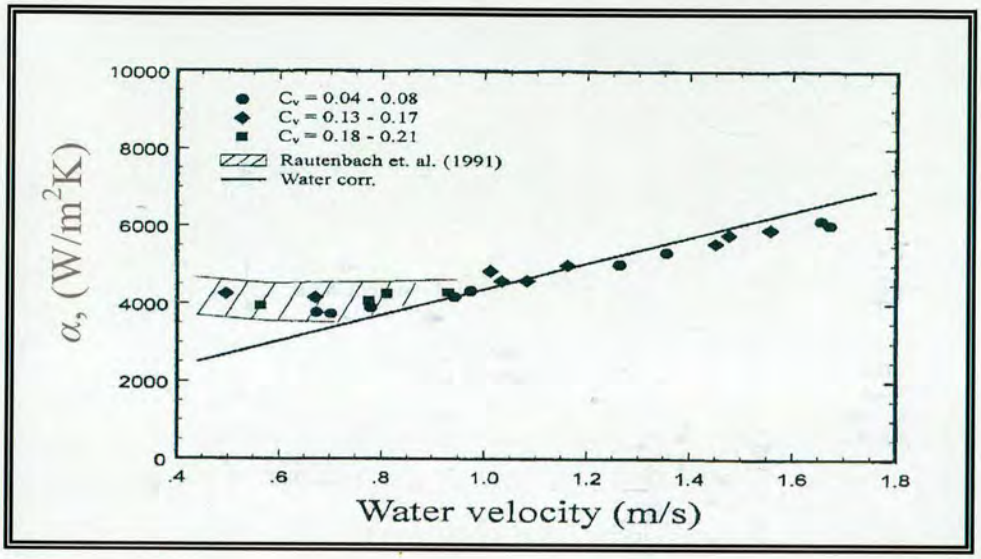

Figure 3.8: The dependence of heat transfer coefficient on superficial fluid velocity using glass beads. Taken from Lee *et al.* [74] where the particle volume fraction is symbolised by Cv.

In 2002, Ahn *et al.* [75] conducted an experimental study to assess the characteristics of fluid flow and heat transfer in a fluidised bed heat exchanger with the circulation of seven different solid particles, as given in Table 3.3 below. Except for the sand grains, all indicated particles had a volume of 14 mm^3, and water was used as the working fluid.

Classification	Material	Geometry	Dimensions
Case (A)	Glass	Bead	3 mm d_p
Case (B)	Aluminium	Cylinder	2 mm d_p, 4.5 mm L
Case (C)	Aluminium	Cylinder	3 mm d_p, 2 mm L
Case (D)	Steel	Cylinder	2 mm d_p, 4.5 mm L
Case (E)	Steel	Cylinder	2.5 mm d_p, 2.8 mm L
Case (F)	Copper	Cylinder	2.5 mm d_p, 2.8 mm L
Case (G)	Sand	Grain	2.0 mm ~ 4.0 mm d_p

Table 3.3: Particles in fluidised bed of Ahn *et al.* [75], where d_p = diameter and L = length.

Appropriated from the authors work, Figure 3.9 shows the improvement of the heat transfer through the operation of the fluidised bed with circulating solid particles. Like Lee *et al.* [73,74], Figure 3.9 illustrates the increase of heat transfer coefficient in the presence of solid

particles for all indicated cases. As with Lee *et al.*, the enhancement effect is more pronounced at lower flow velocities. However, of particular note are the authors' observations concerning heat transfer behaviour at higher flow velocities. From Figure 3.9 it is apparent that over the flow velocity of 1.0 m/s, heat transfer coefficients are lower than those without circulating solid particles (solid line). Noting that turbulent mixing is closely related to increased heat transfer coefficients at higher water velocities, the investigators' suppose that above U = 1.0 m/s solid particles interfere with the growth of these turbulent eddies, thus degrading the measured heat transfer coefficient. However, the authors' do concede that this is unlikely to be the case for actual industrial heat exchangers in fouling environmental conditions. Finally, with respect to the influence of particulate materials, their experimental results indicate that sand grains generally produce the highest heat transfer coefficients. The authors' speculate that the rough geometries of the sand grains may augment the formation of turbulent eddies, thus accounting for the increased rate of heat transfer [75].

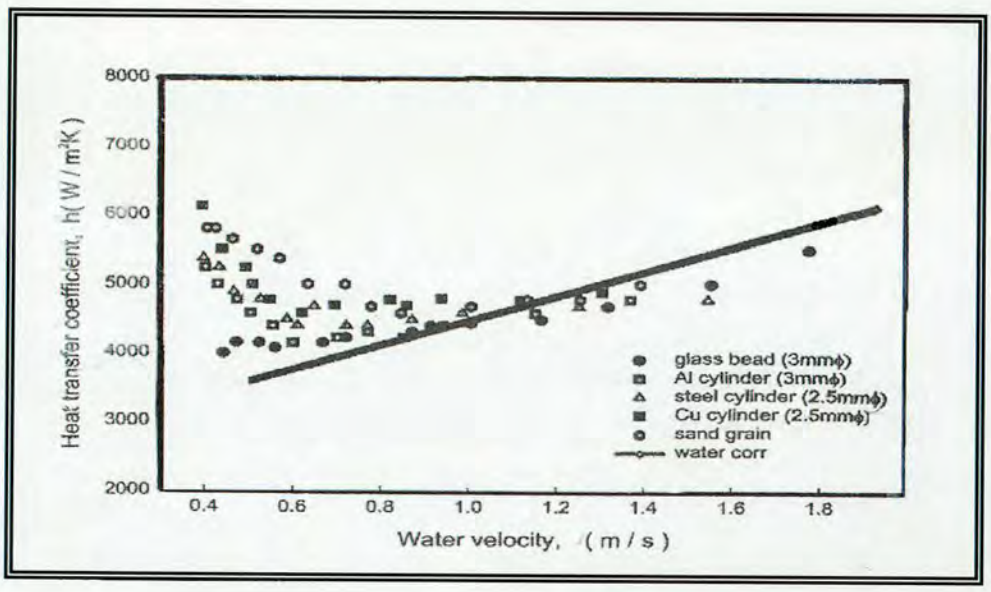

Figure 3.9: Improvement of heat transfer through operation of a circulating fluidised bed with various particles. Taken from Ahn *et al.* [75].

3.3.2.2. FOULING POTENTIAL OF LIQUID-SOLID FLUIDISED BED EXCHANGERS

As well as heat transfer performance, Rautenbach *et al.* [56,63] also examined the fouling behaviour of the circulating fluidised bed heat exchanger. In accordance with the literature, their measurements show that, for most cases, scaling can be totally prevented by the action of the fluidised particles. This is substantiated by Figure 3.10 and Figure 3.11, both taken from the authors' work, for two cases of severe fouling. Figure 3.10 depicts the result of experiments with sugar molasses: whereas the overall heat transfer coefficient of a

conventional forced convection heater is seen to be low, starting to decrease after merely 10 hours of operation due to organic fouling, the heat transfer coefficient of the fluidised bed heat exchanger is high and, more importantly, is shown to remain high for an indefinite period of time. The authors operated such a heater without cleaning for 12 weeks, finally ending the

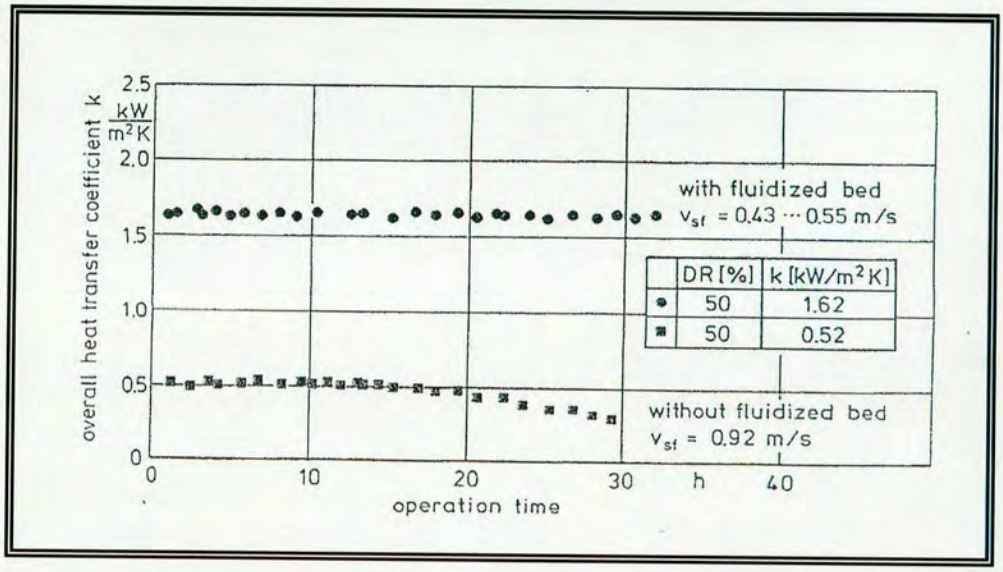

Figure 3.10: Comparison of conventional forced convection and fluidised bed heater – operation with a sugar molasses of 50 % dry matter. Taken from Rautenbach *et al.* [56].

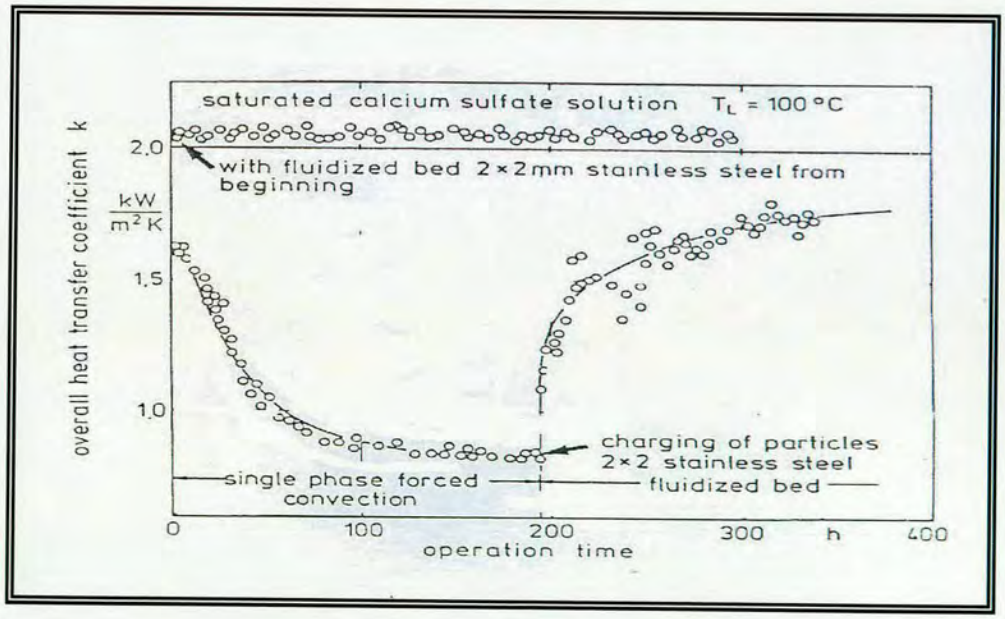

Figure 3.11: Comparison of conventional forced convection and fluidised bed heater – operation with saturated calcium sulphate solutions. Taken from Rautenbach *et al.* [56].

experiment with no noticeable signs of fouling or erosion. Figure 3.11 shows the results of experiments concerning "pure" calcium sulphate scaling. For these conditions, the heat transfer coefficient for single phase forced convection decreases rapidly, due to severe scale deposition, whereas the heat transfer surface of the circulating fluidised bed remains clean. The authors' emphasise the fact that for this particular case, referring to Figure 3.11, scales which had formed during operation without fluidised particles were subsequently removed upon switching to fluidised bed operation [56,63].

Lee *et al.* [74] performed fouling tests using a 3,000 mg/L ferric oxide (Fe_2O_3) slurry both with and without glass beads in a circulating fluidised bed heat exchanger. The ferric oxide used had a mean particle diameter of 0.98 μm and a specific gravity of 5.12. Two types of test were conducted: one with a 0.1 particle volume fraction, and a second without glass beads. During the fouling test the water velocity was maintained at 0.8 m/s with a 30°C inlet water temperature. For an 80 hour test run, the heat transfer coefficients for the two different cases are plotted versus time as shown in Figure 3.12.

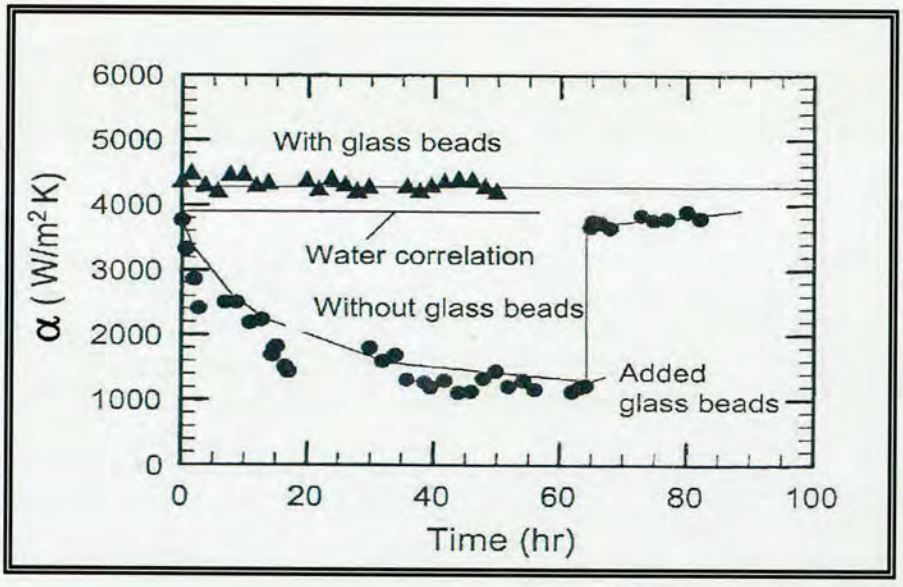

Figure 3.12: Heat transfer characteristics of the circulating fluidised bed heat exchanger with and without glass beads at water velocity 0.8 m/s and volume fraction of glass beads = 0.1 (3000 mg/L ferric oxide added as fouling agent). Adopted from Lee *et al.* [74].

In the first experiment, glass beads were used from the beginning and throughout the test duration; conversely, in the second experiment the system was actually run without glass beads for 65 hours, after which time the glass beads were eventually introduced for the remaining 15 hours. Under the former test conditions the heat transfer coefficient (measured as 4300 ± 215 W/m^{2}K) remains constant over time, proving greater than both the heat transfer

coefficient estimated in the absence of fouling (i.e. using pure water) and without glass particles. In the latter case, i.e. when the foulant-water mixture was for a period circulated without the glass beads, the heat transfer coefficient decreased dramatically from nearly 4000 W/m^2K to 1200 W/m^2K. The generated fouling curve depicts an asymptotic shape, as typically associated with particulate fouling (see *Chapter 2*, subsection 2.2.2). After 65 hours of operation, when the heat transfer coefficient had decreased to one third of its initial value, the glass beads were finally introduced into the circulating fluidised bed heat exchanger. As evidenced by Figure 3.12, following the inclusion of particles, after approximately 5 minutes, the magnitude of the heat transfer coefficient increased rapidly, eventually recovering its initial value. On the authority of the authors', these results demonstrate that under certain circumstances, glass beads are not only effective at eradicating existing fouled deposits, but are also capable of prohibiting the formation of further deposits.

According to Klaren [55], the choice of particle material is an important design parameter for circulating fluidised bed operations, since it influences not only the liquid velocity in the tubes, but also determines the extent of removal of deposits from the tube wall. To this regard, Figure 3.13, taken from the authors work, shows the fouling behaviour in a fluid bed heat exchanger for different particle materials (in this instance glass beads and stainless steel particles). The results illustrated suggest that higher density chopped stainless steel wires are preferable to lower density glass particles. Additionally, within the cited body of work [55], the author also collates some successful operating results, drawn from various industrial applications of the circulating FBHX existing at the time of publication.

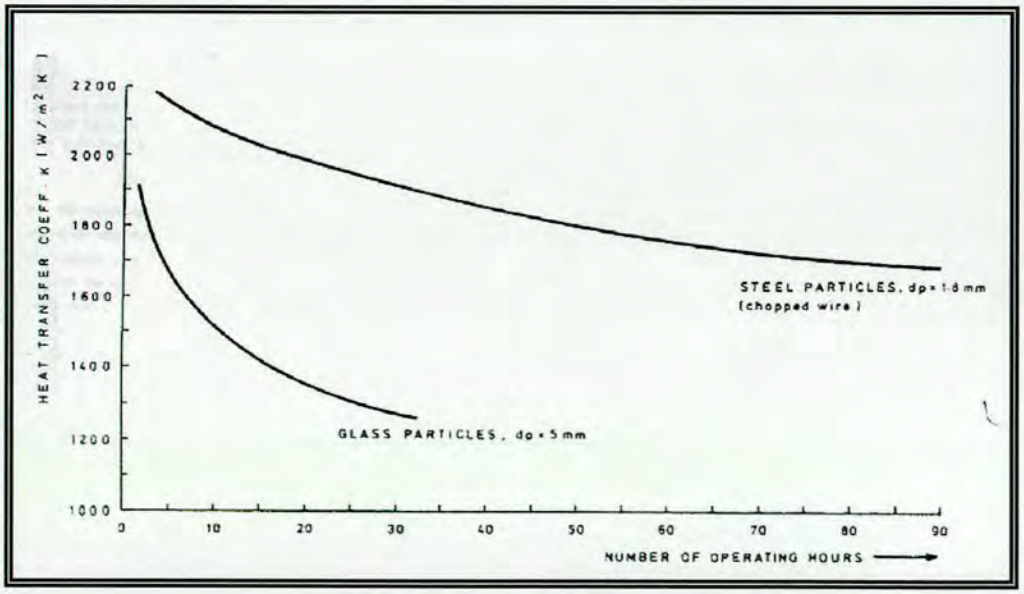

Figure 3.13: Fouling behaviour in circulating FBHX for different particle materials. Taken from Klaren [55].

3.3.2.3. PRESSURE LOSS IN LIQUID-SOLID FLUIDISED BED EXCHANGERS

According to Rautenbach *et al.*, the tube side pressure losses of a conventional tube bundle heat exchanger (of 5 m tube length and 25 mm tube diameter) are approximately 0.5 to 0.8 bar for a fluid velocity of U = 3 m/s; the researchers state that about the same pressure losses may be expected for a FBHX of identical dimensions, and operated with a superficial velocity of less than U = 1.0 m/s (depending to some extent on the material of the fluidised particles; for instance even more reduced pressure losses can be expected for particles of low specific gravity). By way of demonstration, Figure 3.14 depicts a typical set of results taken from the authors' work [63]. It is immediately apparent that compared to single phase forced convection, the presence of solid particles results in a higher pressure drop across the exchanger; however, the fact that FBHXs operate at much lower superficial velocities (U < 0.5 m/s) offsets the increased $\Delta P^{"}$ penalty stemming from the additionally solid phase.

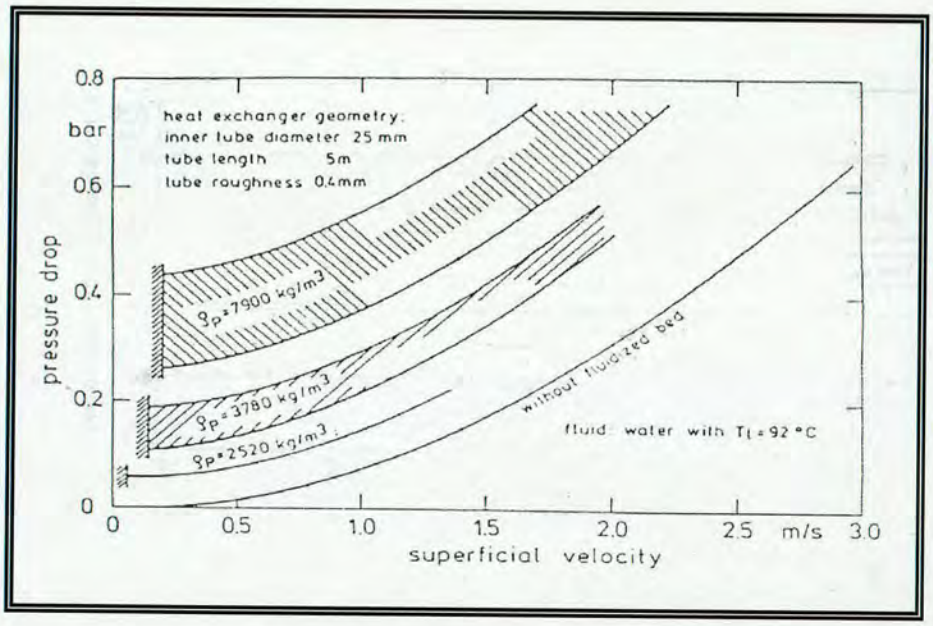

Figure 3.14: Pressure drop of a conventional shell-and-tube heat exchanger compared to a modified shell and tube heat exchanger with a fluidised bed. Taken from Rautenbach *et al.* [56].

Now we return to the work of Lee and Kim [73], where the experimenters measure the heat transfer, fouling behaviour, and pressure loss of a particulate flow in a circulating fluidised bed. Particles used were glass beads of 3.0 mm diameter. From the authors' work, Figure 3.15 depicts the pressure loss per unit length plotted against the flow velocity. The investigators' pressure drop data for pure water is shown to be in good agreement with the widely accepted Petukhov equation [76] for predicting $\Delta P^{"}$ for single-phase liquid flow in tubes. At flow velocities higher than 1.0 m/s, the pressure loss of the particulate flow

becomes independent of the particle volume fraction, gradually approaching that of pure water. However, at flow velocities lower than 1.0 m/s, the foulant-water mixture yields larger pressure loss compared with the pure water flow. The deviation from the pure water increases as the flow velocity decreases and the particle volume fraction increases. In 1961 Newitt *et al.* [77] had noticed a similar trend for sand slurry experiments.

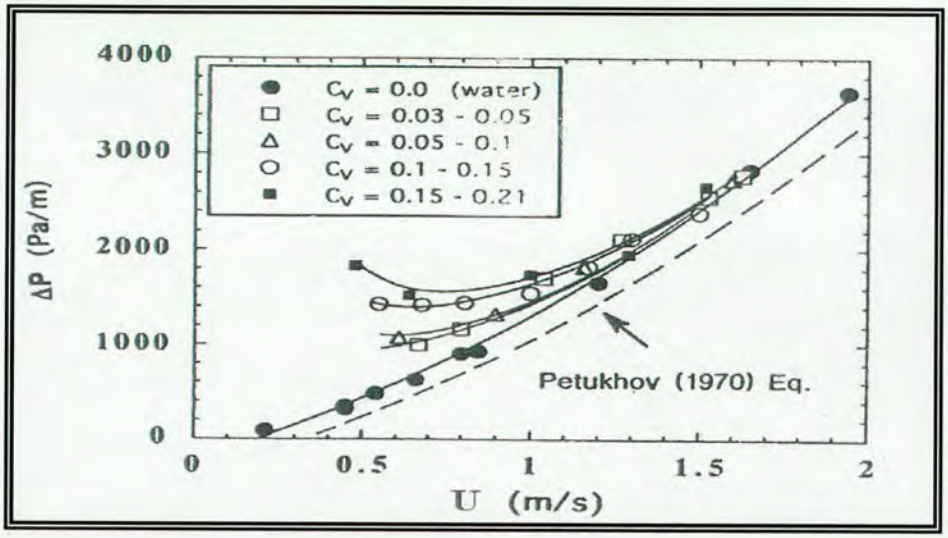

Figure 3.15: Pressure loss per unit length versus flow velocity. For circulating fluidised bed system with 3.0 mm glass beads. Taken from Kim *et al.* [73] where the particle volume fraction is symbolised by Cv.

Continuing with Figure 3.15 above, the results of Lee and Kim [73] show that the pressure loss data at high particle loading/volume fraction (0.15 to 0.20) exhibits an inflection point at a flow velocity of approximately 0.6 m/s. The occurrence of an inflection point at low superficial velocities is typical of a slurry flow when relatively large particles (diameter $\geq$ 50 μm) are involved. Flow visualisation techniques were also applied in an attempt to understand the mechanisms associated with increased pressure loss, and heat transfer augmentation, by the action of fluidised particles. From such explorations, the authors' conclude that particle-wall impact frequency increases as flow velocity decreases; a finding similar to Lee *et al.* [74]. From Lee and Kim [73], Figure 3.16 illustrates the particle behaviour near the tube wall. Below the flow velocity of 1.0 m/s, particles continuously strike the wall, exchanging hydrodynamic momentum with the tube wall, thus resulting in increased pressure loss. However, above a flow velocity of 1.0 m/s all particles migrate towards the centre of the tube, leaving an annulus of clear water near the wall. This may be the reason the slurry flow shows approximately equal pressure loss, and heat transfer coefficient, with that of pure water flow at superficial velocities higher than 1.0 m/s.

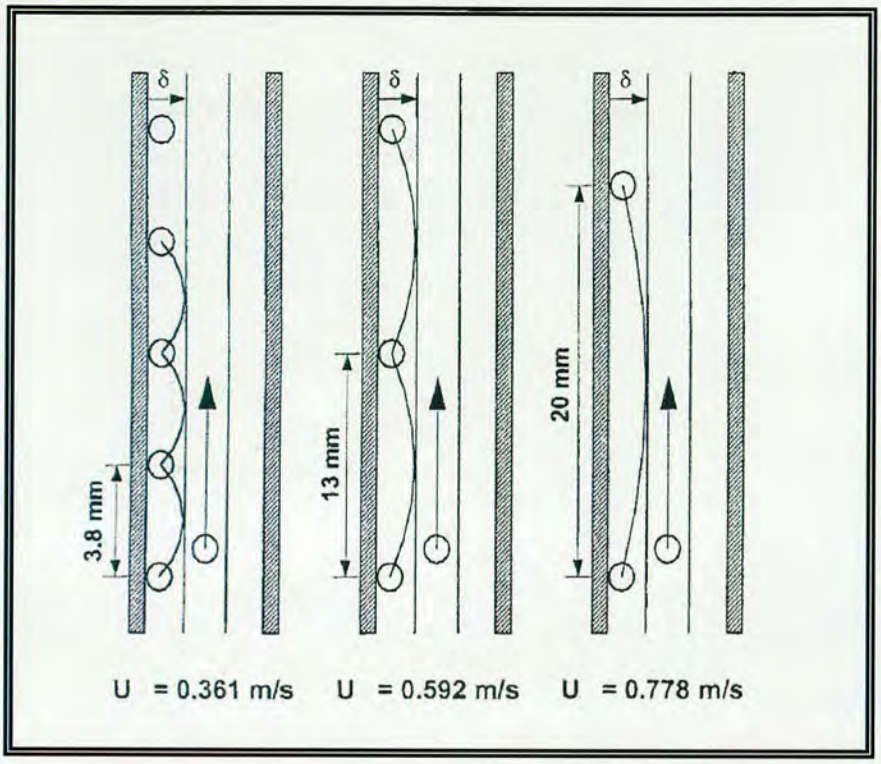

Figure 3.16: Sketch showing the observed particle-wall contact pattern at different flow velocities. Adopted from Lee *et al.* [74].

3.3.2.4. PUMPING POWER REQUIREMENTS OF THE LIQUID-SOLID FBHX

Pumping power requirements for both the transport of liquid and the fluidisation of particles (in either a stationary or circulating state) in the tubes of a FBHX, are determined by the pressure drops according to equations 3.7 and 3.8. Klaren [55] states that when glass particles are used, pumping power requirements for the transport of liquid in the tubes of FBHXs are always lower than in conventional heat exchangers. For steel particles, pumping power requirements are approximately similar to those for plate heat exchangers.

In Rautenbach *et al.*'s [56,63] experimentation with the utilisation of fluidised bed heat exchangers for waste water evaporation, the authors expressed further interest in not only the pressure loss behaviour of the heater, but also the specific power consumption of the evaporator recycle pump. Hence in Figures 3.17(a,b), taken from [56], 3 typical heater designs with identical overall heat transfer coefficients (2000 W/m^2K) and mean temperature driving force (15 K) are discussed: a conventional single phase forced convection heater; and two circulated fluidised bed heaters, one operated with stainless steel particles at $U = 1$ m/s and the other operated with glass spheres at $U = 0.3$ m/s (tube diameter 30 mm, particle size $d_p = 2$ mm). For the 3 cases, Figure 3.17a shows the required tube length as a function of external circulation rate, whilst Figure 3.17b displays their accompanying specific power consumption. According to Figure 3.17b, for steel particles the power consumption of the

recycle pump is equivalent to the conventional forced convection heater; in contrast, and in agreement with Klaren [55], for glass particles the pumping power consumption of the recycle pump is lower than that of the conventional forced convection heater.

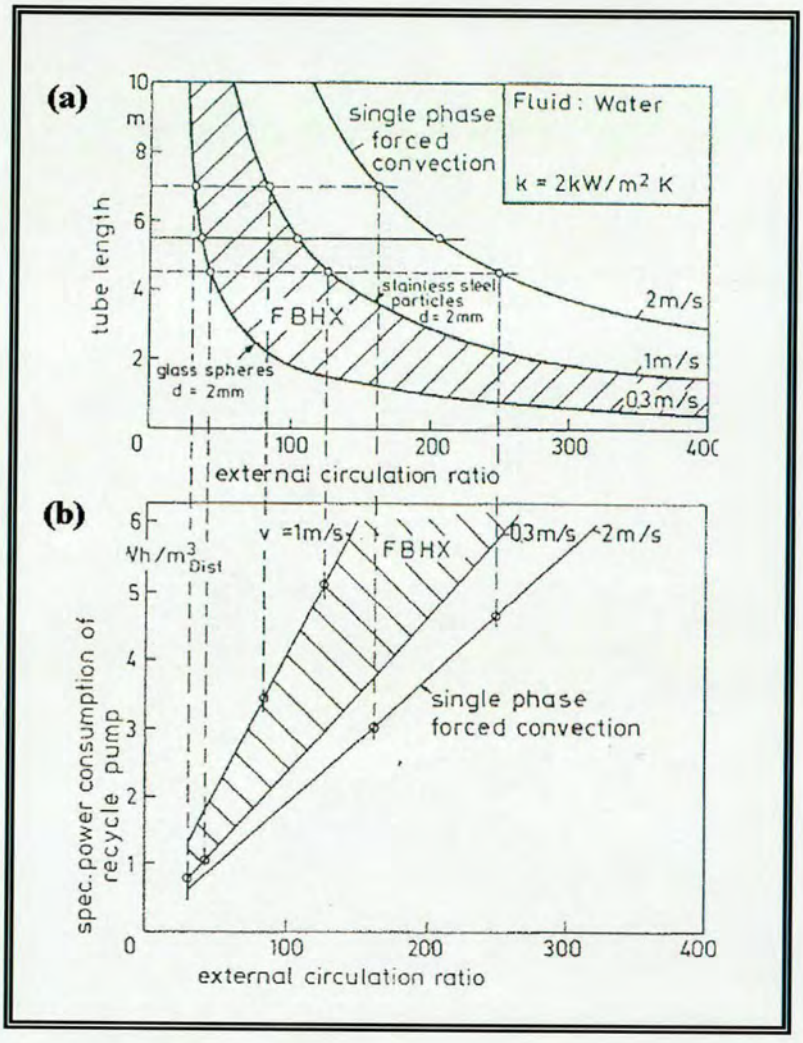

Figure 3.17: Effect of external recirculation rate on (a) tube length, (b) recycle pump power consumption. Comparison of CFB and conventional single-phase forced convection heater. Adopted from Rautenbach [56].

3.3.3. Commercial Installations and Market Potential

3.3.3.1. Quench Coolers

Some of the fouling services which can be provided with the self-cleaning fluidised bed exchanger include the following:

- Forced circulation evaporators and reboilers
- Chemical processes where heating or cooling causes polymerisation fouling or resinous deposits

— Heat recovery from fouling waste-waters
— Concentration of waste-waters by evaporation
— Cooling and evaporative crystallisation
— White-water and black-liquor heating in pulp and paper industries
— Raw juice heating in food processing
— District heating and/power generation with geothermal brines
— Brackish water and sea-water desalinisation, and
— Process cooling with hard scaling and/or biologically fouled waters.

A chemical plant in the United States of America cooled large quench water flows from a proprietary process in open cooling towers [72]. This quench-water released volatile organic compounds (VOCs) into the atmosphere. As a consequence of environmental regulations, the quench-water cycle had to be closed by installing heat exchangers between the quench-water and the cooling water from the cooling towers. In August 1997, after considering other solutions, plant management decided to carry out a test with a small self-cleaning exchanger and compared its performance with that of a conventional shell and tube exchanger. Figure 3.18, taken from [72], shows the results of this test, while Figure 3.19 compares the design consequences for the self-cleaning heat exchangers and the conventional shell and tube exchangers.

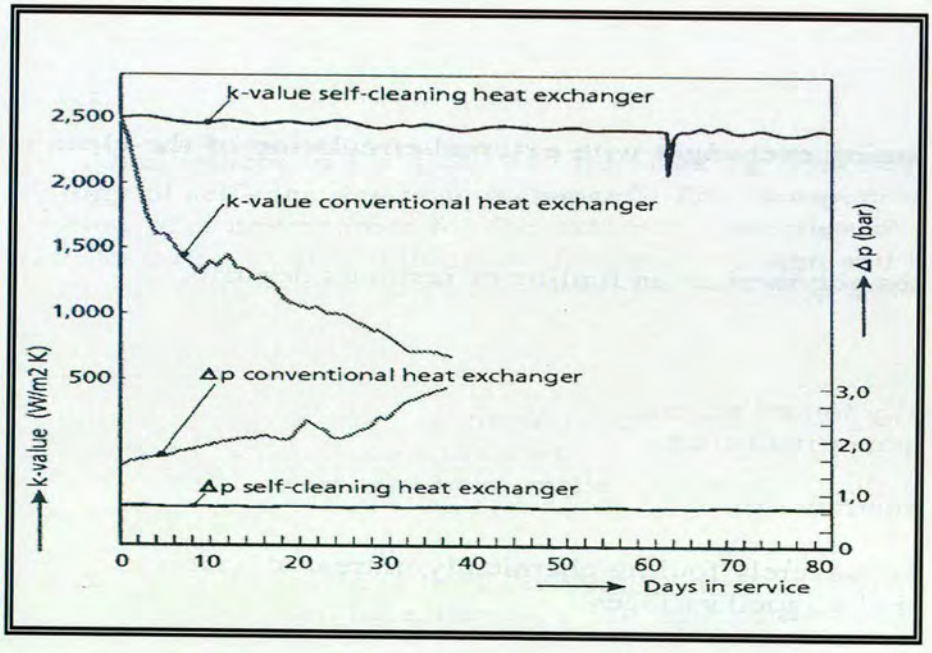

Figure 3.18: Overall heat transfer coefficient (*k*-value) and pressure drop as a function of operating time. Adopted from Klaren [72].

	SELF-CLEANING HEAT EXCHANGER	CONVENTIONAL HEAT EXCHANGER
Heat Transfer Surface	**4,600 m^2**	**24,000 m^2**
Pumping Power	**840 kW**	**2,100 kW**
Number of cleans/year	**0**	**12**

Figure 3.19: Comparing the design consequence between the self-cleaning heat exchangers and the conventional shell and tube exchangers. Adapted from Klaren [72].

For the operation of two parallel production lines, plant management decided in favour of the self-cleaning technology because of the above results, as well as the substantial savings on the investment cost. In each production line two identical self-cleaning heat exchangers were installed. Each exchanger employs a cyclone for the separation of particles, has a shell diameter of 1200 mm, a total height of 20 m, and a heat transfer surface of 1150 m^2 consisting of 700 parallel tubes with an outer diameter of 31.75 mm. Each exchanger uses 9000 kg cut metal wire particles with a diameter of 1.6 mm. The liquid velocity in the tubes is only 0.45 m/s and the particle volume fraction in the tubes approximately 10%. The exchangers serving the first production line were put into operation in October 1998. From start-up till the end of April 1999, Figure 3.20 presents the trend of the observed overall heat transfer coefficient, which has been defined in the diagram as the '*k*-value'. Here, we notice that in spite of some fluctuations at the beginning, a constant '*k*-value' of approximately 2000 W/m^2K was attained. During this period of more than six months, both exchangers operated continuously, with the exception of a few short stops caused by interruptions in the power supply. Figure 3.21 typifies the trend of the two heat exchangers in the first production line, over the period of May 1999 till December 1999. Over such time, there appears a tendency of decreasing '*k*-value', which improves after adjustments to the chemical treatment of the cooling (tower) water. Apparently, this fouling phenomenon was caused by the cooling water in the shell, and not by the severely fouling process liquid in the tubes [72]. Figure 3.21 also shows the '*k*-value' trend of the two exchangers in the second production line, which were put into operation in May 1999. These values began at 2150 W/m^2K and over a period of six months, decreased to approximately 2000 W/m^2K. Both exchangers in the second production line used cooling water from a different cooling tower, which apparently responded better to its chemical treatment and, as a consequence, did not cause much fouling of the exchangers at their shell side. The dotted line in Figure 3.20 shows the trend of the '*k*-value' for conventional shell and tube exchangers as derived from the test results presented in Figure 3.18; this trend, although not shown, is also applicable to all four exchangers during the operating period shown in Figure 3.21.

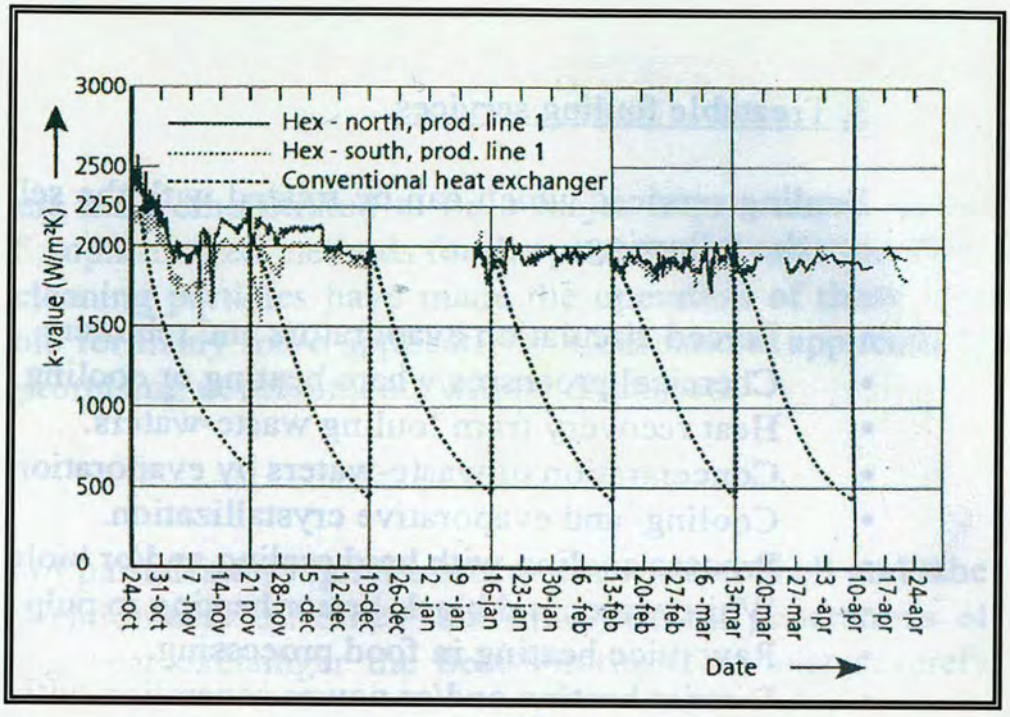

Figure 3.20: The overall heat transfer coefficients (*k*-values) for the self-cleaning heat exchangers of first production line as a function of operating time, and compared with the performance of a conventional heat exchanger. Taken from Klaren [72].

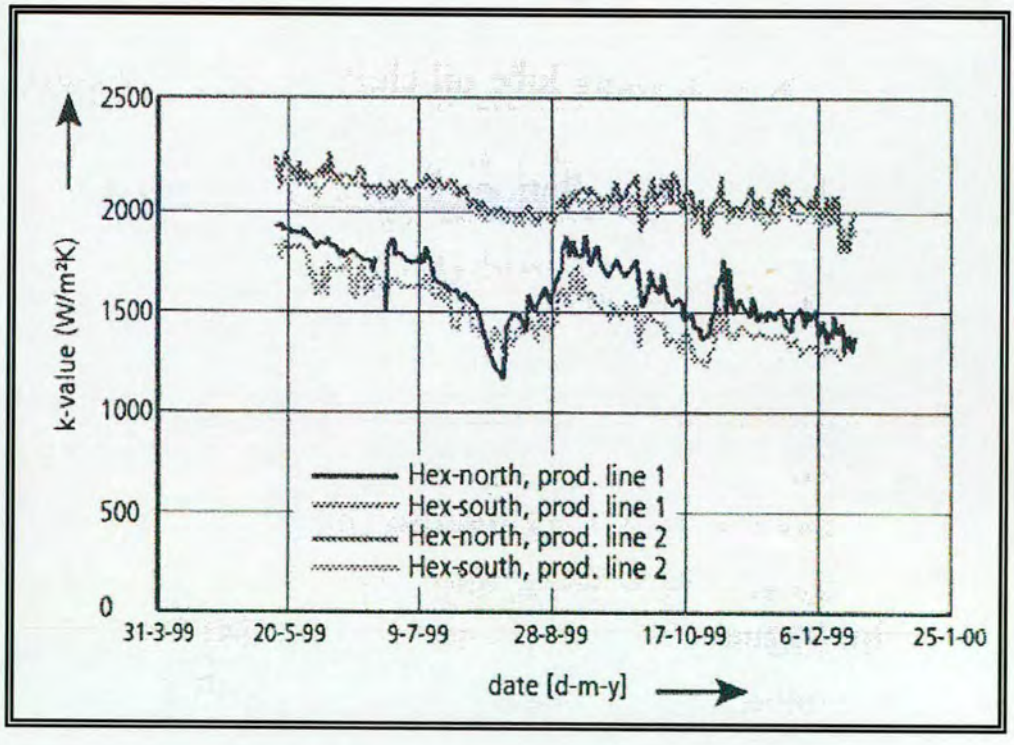

Figure 3.21: Continuation of Figure 3.20, showing the *k*-values for the self-cleaning heat exchangers of both production lines as a function of operating time. Taken from Klaren [72]

Recent publications on the status of the four heat exchangers [1,70,72], report that after 21 months of service, all exchangers were still in operation, maintaining an approximately constant '*k*-value' without having been cleaned. During the operation some minor problems were observed, for example: some piping carrying flow of liquid and particles from the lower part of the external downcomer into the inlet channel, and some parts of the lining of the cyclone separator, needed minor repair after more than 12 months of continuous operation. However, inspection of the heat exchanger tubes did not reveal any measurable wear and the cleaning particles showed a weight loss of only 2% after 12 months of operation.

3.3.3.2. MDF-PLANT

In early 1997, a Belgium manufacturer of Medium Density Fibreboard (MDF) ordered a forced circulation evaporator, without boiling in the tubes, for the concentration of waste-water while producing steam of 200 °C and 14 bar [1,72]. The steam was to be used in the process, whilst the concentrate was set to be combusted together with the bark and the wood scrap. At this high temperature level, the concentration of the waste-water by the evaporation process would cause severe fouling in a conventional exchanger. As a consequence, the client decided to equip the evaporator with a self-cleaning heat exchanger as shown in the process diagram of Figure 3.22 [1].

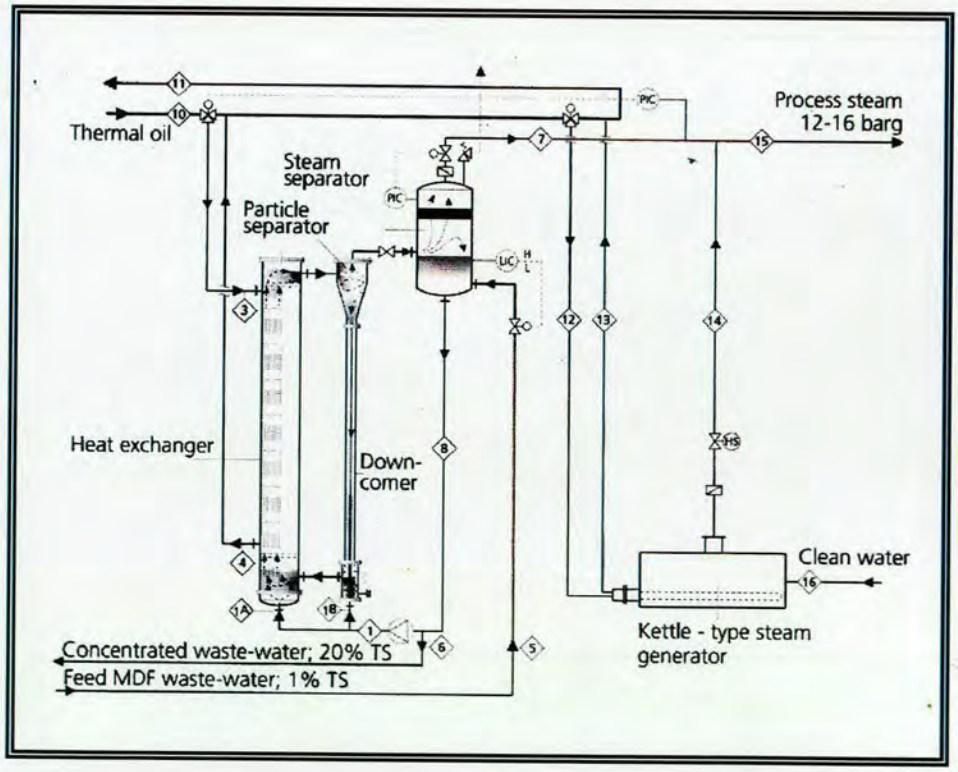

Figure 3.22: Evaporator for MDF wastewater concentrator with self-cleaning heat exchanger. Adopted from Müller-Steinhagen [1].

In the installation depicted above, the self-cleaning heat exchanger has a surface of 250 m^2 and a total height of 12 m. It utilises 4,500 kgs of cut metal wire particles with a diameter of 3 mm. In the tubes, the liquid velocity is 0.8 m/s and the volume fraction of cleaning particles is 5%. The installation successfully eliminated all related fouling problems [1,72].

3.3.3.3. PULP MILL

In December 1996, a producer of pulp and paper-board in Europe ordered two self-cleaning heat exchangers. They replaced conventional exchangers which had suffered from severe fouling due to calcium carbonate and other hard scale deposition, and which, therefore, required cleaning every two weeks [70,72]. The two heat exchangers total 250 m^2 and use cut metal wire of 2 mm diameter as cleaning particles. Both exchangers verified their ability to operate for extended periods of time without fouling. According to Klaren [70,72], due to its technological superiority, this project has been selected and subsidised by the European Commission in Brussels as a demonstration project for the efficient use of energy in industry.

3.3.3.4. FOOD PROCESSING PLANT

In August 1997, a self-cleaning heat exchanger was installed in Japan as an evaporator for the concentration of waste-water in a food processing plant. This forced circulation evaporator operates without boiling in the tubes at a temperature level of approximately 70 °C [70,72]. Conventional heat exchangers were never considered because the severely fouling liquid would cause a fouled blockage in just a few hours. After 30 months of almost continuous operation without cleaning, an inspection of the self-cleaning heat exchanger, with a heat transfer surface of 85 m^2 employing cut metal wire cleaning particles of diameter 2.5 mm, showed clean and shiny tube surfaces [70,72].

3.3.3.5. RETROFITTING EXISTING EXCHANGERS IN FOULING SERVICES

Self-cleaning technology can also be employed for the retrofit of some existing severely fouling vertical heat exchangers.

In Europe a board mill carried out the first revamp of an existing heater into a self-cleaning heat exchanger configuration, applying external circulation of cleaning particles and consisting of glass balls with a diameter of 2 mm [72]. A small existing vertical heater, used for the heating of hard scaling well water, suffered from a variety of operational problems, all caused by very severe fouling due to the precipitation of calcium carbonate. The actual heating source for the heater was the exhaust gas from a combined-cycle power generation plant. The heater revamp was carried out in April 1999. From the literature, available information suggest that since installation the unit has performed satisfactorily, maintaining a constant overall heat transfer coefficient of 2100 W/m^2K. Further to this, the outlet

temperature of the combined-cycle power generation plant has been reduced from 140 °C to 65 °C, resulting in a total heat recovery of 1.2 MW [72].

Unfortunately due to the limitations of time and space, other pertinent examples of successful heat exchanger reconfigurations, cannot readily be accommodated within the confines of this particular body of work. Therefore, for further case studies and details of burgeoning developments in self cleaning technology, the reader is referred to Müller-Steinhagen [1] and Klaren [70,72].

3.3.3.6. MARKET POTENTIAL OF THE SELF-CLEANING LIQUID-SOLID FLUIDISED BED

In general the investment costs of circulating fluidised bed heat exchangers are 60 to 110 % higher than the costs of conventional forced convection heat exchangers of industrial capacity. However, despite higher initial costs, the FBHX is superior to the conventional alternative due to significantly lower maintenance and cleaning costs.

For several cases, Rautenbach *et al.* implemented a dynamic cost evaluation to compare the costs of both systems [62]. According to their results, higher investment costs of the self-cleaning technology are ultimately recovered after 1.5 to 4.5 years at a maximum. For example, appropriated from [62], Tables 3.4 and 3.5 summarise the results of a robust investigation on a 63 m^2 heat exchanger for oil-emulsion/dumpsite leachate treatment and the estimation for the conventional alternative respectively.

According to their presented calculations (which, with regards to frequency and costs of maintenance and cleaning, have been based on detailed discussions with the relevant operators) despite its significantly higher initial costs, the fluidised bed heat exchanger has proven to be a far superior investment. Examination of the figures reveals that, with the circulating fluidised bed heat exchanger, break even point is reached after only 1.5 years of operation. Rautenbach *et al.* performed an identical analysis on five other heat exchangers, all with similar results as presented [62].

COST	PERIOD, y					
	0	1	2	3	4	5
Investment costs	-133,333					
Maintenance & cleaning – Staff		-2,666				
Material						
Replacement - Staff						-9,033
Material		-3,333				-32,666
Capital costs (8% interest)		-10,666	-12,000	-12,960	-13,996	-15,116
Total costs	-133,333	-150,000	-162,000	-174,960	-188,956	-245773

Table 3.4: Development of costs (in US $) for the case of the fluidised bed heat exchanger. From Rautenbach [62].

COSTS	PERIOD, y					
	0	1	2	3	4	5
Investment costs	-56,000					
Maintenance & cleaning – Staff		-6,020	-6,020	-6,020	-6,020	-6,020
Material		-19,133	-19,133	-19,133	-19,133	-19,133
Equipment		-2,100	-2,100	-2,100	-2,100	-2,100
Production Loss		-31,973	-31,973	-31,973	-31,973	-31,973
Replacement - Staff						
Material						
Capital costs (8% interest)		-4,480	-9,576	-15,080	-21,025	-27,445
Total costs	-56,000	-119,706	-188,509	-262,816	-343,069	-429741

Table 3.5: Development of costs (in US $) for the case of a conventional heat exchanger. From Rautenbach [62].

3.3.4. CORRELATING HEAT TRANSFER IN LIQUID-SOLID FLUIDISED BEDS

3.3.4.1. INTRODUCTION

From the discourse so far, it is fair to say that compared with single-phase flow systems, one of the most important advantages of the liquid-solid fluidised bed is the greatly enhanced overall heat transfer effectiveness. Therefore, in applying liquid fluidised bed heat exchangers more widely, there is a requirement for greater superior understanding of both the role of various operating parameters, and of the mechanisms of heat transfer connected with these systems. Such knowledge facilitates the prediction of heat transfer coefficients for any given condition, thus improving the accuracy of fluidised bed heat exchanger design.

As discussed in subsection 3.3.2.1 above, over the past 35 years, numerous studies have successfully identified the main variables influencing the heat transfer performance of liquid fluidised beds. Generally, amongst other key findings (summarised in subsection 3.3.1.), it has been proven that for any given liquid and solid phase system (i.e. particle material, size, or concentration), the measured heat transfer coefficient increases as the bed voidage increases (here bed voidage refers to the volume fraction of the continuous or liquid phase). Typically, a maximum heat transfer coefficient value occurs at a bed voidage between 0.7 and 0.75. Reports from the literature suggest that a further increase in bed voidage culminates in heat transfer deterioration.

This phenomenon is clearly demonstrated by Jamialahmadi *et al.* [82]; here, the authors measured heat transfer coefficients from a liquid-solid fluidised bed within a cylindrical tube, using water as the liquid phase, and three different sized cylindrical steel particles as the circulated solid phase. In the first instance, Figure 3.23, taken from the cited work, shows the results of preliminary experiments conducted to determine the relationship between bed voidage - measured for the three different types of cylindrical steel particles - and liquid superficial velocity. For these measurements, experiments were performed at 35 °C, 200 kPa and with the use of 300 grams of solid particles. Overall, Figure 3.23 shows that for increasing superficial velocity, the shape of the curve is characterised by a gradual increase in voidage, followed by a sharper increase and a subsequent gradual increase towards an asymptotic value of one.

Wilhem and Kwauk [83], who in 1948 studied the fluidisation of particles in water, were actually one of the first to detail the variation of bed voidage with fluid superficial velocity, confirming that their results could be correlated by the expression:

$$Re = C.\varepsilon^{n} \tag{3.24}$$

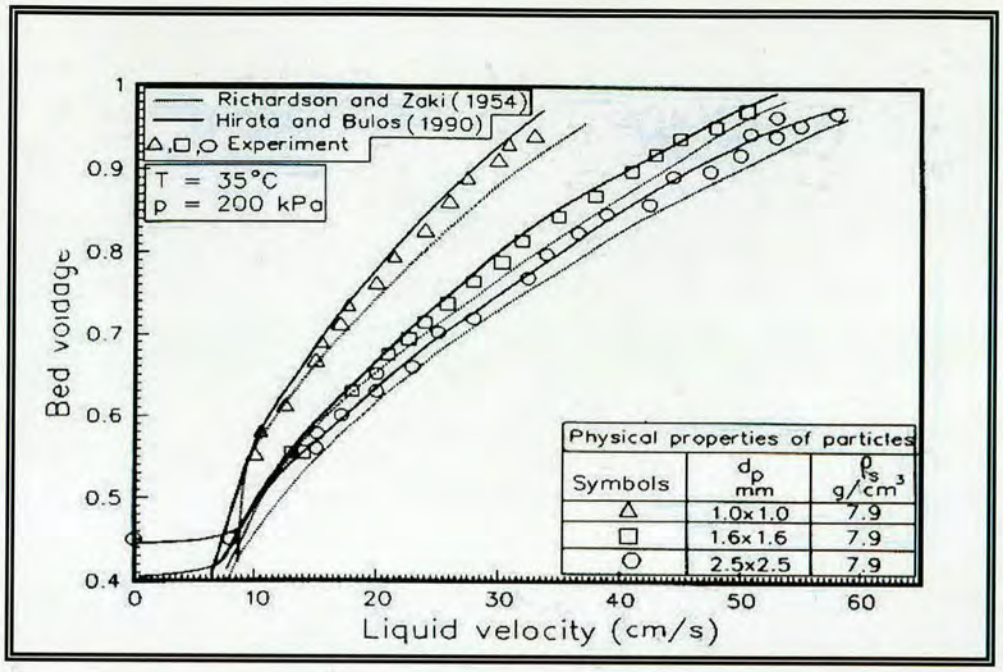

Figure 3.23: Measured and predicted bed voidage as a function of liquid superficial velocity, for LSFB using cylinder steel particles. Taken from Jamialahmadi *et al.* [82].

By 1954 Richardson and Zaki [84] confirmed some of the logic behind this choice by conveniently writing:

$$U = U_t \varepsilon^n \tag{3.25}$$

In equations 3.24 and 3.25 above, Re is the Reynolds number based on the bed diameter; C, a constant of proportionality; ε, the bed voidage; U_t, particle terminal velocity corrected for wall effect, m/s; whilst n is commonly referred to as the Richardson and Zaki exponent, and can be obtained by the equation given by Rowe [85]:

$$n = \frac{2.35\left(2 + 0.175\, Re_{pt}^{\,0.75}\right)}{\left(1 + 0.175\, Re_{pt}^{\,0.75}\right)} \tag{3.26}$$

here Re_{pt} represents the particle terminal velocity corrected for wall effects. To this regard, the experimental results of Jamialahmadi *et al.* [82], shown in Figure 3.23, are also compared with the predictions of two early models, one suggested by Richardson and Zaki (as described in equation 3.25) and the other by Hirata and Bulos [86]. Interestingly enough, the Richardson and Zaki model underpredicts the data of Jamialahmadi *et al.* [82], whilst the Hirata and Bulos equation, which is a modification of the Richardson and Zaki correlation, predicts the experimental result with better accuracy.

In continuing, Jamialahmadi *et al.* [82] performed further experiments for the measurement of heat transfer under various test conditions. For cylindrical steel particles and a bulk liquid temperature of 90 °C, Figure 3.24 shows typical results for the variation of fluidised bed heat transfer coefficient with bed voidage. Here, we can see that the change from static to fluidised bed is typically accompanied by a sharp rise in heat transfer coefficient. According to the authors', this is due to the turbulent motion of the liquid, which causes the particles to move within the fluid bulk, and towards or away from the heat transfer surface. Initially when the bed voidage is increased, achieved by an increase of liquid velocity, the heat transfer coefficient is also increased until it reaches a maximum value. Hereafter, the heat transfer coefficient stabilises momentarily, before gradually declining for further increasing liquid velocity. On the basis of such results, the authors' opine that in circulating fluidised beds, the reduction in heat transfer coefficient is mainly due to increased bed voidage - observed for higher superficial liquid velocities as illustrated in Figure 3.23 - which decreases the probability of particle-wall contact [82]. Their findings are in concordance with the conclusions of similar investigations [78-80].

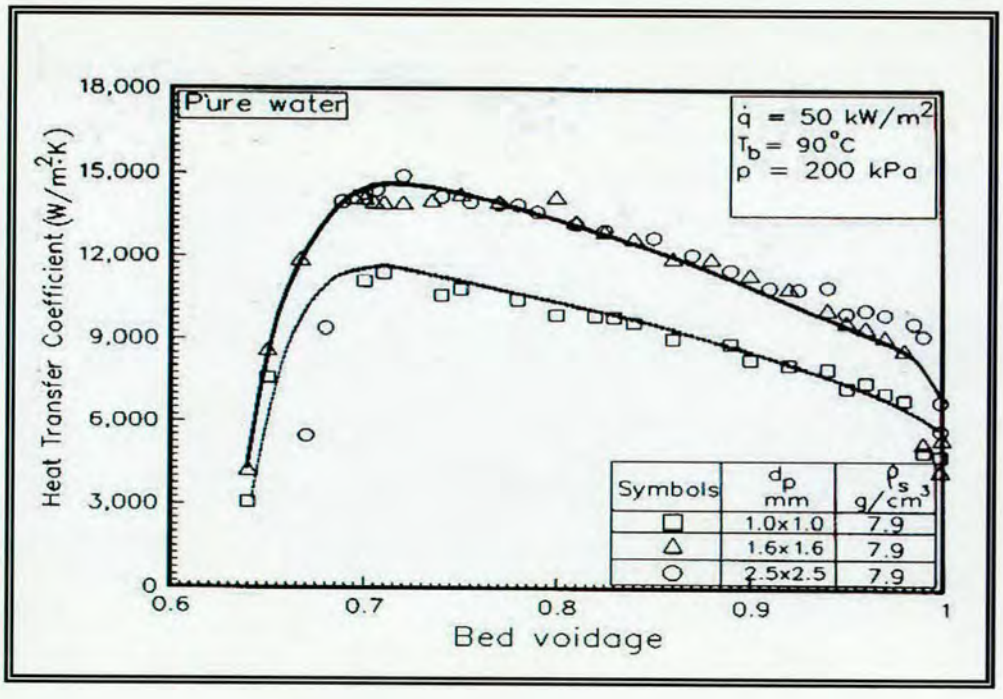

Figure 3.24: Variation in heat transfer coefficient as a function of bed voidage, for LSFB using cylinder steel particles. Adopted from Jamialahmadi *et al.* [82].

By the early 1990's, published results on heat transfer in liquid-solid fluidised beds had led to a considerable number of proposed correlations. However, the formulation of a final conclusion on the mechanism of liquid-solid fluidised bed heat transfer proved an elusive task. At the time, all correlations in the literature could be readily presented in the form:

$$\alpha = \left[\frac{\lambda_L}{d_p}\right] H.Pr^{H1} Re_p^{H2} \left[\frac{d_p}{D}\right]^{H3} \varepsilon^{H4}(1-\varepsilon)^{H5} \qquad (3.27)$$

The values of the coefficients and exponents suggested by the various researchers (i.e. *H* to *H5* in equation 3.27 above), as well as the range of applicability of the individual correlations, are given in [87]. Even though the independent investigators had been reasonably fortunate in correlating their own results, the disparity between the various correlations was found to be rather considerable. The reason for this deficiency was not only the complex nature of the fluidisation process itself, but also the use of dissimilar geometries, which invariably gives rise to different bed hydrodynamics in the separate trials. Hence, in an attempt at developing a unified theoretical model for the prediction of heat transfer, Jamialahmadi *et al.* [50,87] performed extensive investigations on the hydrodynamic and heat transfer behaviour in liquid-solid fluidised beds. Within these publications [50,87], the authors' document all existing published results for the measurement of heat transfer coefficients in liquid fluidised bed systems, comparing the available experimental data, including their own results, with the predictions of the various published correlations. Although the researchers were able to successfully model the collated information, most of the individual working correlations employed in their efforts, were limited to specific particles and usually only for Newtonian fluids.

Start Note: Fluids are classified as Newtonian or non-Newtonian, depending upon Newtons relation between shear stress and the rate of shearing strain, expressed as

$$\text{viscosity} = \frac{\text{shear stress}}{\text{rate of shear strain}} \qquad (3.28)$$

Thus the viscosity is the property of a fluid to resist the rate at which deformation takes place when the fluid is acted upon by shear forces. As a property of the fluid, the viscosity depends upon the temperature, composition, and pressure of the fluid, but is independent of the rate of shear strain. However, Newton's law of viscosity does not predict the shear stress in all fluids; in Newtonian fluids (e.g. pure water) the relation between shear stress and the rate of shearing strain is linear, as shown in Figure 3.25 taken from Welty *et al.* [88]. In non-Newtonian fluids, the shear stress depends on the rate of shear strain. While fluids deform continuously under the action of shear stress, plastics will sustain a shear stress before deformation occurs. The 'ideal plastic' has a linear stress rate-of-strain relation for stresses greater than the yield stress. Thixotropic substances (i.e. substances that show a temporary reduction in viscosity when agitated, example printer's ink) have a resistance to deformation that depends upon deformation rate and time [88]. *End Note*

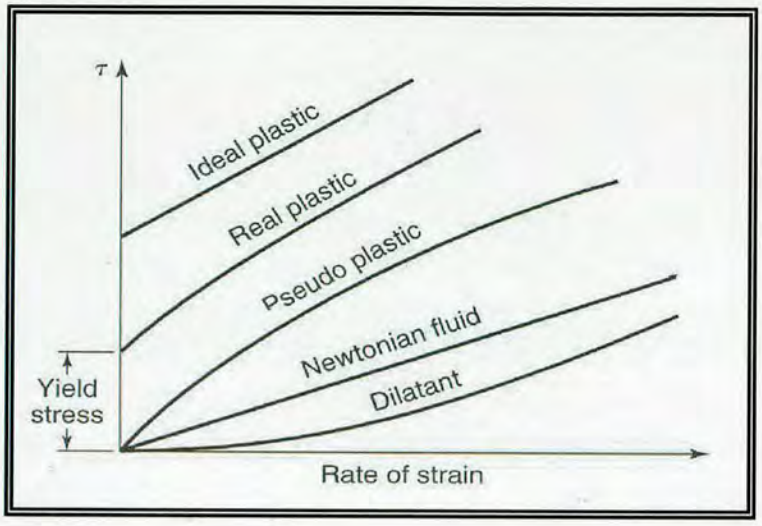

Figure 3.25: Stress rate-of-strain relation for Newtonian and non-Newtonian fluids.

In extending the works of Jamialahmadi *et al.* [50,87], Aghajani [89] obtained a large number of data over a wide range of possible operating parameters (e.g. particle density, shape and size), attempting to cover heat transfer and hydrodynamics of liquid fluidised beds for both Newtonian and non-Newtonian liquids. As a result of these exhaustive works, Aghajani *et al.* [90] have been able to present new universal models for the prediction of hydrodynamic behaviour (e.g. bed voidage) and heat transfer coefficients for liquid-solid fluidised beds in vertical pipes. Comparison with two substantial data banks (which includes more than 2200 data points for Newtonian liquids and more than 800 data points for fluidisation with non-Newtonian liquids), reveals that the proposed mechanistic model, details of which will be discussed later, significantly outperforms previously published correlations. Thus for a wide range of specified conditions, the model advocated by Aghajani *et al.* [90] is currently the most reliable tool for the prediction of hydrodynamic and heat transfer behaviour in liquid fluidised bed systems.

3.3.4.2. HYDRODYNAMICS OF LIQUID-SOLID FLUIDISED BED SYSTEMS

The hydrodynamic behaviour of liquid-solid fluidisation depends on system geometry, bed voidage, and physical properties of the liquid and solid phases. In liquid-solid fluidised beds, since the bed voidage is related to the particle-wall collision frequency, it is logical to assert that bed hydrodynamics also controls the system particle-wall collision frequency which, in turn, influences the rate of heat transfer within the bed.

In liquid-solid fluidised bed heat exchangers, the rate of particle circulation is controlled by the secondary or auxiliary liquid flow rate, as well as the main liquid flow rate. Experimental work has demonstrated that under sufficiently high overall superficial velocity, particle circulation rate will be increased with an increase of the secondary/auxiliary liquid flowrate.

However, lower secondary flow creates a higher resistance to particle fluidisation, subsequently restricting the rate of particle circulation [91]. Therefore, whenever the secondary liquid flow is closed, and the main liquid flow rate is low, particles will remain in a packed or fixed bed state. The introduction of the secondary liquid flow, coupled with an increase of the overall liquid velocity above that required for incipient fluidisation (i.e. above the minimum fluidisation velocity), causes the static bed to expand in particulate mode; here, particles move randomly within the bed, indicating operation in the conventional particulate fluidisation regime. In conventional liquid-solid fluidisation, experienced at lower superficial velocities, there clearly exists a dense bed region at the bottom of the bed and a freeboard region, devoid of solids, above the bed. Under these conditions, particles are not entrained so that external particle circulation is unnecessary. However, further increase of overall liquid flow rate causes significant particle entrainment. When the recirculation of solids to the bottom of the riser becomes necessary to maintain the bed, the fluidised bed enters the liquid-solid circulating fluidisation regime. At this point a pressure balance between the riser column and the downcomer, which can include a solids storage vessel for exchangers with external circulation, is established (see Zheng *et al.* [91] for a comprehensive pressure drop analysis effectuated on a liquid-solid circulating fluidised bed, operated with a return system including a solids storage vessel).

The boundary between the liquid-solid conventional fluidisation and the circulating fluidisation regimes is still not well defined. According to Liang *et al.* [67], the transition to the liquid-solid circulating fluidisation regime is at the velocity where particle circulation rate becomes zero with decreasing liquid velocity. Liang *et al.* [67] termed this experimentally determined velocity the critical transition velocity, also known as the minimum transport velocity or the incipient significant entrainment velocity. As evidenced in [91], this critical transition velocity can be affected by the operating conditions and geometric setup of the liquid-solid fluidised bed.

Of the discussed regimes, conventional liquid-solid fluidisation has been extensively studied [65,83,84,94,95]; as mentioned previously, by proposing a simple relationship between the operating liquid velocity and the bed voidage, Richardson and Zaki [84] made a significant early contribution to this field of science. With regards to flow structure, it has long been considered that liquid-solid fluidisation is a uniformly dispersed homogeneous fluidisation in both the axial and the radial directions, with or without particle circulation (internal or external), and regardless of the fluidisation regime. In other words, all particles are considered to be uniformly suspended so that radial and axial distributions of the phase hold-ups are uniform. This assumption of homogeneity considers liquid-solid fluidisation as an ideal system, and forms the basis of Richardson and Zaki's work. Experimental results confirm that almost all liquid-solid systems fluidised in the conventional low liquid velocity

regime are indeed homogeneous [65,83,84,94,95]. However, information regarding the more recently defined circulating fluidised regime is rather limited, except to say that the flow structure of liquid-solid systems operated at the higher liquid velocities necessary for circulating fluidisation, has also been considered uniform [96]. To redress the balance, Zhu et al [67,91] have implemented studies aimed at clarifying the flow or hydrodynamic characteristics of the circulating fluidisation regime. Though undoubtedly significant, these findings have yet to be sufficiently corroborated by other independent researchers, and are therefore debatable.

3.3.4.2.1. MODELLING 'VELOCITY-VOIDAGE' RELATIONSHIP IN FBHXS

As earlier intimated (see 'introduction' 3.3.4.1), correlations available for the prediction of heat transfer coefficients are strong functions of the bed voidage. Therefore accurate knowledge of this parameter is crucial for the reliable estimation of heat transfer in liquid fluidised bed systems. Jamialahmadi and Müller-Steinhagen [97] compiled all published correlations, as well as conditions recommended for their application, which describe the relationship between operating liquid velocity and bed voidage. Most of these correlations were empirical, applying to specific particles across a restricted range of Reynolds numbers, and usually only for Newtonian fluids. Consequently, a new model covering a wider scope of fluids and operating parameters has been suggested by Aghajani [89]:

$$\varepsilon = \left(\frac{U}{U_t}\right)^{1/Z} \left(1 - \varepsilon_{SB}\right) + \varepsilon_{SB} \tag{3.29}$$

The fluidisation index, Z, can be obtained from [90]:

$$Z = \frac{0.65\left(2 + 0.5Re_{p\infty}^{0.65}\right)}{\left(1 + 0.5Re_{p\infty}^{0.65}\right)} \tag{3.30}$$

Meanwhile, in equation 3.29 above, the static bed voidage, ε_{SB}, can be calculated according to the following expression for spherical particles [90]:

$$\varepsilon_{SB} = \frac{0.15}{\left(\frac{D_e}{d_p} - 1\right)} + 0.38; \qquad \frac{D_e}{d_p} \geq 2.033 \tag{3.31}$$

here D_e represents the equivalent or hydraulic mean diameter of the fluidised bed.

Returning to equation 3.29, U_t symbolises the particle terminal velocity corrected for wall effect. Particle settling velocity is essential for the prediction of bed voidage, as well as heat and mass transfer coefficients. It is well known that the walls of the column exert an

additional retardation effect on a settling solid particle. The extent of this wall effect is usually quantified by introducing a wall factor defined in [90] as:

$$W_f = \frac{\text{Terminal settling velocity in presence of wall effect}}{\text{Terminal settling velocity in absence of wall effect}} = \frac{U_t}{U_\infty};\ 0 < W_f \leq 1 \qquad (3.32)$$

From the work of Aghajani [89] it has been determined that the following equation , proposed by Richardson and Zaki [84], is well suited for calculating particle terminal velocity corrected for wall effect, U_t:

$$\mathrm{Log}_{10}\left(\frac{U_\infty}{U_t}\right) = \frac{d_p}{D_e} \qquad (3.33)$$

When a particle of size d_p falls through a fluid whilst moving at its terminal velocity, the forces which act on the particle are said to be in dynamic equilibrium. In other words, the effective weight (gravitational force minus buoyancy force) is equal to the drag force. For the particle terminal settling velocity in the absence of wall effect, U_∞, this leads to:

$$U_\infty = \left[\frac{4 d_p (\rho_p - \rho_L) g}{3 C_D \rho_L}\right]^{1/2} \qquad (3.34)$$

Equation 3.34 may be written in terms of the free fall particle Reynolds number:

$$Re_{p\infty} = \left[\frac{4 \rho_L d_p^3 (\rho_p - \rho_L) g}{3 C_D \mu_L^2}\right]^{1/2} \qquad (3.35)$$

Equation 3.35 shows that the terminal velocity of a particle is inversely proportional to the drag coefficient, C_D. Theoretically, the drag coefficient can be obtained from the solution of the equation of momentum for the system; as stated by Aghajani *et al.* [90], in the absence of inertial terms the expression is as follows:

$$C_D = \frac{24}{Re_{p\infty}} \qquad (3.36)$$

As the particle Reynolds number increases, the inertial terms become increasingly significant in the momentum equation and no analytical solutions are possible under such conditions. Therefore, almost all drag coefficients reported for higher Reynolds number are experimentally obtained. These results are generally presented in graphical form as a complex function of the flow conditions. Most of the experimental work has been reviewed

and critically evaluated by several investigators [98,99]. Unfortunately, as the unknown velocity, U_∞, appears in both $Re_{p\infty}$ and C_D, the form of these correlations is not convenient for the calculation of the particle free fall velocity for a given liquid-solid system. According to Aghajani *et al.* [90], this difficulty is overcome by writing equation 3.35 in terms of the Archimedes number, which is not a function of the terminal velocity.

$$Ar = \frac{3}{4} C_D Re_{p\infty}^2 = \frac{g \rho_L (\rho_p - \rho_L) d_p^3}{\mu_L^2} \tag{3.37}$$

Equation 3.37 shows that the particle free fall Reynolds number is only a function of Archimedes number and can be best presented in the form:

$$Re_{p\infty} = F(Ar) \tag{3.38}$$

Hartman *et al.* [100] proposed the following explicit relation for the prediction of the free fall velocity of a spherical particle in an infinite medium. As claimed by Aghajani [89], for Newtonian fluids, this is presently the best available correlation for calculating $Re_{p\infty}$:

$$\mathrm{Log}_{10} Re_{p\infty} = P[\mathrm{I}] + \mathrm{Log}_{10} R[\mathrm{I}] \tag{3.39}$$

where

$$P[\mathrm{I}] = [(0.0017795.\mathrm{I} - 0.0573)\mathrm{I} + 1.0315]\mathrm{I} - 1.26222$$

$$R[\mathrm{I}] = 0.99947 + 0.01853 \sin(1.848.\mathrm{I} - 3.14) \tag{3.40}$$

And

$$\mathrm{I} = \mathrm{Log}_{10} Ar \tag{3.41}$$

Few attempts have been made to establish the functional dependence of Archimedes number on particle Reynolds number for solutions with non-Newtonian flow behaviour. However, by non-linear regression analysis of all published data available at the time, Aghajani [89] determined improved values for the constants in equation 3.38, correlating the free fall velocity of particles in non-Newtonian solutions as follows:

$$Re_{p\infty} = 0.334\, Ar^{0.654} \tag{3.42}$$

Aghajani *et al.* [90] compared the new model for the prediction of bed voidage, expressed in equation 3.29, to a large experimental data base including more than 1,000 data from the literature and their own measurements [89]. According to the authors, an average error of 6.18% was achieved for Newtonian liquids, whilst for non-Newtonain fluids a mean error of

6.95% was obtained. A typical result taken from the authors work is demonstrated in Figure 3.26, which illustrates a comparison between the bed voidage data for different investigators [82-84,86,101-108] and values calculated by equation 3.29. Aghajani *et al.* [90] have also compared the aforementioned data base of Aghajani [89] with a plethora of published models for the prediction of the 'bed voidage vs. velocity' relationship. The investigators report that the correlation of Hartman *et al.* [108] performed best for Newtonian liquids (5.79% average error), whilst the correlation of Letan [109] achieved an average error of 8.61% for non-Newtonian liquids. Overall, the authors' findings indicate that for the whole range of investigated fluids, none of the published correlations outperform the bed voidage equation presented in equation 3.29.

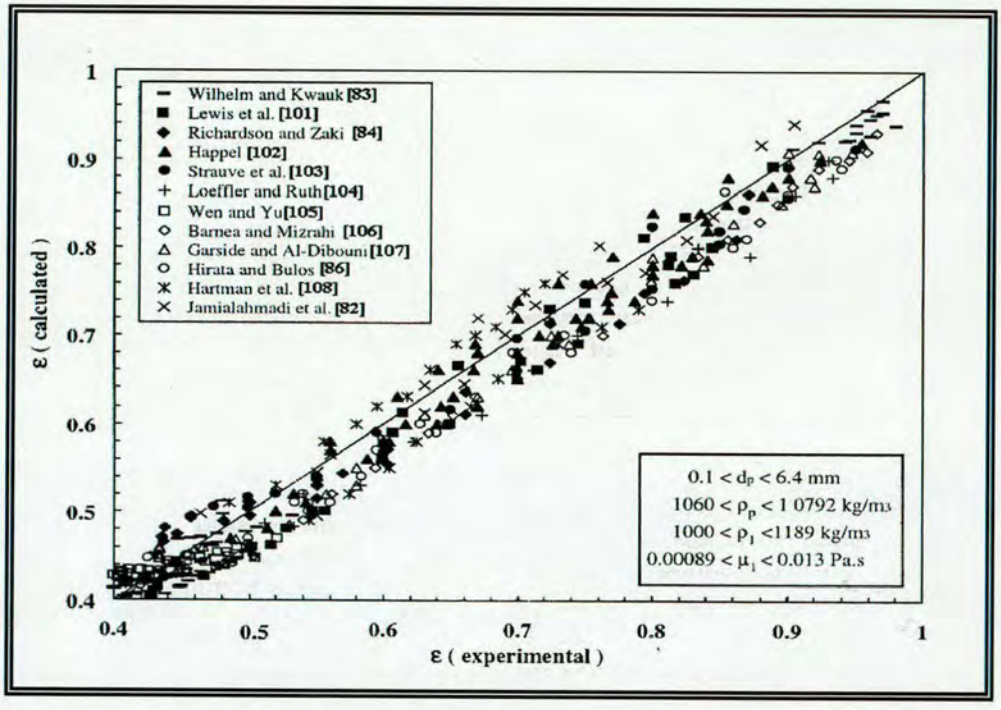

Figure 3.26: Comparison of measured bed voidages with values calculated from equation 3.29 for Newtonian & non-Newtonian solutions. From Aghajani *et al.* [90].

3.3.4.3. THE UNIFIED LIQUID-SOLID FLUIDISED BED HEAT TRANSFER MODEL

In the opinion of Aghajani *et al.* [90] heat transfer to or from liquid-solid fluidised beds must be influenced by the intensity of the interchange between the solid particles and the heater surface, which is, in turn, a function of the velocity of the particles and the frequency and the density of particle contact with the heater surface. On this basis, the authors formulated a new liquid-solid fluidised bed heat transfer model predicated on the following assumptions:

a. The major resistance to heat transfer is a liquid film near the heat transfer surface.

b. The heat transfer surface itself is divided into two zones where heat transfer is governed by different mechanisms. In the first instance, due to the movement of solid particles, there is a steady flow of fluid elements from the bulk of the fluid to the heat transfer surface area affected by particles, A_p, and vice versa. The fluid elements reside for a finite time at the surface, until they return to the bulk in the wake of solid particles scouring the heat transfer surface. In this region, A_p, heat is transferred into the fluid by transient heat conduction from the heat transfer surface. Heat is also transferred by conduction to the particles while they are in contact with the heat transfer surface.

c. On the remaining sections of the heat transfer surface that are not in contact with particles, A_c, heat is transferred to the liquid by forced convection.

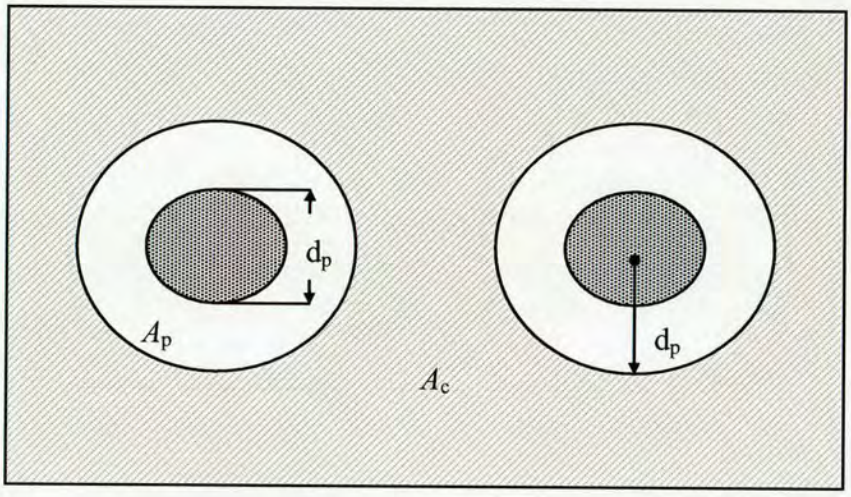

Figure 3.27: Area of heat transfer surface affected by particles, A_p, and by forced convection, A_c, in liquid-solid fluidisation.

Therefore, in liquid-solid fluidised bed systems, at any given moment, heat transfer is composed of two parallel mechanisms, occurring in separate zones of the heat transfer surface as shown in Figure 3.27

Han and Griffith [110] have shown that the area from which the hot liquid layer is pumped away by a vapour bubble leaving the heat transfer surface is πd^2_b. Since small bubbles and solid particles behave similarly (see Jamialahmadi and Müller-Steinhagen [111]) the area of the heat transfer surface affected by a single particle should also be πd^2_p.

The following approach, by Aghajani *et al.* [90], is hence analogous to nucleate boiling heat transfer if "vapour bubble" is replaced by "particle" and "latent heat transfer" by "particle conduction". As elucidated by the authors', time-averaged heat transfer coefficients may be additive if it is assumed that both mechanisms (heat transfer by fluid convection and heat

transfer by transient heat conduction from the heat transfer surface) coexist over the entire heat transfer surface. Therefore in liquid fluidised bed systems, the total heat transfer coefficient, α_{LS}, can be predicted according to:

$$\alpha_{LS} = \alpha_c + \alpha_p \tag{3.43}$$

Aghajani *et al.* [90], suggest that the forced convective heat transfer coefficient, α_c, be calculated from the Gnielinski [112] equation for heat transfer during turbulent flow in pipes if it is modified to apply for local conditions:

$$Nu = \frac{\alpha_c D_e}{\lambda_L} = \frac{\frac{f_i}{8}(Re-1000)Pr}{1+12.7\sqrt{\frac{f_i}{8}}\left(Pr^{2/3}-1\right)}\left[1+\frac{1}{3}\left(\frac{D_e}{L}\right)^{1/3}\right] \tag{3.44}$$

The friction factor, f_i, for turbulent flow may be calculated according to Filonenko [92]

$$f_i = \left[1.82\ \mathrm{Log}(Re)-1.64\right]^{-2} \tag{3.44a}$$

The authors' state, that an average relative error of 5.7% for Newtonian solutions and 8.6% for non-Newtonian solutions confirms a good agreement between their measured single-phase data and the predictions of the modified Gnielinski equation given above.

Quoting Aghajani *et al.* [90], in equation 3.44 above the heat transfer coefficient for the particle-controlled area, α_p, also includes two parallel heat transfer coefficients as shown below:

$$\alpha_p = \alpha_{wl} + \alpha_{wp} \tag{3.45}$$

Here, α_{wl} is the heat transfer coefficient from the wall to the adjacent liquid layer and α_{wp} is the heat transfer coefficient from the wall to the particles. Following the departure of a particle and of the hot liquid layer, the liquid at T_b (i.e. bulk processing temperature) from the main body of the fluid, flows into the area of influence πd_p^2 and comes into contact with the heating surface at T_w (i.e. heat transfer surface temperature) as claimed by Aghajani *et al.* [90]. The authors' suggest that in the area of influence, assuming pure conduction into the liquid, this can be modelled as conduction to a semi-infinite liquid with a step change in temperature ($\Delta T = T_w - T_b$) at the surface:

$$\frac{q_p}{A} = \frac{\sqrt{\lambda \rho c}\,\Delta T}{\sqrt{\pi t}} \tag{3.46}$$

The hot layer is replaced with a frequency f, which is equal to the frequency of the collision of particles with the heat transfer surface. Hence, similar to the study of Mickic and Rohsenow [113] for pool boiling, the average heat flux over the area of influence would be:

$$q_{\mathrm{p}}^{"} = \frac{2\sqrt{\lambda_{\mathrm{L}}\,\rho_{\mathrm{L}}\,C_{\mathrm{p,L}}}\,\sqrt{f}\,\Delta T}{\sqrt{\pi}} \tag{3.47}$$

Taking into account the heat transfer to the particles by conduction when they are in contact with the heat transfer surface, Aghajani *et al.* [90] state that equation 3.47 can be reformulated as below:

$$q_{\mathrm{p}}^{"} = \left[\frac{2}{\sqrt{\pi}}\sqrt{\lambda_{\mathrm{L}}\rho_{\mathrm{L}}C_{\mathrm{p,L}}} + \left(\frac{\pi d_{\mathrm{p}}^{2}}{\pi D_{\mathrm{e}}^{2}}\right)\sqrt{\lambda_{\mathrm{p}}\rho_{\mathrm{p}}C_{\mathrm{p,p}}}\right]\sqrt{f}\,\Delta T \tag{3.48}$$

Therefore, the heat transfer coefficient for the particle-controlled area can now be obtained from:

$$\alpha_{\mathrm{p}} = \left[\frac{2}{\sqrt{\pi}}\sqrt{\lambda_{\mathrm{L}}\rho_{\mathrm{L}}C_{\mathrm{p,L}}} + \left(\frac{d_{\mathrm{p}}}{D_{\mathrm{e}}}\right)^{2}\sqrt{\lambda_{\mathrm{p}}\rho_{\mathrm{p}}C_{\mathrm{p,p}}}\right]\sqrt{f} \tag{3.49}$$

In the equations above, liquid and particle properties are denoted by subscripts L and p respectively, $(\pi d_{\mathrm{p}}^{2}/\pi D_{e}^{2})$ is dimensionless and takes into account the relative area of contact between particles and the heat transfer surface, and f represents the number of particle-wall collisions per unit time of any individual particle, or group(s) of selected particles, within a fluidised system (units of s^{-1}).

By analogy to the kinetic theory of gases (applied to randomly moving solid particles in a fluidised bed) Martin [114,115] has shown that the collision frequency, f, can be described by:

$$f = \frac{1}{t_{\mathrm{c}}} = \frac{C^{"}.U_{\mathrm{p}}}{4d_{\mathrm{p}}} \tag{3.50}$$

For gas and liquid fluidisation, $C^{"}$ is a constant between 2 and 4. Although determining the particle velocity, U_{p}, in fluidised beds is rather difficult and requiring of special equipment, several investigators, such as Latif and Richardson [116], have speculated that in fluidised beds the particle velocity is proportional to the superficial liquid velocity and that is must be zero at $\varepsilon = \varepsilon_{\mathrm{SB}}$. Therefore, in the work of Aghajani *et al.* [90] it is assumed that:

$$U_p = m.U(\varepsilon - \varepsilon_{SB})^a \tag{3.51}$$

Considering that particle contact frequency must be zero at $\varepsilon = 1$, and using equation 3.51, the authors' have modified equation 3.50 to the form:

$$f = Y\left(\frac{U}{d_p}\right)(\varepsilon - \varepsilon_{SB})^a(1-\varepsilon)^b \tag{3.52}$$

In the above equations m, a, and b are constants. By analysing a copious number of experimental data for both Newtonian and non-Newtonian liquid-solid fluidised beds, Aghajani *et al.* [90] have found that for good agreement with experimental data, equation 3.52 above becomes:

$$f = 1.5\left(\frac{U}{d_p}\right)(\varepsilon - \varepsilon_{SB})^{0.2}(1-\varepsilon)^{1.8} \tag{3.53}$$

From these equations we see that, as proclaimed, the collision frequency of contacting particles, f, is indeed a function of the bed voidage, and is thus related to the hydrodynamics of the system. Hence, from the model presented in equation 3.53, it is at once apparent that the liquid-solid fluidised bed heat transfer coefficient is intrinsically linked to the collision frequency of contacting particles, f. According to Aghajani *et al.* [90] for packed or static beds the collision frequency, as calculated by the above model, is zero, generally reaching a maximum for a bed voidage between 0.65 and 0.85 - in accordance with the maximum achievable heat transfer coefficient - before decreasing with further increasing bed voidage. This trend is demonstrated in Figure 3.28, a typical set of results from the authors' work, depicting the calculated collision frequency as a function of bed voidage; here, aqueous solutions of sugar and carboxymethylcellulose (CMC) were adopted as the investigated Newtonian and non-Newtonian liquids.

Returning to the correlation postulated by Aghajani *et al.* [90] and expressed in equation 3.43, taken from the investigators work Figure 3.29a shows typical predictions for different particles fluidised in pure water (a Newtonian liquid). As indicated in the plots, due to the presence of the suspended solids, the heat transfer coefficient increases to a maximum value for a bed voidage between 0.6 and 0.8. For additional information, the same data are plotted as a function of particle Reynolds number in Figure 3.29b. The calculated trends exhibit excellent agreement with the experimental data of Aghajani [89] and of all previous investigators.

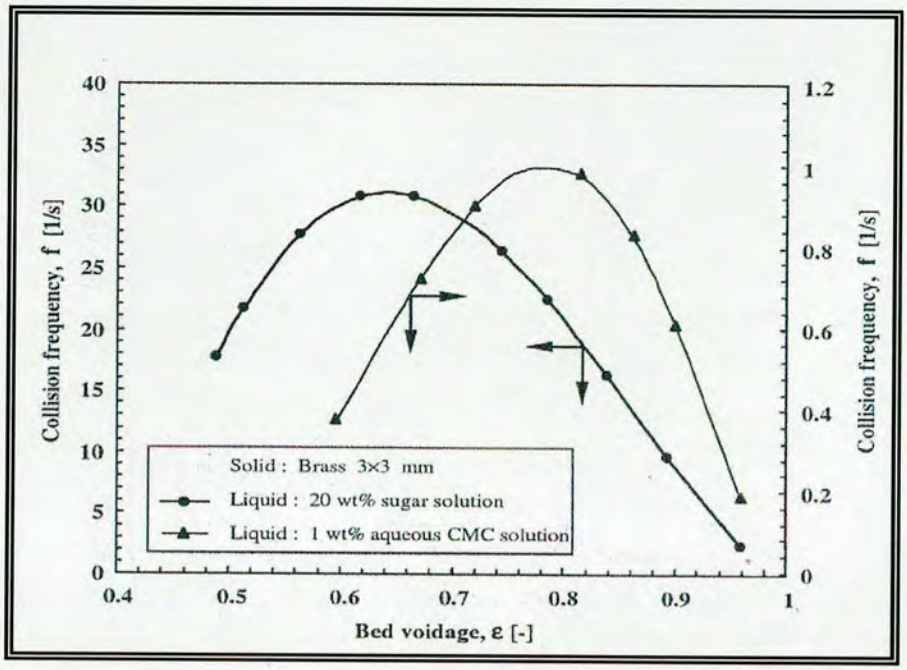

Figure 3.28: Collision frequency, f, as a function of bed voidage, ε, for aqueous solutions of sugar and carboxymethylcellulose (CMC). Adopted from Aghajani *et al.* [90].

In concluding their work, Aghajani *et al.* [90] performed an exhaustive comparison between the measured and calculated values of heat transfer coefficients for 40 published correlations, including their own suggested model, as listed in Table 3.6. As earlier emphasised (referring to subsection 3.3.4.1) for the purpose of this exercise more than 2200 data points for liquid-solid fluidised beds with Newtonian liquids, and more than 800 data points for fluidisation with non-Newtonian liquids, were assimilated from the publications of the authors' featured in the presented list. Bed voidage was calculated according to equation 3.29, as given by Aghajani [89]. The average relative errors (A.R.E) and the standard deviation of prediction, (S.D), for all enumerated correlations are defined as follows:

Relative error -

$$\left|\Delta_{rel}\alpha\right| = \left|\left(\alpha_{cal} - \alpha_{exp}\right)/\alpha_{exp}\right| (\%) \tag{3.54}$$

Average relative error -

$$\left|\text{A.R.E}\right| = \sum\left|\Delta_{rel}\alpha\right| / i \quad (\%), \tag{3.55}$$

Where i = number of data sets

Standard deviation of prediction (S.D) -

$$\text{S.D} = \left(\sum\left(\left|\Delta_{rel}\alpha\right| - \left|\text{A.R.E}\right|\right)^2 / i\right)^{0.5} \quad (\%), \tag{3.56}$$

Where i = number of data sets

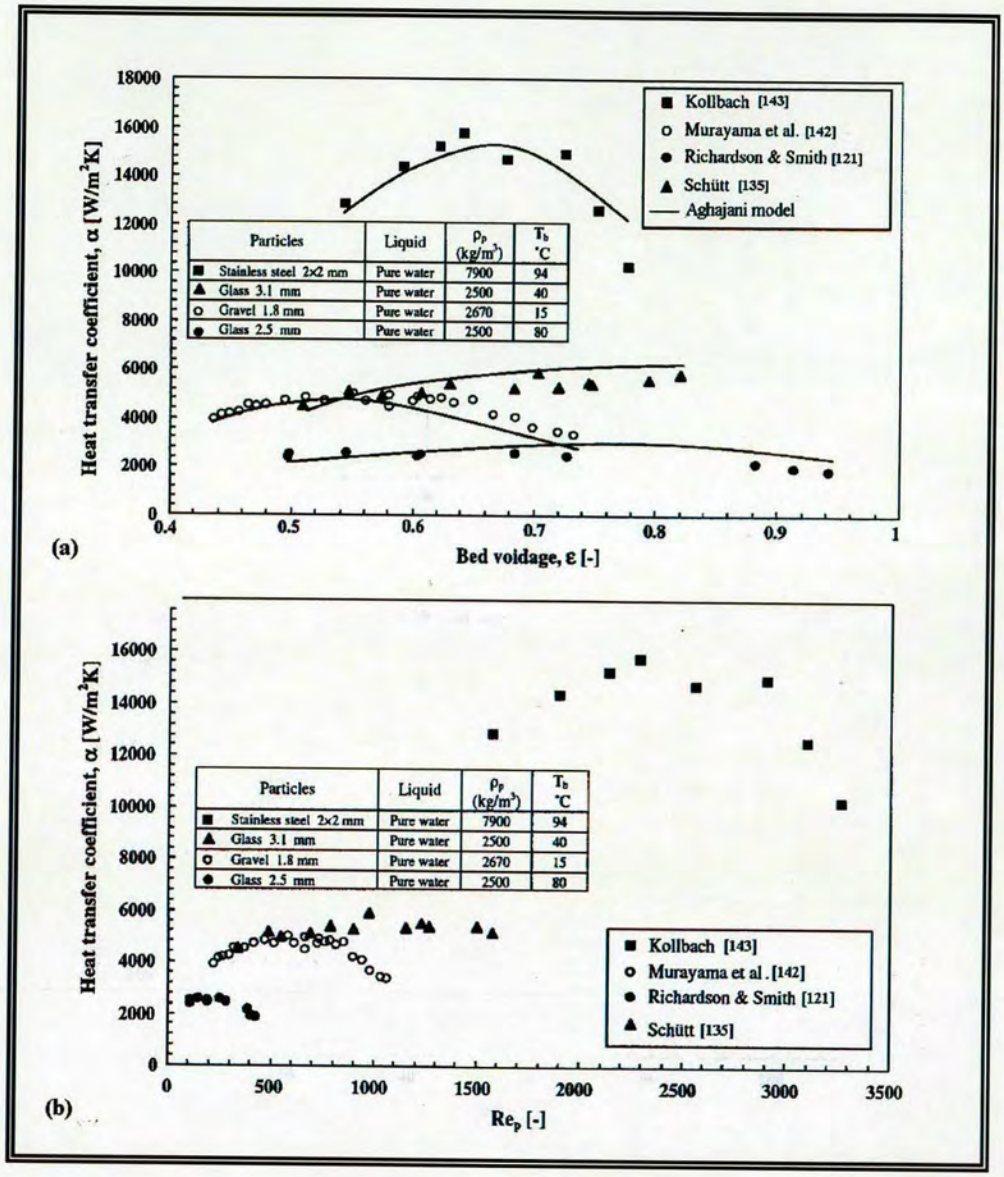

Figure 3.29: (a) Comparison of measured and predicted heat transfer coefficients for fluidisation in pure water,

(b) Heat transfer coefficient as a function of particle Reynolds number for fluidisation in pure water. From Aghajani *et al.* [90].

No.	Author (s)	Newtonian Liquids			Non-Newtonian Liquids		
		A.R.E (%)	S.D (%)	Prediction	A.R.E (%)	S.D (%)	Prediction
1	Wasser and Mardus [117]	48.8	28.7	-	33	16.4	- -
2	Lemlich and Caldas [118]	94.2	14.2	- -	48.6	20.7	- -
3	Richardson and Mitson [119]	66	36.3	±	652	384	+ +
4	Ruckenstein et al. [120]	59.5	39.5	±	96.3	101	±
5	Richardson and Smith [121]	129.8	152.1	- -	65.2	52.8	+ +
6	Wassmund and Smith [80]	73.8	108.9	±	-	-	-
7	Hamilton [122]	43.7	26.6	±	125.6	83.8	+ +
8	Tripathi and Pandey [123]	70.5	11.2	- -	76.8	7.2	- -
9	Brea and Hamilton [78]	32.8	17.8	±	185	113	+ +
10	Varma et al. [124]	81.5	55.9	- -	-	-	-
11	Schimanski et al. [125]	81.2	10.3	- -	91.5	3.6	- -
12	Syromyatnikov et al. [126]	158.7	114.9	+ +	112.6	103	±
13	Richardson et al. [81]	94.9	65.9	+	163.6	118	+ +
14	Allen et al. [127]	35.8	19.5	±	89	79	+
15	Baker et al. [128]	80.9	80.2	-	81.5	77.2	±
16	Khan et al. [129]	109	78.4	+ +	189.8	135.6	+ +
17	Tusin et al. [130]	40.4	25.3	- -	61.5	59.4	±
18	Mersman et al. [131]	40.2	24.6	±	125.9	73.3	+ +
19	Kato et al. [132]	36.6	23.2	±	196.3	89.3	+ +
20	Wehrman and Mersmann [133]	42.8	20.4	±	105.6	66.7	+
21	Schütt [134]	46	23.2	±	152.2	93.1	+ +
22	Schütt [135]	46.8	16.9	±	94.2	70.7	+
23	Khan et al. [136]	36.2	24.8	±	53.5	55.7	±
24	Murayama et al. [137]	45.3	32.2	±	45.5	48.2	±
25	Chiu and Ziegler [79]	78.6	16.6	- -	249	126	+ +
26	Juma and Richardson [138]	41.7	19.6	-	44	42.2	±
27	Coulson and Richardson [139]	47.5	35.2	+	98.6	96.1	+
28	Kim et al. [140]	30.7	14.5	-	52.6	57.3	±
29	Midoux et al. [141]	45.3	31.9	+	88.7	55	+
30	Murayama et al. [142]	43	27.3	±	38.2	34.5	±
31	Kollbach [143]	38.6	15.3	±	80.2	58.3	+ +
32	Grewal and Zimmerman [144]	38.1	28	±	138	131	+
33	Kang et al. [145]	38.7	21.5	±	32.2	32.8	±
34	Macias-Machin et al. [146]	47	31.7	- -	88.6	4.4	- -
35	Jamialahmadi and Müller-Steinhagen [97]	35.8	16.3	±	189	216	±
36	Haid et al. [147]	36.7	22.4	±	135.5	83	+ +
37	Jamialahmadi et al. [82]	38.9	17.3	±	127	161	+ +
38	Jamialahmadi et al. [87]	39.3	16.7	±	123	194	+ +
39	Haid [148]	39.7	15.6	±	121	71	+ +
40	**Aghajani et al. [90]**	**19.9**	**13.4**	±	**21.1**	**16.1**	±

Table 3.6: Comparison of measured data and values predicted by published models. From Aghajani et al. [90].

Comparing the average relative errors and the standard deviation of the values predicted by all published correlations, it is evident from the portrayed list, that having achieved an overall average relative error of 19.9% for Newtonian liquids and 21.1% for non-Newtonian liquids, Aghajani *et al.*'s [90] newly developed model for the prediction of heat transfer in liquid-solid fluidised beds provides better results than all other indicated correlations, thus validating the

veracity of the model presented in equation 3.43. Table 3.6 also indicates whether the highlighted correlations tend to underpredict "-" or overpredict "+" the measurements. Correlations with "- -" or "+ +" have a high tendency to underpredict or overpredict the measurements, and for correlations with "±"Aghajani *et al.* [90] could find no clear tendency.

3.4. SCALE FORMATION DURING BOILING HEAT TRANSFER

3.4.1. INTRODUCTION

As has been discussed so far, the causes of fouling of heat transfer surfaces are many, varied, and extremely complex. Several investigators have studied fouling mechanisms in an effort to understand, quantify, and develop remedial or preventative treatment. Most of these studies have been devoted to fouling during forced convective heat transfer, with hardly any information available on fouling during boiling heat transfer. An observation recently confirmed by Jamialahmadi and Müller-Steinhagen's [149] review on the mechanisms of boiler fouling, which reveals that experimental fouling data under boiling conditions in general, and under sub-cooled flow boiling in particular, are scarce and incomplete (background information on both heat exchanger fouling, and boiling heat transfer has been provided in sections 2.2 and 2.3 respectively). Oufer *et al.* [150] investigated fouling during sub-cooled flow boiling of organic fluids. The researchers studied the effect of surface temperature, velocity, and initial bulk concentration, on chemical reaction fouling of styrene dissolved in pentane during sub-cooled flow boiling. Their results showed that the initial fouling rates increased with increasing surface temperature according to an Arrhenius term, and that the initial fouling rates decreased with increasing flow velocity. Oufer *et al.* [150] also performed experiments to ascertain the effect of flow velocity at relatively high surface temperatures (i.e. temperatures approaching the melting point of the polymer); as claimed by the authors', the shearing action of the adjacent fluid causes the removal term to increase, consequently resulting in fouling rate degredation at higher velocities. Bulk styrene concentration was found to have a somewhat controversial effect, as it only appeared to increase fouling rates at suitable conditions of high surface temperature and low velocity. However, despite being informative, one must accentuate the fact that Oufer *et al.*'s pronounced results did not lead to any generalised conclusions, and cannot be applied to scale formation in aqueous boiling solutions.

Under most conditions, fouling is more severe during boiling heat transfer on account of the following [151]:

— Due to the mechanisms of bubble formation, the local concentration of foulants will increase near the heat transfer surface.

— Heat transfer coefficients for nucleate boiling are considerably higher than forced convection values and are, therefore, more affected by the formation of an additional heat transfer resistance.

— Boilers operate at elevated temperatures and pressures. Overheating of pipes may cause plastic deformation and fracture.

— The interaction of fouling and bubble nucleation phenomena may lead to excessive corrosion of the heat transfer surfaces.

Scale deposition has a substantial effect on the boiling phenomena, by effectively altering the characteristics of the heat transfer surface. Deposits also change the interfacial tension between the growing bubbles and the heated surface. Jakob and Link [152] found that by adding a wetting agent to reduce the surface tension by 45%, the nucleate boiling heat transfer coefficient increased by 23% for the same heat flux. Similar results were obtained by Insinger and Bliss [153]. Initial crystal formation on the surface provides sites for rapid crystal growth. Cavities and impurities on the surface also have a similar effect. Furthermore, it is generally believed that formed deposits provide favourable nucleation conditions, thus reducing the wall superheat necessary for bubble generation. Therefore, as bubble formation is of major significance in the problem of fouling during boiling heat transfer, many of the studies undertaken have explored the effect of bubble formation on heat transfer, and, as discussed following, a host of these researchers have tried to correlate the effects observed.

In 1929, based on experimental observations, Partridge and White [154] proposed the following mechanisms to explain the origin of rings occurring on the heat transfer surface: owing to the local increase in heat transfer surface temperature under the bubble and to fast evaporation at the triple interface, steam and water would throw down a deposit; it would tend to be redissolved if the solubility increases with increasing temperature. To explain the origin of different types of deposits, Freeborn and Lewis [155] suggested a dynamic mechanism similar to that of Partridge and White [154].

The effect of short-time calcium sulphate deposition on nucleate boiling heat transfer has been studied by Palen and Westwater [156]. Tests were made under pool boiling conditions on strips made from aluminium foil. Two types of deposit were observed: one occurring beneath bubbles formed by intermittent boiling sites, and the other on those parts of the surface where no boiling sites were active. Palen and Westwater [156] measured the difference between the strip surface temperature and the bulk solution temperature, as a function of time for constant heat fluxes. From the shape of such curves, for example see Figure 3.30 taken from said work, they defined three different regions.

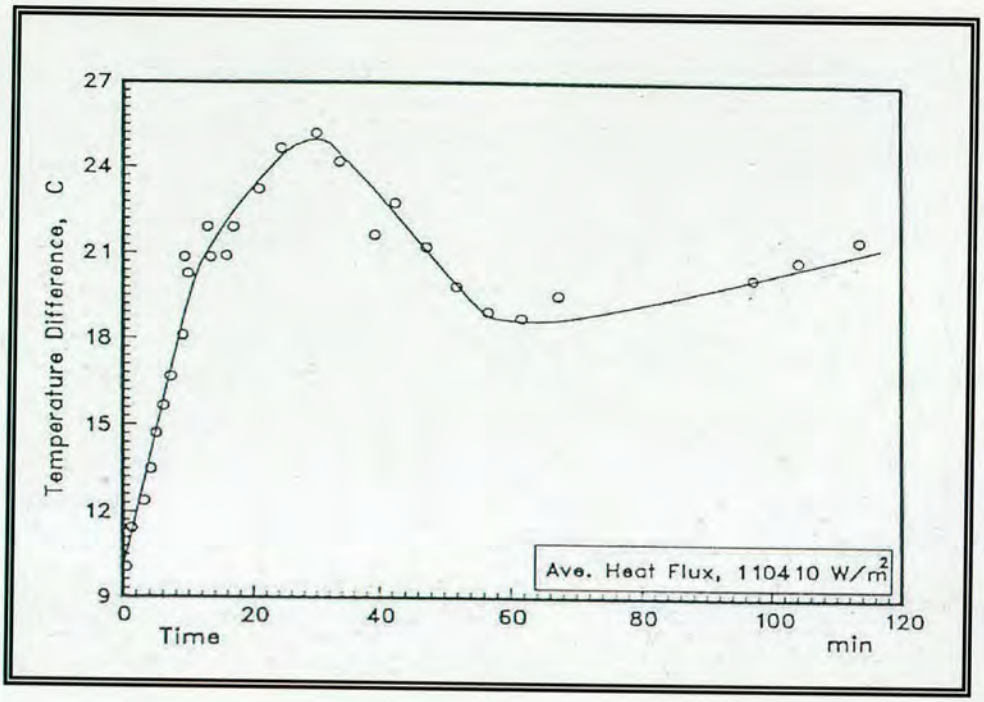

Figure 3.30: The difference between surface and bulk temperatures as a function of time for $CaSO_4$ solution. From Palen *et al.* [156].

In the first two regions the temperature driving force, ΔT, initially increased sharply to a maximum value, before falling to a minimum. In the third region, ΔT increased gradually. Equations for deposition rate and surface temperature were developed from basic mass transfer relations, indicating that the deposition rate is proportional to the heat flux squared. A similar result was found by Müller-Steinhagen *et al.* [157] for CO_2 crystallisation during flow boiling of argon.

Hospeti and Mesler [158] studied deposits formed beneath bubbles during nucleate boiling of saturated calcium sulphate solutions containing radioactive sulphur-35. From the relative distribution of deposits, they concluded that the evaporation occurring at the triple interface (vapour/liquid/solid interface) is not as significant as the evaporation occurring over the entire base of the bubbles. Palethorpe and Bridgwater [159] examined the effect of surface finish on the formation of calcium sulphate deposit. They found that during both static and flowing conditions, air bubbles at the heat transfer surface can significantly affect the amount of deposit formed.

Jamialahmadi *et al.* [160] studied bubble dynamics and scale formation during pool boiling of aqueous calcium sulphate solutions. From their results, they concluded that the fouling process during nucleate boiling of saturated calcium sulphate solutions can be divided into three distinct time regions, during which different phenomena dominate boiling and deposition. For constant heat flux, the heat transfer coefficient at the solid-liquid interface

changes throughout the deposition process due to variations in the number of active nucleation sites. According to the authors', the major contribution towards deposition is due to the evaporation at the base of growing bubbles. Hence, deposition rate increases with increasing number of active sites, i.e. with increasing heat flux.

Most recently, Najibi *et al.* [161] implemented a series of experiments on calcium sulphate and on calcium carbonate scale deposition during sub-cooled flow boiling in a vertical annulus. Figure 3.31, from the authors' work, is a typical example of the measured heat transfer coefficient as a function of time. In this case, the heat flux is 150,000 W/m^2, the calcium sulphate concentration is 2 g/l, the liquid velocity is 0.6 m/s and the bulk temperature is 80 °C. In agreement with Jamialahmadi *et al.* [160] and Helalizadeh *et al.* [162], the authors' suggest that the increase in heat transfer coefficient at the early stage of fouling is caused by the rise in the number of bubble nucleation sites generated by the presence of the deposit. Additional nucleation sites increase the turbulence level in the zone near the heat transfer surface, and, therefore, magnify the heat transfer coefficient, until the insulation effect of the growing deposit becomes prevalent. Furthermore, the authors report that the deposition rate is constant and controlled by different mechanisms depending on flow velocity and surface temperature. Different trends were observed for conditions where either convective heat transfer or nucleate boiling was dominant. As described in subsection 2.2.2 previous, the authors note that there is usually a time interval between the start of their experiments and the detection of a thermal fouling resistance, this is typically known as the

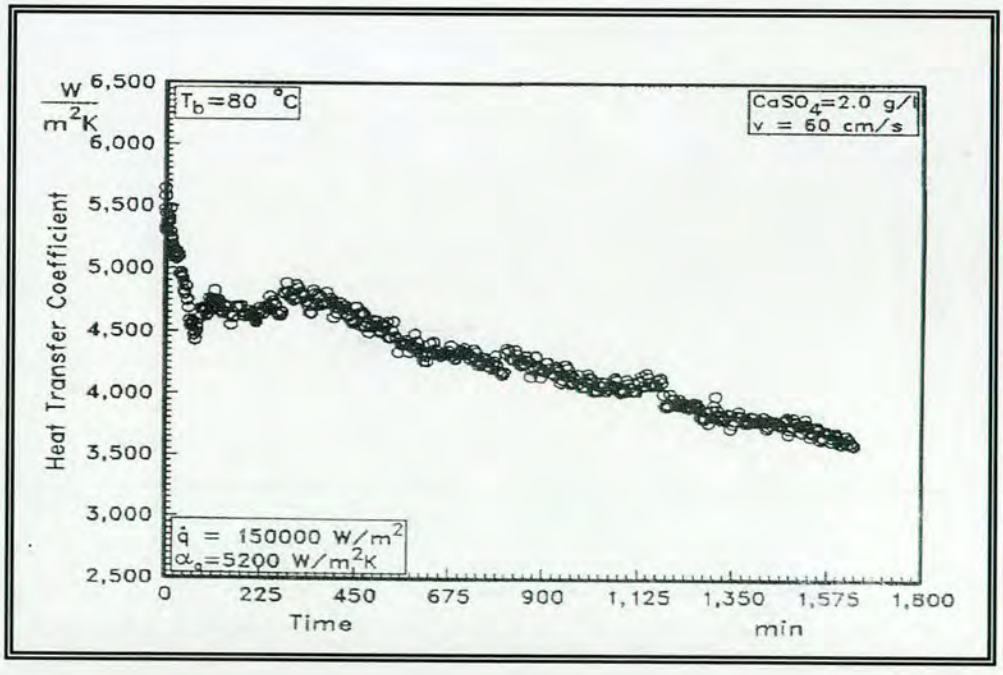

Figure 3.31: Typical variation of heat transfer coefficient with time. From Najibi *et al.* [161].

delay time or initiation period; a critical time period over which conditions conducive for deposition, such as crystal nucleation and heater surface conditioning, are founded.

From the aforementioned work of Najibi *et al.* [161], the effect of fluid velocity on the fouling resistance is shown in Figure 3.32(a) and (b) for constant surface and bulk temperature, under sub-cooled flow boiling conditions. For the researchers' specified range of flow velocity, an almost linear increase in fouling resistance with time has been observed, except during the initial period of testing. A linear relationship is symptomatic of adherent deposits, and

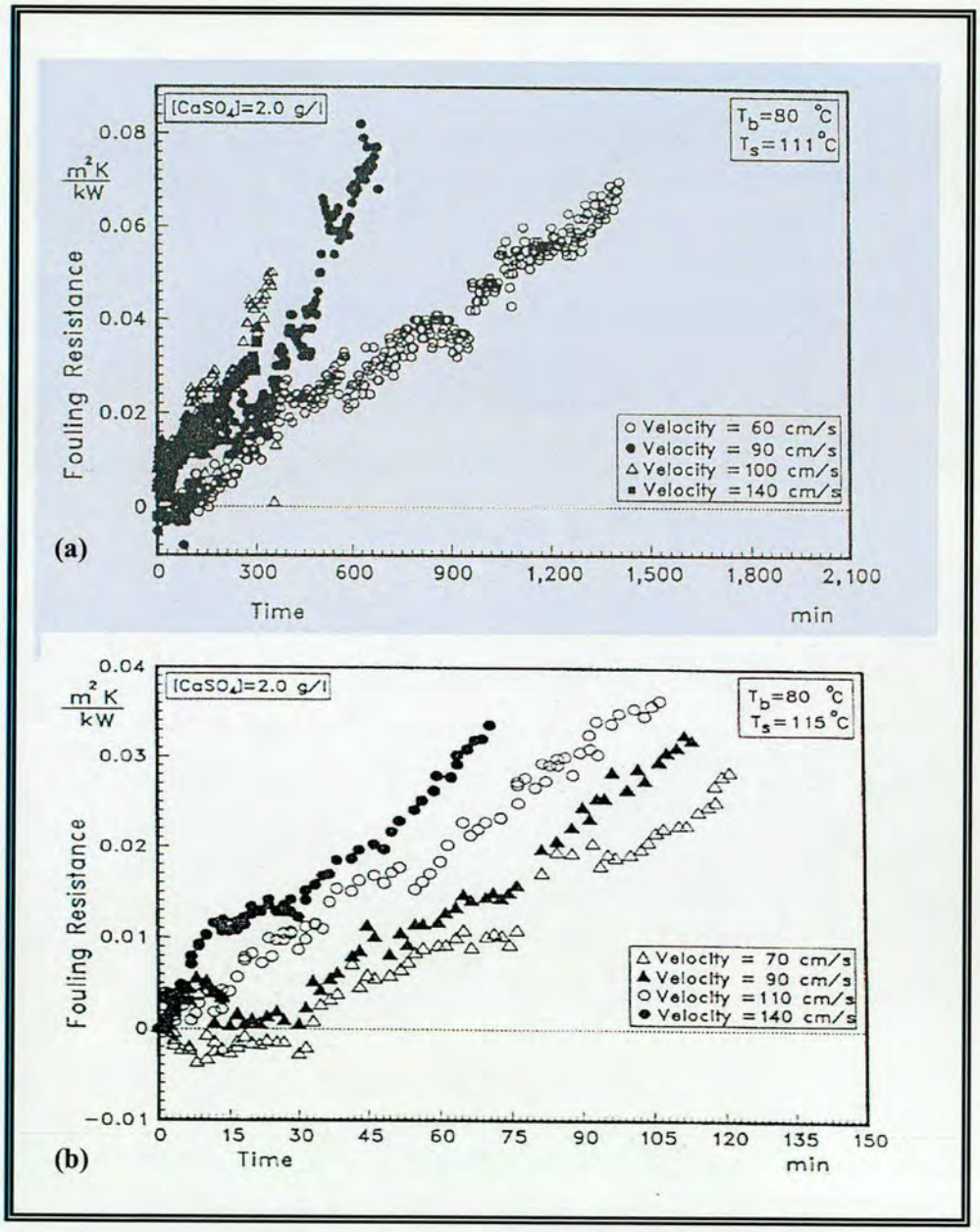

Figure 3.32: (a) Effect of flow velocity on the fouling resistance for a surface temperature of 111 °C, (b) Effect of flow velocity on the fouling resistance for a surface temperature of 115 °C. Adopted from Najibi *et al.* [161].

indicates that the deposition rate is constant with no complementary removal. To find the controlling mechanism, the fouling rates were determined over a range of fluid velocities under constant degree of supersaturation and constant bulk and surface temperatures. Typical results from the authors work are plotted as a function of Reynolds number in Figure 3.33. At low fluid velocities, the mass transfer boundary layer thickness is relatively thick and, therefore, molecular diffusion has some effect on the rate of fouling. In the opinion of Najibi *et al.* [161], as the fluid velocity is increased, the boundary layer thickness is decreased and mass transfer across the boundary layer no longer affects the fouling rate, implying that the fouling process is governed by chemical reaction. Since the reaction rate constant only depends on the surface temperature, the curve shown in Figure 3.33 levels off for higher Reynolds number.

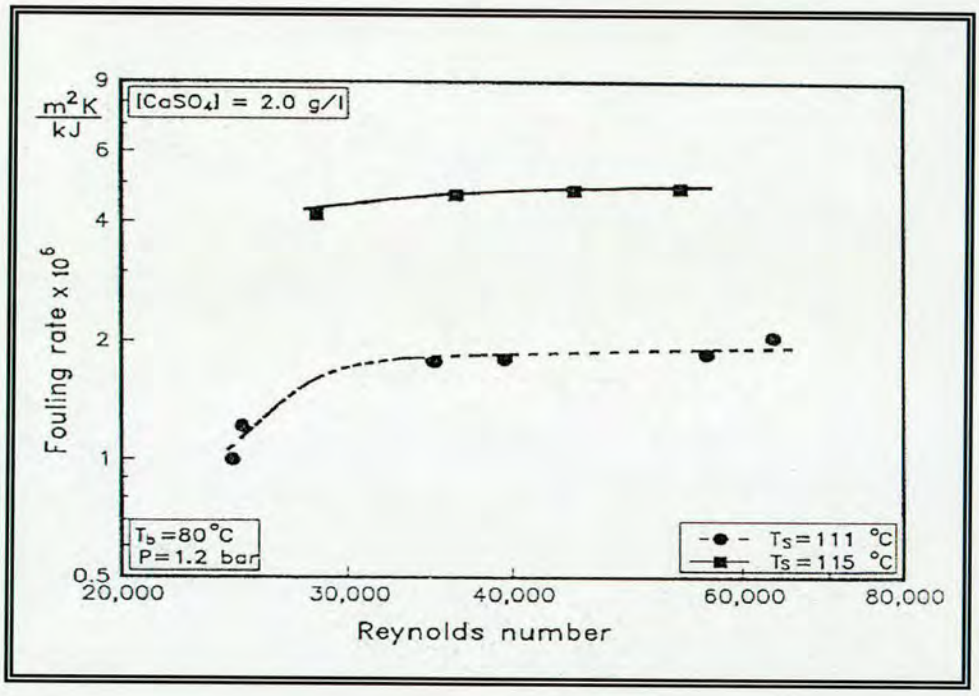

Figure 3.33: Fouling rate as a function of Reynolds number. From Najibi *et al.* [161].

Also from Najibi *et al.* [161], for sub-cooled flow boiling conditions, the variation in fouling resistance with surface temperature at constant bulk temperature and concentration is depicted in Figure 3.34(a) and (b) for two different liquid velocities. The results show that fouling rates depend strongly on the heat transfer surface temperature especially at higher flow velocities. According to the authors', the delay time after the start of the fouling experiments decreases with increasing heat transfer surface temperature. The authors' speculate that since mass transfer coefficients increase linearly with temperature, Hasson *et al.* [163], fouling rates should therefore increase linearly with surface temperature for the mass transfer controlled operating conditions. This trend was indeed observed for liquid velocities below 0.9 m/s. For

liquid velocities above 0.9 m/s, the fouling rate increased exponentially with surface temperature which, as it approaches the Arrhenius relationship expressed in equation 2.5, illustrates that fouling is occurring under reaction controlled conditions. Their investigations also revealed that the rate of fouling is independent of the bulk temperature, both at high and low velocities. Additionally, the bulk temperature was shown to posses a negligible influence on the delay time. Distilling the remainder of the authors' work, the effect of other operating parameters (such as solution concentration and structure of deposit) on sub-cooled flow boiling fouling rates were also examined. Their findings show that bulk composition exerts a strong effect on the fouling rates. Further results are documented in [161].

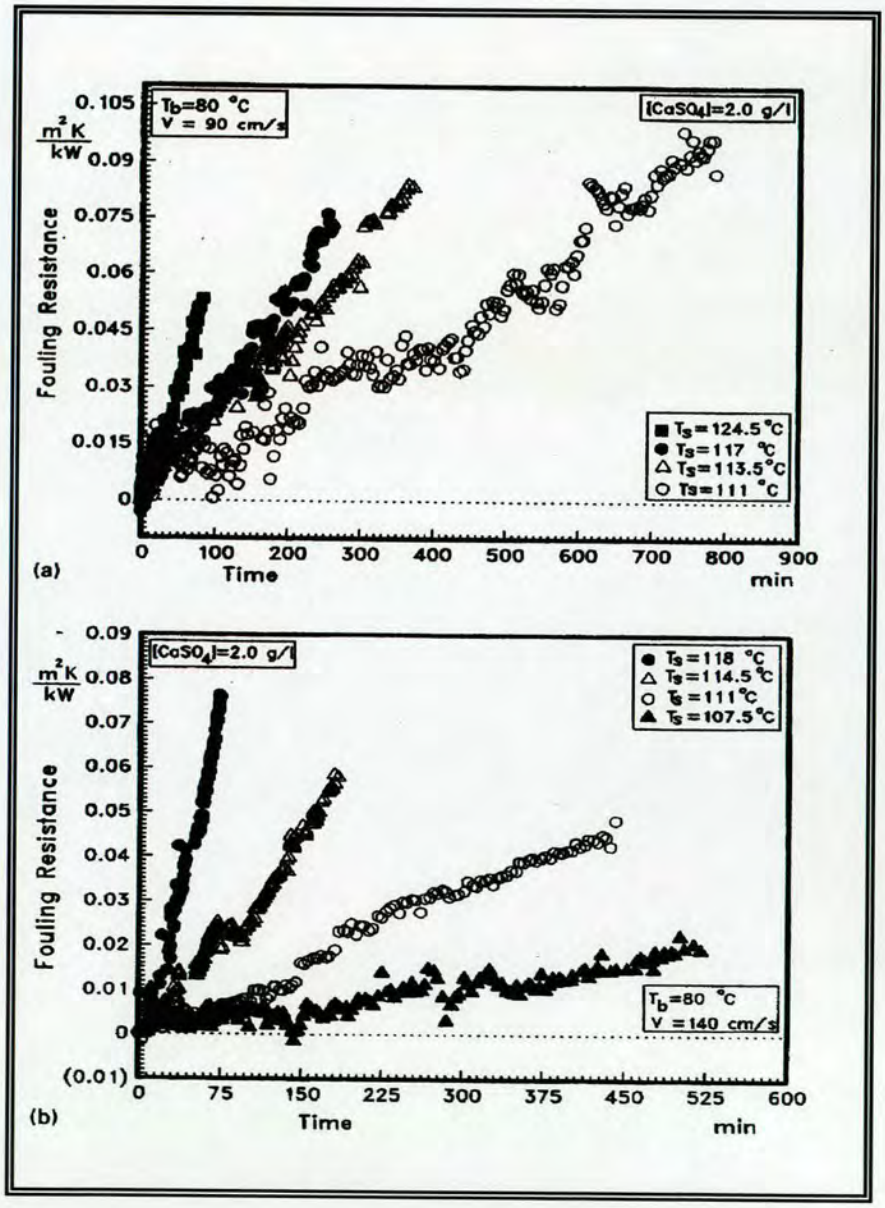

Figure 3.34: (a) Effect of surface temperature on the fouling resistance for a flow velocity of 0.9 m/s, (b) Effect of surface temperature on the fouling resistance for a flow velocity of 1.4 m/s. Taken from Najibi *et al.* [161].

3.4.2. PREDICTION OF FOULING UNDER BOILING CONDITIONS

Like any other heat exchanger, evaporators and boilers are designed using assumed fouling resistances taken from tables of questionable accuracy or similar experience-based sources, the bases of which are at best rather vague in relation to the actual operating conditions [151]. Using a constant value of a fouling resistance (or cleanliness factor) at the design stage can predict the possible boiler performance, indicating the extent of deposit formation that may be expected, but gives no information regarding the rate of the heat transfer deterioration [2,151]. Thus, it is likely that the equipment would have to be taken out for service at an inconvenient and economically undesirable time. As detailed above, the fouling process is a time function, and therefore a rational design procedure for boilers exposed to fouling conditions would allow not only for the forecasting of how much fouling deposit should build up, but also the time and rate at which the phenomena would happen (thus far, in this particular body of work, all of the fouling models described or alluded to, see subsection 2.2.3.1, have been formulated based on experimental data for non-boiling conditions).

Furthermore, with knowledge of the boiling heat transfer fouling rate, the field engineer would be in a position either to plan the cleaning schedule of the evaporators or orchestrate the implementation of fouling mitigation strategies conforming to operation and process requirements.

As clarified in subsection 2.3.2., several investigators [19-29,113,164,165] have recommended models for boiling heat transfer where the total heat surface is divided into two parts, namely the area affected by active nucleation sites, and the remaining area where forced convective heat transfer occurs. As mentioned also, in 1963, by combining the convective and nucleate boiling contributions to flow boiling heat transfer, Chen [20] successfully presented one of the most popular additive boiling correlations for pure fluids and mixtures. In its basic form, the Chen model is expressed as:

$$\alpha_{FB} = \alpha_{npb}\, S\left[f\left(Re_{FB}\right)\right] + \alpha_{LO}\, F\left[f\left(X_{tt}\right)\right] \tag{3.57}$$

Defined earlier, α_{npb} is the nucleate pool boiling heat transfer coefficient which depends on the wall superheat, and α_{LO} is the convective heat transfer coefficient found for liquid-phase flow only. Chen utilised the Dittus-Boelter correlation [166] for the calculation of α_{LO}, and the analysis of Forster and Zuber [167] – which is now obsolete- for the estimation of α_{npb}. The parameter F is a multiplier that accounts for the effective increase in liquid velocity due to the presence of the vapour phase and is a function of the Martinelli parameter X_{tt} [20]. The suppression factor, S, accounts for the decrease in nucleate boiling as forced convective effects increase. According to Chen, S can be defined as the ratio of the mean superheat

around the growing bubble to the wall superheat, and is found to be a function of the two-phase Reynolds number, Re_{FB}. The complete set of equations as applied for the prediction of local subcooled flow boiling heat transfer coefficients is given by Najibi [2] and Wenzel *et al.* [168].

To this regard, Najibi *et al.* [161] adopted an analogous procedure in developing a model for the prediction of calcium sulphate and calcium carbonate fouling rates during sub-cooled flow boiling. The authors used the aforementioned Chen correlation [20] to calculate the fraction of heat transferred by nucleate boiling, *NBF*:

$$NBF = \frac{\alpha_{npb} S}{\alpha_{FB}} \tag{3.58}$$

Najibi *et al.* [161] interpret this parameter as a measure of the fraction of the heat transfer area affected by bubble growth mechanisms. According to the authors, scale formation at the heat transfer surface during sub-cooled flow boiling is, therefore, a combination of the following two mechanisms:

a. In the area which is affected by the vapour bubbles, reaction rate controlled fouling mainly occurs due to the mechanism of bubble formation and microlayer evaporation.

b. In the remaining area, where mass transfer effects are predominant, fouling takes place by forced convective mechanisms.

As shown in Figure 3.35 both of the above mechanisms occur concurrently in independent zones of the heat transfer surface. Therefore, the overall fouling rate can be represented by the following equation:

$$\frac{dR_f}{dt}(\rho_d \lambda_d) = NBF\Phi_{nb} + (1 - NBF)\Phi_{LO}, \tag{3.59}$$

Here subscript d denotes deposit physical properties, and Najibi *et al.* [161] define Φ_{nb} and Φ_{LO} as the rate of mass deposited, kg/m^{2}s, in the nucleate boiling and forced convective zones respectively. As the heat flux increases, the number of active nucleation sites increases and equation 3.58 predicts that the fouling caused by the boiling mechanism will also increase [2,161,162]. In the bounds of this particular review, the predictions of Φ_{nb} and Φ_{LO} shall not be dealt with; however, the reader is directed to the cited work of Najibi *et al.* [161] for a more robust exposition of both terms.

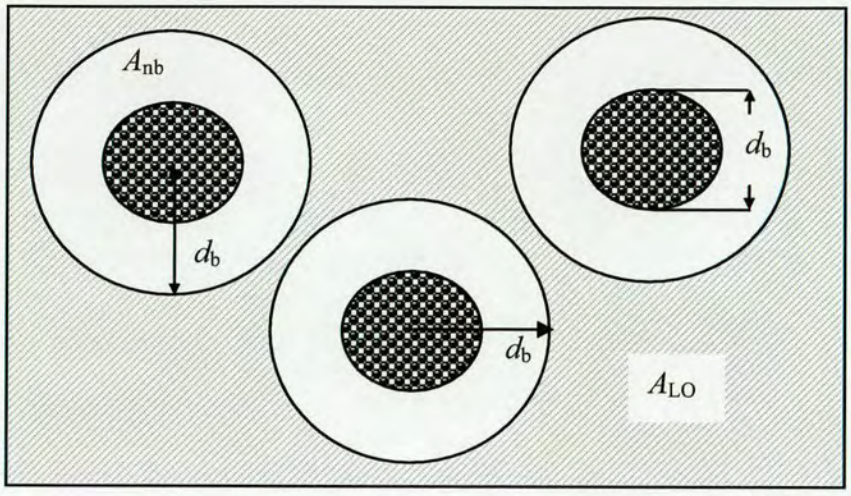

Figure 3.35: Areas affected by nucleate boiling, A_{nb}, and by forced convection, A_{LO}

Figure 3.36 shows a comparison between the authors measured data, and the fouling rate as correlated by equation 3.58 above. Corresponding diagrams for all other fouling experiments (for example, the effect of velocity, bulk concentration and surface temperature on the predictions of the suggested model) are given in Najibi [2].

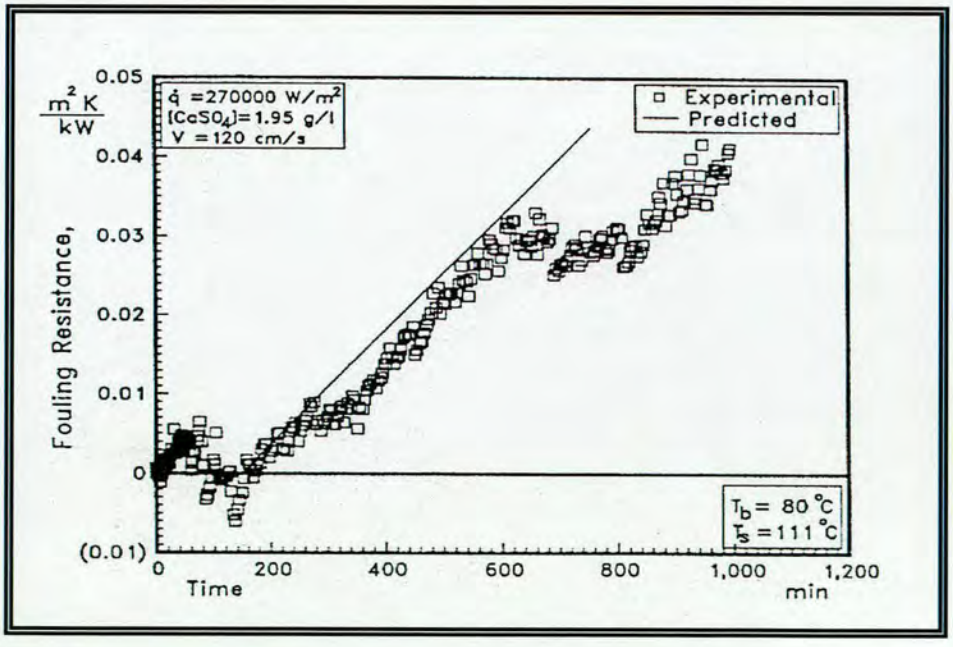

Figure 3.36: Comparison of measured and predicted fouling resistance as a function of time. Taken from Najibi [2].

The trend of Figure 3.36 demonstrates an excellent agreement between the investigators' predicted and experimental results. The suitability of the Najibi *et al.* [161] correlation for the prediction of deposition rates during sub-cooled flow boiling is further verified by Figure 3.37, where all of the authors experimental data, obtained under various operational conditions, are compared with values obtained from equation 3.58. The root mean square error between the predictions and the experimental data is 5.12 %, and the average absolute error is 25 %. The investigators state, that these values are close to the error margins already involved in the prediction of clean sub-cooled boiling heat transfer coefficients [2,161,162].

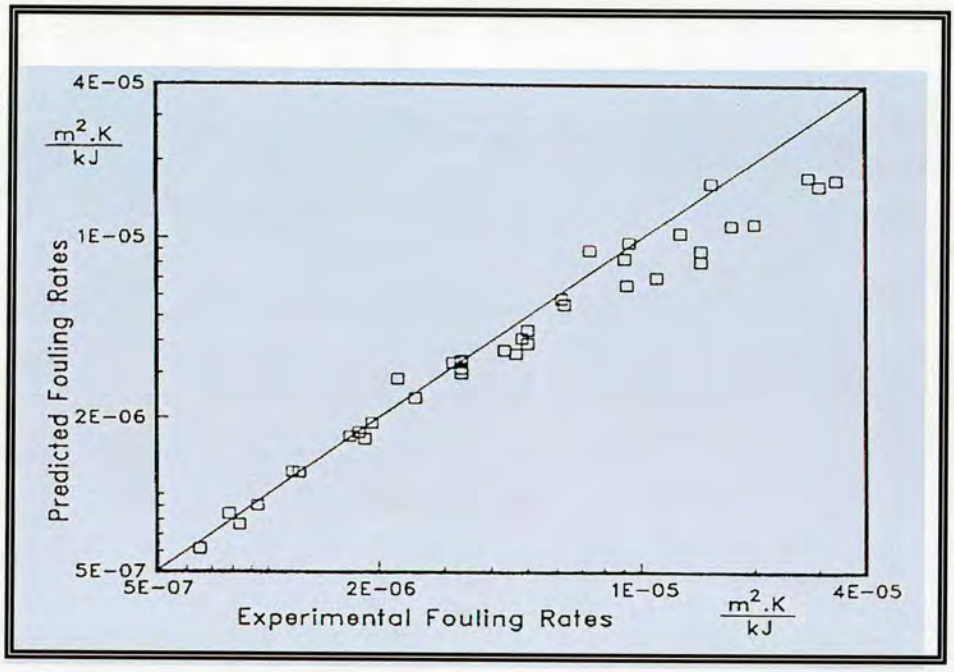

Figure 3.37: Comparison between predicted and experimental fouling rates. From Najibi [2].

3.4.3. Boiling Enhancement And Fouling Prevention Techniques

As the nucleate boiling heat transfer coefficient is higher than most other heat transfer processes, for many industries, it is therefore commercially appropriate to enhance nucleate boiling and inhibit scale deposition by acceptable measures [169]. To date, in studies regarding the enhancement of boiling heat transfer, two salient parameters have received the most attention; the first of these is the boiling nucleation process. As discussed previously, boiling nucleation is a process of major significance as its occurrence determines the wall superheat at which the mechanism of heat transfer passes from the less effective convective mode, to the more effective nucleate boiling mode. Additional to boiling nucleation, the boiling site density - defined as the number of active nucleation sites per unit area on the heated surface - has also been identified as a key enhancement parameter. From the earliest studies of Jakob and Fritz [170], the increase in the number of active nucleation sites,

coinciding with a rise in the boiling heat transfer, has regularly been observed, even for lower heat fluxes. Furthermore, by effecting changes to the properties of the liquid, enhancement can also be achieved by the inclusion of additives. In summary, several effective techniques of boiling enhancement are reported within the literature. A host of these available techniques have been applied to certain fields of thermal engineering [171-173]. However, as alluded to in subsection 3.2.1, many of these techniques are endowed with particular disadvantages such as: complication in manufacture, possible fouling of heat transfer surface, as well as serious boiling hysteresis [174]. Consequently their industrial incorporation has enjoyed varying degrees of success, as illustrated following...

According to the heat transfer enhancement classification scheme decribed by Bergles [42] and presented in subsection 3.2.1, to attain long-term minimum fouling stability and enhanced boiling performance, the most important measures applied to the heat transfer surface are *Enhanced boiling surfaces* (i.e. treated and structured surfaces) and *Additives for boiling liquid systems*. Both of these methods are dealt with in turn.

3.4.3.1. ENHANCED BOILING SURFACES

In these type of techniques, typically used for boiling and condensation operations, the finish of the heat transfer surface is subjected to fine scale alteration [43]. Enhanced boiling surfaces rely either on the treatment of the surface area to augment the bubble site density, or purely on the extension of the overall surface area via the use of fins. The overarching aim is the formation of a surface that comprises a substantial number, and size range, of nucleation sites. In view of this situation it is convenient to categorise treated and structured surfaces, as far as their fouling behaviour is concerned, as involving both area enlargement and heat transfer intensification (recall subsection 3.2.1)

3.4.3.1.1. POROUS LAYER ENHANCEMENT

Porous coatings have emerged as one of the most effective measures for the enhancement of the nucleate boiling heat transfer process. For instance, Universal Oil Products (UOP) (Tonawanda, NY) offers a surface, the High Flux® surface, in which heat transfer is enhanced by the application of a thin porous layer to a smooth surface. It is manufactured by sintering, at a high temperature, fine metallic particles to a smooth metallic surface. The particles are sufficiently dense in number so that the treated surface consists of a large number of minute cavities. Such a surface has the property of initiating nucleate boiling with a much smaller wall superheat than would be true for a plain surface at the same heat flux [43]. The fouling performance of this type of surface has been investigated by Curcio, Jr. [175], and reported by Curio and Somerscales [176]. In these experiments, two types of Praxair High Flux® surfaces (one with a particularly copious amount of minute cavities) and a plain surface were exposed to pool boiling heat transfer in a saturated solution of $CaSO_4$ for approximately 25 hours. The

results of some of the test are shown in Figure 3.38 for the plain surface, and Figure 3.39 for one example of the Praxair High Flux® surface.

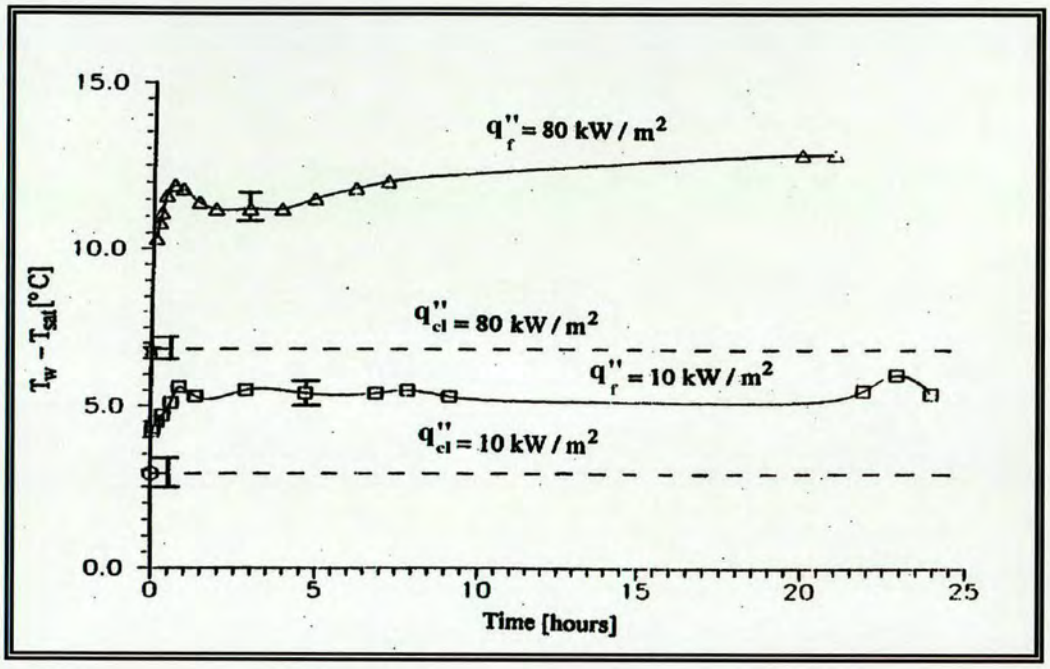

Figure 3.38: The variation of wall superheat with time for a plain surface in a saturated aqueous $CaSO_4$ solution, at two boiling heat fluxes. From Curcio [175].

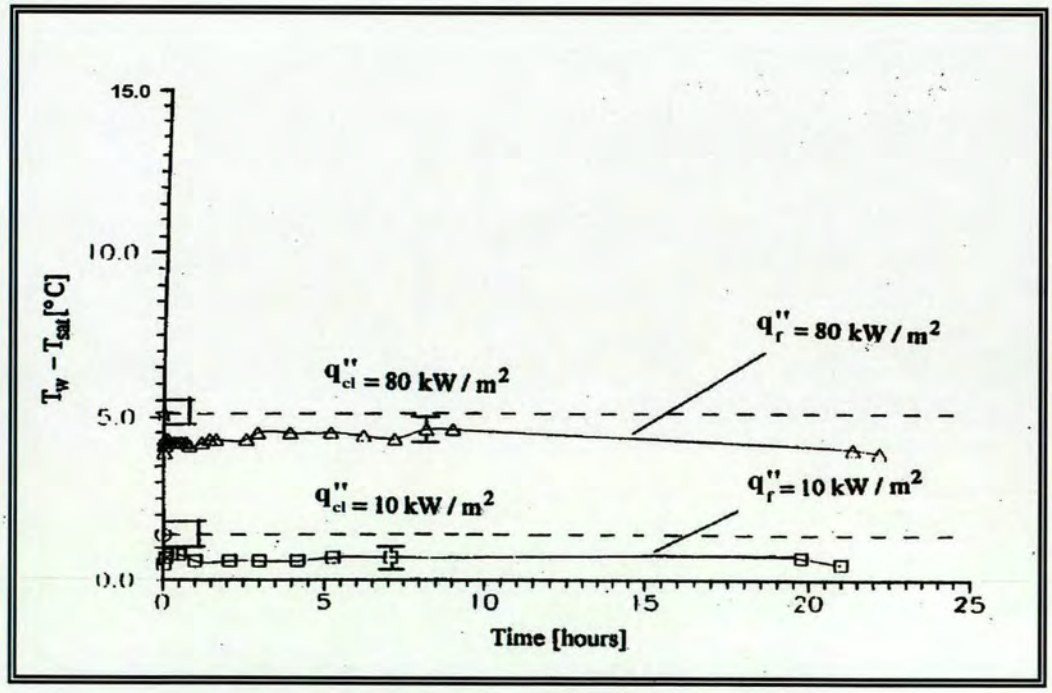

Figure 3.39: The variation of wall superheat with time for a UOP High Flux® small surface in a saturated aqueous $CaSO_4$ solution, at two boiling heat fluxes. Taken From Curcio [175].

According to the authors', the other cavity rich Praxair High Flux® surface also demonstrated similar behaviour to that exemplified in Figure 3.39. A large wall superheat is indicative of a large fouling thermal resistance, so the enhanced heat transfer surface exhibits a much smaller fouling effect than the plain surface. Clearly in this case the enhanced heat transfer surface has a mitigating effect on fouling. As reported by Curio and Somerscales [176], examination of the cavity rich enhanced surface revealed significant boiling enhancement tendencies, as well as sensitivity to fouling.

A series of publications by O'Connor *et al.* [177,178] and Rainey *et al.* [179,180] examined the possibility of simply painting microstructures onto existing heat transfer equipment. By forming microscale cavities on the surface, the performance of these coatings was resultant from an increase in both the number of active nucleation sites and bubble departure frequency per site. Possible applications have been found in phase-change heat exchangers, electronics cooling, refrigeration evaporators or chemical processes. While many of the enhanced surfaces tested have demonstrated the ability to reduce the wall superheat, and to increase the critical heat flux, their feature sizes have been too large to effectively trap a large number of embryonic bubbles when immersed in refrigerants [169].

3.4.3.1.2. STRUCTURED SURFACES

Re-entrant cavities, which posses a small exit section at the inlet, have proven to be quite suitable for aiding nucleation. Hence, a number of commercially available heat transfer surfaces provide enhanced boiling heat transfer by employing re-entrant nucleation sites which are interconnected below the surface [181]. The main difference between structured surfaces and the earlier discussed porous surface is the much greater geometrical regularity of the cavities in the former, and their significantly lower area density. According to Brautsch [169], although higher boiling heat transfer coefficients have been universally noted, in many instances (w.r.t. structured surfaces) these successes have been routinely overshadowed by the more pressing threat posed by fouling of the enhanced surfaces.

In general, the different techniques to obtain structured surfaces can be classified into macroscopic and microscopic structuring. Within these categorises - which are considered in the following sections - three main incentives prescribe the design and application of the various methods adopted by researchers: (1) to decrease the temperature for onset of nucleate boiling, (2) to generate large quantities of bubbles, and (3) to reduce the bubble duration time on the heated surface. The proper exploitation of these objectives favours an increase in both liquid agitation and active bubble site density; two major factors for the enhancement of the boiling heat transfer [169].

A. *Boiling Enhancement by Macroscopic Structuring*: In 1973, Hess tested different designs of fins, which were one of the first methods employed in order to obtain enhanced heat transfer [182]. Under pool boiling conditions, each of these structures exhibited increased evaporation heat transfer coefficients compared to a smooth surface. In most cases, finned tubes allowed higher heat fluxes for a given wall superheat. However, Hess observed that vapour produced at the heated surface typically impeded the re-wetting of the surface; thus, due to an obstructed liquid supply to the heated surface, peak heat fluxes obtainable with finned tubes were routinely lower than was the case for corresponding smooth tubes. Hence, to avoid this drawback, various improved fin types have been developed in order to obtain further improved evaporation heat transfer, also in the peak heat flux region. The intention has been to increase the number of nucleation sites per unit area and to optimise the shape of the nucleation sites. Most of the techniques for producing surfaces with improved fins involve the cold forming of conventional fins. For pool boiling, a great variety of surfaces have been studied in order to determine their potential at improving measured heat transfer coefficients. All of these operate by having thin-film vaporisation internally, and bubbling through the openings of the structure [169]. Nucleation occurs in the interior of the fin arrangement, with an effective vapour-liquid exchange to supply liquid for continuous vaporisation. The development of these structures has been greatly inspired by the quintessential works of Jakob and Fritz [170]. Pate *et al.* [183] provide a representative list of some of these enhanced surfaces; *Thermoexcel-E*, *Gewa-T* and *Turbo-B* are a just a few of the more relevant examples.

Webb [184,185] studied the fin type shown in Figure 3.40(a), as extracted from Brautsch [169]. The heights of the original fins were 0.8 mm at a density of 13 fins/cm. According to Webb, the width of the aperture at the top of the bent fins plays an important role with regards to the evaporation heat transfer. The optimum aperture for the refrigerant Freon R11 as the working fluid was found to lie between 0.0038 and 0.0089 mm. The finned surface shown in Figure 3.40(b) is, to a certain extent, a modification of the structure proposed by Webb. The surface, developed by Fujie *et al.* [186], consists of bent fins with regular grooves on the top. The bent fins produce a porous surface with the individual pores interconnected by channels. Arai *et al.* [187] and Tori *et al.* [188] have also investigated surfaces of this type, which are commercially denominated as *Thermoexcel-E*. The T-shaped surface shown in Figure 3.40(c), known as *Gewa-T*, was produced by splitting the top of a conventional fin and cold forming the outer surface. The structure born from this process is a re-entrant circumferential channel. Compared to a conventionally finned tube, improvements to the pool boiling heat transfer coefficient of between 20% and 40% have been measured by Saier *et al.* [189].

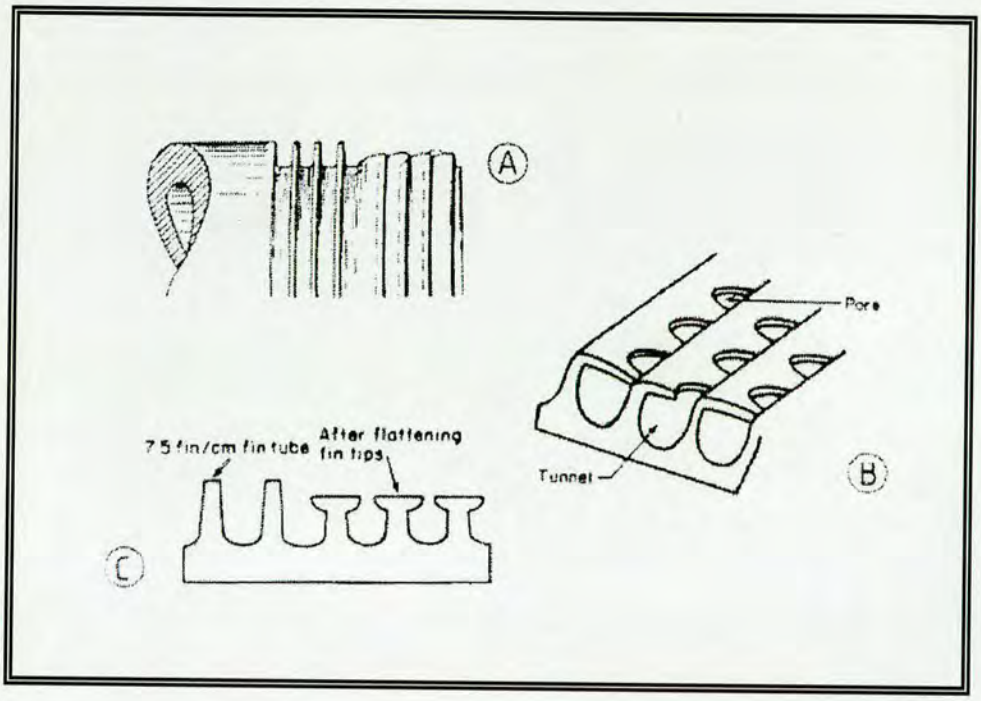

Figure 3.40: Three different types of enhanced fin structures shown in (a), (b), and (c) respectively. From Brautsch [169].

Similar to the examination of porous layer enhancement, as reported in subsection 3.4.3.1.1 previous, fouling tests using the *Turbo-B* structured surface, manufactured by the Wolverine Co. (Decateur, AL), are described by Somerscales and Curcio [190] and by Curcio and Somerscales [176] for pool boiling heat transfer. The test results of one type of *Turbo-B* surface is shown in Figure 3.41. Referring back to Figure 3.38, comparison with the plain surface results shows that contrary to popular belief, as a consequence of the fin-like behaviour of its structured elements, the *Turbo-B* surface, which is used primarily to enhance boiling heat transfer, does indeed demonstrate a capacity to also mitigate fouling.

A number of pool boiling studies have been conducted with the utilisation of woven screen mesh structures as the porous material. Due to its relatively simple installation and maintenance, the addition of a layer of screen mesh to a heater surface provides a promising technology for the enhancement of nucleate boiling heat transfer. According to Brautsch [169], most of the relevant authors especially encourage the use of single layers of mesh screens, as these yield the most effective heat transfer results. Brautsch [169] reports that experimentally, it has been proven that there exists a close relationship between the heat transfer performance and the mesh-fluid system; if the bubble departure diameter of the respective working fluid-bare heater system is of a similar magnitude to the aperture of the employed mesh, a maximum performance would be achieved. To this

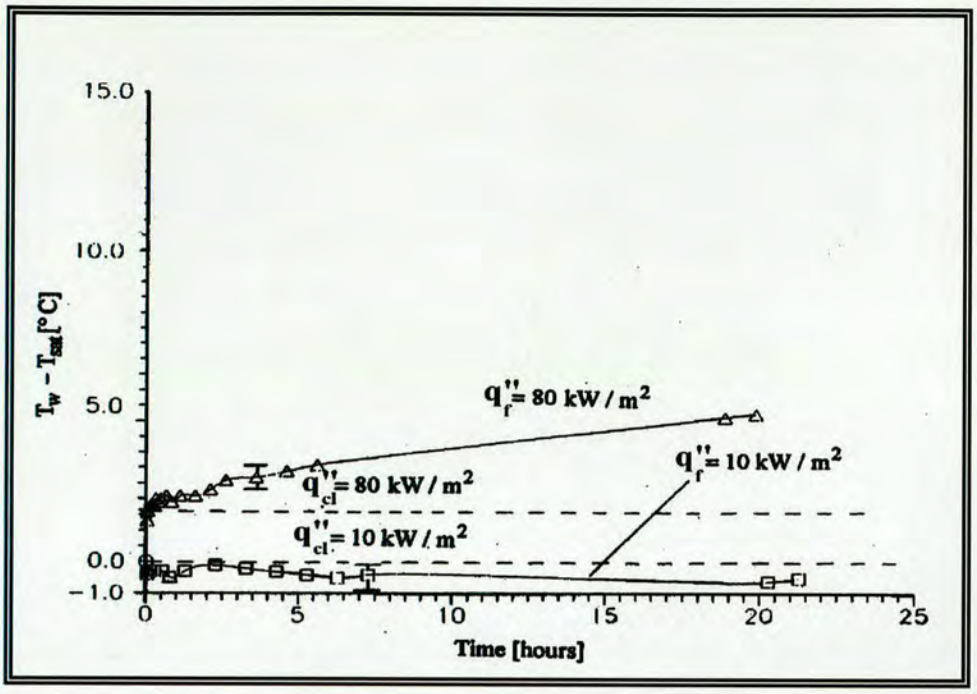

Figure 3.41: The variation of wall superheat with time for a Wolverine Turbo B® surface in a saturated aqueous $CaSO_4$ solution, at two boiling heat fluxes. Taken from Curcio [176].

author's best knowledge, results regarding the fouling performance of the device have not been documented.

Another relatively simple method to improve the evaporative heat transfer is wrapping of wires and/or cords around smooth or finned tubes. Figure 3.42(a), obtained from Webb [184,185], shows a finned tube with wire wrapping between its fins. The void volumes between the wires and the tube (characteristic dimensions for this particular case: 0.013 mm to 0.05 mm) serve as nucleation sites, which facilitate the improvement of the evaporation heat transfer. In Figure 3.42(b), an alternative technique for smooth tubes is indicated. The smooth surface is wrapped with a Nylon cord of a diameter of 0.38 mm at a pitch of 0.25 mm. Results of these two varying techniques, investigated by Webb [184,185] and described by Brautsch [169], are given in Figure 3.43 as wall superheat versus heat flux. The displayed results, again only for pool boiling heat transfer, are satisfactory for the finned tube with the wire and for the smooth tube with the Nylon wrap. Contrastingly, a smooth tube with a wire wrap performs rather inadequately.

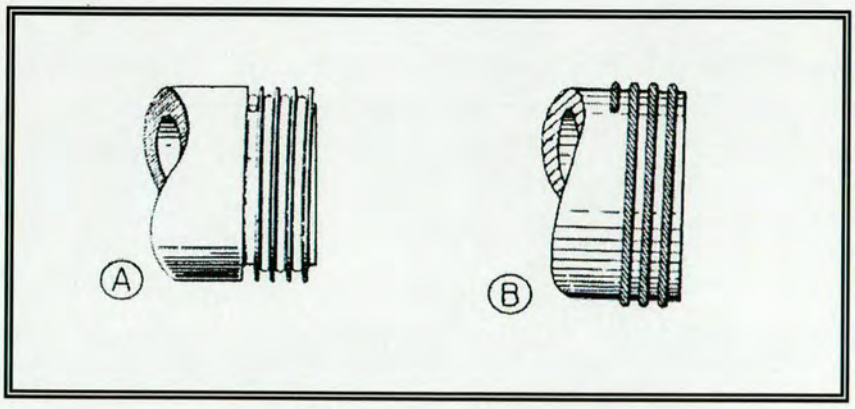

Figure 3.42: (a), (b) – Schematic of heat transfer enhancement by the wrapping of wires and/or cords around smooth or finned tubes. From Webb [185].

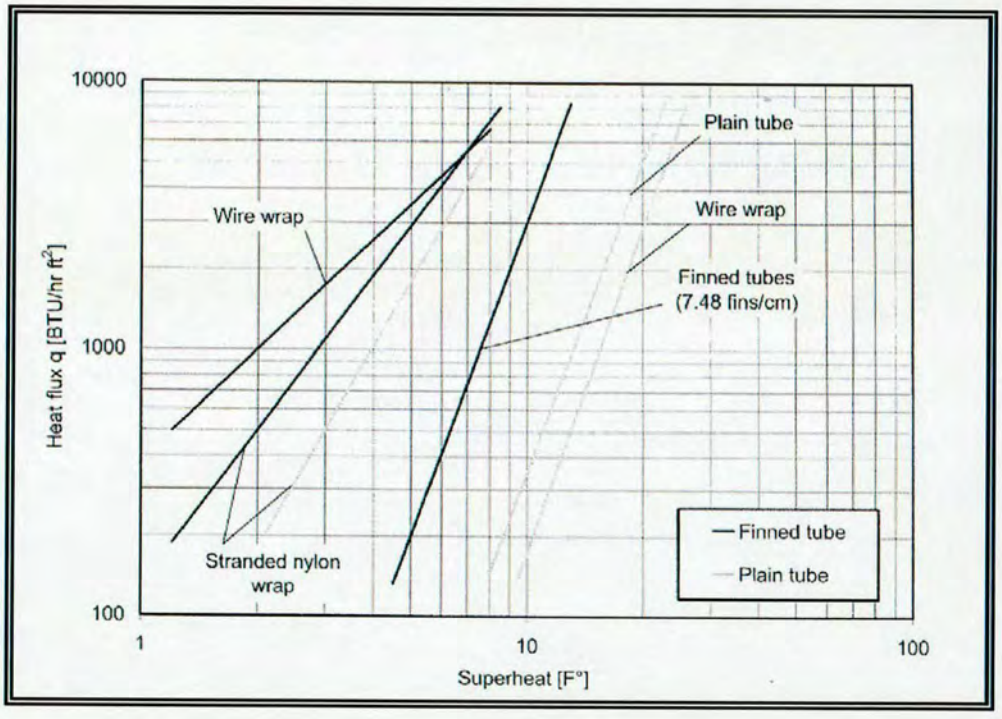

Figure 3.43: Schematic representation of experimental results for surface enhancement using wire and/or cord wraps; working liquid = distilled water. Taken From Brautsch [169].

B. *Boiling Enhancement by Microscopical structuring*: As opposed to the case for abrasive mechanical treatment, mechanical structuring comprises techniques which use mechanical means to produce well defined, regular surface structures. According to Brautsch [169], possible surface treatments include laser or electron beam drilling, milling, shaping and embossing. Different investigations with surface cavities produced by mechanical structuring showed considerably improved evaporation heat transfer coefficients. Griffith and Wallis [191] performed experiments utilising surfaces with a single cavity in order to

observe the phenomena occurring within the cavity during nucleate boiling. The authors' were able to show that a re-entrant cavity performed better compared to a cylindrical or conical cavity. A re-entrant cavity required a lower wall superheat in order to initiate boiling and yielded more homogenous nucleation.

Marto *et al.* [192] investigated boiling of nitrogen from a copper surface enhanced by mechanical structuring. Artificial nucleation sites were produced by embossing. A specimen of the obtained pool boiling results is given in Figure 3.44, as a plot of heat flux versus superheat. The mechanical structuring of the surface had the effect of reducing the wall superheat required for the initiation of nucleate boiling. Hence, for the same wall superheat, compared with the smooth surface, the structured surface of Marto *et al.* allowed for considerably higher heat fluxes, and thus higher boiling heat transfer coefficients.

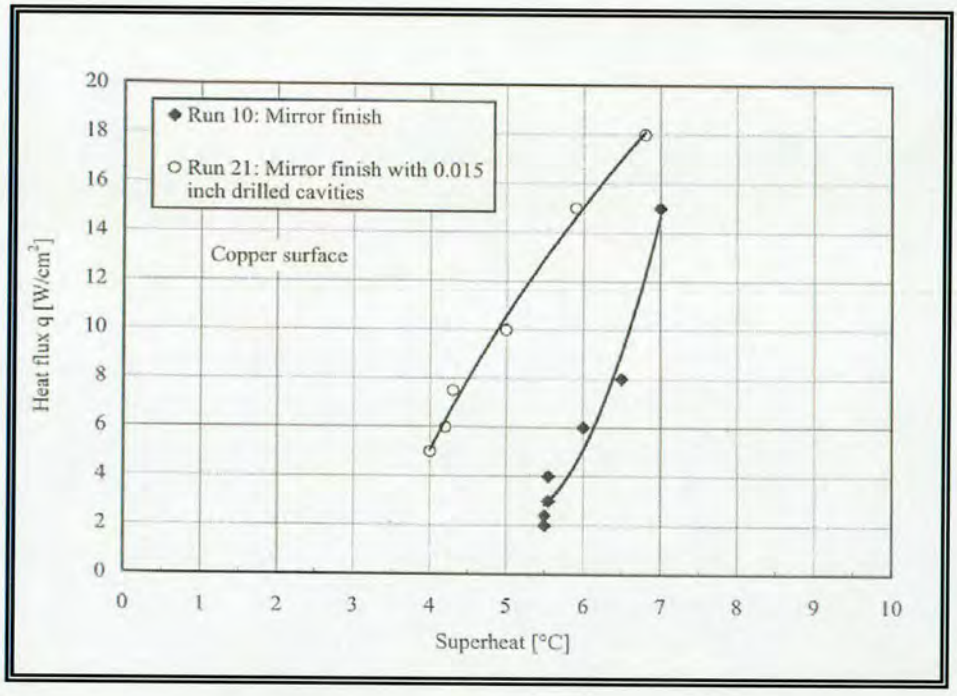

Figure 3.44: Results obtained by Marto [192] for nitrogen boiling from a copper surface.

3.4.3.1.3. SURFACE ENERGY & SURFACE ROUGHNESS TREATMENTS

It has long been known that poorest foulant adhesion occurs on materials with low surface energies. By implanting [193] or sputtering [194] foreign ions onto a metal surface, Müller-Steinhagen and Zhao achieved a remarkable reduction in scale formation during nucleate pool boiling. Capitalising on these successes, Müller-Steinhagen *et al.* [195] studied the effects of surface properties, specifically surface energy and surface roughness, on the deposition of calcium sulphate during convective and sub-cooled flow boiling heat transfer to aqueous

$CaSO_4$ solutions. To reduce surface energy, and hence create low fouling surfaces, several test heaters were treated by the following means:

I. *Ion Beam Implantation*: Ion implantation is the introduction of atoms into the surface layer of a solid substrate, by bombardment of the solid with ions in the keV to MeV energy range. During ion implantation, a beam of dopant ions of fixed energy is swept across the target surface. The ions have a sufficiently high velocity, about 10^6 m/s, so that they penetrate the surface. At present, a number of ion implantation systems, including dynamic mixing ion implantation, multi-beam mixing implantation and vacuum arc ion implantation have been developed [195].

II. *Unbalanced Magnetron Sputtering*: Sputtering is a process whereby materials are dislodged and ejected from the surface of a solid due to the momentum exchange associated with surface bombardment by high energy particles. In the sputtering process, the target (i.e. the source of the coating material) is the negative pole or cathode. The substrate is usually the positive pole or anode, but it can be given an imposed negative bias in order to increase the energy of bombardment during deposition. When the electric field intensity produced between the two poles is above a certain value, it will ignite an electric discharge and ionise the working gas (e.g. Argon). Such a low pressure electric discharge is called a glow discharge, and the ionised gas is called plasma. The target is negatively biased so that its surface is bombarded by positive ions from the plasma. When the atoms are dislodged and ejected from the target, they fly to the substrate and form a deposit on it. If the substrate is biased, it is subjected to positive ion bombardment to form a coating. A number of sputtering techniques have been developed, for example: radio frequency sputtering, ion beam sputtering, bias sputtering, cathodic vacuum arc sputtering, magnetron sputtering and unbalanced magnetron sputtering. To date only one coating type, namely diamond-like carbon (DLC) has been found to combine high hardness with a very low coefficient of friction. According to Müller-Steinhagen *et al.* [195], these DLC-based coatings are now opening up a huge number of new applications with tremendous success.

III. *Mixed Sputtering*: In order to further reduce the surface energy of DLC coated surfaces, Müller-Steinhagen *et al.* [195] sputtered a stainless steel heater rod with DLC and fluorine simultaneously (DLC-F), employing the Teer [196] patented closed-field unbalanced multiple magnetron sputtering ion plating system. The use of multiple ion plating sources allows many different target materials to be used simultaneously, with the object of forming stable or reactive alloy films.

IV. *Plasma Arc Deposition*: The plasma arc deposition process uses an electric arc to flash evaporate materials from the surface of the target or source, and the evaporating material and the reactive gas become highly ionised. The high degree of ionisation helps to promote the reaction and to form a fully dense, well adhered coating. In the investigation of Müller-Steinhagen *et al.* [195], an amorphous carbon (AC) film was prepared on a stainless steel heater rod by the use of this technique.

As well as the application of the above techniques, Müller-Steinhagen *et al.* [195] also electropolished the surface of one heater in order to reduce surface roughness, whilst conversely etching, via electrochemical means, another heater surface to increase surface roughness. The surface roughness of the original rod, the electro-polished rod and the electro-etched rod were 0.14 μm, 0.08 μm, and 11.2 μm respectively. Fouling runs with these various heaters, and with an untreated heater surface as control, were carried out at different heat fluxes, flow velocities and salt concentrations. Taken from the authors' work, Figures 3.45 and 3.46 compare the fouling behaviour of experiments with a DLC-F sputtered surface, a DLC sputtered surface, an electropolished smooth surface, an electroetched rough surface, and an untreated surface as control, for a heat flux of 300 kW/m^2, a $CaSO_4$ concentration of 2.0 g/L and a flow velocity of 60 m/s. This is an experiment with a substantial boiling component; consequently, for the un-treated heater, the authors report similar heat transfer coefficient versus time trends as described by Jamialahmadi and Müller-Steinhagen [151] for the case of pool boiling, i.e. a slight increase at the beginning of the experiment followed by a subsequent gradual decrease (an observation previously noted in subsection 3.4.1).

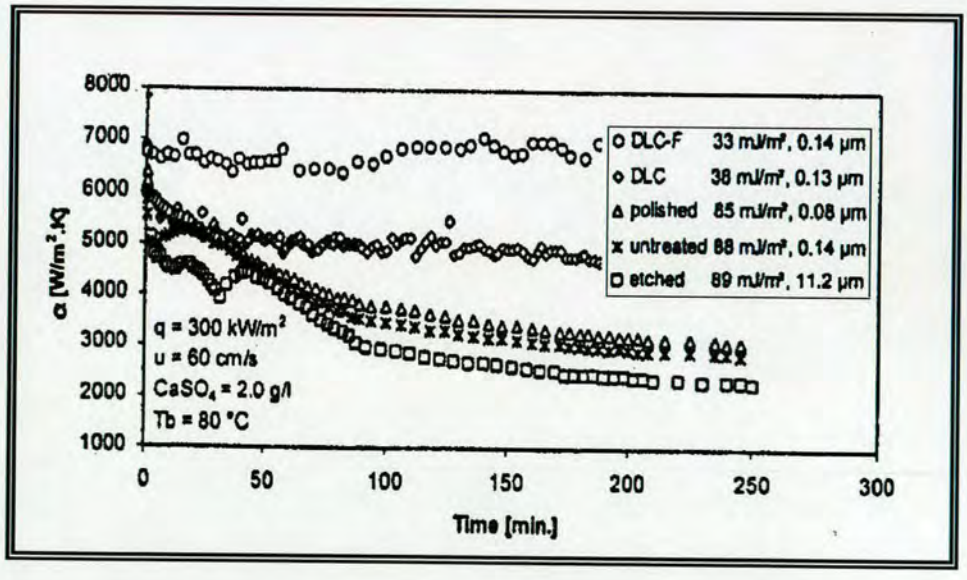

Figure 3.45: Heat transfer coefficient versus time for treated surfaces (DLC-F, DLC, electro-polished and etched) and untreated surface. From Müller-Steinhagen *et al.* [195].

Figure 3.45 shows that boiling heat transfer coefficients for the DLC-F and DLC surfaces with low surface energies (33 and 38 mJ/m^2 respectively) remained almost constant during runs, while the boiling coefficients for the electropolished surface, the untreated surface and the etched surface (all three with high surface energies of 85, 88 and 89 mJ/m^2 respectively) decreased significantly.

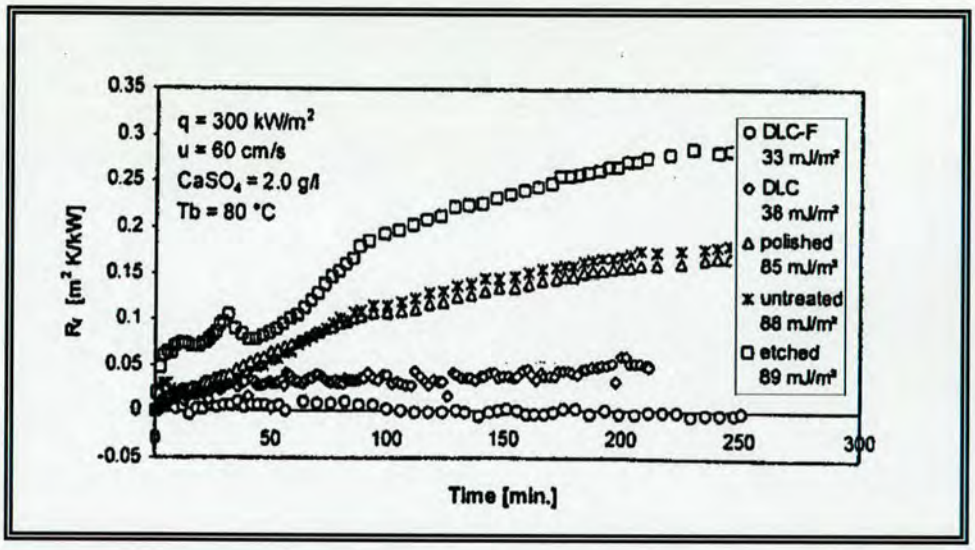

Figure 3.46: Fouling resistance vs. time for treated surfaces (DLC-F, DLC, electropolished and etched) and untreated surface. From Müller-Steinhagen *et al.* [195].

Figure 3.46 displays the fouling resistance-time curves obtained during the fouling runs. Although the investigated surface treatments (i.e. sputtering and ion implantation) do not alter the surface roughness, the reduction in surface energy induced by their application does substantially reduce the $CaSO_4$ scale formation. This is supported by the curve trends of the DLC-F and DLC sputtered surfaces, whose fouling resistances remain low and almost constant, as indicated in Figure 3.46. The authors' claim, that the DLC-F surface was able to outperform its counterparts, primarily due to its lower surface energy. In the opinion of Müller-Steinhagen *et al.*, both surface energy and surface roughness have an effect on the fouling resistance. However, their studies reveal that the effect of surface energy is rather more significant than the effect of surface roughness. Hence, the authors' report that although the electropolishing of some of their tested stainless steel heat transfer surfaces resulted in a reduction in surface roughness, electropolishing does not, however, exhibit any influence on the surface energy, and as such the investigators' report no obvious reduction in scale formation from the implementation of such techniques [195]. Müller-Steinhagen *et al.* [195] also determined that under sub-cooled boiling conditions, flow velocity exerts an additional fouling mitigation effect on heat transfer surfaces modified by magnetron sputtering, plasma arc sputtering and ion beam implantation. As detailed in subsection 3.4.1 and demonstrated

in Najibi *et al.* [161], previous boiling investigations communicate no such flow velocity influence on the fouling prevention of un-treated steel surfaces. Furthermore, Müller-Steinhagen *et al.* state that the combined effect of reduced surface energy and flow velocity on fouling suppression is considerably stronger than has hitherto been documented for pool boiling conditions [195]. Finally, in concluding their study, the investigators proclaim that, excluding ion beam implantation, the above coating techniques are inexpensive and easy to scale-up in industrial practice; preliminary evaluations suggest that additional manufacturing costs for some of the surface modification techniques (for example, mixed sputtering and unbalanced magnetron sputtering) are indeed commercially viable.

3.4.3.2. ADDITIVES FOR BOILING SYSTEMS

For single-phase flows, additives have proven an extremely efficacious heat transfer enhancement and fouling mitigation technique, as exemplified by the mass proliferation of the self-cleaning liquid-solid fluidised bed technology across many engineering areas of industrial interest. The subject of the 'self-cleaning liquid-solid fluidised bed heat exchanger', as applied to non-boiling operations, has been comprehensively addressed in section 3.3 previous.

However, due to the complexity of the boiling phenomena, and the severity of fouling under such conditions, studies regarding the implementation of additives during boiling heat transfer are rather exiguous. Within the limited literature, most of the highlighted three-phase (i.e. vapour and liquid boiling phases plus an additional solid phase) boiling investigations are primarily concerned with the influence of solid particles in boiling liquid pools, with fewer works describing the effect of particles in (vapour-liquid-solid) flow boiling systems. However, knowledge of the enhancement provided by the inclusion of particles to boiling pools, can only serve to further inform our understanding of three-phase (vapour-liquid-solid) flow boiling, which, for the confines of this project, has been identified as the boiling operation of interest.

3.4.3.2.1. ADDITIVES IN POOL BOILING

It has been reported repeatedly in literature that when a proper amount of solid particles are introduced into a pool of boiling liquid, the boiling heat transfer is typically enhanced, with even the partial or complete removal of boiling hysteresis [174]. With its simplicity, it appears an attractive boiling augmentation technique, applied in many situations of technological interest, such as during chemical or food processing (where it is often necessary to boil liquid-solid slurries in which particles tend to settle into a layer on horizontal surfaces), heat pipes, geothermal energy systems and post-accident heat transfer performance in liquid cooled nuclear reactors.

In 1987, Chuah *et al.* [197] experimentally determined the effects of a layer of unconfined particles on the saturated pool boiling heat transfer from a horizontal surface. For this three-phase (vapour-liquid-solid) pool boiling system, the authors' report results for two different types of particles: 0.275 mm and 0.475 mm diameter glass spheres, with low density and low conductivity, as well as 0.100 mm and 0.200 mm diameter copper spheres, with high density and high conductivity. Water was used as the working fluid. To evaluate the interaction between the surface nucleation conditions and the boiling process in the particle layer, the investigators' employed a plain surface and two surfaces with different arrays of artificial cavities. One of the surfaces had 7 artificial cavities, while the other had 19 artificial cavities; for both surfaces the cavities were uniformly distributed over the surface.

Firstly, with regards to hydrodynamic behaviour, Chuah *et al.* [197] report that when a layer of unconfined particles is placed on a heated wall submerged in a pool of boiling liquid, the observed motion states of vapour, liquid, and solid particles can be represented as shown in Figures 3.47(a,b,c,d).

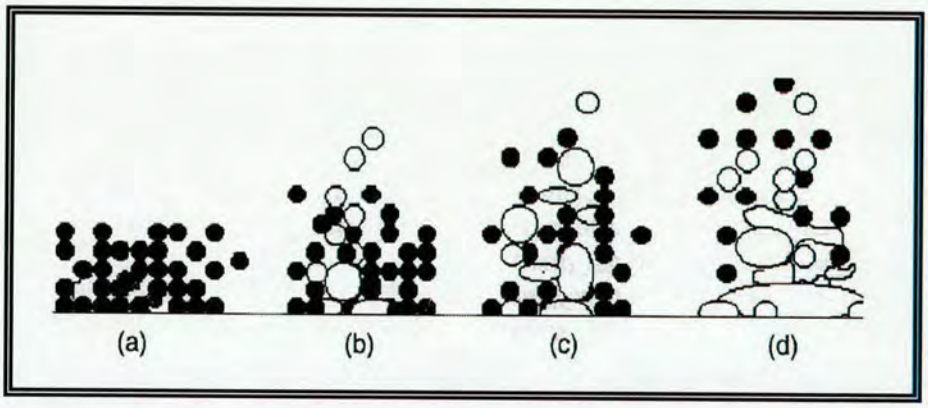

Figure 3.47: (a,), (b), (c), (d) - The hydrodynamic states of vapour-liquid-particles in three-phase pool boiling. Adapted from Chuah *et al.* [197].

According to Chuah *et al.*, at lower heat flux levels, vapour bubbles are generated from one or more nucleation sites on the heated surface - usually within the vicinity of a chimney (i.e. a gap in the particle bed) – and generally coalesce as they grow. Initially, the buoyancy of the bubbles, or the coalesced vapour patches, cannot overcome the resistance of the overlying particle layer and the particle bed is in a fixed state as shown in Figure 3.47(a). With increase of heat flux, the buoyancy of the accumulated vapour eventually becomes substantial enough to overcome the weight or resistance of the particle bed; the vapour flows upwards through the chimneys, partially fluidising the particle layer as depicted in Figure 3.47(b). Still in the lower heat flux regions, Figure 3.47(b) also shows that the region between the vapour chimneys appears to be virtually unaffected by bubble motion in the fluidised chimney

regions. In these identified zones, Chuah *et al.* [197] advise that the presence of the settled particle layer inhibits convective motion of liquid near the surface. Heat transfer in these regions is then mostly by conduction, with some convective effects occurring within the porous structure of the particle layer. Thus, in the opinion of the authors, at lower heat levels, the heat transfer from the heated surface to liquid pool is mainly governed by the convection of the liquid located in the gaps of the particle bed, and the heat conduction of the particles themselves. For middle and progressively higher heat flux levels, Chuah *et al.* [197] observe a rapid increase in nucleation sites juxtaposed with a reduction in their mean spacing. Here, a single chimney may then be fed by several active nucleation sites. Consequently, as the heat flux increases, there may be more chimneys spaced closer together, with the agitation in the chimney regions becoming ever more vigorous. As a result of such trends, the investigators' report the complete fluidisation of the particle layer at higher heat fluxes. Hence, heat transfer by particle conduction, across unfluidised regions of the bed, is expected to diminish with increasing heat flux. Within this high heat flux region, fluidised particles oscillate with the upward vapour and downward liquid flows, as reported by the authors' and shown in Figure 3.47(c). Like a departing vapour bubble, Chuah *et al.* [197] note that a particle ascending from the heated surface draws a portion of the superheated liquid in its wake. When the heat flux rises to a critical value, the upward vapour cushion would hinder the downward motion of particles, thus eliminating the direct contact of particles with the heated surface as demonstrated by Figure 3.47(d)

The experimental measurements of Chuah *et al.* show that for any given heat flux, the presence of a particle layer on the heated surface may increase or decrease the surface superheat depending on the characteristics of the system. In general, compared with ordinary pool boiling at the same heat flux level, the authors' results indicate that the addition of a layer of light, low conductivity glass particles significantly increases the wall/surface superheat, whereas addition of heavier, high conductivity copper particles was found to decrease ΔT; as a consequence, in experiments with a layer of copper particles, measured heat transfer coefficients were found to be as much as twice larger than those measured for ordinary pool boiling at a similar heat flux. For the systems examined by Chuah *et al.* [197], the size of the particles and the initial depth of the particle layer were found to have little effect on the measured heat transfer from the horizontal surface. In concluding their work, the authors' present a tentative analysis of the boiling process, postulating that the shift in the boiling curves, due to the addition of particle layers, can be explained in terms of three distinct effects: (1) enhanced nucleation, (2) partial fluidisation of the particle layer, and (3) the change of the effective conductivity of the medium near the surface.

According to Chuah *et al.* [197], enhancement due to added nucleation sites is greatest for very smooth surfaces at low superheat. For rough surfaces with many available sites, or at

higher wall superheats where even smooth surfaces have many active sites, the particles have little effect on nucleation behaviour. Furthermore, the authors' report that if the conductivity of the particles is much higher or lower than the conductivity of the liquid, the effective conductivity of the solid-liquid mixture may be significantly different from the conductivity of the pure liquid. This may increase or decrease the ability of the medium to conduct heat, thereby altering the overall effectiveness of heat transfer from the surface. For a given heat flux, the effect of conductivity is reflected by a change in the required surface superheat. Particles with a thermal conductivity higher than that of the liquid (e.g. copper) tend to enhance conduction of heat near the surface in both the fluidised and nonfluidised regions. This enhancement is expected to reduce the mean thermal boundary layer thickness near the wall, thus suppressing the resistance to the heat transfer from the surface, which in turn improves the overall heat transfer effectiveness. In addition, the results of Chuah *et al.* [197] also disclose that with the layer of particles present, the thermal boundary layer may be nonuniform over the surface. The thermal boundary layer is expected to be very thin in fluidised regions which are agitated by the vapour motion, and relatively thicker in nonfluidised regions where heat is transferred by conduction of the solid particles.

For experiments utilising surfaces with artificial cavities, Chuah *et al.* [197] state that the presence of particles appeared to have little effect on the density of active nucleation sites. For such surfaces, the effect of particles on the boiling process appears to be primarily a consequence of the earlier expressed partial layer fluidisation and effective conductivity mechanisms. Finally, the authors' developed an equation, not given in the bounds of this review, for predicting the boiling curve shifts attributed to the presence of the particle layer. Excellent agreement between the proposed relation and all the authors' data for glass and copper particles, strongly supports the assumptions utilised in their tentative analysis [197]. Therefore, along with the authors' data, their correlation suggests that under certain circumstances, a thin layer of highly conductivity particles can actually be an effective means of enhancing pool boiling heat transfer.

Recently, Mingheng *et al.* [174] also performed systematic experimental studies to understand the influence of solid particles on the mechanisms of heat transfer in a pool of boiling liquid. Specifically, the researchers' investigated the effect of solid particles on boiling heat transfer enhancement in fixed particle beds (i.e. confined particle layer) and unconfined particle beds respectively. In agreement with Chuah *et al.* [197] previous, their results show that pool boiling heat transfer can be greatly enhanced by the addition of solid particles to the liquid, whether in fixed or unconfined particle bed systems. However, in contrast to Chuah *et al* [197], for the case of the unconfined particle bed, the data of Mingheng *et al.* [174] demonstrates the existence of a close relationship between particle size, initial bed depth and the pool boiling heat transfer enhancement. For particles fluidised in unconfined pool boiling,

Figure 3.48 and 3.49, both taken from [174], depict the effect of particle diameter and initial bed depth on the trend of the boiling curves respectively. In Figure 3.48 we notice that for an unconfined bed of a given initial bed depth, the rate of heat transfer decreases with the increase of particle diameter. In the opinion of Mingheng *et al.* this is because within the liquid pool, the additional volumetric convection caused by smaller particles would be stronger than is the case for larger particles.

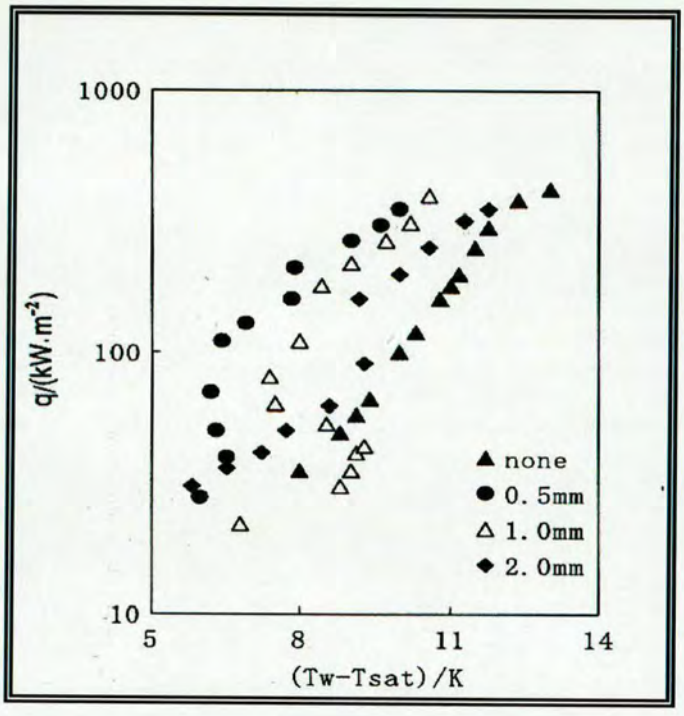

Figure 3.48: The effect of particle diameter for glass beads fluidised in unconfined pool boiling. Initial bed depth = 4.8 mm. Taken from Mingheng *et al.* [174].

Meanwhile, the effect of initial bed depth is rather more involved. For a given particle diameter, if the initial bed depth is relatively small (i.e. less than 9.5 mm for their particular work) , the pool boiling heat transfer increases with increasing initial bed depth as shown in Figure 3.49. However, the authors' advise that for initial bed depths larger than 9.5 mm, the boiling heat transfer decreases with increasing initial bed depth. Hence Mingheng *et al.* speculate that for boiling heat transfer enhancement in a liquid pool with an unconfined particle bed, there exists a saturated initial particle loading.

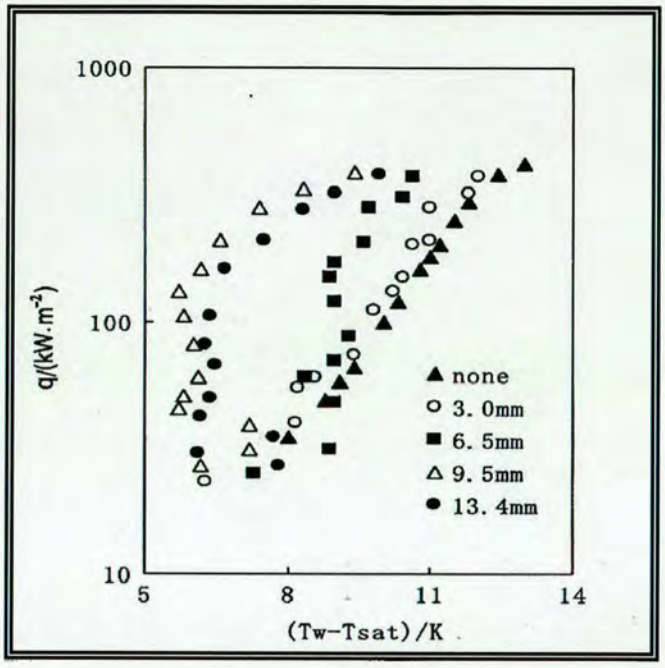

Figure 3.49: The effect of initial bed depth for glass beads (d_p = 1.0 mm) fluidised in unconfined pool boiling. Taken from Mingheng *et al.* [174].

Furthermore, from the authors' analysis, compared with an unconfined particle bed, boiling characteristics are radically altered when a particle layer is fixed in place on the submerged horizontal surface. The key documented effects of a fixed particle bed on nucleate pool boiling heat transfer are: nucleation effect, bubble moving effect and thermal conductivity effect. According to the visual observation of Mingheng *et al.* [174], additional active nucleation sites are provided on the heated surface due to the situation of particles being permanently contacted with the surface. For pool boiling at low heat flux, the required wall superheat, ΔT, is reported to decrease as the nucleation site density increases; the implication being that at the same heat flux, the wall superheat for fixed bed boiling is less than is the case for ordinary pool boiling. This is a clear indication of boiling heat transfer enhancement by the presence of solid particles. Conversely, the authors' findings also reveal that the presence of particles impedes bubble motion, thereby influencing bubble detachment. Their observations show that average bubble sizes with solid particles, are larger than without particles. In the opinion of Mingheng *et al.* [174] this indicates that when particles are present and secured on a heater surface within a boiling liquid pool, bubble diameter is typically increased. As established in the literature, an increase of bubble departure diameter translates to a decrease in bubble frequency, where the higher the bubble frequency, the stronger the boiling heat transfer. Hence, a larger bubble diameter dictates that the heat transfer resulting from the bubble formation process is invariably weakened by the presence of a fixed layer of solid particles. In concluding, the investigators' successfully formulated a correlation for the prediction of boiling heat transfer coefficients in fixed or confined particle beds, see [174].

More importantly or of greater relevance to this project, for the case of the unconfined bed system, Mingheng *et al.* proposed a volumetric convective mechanism, suggesting that boiling heat transfer enhancement, induced by the upward flow of particles from the heat transfer surface, arises from the convective sensible heat transfer caused by the fluidised particle wake flow [174] as shown in Figure 3.50.

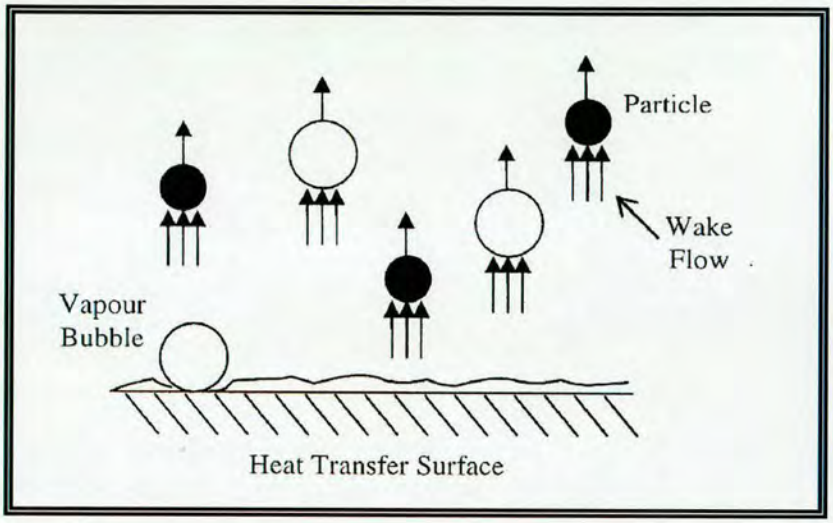

Figure 3.50: Illustration of enhancement mechanism imparted by particles in three-phase (v-l-s) pool boiling heat transfer. Adapted from Mingheng *et al.* [174].

By assuming that an upward flowing particle, diameter d_p, can be treated as a rising bubble departed from the heated surface during nucleate boiling, Mingheng *et al.* [174] correlate the total heat transfer in pool boiling with unconfined fluidised particles as follows:

$$q'' = q''_{\text{npb}} + q''_{\text{p,cs}}$$

$$q'' = q''_{\text{npb}} + \left\{ B'' \varepsilon d_{\text{p}}^{-1.34} \left(\frac{q''}{\Delta h_{\text{v}} \rho_{\text{V}} \nu_{\text{L}}} \right)^{0.66} C_{\text{p,L}} \rho_{\text{L}} \left(T_{\text{w}} - T_{\text{b}} \right) \right\} \qquad (3.60)$$

Equation 3.60 shows that in the three-phase (vapour-liquid-solid) pool boiling system, the total heat flux, q'', can be described as the sum of the nucleate pool boiling heat flux for pure liquid, q''_{npb}, and the convective sensible heat flux supplied by the upward particle wake, $q''_{\text{p,cs}}$. In other words, $q''_{\text{p,cs}}$ symbolises the boiling heat transfer component ascribed to the addition of the solid phase to the boiling liquid pool. In its definition (i.e. $q''_{\text{p,cs}}$) given in

equation 3.60 above, B'' is a coefficient which, according to the authors', can be experimentally determined, whilst ε is the porosity of the initial particle bed.

Extracted from the work of Mingheng *et al.* [174], Figure 3.51 illustrates a comparison between the correlated boiling component, $q''_{p,cs}$, and data obtained by means of contrasting water-only boiling heat transfer measurements with data for pool boiling heat transfer with an unconfined particle layer. Agreement is seen to be satisfactory. Thus, Mingheng *et al.*'s proposed mechanism of pool boiling enhancement by the action of fluidised particles appears realistic and acceptable.

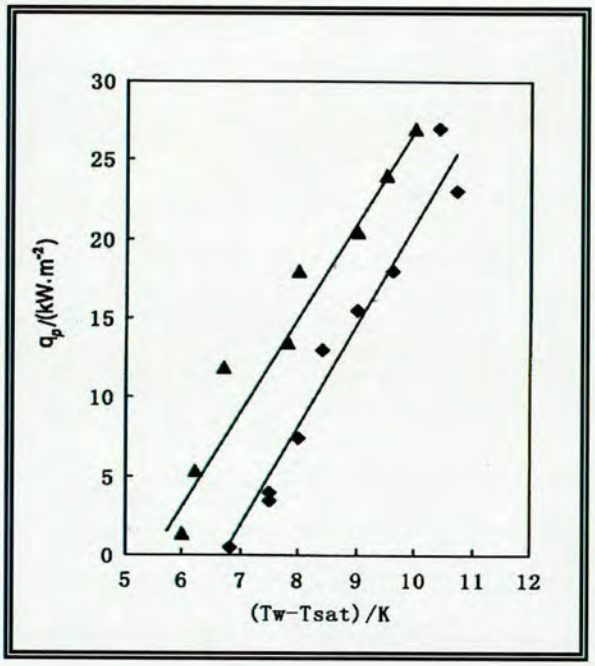

Figure 3.51: Comparison between calculated value, $q''_{p,cs}$, and experimental data obtained from pool boiling with glass beads minus pool boiling with pure water. (♦) d_p = 1 mm; (▲) d_p = 0.5 mm; (–) value calculated by equation 3.60. From [174].

3.4.3.2.2. ADDITIVES IN FLOW BOILING

As discussed in section 3.3 earlier, owing to the increased turbulence caused by the presence of fluidised particles, liquid fluidised bed heat exchangers have been successfully deployed for the enhancement of heat transfer and reduction of heater surface fouling, in non-boiling operations across various process industries. Also, recalling subsection 3.4.3.2.1 above, with regards to boiling operations, the addition of solid particles to pools of boiling liquids has proven a viable heat transfer enhancement strategy, with values of heat transfer coefficients in three-phase (vapour-liquid-solid) pool boiling reportedly twice as large than is the case for

ordinary pool boiling [197]. However, the academic and industrial sector have only over the past decade, become genuinely intrigued by the possibility of exploring the heat transfer and fouling mitigation effect of solid particles, under the combined conditions of liquid fluidisation and flow boiling heat transfer [198-201]. In terms of application, the success of the particle additive technique under industrial flow boiling conditions, would, amongst other things, offer considerable improvements to the power levels of all boilers and boiling water nuclear power reactors, without any increase in equipment size or operating temperature.

A notable piece of work, predating the referenced investigations [198-201], is that of Wei and Maa [202], who in 1982 reported on the influence of soluble polymer additives on the enhancement of flow boiling coefficients. For their boiling chamber configuration, a heating element was placed in the vertical position and housed centrally in a sealed glass tube. System fluid, namely water, flowed upward through the annular space between the heater element and the inner tube wall. The water soluble polymers used in their work were *Polyox* (a polyethylene oxide of molecular weight 2-4 x 10^6) and *Natrosol 250 HR* and *250 GR* (hydroxyethyl cellulose of molecular weight 2 x 10^5 and 7 x 10^4 respectively). Similar to the case for pool boiling, the authors' findings confirm that for the same boiling heat flux, compared with ordinary two-phase flow boiling, the addition of small amounts of soluble polymers (a few hundred p.p.m) generally reduces the necessary wall superheat, thus elevating the measured flow boiling heat transfer coefficient. This favourable effect, displayed in Figure 3.52, is more pronounced when the polymer concentration is higher as shown in Figure 3.53.

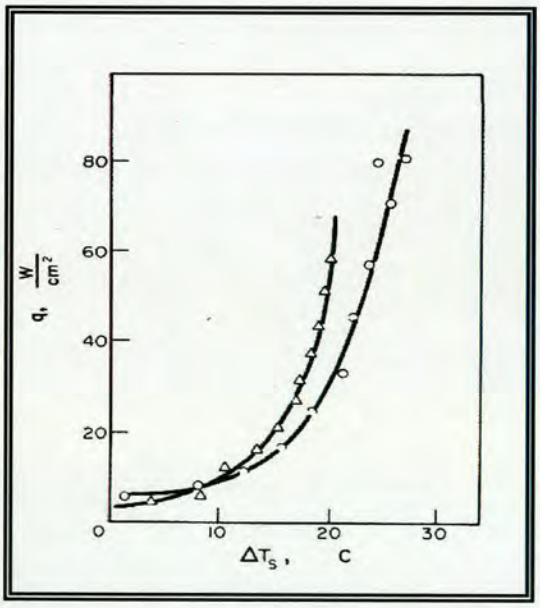

Figure 3.52: Boiling over electrical heating element. $U = 0.107$ m/s; (○) Two-phase flow boiling of distilled H_2O; (Δ) Three-phase flow boiling of 500 p.p.m Natrosol 250 HR aqueous solution. Taken from Wei *et al.* [202].

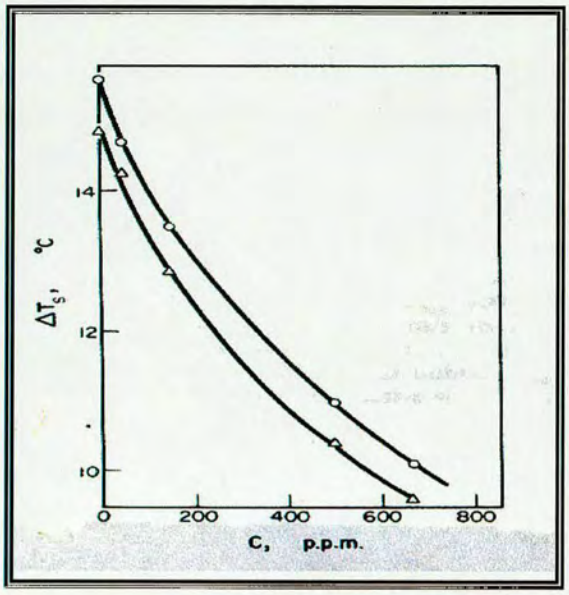

Figure 3.53: Effect of concentration of Natrosol 250 HR aqueous solution on flow boiling superheat. (○) q'' = 1000 kW/m^2; (Δ) q'' = 1400 kW/m^2. From Wei *et al.* [202].

With regards to liquid velocity, Wei and Maa [202] identified the existence of an optimum liquid velocity at which the necessary wall superheat is lowest for the same boiling heat flux. Figure 3.54 depicts a typical set of results for the variation of wall superheat with velocity.

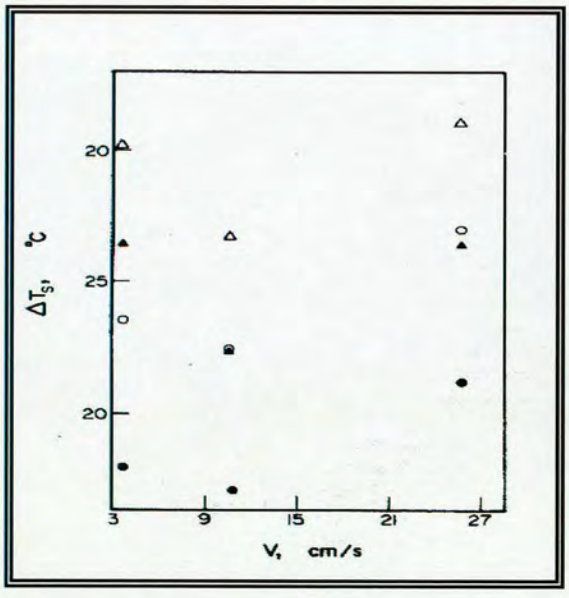

Figure 3.54: The effect of liquid velocity on wall superheat, for a constant heat flux of 720 kW/m^2. (Δ) Boiling of distilled water on stainless steel surface; (○) Boiling of 500 p.p.m Natrosol 250 HR aqueous solution on stainless steel surface; (▲) Boiling of distilled water on nickel plated surface; (●) Boiling of 500 p.p.m Natrosol 250 HR aqueous solution on nickel plated surface. From [202].

Overall, interpreting in terms of the rate of heat transfer, the data trends displayed in Figure 3.54 indicate that in three phase (vapour-liquid-solid) flow boiling, the heat transfer coefficient initially increases with increasing velocity; however, upon attaining a maximum value at an optimum liquid velocity of approximately 0.12 m/s, the boiling coefficient rapidly deteriorates for progressively higher superficial velocities. It is interesting to note that this implied heat transfer versus velocity trend is similar to the case for additives in non-boiling fluidised systems as outlined in subsection 3.3.4.1. Recall the work of Jamialahmadi *et al.* [82] on the variation of the liquid-solid heat transfer coefficient with bed voidage; noting that bed voidage increases as velocity increases, these authors' also give account of an initial rise in non-boiling heat transfer with increasing velocity, which culminates at a peak heat transfer value before eventually declining for progressively higher flowrates as shown in Figure 3.24 above. Recall also that in this particular instance, Jamialahmadi *et al.* [82] identified the suppression of particle-wall collision frequency as the main mechanism involved in the reduction of the liquid-solid fluidised bed heat transfer at higher superficial liquid velocities. For the case of three-phase flow boiling, although the analysis of Wei and Maa [202] neither substantiates, nor repudiates, the claims of Jamialahmadi *et al* [82], the investigators' do offer an alternative explanation for the behaviour of heat transfer coefficient versus liquid velocity. From their experimental work the authors', i.e. Wei and Maa, propose that the reported influence of liquid velocity on boiling heat transfer can be summarised as follows: higher liquid velocity has both the benign effect of increasing the smaller convective heat transfer rate and, by the rapid removal of heat from the top of vapour bubbles via forced convection, the negative effect of impeding the detachment of vapour bubbles from the heating surface, which in turn leads to the inexorable degradation of the boiling coefficient measured with the dilute polymer solution.

In more recent years, i.e. commencing from 1995, the experimenters' Li Xiulin *et al.* [198,200,201] have pioneered the innovation of the three-phase (vapour-liquid-solid) fluidised bed heat exchanger, as a novel concept for the enhancement of heat transfer and prevention of scale formation in the boiling process.

Start Note: At this stage, for the purpose of clarity, it is worth distinguishing heat transfer in 'three-phase fluidised beds' relating to *(gas-liquid-solid) fluidisation*, from those concerning *(vapour-liquid-solid) flow boiling…*

Breifly, Muroyama and Fan [203] define *three-phase (gas-liquid-solid) fluidisation* as an operation in which a bed of solid particles is suspended in a gas and liquid media due to the net gravitational force or buoyancy force on the particles. Gas-liquid-solid fluidised bed reactors have been extensively covered in the literature by investigators' such as Kato *et al.* [132], Kim *et al.* [140], Muroyama and Fan [137,142,203], Chiu and Ziegler [79,204], Epstein [205] and Fan [206]. In these widely utilised systems, as well as even temperature

distribution and ease in handling large quantities of particles, such operations generate considerable and intimate contact among gas, liquid and solid particles, providing substantial advantages for chemical (e.g. hydrogenation of heptane), petrochemical (e.g. coal liquefaction), biochemical (e.g. biological waste treatment) and biological (e.g. production of antibiotics) processes requiring improved inter-phase contact efficiency. Employed for similar fields of biochemical, petrochemical and physical processing etc, gas-solid reactors, and certain applications of liquid-solid fluidised beds, are antecedents of the more recent gas-liquid-solid fluidised bed reactor.

In *three-phase (gas-liquid-solid) fluidisation*, the 'gas phase' is typically *introduced into* the reactor by means of a gas distributor, as opposed to the case for *three-phase (vapour-liquid-solid) flow boiling*, where coupled with liquid-solid fluidisation, the third 'vapour-phase' is *generated within* the system, and emanates from the boiling of the flowing liquid by the action of a heat source. Hence, gas-liquid-solid fluidised beds/reactors are not only functionally different from vapour-liquid-solid fluidised beds - where compared with the former, the latter relates to issues of boiling enhancement and scaling prevention - they are also operationally different. Hence, hereafter, in our discussions on *three-phase (vapour-liquid-solid) flow boiling*, works referring to heat transfer in *three-phase (gas-liquid-solid) fluidisation* are, to a large extent, non-essential, and therefore do not feature in the narrative. *End note*

Returning to the main narrative, Li Xiulun *et al.* [198,200,201] explored the feasibility of their proposed vapour-liquid-solid circulating fluidised bed heat exchanger, examining the effect of operating parameters (such as liquid flowrate, particle concentration and particle type/material) on the boiling heat transfer, fouling mitigation, pressure drop, and recycle pump power consumption performance of the three-phase flow boiling device. Throughout their series of published works, water or saturated brine is utilised as the continuous phase, whilst a variety of solid particles are adopted as the solid phase. Table 3.7 summarises the physical properties of some of the particles they investigated.

Material	**Diameter (mm)**	**Density (kg/m^3)**	**Thermal Conductivity (W/m.K)**	**Specific Heat (J/kg.K)**
Polytetrafluoroethylene	3	2190	0.249	1243
Glass particles	3	2520	1.093	669.9
Titanium particles	3	4505	31.0	524

Table 3.7: Physical properties of particles used by Li Xiulun *et al.* [201]

Firstly, in concordance with Wei and Maa [202], Li Xiulun *et al.* [198,200,201] find that in the presence of solid particles the heat transfer coefficient in three-phase (vapour-liquid-solid) flow boiling is on average 1.5 to 2.0 times greater than is the case for ordinary two-phase (vapour-liquid) flow boiling. According to the authors', this enhancement results from the collision of particles with the heat transfer wall, which consequently increases the number of nucleation sites as well as disrupts the heat transfer boundary layer. Concerning the effect of operating parameters, the researchers' report the following experiences gained from their body of work:

a. In three-phase flow boiling, the heat transfer coefficient increases lightly with an increase in brine flow rate. This is substantiated by Figure 3.55, a typical set of results obtained from the authors' studies. Unlike Wei and Maa [202] above and the earlier cited heat transfer trends in non-boiling fluidised beds (recall section 3.3), for their specified flow range, Li Xiulun *et al.* do not appear to observe the occurrence of heat transfer degradation across their higher flowrate region.

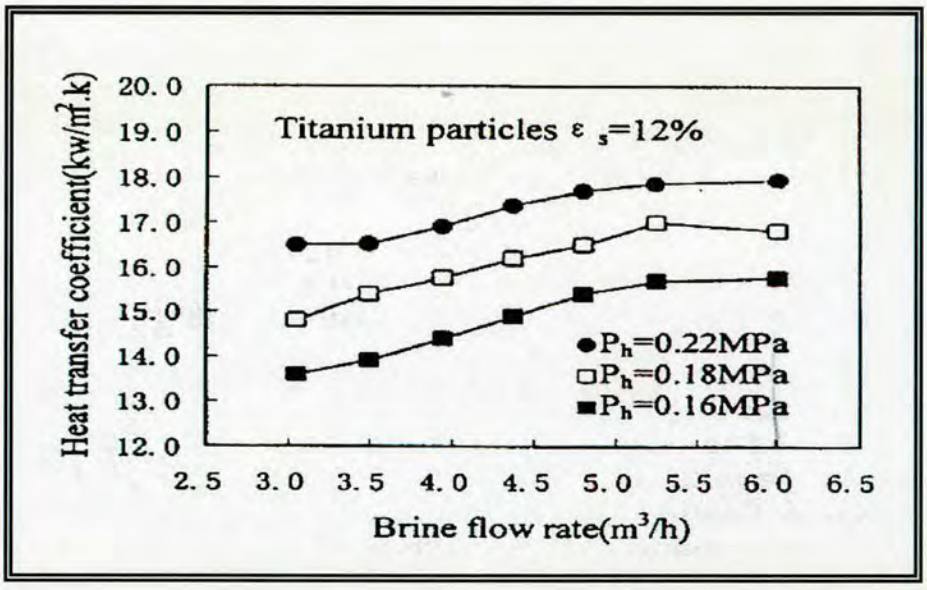

Figure 3.55: Effect of brine flowrate on three-phase flow boiling heat transfer coefficient. Taken from Li Xiulun *et al.* [201] where pressure of heating steam = P_h.

b. The overall pressure drop in the test tube of a three-phase circulating fluidised bed is composed of the gravitational pressure drop (primary factor), the frictional pressure drop and the accelerational pressure drop (both secondary factors). Figure 3.56 depicts the variation of overall pressure drop with brine flowrate as observed by Li Xiulun *et al.* [201]. From the visible trend, it is noticeable that for progressively higher velocities, the overall pressure drop in the test tube has the tendency to firstly increase prior to

decreasing. In the opinion of the authors', the most plausible set of justifications for such a plot are:

— as the brine flowrate approaches, and eventually exceeds, the minimum fluidisation velocity (approximately 4.75 m^3/h) particles are gradually fluidised and suspended within the tube. Hence, as the local solid hold-up steadily increases, the average bed density within the tube also increases, resulting in an elevation of both the gravitational and overall pressure drops.

— when the brine flowarte reaches a value of $\approx$ 5 m^3/h, the bed enters conventional fluidisation region where solid particles are completely fluidised, the local solid hold-up and the average bed density are maximal, and, therefore, the gravitational and overall pressure drop within the tube also reach a maximum.

— with further increase of brine flowrate above the critical transition velocity (i.e. the incipient significant entrainment velocity), the quantity of solid particles carried from the riser tube to the outer return tube increases and a fast circulating fluidised bed is finally formed. As claimed by the authors', this leads to the reduction of the local solid-hold-up within the riser tube, which in turn results in the decrease of the gravitational and overall pressure drops.

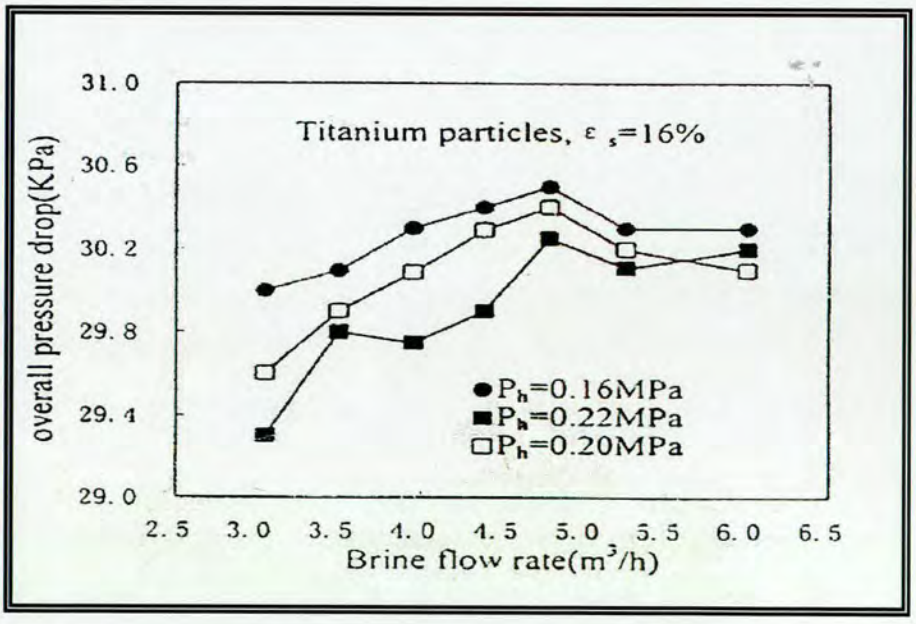

Figure 3.56: Effect of brine flowrate on the overall pressure drop in three-phase evaporator. From Li Xiulun *et al.* [201]

c. Figure 3.57 illustrates the effect of particle material on the measured boiling heat transfer coefficient. Li Xiulun *et al.* [198,200,201] repeatedly found that, for a given particle volume fraction, solid particles with larger density and thermal conductivity (e.g. titanium) register a more enhanced rate of heat transfer than particles whose density and thermal conductivity are lower (e.g. glass). Particles with higher density are more effective at disrupting the boundary layer; meanwhile, the higher the thermal conductivity of the particles, the faster they will acquire heat from the heating surface, ensuring that equilibrium between solid and liquid can be reached rapidly. However, from Figure 3.57 it is immediately apparent that the density and thermal conductivity of polytetrafluoroethylene particles are less than their titanium counterparts; according to the researchers' [201], the non-wetting property of polytetrafluoroethylene particles reduces the degree of wall superheat necessary for the production of vapour bubbles, thereby causing the three-phase flow boiling coefficient measured with polytetrafluoroethylene particles to be virtually equivalent to that measured with titanium particles.

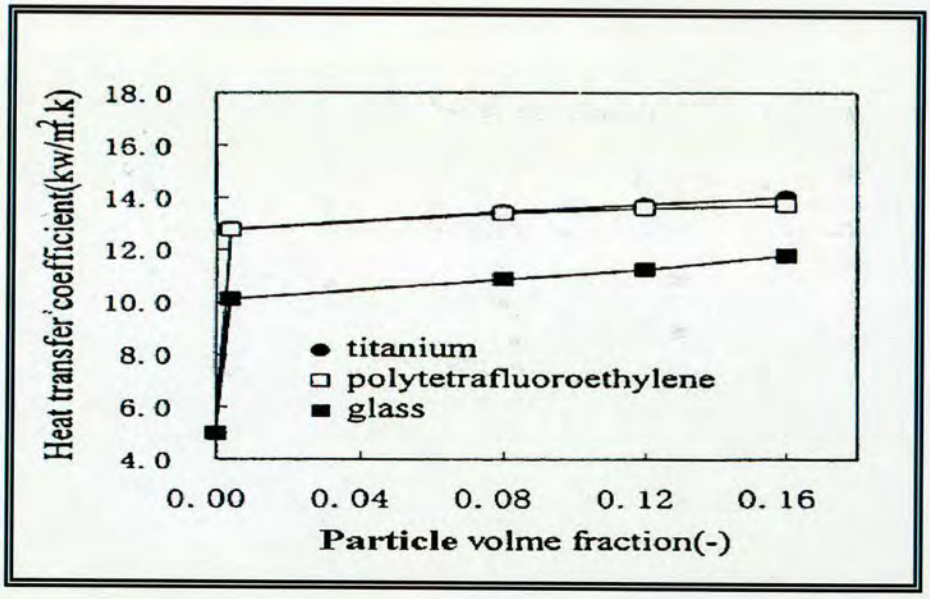

Figure 3.57: Effect of particle material and particle volume fraction on three-phase flow boiling heat transfer coefficient. Adopted from Li Xiulun *et al.* [201].

d. Continuing with Figure 3.57, we also see that flow boiling coefficients are proven to rise moderately for higher particle volume fractions/average solid hold-ups (i.e. the ratio of the initial volume of added particles to the total volume of the vapour-liquid-solid system), thus confirming that the presence of solid particles does indeed bring about more active nucleation sites.

e. In relation to the fouling prevention and cleaning behaviour of their three-phase fluidised bed evaporator, the authors' claim to have successfully operated their experimental apparatus for more than 1000 hours (i.e. in the boiling mode) without any discernable signs of scale deposition within the tubes of their brine evaporator. Appropriated from [200], Figure 3.58 shows the relation of evaporation intensity with time. The authors' report that on closing the circulating or control valve, the heat transfer coefficient rapidly declined due to the absence of particles in the bed. In their estimation, the documented trend indicates the build up of a fouling layer on the heater surface. On opening the circulating valve, the heat transfer coefficient is reported to have recovered its former level, suggesting that particles cannot only prevent fouling but also clean existing fouling. In addition, the authors' attempted to determine the impact of particles on the power consumption of the apparatus. Extracted from their work, Figure 3.59 depicts a comparison of the power consumption of the recycle pump with and without the inclusion of the solid phase. As evidenced from the plots, the presence of solid particles does not lead to any notable increase in the power consumption. Consequently Li Xiulun *et al.* conclude that, excluding material costs, the addition of solid particles would not result in any significant increase to industrial operating costs [201].

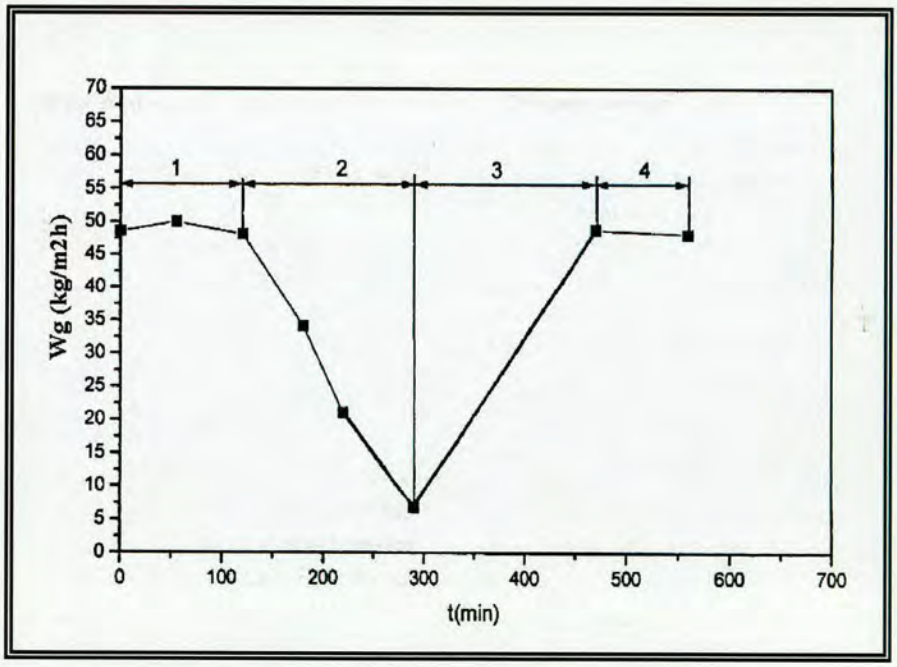

Figure 3.58: Relation of evaporation intensity, W_g (kg/m^2.h), with time. (1) Three-phase flow boiling stable operating zone; (2) Two-phase flow boiling zone; (3) Three-phase flow boiling restarting zone; (4) Three-phase stable operating zone. Flow velocity = 0.41 m/s and pressure of heating steam = 0.18 MPa.. From [200].

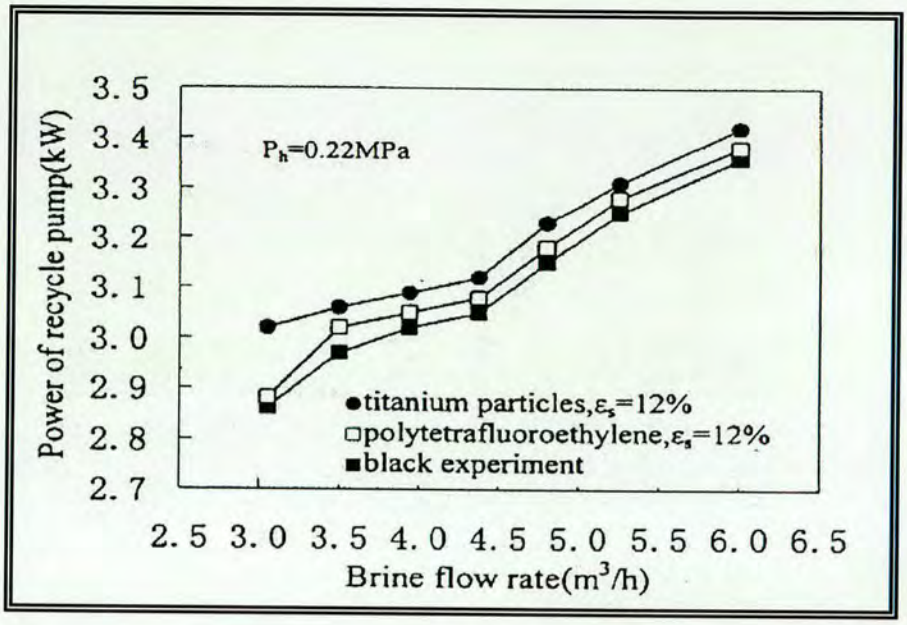

Figure 3.59: Power consumption of recycle pump under various operating conditions. Taken from Li Xiulun *et al.* [201] where solid fraction = ε_s

Finally, based on the heat transfer analysis of their vapour-liquid-solid evaporator, Li Xiulun *et al.* [201] proposed a mathematical model for predicting heat transfer coefficients in three-phase flow boiling, as expressed below:

$$\left(\alpha_{\text{T.F.B}}\right)^{t_R} = \left(\alpha_{\text{LS}}\, F_{\text{CB}}\right)^{t_R} + \left(\alpha_{\text{npb,p}}\, F_{\text{NB}}\right)^{t_R} \tag{3.61}$$

here α_{LS} essentially represents the heat transfer coefficient of liquid-solid fluidised flow and is correlated by the authors' according to the Jamialahmadi equation [82]; meanwhile, $\alpha_{\text{npb,p}}$ is the nucleate pool boiling heat transfer coefficient with solid phase, calculated by Yang and Maa [207] and adapted by Li Xiulun *et al.* [198]. The parameters F_{CB} and F_{NB} are the three-phase convective factor and the three-phase nucleate boiling correction factor respectively. A complete set of equations for the description of equation 3.61 is presented in Li Xiulun *et al.* [198], where the authors' claim good agreement between their experimental data and the results generated from their proposed correlation for three-phase (vapour-liquid-solid) flow boiling. According to the authors, most of their data is proven to lie within ± 20%.

In closing this chapter, it is fair to conclude, that from a review of the profiled literature, the self-cleaning circulating fluidised bed clearly offers great potential as a heat transfer enhancement and antifouling device for a whole range of industries. However, as previously expressed, despite the amount of academic and engineering work devoted to the subject area, there are still many unresolved questions, the comprehension of which would ensure the

proper optimisation and utilisation of the technology. This is particularly true for the case of three-phase (vapour-liquid-solid) fluidised bed heat exchangers, where investigations elucidating the complex mechanisms of boiling heat transfer enhancement and fouling prevention are in their infancy. Hence, to redress this insufficiency, more work is required for the better understanding of circulating fluidised beds, especially as they relate to three-phase flow boiling operations.

CHAPTER 4: EXPERIMENTAL APPARATUS & METHODS

4.1. PROJECT MOTIVATION AND EXPERIMENTAL OBJECTIVES

As summarised in *Chapter 1*, motivated by a desire to contribute to an improved understanding of three-phase flow boiling and its associated fundamentals, the present project explores the boiling heat transfer enhancement and fouling mitigation potential of a contemporary vapour-liquid-solid circulating fluidised bed heat exchanger.

To this effect, based on a combination of multiphase fluidisation and boiling heat transfer, a three-phase boiling device has been developed, and a systematic experimental study duly conducted, for the purpose of achieving the following explicit objectives:

- Firstly, for the more conventional case of two-phase flow boiling, to examine the influence of various operating parameters on the heat transfer rate, and in so doing, to establish consistency between our experimentally obtained results and the well documented two-phase (vapour-liquid) flow boiling trends.

- Secondly, to investigate the heat transfer performance of our proposed three-phase flow boiling device, over a stipulated range of liquid superficial velocities and heat fluxes.

- Thirdly, to determine the influence of particle physical properties, specifically particle size, on the measured three-phase boiling coefficient.

- Next, to compare the observed heat transfer behaviour in three-phase flow boiling with the results of two-phase flow boiling. System discrepancies, which arise from the addition of solid particles to the boiling fluidised bed, are identified and subsequently analysed.

- In the field of heat transfer, the dynamics of bubble formation, growth, and departure are closely related to the mechanisms of boiling. Hence, to enlighten our interpretation of the obtained results, and further our comprehension of the related heat transfer mechanisms, flow visualization studies regarding bubble dynamics and particle-wall interaction, are also to be undertaken.

- Finally, based on an analysis of the contributory heat transfer mechanisms, coupled with the extension of existing two-phase flow boiling and (liquid-solid) fluidised bed heat transfer models, a boiling correlation is to be derived for the prediction of heat transfer in our three-phase fluidised bed.

Figure 4.1 offers a general arrangement sketch of the boiling device as installed in the laboratory. Amongst other things, the illustration displays the riser column, the connected outlet chamber, and the particle return system. Also depicted is the location of the electrical heat source (including the approximate thermocouple spacing along the heater length) relative to the flow channel. From the liquid reservoir, a pre-heater heats the working liquid to within 10 °C of its saturation temperature, before delivery to the test section.

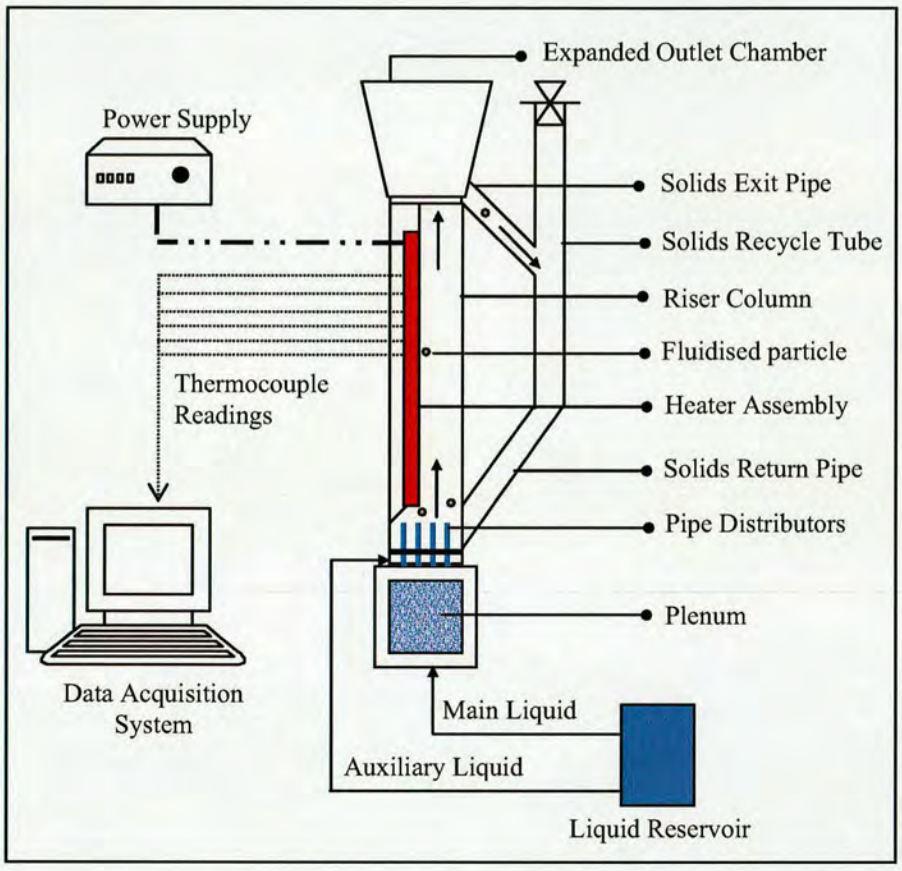

Figure 4.1: Sketch illustrating the 3-phase test unit and some supporting components.

Preliminary testing, conducted to ensure the attainment of the best possible results, revealed that accurate temperature measurements, as well as sustainable particle circulation, were readily achievable with the designated heater arrangement and bed geometry as shown above.

For the purpose of clarity, the next section sets forth the design details and the technical performance of the suggested test unit.

4.2. THE 3-PHASE TEST SECTION: DESIGN & GENERAL DESCRIPTION

4.2.1. ESTIMATION OF BED DIMENSIONS AND FLUIDISING VELOCITIES

For the sizing of the fluidised bed, Table 4.1 (overleaf) shows a summary of some essential bed dimensions and operating conditions, selected from a number of (liquid-solid) and (vapour-liquid-solid) fluidised bed investigations. The presented liquid and solid volumetric terms, Q_L and Q_p respectively, are easily estimated as follows:

$$Q_L = A_{CS} . U_L \tag{4.1}$$

$$Q_p = \left(\varepsilon_p / 1 - \varepsilon_p \right) . Q_L \tag{4.2}$$

Here ε_p is the solid or particle volume fraction (i.e. the ratio of the volume of particles added to the system and the total volume of the system), whilst A_{CS} denotes the cross-sectional area of the fluidised bed. In preparing Table 4.1, the maximum reported values of ε_p and U_L were employed for the calculation of Q_L and Q_p.

Bearing in mind that at the test section, the maximum achievable liquid delivery rate was equivalent to 80 litres/min, the achievability of various design criteria's were subsequently explored. The object of this process was to identify a viable design basis, for the development of a test unit capable of accommodating a broad range of particles and operating conditions, comparable to the references listed in Table 4.1. As a consequence of such trial and error exercises, the following assumptions were selected as the basis upon which our three-phase test unit would be designed:

Prescribed Bed Dimensions			**Prescribed Particles and associated properties**							**Max. U_L**
Shape	*L* (mm)	*W* (mm)	*Type*	*Size* (mm)	*Density* (kg/m^3)	$Re_{p\infty}$	$C_{D,TL}$	U_∞ (m/s)	U_{mf} (m/s)	(m/s)
Square	1200	80	Lead	3	11373	10314	0.422	1.005	0.111	1.5
Assumed Working Medium H_2O								**Limiting Delivery Rate** 80 litres/min		
Liquid Properties read at 100 °C										
Dynamic viscosity, $\mu_L = 2.82 \times 10^{-4}$ kg/ms.								*Density*, $\rho_L = 958.4$ kg/m^3		

Table 4.2: Design assumptions for the estimation of test unit dimensions and operating velocities. here W = width.

AUTHORS	Yr.	SYSTEM BREAKDOWN													
		Boiling Status	**Bed Geometry & Dimensions**				**Liquid Velocity (U_L) Range**		**Solid Fraction (ε_p) Range**		**Particle Size (d_p) Range**		**Particle Density (ρ_p) Range**		**Max. Bed Q_L**	**Max. Bed Q_p**
			Shape	*L* (mm)	D_i (mm)	A_{CS} (m^2)	*min* (m/s)	*max* (m/s)	*min* (%)	*max* (%)	*min* (mm)	*max* (mm)	*min* (kg/m^3)	*max* (kg/m^3)	(m^3/s)	(m^3/s)
Kim et al. [73]	1995	Non-boiling	Circular	1400	14	1.54×10^{-4}	0.5	2.0	4	21	3	3	2520 (*glass*)	2520 (*glass*)	3.08×10^{-4}	8.19×10^{-5}
Li et al. [198]	1995	Boiling	Circular	980	32	8.04×10^{-4}	0.04	0.11	9.61	21.14	0.1	0.9	2520 (*glass*)	8960 (*copper*)	8.84×10^{-5}	2.37×10^{-5}
Zheng [208]	1999	Non-boiling	Circular	3000	76.2	4.56×10^{-3}	0.07	0.5	1.5	25	0.51	0.6	1100 (*plastic*)	7850 (*steel*)	2.28×10^{-3}	7.6×10^{-4}
Zhang and Li [200]	2000	Boiling	Circular	2000	39	1.19×10^{-3}	0.16	0.71	8	20	3	3	2520 (*glass*)	7850 (*steel*)	8.48×10^{-4}	2.12×10^{-4}
Ahn et al. [75]	2002	Non-boiling	Circular	705	16.2	2.06×10^{-4}	0.3	1.8	4.8	4.8	2	4	1500 (*sand*)	8960 (*copper*)	3.17×10^{-4}	1.87×10^{-5}
Lee et al. [74]	2003	Non-boiling	Circular	1400	10	7.85×10^{-5}	0.5	1.7	4	21	3	3	2520 (*glass*)	2520 (*glass*)	1.33×10^{-4}	3.55×10^{-5}
Jianping et al. [201]	2004	Boiling	Circular	2000	45	1.59×10^{-3}	0.52	1.05	4	16	3	3	2520 (*glass*)	4505 (*titanium*)	1.66×10^{-3}	3.16×10^{-4}

Table 4.1: Summary of some essential bed dimensions and operating conditions, adapted from a selection of (l-s) and (v-l-s) fluidised bed investigations. here L = length, whilst D_i = internal diameter.

Returning to Table 4.2 above, it is worth noting that, here, the drag coefficient is obtained from Turton and Levenspiel [100] and expressed as follows:

for $Re_{p\infty} \leq 2 \times 10^5$

$$C_{D,TL} = \frac{24}{Re_{p\infty}}\left[1 + 0.173 Re_{p\infty}^{0.657}\right] + \frac{0.413}{1 + 16300\, Re_{p\infty}^{-1.09}} \tag{4.3}$$

Meanwhile, the particle free-fall velocity in the absence of wall effects, U_∞, and the particle terminal Reynolds number, $Re_{p\infty}$, are determined from equations 3.24 and 3.29 respectively. Furthermore, considering that the apparatus is intended to operate under conditions of boiling, for the purposes of design, the liquid properties listed in Table 4.2 are read at saturation temperature. U_{mf}, also indicated in Table 4.2, refers to the minimum fluidising velocity, whose definition and derivation are addressed below.

Finally, differing from the studies presented in Table 4.1, the adoption of a square-shaped bed is of major significance, as it allows the use of transparent glass sections, thus permitting the implementation of flow visualisation techniques, and thereby making possible a qualitative observation of, and quantitative research into, the complex multiphase flow system. As stated in the objectives, information acquired from such a facility (i.e. flow visualisation) would greatly strengthen our understanding of the heat transfer mechanisms associated with three-phase flow boiling.

The Minimum Fluidising Velocity, U_{mf}

Firstly, consider a bed of particles resting on a distributor designed for uniform upflow of liquid; the onset of fluidisation occurs when

(drag force by upward moving fluid) = (weight of particles) (4.4)

or, with $\Delta P^{"}$ always positive,

$$\Delta P_d^{"} . A_{CS} = A_{CS}\, L_{mf}\left(1 - \varepsilon_{mf}\right)\left[\left(\rho_p - \rho_L\right)g\right] \tag{4.5}$$

here L_{mf} is the height of the bed at minimum fluidisation.

The minimum superficial velocity required for fluidisation, U_{mf}, is a function of the particle and liquid properties, and for spherical shaped particles can be obtained from the following expression [209]:

$$\frac{1.75}{\varepsilon_{mf}^3}\left(\frac{d_p U_{mf}\rho_L}{\mu_L}\right)^2+\frac{150(1-\varepsilon_{mf})}{\varepsilon_{mf}^3}\left(\frac{d_p U_{mf}\rho_L}{\mu_L}\right)=\frac{d_p^3\rho_L(\rho_p-\rho_L)g}{\mu_L^2} \tag{4.6}$$

or,

$$\frac{1.75}{\varepsilon_{mf}^3}Re_{p,mf}^2+\frac{150(1-\varepsilon_{mf})}{\varepsilon_{mf}^3}Re_{p,mf}=Ar \tag{4.7}$$

According to Kunii and Levenspiel [209], the voidage at minimum fluidising conditions, ε_{mf}, may typically be estimated from random packing data. However, in circumstances such as these, where ε_{mf} is unknown, the minimum fluidising velocity can still be calculated by the following means:

Firstly, equation 4.7 can be rewritten as

$$Y_1'' Re_{p,mf}^2+Y_2'' Re_{p,mf}=Ar \tag{4.8}$$

where,

$$Y_1''=\frac{1.75}{\varepsilon_{mf}^3} \quad \text{and} \quad Y_2''=\frac{150(1-\varepsilon_{mf})}{\varepsilon_{mf}^3} \tag{4.9}$$

Rearranging equation 4.8 generates the expression

$$Re_{p,mf}=\left[\left(\frac{Y_2''}{2Y_1''}\right)^2+(Y_1'')^{-1}.Ar\right]^{1/2}-\left(\frac{Y_2''}{2Y_1''}\right) \tag{4.10}$$

Wen and Yu [105] were the first to note that Y_1'' and Y_2'' stayed nearly constant for different kinds of particles over a wide range of conditions, giving predictions of U_{mf} with a 34% standard deviation. For the two constants in equation 4.10, the values recommended by Wen and Yu [105] are:

for fine particles,

$$\left(\frac{Y_2''}{2Y_1''}\right)=33.7 \quad \text{and} \quad (Y_1'')^{-1}=0.0408 \tag{4.11}$$

Hence, solving equation 4.10 for minimum fluidising conditions, and using the values of Y_1'' and Y_2'' as given in equation 4.11 above, gives:

$$Re_{p,mf} = \frac{d_p U_{mf} \rho_L}{\mu_L} = \left[(33.7)^2 + 0.0408. \left(\frac{d_p^3 \rho_L (\rho_p - \rho_L) g}{\mu_L^2} \right) \right]^{1/2} - 33.7 \qquad (4.12)$$

As demonstrated in Table 4.2, the resultant expression (i.e. equation 4.12) provides a useful rough estimate for determining the minimum superficial velocity necessary for the fluidisation of a bed of high density particles such as lead.

The Pumping Power Requirement

For incompressible flow the power required to pump the fluidising liquid through the system, q_{pump}, is the product of the total pressure drop across the system, $\Delta P_t''$, and the liquid volumetric flowrate:

$$q_{pump} = \Delta P_t'' . Q_L \qquad (4.13)$$

As earlier stated in subsection 3.3.1.1, for stable operation of a fluidised bed heat exchanger, Klaren [55] defines the total pressure drop across the system according to equation 3.8. However, here, for the purposes of simplification $\Delta P_t''$ can be expressed as:

$$\Delta P_t'' = g(\rho_p - \rho_L)(1 - \varepsilon)L \qquad (4.14)$$

Hence setting a minimum bed voidage of ε = 0.4, and using particle properties, liquid properties and bed dimensions as stipulated in Table 4.2, from equation 4.14, the predicted overall pressure drop across the 3-phase test unit equates to:

$$\Delta P_t'' = (9.81)(11373 - 958.4)(1 - 0.4)1.2$$
$$= \underline{73560\,\text{Nm}^{-2} \text{ or } 0.7356\,\text{bar}}$$

Therefore, designing with a limiting liquid delivery rate of 80 litres/min (or 1.33 x 10^{-3} m^3/s) and an allowable overall system pressure drop of 73560 Nm^{-2}, from equation 4.13 the fluidising liquid pumping power is then:

$$q_{pump} = (73560).(1.33 \times 10^{-3})$$
$$= \underline{97.83\,\text{Watts}}$$

4.2.2. CONSTRUCTION OF RISER COLUMN

4.2.2.1. THE COLUMN MAINFRAME

To design for a square sectioned riser column, which accommodates a maximum liquid delivery rate of 1.33×10^{-3} m^3/s, as well as having the specified bed dimensions and operating velocities outlined in Table 4.2, necessitates a bed cross-sectional area of the following proportions

$$A_{CS,1} = (Q_L, \text{design})/(U_L, \text{design}) \tag{4.15}$$
$$= (1.33 \times 10^{-3})/(1.5)$$
$$= \underline{8.89 \times 10^{-4}\ \text{m}^2}$$

Such a value is of an order of magnitude comparable with the cross-sectional areas indicated in Table 4.1, which are for studies conducted in circular flow channels.

Hence subject to the prescribed bed dimensions of L = 1200 mm, W = 80 mm, and an implied thickness = 11 mm (i.e. $A_{CS,1}$ / 80 mm width), the body of the riser column has been fabricated from a combination of two 4 mm thick, 980 mm long 'toughened' glass pieces, and two 25 mm thick, 1030 mm long aluminium alloy blocks. The glass pieces act as the front and back face of the column, thus facilitating the observation of phenomena occurring within the bed. Meanwhile, rectangular cross-sectioned grooves are machined out of the aluminium blocks, forming 'frames' into which the glass pieces are subsequently placed.

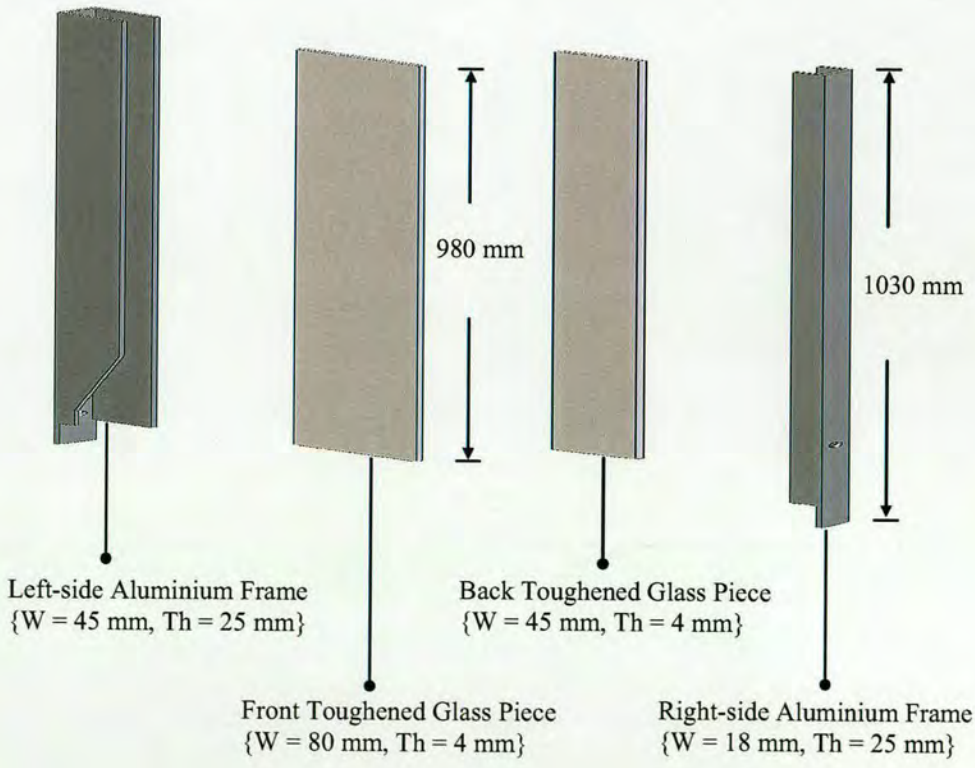

Figure 4.2: Constructing the body/mainframe of the riser column

Figure 4.2 depicts the construction of the column mainframe, illustrating the arrangement of the glass and aluminium sections. A schematic of the initial bed cross-section (i.e. $A_{CS,1}$) resultant from the described arrangement is shown in Figure 4.3 following.

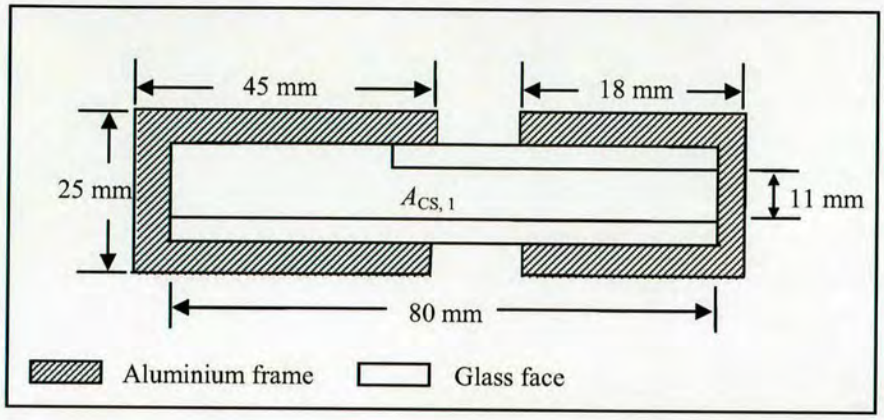

Figure 4.3: Schematic of initial bed area formed by mainframe assembly (i.e. glass and aluminium sections only).

To separate and secure the position of the glass pieces to the aluminium frames, two PTFE (polytetrafluoroethylene) polymer insulators, shown in Figure 4.4, are included in both the left and right sides of the formed channel. Bolts through the aluminium frames fix the insulators into place; furthermore, as indicated in the diagram, a rectangular section is extruded out of the left-side insulating block, in order to provide a compartment for the housing of the intended heater assembly.

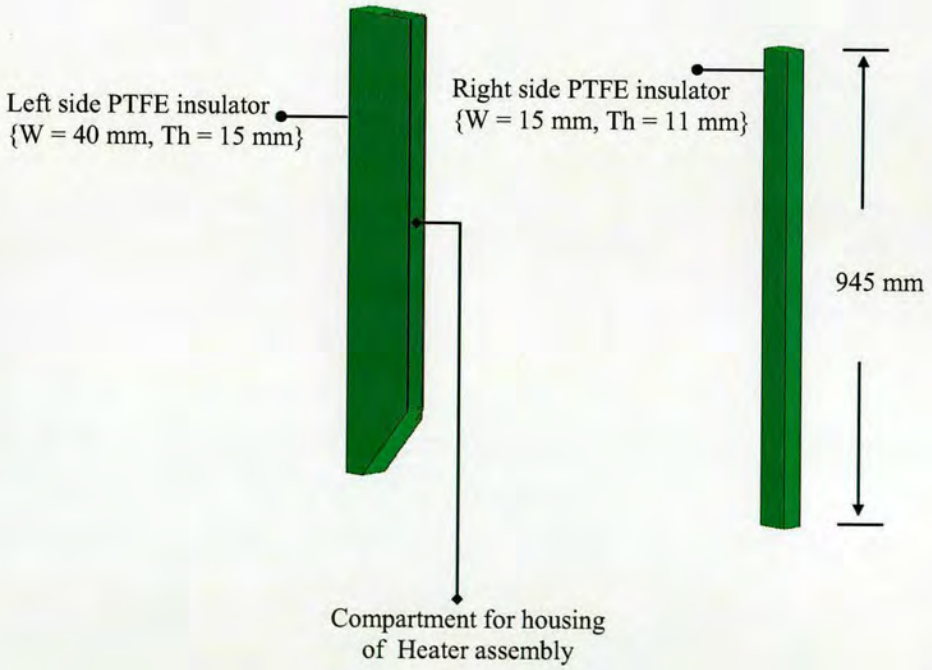

Figure 4.4: Depiction of PTFE insulators showing cavity for heater assembly

4.2.2.2. THE HEATER BLOCK ASSEMBLY

Within the bed, an electric cartridge heater rod of 8mm diameter x 730 mm length serves as the heat source. The heater rod (made of stainless steel and rated at 240 V, 10 Amps, with a maximum power output of 2.5 kW) is encased in a U-shaped channel, machined out of a 24 mm wide, 11 mm thick, and 794 mm length of copper. This assembly creates the heater block, which after being placed in its PTFE insulated compartment, is then fixed to the left-side wall of the riser column. Consequently, this yields a heating surface area of 7.15×10^{-3} m^2 along the flow direction, permitting a maximum attainable heat flux of approximately 350 kW/m^2.

The start of the heated length is located 180 mm downstream of the column entrance, thus allowing for full flow development. Figure 4.5 graphically illustrates the heater block assembly and copper heating surface, whilst Figure 4.6 shows the cartridge heater rod prior to its installation in the test unit.

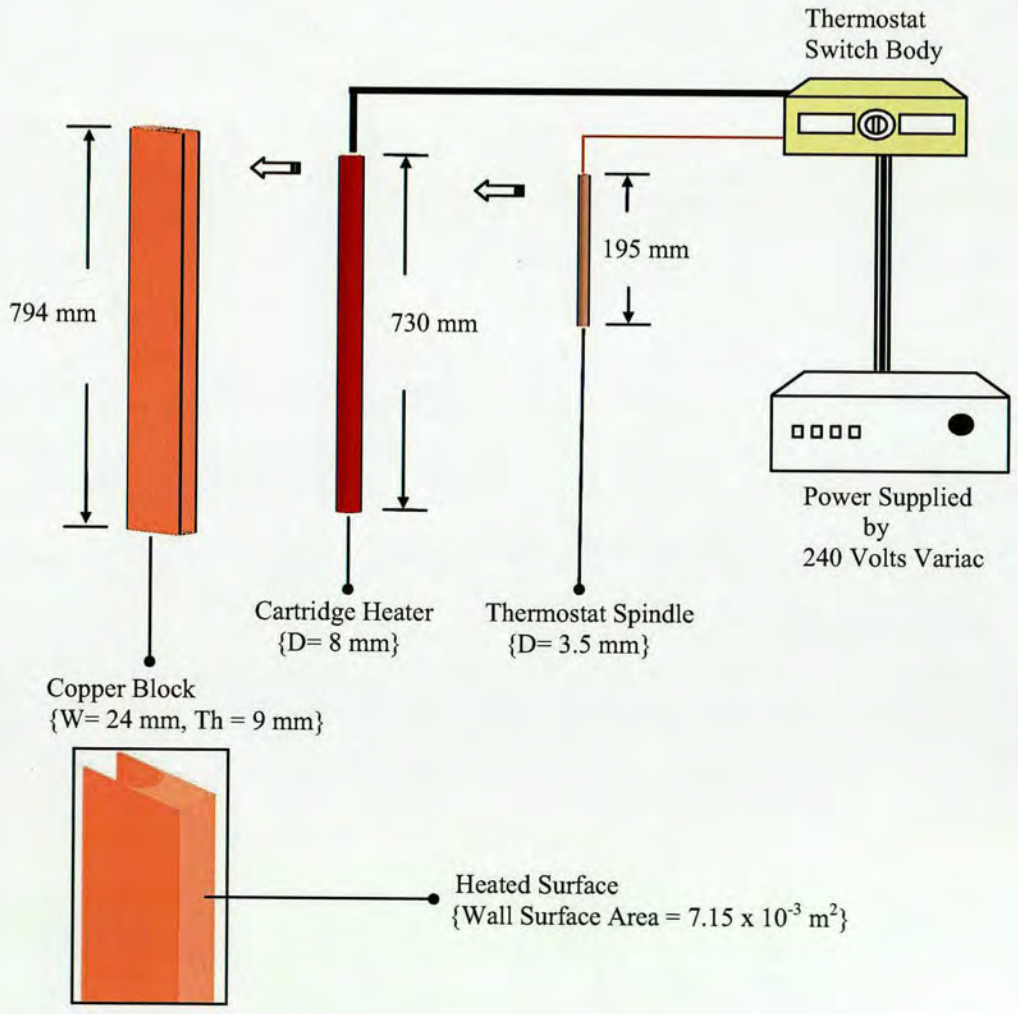

Figure 4.5: Depiction of heater block assembly showing the power supply connection; the copper bar, cartridge heater and control thermostat arrangement; as well as the heat transfer surface area exposed to the flow channel.

As evidenced in Figure 4.5, a control thermostat is also included in the heater block assembly. With an operating temperature range from 0 to 300 °C, the device acts as an on/off safety switch, capable of terminating power supply to the cartridge heater once a determined temperature is reached.

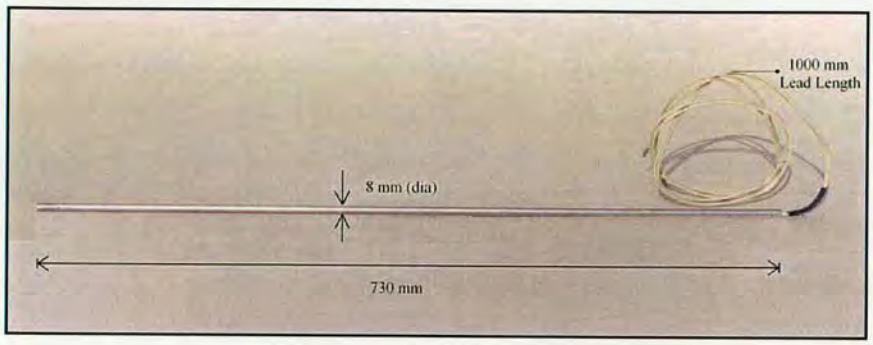

Figure 4.6: Photograph of high density cartridge heater supplied by CHROMALOX, UK.

With its low thermal conductivity, excluding the 11 mm x 794 mm heat transfer surface, the 16 mm thick PTFE material surrounding the heater block (see subsection 4.2.2.1 previous) guarantees sufficient thermal separation from the aluminium frame, thus assuring only negligible heat loss to the surrounding atmosphere. Table 4.3 list some relevant properties of PTFE.

Insulating Material	**Brand Name**	**Operating Range** (°C)	**Density** (kg/m^3)	**Thermal Conductivity** (W/m.K)
PTFE (polytetrafluoroethylene)	Teflon	-200 to 260	2190	0.249

Table 4.3: Physical properties of insulating material

4.2.2.3. THE HEATED FLOW CHANNEL

Along the riser column, the inclusion of the heater assembly forms a one-side heated flow channel with a length of 794 mm and a modified cross-sectional area, A_{CS}, of 2.365 x 10^{-4} m^2. Over this heated flow length, for an intended maximum delivery rate of 80 litres/min, the magnitude of A_{CS} accommodates liquid superficial velocities up to 5 m/s. Taken during the course of fabrication, Figure 4.7 is a photographic plan view of the riser column, showing its internal structure and indicating the 11 mm x 21.5 mm heated flow channel.

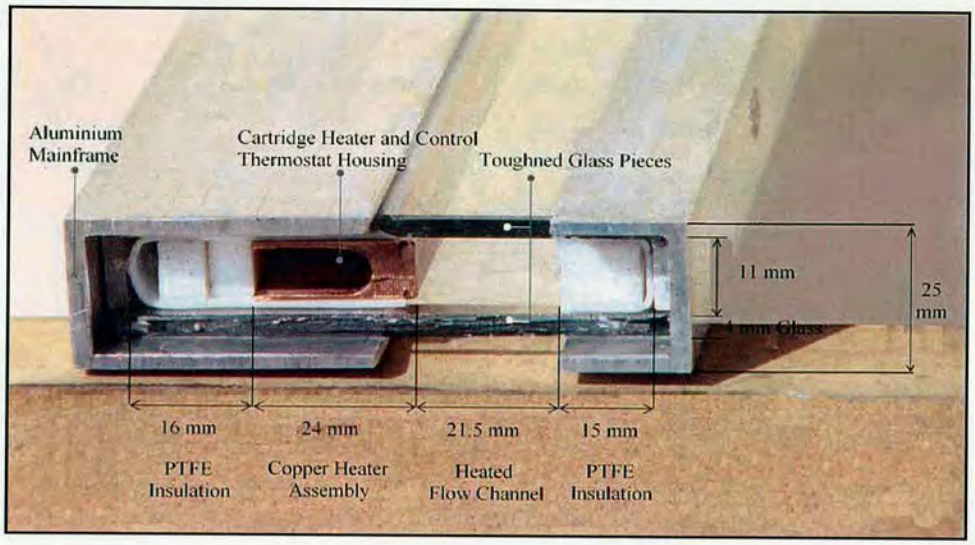

Figure 4.7: Plan view of riser assembly showing heated flow channel and internal structure

Additionally, to prevent leakages from the column structure, a high temperature resistant silicone gel is employed as sealant.

By drilling through the aluminium mainframe and PTFE insulator, pin like holes with a 1 mm diameter opening, are punched along the length of the copper block each to a depth of 5 mm. For the measurement of wall surface temperature, 8 OMEGA K-Type thermocouples (1.5 inch probe length) were inserted into the miniature openings, which are evenly spaced at 91 mm intervals along the heater assembly. A thermal bonding expoxy has been used to seal all probe entrances. To improve measurement accuracy, the thermocouple entrance holes are machined as close to the liquid contacting surface as is feasibly possible. With regards to the bulk fluid temperature, a single probe is installed at the entrance of the heated flow channel in order to evaluate the inlet fluid temperature. Likewise, at the exit or top of the flow channel, another lone probe is inserted for the measurement of the outlet fluid temperature. Figure 4.8 shows a photo of a typical probe. In addition, Figure 4.9 shows a schematic of the finalised riser column, illustrating the thermocouple placements relative to the heated flow length.

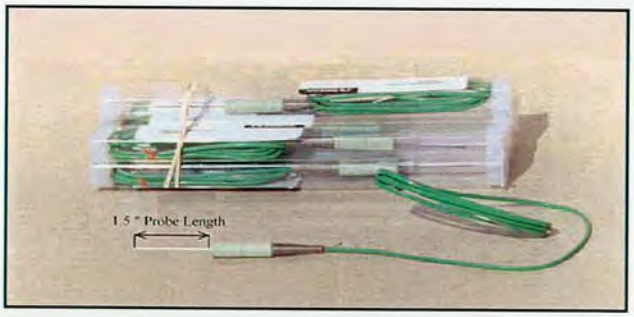

Figure 4.8: Photograph of OMEGA transition junction style (K-type) thermocouple probe

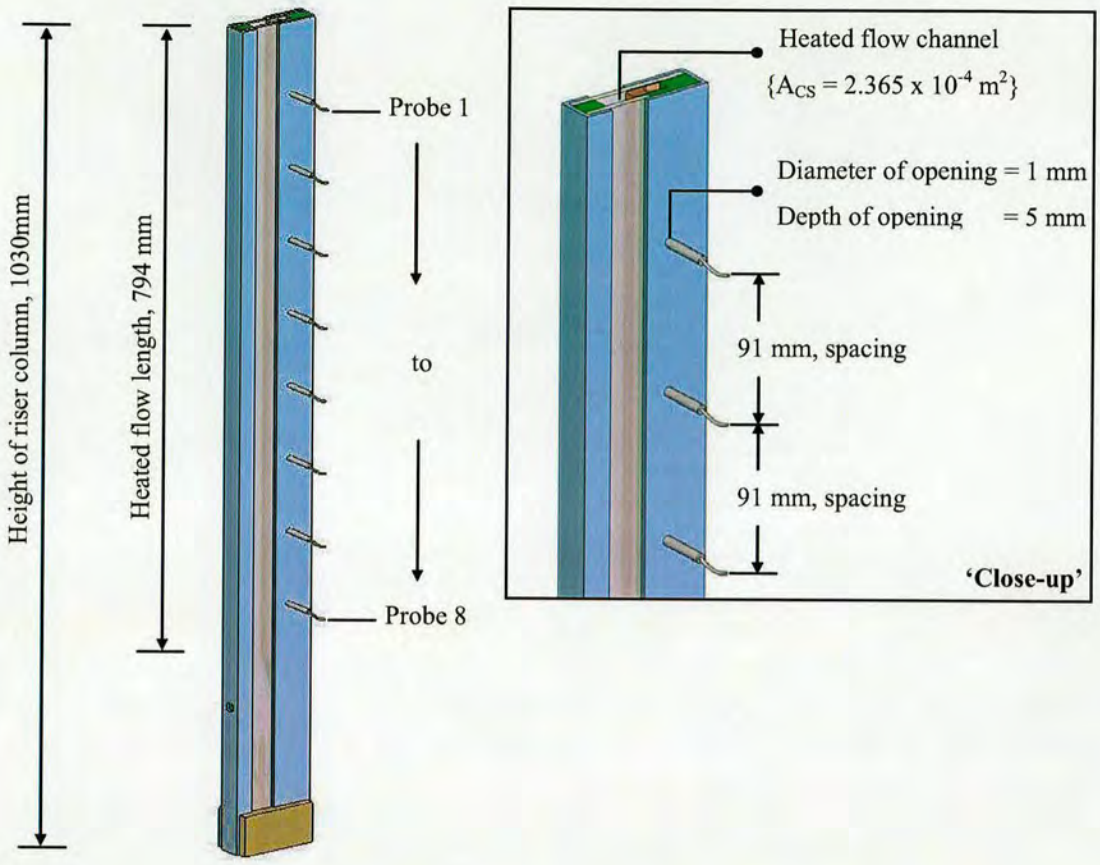

Figure 4.9: Multiple views of finalised riser column, showing thermocouple locations relative to heated flow length.

4.2.3. DESIGNING THE INLET CHAMBER

The particle distribution section and the plenum, or water box, together constitute the inlet chamber of the proposed three-phase boiling device. Let us first begin with the water box…

4.2.3.1. THE PLENUM/WATER BOX

Situated at the very base of the test unit, the plenum or water box is a simple, cube-shaped, stainless steel receptacle, into which main liquid flow is firstly injected. With appropriately sized and evenly spaced holes extruded from its upper surface - to which distribution pipes are fixed - the function of the water box is the regulation, or management, of main liquid flow into the particle distribution section.

4.2.3.2. THE PARTICLE DISTRIBUTION SECTION

The particle distribution section is itself comprised of the following individual components.

A. *Stainless Steel Pipe Distributors*: Screwed into the plenum, these serve as conduits via which main liquid flow is transported up into the riser column. Although not featured in the tabulated summary given in Table 4.1, according to the reviewed literature, main

liquid distributor(s) are usually designed to occupy 20 to 30 % of the available bed cross-sectional area. Again, to ensure even dispersion of the main liquid flow, an arrangement of multiple pipe distributors is commonly preferred to the use of a single distributor.

B. *Copper Porous Plate*: The primary functions of the device are, firstly, to provide a platform upon which introduced solid particles settle, and, secondly, to distribute the fluidising auxiliary liquid uniformly over the bed cross-sectional area. Random mixing in the bed often changes local pressure above the distributor. This causes the flow through individual orifices to fluctuate. More liquid flows through orifices that are subjected to lower downstream pressures; thus channels, or flow paths, of low voidage are established above these orifices, further increasing their through-flow to the detriment of others. Hence, the properties desired of a porous plate distributor can be summarised as follows:

— uniform and stable fluidisation over the entire range of operation.
— minimum amount of dead zones on the plate distributor surface
— minimum plugging over extended periods of operation

In general, Kunii and Levenspiel [209] recommend the fraction of open area on the porous distributor plate be less than 10 %. Figure 4.10(a) shows a typical design of a porous and straight-hole orifice type which traditionally uses vertical orifices through a grid/sintered plate.

C. *Fixing Plate*: Made from rubber, the fixing plate simply secures the junction between the pipe distributors and the water box.

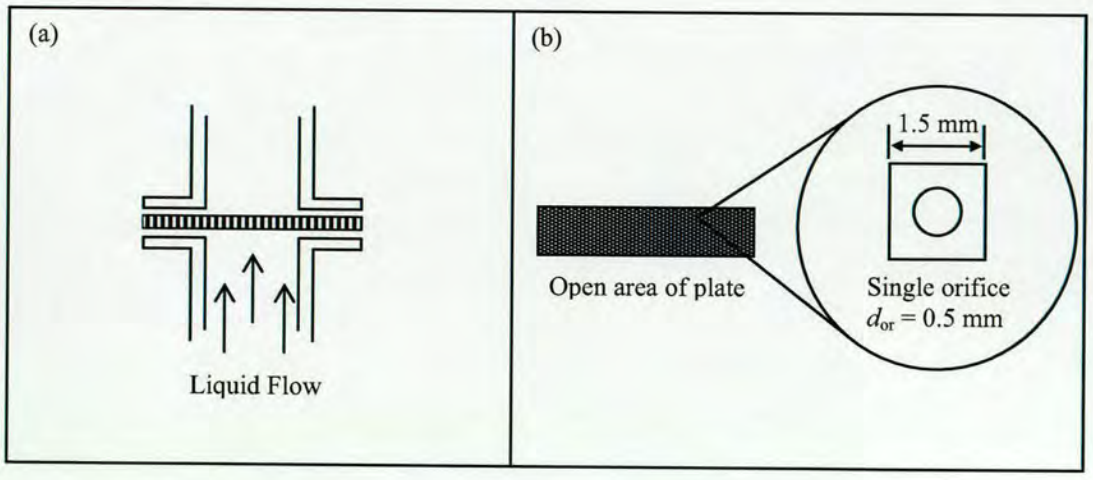

Figure 4.10: (a) Typical design of porous plate with vertical straight-hole orifices, (b) Plain view of porous plate, illustrating open area and orifice specifications.

In designing the particle distribution section, the problem of achieving uniform particle fluidisation over the entire area of the porous plate, can be addressed by a distributor pressure drop, $\Delta P_d^{"}$, considerably in excess of that which would allow for the previously discussed non-homogeneties in local pressure above the plate.

As typified by Klaren [55], design experience suggests a distributor pressure drop 0.1 to 0.3 times that across the entire bed (see equation 3.7). Hence for our purposes, it is sufficient to assume that:

$$\Delta P_d^{"} = 0.1 \Delta P_t^{"} \tag{4.16}$$

Therefore, substituting our value of $\Delta P_t^{"}$ as determined in equation 4.14, from equation 4.16 above the pressure drop across the porous distributor is then:

$$\Delta P_d^{"} = (0.1)(73560)$$

$$= \underline{7356\,\mathrm{Nm^{-2}} \quad \text{or} \quad 0.0736\,\mathrm{bar}}$$

Armed with the above figure, the porous plate can then be modelled directly from orifice theory as described by Kunii and Levenspiel [209] and outlined below:

I. The vessel Reynolds number for the flow approaching the distributor can be determined from the following expression:

$$Re_d = \frac{D_{e,l}\, U_{AL}\, \rho_L}{\mu_L} \tag{4.17}$$

here U_{AL} represents the auxiliary or secondary liquid flow approaching the porous plate.

The relationship between the total, main and auxiliary liquid flows can be simply defined as follows:

Total liquid flow (Q_L) = main liquid flow (Q_{ML}) + auxiliary liquid flow (Q_{AL}) (4.18)

Assuming a constant bed entrance area equivalent to $A_{CS,l}$, equation 4.18 becomes,

$$U_L = U_{ML} + U_{AL} \tag{4.19}$$

In apportioning the ratio of U_{ML} to U_{AL}, one of the main design prerequisites was that the available secondary liquid flow be in excess of the minimum superficial velocity necessary for incipient fluidisation of the particle layer above the plate (i.e. $U_{AL} >> U_{mf}$).

Therefore, designing for high density lead particles with a calculated minimum fluidisation velocity of U_{mf} = 0.111 m/s, and assuming an operating liquid velocity of U_L = 1.5 m/s (see Table 4.2), it is sufficient to allocate U_{AL} as

$$U_{AL} = (13\%)(U_L) = (0.13)(1.5) = \underline{0.2\,\text{m/s}} \tag{4.20}$$

In equation 4.20 above, a percentage proportion of 13% (arrived at by trial and error) has been selected, as it is of a magnitude sufficient enough to meet the aforementioned prerequisite of $U_{AL} >> U_{mf}$ (where, as stated above, U_{mf} is taken as equal to 0.111 m/s, as estimated for lead particles). Meanwhile, returning to equation 4.17, based on the cross-sectional area of the non-heated section of the fluidised bed (i.e. $A_{CS,1}$), the equivalent bed diameter for this region, $D_{e,1}$, is calculated as below:

$$D_e = \frac{4 \times \text{cross - sectional area of flow}}{\text{wetted perimeter}} \tag{4.21}$$

here D_e refers to equivalent or hydraulic mean diameter. Hence,

$$D_{e,1} = \frac{4(A_{CS,1})}{(2 \times 0.08) + (2 \times 0.011)} = \frac{4(8.89 \times 10^{-4})}{0.182} = \underline{19.34 \times 10^{-3}\,\text{m}} \tag{4.22}$$

Finally, inserting the values of equation 4.20 and 4.22 back into equation 4.17 generates a distributor Reynolds number equal to:

$$Re_d = \frac{(19.34 \times 10^{-3})(0.2)(958.4)}{2.82 \times 10^{-4}} = \underline{13{,}155} \tag{4.23}$$

II. For values of Re_d > 3000, the investigators Kunii and Levenspiel [209] recommend the following corresponding value for the orifice coefficient:

$$C_{d,or} = 0.6$$

III. The liquid superficial velocity through the orifice - estimated at an approach temperature of 100 °C – can then be determined as follows:

$$U_{or} = C_{d,or}\left[\frac{2.\Delta P_d''}{\rho_L}\right]^{1/2} = 0.6\left[\frac{2x7356}{958.4}\right]^{1/2} = \underline{2.35\,m/s} \qquad (4.24)$$

IV. The fraction of open area in the porous plate is then given by:

$$\frac{U_{AL}}{U_{or}} = \frac{0.2}{2.35} = \underline{0.085 \text{ or } 8.5\%} \qquad (4.25)$$

This value is acceptable, since it does not exceed Kunii and Levenspiels' specified limit of 10 %.

V. Lastly, to meet the requirements detailed above, the relationship between the number and size of orifices per unit area of distributor (i.e. N_{or} and d_{or} respectively) is obtained from equation 4.26 below:

$$d_{or}^2 . N_{or} = \frac{4}{\pi}\left(\frac{U_{AL}}{U_{or}}\right) \qquad (4.26)$$

Solving, we find the following possible combinations,

d_{or} (m)	0.0002 (0.2 mm)	0.0005 (0.5 mm)	0.0008 (0.8 mm)	0.0010 (1.0 mm)	0.0013 (1.3 mm)
N_{or} (m^{-2})	2.71×10^6	4.33×10^5	1.69×10^5	1.08×10^5	6.41×10^4

Even with every precaution taken to filter the working media, orifices that are too small are still susceptible to clogging, whereas those that are too large may cause uneven distribution of auxiliary liquid flow. In light of these considerations, the following specification was adopted:

$$d_{or} = \underline{0.0005\,m \text{ or } 0.5\,mm} \quad \text{and} \quad N_{or} = \underline{4.33 x 10^5 / m^2}$$

This translates to one orifice in a square of side 1.5 mm. Figure 4.10(b) offers a diagrammatic representation of this orifice arrangement.

Now we turn our attention to the main liquid pipe distributors; for the purposes of approximation, it is sensible to assume the available pressure drop as equivalent to the pressure drop across the porous plate distributor, $\Delta P_d^{"}$, estimated in equation 4.16 earlier. Hence, the length of the pipe distributor(s), and as such the height of the particle distribution section, can therefore be obtained from equation 4.27.

$$L_{pds} = \frac{\Delta P_{pds}^{"}}{g\left(1-\varepsilon_{pds}\right)\left(\rho_p - \rho_L\right)} \tag{4.27}$$

ε_{pds} represents the bed voidage within the particle distribution section. Here we assign a value of $\varepsilon_{pds} = 0.3$. Hence, noting that $\left|\Delta P_{pds}^{"}\right| \approx \left|\Delta P_d^{"}\right|$, and substituting our value of $\Delta P_d^{"}$ from equation 4.16, equation 4.27 above then becomes:

$$L_{pds} = \frac{7356}{9.81(1-0.3)(11373-958.4)}$$
$$= \underline{0.10\,\text{m} \quad \text{or} \quad 100\,\text{mm}}$$

Next, designing for an available pipe distributor occupation area equivalent to 20 % of $A_{CS,l}$ results in equation 4.28 below:

$$A_{pds}\ (\text{i.e. total pipe distributor occupation area}) = \left(20\%\right)\left(A_{CS,l}\right) \tag{4.28}$$
$$= \left(0.2\right)\left(8.89\text{x}10^{-4}\right)$$
$$= \underline{1.78\text{x}10^{-4}\,\text{m}^2}$$

Therefore, considering our stated intention to operate the boiling device using multiple main liquid distributors, the number of pipes compatible with the above occupation area, N_{pipe}, can be derived from,

$$N_{pipe} = \frac{A_{pds}}{\text{cross - sectional area of single pipe}} \tag{4.29}$$

Thus for a nominal pipe distributor outside diameter equal to 7 mm, equation 4.29 gives:

$$N_{pipe} = \underline{4.6}$$

Predicated on the above calculations, the following guidelines were selected for the design of the main liquid pipe distributors.

Material	Length of Pipes (mm)	Outside diameter (mm)	Inside diameter (mm)	No. of Pipes (N_{pipe})
Stainless Steel	100	7	5	5

It is worth emphasising the fact, that although the above specifications represent the 'ideal' calculated dimensions of the main pipe distributors, over the course of fabrication, it became clear, that due to operational technicalities of the circulating system, a lot of the listed figures would have to be slightly revised.

For instance, the length and number of pipe distributors is here shown as 100 mm and 5 respectively. However, bearing in mind that particles are to be introduced into the particle distribution section through the solids return pipe (which itself is connected to the base of the riser column through the right hand side wall of the aluminium frame, and positioned just above the porous plate distributor) sufficient entry room must be made available for particles to settle and be evenly distributed over the area of the porous plate. As a result, 5 pipe distributors, each of length 100 mm, would result in the obstruction of the solid return pipe's entry hole (we discuss the design and construction of the solids return section in subsection 4.2.5 following). Therefore, in order to prevent the blockage, or choking, of particles at the junction between the solids return pipe and the particle distribution section, the number of main liquid distributors (N_{pipe}) was reduced to 4, with each pipe constructed to a uniform length of 84 mm.

In addition to the above, the specified diameter (outside and inside) of the individual pipes was also modified. For the purpose of our design calculations, the nominal pipe distributor outside diameter, as stated above, is given here as 7 mm. However, with an available flow channel thickness equal to 11 mm (see Figure 4.3), and our expressed intention to utilise particles up to $d_p > 2$ mm, such a value (i.e. 7 mm pipe distributor outside diameter) would allow only a 2 mm clearance between either the front/back glass faces and said pipe distributors. Once again, by impeding particle fluidisation within the inlet chamber, such a constriction would affect the proper operation of the test unit. Therefore, as a necessary precaution, the outside diameter of the pipe distributors was reduced to 6 mm, with an internal diameter of 4 mm.

Hence to conclude, Figure 4.11 presents a graphical depiction of the inlet chamber, showing the composition of the plenum, fixing plate and particle distribution section, along with their finalised dimensions.

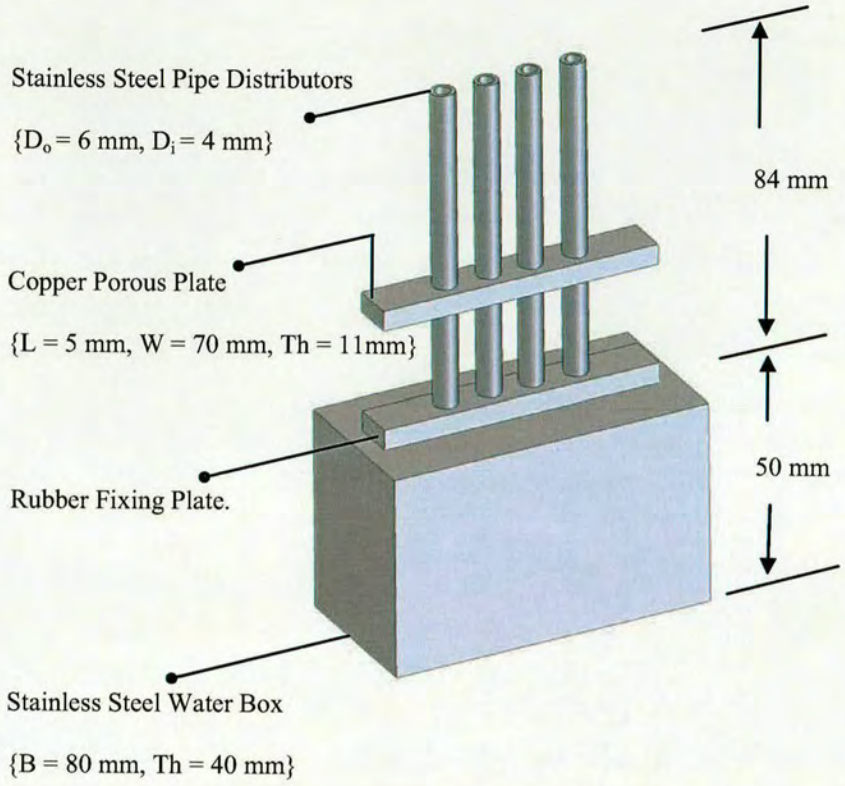

Figure 4.11: Drawing of test section inlet chamber, indicating major components coupled with their actual realised dimensions.

4.2.3.3. PIPE SIZE SELECTION

Figure 4.12 is a three-dimensional block diagram of the inlet section, signalling the desired locations of the main and auxiliary liquid entry pipes.

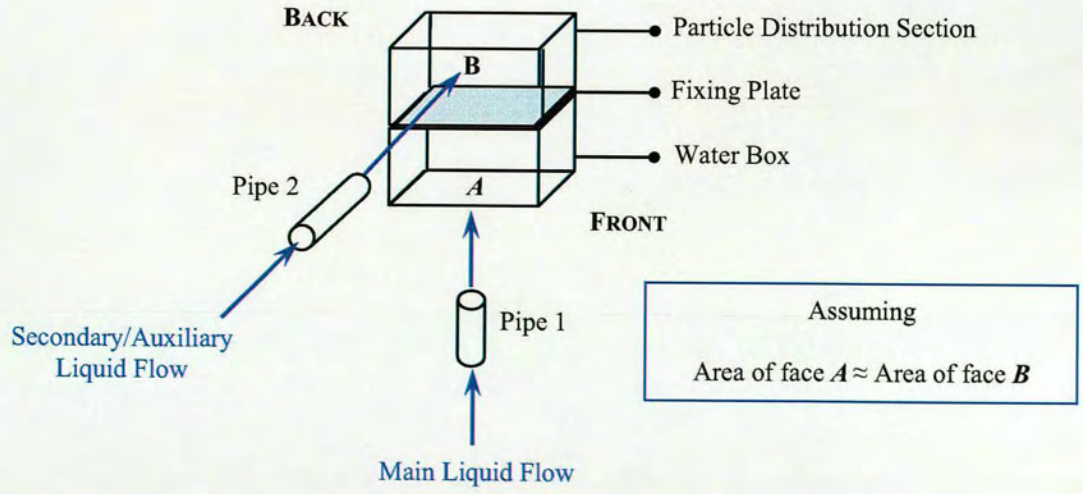

Figure 4.12: Block diagram of inlet chamber indicating pipe entry positions.

A stated earlier, the main liquid flow, Q_{ML}, enters the inlet chamber through the base of the water box (face ***A*** in Figure 4.12), whilst the auxiliary liquid, Q_{AL}, enters underneath the porous plate (not indicated in diagram) via the left-side wall of the nominated test unit (face ***B*** in Figure 4.12). Also, recalling subsection 4.2.3.2 and equations 4.18 and 4.19, we can say that for a suggested total liquid delivery rate of Q_L = 80 litres/min (1.33 x 10^{-3} m^3/s),

$$Q_{AL} = (13\%)(Q_L) = (0.13)(1.33 \times 10^{-3}) \qquad (4.30)$$
$$= \underline{1.73 \times 10^{-4}\, m^3/s}$$

and

$$Q_{ML} = Q_L - Q_{AL} = 1.33 \times 10^{-3} - 1.73 \times 10^{-4} \qquad (4.31)$$
$$= \underline{1.16 \times 10^{-3}\, m^3/s}$$

According to Sinnott [210], for both instances the optimum pipe diameter ($d_{optimum}$) can be calculated as follows:

for turbulent flow,

$$d_{optimum} = 293 \left[\dot{m} \right]^{0.53} \rho_L^{-0.37} \qquad \text{- carbon steel pipe} \qquad (4.32)$$

$$d_{optimum} = 260 \left[\dot{m} \right]^{0.52} \rho_L^{-0.37} \qquad \text{- stainless steel pipe} \qquad (4.33)$$

where,

mass flowrate, $\dot{m}$ (kg/s) = density (kg/m^3) x volumetric flowrate (m^3/s) (4.33a)

A. *Main Liquid Entry Pipe*: We begin with the main liquid entry pipe ('Pipe 1' in Figure 4.12). For a determined liquid volumetric rate flowrate of Q_{ML} = 1.16 x 10^{-3} m^3/s, and utilising stainless steel piping, necessitates an optimum pipe diameter of,

$$d_{optimum} = 260\left[(958.4)(1.16 \times 10^{-3})\right]^{0.52}[958.4]^{-0.37} \qquad (4.34)$$
$$= \underline{2.17 \times 10^{-2}\, m \text{ or } 21.7\, mm}$$

B. *Auxiliary Liquid Entry Pipe*: Likewise for 'Pipe 2', based on an anticipated volumetric flowrate of Q_{AL} = 1.73 x 10^{-4} m^3/s, and selecting for the use of stainless steel piping, leads to an optimum pipe diameter equal to

$$d_{optimum} = 260\left[(958.4)(1.73 \times 10^{-4})\right]^{0.52}[958.4]^{-0.37} \quad (4.35)$$

$$= \underline{8.0 \times 10^{-3}\,\text{m} \text{ or } 8.0\,\text{mm}}$$

Hence, employing these guidelines, the following specifications were adopted:

Main Liquid Entry Pipe

Material = Stainless Steel; Internal Diameter = 20 mm

Auxiliary Liquid Entry Pipe

Material = Stainless Steel; Internal Diameter = 13 mm

4.2.4. DESIGNING THE EXPANSION/OUTLET CHAMBER

Situated on top of the riser column lies the outlet chamber. Here, upon exiting the riser column, the mixed upward flow stream (consisting of vapour, liquid and entrained solids) enters this expanded chamber for the effective separation of solid particles.

As reported in subsection 3.3.1.3 earlier, commercially installed liquid-solid fluidised beds normally resort to the use of cyclone separators; however, with no need to design for mechanical moving parts, the simplicity of the expanded outlet chamber makes it our separator configuration of choice.

To achieve optimal solids separation efficiency, the design of the outlet chamber must address 2 key conditions:

i. Regression of flow velocity, U, towards the particle terminal velocity, U_∞. By successfully engineering the relationship $U \leq U_\infty$, achieved by increasing the cross-sectional area normal to the direction of flow, we devise conditions which encourage the particles to dissociate from the continuing vapour-liquid stream, under the action of gravity.

ii. Secondly, the chamber must be of sufficient volume, not only to fulfil the requirements of (i) above, but also to accommodate a large fraction of entrained particles.

In summary, the overall size of the expansion chamber is dependent on the feedrate to the chamber, as well as the anticipated concentration of solids within the chamber. The mass balance for the overall material flowrate across the chamber can be written as follows:

$$\dot{m}_{TOTAL}\left(\text{i.e. } \dot{m}_V + \dot{m}_L + \dot{m}_p\right) = \left(\dot{m}_{V,1} + \dot{m}_{L,1}\right) + \dot{m}_{p,1} \quad (4.36)$$

here, $\dot{m}_{TOTAL}$ represents the combined vapour, liquid and solid mass flowrate entering the outlet chamber ($\dot{m}_V$, $\dot{m}_L$, and $\dot{m}_p$ respectively), whilst $\dot{m}_{V,1}$, $\dot{m}_{L,1}$ and $\dot{m}_{p,1}$ are, in turn, the vapour, liquid and solid mass flowrates exiting the outlet chamber. Figure 4.13 demonstrates the separator material balance.

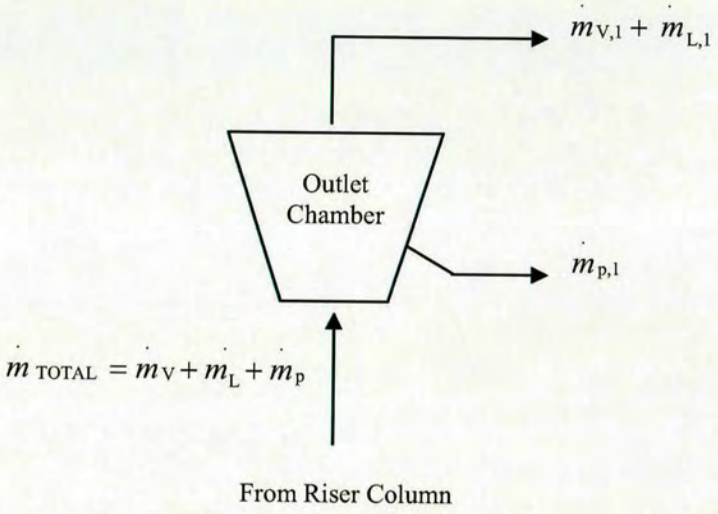

Figure 4.13: Material balance across expansion/outlet chamber

In addition, the overall separation efficiency, S_{EFF}, is simply defined as,

$$S_{EFF} = \frac{\dot{m}_{p,1}}{\dot{m}_p} \tag{4.37}$$

Hence, assuming a maximum liquid volumetric flowrate of Q_L = 1.33 x 10^{-3} m^3/s and a minimum bed voidgae of ε = 0.4, the dimensions of the chamber can be roughly estimated as follows:

firstly,

Total feedrate to outlet chamber = liquid + non-liquid flowrate from riser (4.38)

or,

$$Q_{TOTAL} = Q_L + \frac{(1-\varepsilon)}{\varepsilon}.Q_L \tag{4.38a}$$

inserting our specified values for Q_L and ε, equation 4.38a gives

$$Q_{TOTAL} = \underline{3.325 \times 10^{-3}\ m^3/s}$$

Therefore, modelled on high density lead particles with a calculated particle free-fall velocity of U_∞ = 1.005 m/s (see Table 4.2), the outlet chambers expanded cross-sectional area, $A_{CS,2}$, can be obtained from:

$$A_{CS,2} = Q_{TOTAL} / U \tag{4.39}$$

In order to ensure that $U \leq U_\infty$, design, the minimum acceptable expansion area is then,

$$A_{CS,2}, \text{min} = Q_{TOTAL} / U_\infty, \text{design} = \left(3.325 \times 10^{-3}\right) / \left(1.005\right) \tag{4.39a}$$

$$= \underline{3.308 \times 10^{-3}\ m^2}$$

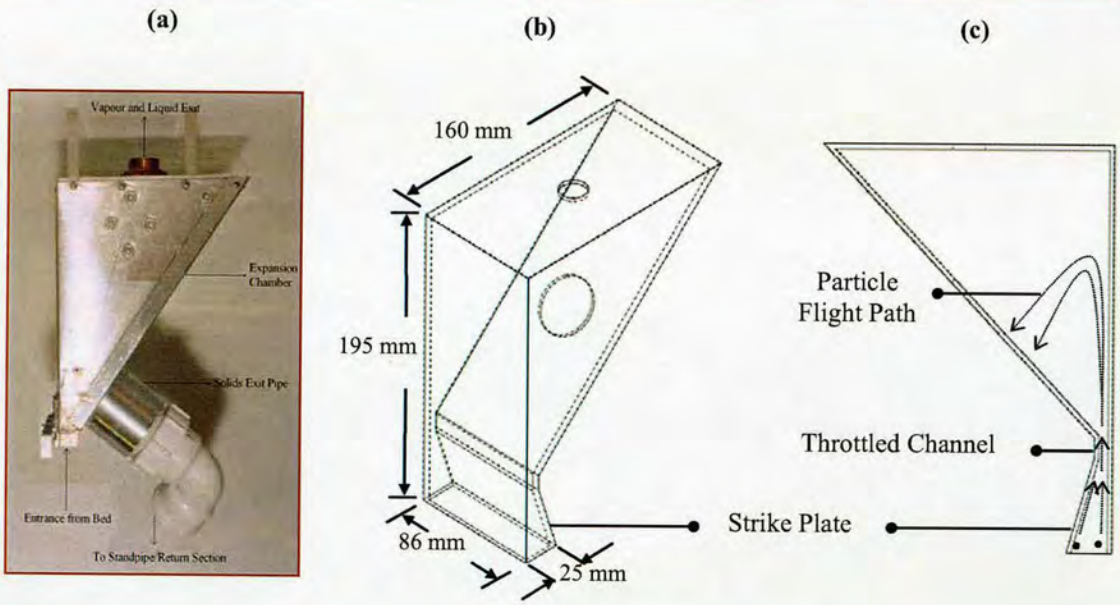

Figure 4.14: (a) Photograph of cone-shaped outlet chamber, (b) Isometric sketch of outlet chamber showing internal structure and realised dimensions, (c) Side-view representation of expansion chamber, indicating the strike plate, the constricted channel and the particle flight path.

By way of illustration, Figure 4.14(a) depicts a photograph of the actual cone-shaped aluminium outlet chamber which, for a length of 195 mm and width of 86 mm, expands from an entrance cross-sectional area approximately equal to $A_{CS,1}$ (i.e. 8.89 x 10^{-4} m^2) to a maximum expansion area of $A_{CS,2}$ = 12.8 x 10^{-3} m^2. In addition to gravity settling effect, an

angled strike plate is included at the expansion chamber's entrance, so as to further suppress the particle momentum. The presence of the strike plate, itself fabricated from malleable aluminium, constricts the chamber's entrance area, and impedes the upward flow of the mixed stream (i.e. vapour, liquid and solid flow from riser column). Whereas fluids flow around the object, in contrast, fluidised particles impact on the strike plate where they forfeit their upward momentum, which in turn effects their separation from the fluid stream. Figures 4.14(b) and (c) are isometric and side-view drawings illustrating the internal configuration of the outlet chamber. The geometry and location of the strike plate is shown in both instances. Furthermore, Figure 4.14(c) clearly displays the throttled channel and the expected particle flight path. Finally, as noted in Figure 4.14(a), whilst vapour and liquid flow exits through the top of the outlet chamber, conversely, separated particles descend into the solids exit pipe for onward transfer to the solids return section

Hitherto, we have progressively charted the evolution of the proposed three-phase boiling device; from the riser column assembly, to the inlet chamber development, finally leading up to the construction of the expansion chamber. Amalgamating these different sections, Figure 4.15(b) offers a photographic image of the fully assembled three-phase test unit. Here, although the downcomer or solids return section is not included, its location is, however, indicated. Meanwhile, Figure 4.15(a) shows an exploded view of the test section, revealing the relative positions of all major constituent parts. Please refer to Appendix D for more technical details concerning the construction of the heated column and outlet chamber.

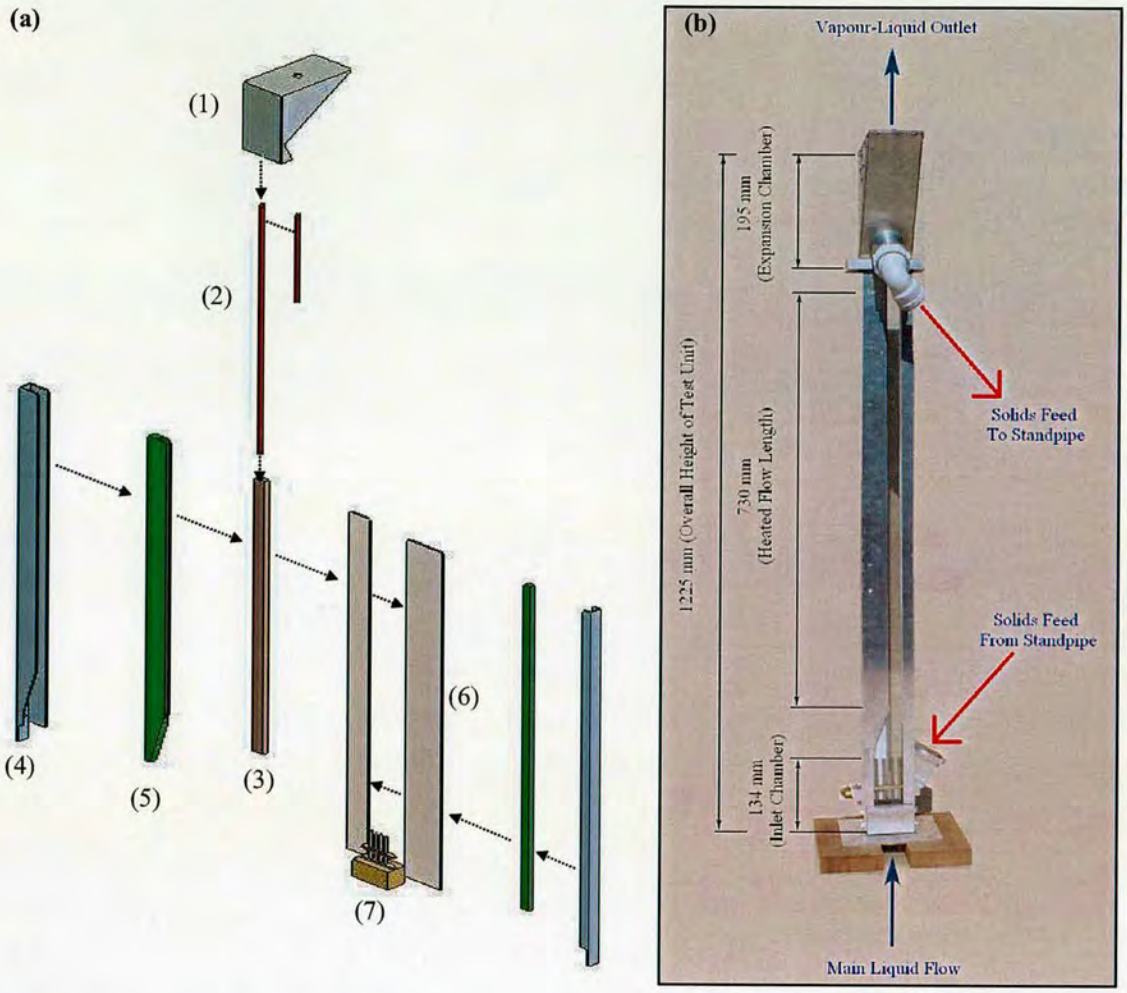

(1) Outlet Chamber	(2) Cartridge Heater & Control Thermostat		(3) Copper Block
(4) Aluminium Frame	(5) PTFE Insulator	(6) Toughened Glass	(7) Inlet Chamber

Figure 4.15: (a) Exploded-view of test section, (b) Photographic image of fully fabricated three-phase circulating fluidised bed. [both exclude the return system]

4.2.5. The Solids Return System

Following on from the outlet chamber, the solids return system facilitates the recirculation of separated solids back to the base of the riser column. For our purposes, a transparent standpipe, fabricated from optical grade polycarbonate (brand name Lexan MP750), serves as the return device in question.

By definition, a standpipe is a length of tube through which solids flow, and is typically formed from a mixture of angled and vertical pipes. Standpipes transfer solids from a region of lower pressure to a region of higher pressure, under the driving force of gravity [211]. This

is schematically shown in Figure 4.16 where solids are being transferred downward in a standpipe, from a lower pressure, $P_1^{"}$, to a higher pressure, $P_2^{"}$.

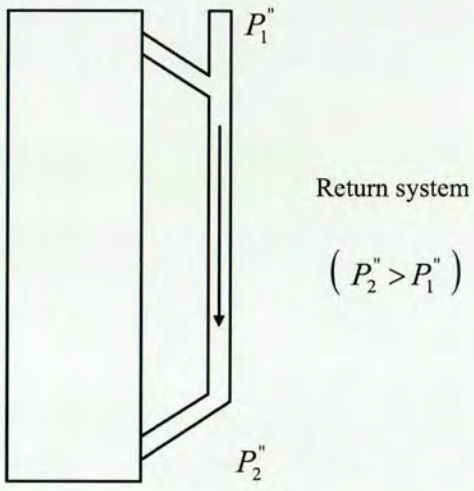

Figure 4.16: Schematic showing concept of solids standpipe/return system.

4.2.5.1: SIZING AND DESCRIBING THE STANDPIPE

The diameter of the standpipe or return system, $d_{S.pipe}$, should be of a value large enough to ensure the smooth flow of solids through the pipe without any possibility of choking. Hence, assuming that the solid circulation rate or mass flowrate through the return leg (kg/s) is equivalent to the particle mass flowrate exiting the outlet chamber, the diameter of the standpipe can then be established by equation 4.40 following

$$d_{S.pipe} = \left[\left(\frac{4}{\pi} \right) \left\{ \frac{\dot{m}_{p,1}}{\left(1 - \varepsilon_{S.pipe}\right).\rho_p.U_{S.pipe}} \right\} \right]^{1/2} \qquad (4.40)$$

here $\dot{m}_{p,1}$ accounts for the solid mass flowrate exiting the outlet chamber, whereas $\varepsilon_{S.pipe}$ and $U_{S.pipe}$ are the bed voidage and solid velocity through the standpipe respectively. Based on experience Luo *et al.* [211] recommend that the solid velocity, $U_{S.pipe}$, should not exceed 0.5 m/s.

Designing for a maximum permissible solid density of 11373 kg/m^3, and assuming a separation efficiency of S_{EFF} = 80 %, the solid circulation rate can be estimated by rearranging equation 4.37 as below:

$$\dot{m}_{p,l} = S_{EFF} . \dot{m}_p \tag{4.41}$$

where, based on equation 4.33a, we define $\dot{m}_p$, the mass flowrate of particles entering the outlet chamber, as

$$\dot{m}_p = Q_p . \rho_p \tag{4.42}$$

by substituting equation 4.2 and equation 4.42, from equation 4.41 we obtain

$$\dot{m}_{p,l} = (0.8).\rho_p.\left[\frac{\varepsilon_p}{(1 - \varepsilon_p)}\right].Q_L \ , \qquad \text{for } \varepsilon_p = 1 - \varepsilon \tag{4.43}$$

Thus, inserting the values of our limiting liquid delivery rate and assumed bed voidage (i.e. Q_L = 1.33 x 10^{-3} m^3/s and ε = 0.4) equation 4.43 yields a particle circulation rate of,

$$\dot{m}_{p,l} = \underline{18 \text{ kg/s}}$$

Finally, returning to equation 4.40 and adhering to an allowable solid velocity of $U_{S.\ pipe}$ equal to 0.5 m/s, the recommended diameter of the standpipe is then established as

$$d_{S.pipe} = \left[\left(\frac{4}{\pi}\right)\left\{\frac{18}{(1 - 0.4).(11373).(0.5)}\right\}\right]^{1/2}$$

$$= \underline{8.2 \text{x} 10^{-2} \text{m} \ \text{ or } \ 82 \text{ mm}}$$

Figure 4.17 shows a photographic image of the actual standpipe employed for use with the three-phase boiling device.

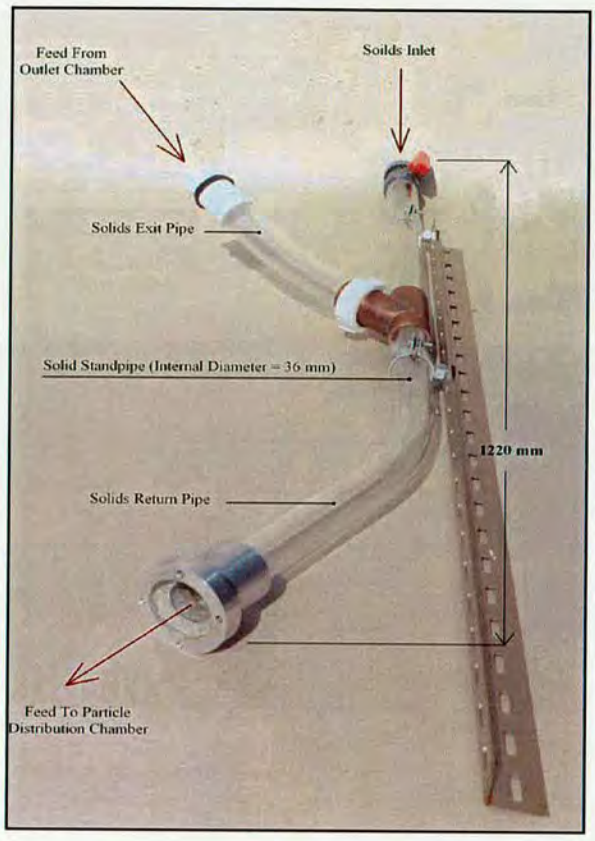

Figure 4.17: Photograph of polycarbonate solids standpipe, detailing dimensions, flow direction and solids inlet valve.

As demonstrated in the above photo, the return leg is comprised of a mixture of straight and angled polycarbonate pipes, coupled together by a copper T-junction. The top angled branch of the standpipe is the solids exit leg, which itself is connected to the test units outlet chamber via the use of a flange incorporated with a double O-ring face seal. Remaining north of the image, located at the top of the straight pipe section we observe the solids inlet valve; solid particles are introduced into the three-phase system through this access. At the bottom of the return leg we note the angled solids return pipe. By means similar to the solids exit pipe, the solids return pipe connects to the particle distribution section (situated at the base of the riser column) thus completing the particle recirculation loop. Furthermore, as shown, the length of the standpipe is comparable with the overall height of the fully assembled fluidised bed section. Also, as with the riser column, all junctions are made leak proof by the use of a high temperature silicone gel.

4.2.5.2. THE NON-MECHANICAL VALVE

Non-mechanical valves are devices that utilise only mobilising fluid, in conjunction with their geometric shape, to effect the flow of solids between the return leg and fluidised bed, without recourse to any external mechanical force. Compared with mechanical solids flow devices, the absence of moving parts makes non-mechanical valves robust, inexpensive and simple to

construct. Figure 4.18(a) depicts the base of the fully assembled three-phase fluidised bed; again, although the return device is not shown, the position of the solid return pipe is, however, indicated. In contrast, the installed inlet chamber (including the particle distribution section, the plenum, as well as the auxiliary and main liquid feed pipes) and the standpipe connection joint are both clearly displayed.

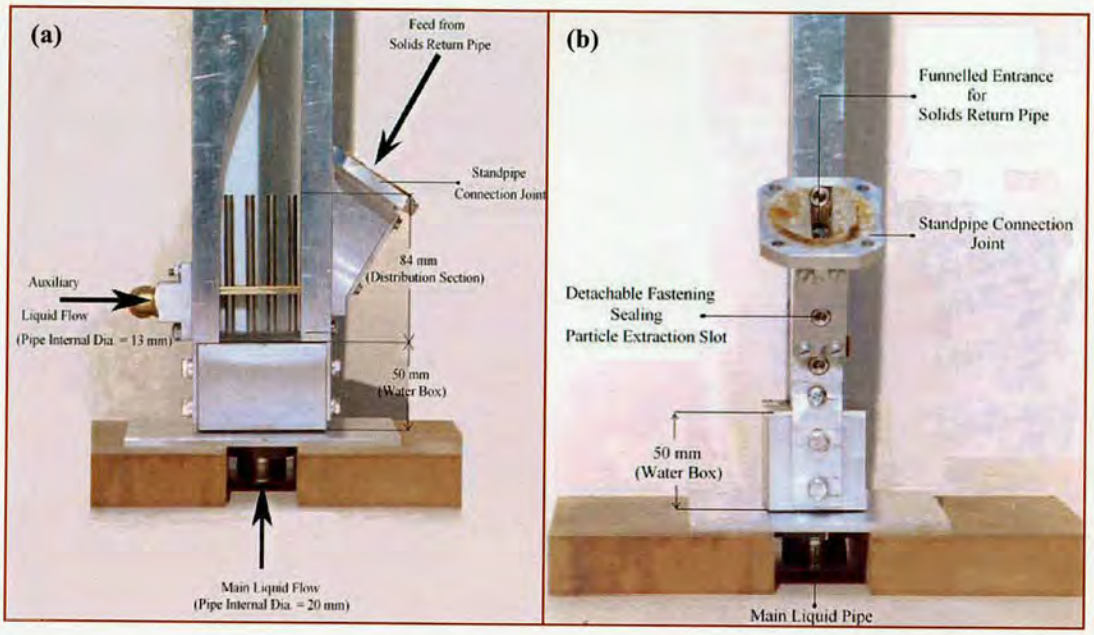

Figure 4.18: (a) Base of three-phase fluidised bed [front-view]; angled solids return pipe, riser bottom and the joint connecting the two, together form non-mechanical valve,
(b) Base of fluidised bed [side-view] indicating secured particle extraction slot.

Introducing auxiliary liquid mobilises solids settled at the bottom of the riser column; this consequently encourages particles remaining in the solids return pipe to feed into the particle distribution section via the connecting standpipe joint. With the auxiliary flow set to zero, particles are prevented from entering the riser and continuous particle circulation can no longer occur. Hence, the V-shaped bend created by the union of the solids return pipe, the standpipe connection joint and the riser bottom, functions as a non-mechanical valve, with the auxiliary liquid flow controlling the solids flowrate into the riser

The Non-Mechanical Valve and Particle Extraction

It is worth noting that our non-mechanical valve offers another beneficial feature…

The standpipe connection joint is fabricated in such a fashion that its back section can be readily disconnected, in order to provide access to the particle distribution section. Hence, when total liquid delivery to the test unit is suspended (for instance after shut-down) and the system drained, particles which settle on the copper porous plate can then be manually

extracted through the revealed exposure. Figure 4.18(b) is a photographic view of the riser bottom, highlighting both the standpipe connection joint and the detachable slot provided for particle extraction.

4.3. Experimental Set-up and Data Acquisition

4.3.1. The Flow Boiling Circuit

Figure 4.19 is a schematic of the experimental set-up as utilised during the course of our boiling investigations. Included in the flow circuit are the three-phase test section and the ancillary test rig.

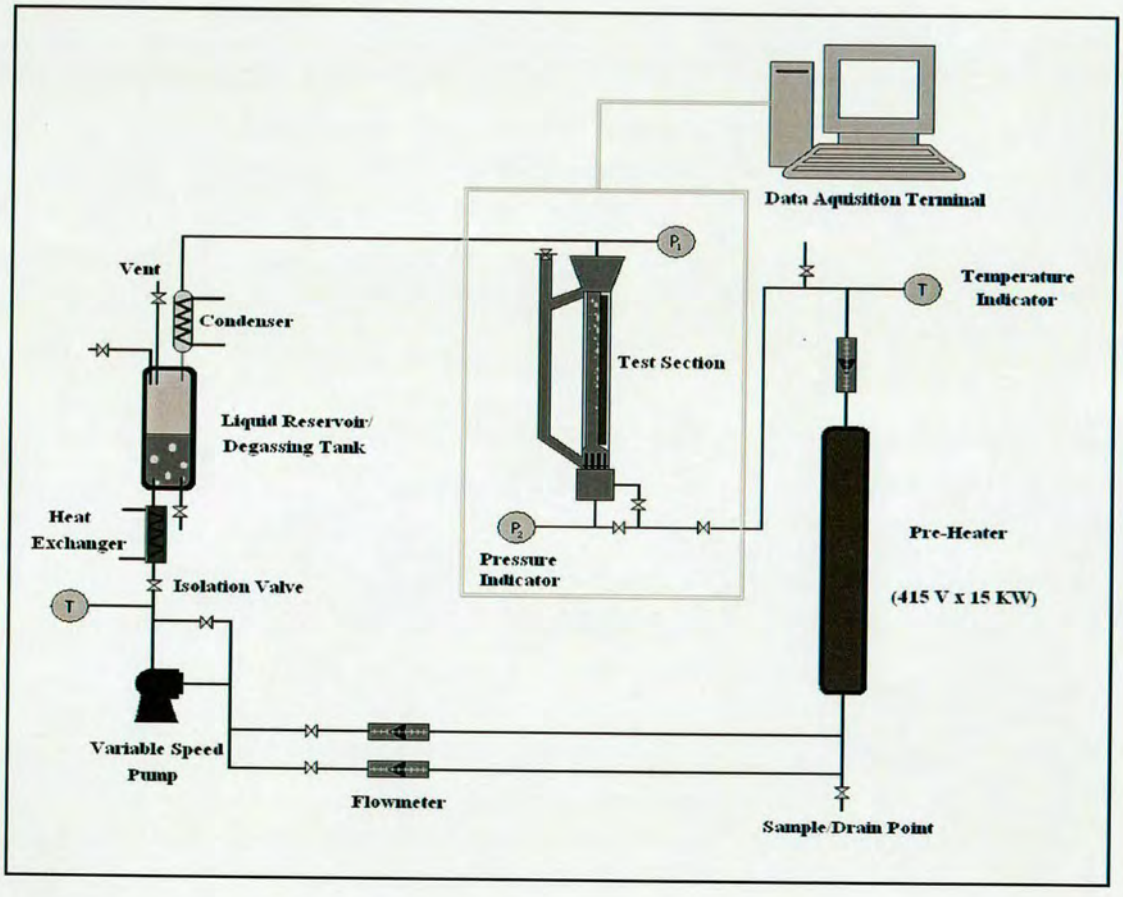

Figure 4.19: Schematic of flow boiling test loop

In actual fact, the test rig, constructed from Type 304 stainless steel, was built before the three-phase test section in anticipation of the current study.

As denoted in Figure 4.19 above, the working medium is supplied to the test unit from its lodgings in the liquid reservoir. Equipped with an internal, thermostat controlled cartridge heater, the liquid reservoir also acts a degassing tank, employed for the removal of dissolved

non-condensable gases. Furthermore, mounted on the degassing vessel, a condenser is provided for condensing the vapour generated within the test section.

Precise control of liquid delivery rate to the test section is a critical factor in the success of the project. In principle, this dictates that the available pumping system should embody a motor capable of having its voltage manipulated. Increasing voltage implies increased motor speed and hence increased liquid delivery. In this regard, the original rig configuration consisted of a COLE-PALMER magnetic drive pump connected to a 'phase-1' (note: 'phase-1' is an electrical terminology and not an inference to a state of matter, i.e. vapour, liquid or solid phase) motor rated at 10 Amps, 115-230 V, and 60 Hz frequency, with a specified maximum flow of 114 litres/min (out of interest, in design section 4.2 previous, this particular property justified the identification of 80 litres/min as our limiting volumetric delivery rate). However, preliminary testing revealed that the existing centrifugal pump was wholly inadequate for the achievement of our purposes. To elaborate, when connected to a 'variac' transformer it was found that the pump and integrated motor could only be operated to within ± 10 % of its stipulated voltage rating. Inevitably, repeated excursions beyond these limits finally culminated in severe, and permanent, damage to the pump.
To remedy the situation, a variable speed PEDROLLO 'phase-3' pump (model CP132A) was procured, in conjunction with a 2.2 kW NORDAC speed controller/frequency inverter. Incorporated with a 0.6 kW induction motor, rated at 220-415 V and 50 Hz frequency, the variable speed pump is capable of a maximum flow equivalent to 100 litres/min, for a total dynamic head of 9 metres. Figure 4.20 is a diagram of the pump-motor control line, which clearly demonstrates the function of the frequency inverter.

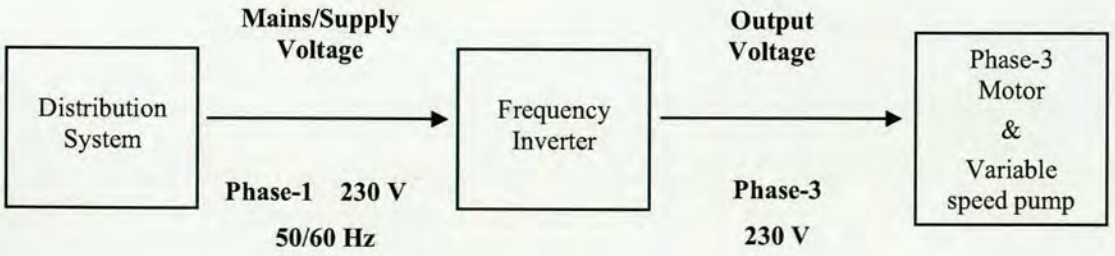

Figure 4.20: Flow diagram illustrating our adopted pump-motor control line

Upon examination, the new speed controlled pump delivery system (shown above) proved an unqualified success, enabling precise and sustainable control of flow up to a value of 65 litres/min.

Immediately after the liquid reservoir, returning to Figure 4.19 earlier, the replacement pump

delivers the degassed liquid to a 'phase-3', 15 kW pre-heater, with a 415 V electrical heating element. The variable speed pump has a suggested maximum inlet temperature of 85 °C; therefore (as indicated in Figure 4.19), before the pumps entrance, an exchanger is deployed for the extraction of heat from the flowing fluid, whilst a hand-held thermometer allows for the pump inlet temperature to be monitored.

The function of the 15 KW pre-heater, which itself is connected to an 'on-off' mains voltage MICROMEGA™ series controller (model CN77000), is to heat the degassed liquid to a predetermined subcooled inlet temperature, prior to achieving vertical upflow in the test section. The setpoint feature on the controller allows the user to define both the subcooled temperature and the rate of rise to set-point.

Throughout the test rig, total liquid flow is metered by the use of variable flow indicators (supplied by FLOWLINE) installed directly in the fluid line. With a range of 5-85 litres/min, and an accuracy of reading within ± 5 %, the flow indicators utilise the technique of differential pressure across a piston which, as the flow increases, moves the piston against a calibrated spring. At the test section, auxiliary flow is metered by the use of a VISION 2000 magnetic turbine flowmeter, with a 1.5-25 litres/min flow range and an accuracy of reading within ± 5 %. 'Double-acting' needle valves are inserted into both the auxiliary and main liquid feed lines. Supplied by RS COMPONENTS Ltd, the valves are designed with a needle adjustment feature for either full shut-off or accurate flow control in both directions. Furthermore, located just beneath its handle, a graduated adjustable scale indicates the valve(s) opening position. With regards to technical capabilities, each valve permits a maximum flow of 80 litres/min, is recommended for operations between -20 °C and 100 °C, and is designed to work up to pressures of 400 bar.

Meanwhile, installed before and after the test section, OMEGA pressure transducers enable pressure readings to be monitored and recorded, in order to evaluate of the total pressure drop across the boiling unit. The transducers have an accuracy within $\pm$ 0.4 % of reading. Factory calibrated K-type thermocouples are employed for the measurement of temperature throughout the entire flow circuit. The estimated bias error of each thermocouple is supplied as $\pm$ 0.4 °C; discussion with the manufacturer reveals that this is a fixed error estimate (i.e. it cannot be reduced by taking the average of multiple readings). We return to the issue of temperature measurement in subsection 4.3.2. proceeding.

Within the test unit, electricity is supplied to the high density cartridge heater (part of the installed heater block assembly), by means of a 240 volt 'variac' transformer. The transformer permits the incremental increase, or decrease, of the imposed power. Figure 4.5 demonstrates our power supply arrangement. The 240 V 'variac' is in turn connected to a power management unit which, by measuring and relating the supplied voltage and current,

generates a direct power display, thus improving the adjustment accuracy to within $\pm$ 0.5 % of reading.

By opening and closing specific isolation valves, located at various strategic points along the experimental rig, it is possible to collect fluid samples; relieve system pressure; and effect drainage. Finally, the entire test rig was encased in insulating foam, so as to minimize heat losses to the ambient air.

4.3.2. DATA ACQUISITION

For both two-phase and three-phase flow boiling, the heat transfer coefficient was calculated by the following equation:

$$\alpha = \frac{q''}{(T_w - T_{f*})} \tag{4.44}$$

here (T_w - T_{f*}) represents the temperature driving force, where T_w is the measured wall temperature and T_{f*} is the estimated mean bulk fluid temperature. In the expression above, the heat flux imposed on the fluid, q'', was obtained from,

$$q'' = \frac{q - q_{loss}}{(\text{surface area of heated wall})} \tag{4.45}$$

q is the electrical power supplied to the heating unit, q_{loss} accounts for the heat losses to the environment, and the heated wall surface area is equivalent to 7.15 x 10^{-3} m^2. As stated in subsection 4.2.2.2, the copper heater assembly is enclosed in a 16 mm thick PTFE insulated housing. With a low thermal conductivity equal to 0.249 W/mK, the teflon insulator assures that virtually all of the power input is available for the boiling process. Consequently, with the heat loss to the surrounding environment no longer a debilitating concern, q_{loss} is assumed as negligible.

The wall temperature, T_w, is the temperature of the heated surface normal to, and in contact with, the flow channel. As described in subsection 4.2.2.3 above, for the determination of T_w, 8 K-type thermocouples were inserted at regularly spaced intervals along the length of the heating block. The thermocouples are connected to a PICO TECHNOLOGY 8-channel interface (TC-08), which in turn connects to the serial port of a DELL compatible personal computer. All measured temperatures were recorded using the accompanying PICOLOG data acquisition software. Capable of collecting up to 1 million samples, the acquisition system facilitates the recording and analysis of rapidly varying signals. A valid experimental run last

between six and seven minutes. At the end of this period, once all wall temperature measurements have been acquired and stored, the software system allows the raw data to be exported to the more user-friendly Windows Excel application. Obtained over various test conditions, and simply entitled 'Wall temperature measurements along heater assembly', Appendix A.1 and Appendix A.3 offer specimens of some exported temperature data sheets. As demonstrated in the cited appendixes, at each individual probe location an estimate of the averaged local wall temperature, T^*, is calculated from the sampled local wall temperature, T, as given in the expression below:

$$T^* = \left(\sum_{i=1}^{N} T_i \right) \Big/ N \tag{4.46}$$

where N represents the number of repeated measurements within a sample. For our purposes, the PICOLOG system records one measurement every second, over a one hundred second sampling period. Thus for any given test condition, the overall measured wall temperature, T_w, can then determined as follows:

$$T_w = \left(\sum_{j=1}^{K} T_j^* \right) \Big/ K \tag{4.47}$$

here, K refers to the total number of thermocouple probes. Subsequently, in addition to graphing the relationship between the investigated parameters and the measured heat transfer coefficient, to generate boiling curve plots for our specified parametric range (i.e. graphs of heat flux versus temperature driving force), the calculated value of T_w is then entered into a second Excel spreadsheet. A specimen entitled 'Data for boiling curves and heat transfer coefficient plots' is presented in Appendix A.2 following.

Meanwhile, at the test section, the mean bulk fluid temperature can be easily defined as:

$$T_{f^*} = \left(T_{f.i} - T_{f.o} \right) / 2 \tag{4.48}$$

$T_{f.i}$ and $T_{f.o}$ are the inlet and outlet fluid temperatures. As described in subsection 4.2.2.3 previous, to measure the inlet and outlet fluid temperatures, two K-type thermocouples were inserted into the bulk fluid flow through the right-hand wall of the riser column. Each probe connects to a hand-held, single input, OMEGA digital thermometer (model HH-81). Powered by a 9 V battery, and with an operating range from -160 to 1372 °C, each thermometer is accurate to within 0.1 % of reading from 0 to 200 °C. Together with the measured wall temperature, at the end of a valid experimental run, once the displayed fluid temperatures

have reached a steady-state, the inlet and outlet fluid temperatures are manually recorded and also entered into spreadsheet B: 'Data for boiling curves and heat transfer coefficient plots'. The uncertainty involved in the evaluation of the experimental heat transfer coefficient is addressed in section 4. 6 following.

4.4. INVESTIGATED RANGE OF MATERIALS AND PARAMETERS

4.4.1. MATERIAL PROCUREMENT

Over the course our investigation into three-phase flow boiling, one of the greatest challenges faced was the procurement of appropriate solid phase material. Although our endeavours lead us to manufactures around the globe, we were eventually able to acquire a broad spectrum of solid materials as summarised below.

Description	Size Range	Supplier Details
Copper Balls	1.0 → 2.5 mm dia.	DULAR STEEL PRODUCTS Ltd, INDIA.
Aluminium Balls	1.0 → 2.5 mm dia.	DULAR STEEL PRODUCTS Ltd, INDIA.
Zirconium Silicate Beads	1.2 → 2.8 mm dia.	AEGIS ADVANCED MATERIALS Ltd, UK.
Glass Balls	1.4 → 3.3 mm dia.	SPHERIC-TRAFALGAR Ltd, UK.
Stainless Steel Balls	**1. 5 → 2. 5 mm dia**	**SPHERIC-TRAFALGAR Ltd, UK.**

Table 4.4: Summary of purchased materials and respective suppliers

As implied by Table 4.4, the initial intention was to systematically examine and compare how the various particles affect the overall performance of the three-phase boiling system. However, in the end, it was necessary to revise these goals, due to both the intended scope of the project and the confines of time.

Therefore, bearing in mind the above, a complete and thorough examination could only be performed on the stainless steel particle range, which, referring to Table 4.4, has been highlighted in bold-type font. Table 4.5 sets out the physical properties of the employed solid particles

Material	Geometry	Density ρ_p (kg/m^3)	Thermal Conductivity λ_p (W/mK)	Specific Heat $C_{p,p}$ (J/kgK)
Stainless Steel	Spherical	7850	48.85	460.5

Table 4.5: Physical properties of investigated particles.

4.4.2. RANGE OF PARAMETERS TESTED

As stated at the beginning of this chapter, for the case of both two-phase and three-phase flow boiling, a key experimental objective has been to clearly identify the influence of various operating parameters on the measured rate of heat transfer. Hence, taking distilled water as the liquid phase, Table 4.6 lists some necessary working fluid parameters. Likewise, details regarding the examined range of heat fluxes and liquid velocities are presented in Table 4.7 and Table 4.8 respectively.

Density ρ (kg/m^3)		Thermal Conductivity	Dynamic Viscosity	Specific Heat	Surface tension	Heat of Vaporisation
Liquid	Vapour	λ_L (W/mK)	μ_L (kg/ms)	$C_{p,L}$ (J/kgK)	σ_L (N/m)	Δh_v (kJ/kg)
965	0.424	0.679	3.05×10^{-4}	4205	0.06082	2283.3

Table 4.6: Summary of some relevant fluid properties for distilled water employed as the working medium. [values obtained for liquid at 90 °C sub-cooled temperature]

Regime	Imposed Heat Flux, q'' (kW/m^2)									
	(1)	(2)	(3)	(4)	(5)	(6)	(7)	(8)	(9)	(10)
Forced Convective	27.97	55.94	83.92	-	-	-	-	-	-	-
Nucleate Boiling	-	-	-	111.89	139.86	167.83	195.8	223.8	251.7	279.7

Table 4.7: Experimentally examined heat flux range characterised with respect to dominant heat transfer mechanisms. Here q'' is calculated according equation 4.45.

As suggested by Table 4.7, in these boiling trials, nucleate boiling heat transfer was only of significance for heat fluxes above 100 kW/m^2. Turning to the investigated liquid velocity range, Table 4.8 also serves as a 'Flowrate *to* Superficial velocity *to* Reynolds number' conversion chart, which is based on the cross-sectional are (A_{CS}) and hydraulic mean diameter (D_e) of the test section's heated flow channel.

Liquid Delivery Rate Q_L		**Liquid Superficial Velocity** U_L	**Reynolds Number** Re
(litres/min)	(... x 10^{-4} m^3/s)	(m/s)	(dimensionless)
10	1.666	0.705	32342
12	2.000	0.846	39087
14	2.333	0.987	45602
16	2.667	1.128	52116
18	3.000	1.269	58631
20	3.333	1.409	65099
22	3.667	1.550	71614
24	4.000	1.691	78128
26	4.333	1.832	84643

Table 4.8: 'Flowrate to Superficial velocity to Reynolds number' conversion chart showing examined liquid flow range.

To clarify, in Table 4.8 above the liquid superficial velocity, U_L, is obtained by simply rearranging equation 4.1 as follows:

$$U_L = Q_L / A_{CS} \tag{4.49}$$

As established earlier, recalling subsection 4.2.2.3, in our boiling device the cross-sectional area of the heated flow channel, A_{CS}, has been determined as 2.365 x 10^{-4} m^2. Meanwhile, for the flow of liquid through its heated length, the vessels Reynolds number is here defined as:

$$Re = \frac{D_e U_L \rho_L}{\mu_L} \tag{4.50}$$

D_e is the equivalent or hydraulic mean diameter of the heated flow length and, from equation 4.21 , is found to be,

$$D_e = \frac{4(A_{CS})}{(2\text{x}0.011)+(2\text{x}0.0215)} = \underline{1.46\text{x}10^{-2}\text{m}} \qquad (4.51)$$

Considering these generated *Re* values, referring to Table 4.8, it is assumed that fully-developed turbulent flow is encountered over the length of the heated section.

4.5. EXPERIMENTAL PROCEDURES

4.5.1. HEAT TRANSFER EXPERIMENTS

Flow boiling experiments were conducted in two series. Firstly, in order to measure the heat transfer enhancement effect in the presence of solid particles, flow boiling curves were first obtained for distilled water only. Upon completion, once heat transfer measurements in the reference (or 'control') two-phase flow boiling series had been secured, particles were finally added to the test section. Boiling curves for the three-phase system were then obtained using similar procedures as employed in the former, and described in due course.

A summary of our adopted test schedule is given in Table 4.9 following. All experiments were conducted at atmospheric pressure.

Test Series	**Flow Boiling Mode**	**Heat flux Range** (kW/m^2)	**Re Range** (dimensionless)	**Particle Sizes** (diameter, mm)
Series-A (reference)	Two-phase (vapour-liquid)	27.97→279.7	32342 → 78128	-
Series-B	Three-phase (vapour-liquid-solid)	27.97→279.7	45602 → 84643	1.5, 2.0 and 2.5

Table 4.9: Summary of implemented heat transfer enhancement test program

4.5.1.1. SERIES-A ; TWO PHASE FLOW BOILING EXPERIMENTS

To prepare for a day of experimental testing, the working fluid was first distilled and demineralised the evening before hand. At the start of test day, the liquid reservoir/degassing tank was typically charged with 10 litres of pure water. With its internal heater fully submerged, the tank's liquid inlet valve was then turned to the fully closed position, so as to prevent air from being drawn into the boiling system (at this point the reader is referred back to Figure 4.19 for a sketch of the flow boiling loop). With all other isolation valves set to

open (excluding the solid inlet valve at the test section and the sample/drain valves along the test rig), the variable speed pump was engaged and the working liquid pumped around the circuit at a desired flow velocity. Before commencing experiments, and with the working liquid still being circulated, all dissolved non-condensable gases were removed by heating the water in the degassing tank to above 95 °C. The use of a thermostat controller allowed the tank's internal heater to be maintained at a predetermined temperature of 115 °C. The degassing process continued for up to 100 minutes prior to the actual start of testing.

After this operation, the water sub-cooling at the test section's inlet was then maintained at a fixed value of 90 °C by the action of the automatically controlled 15kW pre-heater. Preliminary testing revealed that in conjunction with the available heat flux range, see Table 4.9, the selected sub-cooled inlet temperature allows for both the sub-cooled and saturated nucleate boiling regions to be readily attainable over the test section's heated flow length. As described in *Chapter 2*, subsection 2.3.1, in the early stages of sub-cooled boiling (i.e. partial sub-cooled boiling region, where $q'' \leq q''_{OFB}$) only a very limited number of nucleation sites are active, and as such heat transfer is still dominated by the single phase forced convective mechanism. However, once conditions for fully developed nucleate boiling have been attained (i.e. $q'' \geq q''_{OFB}$), nucleation sites then begin to populate the heat transfer surface and the fluid bulk temperature approaches the saturation temperature of the working liquid; this signals the start of the saturated nucleate boiling region, where generated bubbles remain stable in the bulk fluid flow. Nevertheless, for our particular test apparatus and examined parametric range, preliminary findings suggest that sub-cooled temperatures of less than 90 °C delay or, in certain instances, eliminate the occurrence of fully developed nucleate boiling within the flow channel. Not only does this hinder our ability to properly observe the transition between the forced convective and nucleate boiling processes, but it also impedes the characterisation of our obtained results according to the prevalent heat transfer mechanisms. Higher sub-cooled temperatures exhibit similar drawbacks, but for contrary reasons (i.e. suppression of the heat transfer due to single phase forced convection)

With the desired bulk temperature and liquid velocity both selected, the test rig was then left to equilibrate for a few minutes. To begin experiments, the power supply to the test section was switched on and the heat flux set to maximum examined value of 279.7 kW/m^2, equivalent to a displayed power input reading of 2000 W. By adjusting the applied power in steps of 200 watts, test were then carried out from this maximum heat flux value down to a minimum heat flux value of 27.97 kW/m^2, equivalent to a power input reading of 200 W. A decreasing heat flux methodology was adopted so as to eliminate any boiling hysteresis effect resultant from bubble site activation. With the heat flux value specified, thermal conditions were then allowed to stabilise. It is believed that steady-state conditions are attained when the

wall temperature readings - measured by the thermocouples imbedded in the heater assembly – remain relatively constant. This typically occurred 3 to 4 minutes after the wall heat flux had been set. Once it was deemed appropriate, the data logging system was initiated and the temperature profile along the copper heating block recorded. As stated in subsection 4.3.2 earlier, for all experiments, the PICOLOG software was set to record one measurement every second, over a one hundred second sampling period. Subsequent to the acquisition of the wall temperature data, the inlet and outlet fluid temperatures were manually recorded, as has also been described in subsection 4.3.2. This process was repeated for each decreasing value of heat flux. By such means, testing progressed through the two-phase (vapour-liquid) and single-phase (liquid only) heat transfer regions, terminating once the minimum power input was reached (i.e. 200 W). In this manner, the data obtained from the successive experimental runs at the various heat flux settings, together constitute a complete 'set' of results for the specified liquid velocity. The corresponding boiling curve and heat transfer coefficient plots were then generated from the temperature readings taken at each successive heat flux setting.

Upon completion, the liquid flowrate was adjusted and the related boiling curve determined according to the procedure outlined above. This process was repeated to determine boiling curve across the entire liquid velocity range, see Table 4.8 and Table 4.9. Taken as a whole, the results obtained from the fully examined liquid velocity range can be said to represent the findings of a test 'series'.

Multiple test series were conducted in order to substantiate the validity of experiments (for instance test 'Series-A.1', 'Series-A.2', 'Series-A.3' etc). Consequently, to ensure that the experimental results were in harmony, the procedures for acquiring data remained consistent throughout the entire two-phase flow boiling test program. Indeed when the test unit and other supporting components functioned as required, it was possible to complete a valid test series within 1 or 2 days. Although degassing was performed at the start of each test day, the working liquid itself was rarely changed before the end of a legitimate series. For the duplicated tests, plots of boiling curves and heat transfer coefficients proved to be virtually identical, thus verifying both the repeatability of results and the consistency of our experimental procedures. Suppositions and conclusions were derived using data from the most favourable test series.

4.5.1.2. SERIES-B; THREE PHASE FLOW BOILING EXPERIMENTS

Once investigations into reference test 'Series-A' had been successfully accomplished, a measured quantity of solid particles was then added to the test section. Investigations into the three-phase boiling system were then conducted as follows…

Before experiments, the working liquid was first treated and degassed by means similar to those described in subsection 4.5.1.1 above. With degassing complete, the pump was momentarily switched off, in order to facilitate the inclusion of solid particles.

As listed in Table 4.9, there were three different particle sizes employed in the 'Series-B' test program. The relevant particle physical properties are given in Table 4.5. In beginning, a simple KERN & SOHN, battery powered, weighing scale was used to determine a measure of solid particles. At the test section, the solid inlet valve (located at the top of the standpipe) was then opened and 250 grams of solids subsequently added to the system. The particles descend through the standpipe and eventually settle on the porous plate distributor, located at the base of the riser column, as described in subsection 4.2.3.2 earlier. After closing the solid inlet valve, the pre-heater was set to the designated sub-cooled temperature of 90 °C and the variable speed pump re-started. Working liquid was then delivered to the test section via the main and auxiliary entry pipes, whilst the power input to the heater was set to a maximum value of 2000 W.

In the three-phase boiling device, recalling subsection 4.2.3.2, the auxiliary liquid functions by mobilising the layer of particles at the base of the column. Therefore, in performing experiments, the overall or total liquid delivery rate is increased progressively, until enough auxiliary liquid is available to effect the incipient fluidisation of solid particles. With the minimum fluidisation velocity surpassed, and pumping power increased, particles are then fluidised up to the tips of the main liquid pipe distributors, where the total liquid velocity (see equation 4.18) transports the solids up into the riser section. At this stage, the fluidisation of particles continues to develop in the stationary or conventional mode, where the entrainment of solid particles is not experienced. To transcend the critical transition velocity (i.e. the minimum transport velocity) the overall liquid flowrate is further increased, until particles begin to be transported out of the column. Following on from the riser section, the mixed upward flow stream then enters the expansion chamber. Here, entrained particles are filtered out of the flow before being transferred to the solids standpipe. Subsection 4.2.4 sets-out the design and operation of the expansion chamber in greater detail. Meanwhile, the liquid-vapour mixture, which exits through the top of the test section, is directed through the condenser before returning to the liquid reservoir.

Connected to the outlet chamber, the external standpipe returns the particles to the base of the riser, thus enabling the continuous circulation of particles between riser column and return section. At this point the bed is said to be operating in the circulating fluidisation mode; it is important to note that the scope of our investigations into the behaviour of the three-phase boiling system have been restricted to this particular regime (see subsection 3.3.4.2 for definition of terminologies and discourse on fluidisation regimes). Hence, with an observed minimum transport velocity of approximately 13 litres/min (applicable to all examined

particles), the test 'Series-B' flow range given in Table 4.9, represents operating velocities at which sustainable particle circulation was readily achievable.

Furthermore, by manipulating the ratio of the auxiliary liquid flow to the main liquid flow, it is possible to control the particle circulation rate within the three-phase test unit (see subsections 3.3.1.3 and 3.3.4.2). Such a variable would undoubtedly influence the measurable rate of heat transfer. Nonetheless, in this present study and for our specified range of parameters, we are primarily concerned with characterising the boiling enhancement effect of particles in three-phase flow boiling, as opposed to two-phase flow boiling. Therefore, over the course of our investigation, in order to ensure that consistent data acquisition conditions were present in both test 'Series-A and B', it was important that excluding the addition of solid particles to the reference two-phase (vapour-liquid) system, all other test conditions remained fixed. As a result, throughout our experiments with and without the presence of solid particles, the needle valve settings on both the auxiliary and main liquid flow lines were left permanently unchanged. Hence, in both test 'Series-A and B', the total system volumetric rate was regulated solely by the action of the speed controlled pump. As earlier demonstrated, for the 'Series-B' test program, the particle circulation rate and the total liquid delivery rate can be related according to a combination of equations 4.43 and 4.38a.

With the system set at an appropriate heat flux and liquid velocity, time was then given to allow thermal and hydrodynamic conditions to reach steady state, before experiments proceeded as described in subsection 4.5.1.1 above. Again as with test 'Series-A', multiple series of test were performed with the particles, so as to validate procedures and secure optimum results.

Upon completion, the system was shut-down by switching-off the power supply, pre-heater, and variable speed pump in chronological order. After isolating the test section, the system was then drained of liquid, before allowing particles settled on the porous plate to be extracted as described in subsection 4.2.5.2.
Following this, a similar mass of different sized particles was then measured out and added to the test unit. Boiling curves and heat transfer plots for this system were then determined in accordance with the procedures outlined above. The entire process was repeated for each size of particle listed in Table 4.9.

4.5.2. Flow Visualisation Methods

Visualisation is an interdisciplinary imaging science, devoted to providing researchers with additional information by mainly experimental techniques. It is applicable to various phenomena such as flow, heat, sound, electromagnetism, chemical kinetics, as well as their

combinations. In the field of heat transfer enhancement, particularly when the related heat transfer processes are the focus of interest, visualisation techniques are a helpful tool for the interpretation of experimentally obtained results.

Hence, as explained in subsection 4.2.1 above, in order to describe the mechanisms associated with three-phase heat transfer, and explain the enhancing or limiting effects of fluidised particles, it was important that the processes involved could be identified and examined. In accomplishing this, various methods of observing, recording and analysing were attempted.

In the first place, equipping the test unit's riser column with transparent front and back glass sections, made direct visual observation an obvious possibility. Even without magnifying or recording devices, this feature gave us a first impression of the processes occurring within the fluidised bed. However, the limitations of direct observation are undoubtedly the lack of record, and the restricted ability of the viewer to observe short duration or high frequency events.

Hence, in order to conduct viable visualisation investigations, an OLYMPUS digital video camera was initially acquired. Video sequences were recorded at a rate of 25 frames per second and a shutter speed of 1/7500 of a second. The high shutter speed essentially froze the flow, capturing high resolution images (1680 x 1260 pixels) with the aid of a high intensity light source. However, due to the inherent limitations of the digital camera system (such as the necessary trade-off between resolution and speed of imaging) we were unable to successfully track flow behaviour across multiple video frames. With motion sequencing therefore excluded, the growth and development of vapour bubbles, as well as their subsequent interactions with fluidised particles, could not be observed through successive frames. This seriously hindered our ability to recognise and assign processes to heat transfer mechanisms.

In the end, a CMOS high-frame rate camera (Vision Research PHANTOM V.4) was used to capture the flow boiling process. Equipped with an 18-108/2.5 zoom lens, the high-speed camera is capable of recording images at a rate 1000 frames per second, with a resolution of 512 x 512 pixels. Figure 4.21 shows the photographic system as set-up in the laboratory.

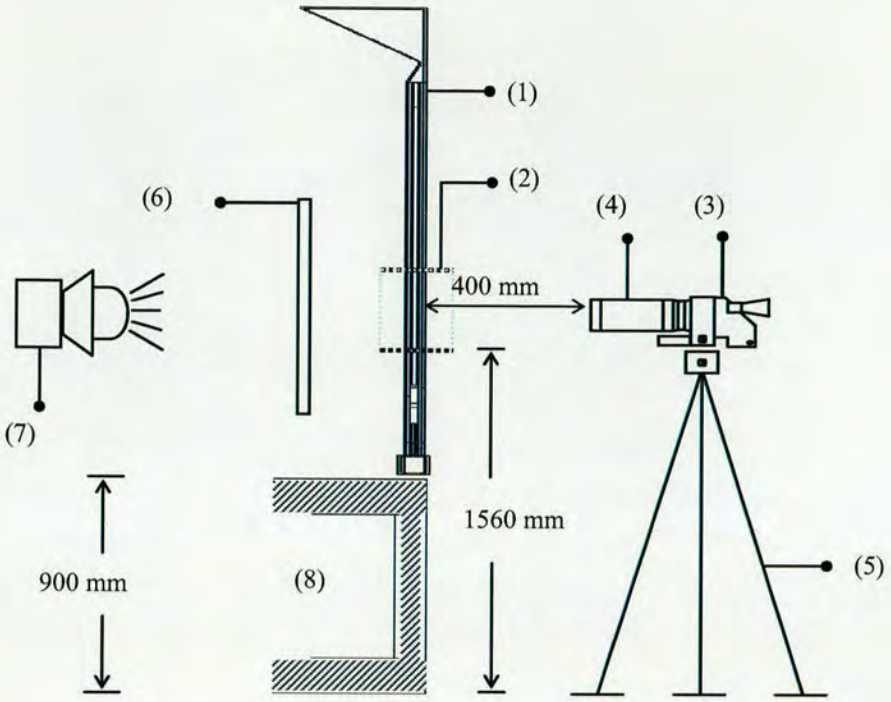

(1) 3-phase CFB (2) 21.5 mm x 45 mm viewing area (3) CMOS Camera [Phantom v4.0] 1000 frames/sec (4) 18-108/2.5 Zoom Lens (5) Tripod (6) Diffuser Paper (7) Light Source [100 W Halogen Projector Lamp] (8) Rig work bench

Figure 4.21: Test section and high-speed camera arrangement for visualisation studies.

As illustrated above, the camera is mounted on a tripod, and positioned in a manner which provides a view parallel to the heated surface and perpendicular to the flow direction. In order to achieve the highest possible resolution and ensure continuity between recordings, the camera lens is then fixed at a constant focal length, and approximately 400 mm away from the front observation window. This results in a viewing area of an order of 21.5 mm x 45 mm, beginning 200 mm from the start of the heated flow length. Additional backlighting is used in all recordings. The advantage of the technique is the high light intensity which is provided; this is necessary if extremely short shutter times are to be obtained at the high frame rates employed. As indicated in Figure 4.21, a 100 W halogen projector lamp and an optical diffuser paper, mounted between lamp and test section, generates the high intensity diffused light source.

The camera connects to a data acquisition PC and short video sequences are recorded and analysed using the specialised PHANTOM software. Selected frames are also edited using JASC Photo Shop Pro. The adopted camera system allowed us to record ongoing heat transfer processes whilst taking experimental measurements at the test section. In this way it has been possible to obtain information which lends credence to our suggested hypotheses.

4.6. ERROR ANALYSIS

In both three and two-phase flow boiling, the experimental error for the measured heat transfer coefficients (determined by equation 4.44) are mostly caused by either instrument specification or deviation estimated from experimental data.

The 95 % confidence uncertainty in the experimental result, α, is derived from the following contributions:

$$U_{\alpha} = \left(P_{\alpha}^{2} + B_{\alpha}^{2}\right)^{1/2} \tag{4.52}$$

here P_{α} represents the precision contribution to the uncertainty U_{α}, whilst B_{α} symbolises the bias contribution. For a measured quantity, the precision interval about a nominal result is the experimenters 95 % confidence estimate of the band within which the average of many such results would fall, if the experiment was repeated many times under the same conditions, and using the same equipment. The precision limit, P_{α}, is thus an estimate of the lack of repeatability caused by random errors and experimental unsteadiness [212]. Meanwhile the bias limit, B_{α}, is an estimate of the systematic error which is considered to remain constant during a given test. Therefore, for repeated test measurements, each measurement is assumed to have the same bias error.

With the imposed heat flux calculated according to equation 4.45, and the power management unit generating a direct power display accurate to within $\pm$ 0.5 % of reading, the main source of uncertainty stems from errors of approximately $\pm$ 0.4 °C in the repeated temperature measurements. As a result, in measuring the rate of heat transfer, the largest experimental errors occurred for the smallest temperature differences between the heated wall and the test fluid.

Hence, following the 1955 propagation equations of Kline and McClintock outlined in 'The Journal of heat transfer ASME Policy on Reporting Uncertainties in Experimental Measurements and Results' [213], the precision and bias limits can be individually estimated as follows:

$$P_{\alpha} = \sqrt{\left(\theta_{\mathrm{Tw}}.P_{\mathrm{Tw}}\right)^{2} + \left(\theta_{\mathrm{Tf}^{*}}.P_{\mathrm{Tf}^{*}}\right)^{2}} \tag{4.53}$$

and

$$B_{\alpha} = \sqrt{\left(\theta_{\mathrm{Tw}}.B_{\mathrm{Tw}}\right)^{2} + \left(\theta_{\mathrm{Tf}^{*}}.B_{\mathrm{Tf}^{*}}\right)^{2}} \tag{4.54}$$

For the experimental result, α, θ_{Tw} and θ_{Tf*} are the sensitivity coefficients of the measured quantities T_w and T_{f*} respectively. The magnitude of these coefficients can be obtained from the expressions below:

$$\theta_{Tw} = \frac{\partial \alpha}{\partial T_w} = -\left[\frac{q''}{(T_w - T_{f*})^2}\right] \tag{4.55}$$

and

$$\theta_{Tf*} = \frac{\partial \alpha}{\partial T_{f*}} = \left[\frac{q''}{(T_w - T_{f*})^2}\right] \tag{4.56}$$

Meanwhile, returning to equation 4.53 above, P_{Tw} and P_{Tf*} are the precision limits of the measured wall temperature and the bulk fluid temperature respectively.

P_{Tw} can be written as follows:

$$P_{Tw} = \left[K \sum_{j=1} \left(P_{T*}^2\right)_j\right]^{\frac{1}{2}} \tag{4.57}$$

where K represents the total number of thermocouple probes; and P_{T*} represents the precision error of the mean local wall temperature (i.e. T^*) as measured by probe number 'j' and defined in equation 4.46 above.

The precision limit of the mean bulk fluid temperature, P_{Tf*}, can be obtained from equation 4.58 below:

$$P_{Tf*} = \left[P_{Tf.i}^2 + P_{Tf.o}^2\right]^{\frac{1}{2}} \tag{4.58}$$

here, $P_{Tf.i}$ and $P_{Tf.o}$ are the precision errors of the inlet and outlet fluid temperatures respectively.

From equation 4.54 above, B_{Tw} and B_{Tf*} are the bias limits of the measured wall temperature and the mean bulk fluid temperature respectively

To this regard, B_{Tw} can be written as follows:

$$B_{Tw} = \left[K \sum_{j=1} \left(B_T^2\right)_j\right]^{\frac{1}{2}} \tag{4.59}$$

where B_T represents the bias error of the local wall temperature (i.e. T) as sampled by probe number 'j'.

Meanwhile, the bias limit of the mean bulk fluid temperature, B_{Tf^*}, can be expressed as:

$$B_{Tf^*} = \left[B_{Tf.i}^2 + B_{Tf.o}^2 \right]^{\frac{1}{2}} \tag{4.60}$$

here, $B_{Tf.i}$ and $B_{Tf.o}$ are the bias errors of the inlet and outlet fluid temperatures respectively. The full complement of expressions employed for the evaluation of U_α are presented in Appendix B.0 following.

For each set of experimentally runs, the uncertainty in the measured heat transfer coefficient changes due to the variation in the temperature driving force (T_w - T_{f^*}). For instance, in a typical two-phase flow boiling run, carried out with distilled water at 90 °C sub-cooling and a volumetric rate of 10 litres/min, the calculated uncertainty, U_α, varies between 10.54 % to 15.6 % as the heat flux is systematically reduced from 279.7 kW/m^2 to 83.92 kW/m^2.

Sample calculations demonstrating the evaluation of U_α are presented in Appendix B.1 to Appendix B.4 following.

CHAPTER 5: FLOW BOILING ENHANCEMENT – EXPERIMENTAL RESULTS

5.1. INTRODUCTION

In this chapter, experimental results detailing the influence of various operating parameters on the boiling heat transfer performance of our proposed three-phase circulating fluidised bed are presented and described. In addition, results which reveal the improvement of the two-phase flow boiling coefficient in the presence of fluidised particles are also set forth and explained. As stated in section 4.1, various aspects of the attainable heat transfer enhancement have been investigated; these include the effect of heat flux, liquid flowrate and particle size.

Test procedures and experimental conditions have been comprehensively described in *Chapter 4*, and are summarised here as follows:

- Experiments are conducted in two different heat transfer test modes. Test 'Series-A', referred to as the reference (or control) series, considers the case of two-phase flow boiling, whilst test 'Series-B' examines heat transfer behaviour in three-phase flow boiling. The results are reported according to these test modes.

- All experiments are performed using distilled water, pre-heated to a sub-cooled temperature of 90 ^{0}C. The physical properties of the working liquid are given in Table 4.6.

- All experiments are conducted at atmospheric pressure.

- In both test modes, the effect of heat flux on the measured rate of heat transfer has been determined for q'' values ranging from 27.97 kW/m^2 to 279.7 kW/m^2. Meanwhile, the influence of liquid superficial velocity has been evaluated at flows ranging from 10 litres/min to 26 litres/min. Tables 4.7, 4.8 and 4.9 give full details regarding the investigated range of heat fluxes and liquid velocities.

- For the case of three-phase flow boiling, the total mass of particles charged to the riser column = 250 grams. For stainless steel particles, with a density of 7850 kg/m^3, this corresponds to volume of added solids = 31.85 ml. Hence, in the riser section, the equivalent particle volume fraction, or average hold-up of particles, can be estimated as shown in equation 5.1 below.

$$\varepsilon_p = \frac{\text{volume of particles added to riser section}}{\text{volume of riser section}} \qquad (5.1)$$

$$= \frac{V_p}{V_{TOTAL}} = \frac{V_p}{\pi.D_e^2.L/4} = \frac{3.18 \times 10^{-5}\ m^3}{\pi.D_e^2.L/4}$$

For an overall bed height, L, approximately equal to 1200 mm and D_e based on the hydraulic mean diameter of the heated channel (see equation 4.51), equation 5.1 yields,

$$\varepsilon_p = \underline{0.16 \text{ or } 16\%}$$

- Finally, as listed in Table 4.9, stainless steel particles of 1.5, 2.0 and 2.5 mm diameter are employed in the 'Series-B' test program. Table 4.5 lists the relevant particle physical properties.

5.2. Results of Two-Phase Investigations (Series-A)

As explained in subsection 4.5.1 and above, at the test section, before exploring the principles of three-phase flow boiling and its associated heat transfer enhancement effect, it was necessary to first consider heat transfer behaviour in conventional two-phase flow boiling. As the reference mode of boiling, our objective was to obtain experimental results consistent with the familiar and extensively reported trends of vapour-liquid flow boiling (see subsection 2.3.1 for the fundamental characteristics of two-phase flow boiling).

Hence, in light of the above, our observations regarding the effect of operating parameters on the rate of heat transfer in two-phase flow boiling, are presented in subsections 5.2.1 and 5.2.2 following

5.2.1. Effect of Heat Flux

For a specified liquid delivery rate of 18 litres/min (*Re* '58631'), Figure 5.1(a) shows the variation of the measured two-phase heat transfer coefficient, $\alpha_{f.b}$, with heat flux, q'', whilst Figure 5.1(b) shows the corresponding boiling curve. From Figure 5.1(a), we see that for heat fluxes below the onset of nucleate flow boiling (where the O.F.B marks the boundary between the forced convective and nucleate boiling regions, and for our test geometry is encountered at q'' values approximately equal to 85 kW/m^2) the heat transfer coefficient is virtually independent of increasing heat flux. However, beyond the O.F.B point, advancing into the nucleate boiling region, the value of

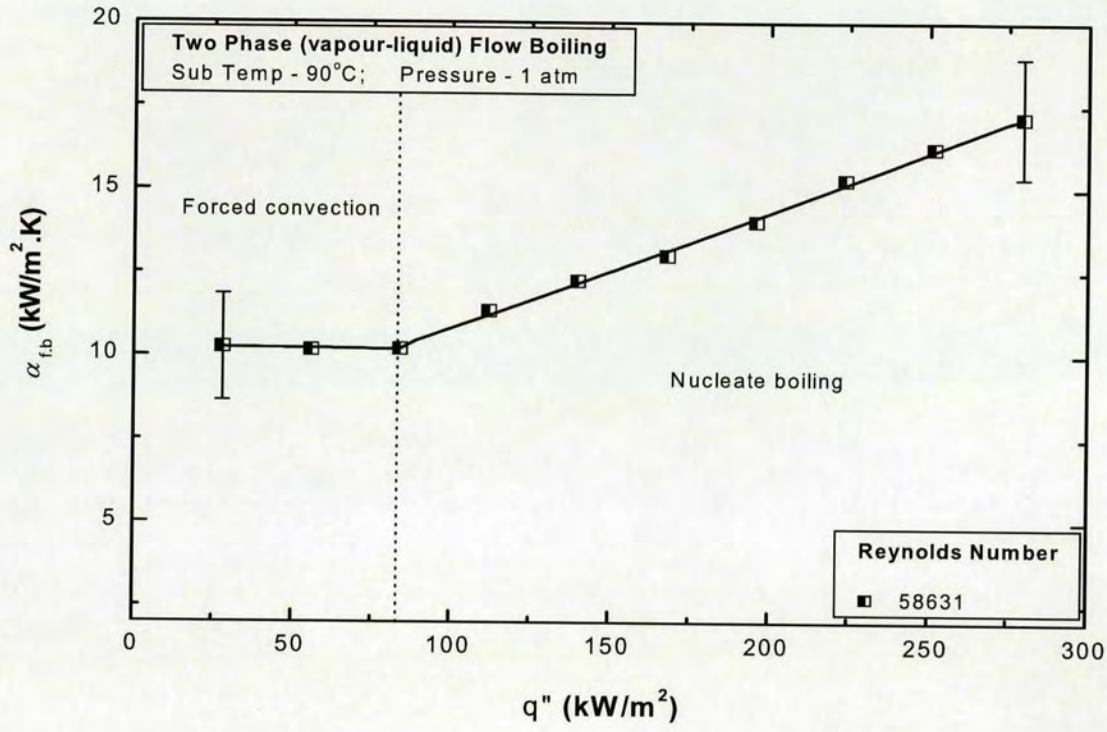

(a)

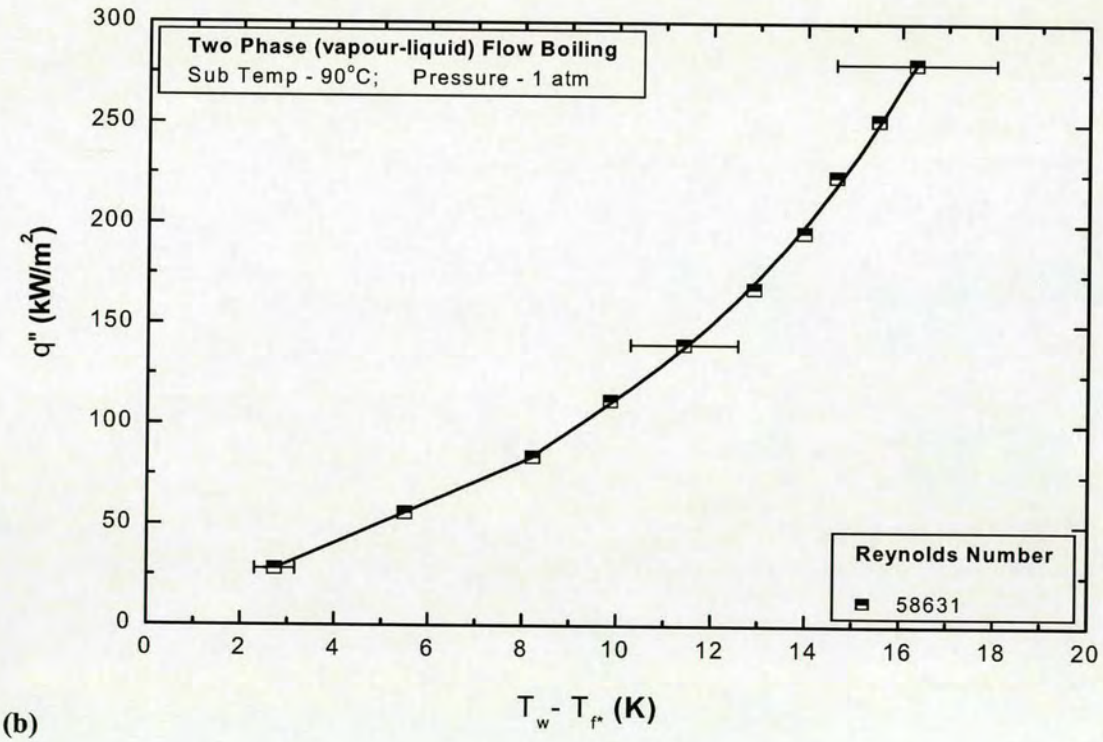

(b)

Figure 5.1: (a) Plot of two-phase heat transfer coefficient vs. heat flux, for distilled water at a liquid flowrate of 18 litres/min (*Re* '58631'), (b) Corresponding boiling curve, showing plot of heat flux versus temperature driving force.

the measured flow boiling coefficient increases almost linearly for successive increases in heat flux.

The trend of the heat transfer coefficient versus heat flux relationship, as shown in Figure 5.1(a) above, is observed for all investigated liquid velocities. This is clearly demonstrated in Figure 5.2(a), which shows a set of results of $\alpha_{f.b}$ vs. $q^{"}$ for a specified range of liquid superficial velocities, which are themselves expressed as dimensionless Reynolds numbers (see Table 4.8 for 'Flowrate to Superficial velocity to Reynolds number' conversion chart) In all instances the two-phase boiling coefficient remains almost constant for heat fluxes below 85 kW/m^2. In contrast, and similar to the result presented in Figure 5.1(a), once we cross the boundary between forced convection and nucleate boiling, indicated on the graph by the dotted line at $q^{"}$ = 83.92 kW/m^2, the two-phase flow boiling coefficient then shows a strong dependency on the heat flux, increasing to a maximum value at $q^{"}$ = 279.70 kW/m^2.

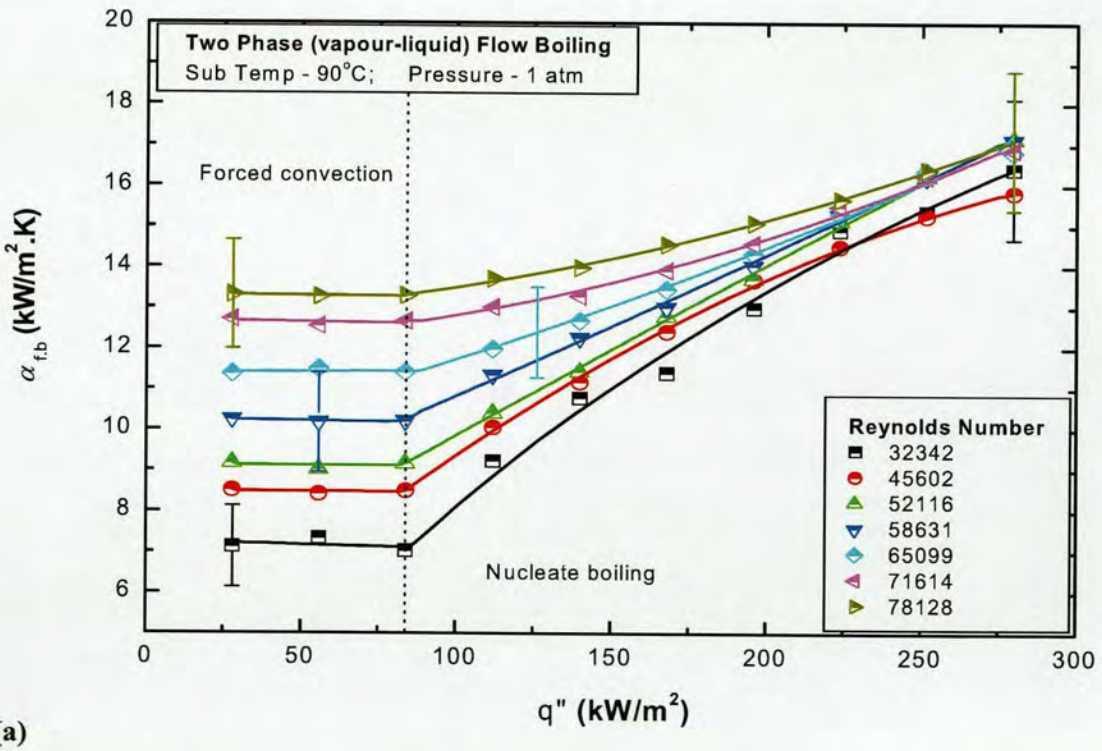

(a)

Figure 5.2: (a) Plots of two-phase heat transfer coefficient vs. heat flux, for specified range of Reynolds number.

For the purpose of visual clarity, error bars have been included for a select number of plots only.

Associated with Figure 5.2(a) above, Figure 5.2(b) depicts the relevant boiling curves for *Re* values of 32342, 52116, 65099 and 78128.

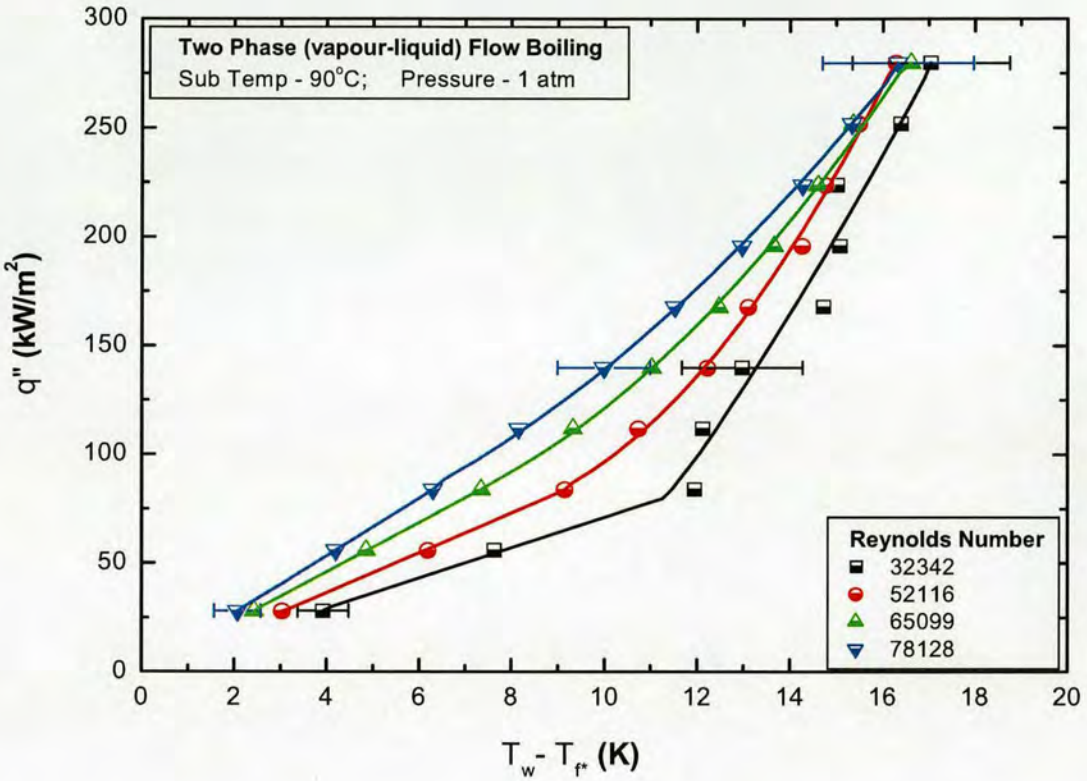

Figure 5.2: (b) Heat flux vs. temperature driving force, determined for indicated values of *Re*.

From the plots of Figure 5.2(b) it is immediately apparent that increasing liquid velocity precipitates a leftward shift of the boiling curve. For the same value of $q^{"}$, higher values of *Re* generate smaller wall excess temperatures (T_w - T_{f*}). For instance at $q^{"}$ = 55.94 kW/m^2, the measured wall excess temperature varies from 7.63 Kelvin to 4.21 Kelvin, reflecting a change of *Re* from 32342 to 78128. Therefore, recalling the expression relating heat transfer coefficient, heat flux and temperature driving force (see equation 4.44) increasing liquid velocity yields higher two-phase boiling coefficients by reducing the wall excess temperature for the same value of $q^{"}$. As well as the heat flux effect, Figure 5.2(a) also illustrates the influence of velocity on the plots of heat transfer coefficient versus heat flux. Over the low to mid-heat flux range (from $q^{"}$ = 27.97 kW/m^2 to 167.83 kW/m^2) increasing *Re* translates to increasingly higher values of $\alpha_{f.b}$. However, in the higher heat flux region (for $q^{"}$ > 167.83 kW/m^2) the measured rate of heat transfer is seemly less affected by fluctuation of the liquid

velocity. We examine the changing nature of the boiling heat transfer coefficient vs. liquid velocity relationship in subsection 5.2.2 following.

5.2.2. Effect of Liquid Superficial Velocity

Figures 5.3 through to 5.5 depict the variation of the two-phase boiling coefficient with liquid velocity, across our given range of heat fluxes. Beginning with Figure 5.3, we see that in the low heat flux range, the two-phase flow boiling coefficient increases linearly with liquid velocity. At the same time, the superimposition of the $\alpha_{f.b}$ vs. *Re* plots validates the boiling coefficients independence of heat flux during forced convective boiling.

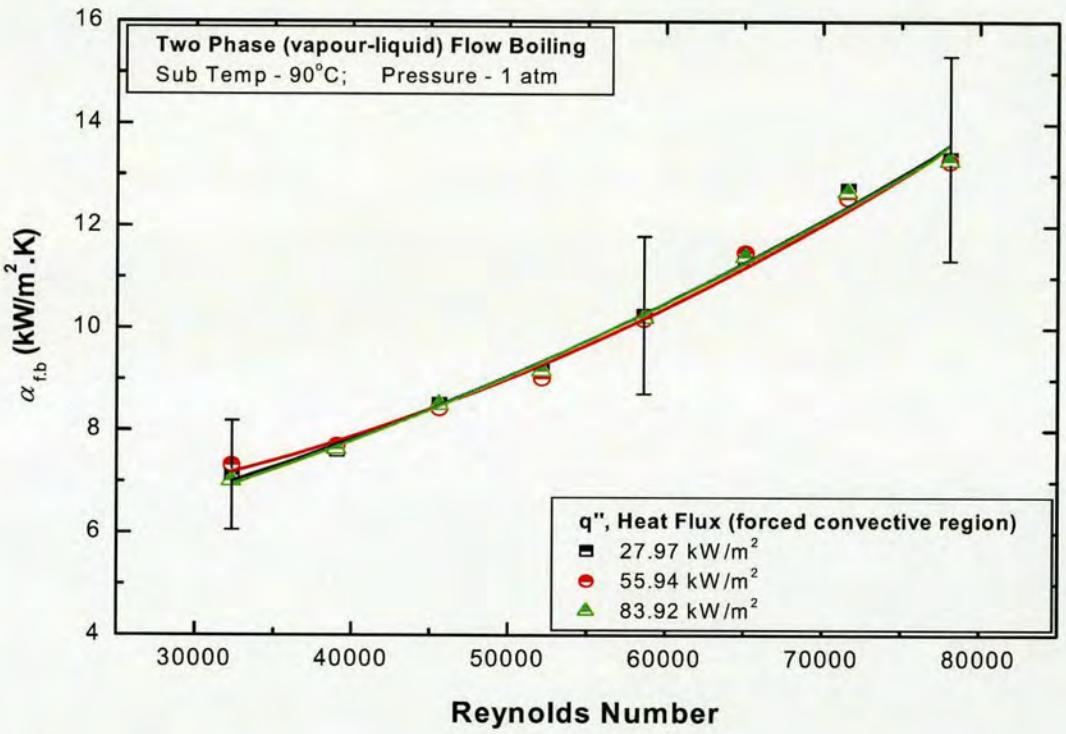

Figure 5.3: Variation of heat transfer coefficient with Reynolds number. Single phase/Forced convective region of two-phase flow boiling.

Following on from above, Figure 5.4 depicts plots of $\alpha_{f.b}$ vs. Reynolds number, for the mid-heat flux range (i.e. $q^{"}$ values in between the forced convective and fully developed nucleate boiling regions). The slope of the curves suggest that in this transitional boiling region, labelled on the graph as 'beyond o.f.b point', although the influence of superficial velocity is still discernible for heat fluxes up to 167.83 kW/m^2, its influence does however begin to diminish as we approach higher heat flux values of around 195.80 kW/m^2. Another noticeable feature of the plot is the variation of the boiling coefficient with heat flux. In

contrast to the forced convective region, for any given liquid velocity, increasing heat flux results in an increased rate of boiling.

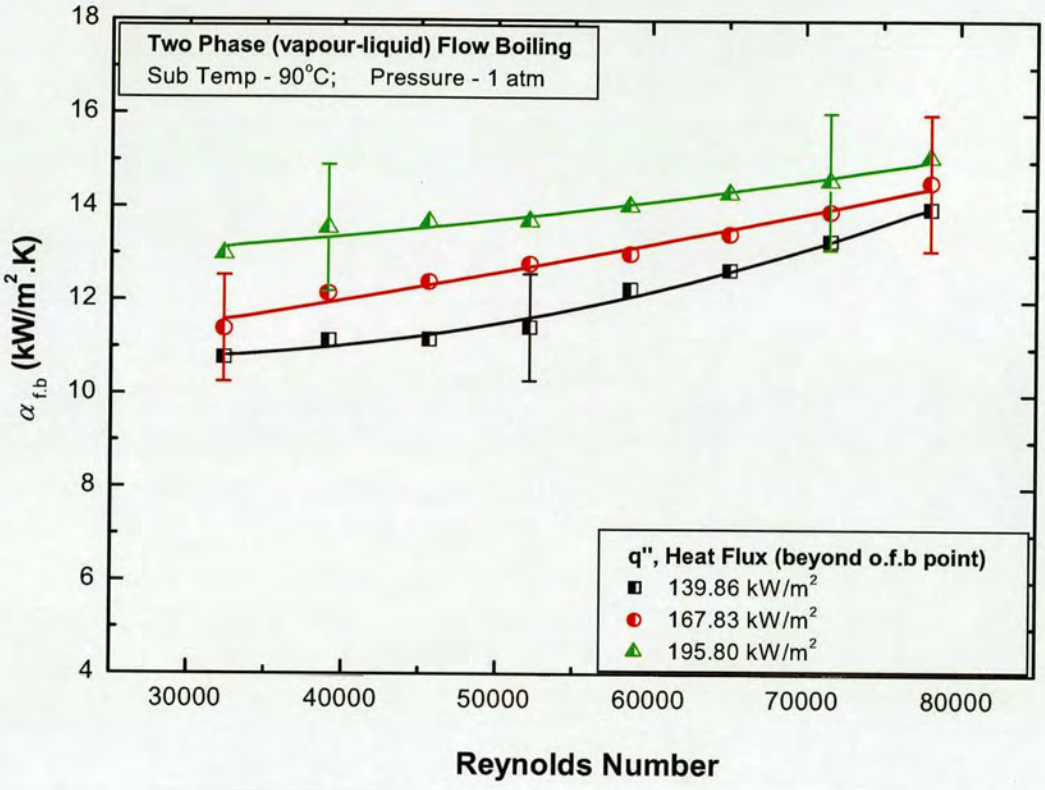

Figure 5.4: Variation of heat transfer coefficient with Reynolds number, for mid-heat flux or transitional boiling region of two-phase flow boiling.

Finally, as evidenced by the plots presented in Figure 5.5, liquid superficial velocity has no effect on the levels of nucleation during fully developed nucleate boiling. In this uppermost boiling region, $\alpha_{f.b}$ appears to be solely dependent on the heat flux.

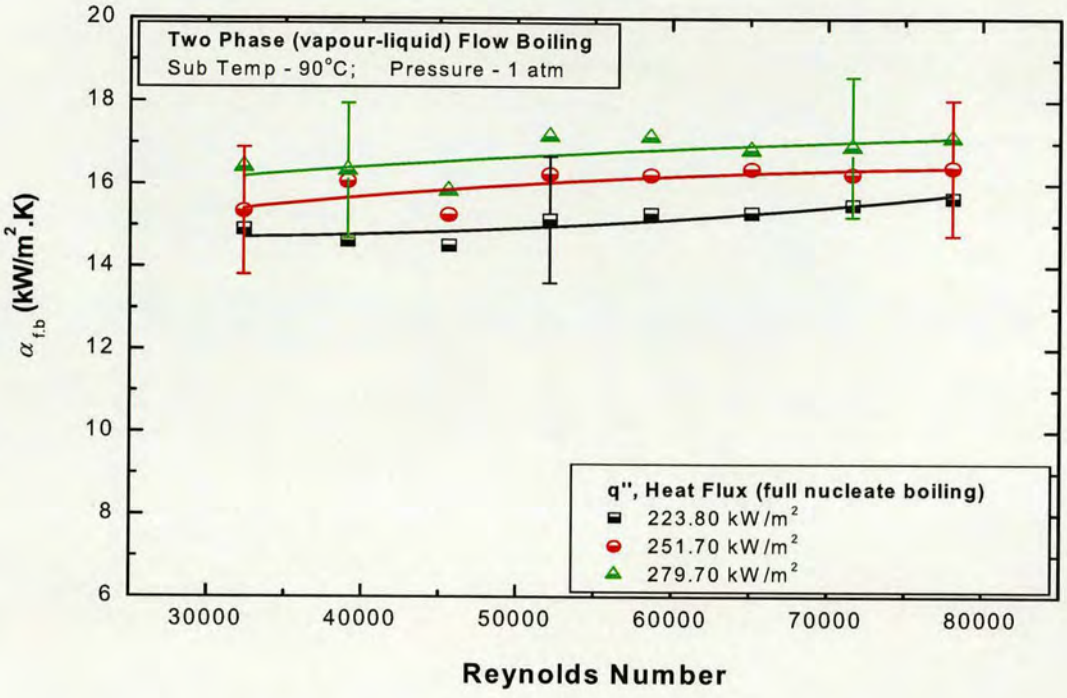

Figure 5.5: Variation of heat transfer coefficient with Reynolds number. Fully developed nucleate boiling region of two-phase flow boiling.

In summary, the findings reported in subsection 5.2.1 and 5.2.2 above are not only reproducible, but also consistent with the main features of two-phase flow boiling as identified by various investigators and stated in *Chapter 2*.

5.3. Results of Three-Phase Investigations (Series-B)

5.3.1. 3-Phase Flow Boiling and The Influence of Heat Flux

For experiments performed with the use of 2.5 mm stainless steel particles, Figure 5.6(a) presents a typical set of results showing the variation of the measured three-phase flow boiling coefficient with heat flux. As indicated on the diagram, these results were obtained for liquid flows of 14 litres/min (*Re* '45602') and 18 litres/min (*Re* '58631'). Figure 5.6(b) depicts the relevant boiling curves.

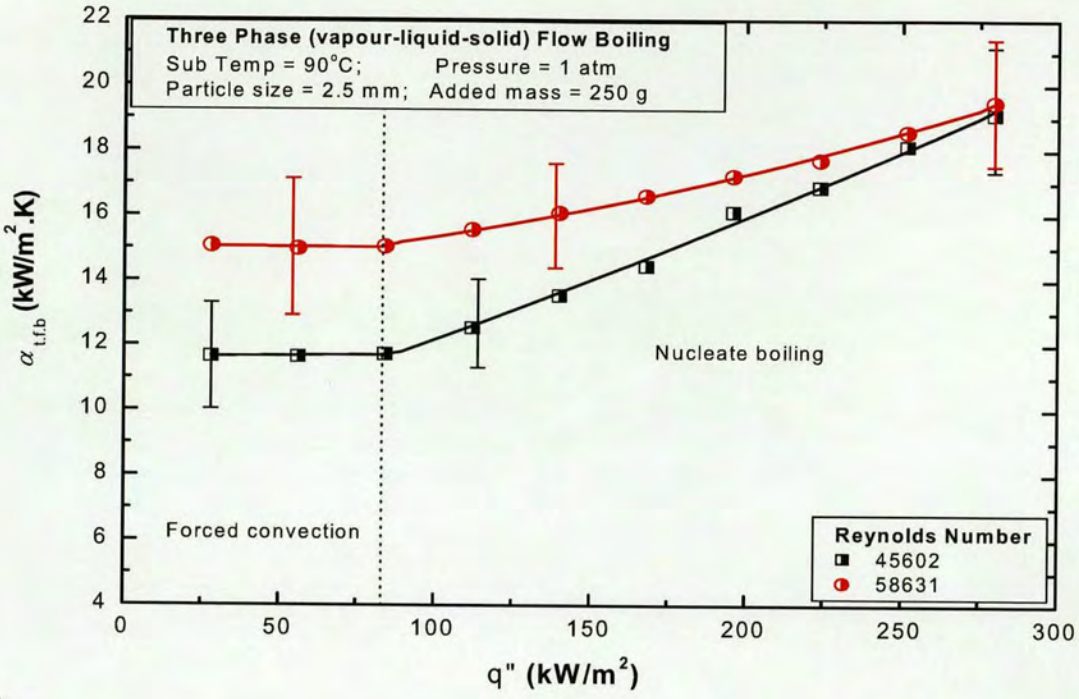

(a)

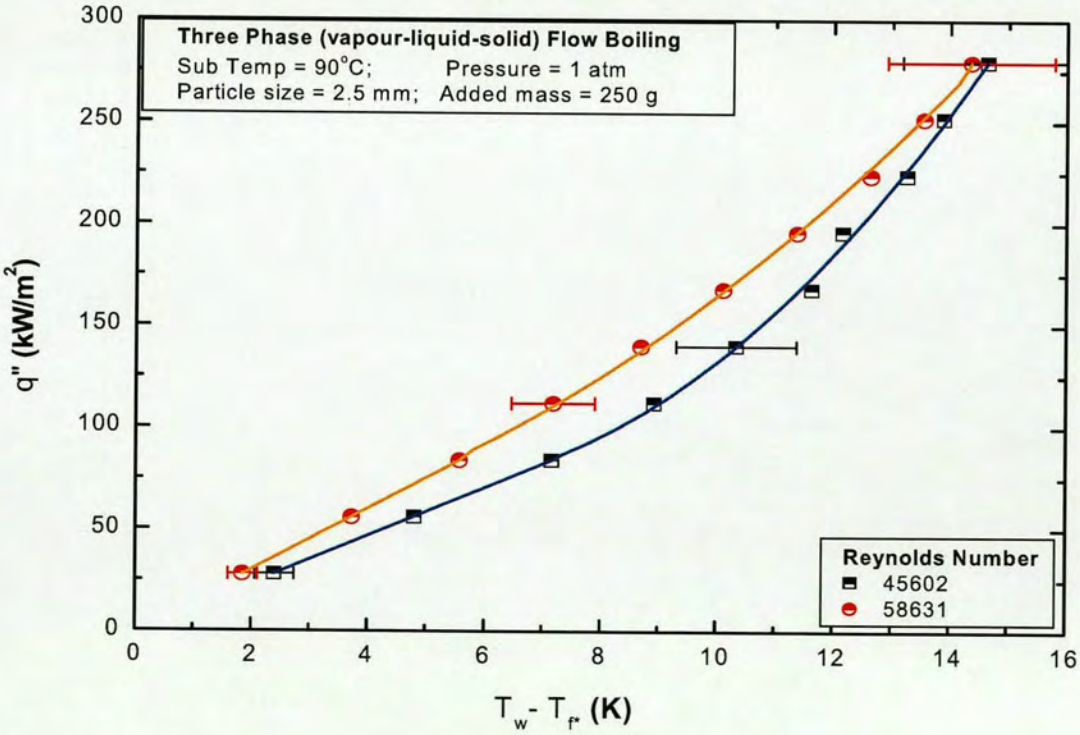

(b)

Figure 5.6: (a) Plot of three-phase heat transfer coefficient vs. heat flux, for 2.5 mm stainless steel particles and liquid flows of 14 and 18 litres/min (*Re* '45602' and '58631'), (b) Associated boiling curves, showing plots of heat flux versus ΔT.

For each examined flowrate, the trend of the three-phase flow boiling coefficient versus heat flux curve ($\alpha_{t.f.b}$ vs. $q^{"}$) displays tendencies similar to those encountered in Figure 5.1(a) for the case of two-phase flow boiling. In both instances, we see that in the forced convective region the three-phase heat transfer coefficient remains unaffected by the variation of the imposed heat flux $q^{"}$. However, upon crossing the o.f.b point ($q^{"}_{OFB} \approx 83.92$ kW/m^2), the plots depart from this behaviour, and the heat transfer coefficient is now magnified by the increase of heat flux. As shown in Figure 5.7(a) below, these tendencies have been observed for all investigated liquid velocities.

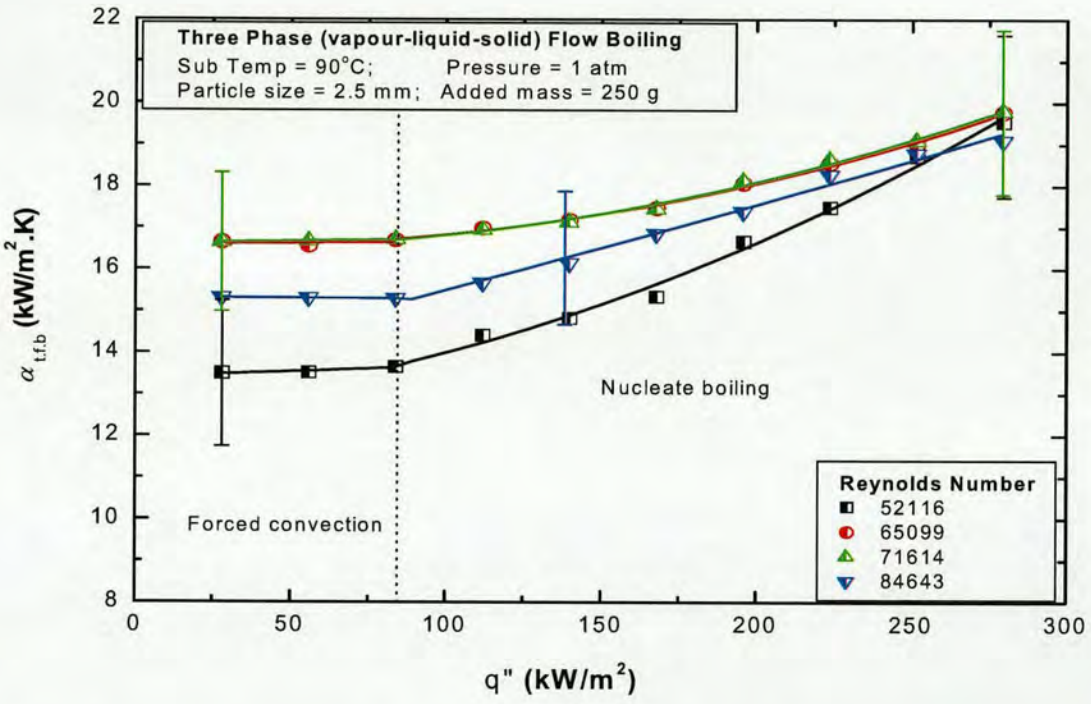

Figure 5.7: (a) Plots of 3-phase heat transfer coefficient vs. heat flux, for specified range of liquid velocities. 2.5 mm stainless steel particles employed as solid phase.

In conjunction with above, Figure 5.7(b) shows the corresponding plots of heat flux versus wall excess temperature. Analogous to the case of two-phase flow boiling (see subsection 5.2.1 above), it is clear that alteration of liquid velocity affects the position of the boiling curve. On first impressions it appears that increasing values of *Re* causes a leftward shift of the boiling curve. As explained in subsection 5.2.1 previous, this results in smaller $(T_w - T_{f*})$ values for the same heat flux, which in turn yields higher three-phase heat transfer coefficients. However, although true, this observation is valid only up to a point. In three-phase flow boiling the relationship between the measured rate of heat transfer and superficial

velocity is rather more involved than that experienced in two-phase flow boiling. We examine this feature in subsection 5.3.2. following.

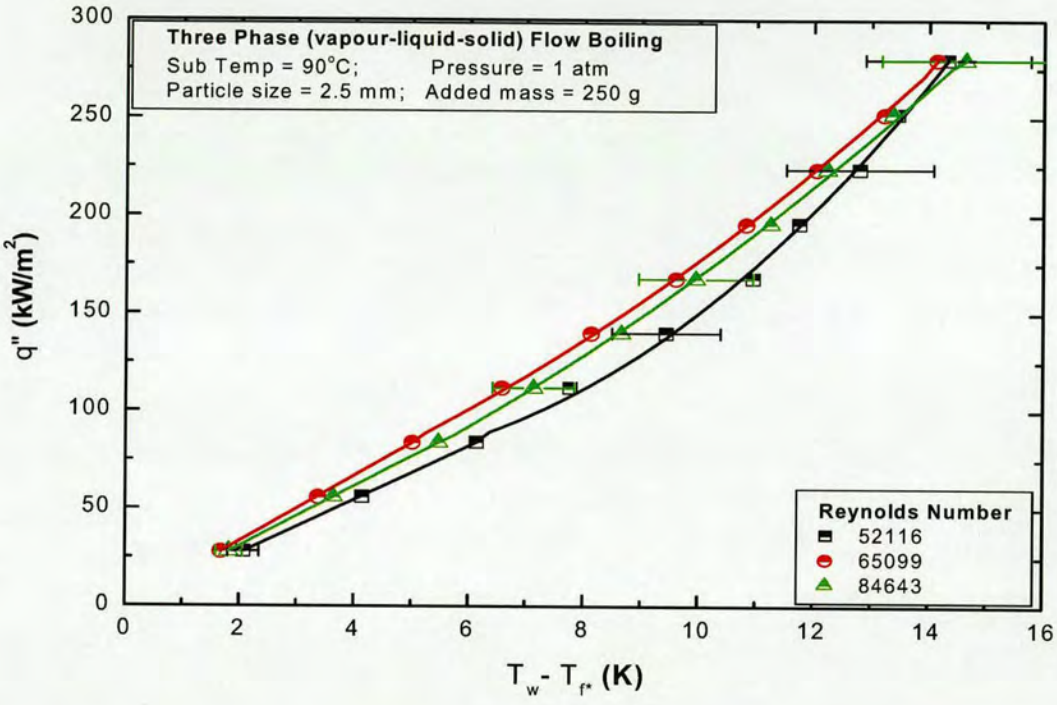

Figure 5.7: (b) Heat flux vs. temperature driving force, for 3-phase flow boiling at indicated liquid velocities. 2.5 mm stainless steel particles employed as solid phase.

However, before going on to describe the effects of liquid superficial velocity, presented in Figure 5.8(a) and Figure 5.9(a) are typical sets of results of heat transfer coefficient versus heat flux for three-phase flow boiling with 1.5 mm and 2.0 mm stainless steel particles respectively. Meanwhile, and in keeping with above, Figure 5.8(b) and Figure 5.9(b) depict the affiliated boiling curves.

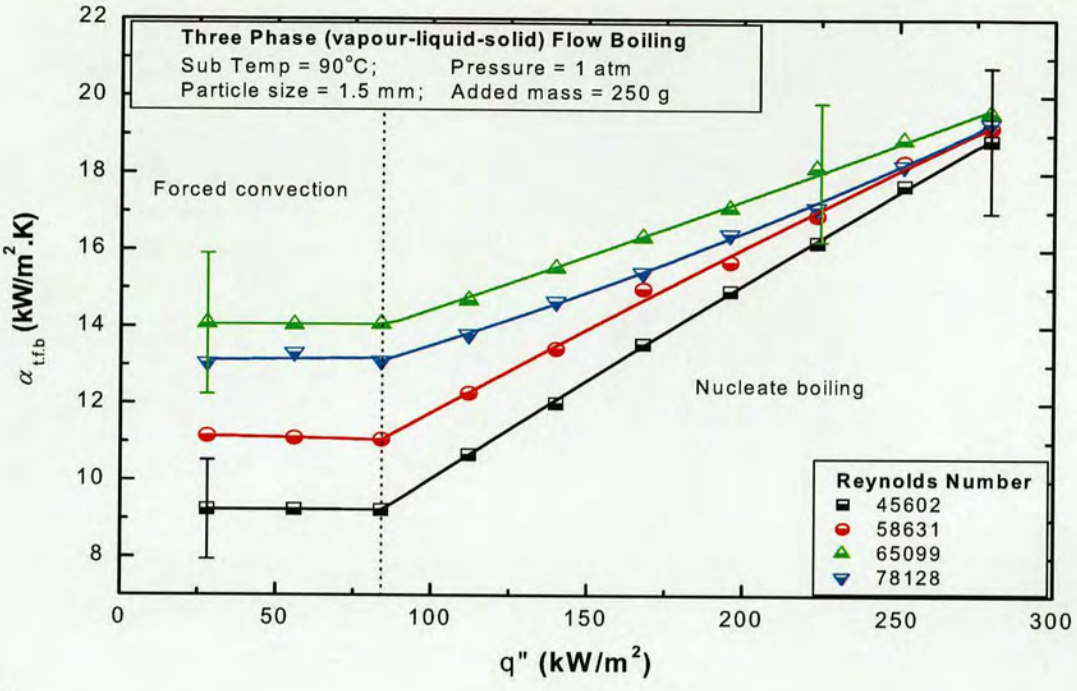

(a)

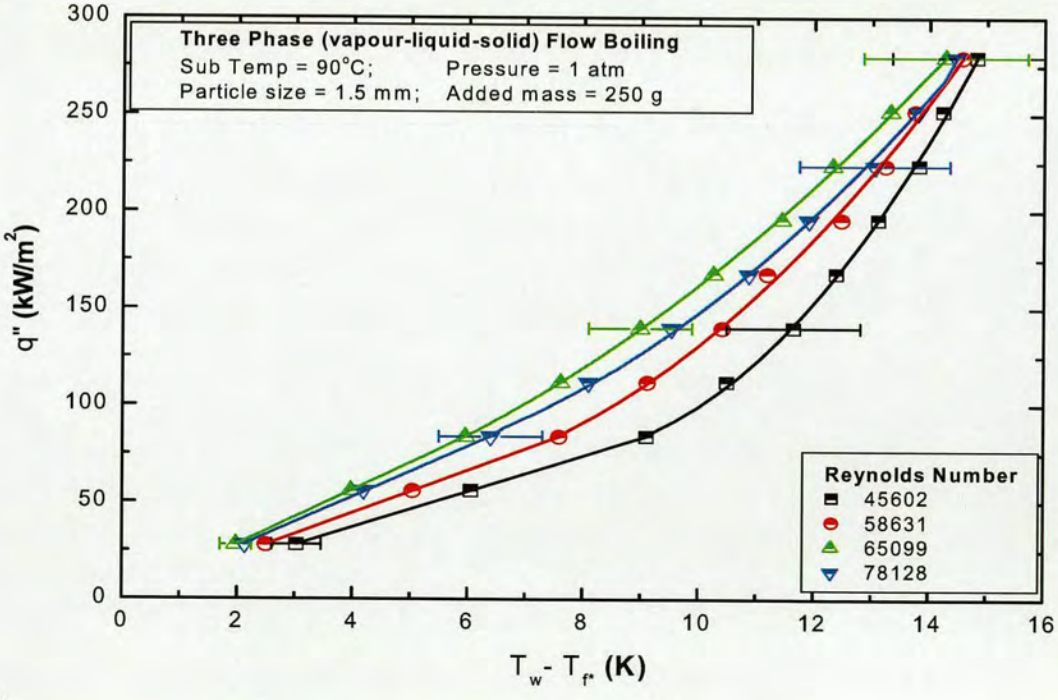

(b)

Figure 5.8: (a) Plots of 3-phase heat transfer coefficient vs. heat flux, for specified range of liquid velocities. 1.5 mm stainless steel particles employed as solid phase. (b) Affiliated boiling curves, showing plots of heat flux versus ΔT.

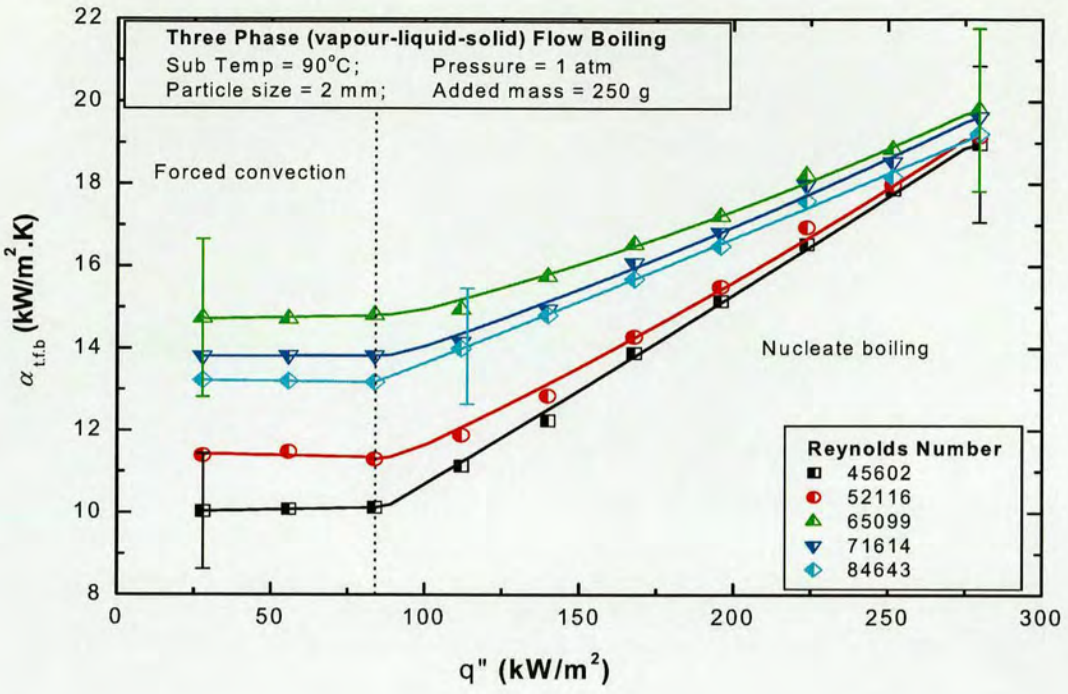

(a)

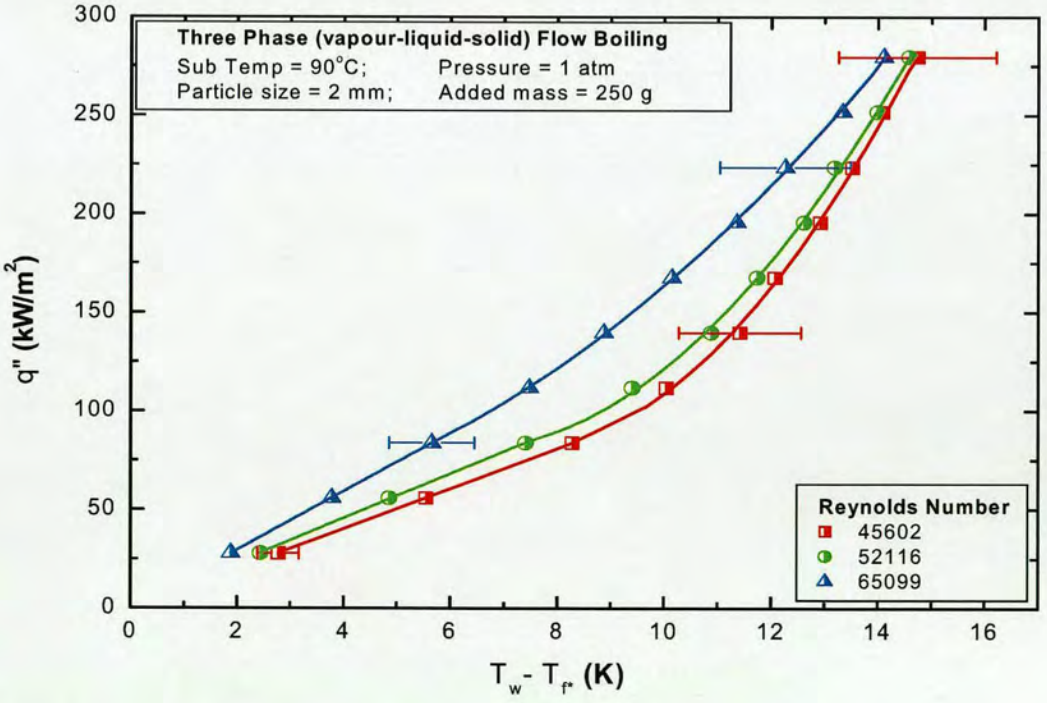

(b)

Figure 5.9: (a) Plots of 3-phase heat transfer coefficient vs. heat flux, for specified range of liquid velocities. 2.0 mm stainless steel particles employed as solid phase. (b) Affiliated boiling curves, showing plots of heat flux versus ΔT.

For both 1.5 mm and 2.0 mm diameter particles, the plots of Figure 5.8(a,b) and Figure 5.9(a,b) display tendencies similar to those presented for the largest sized particles, thereby lending credence to the earlier described three-phase heat transfer results [see Figure 5.6(a,b) and Figure 5.7(a,b)].

5.3.2. 3-PHASE FLOW BOILING AND THE INFLUENCE OF LIQUID VELOCITY

Through the graphs of Figure 5.10 to Figure 5.18, we observe how the three-phase heat transfer coefficient varies with liquid superficial velocity across our range of heat fluxes. To this effect, Figure 5.10 shows a typical set of results obtained during forced convective three-phase flow boiling, and performed with the use of 2.5 mm stainless steel particles

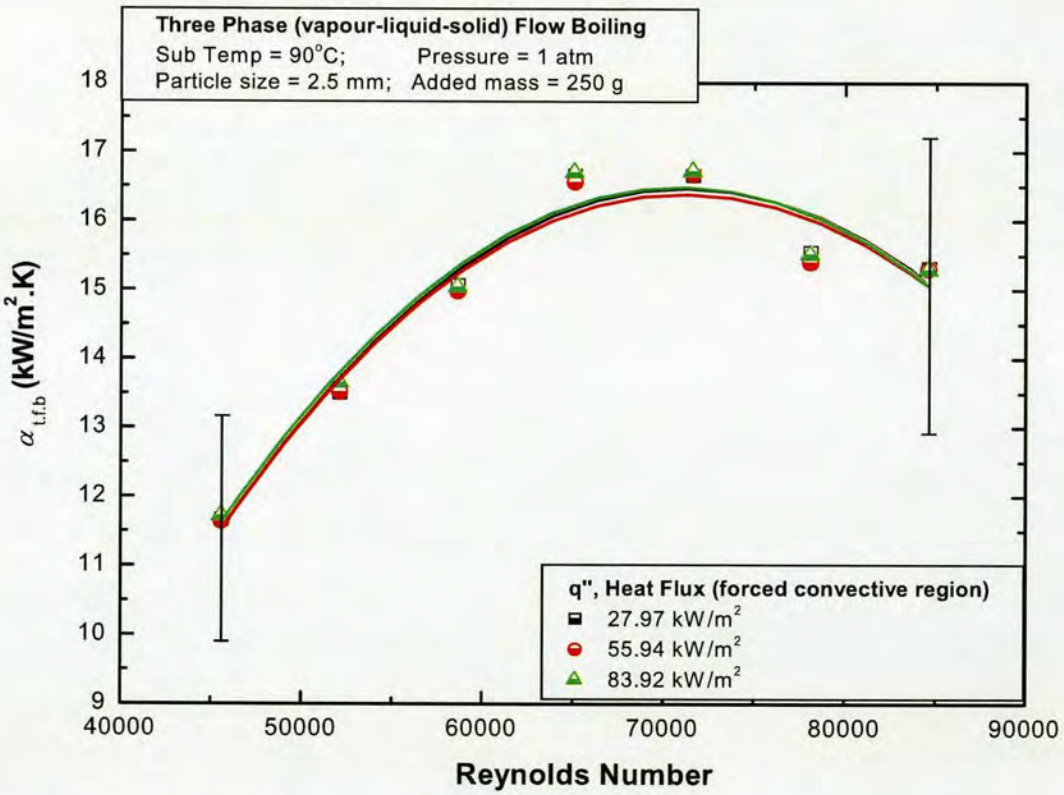

Figure 5.10: Variation of 3-phase heat transfer coefficient with *Re*, for Single phase/Forced convective boiling region and with 2.5 mm stainless steel particles.

By plotting the data points with a second-order polynomial fit, the $\alpha_{t.f.b}$ vs. *Re* relationship describes the parabola-like curve depicted in the diagram above. In this low heat flux region, the first half of the curve indicates an initial increase of the three-phase boiling coefficient with increasing values of *Re*. The linear trend is sustained until $\alpha_{t.f.b}$ attains a maximum at a critical *Re* value. As evidenced by the plot, after this particular point, further increase of *Re*

results in the degradation of the three-phase boiling coefficient. By superimposition, the said plot also illustrates the heat transfer coefficients independence of heat flux across the single phase region. For the same set of test conditions, Figures 5.11 and 5.12 present results for three-phase flow boiling with 2.0 mm and 1.5 mm diameter particles respectively. In each instance, the trend of the $\alpha_{t.f.b}$ vs. *Re* curve demonstrates behaviour similar to that observed in Figure 5.10 for the case of 2.5 mm diameter particles.

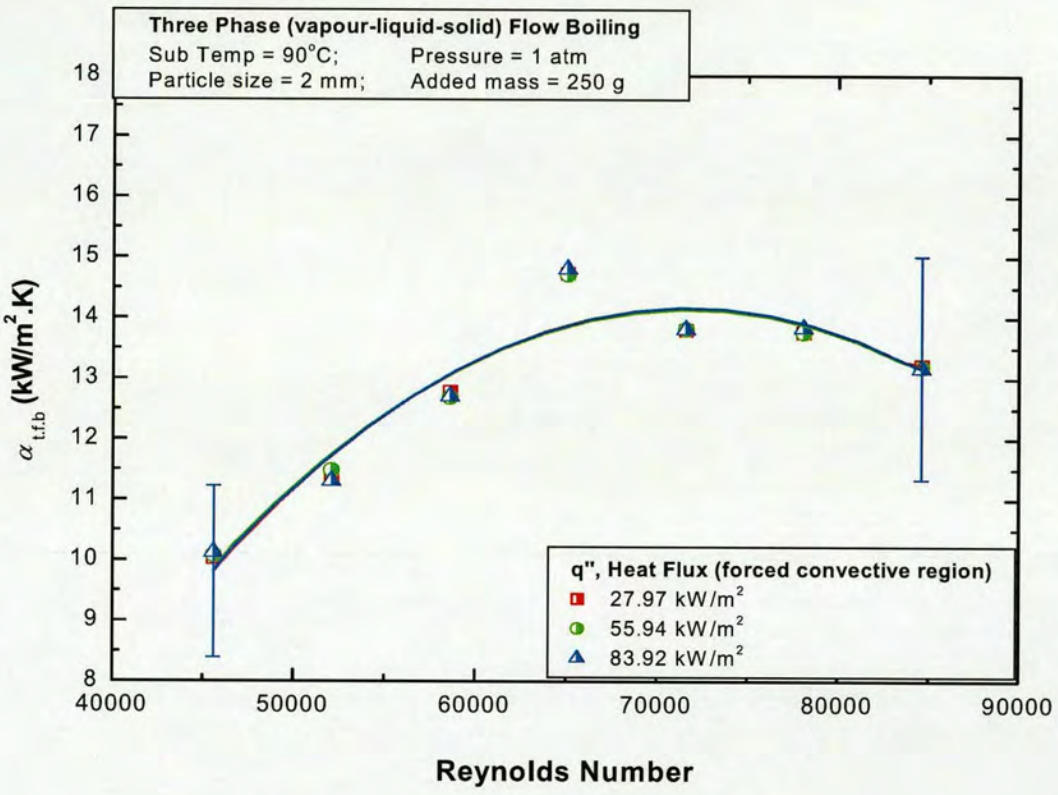

Figure 5.11: Variation of 3-phase heat transfer coefficient with *Re*, for Single phase/Forced convective boiling region and with 2.0 mm stainless steel particles.

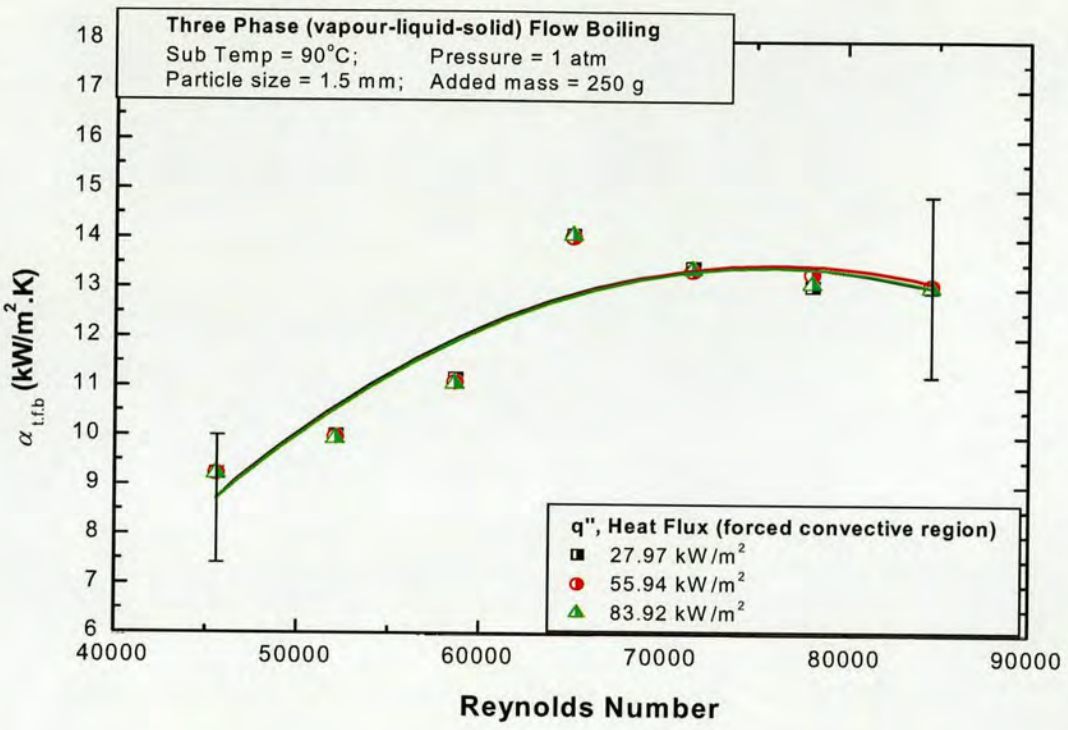

Figure 5.12: Variation of 3-phase heat transfer coefficient with *Re*, for Single phase/Forced convective boiling region and with 1.5 mm stainless steel particles.

Advancing into the nucleate boiling region, the dependence of the three-phase heat transfer coefficient on *Re* gradually begins to decline, before virtually ceasing at higher heat flux values. Firstly, for each individual particle size (presented in descending order from 2.5 mm to 1.5 mm), Figures 5.13 to 5.15 depicts the three-phase heat transfer coefficient versus *Re* relationship for heat fluxes beyond the onset of nucleate flow boiling. In each instance, one can see that at the lower end of the indicated mid-heat flux range (specifically $q^{"}$ = 111.89 kW/m^2), the influence of superficial velocity on the rate of (v-l-s) heat transfer, describes the same pattern as that observed for forced convective boiling (i.e. for increasing *Re*, the three-phase boiling coefficient increases to a threshold value, after which higher liquid flowrate results in deterioration of $\alpha_{t.f.b}$). However, as we transit through to the upper end of the given $q^{"}$ range (i.e. 167.83 kW/m^2 and 195.80 kW/m^2), the overall shape of the $\alpha_{t.f.b}$ vs. *Re* curve begins to plateau, indicating the declining effect of liquid velocity. Furthermore, emphasising the results earlier described in subsection 5.3.1, Figures 5.13 to 5.15 also show that beyond the onset of nucleate flow boiling, the three-phase boiling coefficient is promoted by the increase of heat flux.

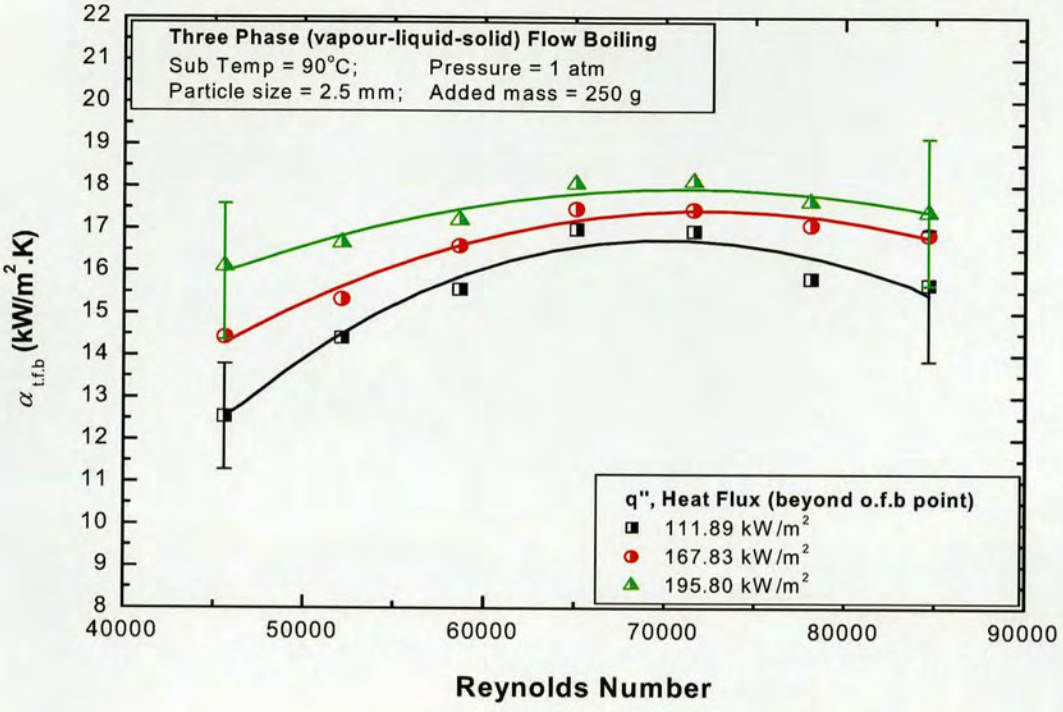

Figure 5.13: Variation of 3-phase heat transfer coefficient with *Re*, for mid-heat flux or transitional boiling region and with 2.5 mm stainless steel particles.

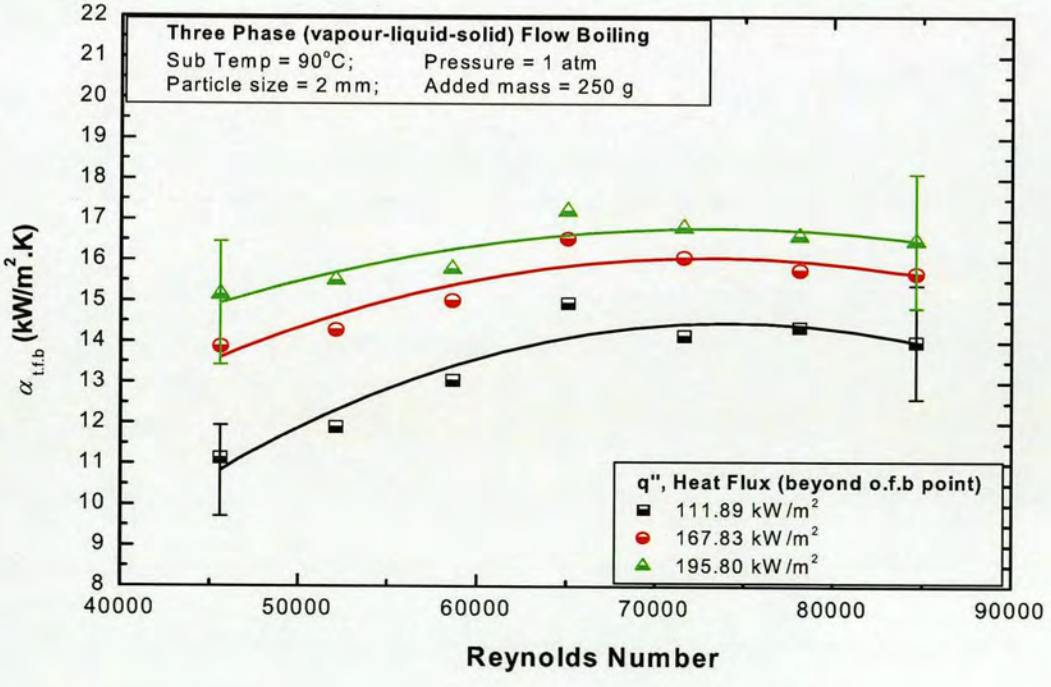

Figure 5.14: Variation of 3-phase heat transfer coefficient with *Re*, for mid-heat flux or transitional boiling region and with 2.0 mm stainless steel particles.

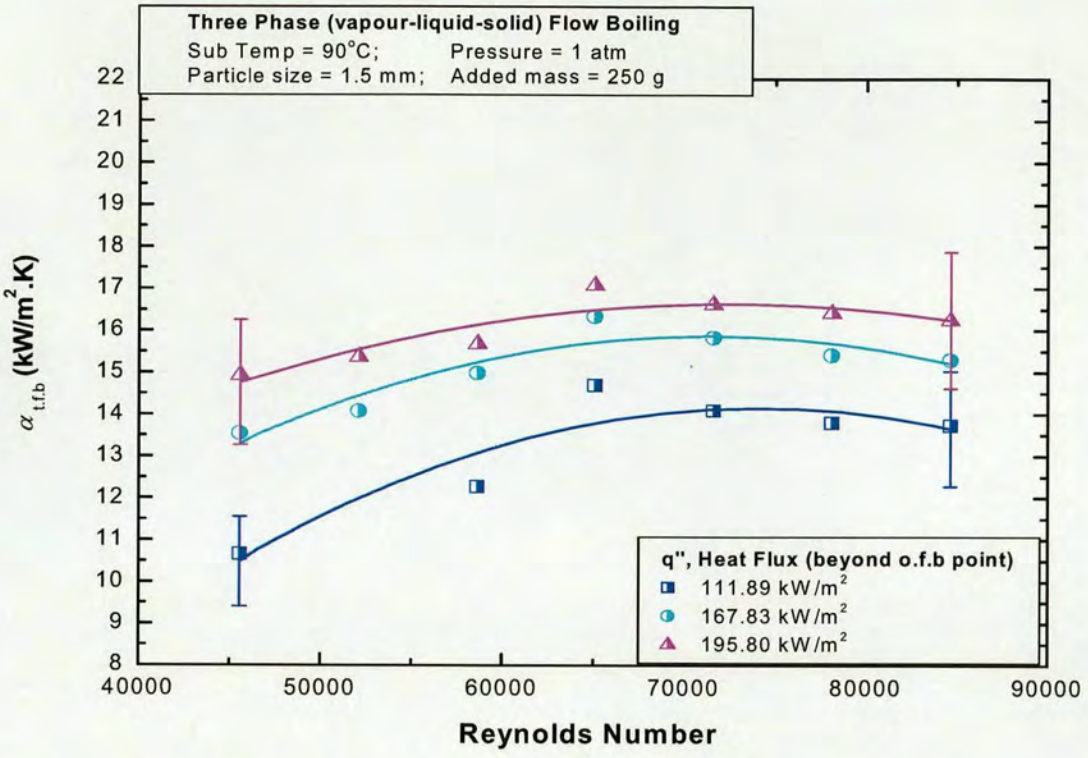

Figure 5.15: Variation of 3-phase heat transfer coefficient with *Re*, for mid-heat flux or transitional boiling region and with 1.5 mm stainless steel particles.

Finally (and again presented in descending order from d_p = 2.5 mm to d_p = 1.5 mm), Figures 5.16 to 5.18 each show the variation of $\alpha_{t.f.b}$ with Reynolds number for heat fluxes within the fully developed nucleate boiling region. For all investigated particle sizes, results indicate that within the upper heat flux region (223.80 kW/m^2 to 279.70 kW/m^2) increase of the three-phase boiling coefficient continues to be dominated by the heat flux relationship, whilst essentially becoming independent of flow velocity.

In subsection 5.3.3 following, we examine the presented three-phase flow boiling results with respect to particle size.

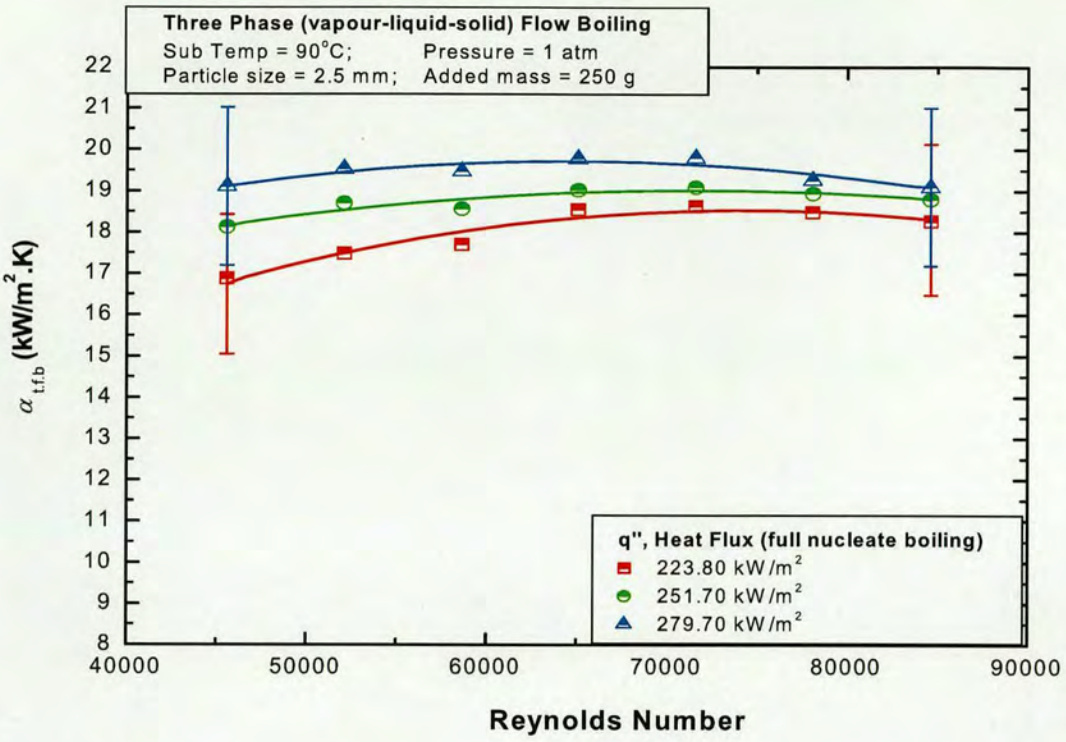

Figure 5.16: 3-Phase heat transfer coefficient vs. Reynolds number, for fully developed nucleate boiling and with 2.5 mm stainless steel particles.

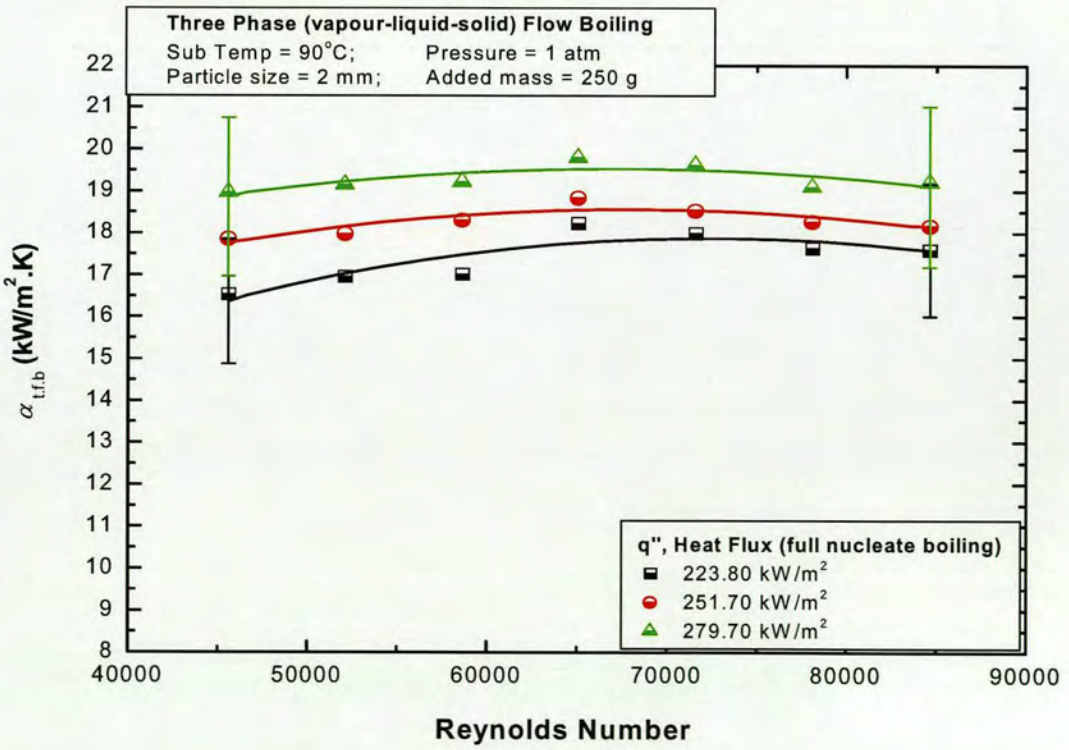

Figure 5.17: 3-Phase heat transfer coefficient vs. Reynolds number, for fully developed nucleate boiling and with 2.0 mm stainless steel particles.

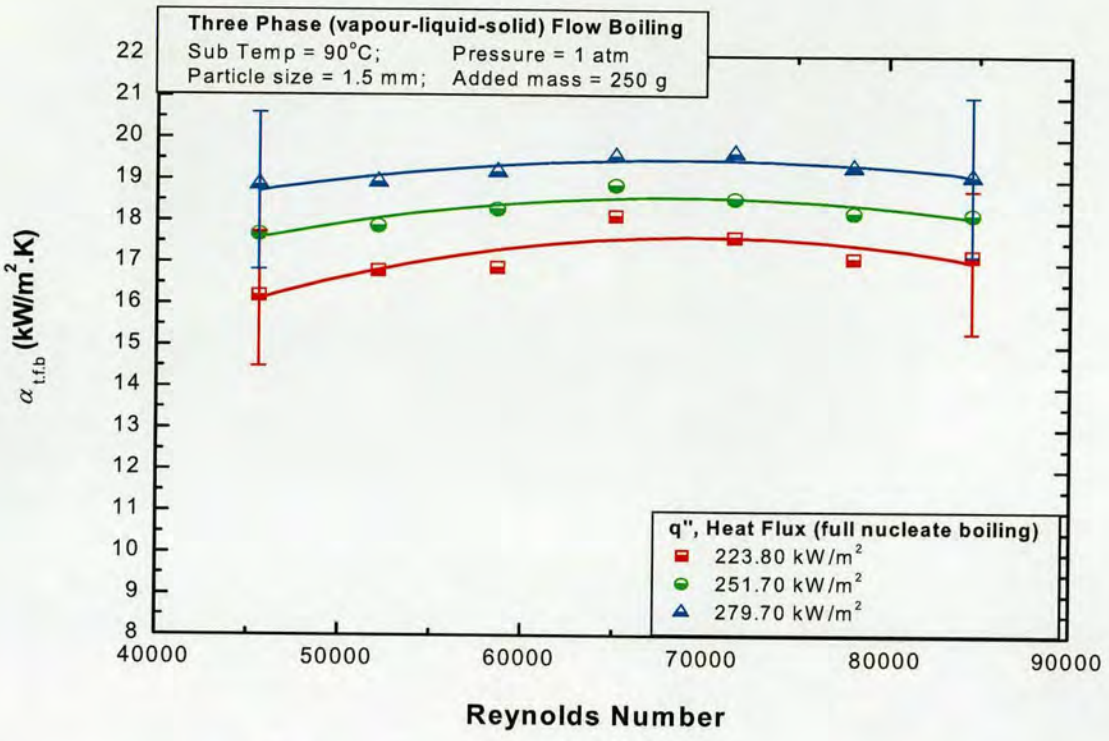

Figure 5.18: 3-Phase heat transfer coefficient vs. Reynolds number, for fully developed nucleate boiling and with 1.5 mm stainless steel particles.

5.3.3. 3-Phase Flow Boiling and The Influence of Particle Size

For a specified liquid delivery rate of 16 litres/min (*Re* '52116') Figure 5.19(a) shows the effect of particle size on the plot of three-phase heat transfer coefficient versus heat flux. Overall, for all examined heat fluxes, the comparison demonstrates that increase of particle diameter promotes the rate of heat transfer in three-phase flow boiling. Some observed features of the enhancement are as follows: In the lower heat flux region (from 27.97 kW/m^2 to 83.92 kW/m^2), the increase of particle diameter from 2.0 mm to 2.5 mm, appears to result in a heat transfer coefficient enhancement which is more pronounced than that observed for the increase from 1.5 mm to 2.0 mm. However, in the nucleate boiling region, we see the enhancement effect of particle size gradually diminish as heat flux is progressively increased. Finally at around $q^{"} = 279.70$ kW/m^2, all curves converge towards a maximum value of $\alpha_{t.f.b}$, and the effect of particle size is no longer discernible. Figure 5.19(b) depicts the accompanying boiling curve comparison. The plot indicates that, generally, the suppression of the wall excess temperature is better achieved with the use of larger sized particles, giving rise to higher values of $\alpha_{t.f.b}$ for the same heat flux setting.

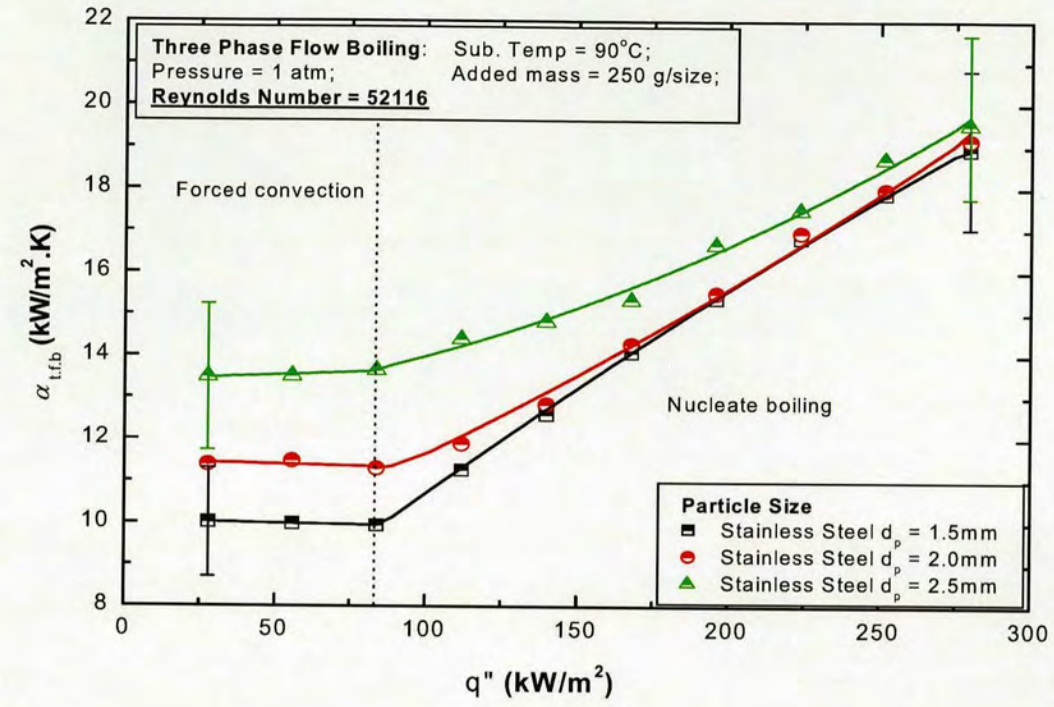

(a)

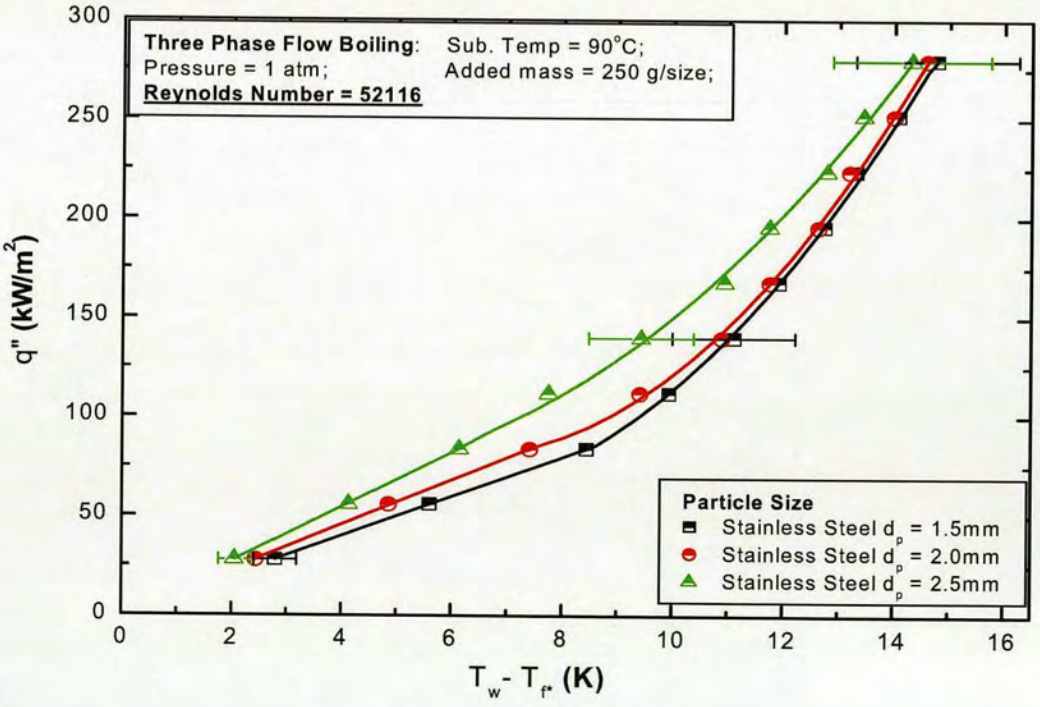

(b)

Figure 5.19: (a) Effect of particle size on plot of 3-Phase heat transfer coefficient vs. heat flux, for *Re* = 52116 (16 litres/min) (b) Related boiling curve comparison.

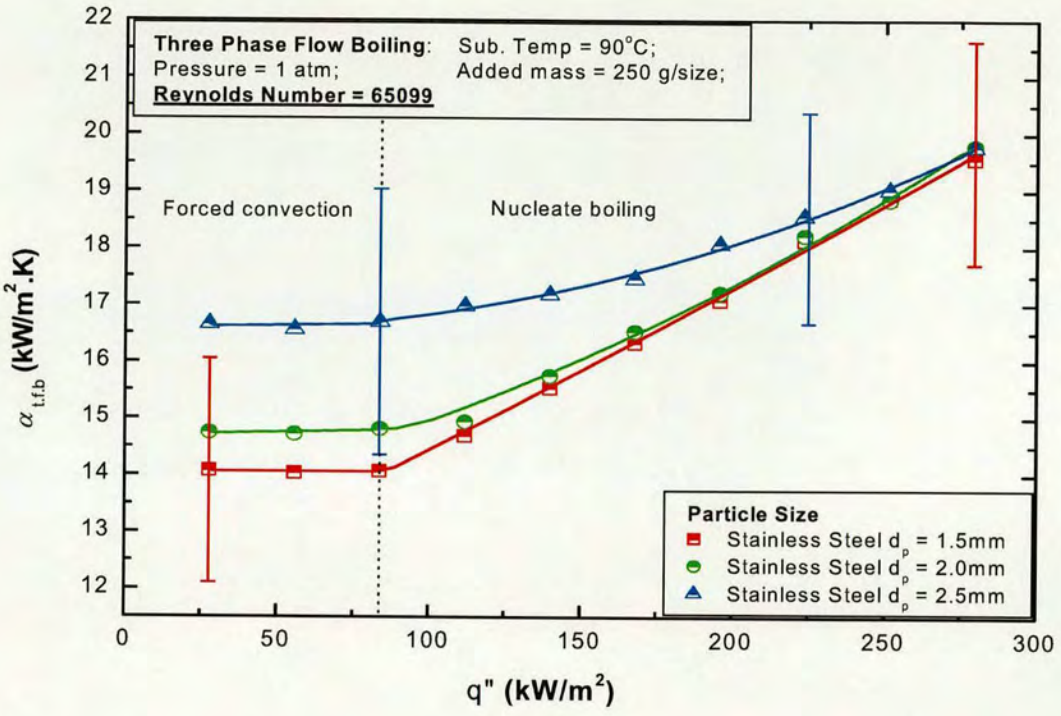

(a)

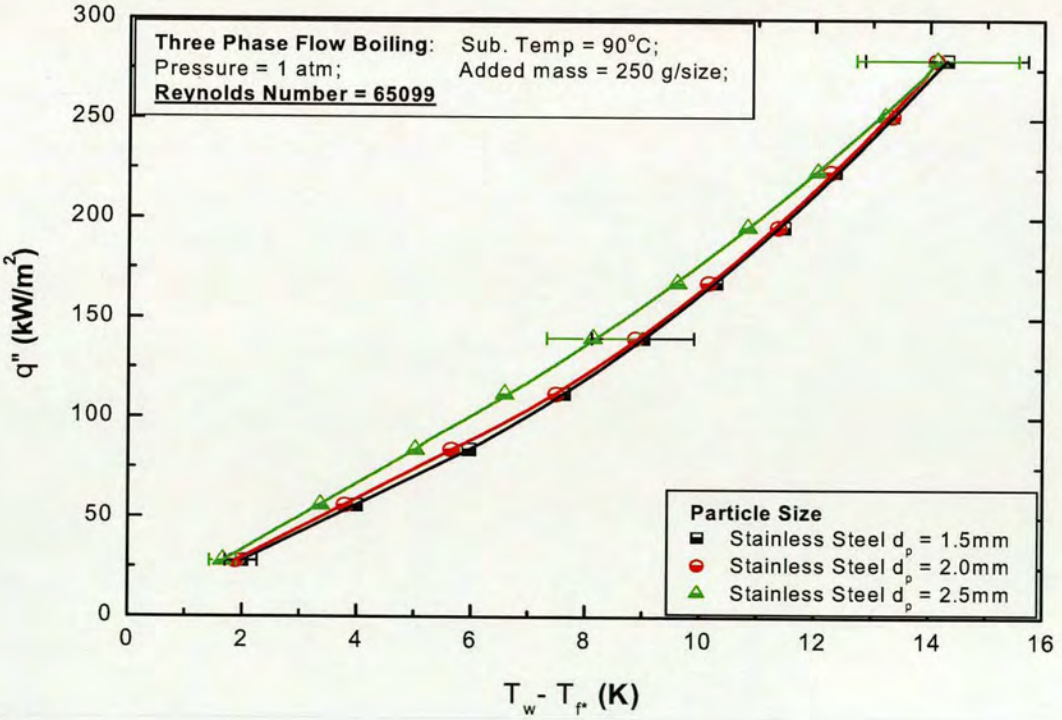

(b)

Figure 5.20: (a) Effect of particle size on plot of 3-Phase heat transfer coefficient vs. heat flux, for *Re* = 65099 (20 litres/min) (b) Related boiling curve comparison.

For a differing set of test conditions, further evidence concerning the effect of particle size is presented in Figures 5.20(a,b) above. Overall, the plots exhibit trends and tendencies consistent with those previously observed in Figures 5.19(a,b).

5.4. Comparison of Heat Transfer in Three-Phase (v-l-s) & Two-Phase (v-l) Flow Boiling.

5.4.1. Comparing Boiling Curves & Plots of Heat Transfer Coefficient Versus Heat Flux.

Figure 5.21(a) compares the variation of heat transfer coefficient with heat flux, for the control run (i.e. two-phase flow boiling) and three-phase circulating fluidised bed boiling. Results for two different liquid velocities are presented (*Re* '52116' and '65099'). In each instance, the three-phase fluidised bed was operated with the use of 2.5 mm stainless steel particles.

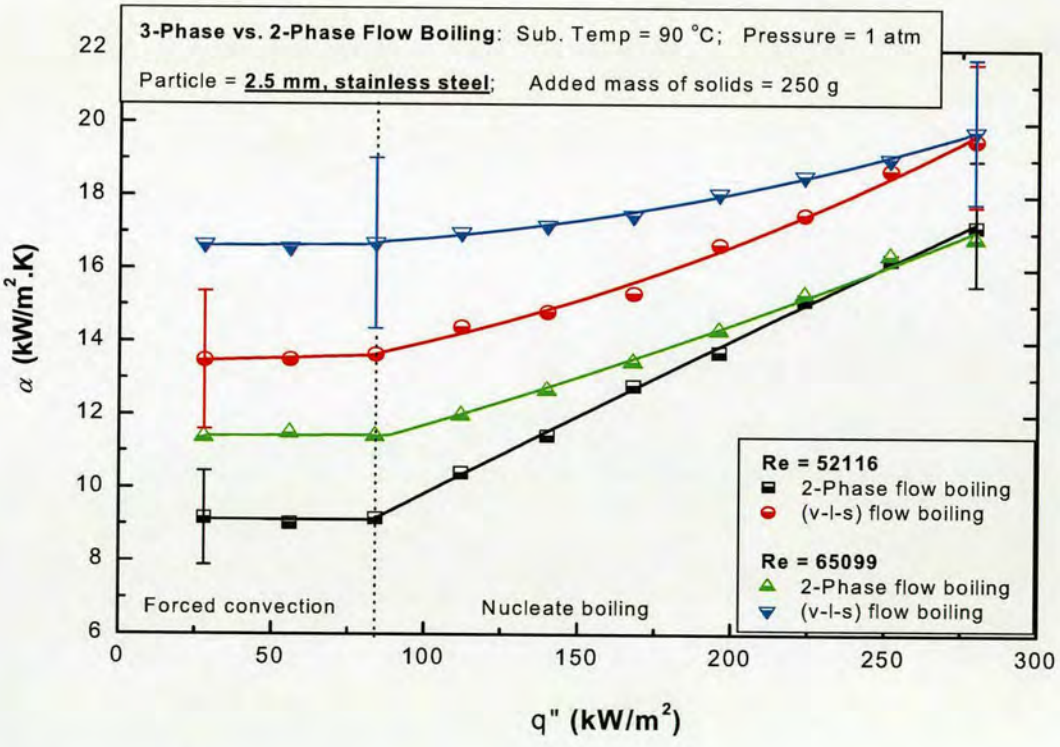

Figure 5.21: (a) Heat transfer coefficient vs. heat flux, for 3-phase and 2-phase flow boiling. Results obtained at 16 and 20 litres/min and for 2.5 mm stainless steel particles.

From the figure above, it is clear that in our boiling system, the overall rate of heat transfer is promoted by the addition of solid particles. For the presented set of test conditions, we see that compared with conventional vapour-liquid flow boiling, 3-phase flow boiling appears to

generate higher heat transfer coefficients for any given value of $q^{"}$. Meanwhile, shown in Figures 5.21(b) and 5.21(c) are the boiling curve plots corresponding to the results of three-phase and two-phase flow boiling, for the test conditions *Re* '52116' and '65099' respectively. In each case, the comparison proves that for the same heat flux setting, wall excess temperature is reduced in the presence of fluidised particles; as explained earlier, the resultant leftward shift in the boiling curve, indicates the increased rate of heat transfer encountered during three-phase flow boiling

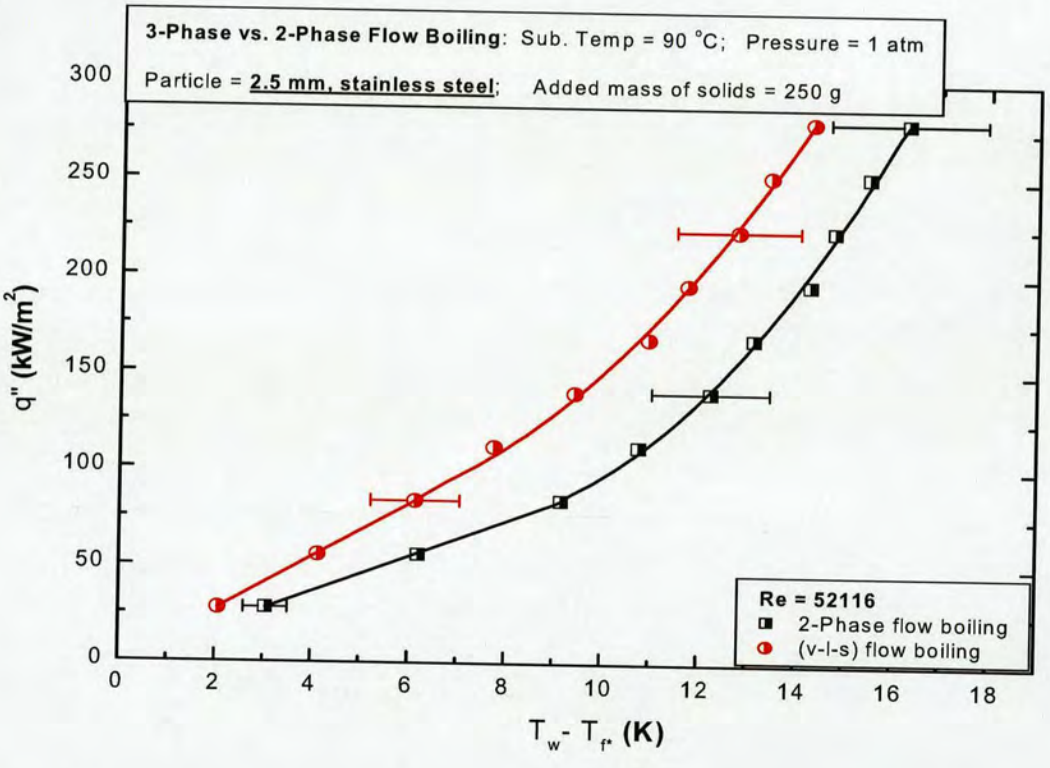

Figure 5.21: (b) Comparing the boiling curves of 3-phase and 2-phase flow boiling. Results obtained at 16 litres/min and for 2.5 mm stainless steel particles.

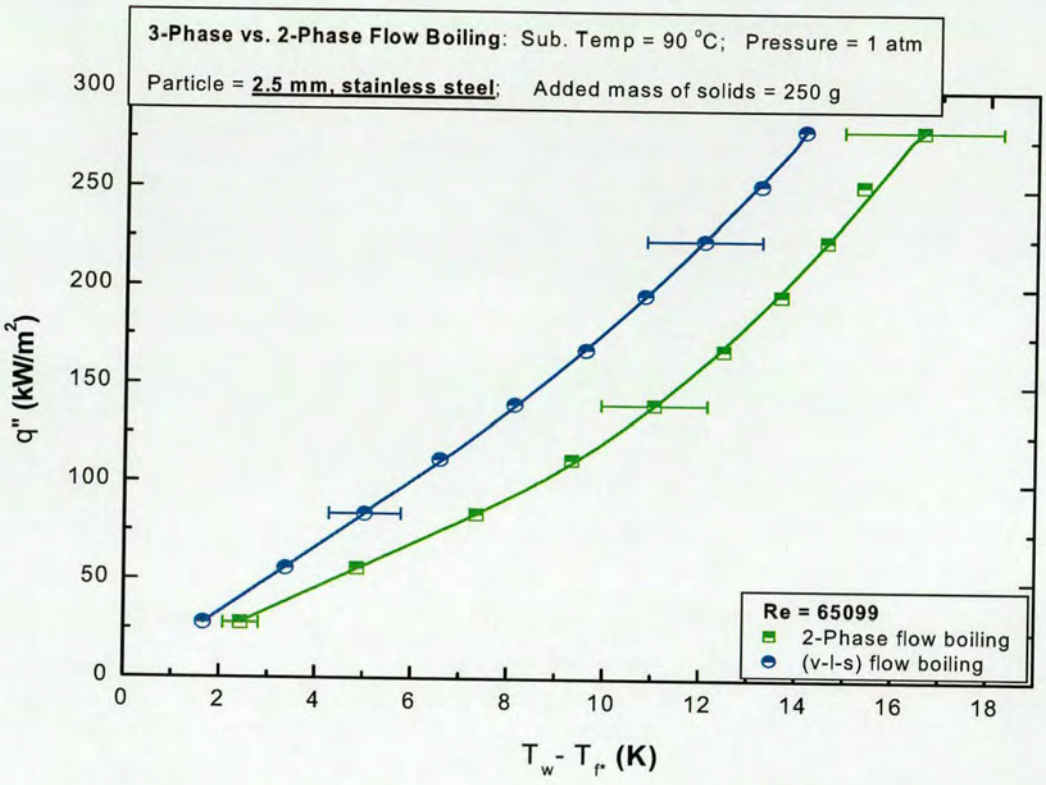

Figure 5.21: (c) Comparing the boiling curves of 3-phase and 2-phase flow boiling. Results obtained at 20 litres/min and for 2.5 mm stainless steel particles.

Emphasising the observations outlined above, for different sized particles (2.0 mm and 1.5 mm respectively), Figures 5.22(a) and 5.23(a) also show the variation of heat transfer coefficient with heat flux for the case of three-phase flow boiling and two-phase flow boiling. As with Figure 5.21(a) above, results for two different liquid velocities are presented in each case. Again, the results prove that over our range of investigated parameters, three-phase flow boiling significantly improves the measured rate of heat transfer.

In connection with Figures 5.22(a) and 5.23(a), Figures 5.22(b,c) and Figures 5.23(b,c) depict associated boiling curve comparisons. The presented results all exhibit tendencies similar to those obtained for the case of 2.5 mm diameter particles as shown in Figures 5.21(b,c).

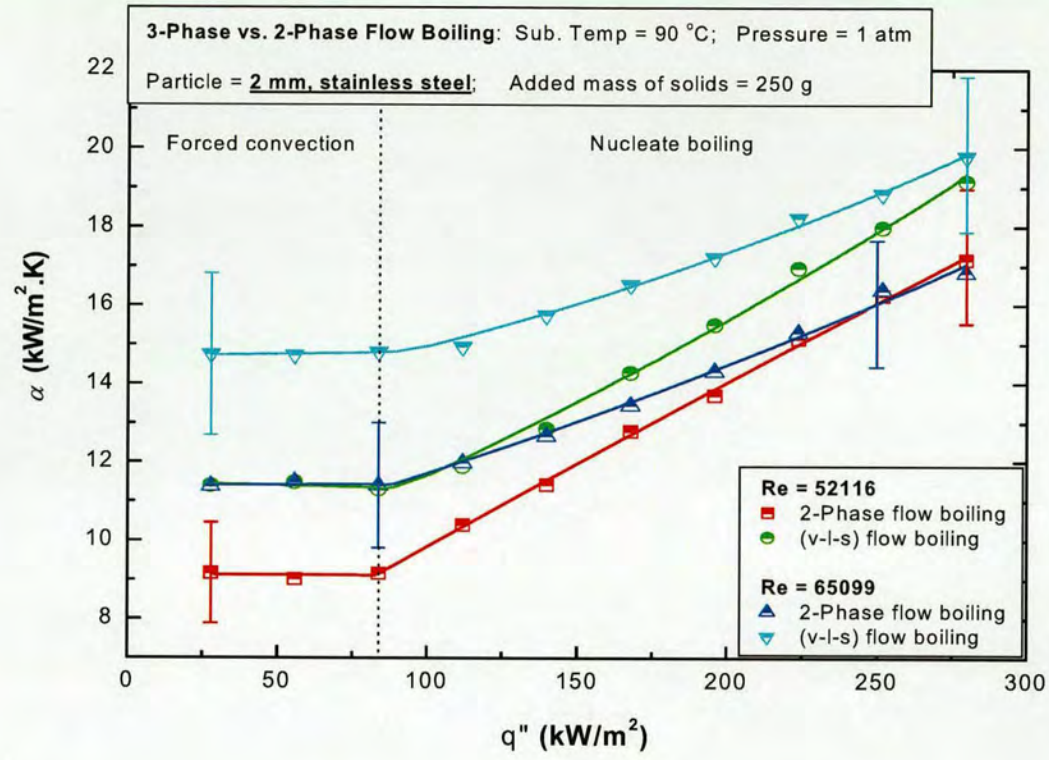

(a)

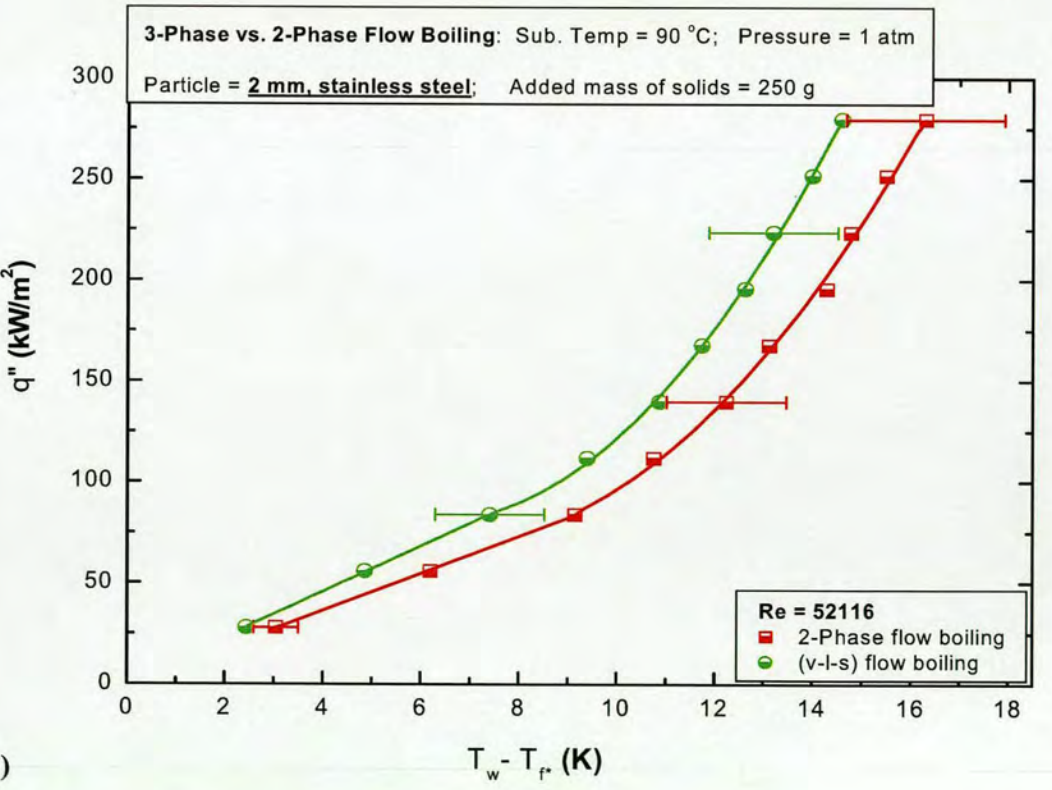

(b)

Figure 5.22: (a) Heat transfer coefficient vs. heat flux, for 3-phase and 2-phase flow boiling. Results obtained at 16 and 20 litres/min and for 2.0 mm stainless steel particles, (b) Comparing the boiling curves of 3-phase and 2-phase flow boiling. Results obtained at 16 litres/min and for 2.0 mm stainless steel particles.

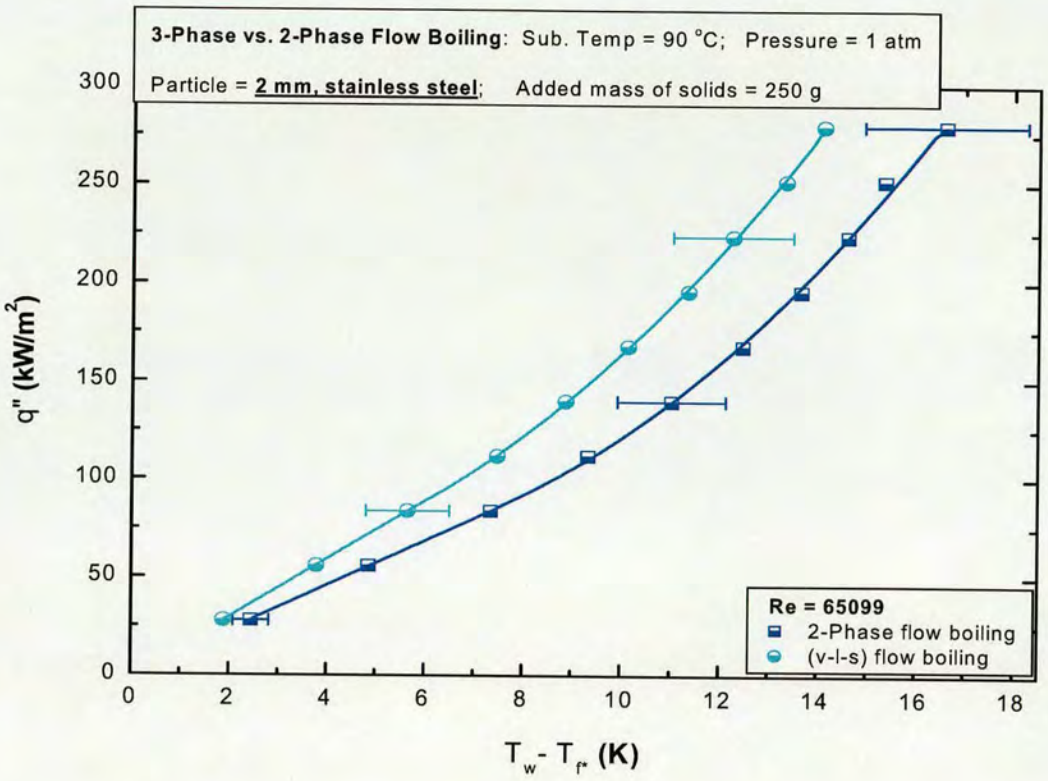

Figure 5.22: (c) Comparing the boiling curves of 3-phase and 2-phase flow boiling. Results obtained at 20 litres/min and for 2.0 mm stainless steel particles.

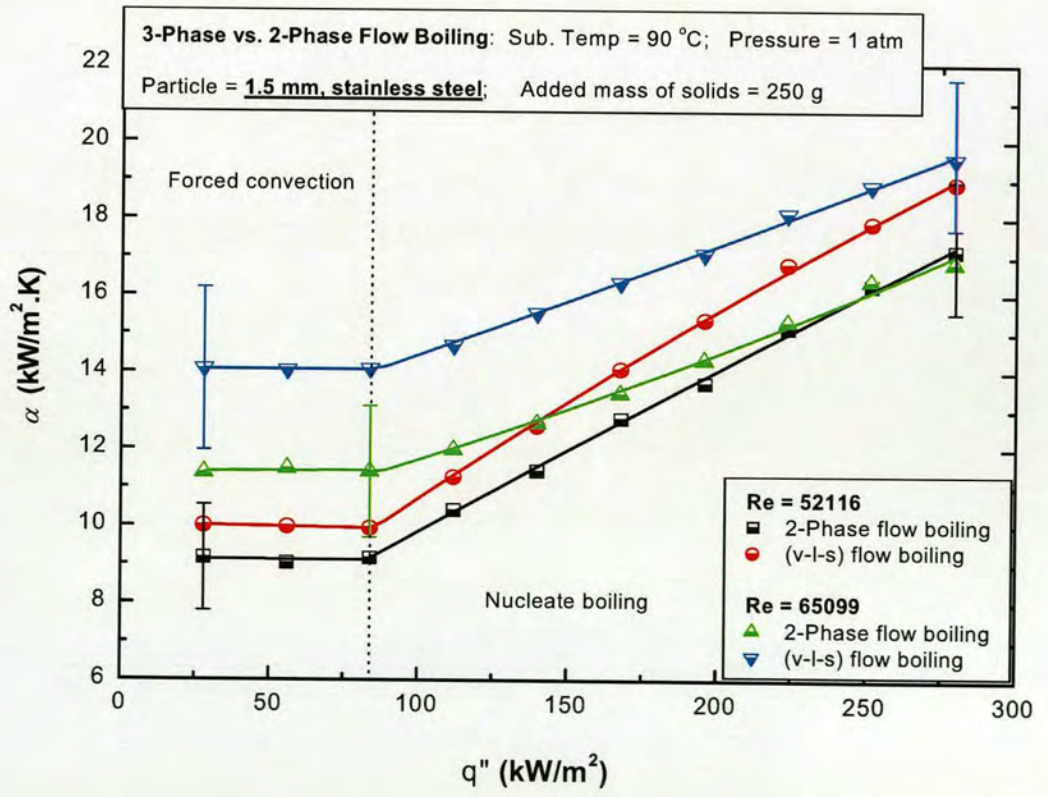

Figure 5.23: (a) Heat transfer coefficient vs. heat flux, for 3-phase and 2-phase flow boiling. Results obtained at 16 and 20 litres/min and for 1.5 mm stainless steel particles.

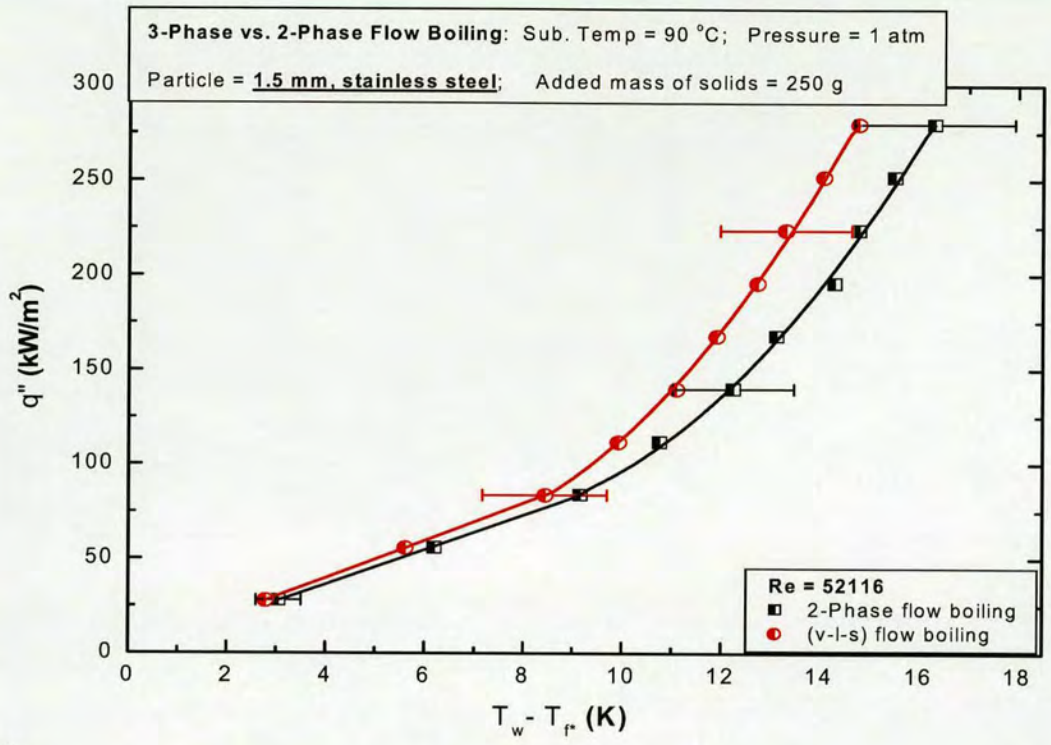

(b)

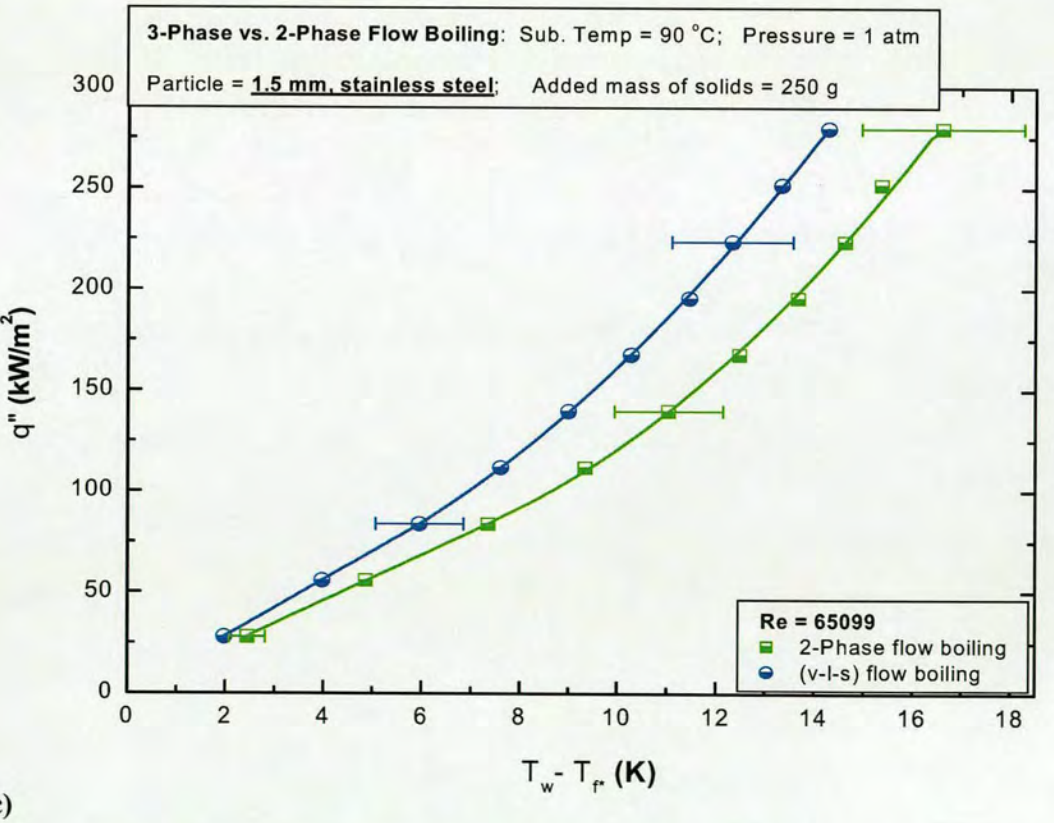

(c)

Figure 5.23: (b) Comparing the boiling curves of 3-phase and 2-phase flow boiling. Results obtained at 16 litres/min and for 1.5 mm stainless steel particles, (c) Comparing the boiling curves of 3-phase and 2-phase flow boiling. Results obtained at 20 litres/min and for 1.5 mm stainless steel particles

5.4.2. Comparing Variation of Heat Transfer Coefficient with Reynolds Number.

For forced convective boiling, Figure 5.24 contrasts the plot of heat transfer coefficient versus liquid superficial velocity for two-phase and three-phase flow boiling. As indicated on the diagram, the results for three-phase flow boiling were obtained with the use of 2.5 mm stainless steel particles. Also (recalling subsections 5.2.2 and 5.3.2), during forced convective boiling, the rate of heat transfer is a function of velocity and effectively independent of heat flux; this is a feature common to both two-phase and three-phase flow boiling. Hence, in light of these considerations, the comparison presented in Figure 5.24 has only been done for one examined value of $q^{"}$.

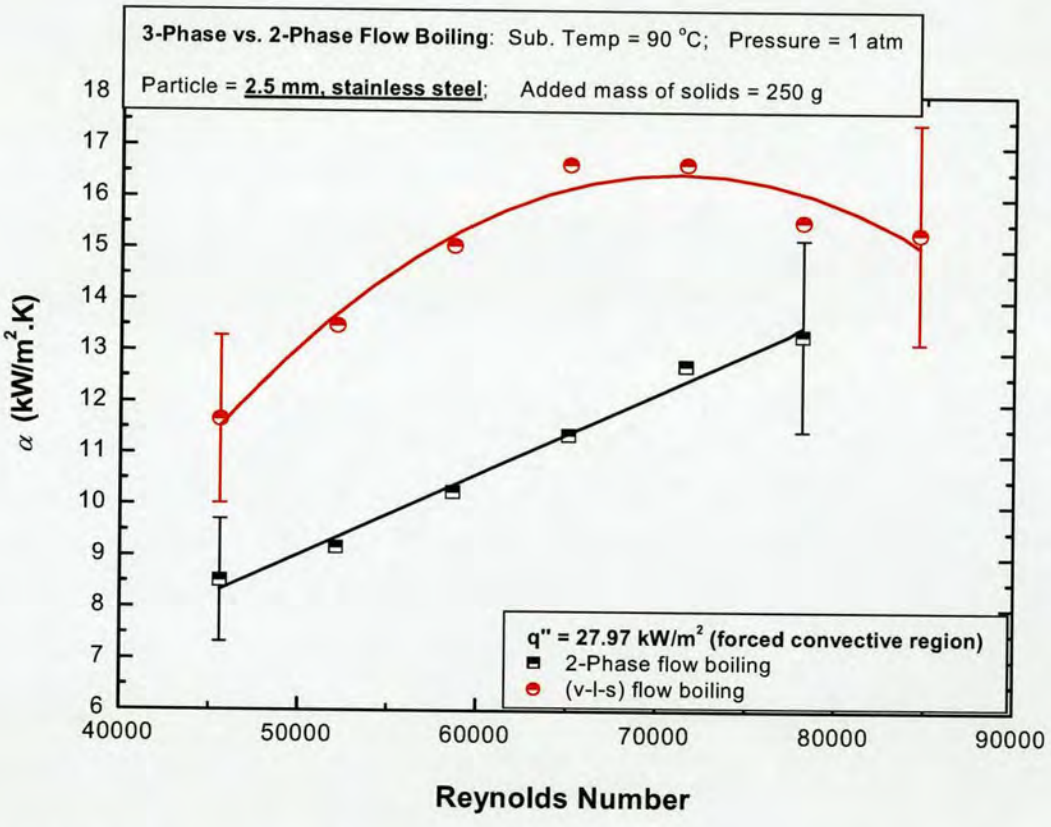

Figure 5.24: Heat transfer coefficient vs. Reynolds number, for 3-phase and 2-phase flow boiling. Results obtained at 27.97 kW/m^2 (single phase region) and 2.5 mm stainless steel particles used as solid phase.

In the diagram above, aside from the visible enhancement effect resultant from the inclusion of solid particles, we clearly see that whilst the rate of heat transfer increases linearly with velocity in the case of two-phase flow boiling (see subsection 5.2.2), in three-phase flow boiling, however, the heat transfer coefficient-velocity dependency describes a more parabola-like plot, being shown to increase to a maximum before declining for progressively

higher flowrates (see subsection 5.3.2). The dissimilar nature of these plots, suggest that the processes governing conventional forced convective heat transfer, are different from those associated with three-phase flow boiling. We return to this matter in due course.

In continuing, Figure 5.25 shows the heat transfer coefficient versus Reynolds number relationship for the fully developed nucleate boiling region of both two-phase and three-phase flow boiling. The comparison has been performed for the q'' values 223.8 kW/m^2 and 279.7 kW/m^2. As demonstrated below, during fully developed nucleate boiling, increasing liquid velocity has no effect on the rate of heat transfer in either two-phase or three-phase flow boiling. Results suggest that for both boiling modes, the nucleate boiling heat transfer coefficient is a function of the heat flux only (see subsections 5.2.1 and 5.3.1). Nevertheless, in this high heat flux region, despite the similar heat flux and liquid velocity tendencies, compared with conventional vapour-liquid flow boiling, three-phase flow boiling still yields higher boiling coefficients at all examined flowrates.

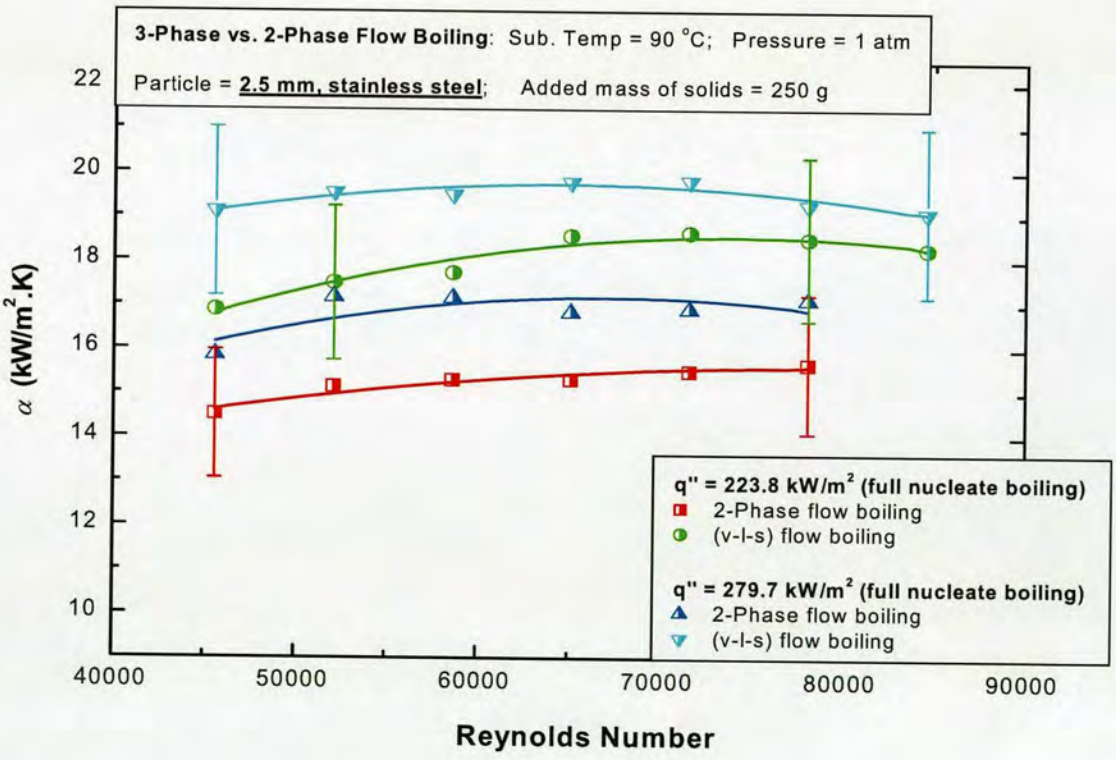

Figure 5.25: Heat transfer coefficient vs. Reynolds number, for 3-phase and 2-phase flow boiling. Results obtained at 223.8 kW/m^2 and 279.7 kW/m^2; 2.5 mm stainless steel particles used as solid phase.

5.4.3. THE HEAT TRANSFER ENHANCEMENT PERCENTAGE, $\alpha_{E.T}$ (%)

Thus far, our presented results have proven the enhancement of boiling coefficients in the presence of fluidised particles. However, our observations also indicate that the *magnitude* of the attainable heat transfer enhancement varies across our examined parametric range. Therefore, quantifying the particle induced enhancement would allow us to characterise its behaviour with respect to the influence of operating parameters. By doing so, it is then possible to accurately identify the limits of heat transfer enhancement in our three-phase boiling device. Moreover, the exercise would provide an invaluable source of information, thus improving our ability to comprehend the mechanisms involved in three-phase boiling enhancement.

Hence, for any particular set of test conditions, the heat transfer enhancement percentage, $\alpha_{E.T}$, can be simply quantified as follows:

$$\alpha_{E.T} = \frac{[\alpha_{t.f.b} - \alpha_{f.b}]}{\alpha_{f.b}} \text{ x } 100 \qquad (5.2)$$

Here $\alpha_{t.f.b}$ and $\alpha_{f.b}$ are the heat transfer coefficients for three-phase circulating fluidised bed boiling and two-phase flow boiling respectively (units of kW/m^2.K).

5.4.3.1. EFFECT OF LIQUID VELOCITY & HEAT FLUX ON HEAT TRANSFER ENHANCEMENT PERCENTAGE

Figure 5.26 illustrates the variation of the heat transfer enhancement percentage with *Re* across our examined heat flux range. Results are presented for three-phase flow boiling operations utilising 2.5 mm stainless steel particles. In general, the trend of the indicated curves, suggest that $\alpha_{E.T}$ initially increases with increasing liquid velocity. For all heat fluxes, the percentage enhancement reaches a maximum value at a certain definite superficial velocity. Further increases of superficial velocity causes a relatively abrupt degradation of the heat transfer percentage enhancement. At the upper end of our investigated flow range, all curves (for the different heat fluxes) decline towards a minimum $\alpha_{E.T}$ value. It is also worth noting that at the highest heat flux setting ($q^{"}$ = 279.7 kW/m^2), the slope of the $\alpha_{E.T}$ vs. *Re* curve flattens out almost completely, suggesting that for higher values of $q^{"}$, velocity has very little effect on the magnitude of the achievable heat transfer enhancement .

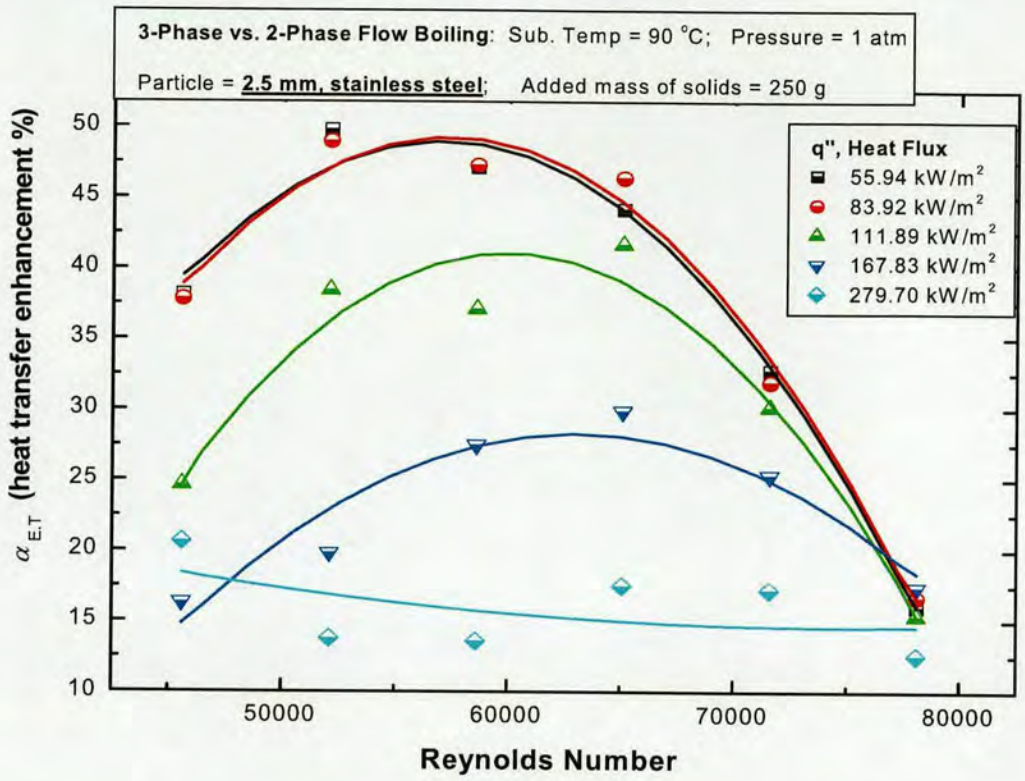

Figure 5.26: Variation of heat transfer enhancement percentage with Reynolds number, for a range of examined heat fluxes. 2.5 mm stainless steel particles used as solid phase.

With regards to the effect of heat flux Figure 5.26 also shows that for all liquid velocities, the calculated enhancement is higher in the single phase region (on graph, $q^{"} = 55.94$ kW/m^2 and 83.92 kW/m^2) than in the nucleate boiling regime (on graph, $q^{"} =$ 111.89 kW/m^2, 167.83 kW/m^2 and 279.7 kW/m^2). Furthermore, for any given value of *Re*, the enhancement percentage appears to remain constant during forced convective boiling. This stems from the fact that neither the three-phase coefficient, $\alpha_{t.f.b}$, nor the two-phase coefficient, $\alpha_{f.b}$, display any heat flux dependencies whilst in the single phase region (see subsections 5.2.2 and 5.3.2). Therefore, in light of equation 5.2 above, it is to be expected that for any given liquid velocity, the calculated heat transfer enhancement percentage should be found as being uniform throughout the lower heat flux region.

Beyond the onset of nucleate flow boiling ($q^{"}_{OFB} \geq$ 83.92 kW/m^2), increasing heat flux generally results in the continued reduction of $\alpha_{E.T}$ for the same superficial velocity. For instance: at an *Re* value of '58631', the heat transfer enhancement percentage drops successively from 47.12 % to 37.12 % to 13.61%, corresponding to heat flux increases from 55.94 kW/m^2 to 111.89 kW/m^2 to 279.7 kW/m^2. Hence, it can be said that throughout the examined liquid velocity range, minimum heat transfer enhancement is experienced at higher $q^{"}$ values, whilst maximum heat transfer enhancement is experienced at lower $q^{"}$ values.

By re-plotting the results of Figure 5.26 as a function of heat flux, we generate the graph shown in Figure 5.27 below. Here we observe the variation of the heat transfer enhancement percentage with heat flux across a range of liquid superficial velocities. The plot provides a good illustration of the heat flux characteristics as described above.

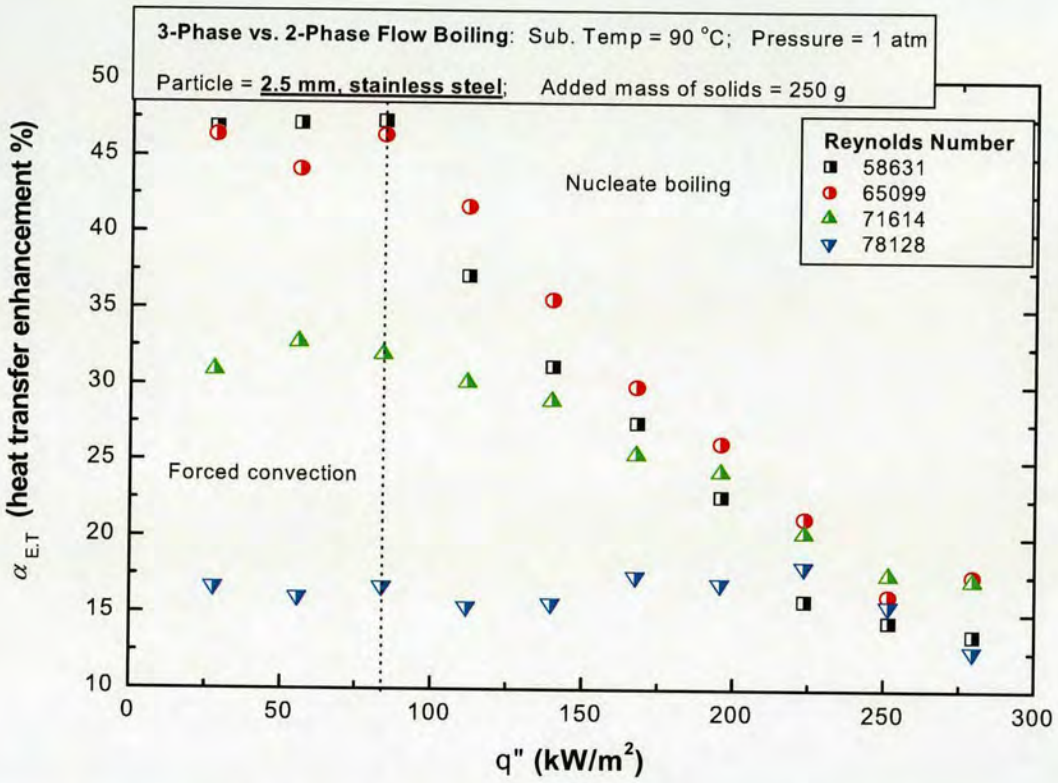

Figure 5.27: Variation of heat transfer enhancement percentage with heat flux, for a range of examined liquid flow rates. 2.5 mm stainless steel particles used as solid phase.

Overall, we see that in the forced convective region, $\alpha_{E.T}$ is almost constant for increasing heat flux; however, advancing into the nucleate boiling region, the value of the coefficient diminishes rapidly, approaching a minimum at the upper heat flux range. This holds true for all investigated liquid flowrates, emphasising the heat flux enhancement limits identified above. Furthermore, some velocity effects are also discernible. For instance, in the low heat flux region, whilst $\alpha_{E.T}$ is undoubtedly independent of heat flux, its value is , however, influenced by liquid velocity. On the other hand, crossing into the nucleate boiling region, in addition to declining enhancement with increasing heat flux, the plots of $\alpha_{E.T}$ vs. $q^{"}$ also begin to converge for successive increases in heat flux. The plots effectively merge at around $q^{"} = 250$ kW/m^2, emphasising velocities decreasing influence on $\alpha_{E.T}$ during fully developed nucleate boiling. We return to examine the effect of liquid superficial velocity in subsection

5.4.3.2 following. For now however, in respect of the heat transfer enhancement boundaries, we can state that across our entire heat flux range, minimum enhancement occurs at maximum velocity (on graph, *Re* '78128'); conversely, we see that for any given value of q'', maximum enhancement is synonymous with low to mid-range values of *Re* (on graph, *Re*'58631' and '65099').

For the purpose of clarity, these relationships are unified in Figures 5.28(a,b) below. The diagrams present 3-Dimensional plots, graphically illustrating the heat transfer enhancement limits as described above. In Figure 5.28(a), velocity – expressed as a function of Reynolds number – is plotted on the y-axis, whilst heat flux is plotted on the x-axis. In defining the limits of boiling enhancement, highlighted in both diagrams, Figure 5.28(a) considers *Re* the fixed/held parameter and heat flux the adjusted variable. Conversely, in Figure 5.28(b) the x-axis represents Reynolds number, whilst the y-axis represents heat flux; again in defining the limits of boiling enhancement, Figure 5.28(b) is presented with q'' considered the fixed parameter, and liquid velocity the adjusted parameter. By default, in both Figures 5.28(a,b) the heat transfer enhancement percentage, $\alpha_{E.T}$, is plotted on the z-axis. In addition, it is worth noting that in both diagrams, the results of $\alpha_{E.T}$ vs. q'' and $\alpha_{E.T}$ vs. *Re* are plotted with point-to-point linear fits, thereby giving rise to the angular 3-dimensional structures depicted.

Admittedly, with respect to consistency, this differs from the graphing techniques utilised in Figure 5.26 (for $\alpha_{E.T}$ vs. *Re*) and Figure 5.27 (for $\alpha_{E.T}$ vs. q''). For instance, considering the variation of heat transfer enhancement percentage with Reynolds number, in Figure 5.26 all data points are plotted with a second-order polynomial fit, thus creating the continuous curve patterns shown. Unlike Figures 5.28(a,b), where maximum and minimum enhancement coefficients have been identified at specific values of *Re*, Figure 5.26 effectively suggests the boundary of maximum heat transfer enhancement over a range of *Re* values. Example: for an imposed heat flux of 83.92 kW/m^2, we see that in Figure 5.26, the crest of the $\alpha_{E.T}$ vs. *Re* curve occurs in-between the data points located at *Re* '52116' and *Re* '65099'; this implies that optimal heat transfer enhancement (approximated to a value of $\alpha_{E.T} = 49$ %) exist within the said range of *Re* values. On the other hand, in the 3-D plot of Figure 5.28(a), for the same test conditions, we see that the point-to-point linear fit peaks at *Re* '52116', signalling a maximum enhancement percentage equal to 50 %. Unlike the curve plot of the former, the specificity of the latter does not recognise the inevitable role of measurement error. Unfortunately, the mathematical software necessary for plotting smooth surfaced 3-D structures (MATHEMATICA) was not readily available at the time of thesis submission. However, with regards to the characteristics of the enhancement percentage, none of this

interferes with the underlying validity of the claims articulated above. For instance, irrespective of the plotting technique employed, the essential point emphasised by both Figures 5.26 and 5.28(a), is that for our examined heat flux range, the plots of $\alpha_{E.T}$ vs. *Re* all reflect an overall rising and falling trend, with maximum heat transfer enhancement generally encountered at lower liquid velocities and minimum enhancement at higher liquid velocities. Similarly, across our stipulated flow range, Figures 5.27 and 5.28(b) both display the overall trend of the heat transfer enhancement percentage vs. heat flux relationship described above, i.e. for any selected liquid velocity, the enhancement percentage is at a maximum and remains roughly constant during forced convective boiling, but drops precipitously to a minimum as nucleate boiling develops.

Therefore, although not acute, such matters should be borne in mind when assessing any of the presented 3-D images.

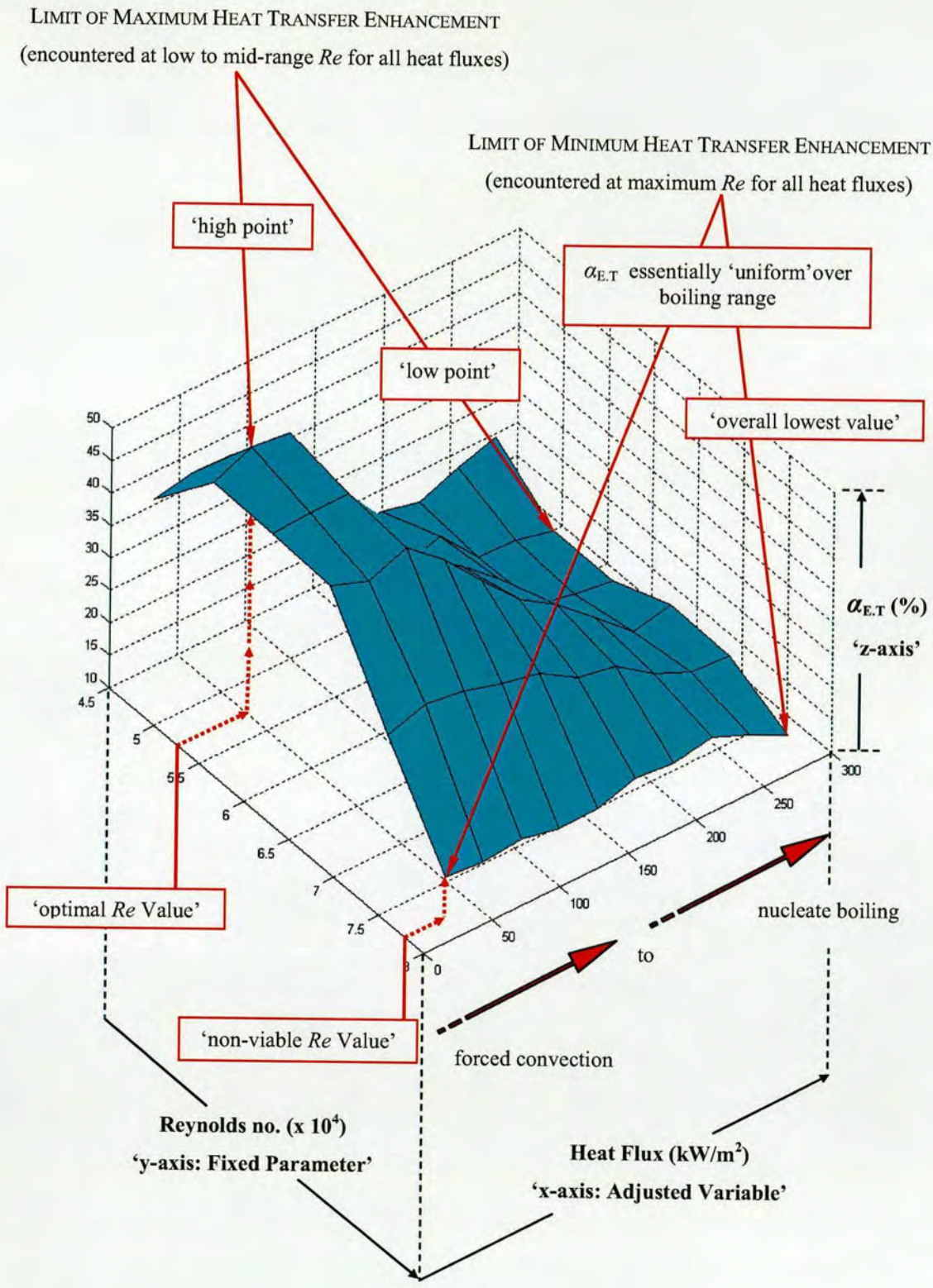

Figure 5.28: (a) 3-D plot showing boiling enhancement limits for 2.5 mm diameter particles. Notation based on *Re* as the fixed parameter and heat flux the adjusted variable.

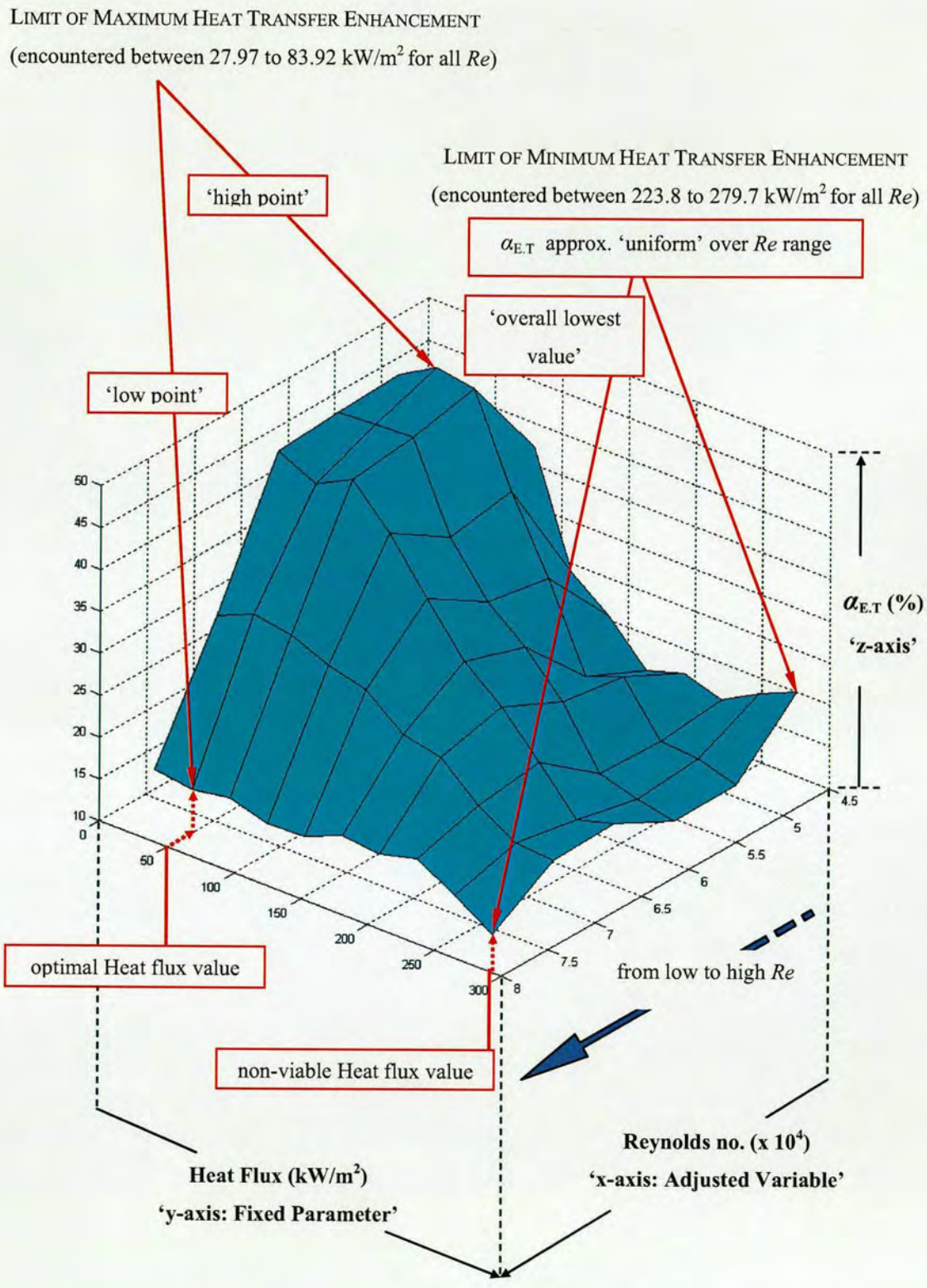

Figure 5.28: (b) 3-D plot showing boiling enhancement limits for 2.5 mm diameter particles. Notation based on heat flux as the fixed parameter and *Re* the adjusted variable.

5.4.3.2. EFFECT OF PARTICLE SIZE ON HEAT TRANSFER ENHANCEMENT PERCENTAGE

Over the course of our investigations, aside from the variables liquid velocity and heat flux, the influence of particle size has also been explored. Hence, by contrasting the experimental results according to particle diameter, it is then possible to establish the enhancement coefficient's functional dependence on d_p.

To this regard, Figures 5.29(a,b,c) each show the effect of particle size on the variation of heat transfer enhancement percentage with heat flux. Results are presented for three different liquid flowrates; Figure 5.29(a) for *Re* '52116', Figure 5.29(b) for *Re* '58631' and Figure 5.29(c) for *Re* '65099'. In each figure, what is immediately apparent is that the trend of the $\alpha_{E.T}$ vs. q'' plot is roughly consistent throughout the examined size range. As with Figure 5.27 above, the results for 2.0 mm diameter particles show a constant $\alpha_{E.T}$ during forced convective boiling, followed by the deterioration of the coefficient in the nucleate boiling region. The plots for the 1.5 mm diameter particles reflect an approximately similar pattern, although in the lower flowrate region, it does appear that $\alpha_{E.T}$ remains fairly uniform throughout the boiling range; at this particle diameter (i.e. 1.5 mm), nucleate boiling deterioration of $\alpha_{E.T}$ is only really distinguishable at the higher liquid velocity shown in Figure 5.29(c).

Concerning the influence of increasing particle size on the magnitude of $\alpha_{E.T}$, Figures 5.29(a,b,c) show that, overall, the use of larger diameter particles *benefits* the calculated heat transfer enhancement percentage. Again this is an expected result, given the fact that the three-phase flow boiling coefficient, $\alpha_{t.f.b}$, has been shown to be a function of d_p (recall subsection 5.3.3). Therefore, with larger particle diameters corresponding to higher values of $\alpha_{t.f.b}$, and $\alpha_{f.b}$ remaining constant, equation 5.2 invariably yields increased values of $\alpha_{E.T}$ for concomitant increases in particle size. However, one must stress the fact that the observation only really applies to the forced convective boiling region, for the plots also reveal that beyond the onset of nucleate flow boiling, as the heat flux is incrementally imposed, the benefit of increased particle diameter is, in turn, steadily eradicated.

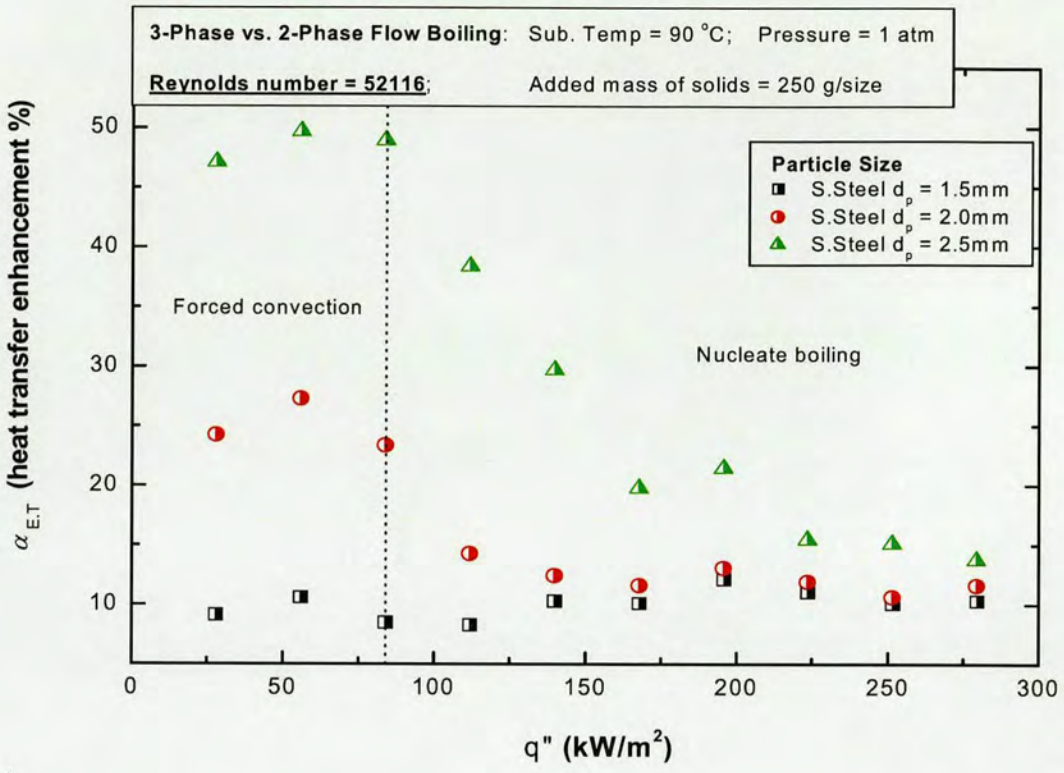

(a)

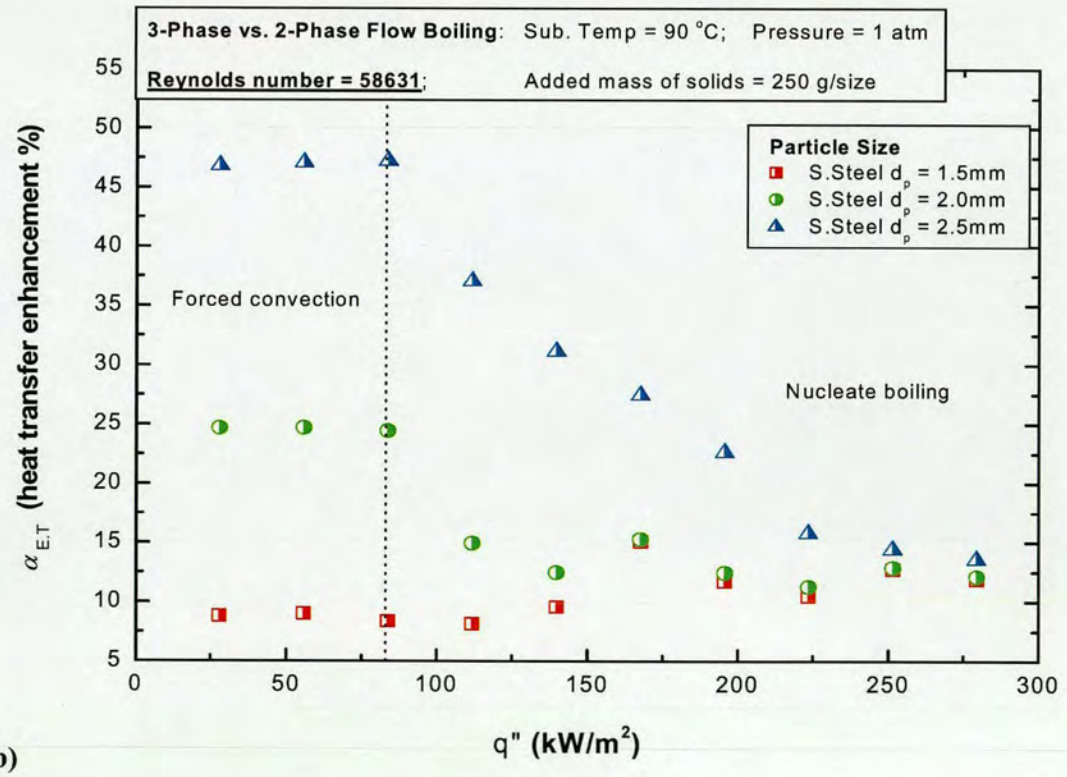

(b)

Figure 5.29: (a) Effect of particle size on variation of heat transfer enhancement percentage with heat flux for *Re* '52116', (b) Effect of particle size on variation of heat transfer enhancement percentage with heat flux for *Re* '58631'.

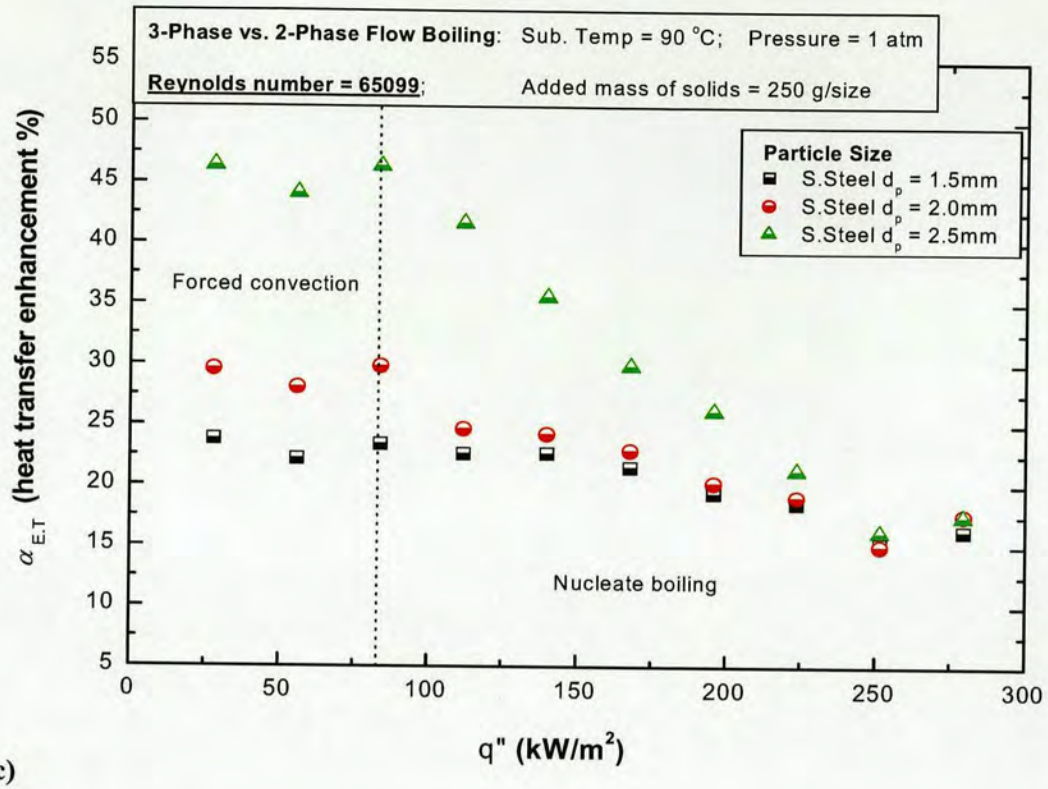

(c)

Figure 5.29: (c) Effect of particle size on variation of heat transfer enhancement percentage with heat flux for *Re* '65099'

In each instance - referring to Figures 5.29(a,b,c) - we see that in the upper heat flux range, all curves converge and increasing particle diameter has little to no effect on the value of the calculated heat transfer enhancement percentage. Table 5.1 offers a snapshot of the behaviour occurring at *Re* '65099' as shown in Figure 5.29(c) above.

Heat Flux (kW/m^2)	**2.5 mm** (d_p) $\alpha_{E.T}$ (%)	**2.0 mm** (d_p) $\alpha_{E.T}$ (%)	**1.5 mm** (d_p) $\alpha_{E.T}$ (%)	**Benefit A** $\alpha_{E.T}$ (%)	**Benefit B** $\alpha_{E.T}$ (%)
55.94	44.14	28.12	22.18	16.02	5.94
111.89	41.70	24.70	22.62	17	2.08
167.83	29.89	22.94	21.50	6.95	1.44
223.80	21.28	19.10	18.53	2.18	0.57
	SECTION (1)			**SECTION (2)**	

Table 5.1: Enhancement comparison chart, adapted from Figure 5.29(c) for *Re* '65099'

In the table above, section (1) demonstrates that at low heat flux, $q^{"}$ = 55.94 kW/m^2, increasing particle size generates higher values of $\alpha_{E.T}$. Nevertheless, as heat flux increases

(descending the individual columns) not only does the magnitude of $\alpha_{E.T}$ decline, but the improvement to the enhancement coefficient resultant from the increase in particle diameter also dissipates. For instance, in the first row of values we see increases in $\alpha_{E.T}$ from 22.18 % to 28.12 % to 44.14 %, representative of diameter increases from 1.5 mm to 2.0 mm to 2.5 mm. However, as we approach fully developed nucleate boiling, the values of the enhancement coefficient start to become more uniform, finally converging at $\alpha_{E.T} \approx 20$ % for a heat flux setting of 223.80 kW/m^2. This simply reflects the activity, or lack of, occurring in the three-phase flow boiling mode. As explained in subsection 5.3.3 earlier, although increasing particle size augments the three-phase boiling coefficient whilst in the forced convective region, in the nucleate boiling region, however, our results show that for any given value of *Re*, the benefit to the three-phase coefficient, $\alpha_{t.f.b}$, steadily disappears as we approach the uppermost heat flux region. Recall Figures 5.19(a) and 5.20(a), where we see the plots of $\alpha_{t.f.b}$ vs q'' for the different sized particles virtually merging at maximum heat flux; the implication being that during fully developed nucleate boiling, the three-phase flow boiling coefficient is a function of the heat flux but not the size of particle. Therefore, in the higher heat flux region, with the measured values of $\alpha_{t.f.b}$ becoming more consistent over our examined size range, the benefit of a larger particle diameter on the magnitude of the attainable heat transfer enhancement is also diminished, based on the fact that equation 5.2 yields similar $\alpha_{E.T}$ values for all particle diameters, thus accounting for the curve convergence observed at all examined liquid flowrates.

Continuing with Table 5.1, the information provided in section (2) is also quite interesting. Here the categories 'Benefit A' and 'Benefit B' are defined as follows:

$$\text{Benefit A} = \alpha_{E.T}(2.5 \text{ mm diameter}) - \alpha_{E.T}(2.0 \text{ mm diameter}) \tag{5.3}$$

$$\text{Benefit B} = \alpha_{E.T}(2.0 \text{ mm diameter}) - \alpha_{E.T}(1.5 \text{ mm diameter}) \tag{5.4}$$

For the same size interval ($\Delta d_p = 0.5$ mm) the increase of particle diameter from 2.0 mm to 2.5 mm provides an enhancement benefit much more substantial than that experienced for the increase from 1.5 mm to 2.0 mm. For example, at $q'' = 111.89$ kW/m^2, a diameter increase from 1.5 mm to 2.0 mm yields an enhancement benefit equal to 2.08 %, on the other hand, for the same set of test conditions, a diameter increase from 2.0 mm to 2.5 mm produces an enhancement benefit equal to 17 %. Figure 5.29(a) and 5.29(b) exhibit similar tendencies. However, as well as particle size, a broader range of size intervals would have to be investigated in order to substantiate the observed phenomena.

Returning to the general influence of particle size on the percentage heat transfer enhancement, Figures 5.30(a,b,c,d) each show the effect of d_p on the variation of heat transfer enhancement percentage with Reynolds number. Results are presented for four different heat flux settings. Looking at the series of diagrams as a whole, we see that for any given liquid velocity, the effect of increasing particle diameter can be discerned for q'' values in the low to mid-heat flux range (Figures 5.30(a,b) for q'' = 55.94 kW/m^2 and 111.89 kW/m^2 respectively) but is almost non-existent for higher heat flux settings (Figures 5.30(c,d) for q'' = 251.70 kW/m^2 and 279.70 kW/m^2 respectively). At the same time, it is quite clear that for all examined liquid velocities, where present (i.e. at lower heat fluxes), the heat transfer enhancement benefit is more pronounced for diameter increases from 2.0 mm to 2.5 mm, as opposed to 1.5 mm to 2.0 mm. In such regards, the presented results support the observations detailed above. Furthermore, for each size of particle, Figures 5.30(a,b,c,d) captures the changing and decreasing dependency of $\alpha_{E.T}$ on liquid flowrate. In the low to mid-heat flux region, Figure 5.30(a) and 5.30(b), we see that for all particles, the variation of $\alpha_{E.T}$ with Re describes the now familiar parabola-like curve: initial increase to a maximum, followed by rapid decrease to a minimum at highest Re

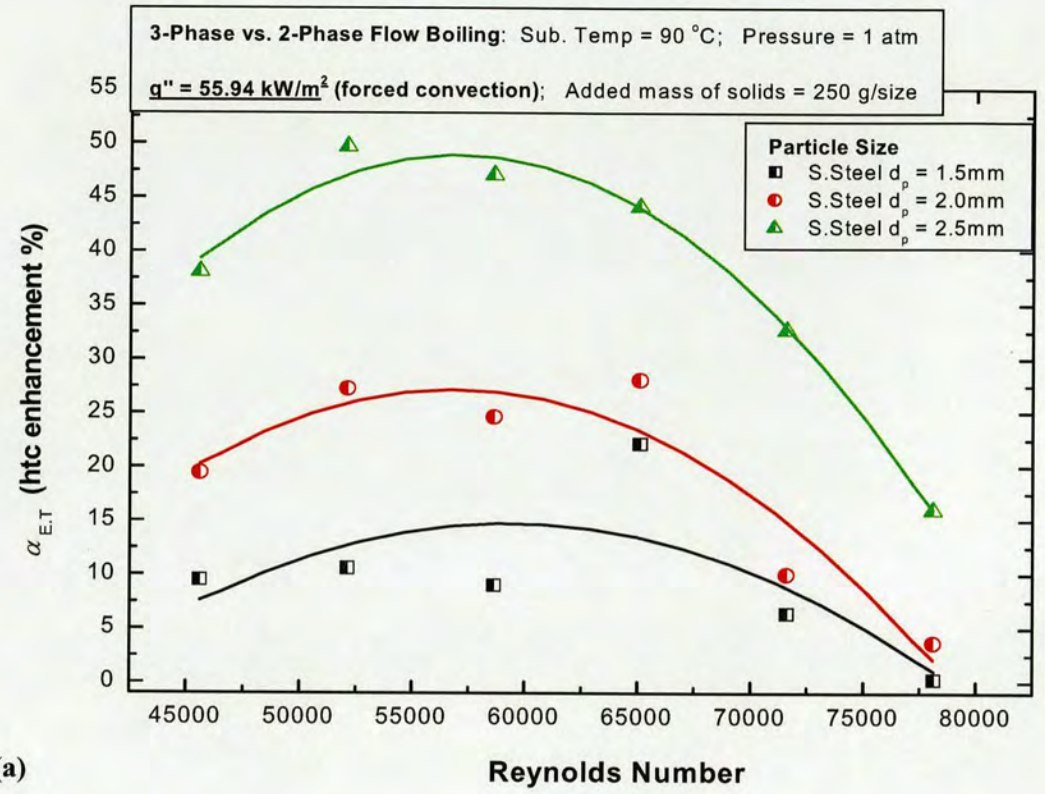

(a)

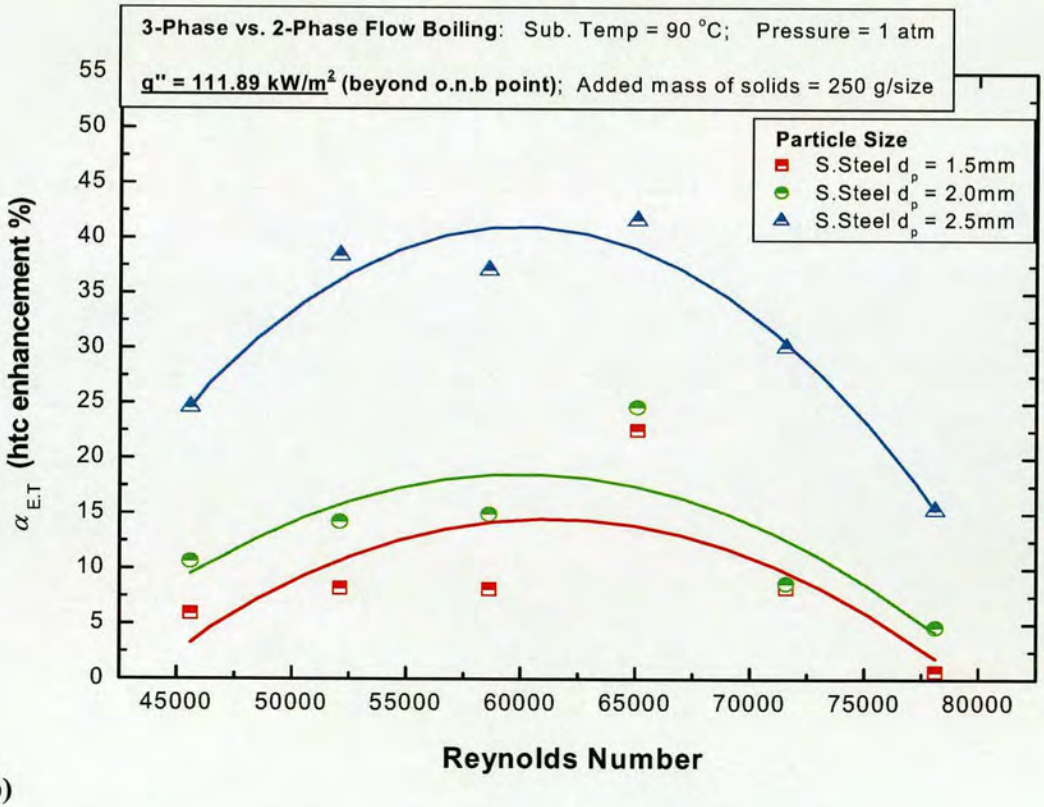

(b)

Figure 5.30: (a) Effect of particle size on variation of heat transfer enhancement percentage with *Re*. Heat flux = 55.94 kW/m^2, (b) Effect of particle size on variation of heat transfer enhancement percentage with *Re*. Heat flux = 111.89 kW/m^2.

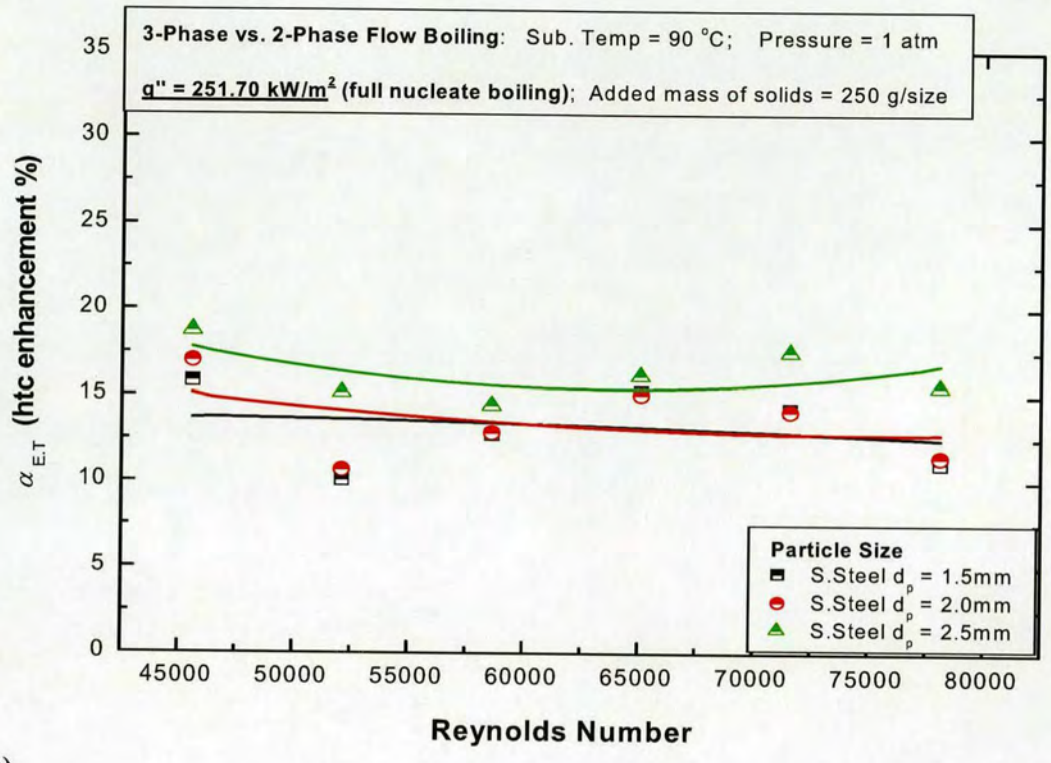

(c)

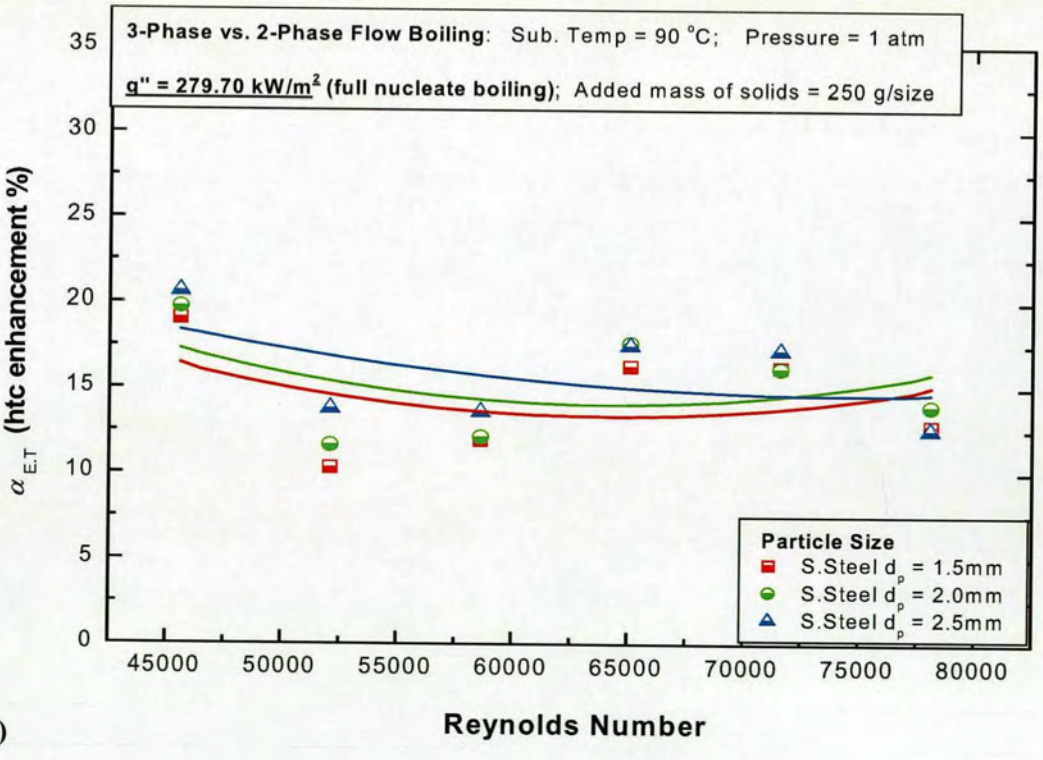

(d)

Figure 5.30: (c) Effect of particle size on variation of heat transfer enhancement percentage with *Re*. Heat flux = 251.70 kW/m^2, (d) Effect of particle size on variation of heat transfer enhancement percentage with *Re*. Heat flux = 279.70 kW/m^2.

In addition to the above, the plots also indicate that higher liquid velocity does not only degrade the attainable heat transfer enhancement percentage (as demonstrated in subsection 5.4.3.1) but like the effect of a high heat flux, it also suppresses the enhancement benefit resultant from increasing particle size. The suppression is more noticeable between the diameters 2.0 mm and 1.5 mm. Adapted from Figure 5.30(a) and Figure 5.30(b), Table 5.2 performs a similar exercise as Table 5.1 above

Heat Flux (kW/m^2)	***Re*** (dimensionless)	**2.5 mm** (d_p)	**2.0 mm** (d_p)	**1.5 mm** (d_p)	**Benefit A**	**Benefit B**
		$\alpha_{E.T}$ (%)	$\alpha_{E.T}$ (%)	$\alpha_{E.T}$ (%)	$\alpha_{E.T}$ (%)	$\alpha_{E.T}$ (%)
55.94	60000	47.84	26.32	14.66	21.52	11.66
	70000	38.13	18.88	11.04	19.25	7.84
	75000	24.24	8.37	4.05	15.87	4.32
111.89	60000	41.02	18.57	14.54	22.45	4.03
	70000	34.70	15.01	11.84	19.69	3.17
	75000	23.09	8.44	5.85	14.65	2.59
			SECTION (1)		**SECTION (2)**	

Table 5.2: Enhancement chart, adapted from Figures 5.30(a,b) for $q^{"} = 55.94$ kW/m^2 and $q^{"} = 111.89$ kW/m^2.

Focusing on section (2), Table 5.2 shows that for the selected heat flux settings, the calculated enhancements benefits 'A' and 'B' both diminish with increasing flowrate. For instance for $q^{"} = 55.94$ kW/m^2, enhancement benefit 'A' decreases from 21.52 % to 19.25 % to 15.87 %, corresponding to *Re* increases from 60000 to 70000 to 75000. Benefit 'B' better reflects the falling trend; for the same value of $q^{"}$ and similar increases in *Re*, benefit 'B' drops from 11.66 % to 7.84 % and finally culminates at 4.32 %.

Turning our attention to Figures 5.30(c) and 5.30(d), as mentioned in subsection 5.4.3.1 above, here in the high heat flux region - and especially for $q^{"} = 279.70$ kW/m^2 - as well as increasing particle size, it is quite clear that for our specified boiling system, an increase in the liquid delivery rate has no real significant effect on the achievable heat transfer enhancement during fully developed nucleate boiling. Once more this can easily be understood by recognising the fact that according to our obtained results, in the high heat flux region, neither the two-phase boiling coefficient nor the three-phase boiling coefficient are affected by

increasing liquid velocity. Hence, for any particular size of particle, the differential in equation 5.2 above (i.e. $\alpha_{t.f.b} - \alpha_{f.b}$) remains approximately constant for successive increases in liquid superficial velocity, thereby giving rise to the roughly horizontal plot(s) of $\alpha_{E.T}$ vs. *Re* as shown in Figures 5.30(c,d).

Overall, the results presented in this chapter provide a basis for further analysis of the heat transfer mechanisms governing boiling enhancement in the three-phase circulating fluidised bed.

CHAPTER 6: FLOW BOILING ENHANCEMENT – DISCUSSION OF MECHANISMS

6.1. INTRODUCTION

Thus far, by analytically comparing the findings from our 'Series-A' (two-phase) and 'Series-B'(three-phase) boiling experiments, several heat transfer enhancing and limiting effects resultant from the addition of solid particles have been identified and described. At the test section, although direct visual observation allows for a first impression of the processes occurring within the three-phase fluidised bed, realistically however, an in depth analysis to determine the heat transfer mechanisms responsible for these effects cannot not be performed by such means only. Therefore, as explained in *Chapter 4*, to gain insight into the mechanisms of three-phase boiling enhancement, the multiphase flow system has been recorded via the use of a high-speed camera equipped with a zoom lens.

In light of the above, here in *Chapter 6*, the intention is to further analyse our earlier reported trends, and in so doing, explain the prevalent heat transfer mechanisms. To accomplish this, some effects and features of the heat transfer results, presented in *Chapter 5*, are interpreted by means of the obtained visualisation results.
Continuing with the norm, we begin discussions by examining the significance of the results obtained during the control 'Series-A' test program, for the case of conventional sub-cooled flow boiling.

6.2. VERIFYING MECHANISMS OF SUB-COOLED FLOW BOILING

Sub-cooled flow boiling has long been recognised as one of the most effective heat transfer modes, receiving considerable attention in applications where highly efficient cooling is required, such as in emergency core cooling of nuclear reactors, high-electronic cooling, and cooling of rocket nozzles. A comprehensive literature review on the fundamental mechanisms and observations in two-phase flow boiling has been performed in *Chapter 2*, section 2.3.

Although a huge number of publications on the topic of sub-cooled boiling heat transfer exist, the basic knowledge of the physical mechanisms governing the boiling process is still incomplete; predictive models have been derived on semi-empirical basis or highly simplified representation of the real processes. However, this not withstanding, the results obtained from our two-phase flow boiling experiments, reveal observations consistent with the basic sub-cooled flow boiling characteristics, and sufficient for the requirements of this particular body of work.

In brief, our findings show that in the low heat flux region, the two-phase boiling coefficient is independent of heat flux but a function of liquid velocity. In this region, the heat transfer coefficient is dominated by the forced convective contribution. However, crossing into the nucleate boiling regime (where $q'' \geq q''_{OFB}$) the two-phase boiling coefficient displays a strong heat flux dependency, but becomes insensitive to fluctuating flow velocity (see section 5.2 for details concerning the results of our two-phase flow boiling investigations).

Regarding the mechanisms governing heat transfer within the high heat flux region, nucleate boiling is typically characterised by the presence of small bubbles, which grow and then rapidly collapse on, or near, the heated surface. These bubbles are responsible for the increased rate of heat transfer typically associated with sub-cooled nucleate boiling. In the past, many investigations have sought to visually examine the bubble growth and detachment processes in vertical flow boiling. The pioneering work of Gunther [15] is well known. He was the first to study the bubble behaviour during sub-cooled flow boiling using high-speed photography, and quantified successfully the bubble size, population, growth rate etc., as functions of system parameters such as pressure, heat flux and velocity. According to the author, bubble population (i.e. number of existing bubbles per unit heat transfer surface area) increases with increasing heat flux. In contrast, increase of the liquid mass flux causes a reduction in the size, and life-span, of the generated bubbles. In 1972, Abdelmessih *et al* used high-speed photography to observe bubble growth and collapse from an artificial nucleation site [214]. The researchers concluded that the increase of heat flux engenders the increase of bubble size and life-span, whereas increased liquid velocity precipitates the opposite effect. As well as the above, many other researchers have attempted to study bubble behaviour with optical high-speed techniques [215-217]. In terms of the areas of contention, the related literature is abound with various opinions regarding the effect of heat flux on bubble population and maximum bubble diameters. In this present study, based on the results of our flow visualisation investigations, it can be stated that, generally, increasing heat flux promotes the observed bubble generation frequency (which refers to the rate at which bubbles are generated from the heater surface) as well as the number of bubbles existing on the heater surface. Therefore, due to the elevated vapour levels, significant bubble coalescence was also observed, yielding larger diameter bubbles for higher values of q''. These larger sized bubbles move vigorously within the flow, thereby enhancing the boiling heat transfer coefficient as shown in results section 5.2.

Evidence of the described bubble behaviour is presented in Figures 6.1(a)-(c), which show the development of (vapour-liquid) two-phase flow boiling over a fixed length of column.

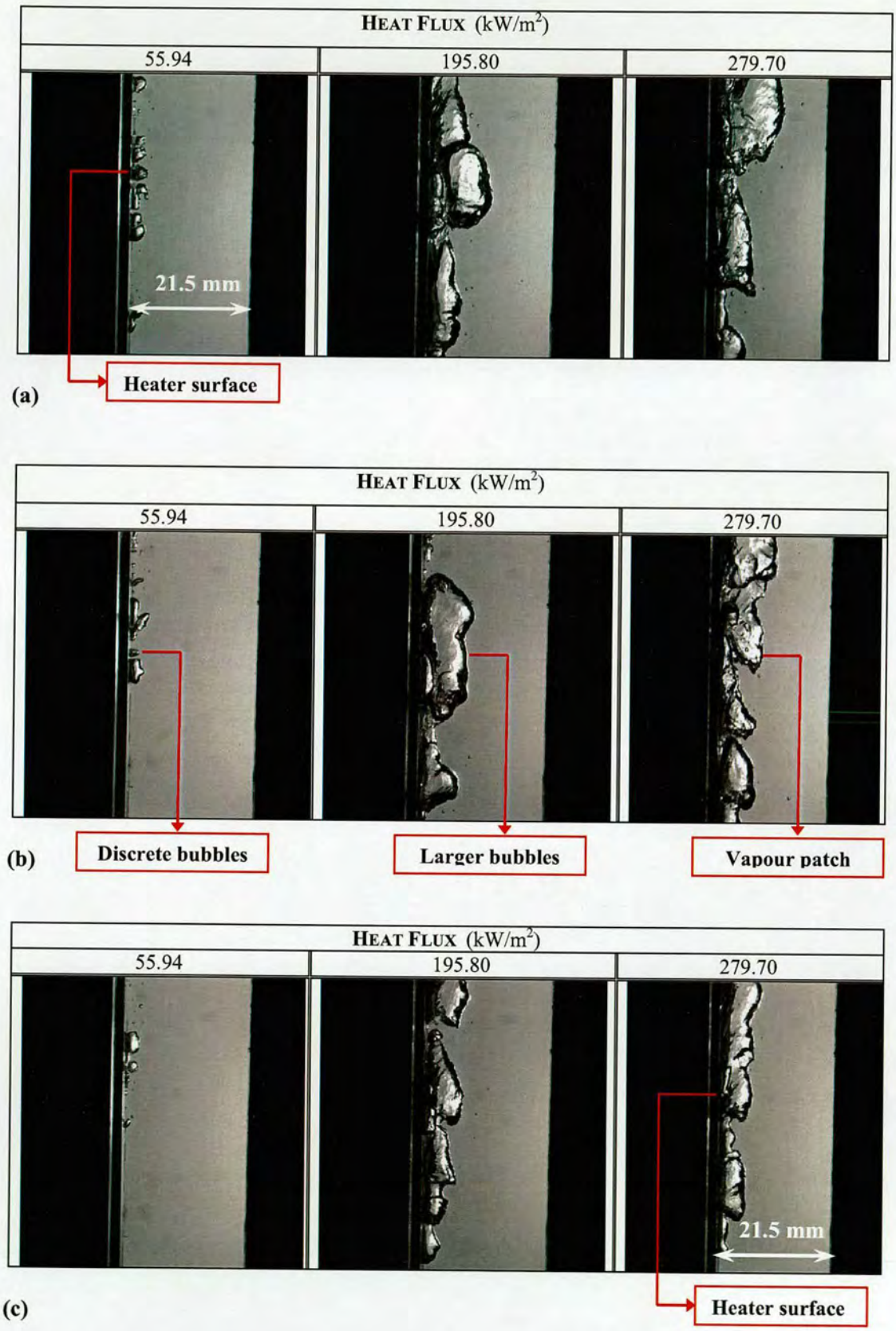

Figure 6.1: Video images depicting the development of two-phase flow boiling for a liquid subcooled temperature of 90°C. Filmed at (a) *Re* '45602' (b) *Re* '58631' and (c) *Re* '78128'.

The sequences have been filmed at three different flowrate settings, each recorded at a frame rate of 1000 fps (i.e. frames per second). The camera arrangement and applied visualisation techniques have been described in *Chapter 4*, subsection 4.5.2.

In all instances, it can be seen that in the low heat flux region ($q^{"}$ = 55.94 kW/m^2) the observed bubble population is relatively low and, where present, the vapour mainly takes the form of small , discrete bubbles, which do not change significantly in shape or size. Also typical for this region was that most of the detached bubbles remained close to the wall, eventually reattaching a few frames later. Overall, very few actually collapsed in the bulk fluid. Extending beyond the O.F.B point, the results indicate that at a higher imposed heat flux, a larger fraction of the heater surface is covered by bubbles, suggesting that more nucleation sites are being activated by the increase of heat flux. Considering the mid-heat flux range, symbolised here by $q^{"}$ = 195.80 kW/m^2, we see that prior to detachment, many of the generated bubbles merge to form larger bubbles, which then extend into the bulk fluid before eventually collapsing. As demonstrated in Figures 6.1(a) – 6.1(c), bubbles in this region are not spherical. As they merge and grow, the sliding bubbles adopt a more rhombus-like shape, whilst simultaneously becoming more elongated. Similar observations were encountered at maximum heat flux, represented here by $q^{"}$ = 279.70 kW/m^2 . However, due to the significant increase in the overall number and frequency of generated bubbles, a higher degree of bubble coalescence is typically observed during fully developed nucleate flow boiling region. As is clearly shown, vapour bubbles coalesce into large, elongated patches which travel along the heater wall. After merging, although bubble detachment does occur, a greater portion of the enlarged bubbles (or vapour patches) remain in contact with the heated surface, restricting liquid access to the immediate near wall region. Observations of different bubble behaviour, indicates that the mechanisms of heat transfer varies across our examined range of heat fluxes. While in the lower heat flux region, latent heat transport through the sliding bubbles can be considered the main heat transfer mode. Meanwhile, in the higher heat flux region, where bubble generation frequency and bubble population are both substantially increased, the overall flow boiling coefficient is augmented by the combined effects of increased bubble agitation (i.e. additional turbulent mixing) and increased latent heat transport.

Though not new or revolutionary, but by capturing the heat transfer processes involved in conventional two-phase flow boiling, the observations and mechanistic interpretations reported above, do, however, give substance to the results obtained during the reference/control 'Series-A' test program.

6.3. HEAT TRANSFER IN THREE-PHASE FLOW BOILING

6.3.1. CHARACTERISTICS OF (VAPOUR-LIQUID-SOLID) FLOW BOILING

As earlier intimated (see *Chapter 3*, subsection 3.3.4.3) for investigations involving the fluidisation of solid particles, the rate of heat transfer to/from the bed is dependent on the intensity of the interaction between the solid particles and the heater surface. This is primarily due to the fact that upon contact, as well as exchanging hydrodynamic momentum with the wall, particles moving in the upward flow stream agitate the fluid in the near wall region, giving rise to the erosion of the thermal boundary layer, which itself forms the major resistance to heat transfer. Figure 6.2 offers a sketch of the boundary layer disruption occurring in the vicinity of the heated wall.

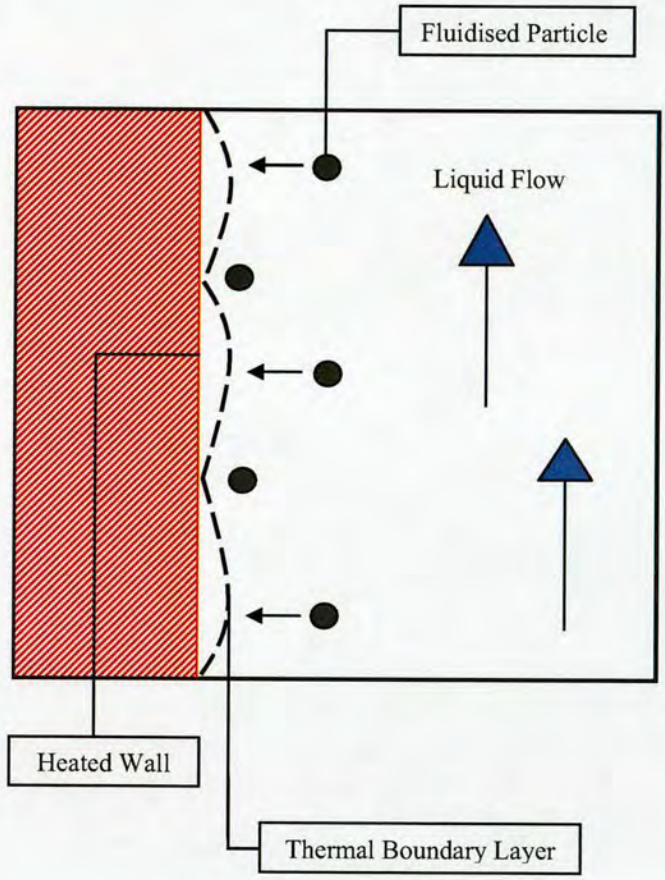

Figure 6.2: Sketch showing erosion of thermal boundary layer by the action of fluidised particles. Illustration assumes $q'' < q''_{OFB}$.

Regarding the characteristics of the three-phase heat transfer coefficient, the results of our 'Series-B' test program have unveiled some notable attributes…

Firstly, for our particular boiling system and range of examined parameters, the results shown in section 5.3, indicate that for $q^{"}$ values in the lower heat flux range, the three-phase heat transfer coefficient is a function of velocity, but independent of increasing heat flux. Presumably, this would suggest that within this boiling region (where $q^{"} < q^{"}_{OFB}$) the rate of heat transfer is mainly controlled by the mechanisms of forced convection, including the additional energy transfer and turbulent mixing brought about by the movement of the fluidised particles. However, once the appropriate conditions for the commencement of boiling have been satisfied, i.e. for $q^{"} \geq q^{"}_{OFB}$, the three-phase boiling coefficient then increases with increasing heat flux, but loses its velocity dependency. A plausible explanation for this, could be the fact that the increase of heat flux produces more active nucleation sites and elevates the vapour fraction within the bed (see section 6.2 above); the former heightens the degree of nucleate boiling, whilst the latter increases the level of turbulence in the already agitated liquid-solid flow. Taken together, these effects could account for the overall increase of the three-phase boiling coefficient with progressively increasing heat flux . In subsection 6.3.2 following, we continue discussions regarding the contribution of solid particles during nucleate boiling heat transfer.

Meanwhile, for our prescribed liquid delivery range, the curve trend described by the three-phase boiling coefficient versus Reynolds number relationship - particularly evident across the forced convective to lower mid-heat flux range - could be due to the effect of reduced particle concentration (or local solid hold-up), resultant from the general increase in bed voidage with increasing liquid velocity; perhaps combined with a flow regime change to one in which the particle motion is more ordered and nearly parallel to the walls at higher Reynolds number. This can be explained qualitatively as follows:
In the low velocity (vapour-liquid-solid) circulating fluidised bed state, the particle motion has a high degree of turbulence; as such, fluidised particles move randomly throughout the bed frequently colliding with each other and with the heat transfer surface. Hence, if the improvement in the three-phase heat transfer coefficient is truly dependent on the erosion of the boundary layer by the action of the fluidised particles, it is to be expected that the coefficient may pass through a maximum as liquid velocity is further increased. Recalling the review presented in *Chapter 3*, subsection 3.3.4, numerous studies have proven that in circulating fluidised bed systems, increasing liquid velocity is accompanied simultaneously by higher bed voidage and increased average particle speed [81]. These combined effects decrease the local solid hold-ups within the riser column, $\varepsilon^{"}_{p}$, thereby reducing the probability of particles colliding with the heater surface. Therefore, based on the widely accepted literature [73,74,81,82], after the initial rise to a threshold value, the degradation of the three-phase boiling coefficient with further increasing flowrate (as shown in results section 5.3)

must simply be a consequence of a reduced particle-wall collision frequency, typical of higher liquid velocities. As explained in subsection 3.3.4.3, the particle-wall collision frequency, f (s^{-1}), represents the number of wall collisions per unit time of any individual particle, or group(s) of selected particles, within the fluidised system [114-116].

To corroborate these claims, a series of flow visualisation studies were undertaken at the three-phase test section. In all, we sought to determine the relationship between increasing liquid delivery rate, the bed voidage and the average upward solid velocities within the riser column. It is assumed that the increase in the average solid velocities', reduces the overall residence time of the particles within the bed, and as such, increases the bed voidage (i.e. volume fraction of the fluid phase). Continuing the logic, reduced bed residence time would suggest that fluidised particles have less time to impact the heat transfer surface. Now imagine an 'isolated' particle in the flow stream; as we travel through the heated channel from this point-of-view, it can reasonably be assumed that along the heater surface, as well as less contact time, a higher particle rise velocity would increase the distance between the particle-wall impact points. In these conditions - now referring to the particulate system as a whole - particles would be prevented from effecting the increase of heat transfer, either through the energy interchange at the surface, or the disruption of the thermal boundary layer in the near wall vicinity. For our boiling system, such a scenario would concur with the observed reduction in the three-phase boiling coefficient encountered at higher examined liquid superficial velocities.

To this effect, Figure 6.3 depicts a typical set of results showing the variation of average particle rise velocity, U_p, with liquid superficial velocity, U_L. Meanwhile, Figure 6.4 shows the effect of liquid velocity on the estimated bed voidage, ε. In both figures, results are presented for all investigated particle sizes. As above, the camera arrangement and applied visualisation techniques are described in *Chapter 4*, subsection 4.5.2. Hence, by employing the use of the specialised PHANTOM software accompanying the high-speed camera, we have been able to ascertain the average particle rise velocities from selected film sequences. Recordings have also been used to determine the bed voidage for any particular set of test conditions; within the riser section, the local solid hold-ups are low enough that by freezing a frame one can count the number of particles in a given height of riser. An estimate of the bed voidage, ε, can then be obtained from the expression below:

$$\varepsilon = \frac{\text{volume of viewed section} - (\text{particle volume x no. in viewed section})}{\text{volume of viewed section}} \qquad (6.1)$$

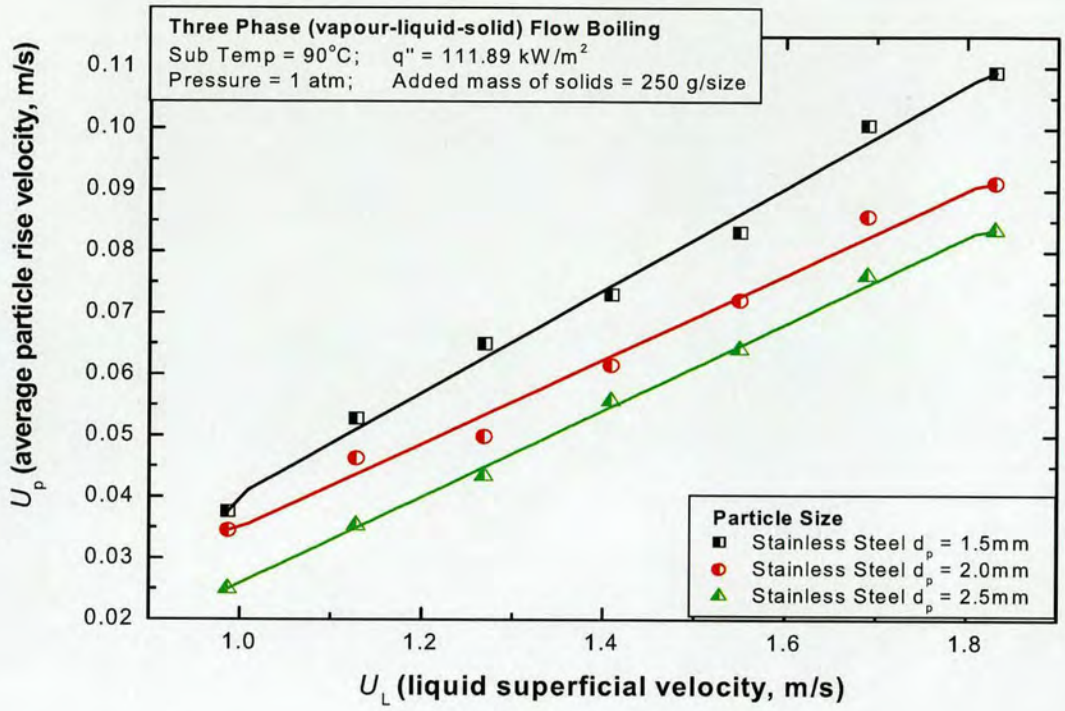

Figure 6.3: Variation of average particle rise velocity with liquid flowrate for all examined values of d_p. Data obtained via the use of flow visualisation.

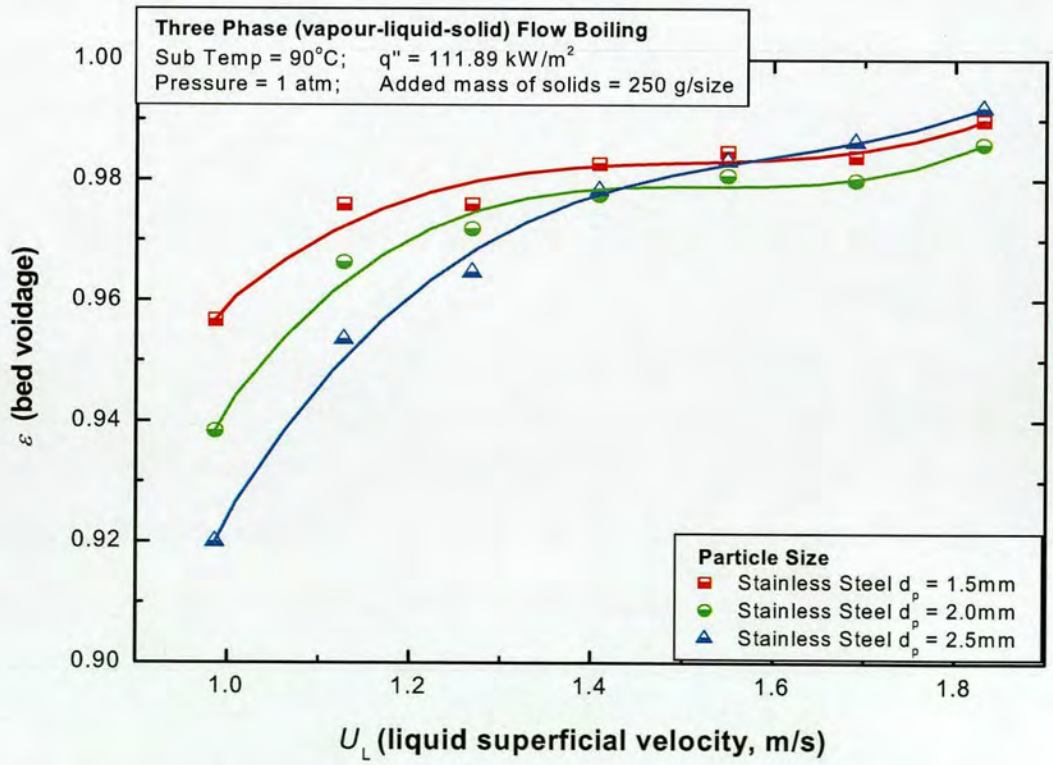

Figure 6.4: Variation of fluid volume fraction with liquid flowrate for all examined values of d_p. Data obtained via the use of flow visualisation.

For the results presented in Figures 6.3 and 6.4, the related video sequences were all filmed at a heat flux setting of $q^{"}$ = 111.89 kW/m^2. Finally, for each examined value of d_p, the total mass of particles charged to the test section was equal to 250 grams; this translates to an average solid hold-up, or particle volume fraction, of ε_p = 16 % (see *Chapter 5*, section 5.1)

Beginning with Figure 6.3, we see that for all particle sizes, average particle rise velocity increases linearly with increasing liquid superficial velocity. Therefore, bearing in mind the trend of the $\alpha_{t.f.b}$ vs. *Re* curve (as shown in Figure 5.10) the depicted linear fit proves that in the higher flow range, the deterioration of the three-phase heat transfer coefficient does correspond with higher particle speeds. In addition, the depicted results also show that for any given liquid flow rate, increasing particle size reduces the estimated average particle rise velocity. This can be explained as follows: when particles are suspended in an up-flowing fluid, the forces acting on the particles include drag force, buoyancy force and gravity. As stated in section 4.2, particles are carried up into the riser section once the drag and buoyancy forces overcome gravity. Therefore, as larger sized particles have less contact surface area (per unit volume of fluidising liquid) available for the generation of drag force, it is no surprise that they are shown to travel slower than smaller diameter particles for an equivalent liquid velocity.

Continuing with the results of our flow visualisation studies, from Figure 6.4, it is clear that in our test section, the volume fraction of the continuous fluid phase, ε, increases as liquid velocity is also increased. This proves that the concentration, or local solid hold-up, of particles flowing through the heated flow channel reduces as liquid velocity increases.
The combined effects, i.e. increased particle speed and reduced local solid hold-up, strongly support the notion that increasing liquid velocity reduces the particle-wall collision frequency, thereby giving rise to the deterioration of the three-phase flow boiling coefficient; as explained above, this is particularly true for heat transfer in the low to mid-heat flux region (see *Chapter 5,* subsection 5.3.2). In the higher heat flux region, the diminishing influence of liquid velocity (again see *Chapter 5*, subsection 5.3.2) suggests that the forced convective contributions are gradually suppressed as the mechanisms of nucleate boiling become more dominant.

6.3.2. Three-Phase Flow Boiling and The Mechanisms of Heat Transfer Enhancement

From the results presented in *Chapter 5*, it is evident that significantly higher boiling coefficients are achievable in three-phase flow boiling as opposed to conventional two-phase flow boiling. Contrasting the respective boiling curves, our observations show that in our

boiling system, the fluidisation of solid particles leads to a reduction in the measured wall excess temperature at all heat flux settings. The result is a leftward shift of the boiling curve, proving that in three-phase flow boiling, a higher rate of heat transfer can be obtained with less temperature driving force. This holds true for all examined liquid superficial velocities. See section 5.4 for full details concerning the comparison of heat transfer in three-phase flow boiling and two-phase flow boiling.

The findings summarised above are in accord with the observations of Wei and Maa [202] and Li Xiulun *et al.* [198,200,201] who initially reported the enhancement of the vapour-liquid flow boiling coefficient in the presence of solid particles (see subsection 3.4.3.2). However, from the analysis of our heat transfer results, not only have we been able to identify an enhancement effect, but we have also been able to quantify the observed enhancement and examine its behaviour over a range of operating conditions. Therefore, as a means of explaining the fundamentals and nature of the particle induced enhancement, the following series of mechanisms are tentatively proposed:

I. As explained in *Chapter 3*, in the wall area affected by particles – referring to the heater surface - heat is transferred to a particle mainly by the process of conduction. This occurs during its contact with the heat transfer surface and results in the increase of the particle's internal energy. By the more or less random motion of the particulate system, this surplus energy is then carried into the bulk of the bed, where it is almost immediately transferred to the fluid and other particles. Heat is also transferred into the fluid by transient heat conduction from the heater surface to the adjacent fluid layer. As particles depart from the heated surface, the hot fluid layer is transported into the main flow and replaced by a cooler liquid; this improves the overall thermal mixing within the bed. In all, both processes enhance the rate of convective heat transfer, thereby giving rise to increased three-phase flow boiling coefficients.

II. Near the wall, as well as erosion of the thermal boundary layer, the stirring motion of the particles may help to sweep away bubbles from the heating surface. This reduces the time available for the vapour bubbles to grow on the wall. As is well known, nucleate boiling is a high efficiency heat transfer mode, fundamentally reliant on the bubble generating and departing process. Therefore, by shorten the time of growth of vapour bubbles forming on the heater surface, the flux of particles effectively accelerates the said process, causing a significant increase in the boiling heat transfer.

III. It is possible that more active nucleation sites are provided on the heating surface due to the continually contact between the wall and the fluidised particles. This could probably

be the result of micro-abrasion of the heating surface around the particle-wall impact zone. Furthermore, the additional particle surface area also contributes to the overall increase in the boiling site density (defined as the number of active nucleation sites per unit heat transfer surface area). As explained in subsection 3.4.3, and demonstrated above, right from the earliest studies of Jakob and Fritz [170] an increase in boiling site density coupled with a rise in boiling heat transfer coefficients, has been a regularly observed phenomena occurring even at lower heat fluxes. As explained above, this is mainly due to fact that an increase in the number of active nucleation sites allows for more bubbles to form on the heater surface, consequently heightening the vapour fraction and furthering the level of turbulence; bubble generation frequency is also promoted, giving rise to stronger nucleate boiling. Therefore, if our assumptions are valid (i.e. boiling site density is increased by the particle-wall interactions and the additional particle surface area) then the effects described above would certainly contribute to the enhancement of the three-phase flow boiling coefficient when compared against conventional two-phase flow boiling.

IV. Fluidised particles affect the level of flow stability within the bed. When particles interact with the vapour bubbles, big bubbles are disrupted to form a large number of smaller bubbles which move vigorously within the bulk fluid. Although the mechanisms involved in the event are not very clear, the agitation of the bulk fluid (arising from the particle-bubble interaction) would undoubtedly influence the flow field, by increasing the degree of turbulent mixing, thereby engendering the enhancement of the convective contribution to the flow boiling heat transfer coefficient.

If we assume that the suppositions outlined above are reasonable justifications for the observed boiling enhancement, then the results of our analysis concerning the magnitude of the attainable enhancement, suggest that the identified mechanisms participate in the promotion of the boiling coefficient to varying degrees, depending on the specified set of bed operating conditions. For our particular case, this (referring to said operating conditions) mainly comprises the regime of boiling and the rate of liquid delivery. Hence in the following subsections, we discuss the nature of the heat transfer enhancement percentage, $\alpha_{E.T}$, and by such means, we attempt to identify the factors which encourage, or inhibit, the mechanisms connected to the promotion of the boiling coefficient in the presence of solid particles.

6.3.2.1. THE ENHANCEMENT PERCENTAGE & FORCED CONVECTIVE HEAT TRANSFER

As shown in results section 5.2 and 5.3, in the lower heat flux region, the two-phase and three-phase heat transfer coefficients ($\alpha_{f.b}$ and $\alpha_{t.f.b}$ respectively) share a similar heat flux dependency. For both boiling modes, our results show that the measured boiling coefficient is essentially independent of heat flux, but increases with liquid superficial velocity. However, the similarity ends there, for whilst the two-phase heat transfer coefficient increases linearly with liquid velocity, in contrast, the trend of the three-phase boiling coefficient versus liquid velocity relationship is described by a parabolic shaped curve. Recalling *Chapter 5*, Figure 5.24 shows a comparison of the respective two-phase and three-phase α vs. *Re* relationships, clearly insinuating the difference between the related heat transfer processes.

Therefore – and referring particularly to the low heat flux region - with regards to the effect of liquid velocity on the magnitude of the attainable heat transfer enhancement, $\alpha_{E.T}$, it is to be expected that the results presented in subsection 5.4.3 would reflect this difference. To recall, our findings show that $\alpha_{E.T}$ experiences an initial increase to maximum value at some definite liquid superficial velocity (see Figure 5.26); bearing in mind the expression for $\alpha_{E.T}$ defined in equation 5.2, the rising tendency of the $\alpha_{E.T}$ vs. *Re* curve simply represents the growth in the magnitude of $\Delta\alpha$, i.e. $(\alpha_{t.f.b} - \alpha_{f.b})$, observed for velocity increases within the lower Reynolds number range. Here, the significance of the differential, $(\alpha_{t.f.b} - \alpha_{f.b})$, arises from the favourable operating conditions within the (v-l-s) fluidised bed, which allow the mechanisms responsible for boiling enhancement to be exploited to their full potential. However, as the circulating bed passes into the high flowrate region, the number of particle collisions experienced on the heater transfer surface gradually begins to diminish, mainly due to increasing particle speed and increasing bed voidage. As explained above, the former is likely to widen the distance between the particle-wall impact points, whilst the latter reduces the local solid hold-ups along the length of the heated channel. Hence, with particle-wall impact frequency reduced, Figure 5.24 shows that the measured three-phase heat transfer coefficient passes through a maximum, before declining towards values more in keeping with two-phase flow boiling. Imitating the lessen differential, $\Delta\alpha$, the calculated heat transfer enhancement percentage, $\alpha_{E.T}$, also decreases, approaching its lowest value at highest *Re* (see Figure 5.26). Therefore, by minimising the contact between the flux of particles and the heating surface, higher liquid velocities hinder the mechanisms which control the enhancement of the boiling coefficient.

With regards to the third investigated parameter, our findings show that, overall, larger diameter particles augment the rate of three-phase boiling heat transfer (see subsection 5.3.3).

As a result, increasing particle size promotes the magnitude of the attainable heat transfer enhancement, $\alpha_{E.T}$, especially in the forced convective region (see subsection 5.4.3.2). In our estimation, having possession of a higher momentum, larger diameter particles are perhaps more effective at thinning and disrupting the thermal boundary layer in the near wall region. Therefore, the additional convective heat transfer stemming from any one particle at any one time, would increase with increasing particle diameter. These effects may account for the enhancement of the three-phase flow boiling coefficient and, in turn, the attainable heat transfer enhancement percentage.

In addition to the above, it is also worth noting that although larger diameter particles may assure a greater momentum effect, for the same solid fraction, ε_p, a larger particle size would, however, allow for less units of particles compared to a smaller size of particle diameter. Put simply, this implies that less additional nucleation sites would be made available on the heating surface via the use of larger solid particles.

Meanwhile, the results presented in subsection 5.4.3.2 also suggest that the benefit to the enhancement coefficient, brought about by the use of larger diameter particles, evaporates at higher liquid velocities; a corresponding reduction in the frequency of particle-wall collisions, experienced throughout the examined size range, is undoubtedly the most plausible explanation for the observed behaviour at higher liquid velocities.

6.3.2.2. THE ENHANCEMENT PERCENTAGE & NUCLEATE BOILING HEAT TRANSFER

As stated above, bubble disruption by the action of fluidised particles is one of the possible means by which particles promote the boiling coefficient. Therefore, considering the fact that increasing heat flux favours the growth and detachment of vapour bubbles from the heating surface, one would expect that within the bed, the resulting increase in vapour fraction should lead to greater particle-bubble interactions and hence a more pronounced boiling heat transfer enhancement for progressive increases of the heat flux.

Rather contrastingly, the results from our particular experimental setup and bed geometry point in the other direction. Recalling *Chapter 5*, Figures 5.29(a)-(c) show that throughout the examined size range, the magnitude of the attainable enhancement, $\alpha_{E.T}$, generally deteriorates with increasing heat flux at both low and high superficial velocities. The observed trend suggests that whilst increasing heat flux may indeed improve the overall particle-bubble interactions, especially in the region away from the wall, in the near wall region, however, the elevated growth and detachment of vapour bubbles appears to reduce the momentum carried to the impact between solid particles and heat transfer surface, thereby suppressing the important heat transfer contribution from such particle-wall interactions.

To this effect, Figures 6.5(a,b) present sample images from selected video sequences, allowing us to compare the development of two-phase and three-phase flow boiling under similar test conditions. Results are presented for two different flowrate settings. Figure 6.5(a) for *Re* '45602' and Figure 6.5(b) for *Re* '58631'.

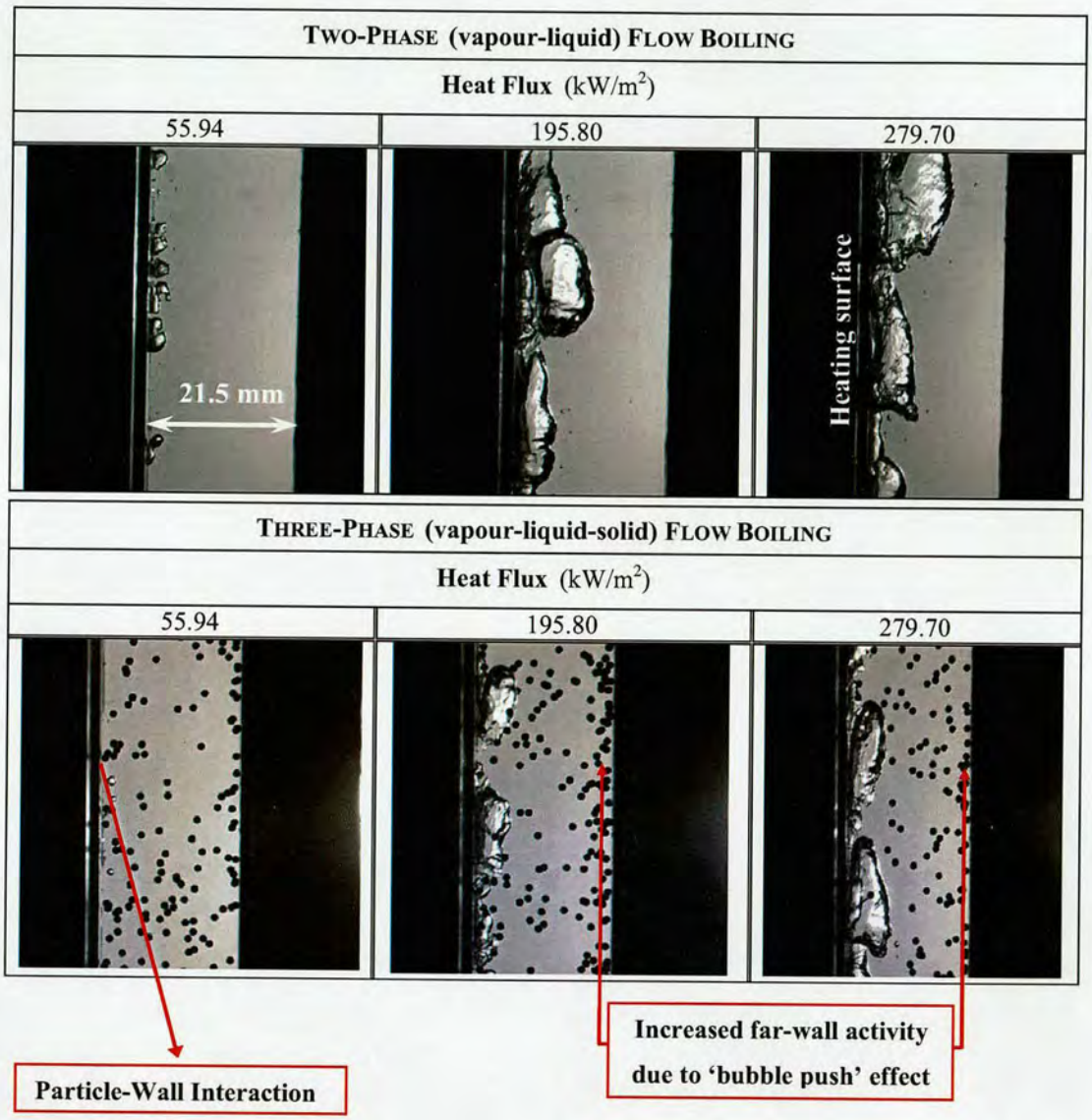

Figure 6.5: (a) Video images comparing state of fluidised bed during two phase & three-phase flow boiling. Filmed at a liquid flowrate of 14 litres/min (*Re* '45602') and using 1.5 mm diameter particles as the solid phase.

Heating surface

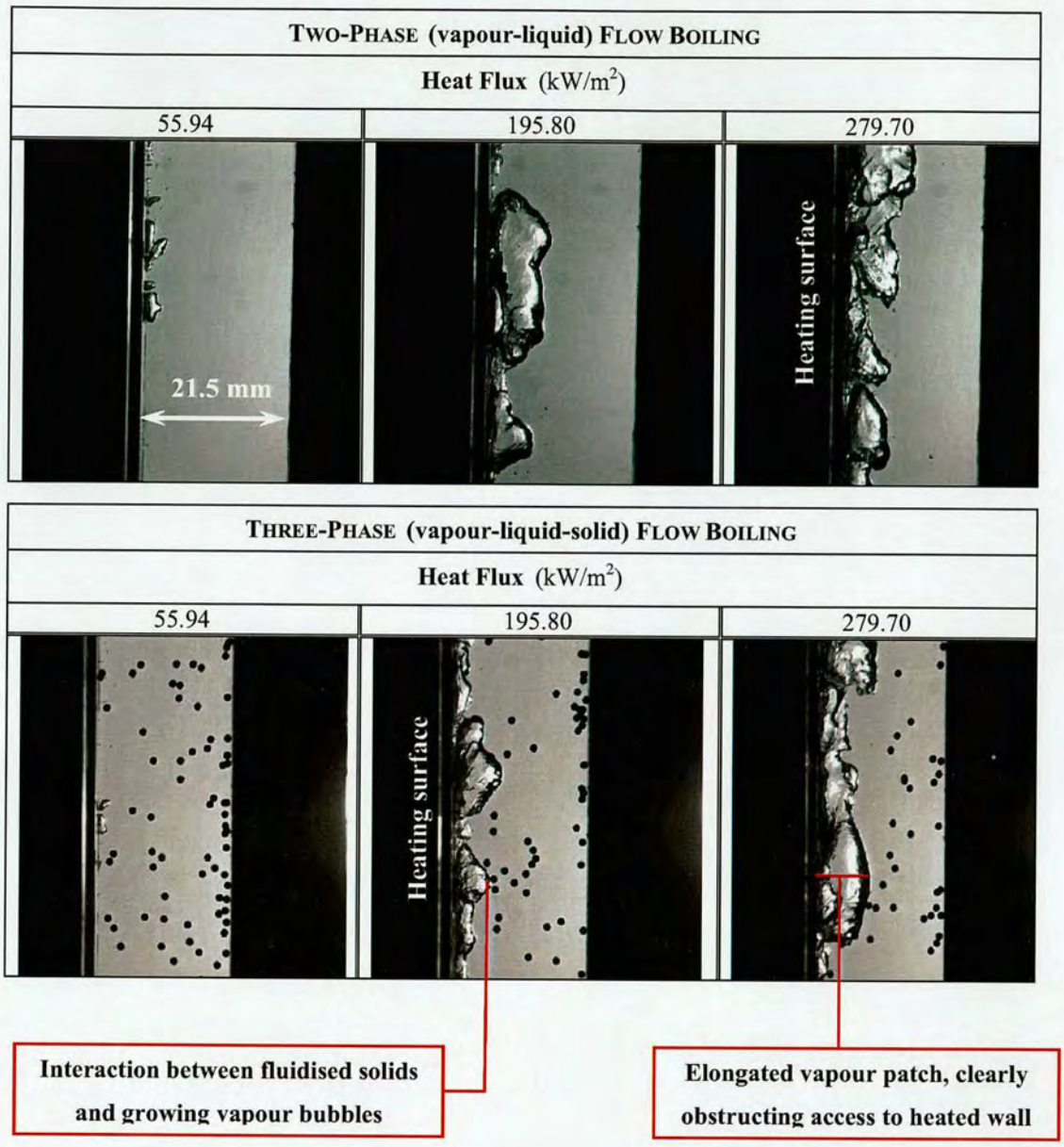

Figure 6.5: (b) Video images comparing state of fluidised bed during two phase & three-phase flow boiling. Filmed at a liquid flowrate of 18 litres/min (*Re* '58631') and using 1.5 mm diameter particles as the solid phase.

In the first instance, the video comparisons demonstrate the general nature of the particle-bubble interactions experienced within the three-phase fluidised bed, emphasising the difference between the flow field with solid particles and that without. For the case of three-phase flow boiling, due to the random motion of the fluidised particles, one gets a clear sense of the heightened degree of chaos within the heated channel. As explained above, compared with conventional two-phase flow boiling, the increase in the level of fluid agitation, brought about by the addition of solid particles, is a key component in the enhancement of the boiling heat transfer coefficient. Nevertheless, returning to the main subject, i.e. decreasing $\alpha_{E.T}$ with increasing heat flux, Figures 6.5(a,b) both show that in the lower heat flux region ($q^{"}$ = 83.92 kW/m^2) bubbles forming on the heater surface are spherical and discrete in nature, and the distribution of particles within the bed is fairly uniform. In both figures, the contact between heater wall and the flux of particles is clearly discernible.

However, transiting towards the upper heat flux region ($q^{"}$ = 195.80 kW/m^2 and 279.70 kW/m^2) most of the generated bubbles coalesce to form large, elongated vapour patches, which typically remain in contact with the heater surface, visibly preventing the fluidised particles from engaging the wall. In both Figures 6.5(a) and (b), this 'bubble push' effect is most apparent at maximum heat flux, where it appears that the growing and expanding vapour patch effectively 'pushes' the flux of particles away from the heating surface, and on towards the opposite side of the channel. Hence, with such conditions present within the bed during fully developed nucleate boiling, particles are obviously restricted from effecting heat transfer enhancement at the wall contact area, subsequently leading to the degradation of the enhancement coefficient at higher heat flux values. With regards to the heat transfer benefit gained from the use of larger diameter particles during nucleate boiling, the proposed 'bubble push' theory could also account for the declining effect of particle size on the improvement of the three-phase flow boiling coefficient, and, by the extension, the heat transfer enhancement percentage. As demonstrated in subsections 5.3.3 and 5.4.3.2, in contrast to the forced convective region, our results show that for heat fluxes beyond the onset of nucleate flow boiling, the benefit of increasing particle size on the magnitude of both $\alpha_{t.f.b}$ and $\alpha_{E.T}$ gradually diminishes for successively increasing heat flux.

Given that the contact between solid particles and the heater surface is the means via which larger diameter particles transmit their heightened momentum for the enhancement of heat transfer, the suppression of this critical interaction, stemming from the resulting 'push' of growing vapour bubbles, appears to be the only credible justification for the observed tendency. However, the overall result does emphasis the dominance of the bubble formation process on the rate of nucleate flow boiling heat transfer. This is further evidenced by the fact that, as well as increasing particle size, the results presented in subsection 5.4.3.2 indicate that

during fully developed nucleate boiling, increasing liquid velocity has virtually no influence on the magnitude of the attainable heat transfer enhancement. As explained in *Chapter 5*, the observation testifies to the fact that in the higher heat flux region, the forced convective contributions to both the two-phase and three-phase boiling coefficients' are overshadowed by the nucleate boiling heat transfer. However, like the forced convective region, for heat fluxes beyond the onset of nucleate flow boiling, our findings indicate that the heat transfer enhancement percentage obtains its lowest value at maximum liquid superficial velocity.

Regarding the limits of the enhancement: by studying the behaviour of the coefficient (i.e. $\alpha_{E.T}$) with reference to our specified range of operating parameters, we have been able to successfully determine the enhancement boundaries within our three-phase boiling device. Essentially, for the promotion of the boiling coefficient, the presented results suggest that the most undesirable bed conditions are a high heat flux and a high liquid delivery rate. Both reduce the contact between the heater surface and the flux of particles; the former by the above described 'bubble-push' effect, and the latter by the reduction of the particle-wall impact frequency, which itself is a consequence of the increased bed voidage and particle speed(s) encountered at higher liquid velocities. Together these limitations have been identified in the 3-dimensional diagrams presented in *Chapter 5*, Figures 5.28(a,b).

Further to this, Figure 6.6 shows a series of images capturing the heat and mass transfer processes occurring within the bed at various test conditions. The images have all been selected from video sequences recorded at a frame rate of 1000 fps (frames per second). Furthermore, the investigation employed the use of 1.5 mm diameter particles at our standard solid loading of ε_p = 16 %. As above, see *Chapter 4* for camera arrangement and applied visualisation techniques. In the diagram presented, it is clear that as we descend a column (increasing liquid delivery) the concentration of particles within the bed is gradually depleted. For instance, if we compare the development of boiling at 14 litres/min (*Re* '45602') to that observed for a maximum liquid delivery of 26 litres/min (*Re* '84643'), we see that for all heat fluxes (increasing from left to right), the local solid hold-up appears to be much higher in the former than the latter. Likewise, for the higher heat fluxes ($q^{"}$ = 195.80 kW/m^2 and 279.70 kW/m^2), the 'push' effect brought about by the accompanying increase in bubble diameter is also quite noticeable.

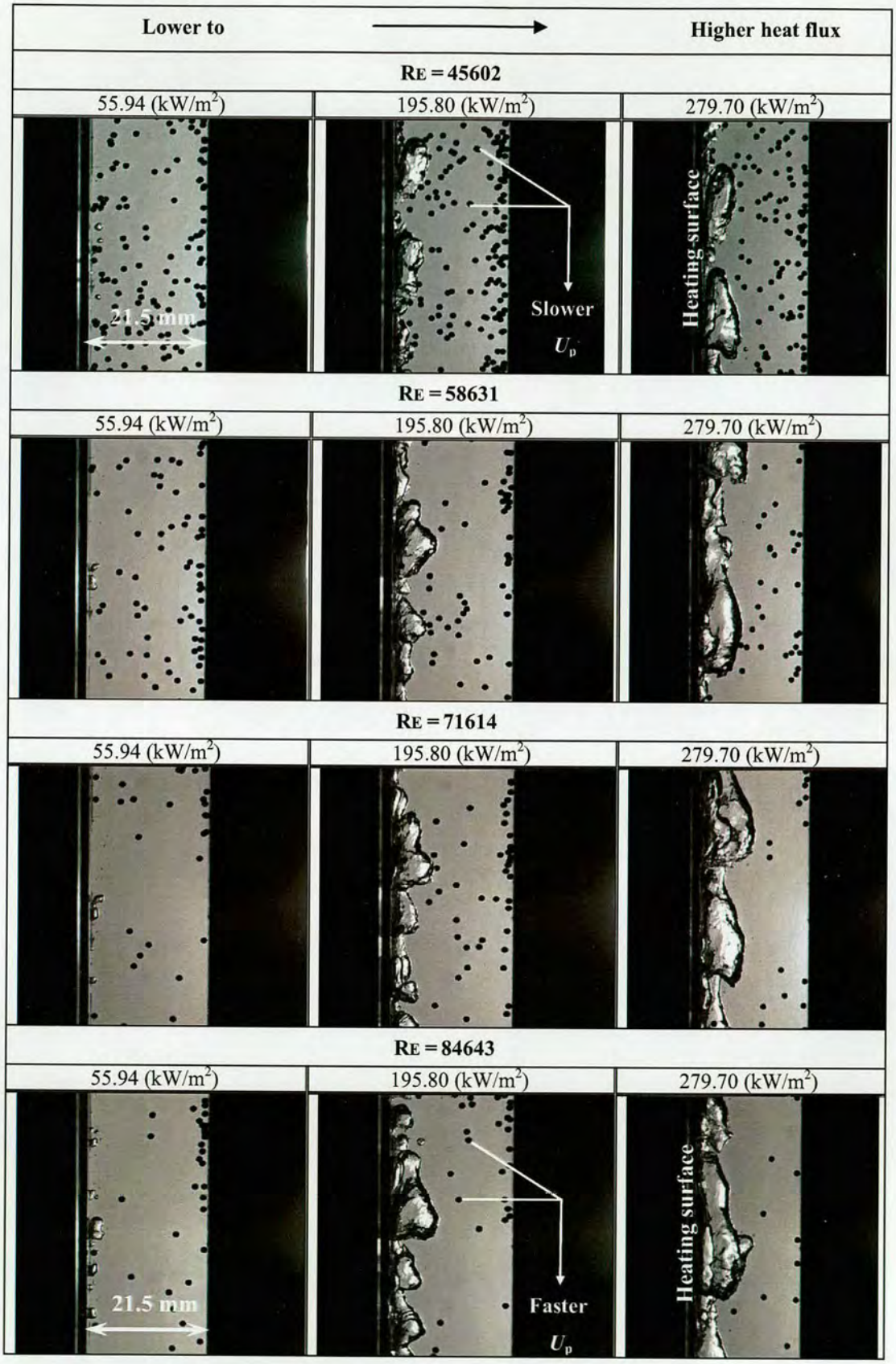

Figure 6.6: Photographic chart showing physical processes occurring within the three-phase circulating fluidised bed at various liquid flowrates (from 14 to 26 litres/min).

Hence, based on our results and considerations presented thus far, it can be said that in Figure 6.6 above, the first half of the chart (where particle speed and bed voidage have been shown to be at their least) represents the state of the fluidised bed during maximum heat transfer enhancement; whilst the bottom half of the chart (where particle speed and bed voidage have been shown to be at their greatest) represents the state of the bed during reduced heat transfer enhancement.

In summary, the heat transfer mechanisms responsible for the observed particle enhancement effect have been examined in great detail. Our analysis has shown that the governing processes are fairly dependable, and can therefore be predicted with some degree of accuracy.

CHAPTER 7: CORRELATING THE THREE-PHASE (V-L-S) FLOW BOILING EXPERIMENTAL RESULTS

7.1. INTRODUCTION

Three-phase flow boiling enhancement and limiting heat transfer effects have been experimentally determined as described in *Chapter 5*. The heat and mass transfer processes causing these effects have also been visualised and clearly connected to the heat transfer data, resulting in a comprehensive theory regarding the heat transfer mechanisms of vapour-liquid-solid flow boiling (see *Chapter 6*).

However, the ultimate objective of any fundamental approach to the problem of heat transfer in three-phase fluidisation is to be able to predict the boiling heat transfer coefficient for any given condition, through a knowledge and understanding of the processes involved.

As stated in the review performed in *Chapter 3*, due to the complex nature of the three-phase flow boiling system, correlations for the prediction of vapour-liquid-solid heat transfer appear fleeting within the available literature. Of the few studies undertaken, the work of Li Xiulun *et al.* [201] features most prominently. The authors' investigated fouling mitigation and heat transfer characteristics of a three-phase CFB evaporator, measuring the heat transfer coefficient for various superficial velocities, particle volume fractions and particle types. In the main, their findings are consistent with the observations recorded within this particular body of work, i.e. compared with two-phase (vapour-liquid) flow boiling, in (vapour-liquid-solid) flow boiling, the additionally solid phase promotes the measured rate of boiling heat transfer (see subsection 3.4.3.2). Developing upon their experimental work, Li Xiulun *et al.* also went on to propose a mathematical model for predicting heat transfer to/from vapour-liquid-solid circulating fluidised beds. As claimed by the authors', the correlation – given in equation 3.61- is capable of predicting their experimental data to within a deviation of ± 20%.

However, compared with Li Xiulun *et al.*, for our particular test geometry and investigated parametric range, an analysis of both the experimental and visualisation results, has lead to some differing conclusions regarding the behaviour of the multiphase flow system. For instance, across our stipulated flow range (from 0.99 m/s up to 1.85 m/s), the measured three-phase boiling heat coefficient, $\alpha_{t.f.b}$, exhibits non-linear functionality with fluid superficial velocity; a finding which stands in contrast to the work(s) of Li Xiulun *et al.* [200,201], who report that for liquid velocities ranging from 0.5 m/s up to 1 m/s, an increase in fluid flowrate gives rise to a corresponding increase in three-phase flow boiling coefficient, with no sign of heat transfer degradation occurring at higher liquid velocities. Presumably the dissimilarity between our examined fluid velocity range accounts for such discrepancies.

Therefore, in order to reflect some of our distinct experimental findings, this chapter aspires to develop a modified approach for predicting our measured three-phase flow boiling heat transfer coefficients. This will be accomplished by converting our postulated (v-l-s) flow boiling mechanisms into assumptions which form the basis for theoretical models of the heat transfer process. As a consequence, both our experimental and theoretical heat transfer results can then be compared, and an analysis made regarding the accuracy, and validity, of the three-phase flow boiling correlation presented.

7.2. INFLUENCING PARAMETERS AND GOVERNING EQUATIONS

Of the many different parameters which control the mechanisms of three-phase heat transfer, the most important ones have been taken into account in order to correlate the overall heat transfer coefficient for (v-l-s) circulating fluidised bed boiling.

In beginning, let us first consider a stable saturated three-phase flow boiling system. It has been noted that, excluding the addition of solid particles, there is no essential fundamental difference between the boiling regimes of two-phase (vapour-liquid) and three-phase (vapour-liquid-solid) flow boiling. However, as earlier demonstrated in *Chapters 5* and *6*, the presence of solid particles does affect the levels of nucleation and convection in the boiling process. Therefore, through an analysis of the heat transfer performance of our three-phase flow boiling device, any number of available and dependable two-phase flow boiling heat transfer model(s) can be readily adopted to serve as a basis upon which a mathematical correlation for the prediction of heat transfer in vapour-liquid-solid flow boiling might be founded.

Hence, based on Steiner's two-phase flow boiling asymptotic model discussed in background *Chapter 2*, the proposed general equation describing the vapour-liquid-solid flow boiling coefficients, can thus be correlated as expressed in equation 7.1 below. The correlation covers both the three-phase forced convective region and the three-phase nucleate boiling region. Both contributions (i.e. forced convective and nucleate boiling) interact via an intricate mechanism, and occur to some extent over the entire range of the correlation. Analogous to Steiner's previously considered two-phase flow boiling model, the contributions of both mechanisms are asymptotically added according to their respective magnitudes:

$$\alpha_{\text{T.F.B}} = \left[\left(\alpha_{\text{NB}}\right)^{t_R} + \left(\alpha_{\text{CB}}\right)^{t_R} \right]^{1/t_R} \tag{7.1}$$

nucleate boiling contribution — convective boiling contribution

$$\alpha_{\text{T.F.B}} = \left[\left\{ \left(\alpha_{\text{npb,p}} . F_{\text{NB}}\right)^{b_E} \right\}^{t_R} + \left\{ \alpha_{\text{LS}} . F_{\text{CB}} . \text{f}(U) \right\}^{t_R} \right]^{1/t_R}$$

here α_{NB} and α_{CB} are the nucleate boiling and convective boiling contributions to the three-phase flow boiling correlation respectively. $\alpha_{npb,p}$ is the nucleate pool boiling coefficient with solid phase, developed from Yang and Maa's 1984 correlation of nucleate boiling heat transfer for solids suspended in a pool of water [207]. The value of $\alpha_{npb,p}$ is significantly influenced by the heat flux q''. F_{NB} is the three-phase nucleate flow boiling correction factor to $\alpha_{npb,p}$, which compensates for differences between pool and flow boiling conditions; correlated by Steiner [29], its influencing parameters include reduced pressure, heat flux, tube diameter, and surface roughness, as well as a blanket residual correction, expressed as a function of molecular weight. For the correlation of our experimental data, we have introduced a new nucleate boiling enhancement exponent, b_E. The modification was implemented in order to augment the value of the calculated nucleate boiling contribution.

In equation 7.1, α_{LS} is the convective heat transfer coefficient, which accounts for heat transfer in the forced convective (i.e. liquid-solid only) region of three-phase circulating fluidised bed boiling. A satisfactory correlation as proposed by Aghajani *et al.* [90] was used in our developments. The parameters of Aghajani's correlation include bed voidage, liquid flow velocity, particle size and particle density. F_{CB} is the three-phase flow multiplier to the convective α_{LS} value, accounting for the enhancement of the coefficient in the vapour-liquid-solid mixture. It is a function of the vapour quality, x, and the ratio of liquid/vapour densities.

To account for the observed novel relationship between superficial velocity and our measured three-phase flow boiling coefficient, we have modified the three-phase model by including a convective velocity adjustment factor, $\mathrm{f}(U)$. This new correction factor influences the dependency of α_{CB} on flow velocity.

Finally, in the presented three-phase flow boiling model, t_R is an exponent that dictates the range of transition between the nucleate and convective components. High values of t_R would indicate an abrupt transition, while low values would extend the transition range. Apparently a function of the nucleation cavity size distribution, for commercial tubes the t_R value ranges from 2.5 to 3.5. The work of Steiner *et al.* [29] documents that, within the range of other uncertainties, the demonstrated effect of t_R on the two-phase flow boiling correlation is moderate at best. Therefore, imitating the authors, $t_R = 3$ is accepted for our purposes.

7.2.1. Correlating Convective Component of (v-l-s) Flow Boiling

Firstly, in the convective region of three-phase flow boiling, the heat transfer is dominated by a forced convective mechanism existing for heat fluxes below the onset of nucleate flow

boiling. Thus for low heat fluxes (i.e. $q^{"} \leq q^{"}_{OFB}$) the nucleate boiling term in equation 7.1 reduces to zero, the equation remaining valid for three-phase forced convective boiling only (i.e. for $q^{"} \leq q^{"}_{OFB}$, $\alpha_{T.F.B} \approx \alpha_{CB}$).

Therefore, in light of the above, it is to be expected that the convective contribution to the calculated three-phase boiling coefficient, as written in equation 7.2 below, is largely independent of heat flux over a range of superficial velocities and particle characteristics:

$$\alpha_{CB} = \alpha_{LS} . F_{CB} . \mathrm{f}(U) \tag{7.2}$$

here α_{LS} is the convective heat transfer coefficient based on the total flow assumed as liquid-solid only, i.e. liquid-solid mass velocity without a vapour adjustment term $(1 - x)$; the fact that the forced convective regime of three-phase circulating fluidised bed boiling can be envisaged as a liquid-solid fluidised bed system, allows for such a supposition. To reflect this condition, Aghajani *et al*'s [90] unified correlation for predicting heat transfer in liquid-solid fluidised beds has been employed for the calculation of α_{LS}. Subsection 3.3.4.2.1 and subsection 3.3.4.3 present a fully comprehensive discourse on the derivation of α_{LS} which is defined according to equation 3.43 and repeated below for the purposes of clarity:

$$\alpha_{LS} = \alpha_c + \alpha_p \quad \text{- equation 3.43}$$

Therefore, based on the particulars of Aghajani's correlation detailed in *Chapter 3*, for the convective boiling regime of vapour-liquid-solid three-phase flow boiling, we can rightly assume the heat transfer to be composed of two parallel mechanisms occurring in separate zones of the heater surface as shown in earlier Figure 3.27. In the 'liquid flow only' zone, the heat transfer coefficient, α_c, can be determined from the Gnielinski correlation [112] as given in equation 3.44, whilst in the particle-controlled area of the heater surface, the heat transfer coefficient, α_p, can be derived from the equation of Aghajani *et al.* as written in equation 3.49. These relationships can be summarised as follows:

Aghajani et al's unified correlation, adapted from Chapter 3

Heat transfer in liquid-solid fluidised flow ~ Equation 3.43

$$\alpha_{LS} = \alpha_c + \alpha_p$$

Heat transfer from 'Particle-controlled' region ~ Equation 3.49

Heat transfer from 'Liquid flow only' region ~ Equation 3.44

$$\alpha_c = \frac{\lambda_L}{D_e} \cdot \frac{\frac{f_i}{8}(Re-1000)Pr}{1+12.7\sqrt{\frac{f_i}{8}}\left(Pr^{2/3}-1\right)}\left[1+\frac{1}{3}\left(\frac{D_e}{L}\right)^{1/3}\right]$$

with friction factor, f_i, determined from equation 3.44a

$$f_i = \left[1.82\ \mathrm{Log}(Re)-1.64\right]^{-2}$$

$$\alpha_p = \left[\frac{2}{\sqrt{\pi}}\sqrt{\lambda_L \rho_L C_{p,L}} + \left(\frac{d_p}{D_e}\right)^2 \sqrt{\lambda_p \rho_p C_{p,p}}\right]\sqrt{f}$$

with particle-wall collision frequency, f, determined from equation 3.53

$$f = 1.5\left(\frac{U}{d_p}\right)\left(\varepsilon - \varepsilon_{SB}\right)^{0.2}\left(1-\varepsilon\right)^{1.8}$$

bed voidage, ε, determined from equation 3.29

$$\varepsilon = \left(\frac{U}{U_t}\right)^{1/Z}\left(1-\varepsilon_{SB}\right)+\varepsilon_{SB}$$

and static bed voidage, ε_{SB}, determined according to equation 3.31

$$\varepsilon_{SB} = \frac{0.15}{\left(\frac{D_e}{d_p}-1\right)} + 0.38$$

Returning to equation 7.2, as explained above F_{CB} - the three-phase enhancement factor to the convective α_{LS} value - can be derived as a function of the vapour quality x and the ρ_L / ρ_V ratio; according to Steiner *et al.* [29] the expression can be written as follows:

$$F_{CB} = \left[(1-x)^{1.5} + 1.9(x)^{0.6} \left(\frac{\rho_L}{\rho_V} \right)^{0.35} \right]^{1.1}_{x \leq 0.6} \tag{7.3}$$

The above correlation is recommended for boiling operations. The value of x has been arbitrarily set to 0.1. A parametric study on the variation of x has shown negligible effect on the calculated vapour-liquid-solid flow boiling heat transfer coefficient, $\alpha_{T.F.B}$.

7.2.1.1. THE CONVECTIVE VELOCITY ADJUSTMENT FACTOR, $f(U)$

Compared with Li Xiulun *et al.* [200,201], for an examined liquid velocity range of 0.99 m/s up to 1.85 m/s, the results of our heat transfer investigations clearly show a contravening effect of superficial velocity on the magnitude of the measured three-phase flow boiling coefficient. As shown in Figures 5.10 to 5.12, for heat fluxes in the forced convective and lower transitional boiling regions, the experimental heat transfer coefficient, $\alpha_{t.f.b}$, is initially shown to increase for increasing velocity, attaining a maximum value at a definite Reynolds number. It should be noted that within this lower velocity region ($0.99\ \text{m/s} \leq U_L < 1.41\ \text{m/s}$), the observed sensitivity of heat transfer coefficient to liquid flowrate corresponds with the linear relationship reported by Li Xiulun *et al.*, for an investigated flow range of 0.5 m/s to 1.0 m/s.

However above a critical Reynolds number, Re_{CR}, the heat transfer coefficient and liquid velocity relationship deviates from the positive linear trend experienced at lower flow velocities. In this higher flow regime ($1.41\ \text{m/s} < U_L \leq 1.85\ \text{m/s}$) further increases in flow velocity result in deterioration of the measured heat transfer coefficient. The heat transfer mechanisms governing this phenomenon have been discussed in *Chapter 6*.

Therefore, in order to accurately predict our experimental results a new velocity adjustment factor, $f(U)$, has been incorporated into the 3 phase flow boiling model, so as to account for our observed non-linear relationship between the experimental three-phase heat transfer coefficient and Reynolds number.

For our stipulated flow range, the velocity adjustment factor has been separately established for $Re < Re_{CR}$ and $Re \geq Re_{CR}$. This was achieved by systematically varying $f(U)$ to

obtain the best fitting curve for the comparison between the predicted and experimental three-phase heat transfer coefficients.

By such means, the convective adjustment factor has been identified as follows:

I. $f(U) = 10^{-1.47}$ or 0.0341 for $Re < Re_{CR}$ and

II. $f(U) = (1660.5/Re)^{0.89}$ for $Re \geq Re_{CR}$

Figure 7.1 illustrates the predicted and experimental dependence of the adjustment factor $f(U)$ on Reynolds number.

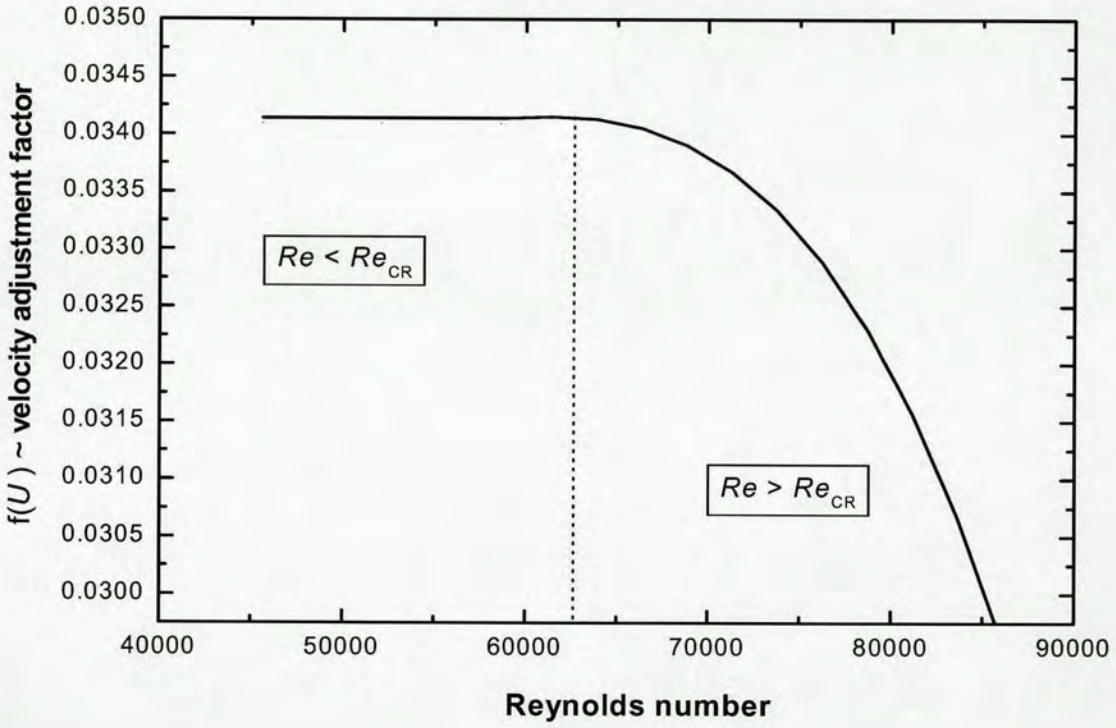

Figure 7.1: Variation of convective velocity adjustment factor, $f(U)$, with Reynolds no.

The arguments justifying the adoption of such a plot can be written as follows:

- As explained above, for $Re < Re_{CR}$ the trend of our experimental heat transfer data is characterised by a positive linear variation of three-phase flow boiling coefficient with velocity (see Figures 5.10 to 5.12); a finding in accord with behaviour observed and correlated by Li Xiulun *et al.* [201]. Hence, in the lower flow velocity range, $f(U)$ should be represented by a constant as shown in Figure 7.1 above. As a result, within

this reduced flow region, the existing three-phase flow boiling correlation (as expressed in equation 3.61) remains unaffected.

- However, $Re \geq Re_{CR}$ exceeds the fluid velocity range examined by Li Xiulun *et al.* For this higher flow region, results from our experimental work suggest a boiling heat transfer behaviour contrary to that previously observed, and predicted, for $Re < Re_{CR}$ (at higher flow rates, increasing superficial velocity results in decreasing three-phase flow boiling heat transfer). Thus, by setting $f(U)$ as an inverse function of superficial velocity, the three-phase flow boiling correlation has been modified in order to accurately correlate our experimental heat transfer results.

7.2.2. PREDICTING NUCLEATE BOILING IN 3-PHASE CIRCULATING FLUIDISED BED

In predicting the three-phase flow boiling heat transfer coefficient, $\alpha_{T.F.B}$, the nucleate boiling contribution term in equation 7.1 can be used only if the wall superheat is above a certain minimum value required for the onset of nucleate flow boiling; for our experimental heat flux range, the corresponding minimum heat flux value has been estimated as $q_{OFB} \approx 85\ kW/m^2$. Beyond the O.F.B point, the nucleate and convective boiling coefficients are superimposed according to their relative magnitudes, with the nucleate boiling coefficient, α_{NB} (defined in equation 7.4 below), becoming dominant for increasing heat flux. In this boiling region, the three-phase flow boiling coefficient, $\alpha_{T.F.B}$, is predicted according to the asymptotic addition of the nucleate and convective components as given in equation 7.1.

$$\alpha_{NB} = \left(\alpha_{npb,p}.F_{NB}\right)^{b_E} \tag{7.4}$$

α_{NB} is based on the nucleate pool boiling heat transfer coefficient for a bed of shallow fluidised solids, $\alpha_{npb,p}$, corrected for effects of the flowing liquid, and tube geometry, by the three-phase nucleate flow boiling correction factor, F_{NB}. To facilitate a true prediction of our experimental data, a new nucleate boiling enhancement exponent, b_E, has been introduced in order to improve the calculated value of α_{NB}, thereby increasing the dependence of the predicted three-phase boiling coefficient on heat flux. In the three-phase model, b_E is a constant, established via the best-fitting curve method, and identified as: $b_E = 1.05$.

7.2.2.1. DERIVATION OF NUCLEATE POOL BOILING COEFFICIENT FOR LIQUID FLUIDISED PARTICULATE BEDS, $\alpha_{npb,p}$

As stated above, for nucleate boiling, Yang and Maa [207] have developed a correlation for nucleate pool boiling heat transfer of water with suspended particles, compared with nucleate pool boiling of pure water.

$$\frac{\alpha_{npb,p}}{\alpha_{npb}} = \left[1+\beta\left(\frac{q''}{q''_{CR}}\right)^{-\gamma}\right]^{-1}\left(\frac{\lambda_M}{\lambda_L}\right)^{\xi} \tag{7.5}$$

According to Li XiuLun *et al.* [198], equation 7.5 can be simplified to:

$$\frac{\alpha_{npb,p}}{\alpha_{npb}} = \left(\frac{\lambda_M}{\lambda_L}\right)^{\xi} = Y'' \tag{7.6}$$

where α_{npb} is the nucleate pool boiling heat transfer coefficient of pure liquid, λ_M and λ_L are the thermal conductivities for solid-liquid mixtures and pure liquid respectively. For ordinary pool boiling, Rohsenow's 1952 correlation suggests a value for the constant, ξ, approximately equal to 1.7.

For the prediction of α_{npb}, the physical properties-based method of Stephan and Preusser [93] has been utilised:

$$\alpha_{npb} = 0.1\left(\frac{\lambda_L}{d_b}\right)\left(\frac{\rho_L}{\rho_V}\right)^{-0.156}\left(\frac{q'' d_b}{\lambda_L T_{sat}}\right)^{0.674}\left(\frac{\Delta h_v (d_b)^2}{\Omega^2}\right)^{0.371}\left(\frac{\Omega^2 \rho_L}{\sigma_L d_b}\right)^{0.35}\left(\frac{\mu_L C_{p,L}}{\lambda_L}\right)^{-0.16} \tag{7.7}$$

here Ω is thermal diffusivity (units of m^2/s) and expressed as $\Omega = \lambda_L / (\rho_L C_{p,L})$; furthermore, d_b is the bubble departure diameter and from Steiner *et al.* [29] is defined as:

$$d_b = 0.0146\Theta\left[\frac{2\sigma_L}{g(\rho_L - \rho_V)}\right]^{1/2} \tag{7.8}$$

According to the authors', the bubble contact angle, Θ, is to be substituted as 45° for water. Referring back to equation 7.6, the mean thermal conductivity of the solid-liquid mixture, λ_M, may be estimated using the 1964 relation developed by Brailsford and Major for a matrix of spheres filled with a fluid [218]:

$$\lambda_M = \frac{\lambda_L (1-2J)}{1+J} \tag{7.9}$$

here J is a dimensionless number and is defined as:

$$J = \varepsilon_p \left(\frac{\lambda_L - \lambda_p}{2\lambda_L + \lambda_p} \right) \tag{7.10}$$

7.2.2.2. DERIVATION OF NUCLEATE BOILING CORRECTION FACTOR, F_{NB}

The factors affecting F_{NB} are formulated upon "normalised" values of the parameters involved, determined from the literature as documented by Steiner [29], and defined in equation 7.11. The use of normalised parameters permits the formulation of dimensionless terms, which contributes to greater accuracy and generalisation of the method:

$$F_{NB} = f(m,x) F_{pr} \left(\frac{q''}{q''_0} \right)^r F(d) F(R_a) F(M) \tag{7.11}$$

$f(m, x)$ correlates the possible effects of mass velocity, $\dot{m}$, and vapour quality, x, in vertical nucleate flow boiling. From the results of Steiner [219], it is concluded that flow velocity (given by mass velocity and vapour quality) has no effect on the heat transfer coefficient in vertical flow nucleate boiling, resulting in $f(m, x)$ equal to 1. Also, according to the data source located in [29], for nucleate flow boiling of water the reference/normalised heat flux, q''_0, is equal to 150000 W/m^2.

In equation 7.11 above, F_{pr} is the pressure correction factor and correlated according to Steiner *et al.* [29] as follows:

$$F_{pr} = \left\{ 2.816 \left(P''_R\right)^{0.45} + \left[3.4 + \frac{1.7}{1-\left(P''_R\right)^7} \right] \left(P''_R\right)^{3.7} \right\}_{P''_R \le 0.95} \tag{7.12}$$

here $P_R^{"}$ is the reduced pressure (dimensionless) and expressed as $P_R^{"} = P^{"}/P_{CR}^{"}$. Equation 7.12 has a similar form, but is slightly lower than for nucleate pool boiling, especially at low and high reduced pressures. Referring to the findings of the aforementioned authors, $P_{CR}^{"}$ for water is approximately 220.64 bar.

Returning to equation 7.11, the exponent *r* on the $(q^{"}/q_0^{"})$ term is derived from the equation of Steiner *et al.* [29] and written as:

$$r = 0.8 - (0.1)\exp(1.75\,P_R^{"}) \tag{7.13}$$

For tube side flow boiling, Steiner *et al.* [219] report a decrease in heat transfer coefficient with increasing tube diameter. From their results the diametral correction factor $F(d)$, based on normalised diameter of $D_{nor} = 0.01$ m, can be written as:

$$F(d) = \left(\frac{D_e}{D_{nor}}\right)^{-0.4} \tag{7.14}$$

$F(R_a)$ accounts for surface roughness effects in equation 7.11. Tests in flow boiling with surface roughness between 0.1 and 5 μm indicate similar dependencies as found in pool boiling. Taking reference roughness as $R_{a,0} = 1$ μm (about average for most commercial tubes), the correction factor can be correlated by Steiner *et al.* as shown in equation 7.15:

$$F(R_a) = \left(\frac{R_a}{R_{a,0}}\right)^{0.133} \tag{7.15}$$

However, because of very incomplete data on this subject and unknown effects of possible corrosion, $F(R_a) = 1$ is recommended as a safe value for industrial designs, unless specific information is available [29]. Finally, in the correlation of F_{NB}, $F(M)$ is the residual correction factor, which reflects the trend of error that appears as a function of molecular weight *M* (within the tested range of $M = 2$ to 187). The effect of molecular weight is not surprising, as *M* influences most properties included in the boiling correlation. According to Steiner [29] the molecular weight correction factor can be obtained from:

$$F(M) = 0.36(M)^{0.27} \tag{7.16}$$

where for water $M = 18$. The authors' also suggest an alternative equation for fluids with $M > 10$ and with the limit $F(M) \leq 2.5$:

$$F(M) = \left(0.377 + 0.199 \ln\ (M) + 2.843\text{E-}5[M]^2\right)_{\leq 2.5} \qquad (7.17)$$

Both methods were employed in our calculations, but equation 7.17 was found to be the more agreeable expression.

Using data obtained for three-phase flow boiling with 2.0 mm (d_p) stainless steel particles, Appendix C summarises the steps required for calculating $\alpha_{T.F.B}$ over a given range of liquid velocities and heat fluxes. Furthermore, for a given set of operating conditions, a detailed sample calculation has also been performed below, in order to demonstrate the procedure.

SAMPLE CALCULATION FOR THE DETERMINATION OF $\alpha_{T.F.B}$

CONDITIONS:

Stainless Steel Particles, $d_p = 1.5 \times 10^{-3}$ m; Heat Flux, $q'' = 167.83$ kW/m^2; Liquid Superficial Velocity, $U = 1.832$ m/s equivalent to Reynolds Number, $Re = 84643$. Subcooled Temperature of Working Liquid = 90 °C

STEP A: CALCULATING CONVECTIVE CONTRIBUTION, α_{CB}

Recall, from equation 7.2

$$\alpha_{CB} = \alpha_{LS} . F_{CB} . \text{f}(U)$$

I. Firstly from equation 3.43, the heat transfer coefficient in liquid solid fluidised flow, α_{LS} -

$$\alpha_{LS} = \alpha_c + \alpha_p$$

II. From equation 3.44, the heat transfer from 'liquid flow' only region, α_c -

$$\alpha_c = \frac{\lambda_L}{D_e} . \frac{\frac{f_i}{8}(Re - 1000)Pr}{1 + 12.7\sqrt{\frac{f_i}{8}}\left(Pr^{2/3} - 1\right)} \left[1 + \frac{1}{3}\left(\frac{D_e}{L}\right)^{1/3}\right]$$

here, λ_L (read at 90 °C) = 0.679 W/mK; $D_e = 0.0146$ m; $L = 1.2$ m

and $Pr = \mu_L C_{p,L} / \lambda_L = (2.42 \times 10^{-4})(4239)/0.679 = 1.511$

III. Meanwhile, from equation 3.44a, friction factor, f_i –

$$f_i = [1.82\ \mathrm{Log}(Re) - 1.64]^{-2} = [1.82\ \mathrm{Log}(84643) - 1.64]^{-2} = \underline{0.01862}$$

IV. Substituting the value of f_i back into (II) above –

$$\alpha_c = \frac{0.679}{0.0146} \cdot \frac{\frac{0.01862}{8}(84643 - 1000)1.511}{1 + 12.7\sqrt{\frac{0.01862}{8}}\left(1.511^{2/3} - 1\right)} \left[1 + \frac{1}{3}\left(\frac{0.0146}{1.2}\right)^{1/3} \right] = \underline{11{,}008.2\ \mathrm{W/m^2K}}$$

V. Next from equation 3.49, the heat transfer from the particle controlled region, α_p -

$$\alpha_p = \left[\frac{2}{\sqrt{\pi}} \sqrt{\lambda_L \rho_L C_{p,L}} + \left(\frac{d_p}{D_e} \right)^2 \sqrt{\lambda_p \rho_p C_{p,p}} \right] \sqrt{f}$$

here (liquid and particle properties read at 90 °C), λ_L = 0.679 W/mK; ρ_L = 946.66 Kg/m^3; $C_{p,L}$ = 4239 J/Kg.K; λ_p = 48.85 W/mK; ρ_p = 7850 Kg/m^3; $C_{p,p}$ = 460.5 J/Kg.K

VI. For the calculation of α_p in (V) above, f (i.e. the particle collision frequency) is established from equation 3.53 –

$$f = 1.5\left(\frac{U}{d_p}\right)(\varepsilon - \varepsilon_{SB})^{0.2}(1 - \varepsilon)^{1.8}$$

where, U = 1.832 m/s, d_p = 1.5 x 10^{-3} m and, from equation 3.31, $\varepsilon_{SB} = \dfrac{0.15}{\left(\frac{D_e}{d_p} - 1\right)} + 0.38 = \underline{0.40}$

VII. Meanwhile, bed voidage, ε is determined as follows –

- From equation 3.29:

$$\varepsilon = \left(\frac{U}{U_t}\right)^{1/Z}\left(1-\varepsilon_{SB}\right)+\varepsilon_{SB}$$

where fluidisation index, Z is found from equation 3.30, $Z = \dfrac{0.65\left(2 + 0.5Re_{p\infty}^{0.65}\right)}{\left(1 + 0.5Re_{p\infty}^{0.65}\right)}$

- From equation 3.33, particle terminal velocity corrected for wall effect, U_t:

$$\mathrm{Log}_{10}\left(\frac{U_\infty}{U_t}\right) = \frac{d_p}{D_e} = \underline{0.1027\,\mathrm{m/s}}$$

- From above, particle terminal velocity in the absence of wall effect, U_∞ is found from equation 3.34:

$$U_\infty = \left[\frac{4\,d_p\left(\rho_p-\rho_L\right)g}{3C_D\,\rho_L}\right]^{1/2}$$

- In equation 3.34, drag coefficient, C_D, is given by equation 3.36 :

$$C_D = \frac{24}{Re_{p\infty}}$$

- Particle free fall Reynolds Number, $Re_{p\infty}$, is itself expressed as shown in equation 3.39:

$$\mathrm{Log}_{10}\,Re_{p\infty} = P[\mathrm{I}]+\mathrm{Log}_{10}\,R[\mathrm{I}]$$

where

$$P[\mathrm{I}] = \left[\left(0.0017795.\mathrm{I}-0.0573\right)\mathrm{I}+1.0315\right]\mathrm{I}-1.26222$$

$$R[\mathrm{I}] = 0.99947+0.01853\sin\left(1.848.\mathrm{I}-3.14\right)$$

and

$$\mathrm{I} = \mathrm{Log}_{10}\,Ar = \mathrm{Log}_{10}\left[\frac{g\,\rho_L\left(\rho_p-\rho_L\right)d_p^3}{\mu_L^2}\right] = \underline{6.5676}$$

- Working back to equation 3.29, the above value of I (defined by equation 3.41) gives:

$Re_{p\infty} = 3514 \rightarrow C_D = 6.83\ \mathrm{x}10^{-3} \rightarrow U_\infty = 4.577\ \mathrm{m/s} \rightarrow U_t = 3.613\ \mathrm{m/s} \rightarrow$

$Z = 0.656 \rightarrow$ and finally $\underline{\varepsilon = 0.613}$

VIII. Substituting the value of ε back into (VI) above generates -

$$f = 1.5\left(\frac{U}{d_p}\right)(\varepsilon - \varepsilon_{SB})^{0.2}(1-\varepsilon)^{1.8} = 1.5\left(\frac{1.832}{0.0015}\right)(0.613-0.4)^{0.2}(1-0.613)^{1.8}$$

$$f = \underline{243.5\,s^{-1}}$$

IX. We can now return to (V) above for the determination of α_p -

$$\alpha_p = \left[\frac{2}{\sqrt{\pi}}\sqrt{\lambda_L \rho_L C_{p,L}} + \left(\frac{d_p}{D_e}\right)^2 \sqrt{\lambda_p \rho_p C_{p,p}}\right]\sqrt{f}$$

$$\alpha_p = \underline{31{,}252\,W/m^2.K}$$

X. Returning to (I), we now insert the calculated values of α_p and α_c for the determination of α_{LS} -

$$\alpha_{LS} = 11{,}008.2 + 31{,}252 = \underline{42{,}260.24\,W/m^2.K}$$

XI. From equation 7.3, the three phase enhancement factor to the convective α_{LS} value, i.e. F_{CB}, is then -

$$F_{CB} = \left[(1-x)^{1.5} + 1.9(x)^{0.6}\left(\frac{\rho_L}{\rho_V}\right)^{0.35}\right]^{1.1}_{x \le 0.6}$$

where, as stated in subsection 7.2.1 above, $x = 0.1$ and ρ_V (read at 90 °C) = 0.424 Kg/m^3 hence,

$$F_{CB} = \left[(1-0.1)^{1.5} + 1.9(0.1)^{0.6}\left(\frac{946.66}{0.424}\right)^{0.35}\right]^{1.1}_{x \le 0.6} = \underline{9.8}$$

XII. Finally, from equation 7.2, the convective contribution can then be computed as –

$$\alpha_{CB} = \alpha_{LS} . F_{CB} . f(U)$$

where, as discussed in subsection 7.2.1.1, for $Re \ge Re_{CR}$

$$f(U) = (1660.5/Re)^{0.89} = (1660.5/84643)^{0.89} = 0.0302$$

hence

$$\alpha_{CB} = 42{,}260.24(9.8)(0.0302) = \underline{12{,}520.3\ \text{W/m}^2\text{.K}}$$

STEP B: CALCULATING NUCLEATE BOILING CONTRIBUTION, α_{NB}

Recall, from equation 7.4

$$\alpha_{NB} = \left(\alpha_{npb,p}.F_{NB}\right)^{b_E}$$

XIII. From equation 7.6, the nucleate pool boiling heat transfer of water with suspended particles, $\alpha_{npb,p}$, is calculated as –

$$\frac{\alpha_{npb,p}}{\alpha_{npb}} = \left(\frac{\lambda_M}{\lambda_L}\right)^{1.7}$$

- From equation 7.9 the thermal conductivity of solid liquid mixtures, λ_M, is found as :

$$\lambda_M = \frac{\lambda_L(1-2J)}{1+J}$$

- Where from equation 7.10, J is written as:

$$J = \varepsilon_p\left(\frac{\lambda_L - \lambda_p}{2\lambda_L + \lambda_p}\right) = 0.16\left(\frac{0.679 - 48.85}{2(0.679) + 48.85}\right) = \underline{-0.16}$$

- Substituting back into equation 7.9:

$$\lambda_M = \frac{0.679(1-2(-0.16))}{1+(-0.16)} = \underline{1.067\ \text{W/m.K}}$$

- Substituting back into equation 7.6, the above value of λ_M leads to:

$$\frac{\alpha_{npb,p}}{\alpha_{npb}} = \left(\frac{\lambda_M}{\lambda_L}\right)^{1.7} = \underline{2.16}$$

XIV. For the calculation of $\alpha_{npb,p}$ in (XIII) above, α_{npb} (the nucleate pool boiling of pure water) is found from equation 7.7 -

$$\alpha_{npb} = 0.1\left(\frac{\lambda_L}{d_b}\right)\left(\frac{\rho_L}{\rho_V}\right)^{-0.156}\left(\frac{q^{"} d_b}{\lambda_L T_{sat}}\right)^{0.674}\left(\frac{\Delta h_v (d_b)^2}{\Omega^2}\right)^{0.371}\left(\frac{\Omega^2 \rho_L}{\sigma_L d_b}\right)^{0.35}\left(\frac{\mu_L C_{p,L}}{\lambda_L}\right)^{-0.16}$$

here, $q^{"} = 167{,}830\ \text{W/m}^2$; $\Delta h_v = 2.28 \times 10^6\ \text{J/Kg}$; $T_{sat} = 373\text{K}$;

$\sigma_L = 0.060822\ \text{N/m}$ and $\Omega = \left(\lambda_L / \rho_L . C_{p,L}\right) = 1.67 \times 10^{-7}\ \text{m}^2/\text{s}$

XV. Meanwhile, the bubble departure diameter is obtained from equation, 7.8 -

$$d_b = 0.0146\Theta\left[\frac{2\sigma_L}{g(\rho_L - \rho_V)}\right]^{1/2}$$

where, as discussed in subsection 7.2.2.1, a bubble contact angle (i.e. Θ), of 45° is recommended for water

hence

$$d_b = 0.0146\Theta\left[\frac{2\sigma_L}{g(\rho_L - \rho_V)}\right]^{1/2} = \underline{0.00236\,\text{m}}$$

XVI. Substituting the value of d_b back into (XIV) above gives -

$$\alpha_{npb} = \underline{12{,}760\ \text{W/m}^2.\text{K}}$$

XVII. Substituting the value of α_{npb} back into (XIII) produces -

$$\alpha_{npb,p} = (2.16)(12{,}760) = \underline{27{,}561.6\ \text{W/m}^2.\text{K}}$$

XVIII. From equation 7.11, the nucleate boiling correction factor, F_{NB}, is obtained from -

$$F_{NB} = f(m, x) F_{pr}\left(\frac{q^{"}}{q_0^{"}}\right)^r F(d) F(R_a) F(M)$$

where $f(m, x) = 1$; $F(R_a) = 1$ and $q_0^{"} = 150{,}000\ \text{W/m}^2$.

XIX. From equation 7.12, the pressure correction factor, F_{pr} is found from –

$$F_{pr} = \left\{ 2.816\left(P_{\mathrm{R}}^{''}\right)^{0.45} + \left[3.4 + \frac{1.7}{1-\left(P_{\mathrm{R}}^{''}\right)^{7}} \right] \left(P_{\mathrm{R}}^{''}\right)^{3.7} \right\}_{P_{\mathrm{R}}^{''} \le 0.95}$$

where $P_{\mathrm{R}}^{''} = P^{''}/P_{\mathrm{CR}}^{''} = 1/220.64 = \underline{0.00453}$

hence,

$$F_{pr} = \underline{0.2483}$$

XX. In calculating F_{NB}, the r on the $(q^{''}/q_0^{''})$ term is derived from equation 7.13 -

$$r = 0.8 - (0.1)\exp\left(1.75\, P_{\mathrm{R}}^{''}\right) = 0.8 - (0.1)\exp(1.75 \text{ x } 00453) = \underline{0.699}$$

XXI. From equation 7.14, the diameteral correction factor $F(d)$ is determined as -

$$F(d) = \left(\frac{D_{\mathrm{e}}}{D_{\mathrm{nor}}} \right)^{-0.4}$$

where $D_{\mathrm{nor}} = 0.01$ m

and hence

$$F(d) = \left(\frac{0.0146}{0.01} \right)^{-0.4} = \underline{0.859}$$

XXII. Meanwhile, from equation 7.16, the molecular weight correction factor is calculated as -

$$F(M) = 0.36(M)^{0.27}$$

where for H_2O as the working liquid $M = 18$,

$$F(M) = \underline{0.7856}$$

XXIII. Hence substituting the values established in (XIX), (XX), (XXI) and (XXII) back into (XVIII), F_{NB} proves to be

$$F_{\mathrm{NB}} = \underline{0.1814}$$

XXIV. Finally, returning to equation 7.4, α_{NB} then computes as –

$$\alpha_{NB} = \left(\alpha_{npb,p}.F_{NB}\right)^{b_E}$$

where, as stated in subsection 7.2.2, $b_E = 1.05$

hence

$$\alpha_{NB} = \left((27{,}561.6)(0.1814)\right)^{1.05}$$

$$\alpha_{NB} = \underline{7{,}654 \text{ W/m}^2.\text{K}}$$

FINAL STEP C: CALCULATING THE 3-PHASE FLOW BOILING COEFFICIENT, $\alpha_{T.F.B}$

Finally from equation 7.1, the predicted overall three-phase flow boiling heat transfer coefficient is determined as below -

$$\alpha_{T.F.B} = \left[(\alpha_{NB})^{t_R} + (\alpha_{CB})^{t_R} \right]^{1/t_R}$$

where $t_R = 3$

$$\alpha_{T.F.B} = \left[(7{,}654)^3 + (12{,}520.3)^3 \right]^{1/3}$$

$$\alpha_{T.F.B} = \underline{\underline{13{,}409 \text{ W/m}^2.\text{K}}}$$

7.3. COMPARISON WITH HEAT TRANSFER EXPERIMENTAL RESULTS

7.3.1. COMPARING THE PREDICTED & EXPERIMENTAL BOILING COEFFICIENTS

The experimentally obtained heat transfer data has been compared with the model calculation for vapour-liquid-solid three-phase flow boiling. The heat transfer coefficients proposed by the presented correlation have been calculated across our given heat flux and flow velocity range.

Figures 7.2-7.4 present results comparing the correlated and experimental three-phase flow boiling coefficient(s), for our three different stainless steel particle sizes (d_p = 1.5, 2.0 and 2.5 mm). The graphs prove that the proposed correlation is able to describe the experimental data within a maximum deviation of 20-30 % for all employed particle sizes. To allow for a better examination of the presented results, the calculated and experimental three-phase heat transfer coefficients have been compared over the separate boiling regions as shown in Figures 7.5(a)-(c), for the case of stainless steel 2.0 mm diameter particles, at a particle volume fraction of 16 %.

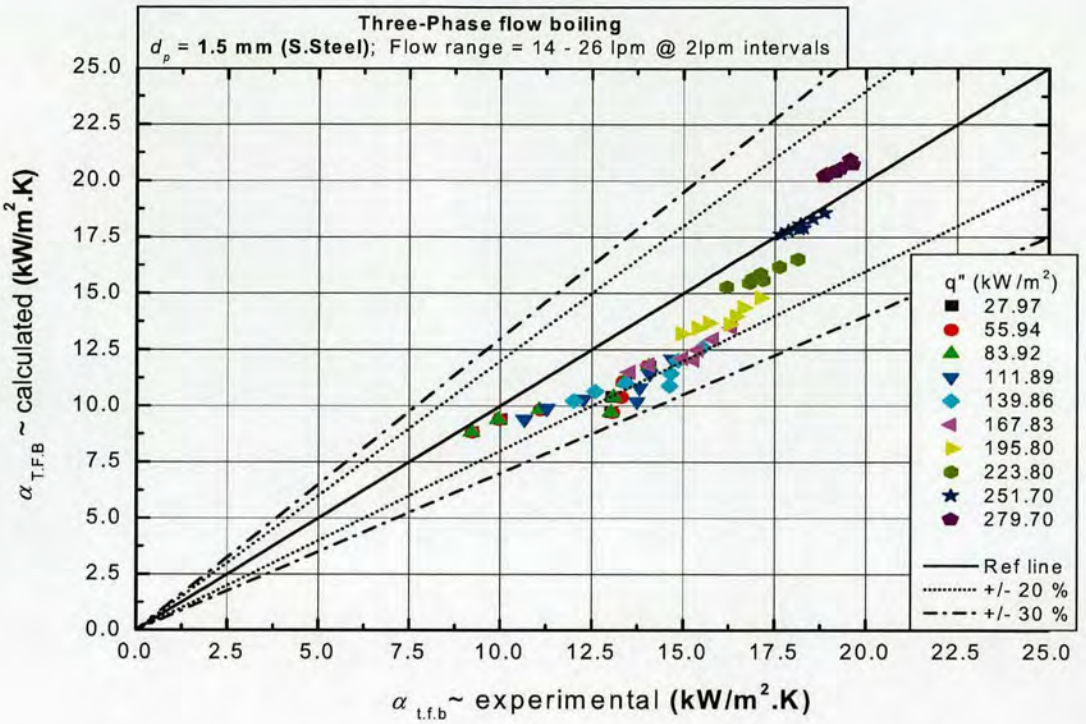

Figure 7.2: Comparison between calculated and experimental heat transfer coefficient for three-phase flow boiling, using 1.5 mm stainless steel particles at 16 % particle volume fraction.

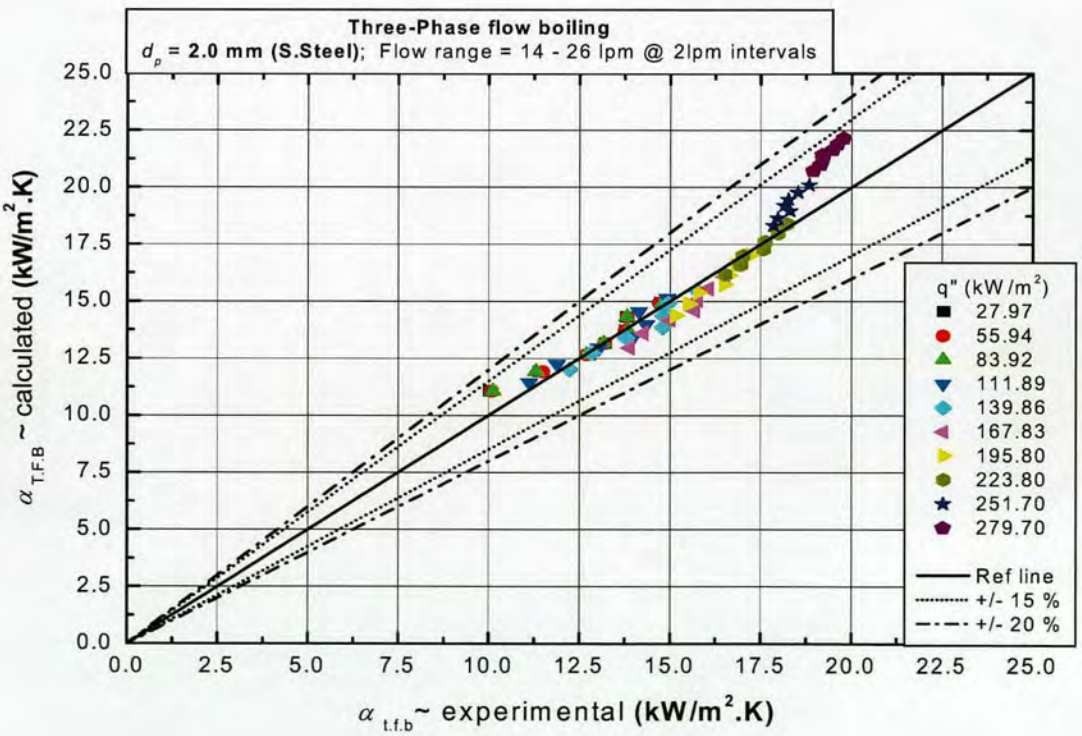

Figure 7.3: Comparison between calculated and experimental heat transfer coefficient for three-phase flow boiling, using 2.0 mm stainless steel particles at 16 % particle volume fraction.

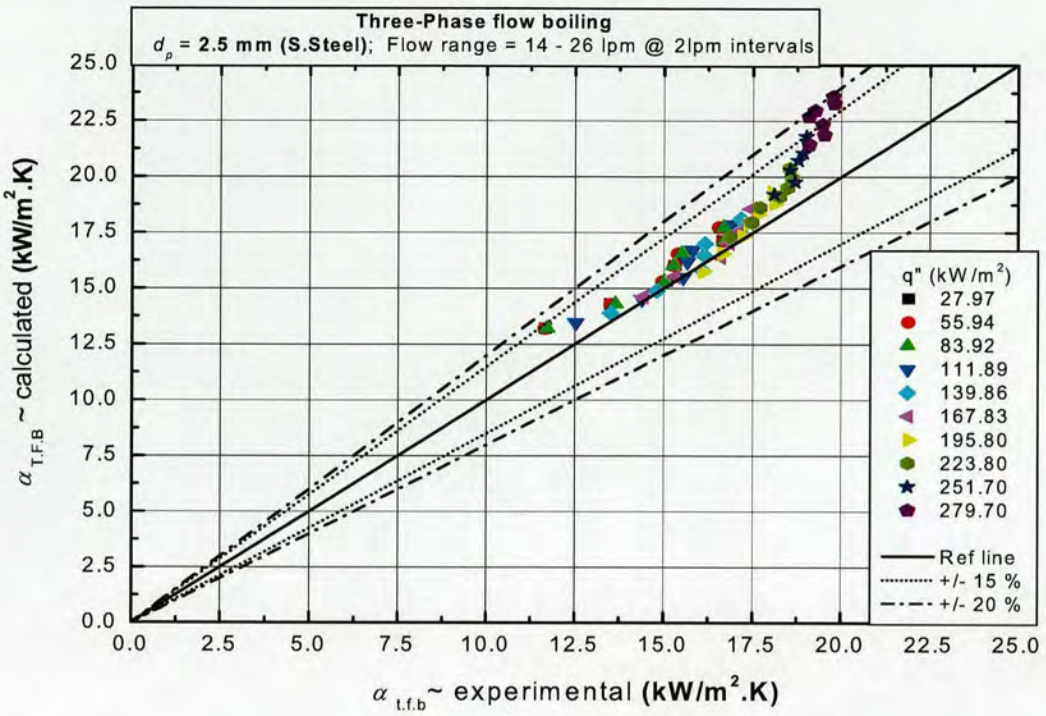

Figure 7.4: Comparison between calculated and experimental heat transfer coefficient for three-phase flow boiling, using 2.5 mm stainless steel particles at 16 % particle volume fraction.

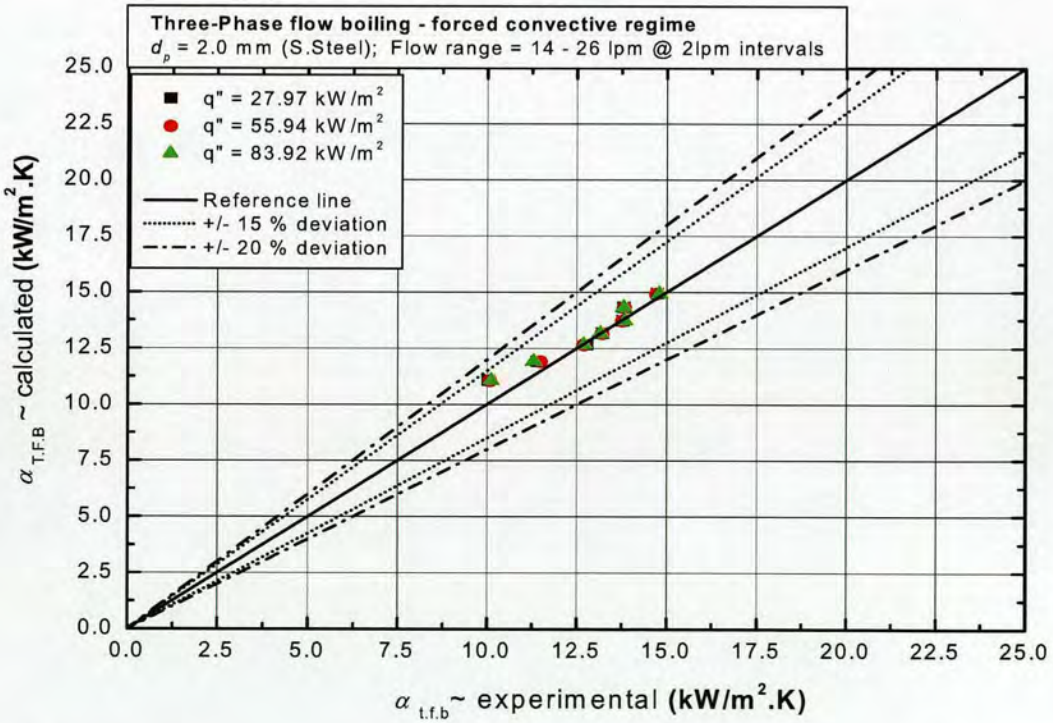

(a)

Figure 7.5: (a) Comparison between calculated and experimental heat transfer coefficient over forced convective region of 3-phase boiling. Results obtained for 2 mm stainless steel particles at 16 % particle volume fraction.

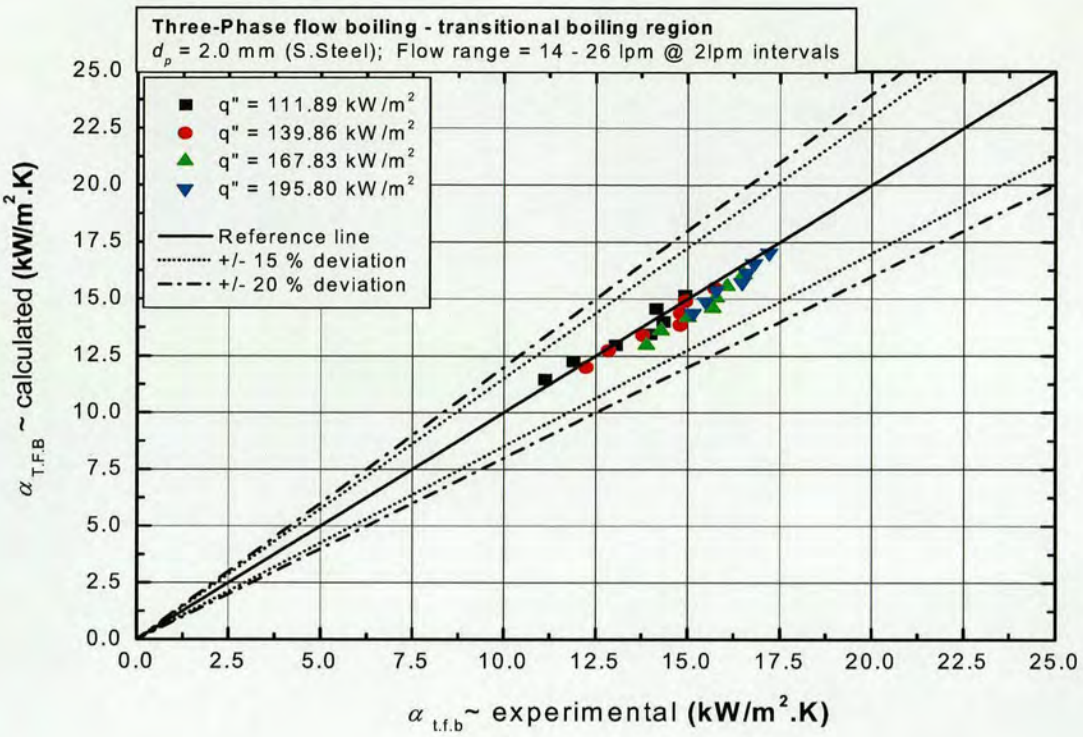

(b)

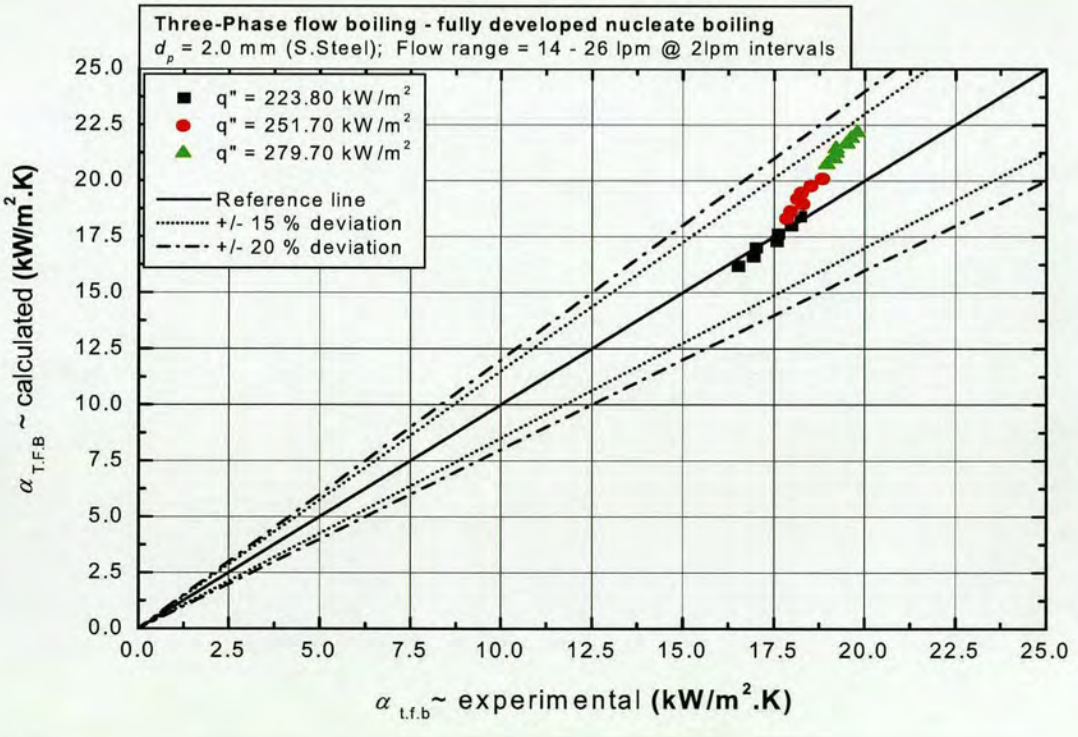

(c)

Figure 7.5: Comparison between calculated and experimental heat transfer coefficient over (b) transitional boiling region and (c) fully developed nucleate boiling region of 3-phase boiling. Results obtained for 2 mm stainless steel particles at 16 % particle volume fraction.

7.3.2. Effect of Operating Parameters on The Correlation For Three-Phase (v-l-s) Flow Boiling

The effects of Reynolds number and heat flux on the prediction of the suggested model are shown in Figures 7.6-7.7, for the case of stainless steel 2.5 mm diameter particles at a particle volume fraction of 16 %.

Figure 7.6 shows that across our flow boiling range, fluid velocity influences the predicted boiling coefficient in a manner similar to the trend identified for the measured three-phase heat transfer coefficient, as previously depicted in *Chapter 5*, Figures 5.10 to 5.12. From the plot of Figure 7.6, we see that, initially, the heat transfer coefficient increases with increasing superficial velocity, approaches a maximum value, after which further increase of liquid flowrate results in heat transfer retardation.

Meanwhile, Figure 7.7 presents the effect of heat flux on the calculated heat transfer coefficient. In the forced convective region, the three-phase boiling coefficient is affected by velocity, but independent of heat flux. However, above a minimum wall superheat the calculated boiling coefficient rapidly increases with heat flux, becoming less responsive to variation in fluid velocity. The generated trend is consistent with experimentally observed behaviour as reported in *Chapter 5*.

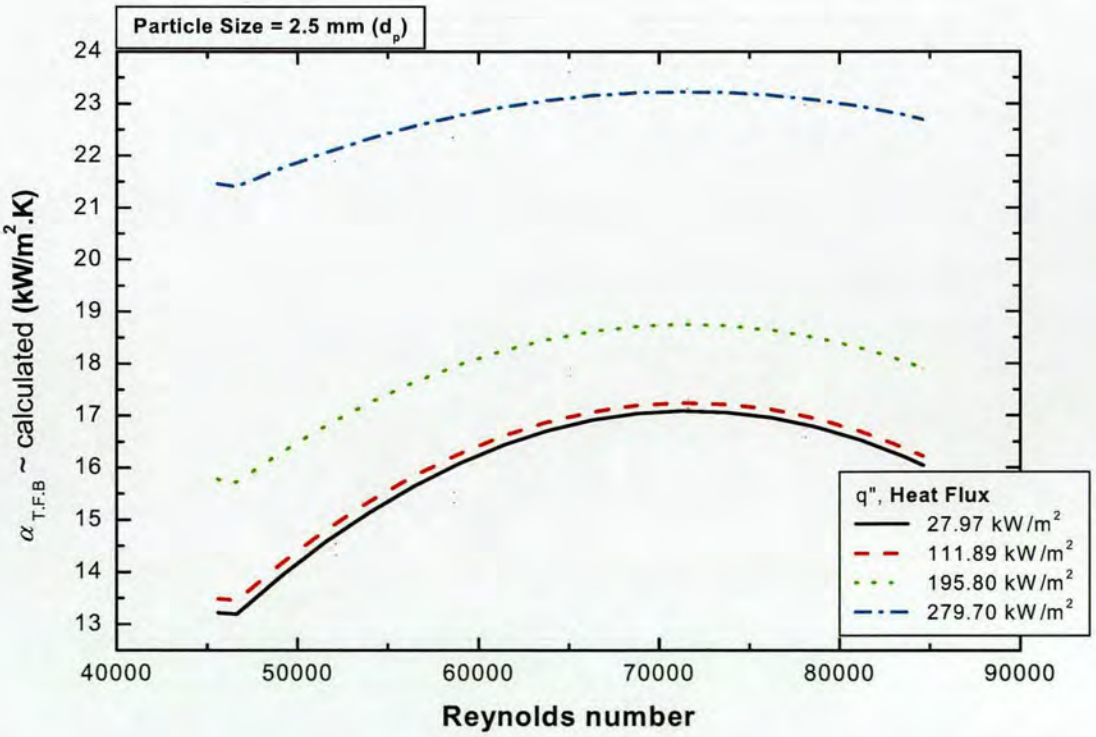

Figure 7.6: Effect of *Re* on the predicted three-phase flow boiling coefficient $\alpha_{T.F.B}$. Results presented over a range of heat fluxes.

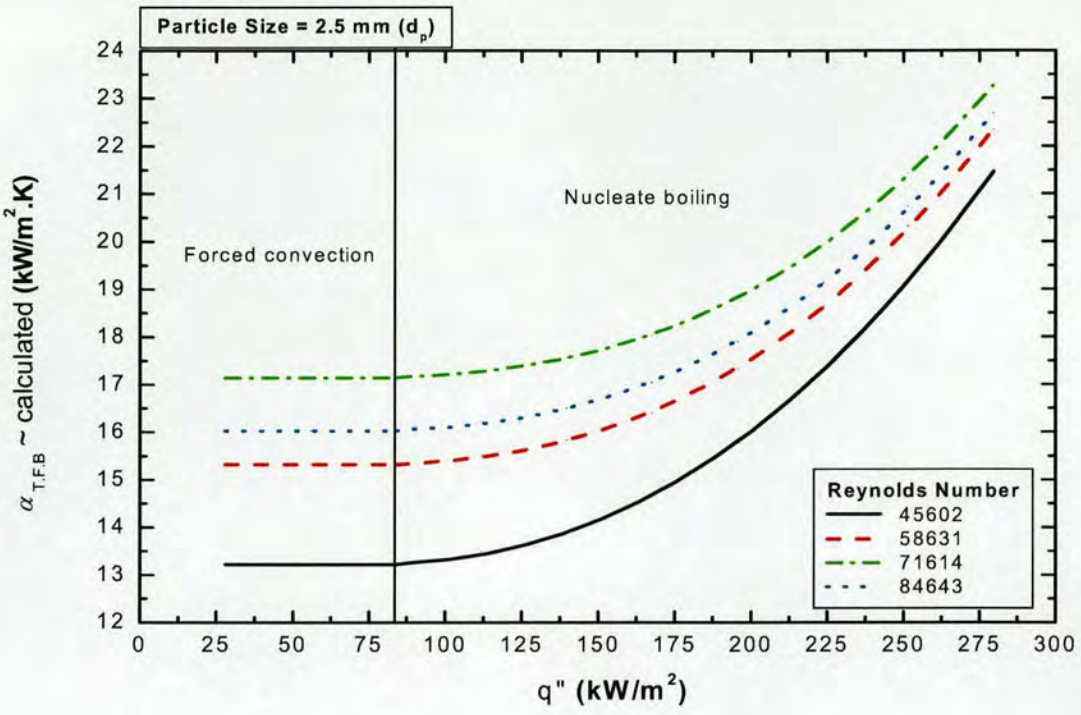

Figure 7.7: Effect of $q^{"}$ on the predicted three-phase flow boiling coefficient $\alpha_{T.F.B}$. Results presented for a range of Reynolds numbers.

In addition to the final results shown in Figures 7.2 through to Figures 7.5(a,b,c), the effect of modified $f(U)$ and b_E on the accuracy of our proposed correlation is presented in Figures 7.8-7.9; in this manner it is possible for one to gauge the sensitivity of the velocity adjustment factor and nucleate boiling enhancement exponent respectively. As discussed earlier, the aim has been to find a correlation that best describes our experimental data. For such a comparison, the best fitting curve has been defined as the level where the mean deviation between the experimental and the correlated heat transfer coefficient can no longer be improved by the modification of either $f(U)$ or b_E.

To this effect, Figure 7.8 presents the influence of the convective velocity adjustment factor, $f(U)$, on the variation of heat transfer coefficient with Reynolds number. In the main graph label, our working $f(U)$ value has been highlighted with a bold-type font. Experimental data for the case of stainless steel 2.0 mm diameter particles, at a particle volume concentration of 16%, have also been included for a better comparison.

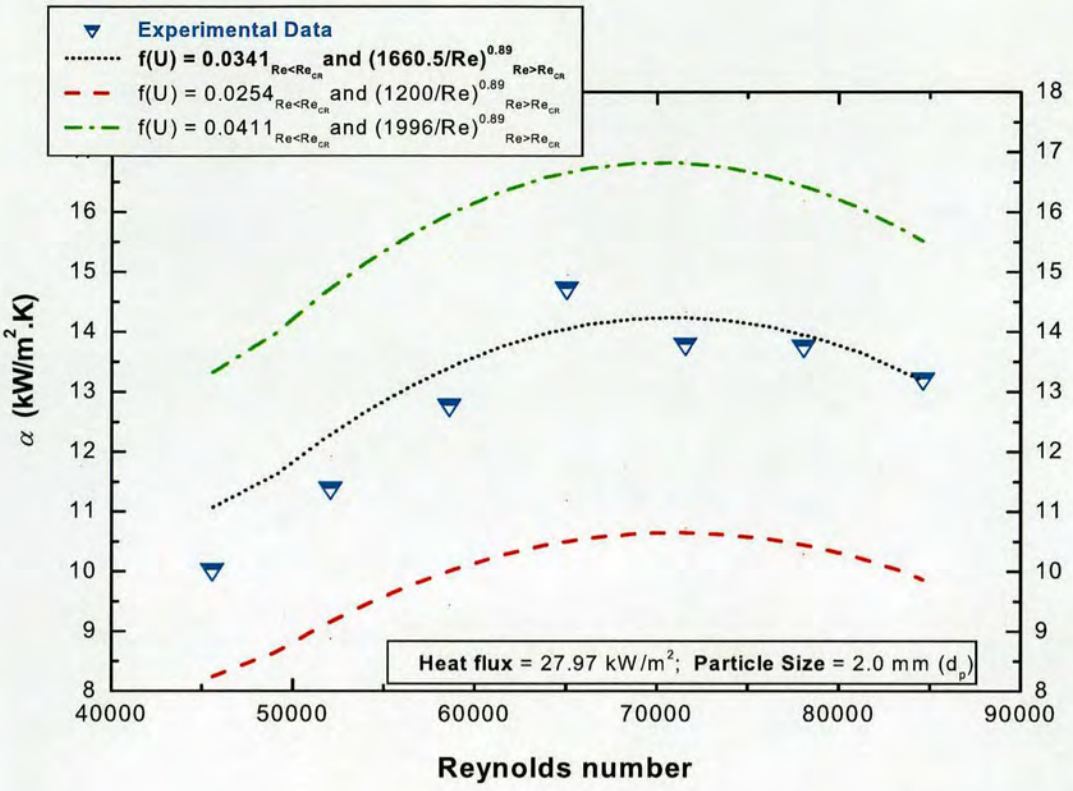

Figure 7.8: Influence of the convective velocity adjustment factor, $f(U)$, on the variation of heat transfer coefficient with Reynolds number, for 2.0 mm stainless steel particles at 16 % particle volume concentration.

Meanwhile, Figure 7.9 demonstrates the effect of modified b_E on the accuracy of the suggested correlation. Again, in the main graph label, our working b_E value has been highlighted with a bold-type font and experimental data for the case of stainless steel 2.0 mm diameter particles have also been included. More importantly, as well demonstrating the sensitivity of the adjustment and enhancement factors, Figure 7.9 clearly shows that with b_E and $f(U)$ set to a value of 1, Li Xiulun's original correlation (as defined in equation 3.61) overpredicts the experimental result by a fairly significant margin.

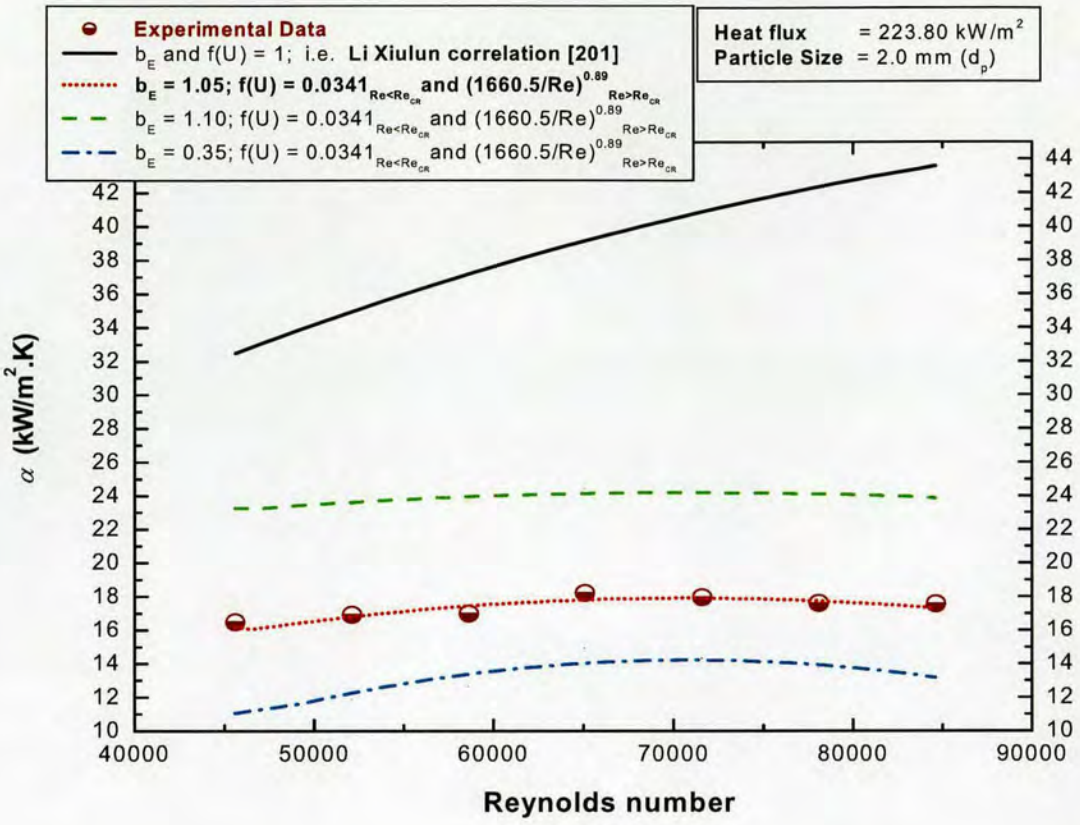

Figure 7.9: Effect of modified b_E, nucleate boiling enhancement exponent, on the accuracy of the theoretical values predicted by equation 7.1. Also compares the result obtained from the correlation of Li Xiulun *et al.* [201].

7.4. SUMMARISING THE CORRELATION OF HEAT TRANSFER IN (V-L-S) CIRCULATING FLUIDISED BED BOILING

A general equation has been developed for the prediction of our experimentally obtained three-phase flow boiling heat transfer coefficients. The correlation is based on the two-phase flow boiling asymptotic model and covers both the three-phase forced convective region and the three-phase nucleate boiling region.

The expression:

$$\alpha_{\text{T.F.B}} = \left[\left(\alpha_{\text{NB}}\right)^{t_R} + \left(\alpha_{\text{CB}}\right)^{t_R} \right]^{1/t_R}$$

$$\alpha_{\text{T.F.B}} = \left[\left\{ \left(\alpha_{\text{npb,p}} . F_{\text{NB}}\right)^{b_E} \right\}^{t_R} + \left\{ \alpha_{\text{LS}} . F_{\text{CB}} . \text{f}(U) \right\}^{t_R} \right]^{1/t_R}$$

In this *Chapter* the model's ability to predict the experimental data has been successfully demonstrated. When applied to experimentally obtained data for stainless steel particles (d_p = 1.5, 2.0 and 2.5 mm, ε_P = 16 %), the correlation is able to predict the experimental data within a 20-30 % maximum deviation.

Further still, the model accurately predicts the experimentally observed operating parameter trends, i.e. the effect of varying heat flux and superficial velocity on the rate of heat transfer in three-phase flow boiling as reported in *Chapter 5*.

CHAPTER 8: CONCLUSIONS AND FUTURE OUTLOOKS

8.1. CONCLUSIONS

A three-phase (vapour-liquid-solid) circulating fluidised bed combines the features of heat transfer enhancement and fouling prevention. However, the mechanisms of flow and heat transfer are still not well understood due to the complexity of the multiphase system. Hence, to contribute to the development of the fluidised bed enhancement technique, the present study has attempted to systematically investigate the heat transfer performance of a proposed three-phase flow boiling device, and in so doing, to determine the mechanisms responsible for the improvement of the boiling coefficient. To this regard, an extensive series of experiments have been carried out over a stipulated range of operating parameters, resulting in a comprehensive theory regarding the enhancement of the boiling coefficient in the presence of fluidised particles

Beginning with a detailed explanation regarding the principles of heat exchanger fouling and boiling heat transfer, the basic background information on this field of heat transfer science has been given in *Chapter 2*. The literature review performed in *Chapter 3* has been able to summarise the various fouling and heat transfer enhancement techniques, and by comparing the benefits and penalties of the different strategies, has also been able to contextualise the importance of the circulating fluidised bed within the current state of research, and thereby emphasise the relevance of the present study.

The application of the technology was originally confined to non-boiling operations where numerous investigators were able to successfully establish the fact that fluidised particles had the ability to promote the rate of heat transfer, not only by removing large quantities of heat per unit time and area from a heated surface, but also by promoting the level of turbulence within the liquid flow. To this regard, both the experimental results and the established heat transfer models from the most relevant publications have been analysed, and where present, differences and discrepancies have been compared and discussed.

However, although scale formation is much more severe during boiling heat transfer, information regarding the mechanisms of boiler fouler is still relatively arcane, with no generalised conclusions on the topic readily existent. Nevertheless, despite these limitations, the review of the available literature does show that scale deposition substantial affects the boiling phenomena by effectively altering the characteristics of the heater surface. Therefore, given that nucleate boiling is the preferred heat transfer process for many industrial applications, it is of vital commercial interest that methods are developed for the enhancement of the nucleate boiling coefficient and prevention of boiler fouling. According to the available literature the most proficient methods for the attainment of long-term minimum fouling stability and enhanced boiling performance are *Enhanced boiling surfaces*

(i.e. treated and structured surfaces) and *Additives* for boiling liquid systems. Both of these categorises have been extensively reviewed, with key emphasis placed on the latter. Unlike single-phase flow, studies regarding the implementation of additives during boiling heat transfer are quite rare, and within the limited literature available, most of the investigations are primarily concerned with the influence of solid particles in boiling liquid pools. However, the scientific and commercial sectors have recently awakened to the possibility of exploring the heat transfer and fouling mitigation effect of solid particles, under the combined conditions of liquid fluidisation and flow boiling heat transfer. Therefore, as well as three-phase flow boiling experimental effects and tendencies, the most important correlations from the few contributing authors' have been described, including the heat transfer mechanisms that are held responsible for the observed particle enhancement effect.

Hence, in order to gain relevant and accurate experimental results concerning the nature of heat transfer in (vapour-liquid-solid) fluidisation, a three-phase boiling device has been successfully designed and developed as described in *Chapter 4*. Within the test unit, a cartridge heater rod encased in a length of copper has been employed as the electrical heat source, and the surface from which we have been able to accurately measure the wall excess temperature as a function of heat flux, liquid velocity and particle diameter. To properly establish the effect of solid particles on the rate of boiling heat transfer, experiments have first been conducted in the conventional two-phase flow boiling mode; upon completion, particles have then been introduced into the boiling system and the enhanced boiling coefficient determined over our given particle size range. Furthermore, in designing our three-phase circulating fluidised bed, the use of transparent glass sections has allowed us to visualise the processes occurring within the bed, and as a result, we have been able to perform an in-depth analysis on the behaviour of the multiphase flow system via the use of a high-speed video recorder equipped with a zoom lens

Therefore, by combining the results obtained from our heat transfer and flow visualisation experiments, recognised effects and features have been clearly assigned to heat transfer tendencies, allowing for a comprehensive description of the enhancement process in three-phase flow boiling.

From the work detailed above our main conclusions can be summarised as follows

I. **Boiling heat transfer and the enhancement effect of particles**: For our particular test geometry and examined parametric range, the investigation has revealed that compared with conventional two-phase flow boiling, the addition of solid particles to the boiling system significantly increases the measured rate of boiling heat transfer. The observed tendency has been justified by way of a series of mechanistic suppositions. For instance,

it is believed that in the vicinity of the heater surface, the motion of the fluidised particles causes the erosion of the laminar sublayer, which itself is an impediment to the heat transfer process. Furthermore, the flux of particles sweep bubbles away from the heating surface, shorten their time of growth, and thus elevating the boiling heat transfer. The interaction of particles with generated vapour bubbles also influences the flow field within the fluidised bed, this is essentially due to the fact that when particles penetrate large bubbles, the interaction yields an increased number of smaller bubbles which agitate the fluid flow, thereby promoting the convective heat transfer and, in turn, the flow boiling heat transfer coefficient.

In addition to the above, the contact between the particles and the heating surface has also been identified as a key factor in the boiling heat transfer enhancement. In our estimation, the boiling site density (i.e. number of active nucleation sites per unit heat transfer surface area) is increased due to the particle-wall interactions, as well as the additional surface area brought about by the fluidised solid phase. This increase in the number of active nucleation sites supplements the bubble formation process, thereby giving rise to higher boiling coefficients when compared to conventional two-phase flow boiling.

II. **The attainable heat transfer enhancement and the influence of liquid velocity**: Analysis has shown that the magnitude of the attainable heat transfer enhancement varies according to the selected set of operating conditions. For instance, over most of the examined heat flux range (especially referring to q'' values in the forced convective and transitional boiling regimes), the results obtained at our test section show that in the lower liquid velocity region, the estimated heat transfer enhancement percentage varies linearly with increasing Reynolds number. However, after attaining a maximum at a critical value of *Re*, further increases of liquid flowrate results in the degradation of the enhancement coefficient. As discussed in *Chapter 3*, the observed trend is a feature commonly associated with heat transfer enhancement in non-boiling liquid-solid fluidised bed operations [73,74,81,82], here the cited investigators' have also identified the particle-wall interaction as a key factor in the enhancement of heat transfer. Generally, the accepted theory states that at higher liquid velocities, the increase in the volume fraction of the continuous phase reduces the particle-wall impact frequency and, in turn, the measured rates of heat transfer. Therefore, in the context of our own three-phase flow boiling investigations, the trend described by the liquid velocity relationship, leads us to believe that in the high flowrate region (where the concentration, or local solid hold-up, of particles within the heated flow channel is visibly reduced) deterioration of the three-phase boiling coefficient, and by extension the attainable percentage enhancement,

stems from the reduction in the number and frequency of particle-wall collisions experienced on the heater surface. Through the use of our described flow visualisation techniques, we have been able to substantiate the above hypothesis, by establishing the unique relationship between bed voidage, liquid velocity and particle speed.

In summary, the results have been able to prove that in our specific boiling system, increasing liquid velocity causes a corresponding increase in the estimated average particle rise velocity as well as the volume fraction of the continuous fluid phase. Both conditions engender the reduction of the particle-wall collision frequency, thus explaining the accompanying decrease in the measured rate of heat transfer at higher liquid superficial velocities.

III. **The attainable heat transfer enhancement and the influence of heat flux**: As stated above, and discussed in *Chapter 6*, increasing heat flux promotes the nucleate boiling heat transfer, by making available more active nucleation sites on the heater surface. The result of the heightened bubble formation process is an increased vapour fraction within the test section. Given the importance of the particle-bubble interactions as outlined above, one would expect that at higher heat fluxes, the increased vapour production would lead to greater bubble disruption in the presence of solid particles, and hence a more pronounced boiling heat transfer enhancement. However, results obtained at our test section, show that for any given liquid delivery rate, although increasing heat flux augments the three-phase flow boiling coefficient (i.e. $\alpha_{\text{t.f.b}}$), conversely, in respect of two-phase flow boiling enhancement, the magnitude of the attainable heat transfer enhancement percentage (i.e. $\alpha_{\text{E.T}}$), steadily diminishes as we transit towards higher q'' values. Analysis of our flow visualisation experiments reveals that as heat flux is progressively increased, bubbles forming on the heater surface coalesce to create larger, elongated vapour patches, which typically remain attached to the wall, thereby preventing the flux of particles from engaging the heater surface and effecting the enhancement of heat transfer. The end result is an overall decrease in the value of the calculated enhancement percentage $\alpha_{\text{E.T}}$. Therefore, it can be said that for our particular test geometry and heater arrangement, increasing heat flux exhibits a counter-intuitive effect on the enhancement of the two-phase flow boiling coefficient (in other words minimum $\alpha_{\text{E.T}}$ is encountered at maximum q'' for all examined liquid flowrates).

IV. **The attainable heat transfer enhancement and the influence of particle diameter**: Three-phase flow boiling heat transfer enhancement strongly depends on particle size. In our opinion, larger diameter particles have a higher momentum for the disruption of the thermal boundary layer, thereby assuring a greater heat transfer enhancement. However,

our findings also show that the benefit to the estimated enhancement coefficient, resultant from the use of progressively larger sized particles, is overshadowed by the heat transfer limitations identified in points (II) and (III). In the case of the former, the reduced particle-wall collision frequency, observed at higher liquid velocities, obliterates the enhancement benefit of increasing particle size; likewise, for the case of the latter, during fully developed nucleate boiling, the described 'bubble-push' effect suppresses the increased momentum contribution of the larger sized particles.

V. **Defining the boundaries of the enhancement**: As implied in point (IV) above, by combining our reported parametric tendencies, we have been able to successfully determine the enhancement boundaries within our three-phase (v-l-s) circulating fluidised bed. In summary, our findings have shown that as well as a reduced particle diameter, a high heat flux, and a high liquid delivery rate are detrimental to the achievable heat transfer enhancement. These limitations have been clearly identified, both by graphical representation, and digital imaging, as shown in *Chapter 5*, Figures 5.28(a,b) and *Chapter 6*, Figure 6.6 respectively. Knowledge of such operating boundaries could be of vital benefit to the design of the three-phase boiling device for use in industrial applications.

VI. **Correlating heat transfer in (v-l-s) flow boiling**: In the final stage of the project, a modified approach for predicting heat transfer in our three-phase flow boiling system has been developed. This has been accomplished by converting the conclusions drawn from the experimental results into assumptions which form the basis for theoretical considerations of the three-phase flow boiling process. Our correlated heat transfer coefficient has been compared with the experimental data and the agreement has been shown to be very good. The measured boiling coefficients have also been compared with another available three-phase flow boiling model (see [201]), which was found to overpredict our experimental data.

8.2. FUTURE OUTLOOKS

Future work should concentrate on the following areas:

Fouling mitigation potential of the boiling device: At this stage, although no work has been done to establish the cleaning effect of the fluidised particles, their proven ability to suppress the measured wall excess temperature, presumably not only enhances the heat transfer coefficient, but also disrupts conditions favourable to fouling (as explained in *Chapter 3*, for many fluids fouling increases with increase in heat transfer surface temperature). Thus, compared with other boiling heat transfer enhancement techniques, our three-phase circulating fluidised bed certainly appears to have the potential to mitigate fouling by a combination of abrasive action and wall temperature suppression. However, systematic and detailed work must be undertaken in order to verify such an assumption.

Pressure loss in the three-phase circulating fluidised bed: The pressure loss across the bed, resultant from the inclusion of solid particles, is undoubtedly a parameter worthy of proper investigation. Although provision was made for pressure drop measurements at the test section, no visible tendency could be discerned from results obtained during extensive preliminary testing. It is possible that due to the size of the flow channel, our installed pressure transducers could not readily detect any fluctuation in $\Delta P''$. Nevertheless, this knowledge gap must be addressed, even though it probably would require the future redesign of the test section.

Influence of alternative particle physical properties: As explained in *Chapter 4*, a wide range of particles of varying materials and sizes were actually procured for use in our heat transfer enhancement investigations; however, for this present study, due to the limitations of time, we have not been able to examine the influence of parameters such as particle material and initial particle volume fraction. Presumably the larger density particles (i.e. copper, with ρ_p = 8960 kg/m^3) would have a higher momentum to collide with the wall and disrupt the boundary layer. Also, increasing the average solid holdup in the system (i.e. the initial particle volume fraction) would result in higher local solid hold-ups, ε_P'', both in the near wall and bulk flow regions. As a consequence, the probability of particle-bubble and particle-wall collisions would be greatly improved. The former would elevate the level of turbulence, whilst the latter would increase the number of nucleation sites available for boiling heat transfer. These suppositions would all have to be confirmed in order to fully appreciate the role of fluidised particles in the enhancement of heat transfer in three-phase flow boiling.

Bed hydrodynamics: Finally, as demonstrated in *Chapter 6*, the hydrodynamic behaviour of the bed clearly controls both the particle-wall collision frequency and the state of aggregation

of the solid phase within the bed. All of these factors influence the measured rate of heat transfer at the test section. Therefore, for a more comprehensive description of the governing heat transfer enhancement mechanisms, further work must be done to determine the hydrodynamic characteristics of our three-phase flow boiling device, including the estimation of the axial and radial profiles of solid holdup and solid velocity.

In conclusion, within the limits of our set objectives, this work has lead to an understanding of the heat transfer mechanisms during three-phase (vapour-liquid-solid) circulating fluidised bed boiling. Based on an extensive series of heat transfer and visualisation experiments, the main influencing effects on the performance of the multiphase boiling device have been identified, leading to a predictive semi-theoretical correlation which could help improve the design of fluidised bed heat exchangers.

REFERENCES

1. Müller-Steinhagen, H., "Heat exchanger fouling: Mitigation and cleaning technologies," Publico Publications, Germany, ISBN 0-85295-4360, 2000.

2. Najibi, S.H., "Heat transfer and heat transfer fouling during subcooled flow boiling for electrolyte solutions," Ph.D Thesis, The University of Surrey, UK, 1997

3. Epstein, N., "Thinking about heat exchanger fouling: A 5x5 matrix," *Heat Transfer Engng.*, vol. 4, pp. 43-56, 1983.

4. Kern, D.Q. and Seaton, R.A., "A theoretical analysis of thermal surface fouling," *Brit. Chem. Eng.*, vol. 4, no. 5, pp. 258-262, 1959.

5. Taborek, J. *et al.*, "Fouling-the major unresolved problem in heat transfer," *Chem. Eng. Prog.*, vol. 68, no.2: pp. 59-67 and no. 7: pp. 69-78, 1972.

6. Taborek, J., "Assessment of fouling research in the design of heat exchangers," In: *Proceedings of 'Fouling mitigation of industrial heat exchange equipment,'* an international conference, San Luis Obispo, California, USA, June 1995.

7. Garrett-Price, B.A. *et al.*, "Fouling of heat exchangers-characteristics, costs, prevention, control and removal," Noyes Publications, Park Ridge, New Jersey, 1985.

8. Pritcahrd, A.M., "The economics of fouling," In: *Fouling science and technology*, Melo, L.F., Bott, T.R. and Bernardo, C.A., eds., NATO ASI Series E, vol. 145, Kluwer Academic Publishers, 1987.

9. Müller-Steinhagen, H., "Fouling of heat exchangers surfaces," *Chemistry and Industry*, vol. 5, pp. 171-175, 1995.

10. Kreith, F. and Black, W.Z., "Basic heat transfer," Harper & Row Publishers, New York, pp. 464-479, 1980.

11. Incropera, F.P. and DeWitt, D.P., "Fundamentals of heat and mass transfer," Wiley, J. and Sons, Inc., 4th edition, ISBN 0-471-30460-3, 1996.

12. Moscik, I. and Broder, J., "Discussion of heat transfer from a platinum wire submerged in water," *Recznicki Chemie*, vol. 6, pp. 329-354, 1926.

13. McAdams, W.H., Woods, W.K. and Brayan, R.L., "Vaporization inside horizontal tubes," *Trans. ASME*, vol. 63, pp. 545-552, 1941.

14. Davidson, W.F., "Studies of heat transmission through boiler tubing at pressures from 500 to 3300 psi," *Trans. ASME*, vol. 65, pp.551-554, 1943.

15. Gunther, F.C., "Photographic study of surface boiling heat transfer to water with forced convection," *Jet Propulsion Laboratory, Pasadena, CA, Progress Report* no. 4-120; also *Trans. ASME*, vol. 73, pp. 115-124, 1951.

16. Lienhard IV, J.H. and Lienhard V, J.H., "A heat transfer text book," 3rd edition, Published by Phlogiston Press, Cambridge, Massachusetts, USA, 2003.

17. Bergles, A.E. and Rohsenow, W.M., "The determination of forced convection surface boiling," *ASME J. Heat Transfer*, vol. 86, pp. 365-372, 1964.

18. Steiner, D. and Ozawa, M., "Flow boiling heat transfer in horizontal and vertical tubes," In: *Heat exchangers-Theory and Practise*, Taborek, J., Hewitt, G.F. and Afgan, N., eds., Hemisphere, New York, 1983.

19. Rohsenow, W.M., "A method of correlating heat transfer data for surface boiling of liquids," *Trans. ASME*, vol. 74, pp. 969-976, 1952.

20. Chen, J.C., "A correlation for boiling heat transfer to saturated fluids in convective flow," *Ind. Eng. Chem. Process Design Develop.*, vol. 5, no. 3, pp. 322-329, 1966. Reprint of ASME paper 63-HT-34, 1963.

21. Churchill, S.W., "The interpretation and use of rate data," Hemisphere, New York, 1974.

22. Shah, M.M., "A new correlation for heat transfer during boiling flow through pipes" *ASHRAE Trans.*, vol. 82, no. 2, pp. 66-86, 1976.

23. Shah, M.M., "Chart correlation for saturated boiling heat transfer: equations and further study," *ASHRAE Trans.*, vol. 88, part 1, no. 2673, pp. 185-196, 1982.

24. Chawla, J.M., "Wärmeübergang und druckabfall in waa-grechten rohren bei der strömung von verdampfenden kältemitteln," *Kältetechnik-Klimatisierung*, vol. 19, no. 8, pp. 246-252, 1967.

25. Gungor, K.E. and Winterton, R.H.S., "A general correlation for flow boiling in tubes and annuli," *Int. J. Heat Mass Transfer*, vol. 29, no. 3, pp. 351-358, 1986.

26. Gungor, K.E. and Winterton, R.H.S., "Simplified general correlation for saturated flow boiling and comparison of correlations with data" *Chem. Eng. Res. Des.*, vol. 65, pp. 148-156, 1987.

27. Kandlikar, S.G., "An improved correlation for predicting boiling heat transfer in horizontal and vertical tubes" In: *Heat Exchangers for Two-Phase Flow Applications*, ASME, New York, 1983.

28. Kandlikar, S.G., "A general correlation for saturated two-phase flow boiling heat transfer inside horizontal and vertical tubes" *ASME J. Heat Transfer* , vol. 112, pp. 219-228, 1990; Boiling and Condensation in Heat Transfer Equipment, ASME HTD vol. 85, 1987.

29. Steiner, D. and Taborek, J., "Flow boiling heat transfer in vertical tubes correlated by an asymptotic model" *Heat Transfer Engineering*, vol. 13, no. 2, pp. 43-69, 1992.

30. Chenoweth, J.M., "General design of heat exchangers for fouling conditions," In: *Proceedings of the NATO Advanced Study Institute on Advances in Fouling Science and Technology*, Alvor, Portugal, 1987.

31. French, M.A., "Chemical cleaning in practice," *Conference on Progress in the Prevention of Fouling in Industrial Plant*, University of Nottingham, UK, 1981.

32. Lewis, R.O., "Influence of biofouling counter measures on corrosion of heat exchanger materials in seawater," *Materials Performance*, vol. 21, no. 9, pp.31-38, 1982.

33. Sasscer, D.S., Morgan, T.O., Rivera, C., Ernst, R., Scot, A.C. and Summerson, T.J., "Oceanic corrosion tests of bare and zinc-protected aluminum alloys for seawater heat exchangers," *Ocean Science and Engineering*, vol. 9, no. 3, pp. 269-371, 1984.

34. Bell, R., "State of the art mechanical systems for scale and biofilm controls," Electric Power Research Institute (EPRI), Report CS-4339, November 1985.

35. Haluska, J.L., "Process fouling control by effective antifoulant selection," Paper no. 153, presented at *Corrosion/76*, Houston, March 22-26, 1976.

36. Birchall, G.A., "Achieving microbiolocal control in open recirculating cooling systems," *Conference on Progress in the Prevention of Fouling in Industrial Plant*, University of Nottingham, UK, 1981.

37. Miller, P.C. and Bott, T.R., "The removal of biolocal films using sodium hypochloride," *Int. Chem. Eng. Conf. on Fouling Science or Art?*, The University of Surrey, UK, 1979.

38. Ryznar, J.W., "A new index for determining the amount of calcium carbonate formed by water," *J. Amer. Water Works Ass.*, vol. 36, pp. 472, 1944.

39. KALVO VOGLER GMBH, "Automatisches reinigungssystem für kondensatoren und röhrenwärmeaustauscher."

40. Troup, D.H. and Richardson, J.A., "Scale nucleation on heat transfer surface and its prevention," *Chem. Eng. Commun.*, vol. 2, pp. 167-180, 1978.

41. Müller-Steinhagen, H., "Control of heat exchanger fouling," *Process and Control Engineering*, pp. 34-38, November 1988.

42. Bergles, A.E., "Techniques to augment heat transfer," In: *Handbook of Heat Transfer Applications*, Rohsenow, W.M., Hartnett, J.P. and Ganic, E.N., eds., 2nd edition, pp. 3-1 to 3-80, McGraw-Hill

43. Somerscales, E.F.C. and Bergles, A.E., "Enhancement of heat transfer and fouling mitigation," *Advances in Heat Transfer*, vol. 30, pp. 196-253, 1997.

44. Panchal, C.B., "Experimental investigation of seawater biofouling for enhanced surfaces," In: *Heat Transfer Fundamentals, Design, Applications, and Operating Problems*, Shah, R.K., ed., HTD-vol. 108, pp. 231-238, ASME, New York, 1989.

45. Panchal, C.B. and Sasscer, D.S., "Biofouling and corrosion fouling of plain and enhanced aluminum surfaces," In: *Fouling and Enhancement Interactions*, Rabas, T.J. and Chenoweth, J.M., eds., HTD-vol. 164, pp. 9-15, ASME, New York, 1991.

46. Somerscales, E.F.C., Ponteduro, A.F. and Bergles, A.E., "Particulate fouling of heat transfer tubes enhanced on their inner surface," In: *Fouling and Enhancement Interactions*, Rabas, T.J. and Chenoweth, J.M., eds., HTD-vol. 164, pp. 17-28, ASME, New York, 1991.

47. Gough, M.J. and Rogers, J.V., "Insert for placement in a vessel and method of forming the insert," U.S. Pat. 4-481-154, 1984

48. Gough, M.J. and Rogers, J.V., "Reduced fouling by enhanced heat transfer using wire matrix radial mixing elements," In: *Heat Transfer-Pittsburgh 1987*, Lyczkowski, R.W., ed., AIChE Symposium Series, vol. 83, no. 257, pp. 16-21. AIChE, New York, 1987.

49. Hatch, L.P. and Weth, G.G., "Scale control in high temperature distillation utilizing fluidised bed heat exchangers," *Research and Development Progress Report*, no. 571, 1970.

50. Klaren, D.G., "Fluid bed heat exchanger: a major improvement in severe fouling heat transfer," In: *Heat exchangers-Theory and Practise*, Taborek, J., Hewitt, G.F. and Afgan, N., eds., pp. 885-896, Hemisphere, Washington, DC., 1983.

51. Jamialahmadi, M. and Müller-Steinhagen, H., "Hydrodynamics and heat transfer of liquid fluidised bed systems," *Chem. Eng. Commun.*, vol. 176, pp. 35-79, 2000.

52. Allen, C.A. and Grimmett, E.S., "Liquid-fluidised bed heat exchanger design parameters," Department of Energy, Idaho Operations Office, under contract I-(322)-1570, 1978.

53. Klaren, D.G., "Development of a vertical flash evaporator," Ph.D Thesis, Delft University of Technology, the Netherlands, 1975.

54. Meijer, J.A.M., "Inhibition of calcium sulphate scale by a fluidised bed" Ph.D Thesis, Delft University of Technology, the Netherlands, 1984.

55. Klaren, D.G., "The fluidised bed heat exchanger: principles and modes of operation and heat transfer results under severe fouling conditions," *Fouling Prev. Res. Dig.*, vol. 5, no. 1, 1983.

56. Rautenbach, R., Erdmann, C. and Kollbach, J.S., "The fluidised bed technique in the evaporation of wastewaters with severe fouling/scaling potential – latest developments, applications, limitations." *Desalination,* vol. 81, pp. 285-298, 1991.

57. Klaren, D.G. and Bailie, R.E., "The non-fouling fluidised bed heat exchanger," 1989 National Conference, HTD-vol. 108, *Heat Transfer Equipment Fundamentals, Design, Applications and Operating Problems*, Philadelphia, 1989.

58. Klaren, D.G., "Handbook on industrial applications of self-cleaning fluidised bed exchangers for severely fouling liquids," ISBN 90-802554-1-6, 1995.

59. Klaren, D.G. and Sullivan, D.W., "Non-fouling heat exchanger performance in severe fouling services: principle, industrial applications and operating installations," Spring National Meeting AIChE, Houston, 1999.

60. Dirk, W.J., Allen, C.A. and McAtee, R.E., "Preliminary evaluation of materials for fluidised bed technology in geothermal wells at Raft River, Idaho, and East Mesa, California," In: *Geothermal Scaling and Corrosion*, ASTM Publ. 04-71700-27, pp. 69-80, American Society for Testing and Materials, New York, 1979.

61. Klaren, D.G. and Bailie, R.E., "Consider nonfouling fluidised bed exchangers," *Hydrocarbon Processing*, pp. 48-50, July 1989.

62. Rautenbach, R. and Katz, T., "Survey of long-time behaviour and cost of industrial fluidised bed heat exchangers." *Desalination*, vol. 108, pp. 335-344, 1996.

63. Kollbach , J.S., Dahm, W. and Rautenbach, R., "Continuous cleaning of heat exchanger with recirculating fluidised bed," *Heat Transfer Engineering*, vol. 8, no. 4, pp. 26-32, 1987.

64. Tianqing, T., "Mechanism study on circulating flow of particles within a fluid bed antifouling heat exchanger," In: *Proceedings of 'Fouling mitigation of industrial heat exchange equipment,'* an international conference, San Luis Obispo, California, USA, June 1995.

65. Fan, L.S., "Gas-liquid-solid fluidisation engineering," Butterworth, Boston, 1989.

66. Felice, R.D., "Hydrodynamics of liquid fluidisation," *Chem. Eng. Sci.*, vol. 50, pp. 1213-1245, 1995.

67. Liang, W., Zhang, S., Zhu, J.X., Jin, Y., Yu, Z. and Wang, Z., "Flow characteristics of the liquid-solid circulating fluidised bed," *Powder Technology*, vol. 90, pp. 95-102, 1997.

68. Liang, W., Yu, Z., Jin, Y., Wang, Z.W., Wang, Y., He, M. and Min, E., "Synthesis of linear alkylbenzene in a liquid-solids circulating fluidised bed reactor," *J. Chem. Technol. Biotechnol.*, vol. 62, pp. 98-102, 1995.

69. U.S. Pat. 5-012-210, 1991.

70. Klaren, D.G., "Self cleaning heat transfer," *Hydrocarbon Engineering*, pp. 83-92, March 2001.

71. Klaren, D.G. and Sullivan, D.W., "Self-cleaning heat exchangers in foul water steam generators," In: *Proceedings of 34th National Heat Transfer Conference*, Pittsburgh, Pennsylvania, USA, August 20-22, 2000.

72. Klaren, D.G, "Self-cleaning heat exchangers: principle, industrial applications and operating installations," Presented at the Industrial Heat Transfer Conference, Dubai, Saudi Arabia, September 24-26, 2000.

73. Kim, N.H. and Lee, Y.P., "A study on the pressure loss, heat transfer enhancement and fouling control in liquid fluidised bed heat exchangers," In: *Proceedings of 'Fouling mitigation of industrial heat exchange equipment,'* an international conference, San Luis Obispo, California, USA, June 1995.

74. Lee, H.C., Kang, G., Lee, Y.P., Han, H.S. and Stevens, D.K., "Development of an advanced evaporation system with fouling free technology using a circulating fluidised bed heat exchanger," *Environmental Engineering Science*, vol. 20, no. 4, 2003.

75. Ahn, S.W., Lee, B.C., Kim, W.C., Bae, M.W. and Lee, Y.P., "Characteristics of fluid flow and heat transfer in a fluidised heat exchanger with circulating solid particles," *KSME International Journal*, vol. 16, no. 9, pp. 1175-1182, 2002.

76. Petukhov, B.S., "Heat transfer in turbulent pipe flow with variable physical properties," In: *Advanced Heat Transfer*, vol. 6, Irvine, T.F. and Hartnett, J.P., eds., Academic Press, New York, pp. 504-564, 1970.

77. Newitt, D.M., Richardson, J.F. and Gliddon, B.J., "Hydraulic conveying of solids in vertical pipes," *Trans. Instn. Chem. Engnrs.*, vol. 39, pp. 93-100, 1961.

78. Brea, F.M. and Hamiliton, W., "Heat transfer in liquid fluidised beds," *Trans. Instn. Chem. Engnrs*, vol. 49, pp. 196-203, 1971.

79. Chiu, T.M. and Ziegler, E.N., "Liquid hold-up and heat transfer coefficient in liquid-solid and three-phase fluidised beds," *AIChE J.*, vol. 31, pp. 1504-1509, 1985.

80. Wasmund, B.W. and Smith, J.W., "Wall to fluid heat transfer in liquid fluidised beds," *Canadian Journal of Chemical Engineering*, vol. 45, pp. 156-165, 1967.

81. Richardson, J.F., Roman, M.N. and Shakiri, K.J., "Heat transfer from immersed surfaces in liquid fluidised beds," *Chem. Eng. Sci.*, vol. 31, pp. 619-624, 1976.

82. Jamialahmadi, M., Malayeri, M.R. and Müller-Steinhagen, H., "Prediction of heat transfer to liquid-solid fluidised beds," *Canadian Journal of Chemical Engineering*, vol. 73, pp. 444-455, August 1995.

83. Wilhelm, R.H. and Kwauk, M., "Fluidisation of solid particles," *Chem. Eng. Prog.*, vol. 44, pp. 201-218, 1948.

84. Richardson, J.F. and Zaki, W.N., "Sedimentation and fluidisation," *Trans. Inst. Chem. Eng.*, vol. 32, pp. 35-53, 1954.

85. Rowe, P.N., "A convenient empirical equation for estimation of the Richardson-Zaki exponent," *Chem. Eng. Sci.*, vol. 42, no. 11, pp. 2795-2796, 1987.

86. Hirata, A. and Bulos, F.B., "Prediction of bed voidage in solid-liquid fluidisation," *J. Chem. Eng. Japan*, vol. 23, pp. 599-604, 1990.

87. Jamialahmadi, M., Malayeri, M.R. and Müller-Steinhagen, H., "A unified correlation for the prediction of heat transfer coefficients in liquid/solid fluidised bed systems," *Journal of Heat Transfer*, vol. 118, pp. 952-959, November 1996.

88. Welty, J.R., Wicks, C.E., Wilson, R.E. and Rorrer, G., "Fundamentals of momentum, heat and mass transfer," Wiley, J and Sons, Inc., 4th edition, ISBN 0-471-38149-7, 2001.

89. Aghajani, M., "Studies of bed voidage and heat transfer in solid-liquid fluidised bed heat exchangers," Ph.D Thesis, University of Surrey, UK, 2001.

90. Aghajani, M., Müller-Steinhagen, H. and Jamialahmadi, M., "New design equations for liquid/solid fluidised bed heat exchangers," *Int. J. Heat Mass Transfer*, vol. 48, pp. 317-329, 2005.

91. Zheng, Y. and Zhu, J.X., "The onset velocity of a liquid-solid circulating fluidised bed," *Powder Technology*, vol. 114, pp. 244-251, 2001.

92. Filonenko, G.K., "Hydraulic resistance in pipes," *Teploenergetika*, vol. 1, pp. 40-44, 1954.

93. Stephan, K. and Preusser, P., "Wärmeübergang beim behältersieden" *Chem. Ing. Tech.*, vol. 51, pp. 649-679, 1979.

94. Lapidus, L. and Elgin, J.C., "Mechanics of vertical-moving fluidised systems," *AIChE J.*, vol. 3, pp. 63-68, 1957.

95. Mertes, T.S. and Rhodes, H.B., "Liquid-particle behaviour (part 1)," *Chem. Eng. Prog.*, vol. 51, pp. 429-432, 1955.

96. Kwauk, M., "Fluidisation-idealised and bubbleless, with applications," Science Press and Ellis Horwood, Beijing, China, 1992.

97. Jamialahmadi, M. and Müller-Steinhagen, H., "Bed voidage in annular solid-liquid fluidised beds," *Chem. Eng. Process.*, vol. 31, pp. 221-227, 1992.

98. Clift, R., Grace, J.R. and Weber, M.E., "Bubbles, drops and particles," Academic Press, New York, 1978.

99. Khan, A.R. and Richardson, J.F., "The resistance to motion of a solid sphere in a fluid," *Chem. Eng. Commun.*, vol. 62, pp. 135-147, 1987.

100. Hartman, M., Havlin, V., Trnka, O. and Čársky, M., "Predicting the free-fall velocities of spheres," *Chem. Eng. Sci.*, vol. 44, no. 8, pp. 1743-1745, 1989.

101. Lewis, W.K., Gililand, E.R. and Bauer, W., "Characteristics of fluidised particles," *Ind. Eng. Chem.*, vol. 41, pp. 1104-1117, 1949.

102. Happel, J., "Viscous flow in multiparticle systems: slow motion of fluids relative to beds of spherical particles and particulate fluidisation and sedimentation of spheres," *AIChE J.*, vol. 4, pp. 197-201, 1958.

103. Strauve, D.L., Lapidus, L. and Elgin, J.C., "The mechanics of moving vertical fluidised systems," *Canadian Journal of Chemical Engineering*, vol. 36, pp. 141-152, 1958.

104. Loeffler, A.L. and Ruth, B.F., "Particulate fluidisation and sedimentation of spheres," *AIChE J.*, vol. 5, pp. 310-315, 1959.

105. Wen, C.Y. and Yu, Y.H., "Mechanism of fluidisation," *Chem. Eng. Progress Synpos. Series* 44, pp. 201-218, 1966.

106. Barnea, E. and Mizrahi, J., "A generalised approach to the fluid dynamics of particulate systems. Part 1: general correlation for fluidisation and sedimentation in solid multiparticle systems," *Chem. Eng. J.*, vol. 5, pp. 171-189, 1973.

107. Garside, J. and Al-Dibouni, M.R., "Velocity-voidage relationships for fluidisation and sedimentation in solid-liquid systems," *Ind. Eng. Chem. Process Des. Dev.*, vol. 16, pp. 206-213, 1977.

108. Hartman, M., Trnka, O. and Havlin, V., "A relationship to estimate the porosity in liquid-solid fluidised beds," *Chem. Eng. Sci.*, vol. 47, no. 12, pp. 3162-3166, 1992.

109. Letan, R., "On vertical dispersion two-phase flow," *Chem. Eng. Sci.*, vol. 29, pp. 621-624, 1974.

110. Han, C.Y. and Griffith, P., "The mechanism of heat transfer in nucleate pool boiling-Part I and II," *Int. J. Heat Mass Transfer*, vol. 8, pp. 887-917, 1965.

111. Jamialahmadi, M. and Müller-Steinhagen, H., "Gas hold-up in bubble columns," In: *Encyclopedia of Fluid Mechanics*, Chapter II, Supplement 2, Cheremisinoff, N., ed., Gulf Publ. Corp., Houston, TX, 1993.

112. Gnielinski, V., "Wärmeübertragung in rohren", *VDI-Wärmeatlas*, 5th ed., VDI-Verlag, Düsseldorf , 1986.

113. Mickic, B.B. and Rohsenow, W.M., "A new correlation of pool boiling data including the effect of heat surface characteristics," *J. Heat Transfer*, vol. 5, pp. 245-250, 1969.

114. Martin, H., "Heat transfer between gas fluidised bed of solid particles and the surfaces of immersed heat exchanger elements, Part II," *Chem. Eng. Process.*, vol. 18, pp. 199-223, 1984.

115. Martin, H., "Fluid bed heat exchangers-a new model for particle convection energy transfer," *Chem. Eng. Commun.*, vol. 13, pp. 1-16, 1981.

116. Latif, B.A.J. and Richardson, J.F., "Circulation patterns and velocity distributions for particles in a liquid fluidised bed," *Chem. Eng. Sci.*, vol. 72, pp. 1933-1949, 1972.

117. Wasser, U. and Mardas, G., "Zum wärmeübergang in wirbelschichten," *Chem. Ing. Techn.*, vol. 29, pp. 332-335, 1957.

118. Lemlich, R. and Caldas, I., "Heat transfer to liquid fluidised bed," *AIChE J.*, vol. 4, pp. 376-380, 1958.

119. Richardson, J.F. and Mitson, A.E., "Sedimentation and fluidisation. Part II- Heat transfer from a tube wall to a liquid fluidised system," *Trans. Inst. Chem. Eng.*, vol. 36, pp. 270-282, 1958.

120. Ruckenstein, E., Shorr, V. and Suciu, G., "Despre transferul de caldurs dintre un strat fluidizat culichid si peretelerasuluicare – I contine, studdi cercetari fizica," *Akad. Rep. Populare Romine*, vol. 10, pp. 235, 1959.

121. Richardson, J.F. and Smith, J.W., "Heat transfer to liquid-fluidised systems and to suspensions of coarse particles in vertical transport," *Trans. Inst. Chem. Eng.*, vol. 40, pp. 13-22, 1962.

122. Hamilton, W., "A correlation for heat transfer in liquid fluidised beds," *Canadian Journal of Chemical Engineering*, vol. 48, pp. 52-55, 1970.

123. Tripathi, G. and Pandey, G.N., "Heat transfer in liquid fluidised beds," *Indian J. Technol.*, vol. 8, pp. 285-289, 1970.

124. Varma, R.L., Pandey, C.N. and Tripathy, G., "Heat transfer in semifluidised beds," *Indian J. Technol.*, vol. 10, pp. 11-15, 1972.

125. Schimanski, G.N., Jancuk, E.N. and Nikitin, P.G., "Untersuchung der wärmeübertragung zwischen einem waagerechten rohrbündel und einer wirbelschicht," *Arch. Energiewirt.*, vol. 27, pp. 25-29, 1972.

126. Syromyatnikov, N.I., Vasanora, L.K. and Karpenko, A.I., "Heat transfer in liquid fluidised bed," *Heat transfer Sov. Res.*, vol. 6, pp. 135-139, 1973.

127. Allen, C.A., Fukuda, O., Grimmett, E.S. and McAtee, R.E., "Liquid fluidised bed heat exchanger-horizontal configuration experiments and data correlations," In: *12th Intersociety Energy Conversion Engineering Conference*, Preprints, pp. 831-838, 1977.

128. Baker, C.G.J., Armstrong, E.R. and Bergougnou, M.A., "Heat transfer in three-phase fluidised beds," *Powder Technol.*, vol. 21, pp. 195-204, 1978.

129. Khan, A.R., Richardson, J.F. and Shakiri, K.J., "Heat transfer between a fluidised bed and a small immersed surface," Cambridge University Press, pp. 351-356, 1978.

130. Tusin, A.M., Vasanova, L.K. and Syromyatnikov, N.I., "Heat transfer from a transverse streamlined cylinder during surface boiling in a liquid fluidised bed," *J. Eng. Phys.*, vol. 32, pp. 263-266, 1979.

131. Mersman, A., Noth, H., Ringer, O. and Wunder, R., "Maximaler wärmeübergang in apparaten mit dispersen zweiphasensystemen," *Chem. Ing. Tech.*, vol. 52, pp. 189-198, 1980.

132. Kato, Y., Kago, T., Uchida, K. and Morroka, S., "Liquid hold-up and heat transfer coefficient between bed and wall in liquid-solid and gas-liquid-solid fluidised beds," *Powder Technol.*, vol. 28, pp. 173-179, 1981.

133. Wehrman, M. and Mersmann, A., "Wärmeübergang in flüssigkeits durchströmten fest und fliess betten," *Chem. Ing. Techn.*, vol. 53, pp. 804-805, Ms 940/81, 1981.

134. Schütt, U., "Wärmeübertragung in der flüssigkeitswirbelschicht mit senkrechten rohren," Wiss Zeitung Techn. Hochschule Magdeburg, vol. 26, pp. 71-74, 1982.

135. Schütt, U., "Wärmeübertragung in der flüssigkeitswirbelschicht mit senkrechten rohren," Ph.D Thesis, Universität Magdeburg, 1983.

136. Khan, A.R., Juma, K.A. and Richardson, J.F., "Heat transfer from a plane surface to liquids and liquid-solid fluidised beds," *Chem. Eng. Sci.*, vol. 38, pp. 2053-2066, 1983.

137. Muroyama, K., Fuluma, M. and Yasunishi, A., "Wall-to-bed heat transfer in gas-liquid-solid fluidised beds," *Canadian Journal of Chemical Engineering*, vol. 62, pp. 199-208, 1984.

138. Juma, A.K.A. and Richardson, J.F., "Heat transfer to cylinders from segregating liquid-solid fluidised beds," *Chem. Eng. Sci.*, vol. 40, pp. 687-694, 1985.

139. Coulson, J.M. and Richardson, J., "Chemical Engineering," Vol. 2, 3rd edition, Pergamon Press, Oxford, 1985.

140. Kim, S.D., Kang, Y. and Kwon, H.K., "Heat transfer characteristics in two and three phase slurry fluidised beds," *AIChE J.*, vol. 32, pp. 1397-1400, 1986.

141. Midoux, N., Wild, J., Purwasamita, M., Chapentier, J.C. and Martin, H., "Zum flüssigkeitsinhatt und zum wärmeübergang in rieselbettreaktoren bei boher wechselwirkung des gases und der flüssigkeit," *Chem. Eng. Tech.*, vol. 58, pp. 142-143, MS1445/86, 1986.

142. Muroyama, K., Fuluma, M. and Yasunishi, A., "Wall-to-bed heat transfer in liquid-solid and gas-liquid-solid fluidised beds," *Canadian Journal of Chemical Engineering*, vol. 64, pp. 399-408, 1986.

143. Kollbach, J., Ph.D Thesis, Universität Achen, Achen, 1987.

144. Grewal, N.S and Zimmerman, A.T., "Heat transfer from tube immersed in a liquid-solid fluidised bed," *Powder Technol.*, vol. 54, pp. 137-145, 1988.

145. Kang, Y., Fan, L.T. and Kim, S.D., "Immersed heater-type bed heat transfer in liquid-solid fluidised beds," *AIChE J.*, vol. 37, pp. 1101-1106, 1991.

146. Macias-Machin, A., Oufer, L. and Wannenmacher, N., "Heat transfer between an immersed wire and a liquid fluidised bed," *Powder Technol.*, vol. 66, pp. 281-284, 1991.

147. Haid, M., Martin, H. and Müller-Steinhagen, H., "Heat transfer to liquid-solid fluidised beds," *Chem. Eng. Process.*, vol. 33, pp. 211-225, 1994.

148. Haid, M., "Correlations for the prediction of heat transfer to liquid-solid fluidised beds," *Chem. Eng. Process.*, vol. 36, pp. 143-147, 1997.

149. Jamialahmadi, M. and Müller-Steinhagen, H., "Scale formation during nucleate boiling - A review," *Corrosion Rev.*, vol. 11, pp. 25-54, 1993.

150. Oufer, L., Breber, G. and Knudsen, J., "A study of chemical reaction fouling under subcooled boiling conditions," *AIChE Symposium on Heat Exchanger Fouling in Chemical and Food Processing*, Paper no. 35e, AIChE National Meeting , San Diego, USA, 1990.

151. Jamialahmadi, M. and Müller-Steinhagen, H., "The effect of scale formation on nucleate pool boiling," *EUROTHERM Seminar No 48: Pool Boiling 2*, Paderborn, Germany, Gorenflo, D., Kenning, D.B.R., Marvillet, Ch., eds., pp. 77-86, 1996.

152. Jakob, M. and Link, W., *Forschung, a.d., Geb. D. Ingenieurwes*, vol. 4, pp. 75, 1993.

153. Insinger, T. and Bliss, H., *Trans. Am. Inst. Chem. Eng.,* 36, pp. 491, 1940.

154. Patridge, E.P. and White, A.H., "Mechanism of formation of calcium sulphate boiler scale," *Ind. Eng. Chem.*, vol. 21, pp. 834-838, 1929.

155. Freeborn, J. and Lewis, D., "Initiation of boiler scale formation," *J. Mech. Sci.*, vol. 4, pp. 46-52, 1962.

156. Palen, J.W. and WestWater, W., "Heat transfer and fouling rates during pool boiling of calcium sulphate solutions," *Chem. Eng. Prog. Symp. Series*, vol. 62, pp. 77-86, 1966.

157. Müller-Steinhagen, H., Hechler, C., Steiner, D. and Schlunder, E.U., "Fouling-vorgänge bei der verdampfung von argon im waagerecht durchströmten rohr," *Wärme und Stoffubertragung*, vol. 17, pp. 47-53, 1982.

158. Hospeti, N.B. and Mesler, R.B., "Deposits formed beneath bubbles during nucleate boiling of radioactive calcium sulphate solutions," *AIChE J.*, pp. 662-665, 1965.

159. Palethorpe, S.J. and Bridgwater, J., "The influence of surface finish on calcium sulphate fouling," *Int. Conf. Fouling in Process Plant*, Oxford, pp. 355-372, 1988.

160. Jamialahmadi, M., Blöchl, R. and Müller-Steinhagen, H., "Bubble dynamics and scale formation during boiling of aqueous calcium sulphate solutions," *Chem. Eng. Process.*, vol. 26, pp. 15-26, 1989.

161. Najibi, S.H., Müller-Steinhagen, H. and Jamialahmadi, M., "Calcium sulphate scale formation during sub-cooled flow boiling," *Chem. Eng. Sci.*, vol. 52, no. 8, pp. 1265-1284, 1997.

162. Helalizadeh, A., Müller-Steinhagen, H. and Jamialahmadi, M., "Mixed salt crystallization fouling," *Chem. Eng. Process.*, vol. 39, pp. 29-43, 2000.

163. Hasson, D., Avriel, M., Resnick, W., Rozenman, T. and Windreich, S., "Mechanism of calcium carbonate scale deposition on heat transfer surfaces," *I & EC Fundamentals 7*, pp. 59-65, 1968.

164. Lorenz, J.J., Mickic, B.B. and Rohsenow, W.M., "The effect of surface conditions on boiling characteristics," In: *Proceedings of the 5th International Heat Transfer Conference*, Tokyo, vol. 4, pp. 35-39, 1974.

165. Shoukri, M. and Judd, R.L., "On the influence of surface conditions in nucleate boiling – the concept of bubble flux density," *ASME J. Heat Transfer*, vol. 100, pp. 618-623, 1987.

166. Dittus, F.W. and Bölter, L.M.K., "Heat transfer in automobile radiators of the tubular type," University of California Press, vol. 2, no. 13, 1930.

167. Forster, H.K. and Zuber, N., *J. Appl. Phys.*, vol. 25, pp. 474, 1954.

168. Wenzel, U. and Müller-Steinhagen, H., "Heat transfer to ternary mixtures of acetone, iso-propanol and water under sub-cooled flow boiling conditions," *Int. J. Heat Mass Transfer*, vol. 37, pp.175-194, 1994.

169. Brautsch, A.H., "Heat transfer mechanisms during the evaporation process from mesh screen porous structures," Ph.D Thesis, Heriot-Watt University, Edinburgh, UK, November 2002

170. Jakob, M. and Fritz, W., "Versuche über den verdampfungsvorgang," *Forschung auf dem Gebiet des Ingenieurwesens*, 2, pp. 435-437, 1931.

171. Mingheng, S., Yongping, G. and Chongfang, M., "Boiling and condensation heat transfer," Higher education press, Beijing, 1995.

172. Weizao, G., Jiani, S., Chongfang, M. *et al.*, "Enhancement heat transfer," Science Press, Beijing, 1990.

173. Hetsroni, G., Mosyak, A. and Rozenblit, R., "Effect of fluid properties on pool boiling, bubble dynamics and thermal patterns on the wall," In: *Proceedings of Symposium on Energy Engineering in the 21st Century*, vol.1, Begell House Press, pp. 72-83, 2000.

174. Mingheng, S., Yanbing, Z. and Zhongliang, L., "Study on boiling heat transfer in liquid saturated particle bed and fluidised bed," *Int. J. Heat Mass Transfer*, vol. 46, pp. 4695-4702, 2003.

175. Curcio, L.A., Jr., "Pool boiling of enhanced heat transfer surfaces in refrigerant-oil mixtures and aqueous calcium sulphate solutions," MS Thesis, Rensselaer Polytechnic Institute, Troy, NY, 1989.

176. Curcio, L.A., Jr. and Somerscales, E.F.C., "Pool boiling of enhanced heat transfer surfaces in refrigerant-oil mixtures and aqueous calcium sulphate solutions," Rep. No. HTL-5. Heat Transfer Laboratory, Department of Mechanical Engineering, Aeronautical Engineering and Mechanics, Rensselaer Polytechnic Institute, Troy, NY, 1989.

177. O'Connor, J.P., You, S.M. and Price, D.C., "A dielectric surface coating technique to enhance boiling heat transfer from high power microelectronics," *IEEE Trans. on Components, Packaging, and Manufacturing Technology*, vol. 18, no. 3, pp. 656-663, 1995a.

178. O'Connor, J.P., You, S.M. and Price, D.C., "A painting technique to enhance pool boiling heat transfer in FC-72," *ASME Journal of Heat Transfer*, vol. 117, no. 2, pp. 387-393, 1995b.

179. Rainey, K.N. and You, S.M., "Pool boiling heat transfer from plain and microporous, square pin finned surfaces in saturated FC-72," *ASME Journal of Heat Transfer*, vol. 122, no. 3, pp. 509-516, 2000.

180. Rainey, K.N. and You, S.M., "Effects of heater orientation on pool boiling heat transfer from microporous coated surfaces," *Int. J. Heat Mass Transfer*, vol. 44, no. 14, pp. 2589-2599, 2001.

181. Webb, R.L., "Principles of enhanced heat transfer," Wiley, New York, 1994.

182. Hess, G., "Heat transfer in nucleate boiling, maximum heat flux and transient boiling," *Int. J. Heat Mass Transfer*, vol. 16, pp. 1611-1627, 1973.

183. Pate, M.B., Ayub, Z.H. and Kohler, J., "Heat exchangers for the air conditioning and refrigeration industry: state-of-the-art design and technology," In: *Compact Heat Exchangers*, Hemisphere, New York, pp. 567-590, 1990.

184. Webb, R.L., "Heat transfer surface which promotes nucleate ebullition," U.S. Pat. 3-521-708, 1970.

185. Webb, R.L. "Heat transfer surface having a high boiling heat transfer coefficient," U.S. Pat. 3-696-861, 1972.

186. Fujie, K., Nakayama, W., Kuwahara, H. and Kakizak, K., "Heat transfer wall for boiling liquids," U.S. Pat. 4-060-125, 1977.

187. Arai, N., Fukashima, T., Arai, A., Nakajima, T., Fujie, K. and Nakayama, Y., "Heat transfer tubes enhancing boiling and condensation in heat exchangers of a refrigeration machine," *ASHRAE Transactions*, vol. 83, pp. 58-70, 1977.

188. Tori, T., Hirasawa, S., Kuwahara, H., Yanagida, T. and Fujie, K., "The use of heat exchangers with THERMOEXCEL tubing in ocean thermal energy plants," ASME Paper no. 78-WA-HT-65, 1978.

189. Saier, M., Kästner, H.W. and Klöckner, R., "Y- and T-finned tubes and methods and apparatus for their making," U.S. Pat. 4-179-911, 1979.

190. Somerscales, E.F.C. and Curcio, L.A., Jr., "Effect of calcium sulphate on pool boiling of enhanced heat transfer surfaces," *Am. Soc. Mech. Eng.*, Paper No. 90-WA/HT-2, 1990.

191. Griffith, P. and Wallis, J.D., "The role of surface conditions in nucleate boiling," *Chem. Eng. Prog. Symposium Series.*, vol. 56, pp. 49-63, 1960.

192. Marto, P.J., Manslon, J.A. and Maynard, M.D., "Nucleate boiling in nitrogen with different surface conditions," *Journal of Heat Transfer*, vol. 90, pp. 437-444, 1968.

193. Müller-Steinhagen, H. and Zhao, Q., "Anti-fouling by metal surface modification," UK Pat. P31807GB, PCT Application GB96/02681, 1996.

194. Müller-Steinhagen, H. and Zhao, Q., "Investigation of low fouling surface alloys made by ion implantation technology," *Chem. Eng. Sci.* vol. 52, pp. 3321-3332, 1997.

195. Müller-Steinhagen, H., Zhao, Q., Helalizadeh, A. and Ren, X.G., "The effect of surface properties on $CaSO_4$ scale formation during convective heat transfer and subcooled flow boiling," *Can. J. Chem Eng.*, vol. 78, pp. 12-20, 2000.

196. Teer, D.G., "Uniform deposition and plasma system," UK Patent Application, 9006073.2. 1990.

197. Chuah, Y.K. and Carey, V.P., "Boiling heat transfer in a shallow fluidised particulate bed," *Journal of Heat Transfer*, vol. 109, pp. 196-203, 1987.

198. Li, X.L., Jianping, W. and Gu, J., "Flow boiling heat transfer with fluidised solid particles," *Chinese J. of Chem. Eng.*, vol. 3, no. 3, pp. 163-170, 1995.

199. Klaren, D.G., "Self-cleaning heat exchangers," *Int. Journal of Hydrocarbon Engineering*, vol. 4, no. 3, pp. 42-44, 1999.

200. Zhang, L. and Li, X.L., "A study on boiling heat transfer in three-phase circulating fluidised bed," *Chemical Engineering Journal*, vol. 78, pp. 217-223, 2000.

201. Jianping, W., Zhou, H. and Li, X.L., "Performance of a new vapour-liquid-solid three-phase circulating fluidised bed evaporator," *Chemical Engineering and Processing*, vol. 43, pp. 49-56, 2004.

202. Wei, H. and Maa, J.R., "Enhancement of flow boiling heat transfer with polymer additives," *Int. J. Heat Mass Transfer*, vol. 25, no. 3, pp. 431-434, 1982.

203. Muroyama, K. and Fan, L.S., "Fundamentals of gas-liquid-solid fluidisation," *AIChE Journal*, vol. 31, no. 1, pp. 1-34, 1985.

204. Chiu, T.M. and Ziegler, E.N., "Heat transfer in three-phase fluidised bed," *AIChE Journal*, vol. 29, no. 4, pp. 677-685, 1983.

205. Esptein, N., "Three-phase fluidisation: some knowledge gaps," *Can. J. Chem Eng.*, vol. 59, pp. 649-657, 1981.

206. Fan, L.S., "Summary paper on fluidisation and transport phenomena," *Powder Technol.*, vol. 88, pp. 245-253, 1996.

207. Yang, Y.M. and Maa, J.R., "Boiling of suspension of solid particles in water," *Int. J. Heat Mass Transfer*, vol. 27, pp. 145-147, 1984.

208. Zheng, Y., "Flow structure in a liquid-solids circulating fluidised bed," Ph.D Thesis, The University of Western Ontario, Canada, July 1999.

209. Kunni, D. and Levenspiel, O., "Fluidisation engineering," Butterworth-Heinemann series in Chemical Engineering, 2nd edition, ISBN 0-409-90233-0, 1991.

210. Sinnott, R.K., "Chemical engineering design," vol. 6, 2nd edition, Coulson and Richardson's Chemical Engineering , Butterworth-Heinemann, ISBN 0-7506-2558-9, 1993.

211. Luo, Z., Ni, M., Zhou, J., Cheng, L., Chang, Z. and Cen, K., "Solid recycle system for CFB," In: *Proceedings of 10th Int. Conf. on Fluidised Bed Combustion*, Manaker, A., ed., ASME, pp. 557-562, 1989.

212. Hetsroni, G., Zakin, J.L., Gurevich, M., Mosyak, A., Pogrebnyak, E. and Rozenblit, R., "Saturated flow boiling heat transfer of environmentally acceptable surfactants," *Int. Journal of Multiphase flow,* vol. 30, pp. 717-734, 2004.

213. ASME Journal of Heat Transfer Editorial Board, "Policy on reporting uncertainties in experimental measurements and results", *Journal of Heat Transfer*, vol. 115, pp. 5-6, 1993.

214. Abdelmessih, A.H., Hooper, F.C. and Nangia, S., "Flow effects on bubble growth and collapse in surface boiling," *Int. J. Heat Mass Transfer*, vol. 15, pp. 115-125, 1972.

215. Bibeau, E., "Void growth in sub-cooled flow boiling for circular and finned geometries for low values of pressure and velocity," Ph.D Thesis, University of British Columbia, 1993.

216. Kandlikar, S., Mizo, V. and Cartwright, M., "Investigation of bubble departure mechanism in subcooled flow boiling of water using high-speed photography," *Convective Flow Boiling Conference*, Banff, Canada, pp. 161-166, 1995.

217. Klausner, J.F., Mei, R., Bernhard, D.M. and Zeng, L.Z., "Vapour bubble departure in forced convective boiling," *Int. J. Heat Mass Transfer*, vol. 36, no. 3, pp. 651-662, 1993.

218. Braislford, A.D. and Major, K.G., "The thermal conductivity of aggregates of several phases, including porous material," *British. J. of Applied Physics*, vol. 15, pp. 313-319, 1964.

219. Steiner, D., "Wärmeüberagung beim sieden gesättigter flüssigkeiten, sect. hbb" in *VDI Wärmeatlas*. VDI Verlag, Düsseldorf, 1988.

220. Polyanin, A.D., Kutepov, A.M., Vyazmin, A.V. and Kazenin, D.A., "Hydrodynamics, mass and heat transfer in chemical engineering," Taylor and Francis, London, ISBN 0-415-27237-8, 2002.

221. http://www.grc.nasa.gov/WWW/K-12/airplane/nseqs.html

222. Batchelor, G.K., "An introduction to fluid dynamics," Cambridge University Press, 1967.

223. http://www.grc.nasa.gov/WWW/K-12/airplane/eulereqs.html

224. http://www.fluidmech.net/tutorials/bernoulli/bernoulli-intro.htm

225. Landau, L.D. and Lifshitz, E.M., "Fluid mechanics," Pergamon Press, 1987.

226. Acheson, D.J., "Elementary fluid dynamics," Clarendon Press, 1990.

APPENDIX A

Determining

the

Experimental Boiling Coefficients

Appendix	Description	Numbering
A.1	**Wall temperature measurements along heater assembly** Test Conditions ▪ Stainless steel particles, 2.5 mm d_p ▪ Re = 45602 (fixed) ▪ q'' = 27.97 → 279.7 kW/m^2 (adjusted)	**A.1/1:1** **to** **A.1/10:2**
A.2	**Data for boiling curves and heat transfer coefficient plots** Test Conditions ▪ Stainless steel particles, 2.5 mm d_p ▪ Re = 45602 → 84643	**A.2/1** **to** **A.2/7**
A.3	**Wall temperature measurements along heater assembly** Test Conditions ▪ Stainless steel particles, 2 mm d_p ▪ Re = 45602 (fixed) ▪ q'' = 27.97 → 279.7 kW/m^2 (adjusted)	**A.3/1:1** **to** **A.3/10:2**
A.4	**Data for boiling curves and heat transfer coefficient plots** Test Conditions ▪ Stainless steel particles, 2 mm d_p ▪ Re = 45602 → 71614	**A.4/1** **to** **A.4/5**

Wall Temperature Measurements Along Heater Assembly

Stainless Steel Particles- 2.5 mm dia - 250 g loading

Re = 45602 q" = 27.972 kW/m2 T_W = 91.99323

Measure-ment no. (N)	T* =	90.3959 Probe 1 T_1 (°C)	91.0654 Probe 2 T_2 (°C)	93.8232 Probe 3 T_3 (°C)	95.0254 Probe 4 T_4 (°C)	95.0663 Probe 5 T_5 (°C)	94.2257 Probe 6 T_6 (oC)	88.7626 Probe 7 T_7 (oC)	87.5813 Probe 8 T_8 (oC)
1		90.67	91.31	94.03	95.28	95.26	94.53	88.42	87.22
2		90.81	91.4	94.12	95.35	95.39	94.64	88.4	87.22
3		90.81	91.4	94.12	95.35	95.39	94.64	88.4	87.35
4		90.87	91.49	94.21	95.37	95.39	94.69	88.4	87.35
5		90.96	91.55	94.27	95.43	95.39	94.69	89.73	88.59
6		90.96	91.55	94.27	95.43	95.39	94.69	89.75	88.62
7		91	91.62	94.29	95.43	95.39	94.69	89.75	88.62
8		91	91.62	94.32	95.41	95.37	94.62	89.67	88.59
9		91	91.62	94.32	95.41	95.37	94.62	89.64	88.57
10		90.98	91.64	94.32	95.41	95.41	94.58	89.64	88.57
11		90.94	91.64	94.34	95.46	95.37	94.53	89.64	88.57
12		90.94	91.64	94.34	95.46	95.37	94.53	88.38	87.24
13		90.94	91.62	94.34	95.48	95.41	94.53	88.38	87.24
14		90.92	91.6	94.32	95.48	95.37	94.51	88.38	87.24
15		90.92	91.6	94.32	95.48	95.37	94.51	88.38	87.24
16		90.74	91.51	94.25	95.41	95.37	94.4	89.27	87.94
17		90.63	91.38	94.1	95.3	95.3	94.4	89.27	87.94
18		90.63	91.38	94.1	95.3	95.3	94.4	89.27	87.94
19		90.48	91.29	93.99	95.19	95.19	94.23	89.14	87.83
20		90.28	91.07	93.83	95.02	95.1	94.16	88.88	87.52
21		90.28	91.07	93.83	95.02	95.1	94.16	88.88	87.52
22		90.15	90.96	93.68	94.86	94.93	94.01	88.7	87.41
23		90	90.78	93.55	94.8	94.89	93.9	88.7	87.41
24		90	90.78	93.55	94.8	94.89	93.9	88.7	87.41
25		89.82	90.67	93.5	94.73	94.84	93.83	88.68	87.33
26		89.73	90.61	93.37	94.6	94.8	93.75	88.66	87.33
27		89.73	90.61	93.37	94.6	94.8	93.75	88.66	87.33
28		89.75	90.5	93.35	94.56	94.69	93.66	88.66	87.33
29		89.73	90.5	93.35	94.47	94.58	93.64	88.66	87.37
30		89.73	90.5	93.35	94.47	94.58	93.64	88.66	87.37
31		89.78	90.5	93.35	94.47	94.58	93.66	87.57	86.38
32		89.86	90.54	93.35	94.49	94.58	93.66	88.68	87.46
33		89.86	90.54	93.35	94.49	94.58	93.66	88.68	87.46
34		89.91	90.61	93.44	94.58	94.6	93.72	87.7	86.56
35		89.91	90.61	93.44	94.58	94.6	93.72	88.81	87.68
36		89.93	90.65	93.48	94.67	94.71	93.79	88.81	87.68
37		90.1	90.74	93.55	94.73	94.71	93.85	89.03	87.94
38		90.1	90.74	93.55	94.73	94.71	93.85	89.14	88
39		90.15	90.78	93.59	94.78	94.75	93.94	89.14	88
40		90.21	90.85	93.61	94.8	94.78	94.03	89.14	88
41		90.21	90.85	93.61	94.8	94.78	94.03	89.19	88.05
42		90.3	90.89	93.72	94.89	94.89	94.12	89.19	88.05
43		90.37	90.98	93.79	95	94.91	94.14	89.4	88.29
44		90.37	90.98	93.79	95	94.91	94.14	89.4	88.29
45		90.5	91.07	93.85	95.13	94.95	94.14	89.4	88.29
46		90.63	91.18	93.9	95.15	94.95	94.21	89.49	88.31
47		90.63	91.18	93.9	95.15	94.95	94.21	89.58	88.38
48		90.67	91.27	93.99	95.24	95.1	94.32	89.58	88.38
49		90.72	91.31	94.03	95.28	95.24	94.47	89.56	88.35
50		90.72	91.31	94.03	95.28	95.24	94.47	88.42	87.35
51		90.78	91.35	94.1	95.32	95.39	94.6	88.42	87.35

Wall Temperature Measurements Along Heater Assembly

Stainless Steel Particles- 2.5 mm dia - 250 g loading

Re = 45602 q" = 27.972 kW/m2 T_W = 91.99323

Measure-ment no. (N)		Probe 1 T_1 (°C)	Probe 2 T_2 (°C)	Probe 3 T_3 (°C)	Probe 4 T_4 (°C)	Probe 5 T_5 (°C)	Probe 6 T_6 (oC)	Probe 7 T_7 (oC)	Probe 8 T_8 (oC)
52		90.87	91.44	94.23	95.41	95.43	94.69	88.42	87.35
53		90.87	91.44	94.23	95.41	95.43	94.69	88.42	87.35
54		90.96	91.46	94.25	95.39	95.46	94.67	88.49	87.37
55		91.03	91.55	94.29	95.46	95.54	94.8	88.49	87.39
56		91.03	91.55	94.29	95.46	95.54	94.8	88.49	87.39
57		91.05	91.55	94.34	95.59	95.54	94.84	88.49	87.41
58		91.03	91.6	94.34	95.59	95.57	94.84	89.64	88.49
59		91.03	91.6	94.34	95.59	95.57	94.84	89.64	88.49
60		91.03	91.6	94.34	95.57	95.59	94.86	89.67	88.51
61		91.03	91.6	94.34	95.57	95.59	94.86	89.49	88.35
62		90.96	91.6	94.34	95.5	95.59	94.84	89.49	88.35
63		90.87	91.55	94.34	95.48	95.57	94.78	89.23	88.11
64		90.87	91.55	94.34	95.48	95.57	94.78	89.12	87.85
65		90.65	91.4	94.12	95.32	95.46	94.69	89.12	87.85
66		90.57	91.31	93.99	95.24	95.43	94.6	87.94	86.73
67		90.57	91.31	93.99	95.24	95.43	94.6	88.77	87.5
68		90.39	91.2	93.88	95.04	95.19	94.38	88.77	87.5
69		90.24	91.05	93.79	95	95.13	94.18	88.7	87.39
70		90.24	91.05	93.79	95	95.13	94.18	88.7	87.39
71		90.04	90.81	93.57	94.82	94.97	94.03	88.7	87.39
72		89.97	90.78	93.5	94.82	94.93	94.01	88.64	87.28
73		89.97	90.78	93.5	94.82	94.93	94.01	87.26	85.99
74		89.82	90.7	93.39	94.56	94.73	93.9	87.26	85.99
75		89.69	90.52	93.33	94.56	94.73	93.81	87.28	86.01
76		89.69	90.52	93.33	94.56	94.73	93.81	88.62	87.33
77		89.69	90.48	93.26	94.53	94.69	93.68	88.62	87.33
78		89.73	90.48	93.24	94.53	94.69	93.72	88.62	87.37
79		89.73	90.48	93.24	94.53	94.69	93.72	88.7	87.46
80		89.73	90.46	93.22	94.51	94.67	93.7	88.7	87.46
81		89.73	90.46	93.22	94.51	94.67	93.7	88.73	87.63
82		89.8	90.46	93.26	94.56	94.69	93.75	88.79	87.61
83		89.89	90.52	93.35	94.64	94.75	93.88	88.79	87.61
84		89.89	90.52	93.35	94.64	94.75	93.88	88.81	87.63
85		89.93	90.63	93.44	94.67	94.75	93.9	87.89	86.71
86		90.06	90.72	93.5	94.73	94.75	93.9	87.89	86.71
87		90.06	90.72	93.5	94.73	94.75	93.9	87.92	86.73
88		90.13	90.74	93.53	94.75	94.82	94.03	88.14	86.98
89		90.21	90.81	93.57	94.78	94.89	94.03	88.14	86.98
90		90.21	90.81	93.57	94.78	94.89	94.03	88.18	87.04
91		90.28	90.83	93.68	94.86	94.89	94.16	88.18	87.04
92		90.41	90.96	93.72	94.95	94.95	94.16	88.18	87.04
93		90.41	90.96	93.72	94.95	94.95	94.16	88.18	87.19
94		90.5	91.03	93.77	94.95	94.97	94.18	88.29	87.26
95		90.52	91.11	93.79	94.95	95	94.27	88.29	87.26
96		90.52	91.11	93.79	94.95	95	94.27	88.29	87.26
97		90.57	91.16	93.9	95.1	95.15	94.36	88.29	87.26
98		90.67	91.22	93.99	95.15	95.15	94.38	88.44	87.37
99		90.67	91.22	93.99	95.15	95.15	94.38	89.64	88.49
100		90.67	91.29	94.01	95.24	95.28	94.38	89.64	88.49

Wall Temperature Measurements Along Heater Assembly

Stainless Steel Particles- 2.5 mm dia - 250 g loading

Re = 45602 q" = 55.944 kW/m2 T_W = 94.70918

Measure-ment no. (N)	T* =	90.4559 Probe 1 T_1 (°C)	92.1863 Probe 2 T_2 (°C)	97.41 Probe 3 T_3 (°C)	99.4794 Probe 4 T_4 (°C)	99.1648 Probe 5 T_5 (°C)	98.1069 Probe 6 T_6 (oC)	91.4871 Probe 7 T_7 (oC)	89.383 Probe 8 T_8 (oC)
1		89.91	91.82	97.08	99.12	98.64	97.85	91.55	89.49
2		89.97	91.79	97.03	99.1	98.61	97.82	91.55	89.49
3		90.04	91.84	97.06	99.25	98.64	98.17	91.55	89.49
4		90.04	91.84	97.06	99.25	98.64	98.17	91.55	89.58
5		90.26	92.1	97.28	99.45	99.12	98.2	91.55	89.58
6		90.32	92.12	97.28	99.45	99.12	98.39	91.71	89.75
7		90.32	92.12	97.28	99.45	99.12	98.39	91.84	89.89
8		90.37	92.12	97.36	99.38	99.14	98.39	91.84	89.89
9		90.39	92.17	97.41	99.36	99.14	98.39	91.84	89.89
10		90.39	92.17	97.41	99.36	99.14	98.39	90.76	88.77
11		90.57	92.32	97.54	99.38	99.29	98.59	90.76	88.77
12		90.67	92.34	97.54	99.67	99.38	98.59	90.76	88.77
13		90.67	92.34	97.54	99.67	99.38	98.59	90.76	88.77
14		90.76	92.34	97.54	99.67	99.38	98.44	90.96	88.88
15		90.85	92.41	97.56	99.67	99.42	98.35	92.32	90.28
16		90.85	92.41	97.56	99.67	99.42	98.35	92.32	90.28
17		90.98	92.5	97.65	99.73	99.53	98.46	92.32	90.28
18		90.98	92.52	97.71	99.78	99.53	98.46	91.2	89.19
19		90.98	92.52	97.71	99.78	99.53	98.46	91.2	89.19
20		91.05	92.58	97.71	99.78	99.71	98.59	91.2	89.19
21		91.09	92.63	97.71	99.78	99.71	98.59	92.5	90.39
22		91.09	92.63	97.71	99.78	99.71	98.59	92.5	90.39
23		91.11	92.65	97.74	99.8	99.71	98.59	92.5	90.39
24		91.11	92.65	97.74	99.8	99.71	98.59	92.39	90.37
25		91	92.67	97.67	99.89	99.69	98.55	92.39	90.37
26		90.98	92.69	97.69	99.93	99.8	98.53	91.16	89.23
27		90.98	92.69	97.69	99.93	99.8	98.53	92.12	90.1
28		90.94	92.6	97.69	99.93	99.8	98.37	92.12	90.1
29		90.76	92.54	97.74	99.93	99.64	98.39	91.05	88.88
30		90.76	92.54	97.74	99.93	99.64	98.39	91.88	89.82
31		90.72	92.5	97.74	99.62	99.1	98.26	91.88	89.82
32		90.46	92.34	97.6	99.47	98.88	98.17	90.72	88.62
33		90.46	92.34	97.6	99.47	98.88	98.17	91.53	89.36
34		90.41	92.23	97.52	99.34	98.88	97.71	91.53	89.36
35		90.28	92.08	97.21	98.88	98.66	97.58	91.4	89.14
36		90.28	92.08	97.21	98.88	98.66	97.58	91.4	89.14
37		90.13	91.99	97.01	98.83	98.39	97.56	91.4	89.14
38		89.84	91.73	96.82	98.64	98.11	97.56	91.25	89.1
39		89.84	91.73	96.82	98.64	98.11	97.56	89.93	87.87
40		89.8	91.71	96.82	98.64	98.11	97.56	89.93	87.87
41		89.8	91.6	96.82	98.77	98.35	98.59	89.93	87.87
42		89.8	91.6	96.82	98.77	98.35	98.59	89.93	87.87
43		90	91.71	97.01	98.85	98.57	98.59	90.15	87.85
44		90	91.71	97.01	98.85	98.57	98.59	90.19	87.89
45		90	91.88	97.01	99.12	98.77	98.5	90.19	87.89
46		90	91.88	97.14	99.25	98.92	98.42	90.26	87.98
47		90	91.88	97.14	99.25	98.92	98.42	91.49	89.21
48		90.13	91.88	97.28	99.29	98.96	98.17	91.49	89.21
49		90.21	91.9	97.34	99.29	98.92	98.15	91.62	89.47
50		90.21	91.9	97.34	99.29	98.92	98.15	91.64	89.67
51		90.24	91.92	97.3	99.36	99.07	97.98	91.64	89.67

Wall Temperature Measurements Along Heater Assembly

Stainless Steel Particles- 2.5 mm dia - 250 g loading

Re = 45602 q" = 55.944 kW/m2 T_W = 94.70918

Measure-ment no. (N)		Probe 1 T_1 (°C)	Probe 2 T_2 (°C)	Probe 3 T_3 (°C)	Probe 4 T_4 (°C)	Probe 5 T_5 (°C)	Probe 6 T_6 (oC)	Probe 7 T_7 (oC)	Probe 8 T_8 (oC)
52		90.28	91.95	97.36	99.36	99.07	97.96	91.66	89.69
53		90.28	91.95	97.36	99.36	99.07	97.96	91.71	89.78
54		90.32	92.01	97.25	99.36	99.16	97.96	91.71	89.78
55		90.41	92.03	97.28	99.36	99.25	97.96	91.73	89.91
56		90.41	92.03	97.28	99.36	99.25	97.96	91.71	89.89
57		90.48	92.17	97.28	99.38	99.29	97.98	91.71	89.89
58		90.65	92.36	97.6	99.64	99.4	98.28	91.88	89.95
59		90.65	92.36	97.6	99.64	99.4	98.28	90.89	88.92
60		90.89	92.56	97.8	99.95	99.75	98.55	90.89	88.92
61		90.89	92.56	97.8	99.95	99.75	98.57	92.14	90.21
62		90.89	92.56	97.8	99.95	99.75	98.57	92.43	90.35
63		90.83	92.45	97.8	99.95	99.75	98.57	92.43	90.35
64		90.83	92.45	97.91	100	99.91	98.48	92.52	90.35
65		90.83	92.45	97.91	100	99.91	98.48	92.54	90.37
66		90.89	92.6	97.91	100	99.91	98.48	92.54	90.37
67		90.98	92.63	97.87	99.93	99.67	98.09	92.58	90.5
68		90.98	92.63	97.87	99.93	99.67	98.09	91.29	89.19
69		91	92.69	97.87	99.93	99.67	98.09	91.29	89.19
70		91.09	92.91	97.93	100.39	99.86	98.2	92.6	90.48
71		91.09	92.91	97.93	100.39	99.86	98.2	92.58	90.41
72		91.18	92.93	98.09	100.39	99.89	98.28	92.58	90.41
73		91.18	92.93	98.09	100.39	99.89	98.28	92.58	90.41
74		91.07	92.89	97.98	100.39	99.84	98.17	92.52	90.24
75		91	92.85	97.98	99.97	99.8	97.93	92.52	90.24
76		91	92.85	97.98	99.97	99.8	97.93	92.12	89.93
77		90.76	92.5	97.69	99.84	99.64	97.91	92.12	89.93
78		90.74	92.47	97.69	99.84	99.6	97.89	91.95	89.78
79		90.74	92.47	97.69	99.84	99.6	97.89	91.95	89.78
80		90.61	92.41	97.45	99.69	99.4	97.82	91.95	89.78
81		90.57	92.25	97.45	99.67	99.25	97.74	90.5	88.27
82		90.57	92.25	97.45	99.67	99.25	97.74	90.5	88.27
83		90.26	92.19	97.43	99.23	98.61	97.45	90.5	88.27
84		90.17	91.99	97.23	98.88	98.55	97.19	90.39	88.11
85		90.17	91.99	97.23	98.88	98.55	97.19	91.31	89.14
86		89.93	91.88	97.1	98.88	98.44	97.19	91.31	89.14
87		89.93	91.71	96.88	98.83	98.44	97.58	90.19	87.96
88		89.93	91.71	96.88	98.83	98.44	97.58	91.31	89.1
89		89.93	91.6	96.82	98.9	98.5	97.58	91.31	89.1
90		89.93	91.6	96.82	98.9	98.5	97.58	91.31	89.1
91		89.75	91.51	96.82	98.94	98.5	97.5	91.33	89.12
92		89.71	91.49	96.84	98.99	98.5	97.5	91.33	89.12
93		89.71	91.49	96.84	98.99	98.5	97.5	91.49	89.23
94		89.71	91.49	96.86	99.01	98.68	97.74	91.6	89.38
95		89.8	91.49	97.03	99.21	98.7	97.78	91.6	89.38
96		89.8	91.49	97.03	99.21	98.7	97.78	91.6	89.38
97		89.95	91.62	97.01	99.25	99.01	97.78	90.54	88.4
98		89.97	91.68	97.08	99.45	99.1	97.82	90.54	88.4
99		89.97	91.68	97.08	99.45	99.1	97.82	90.54	88.4
100		90.08	91.71	97.08	99.45	99.16	97.82	90.74	88.57

Wall Temperature Measurements Along Heater Assembly

Appendix A.1/3:1

Stainless Steel Particles- 2.5 mm dia - 250 g loading

Re = 45602 q" = 83.916 kW/m2 T_W = 97.99263

Measure-ment no. (N)	T* =	91.5107 Probe 1 T_1 (°C)	94.2701 Probe 2 T_2 (°C)	101.7102 Probe 3 T_3 (°C)	104.1417 Probe 4 T_4 (°C)	103.9092 Probe 5 T_5 (°C)	102.1321 Probe 6 T_6 (oC)	94.1181 Probe 7 T_7 (oC)	92.1489 Probe 8 T_8 (oC)
1		91.14	94.07	101.62	104.03	103.94	102.37	94.49	92.25
2		91.14	94.07	101.62	104.03	103.94	102.37	93.44	91.11
3		91.27	94.12	101.62	104.2	104.16	102.4	93.44	91.11
4		91.33	94.25	101.67	104.38	104.44	102.48	94.4	92.36
5		91.33	94.25	101.67	104.38	104.44	102.48	94.4	92.58
6		91.55	94.47	101.78	104.47	104.44	102.73	94.4	92.58
7		91.6	94.49	101.89	104.49	104.53	102.7	94.56	92.65
8		91.6	94.49	101.89	104.49	104.53	102.7	94.56	92.8
9		91.73	94.6	101.89	104.49	104.33	102.7	94.56	92.8
10		91.86	94.69	101.87	104.47	104.18	102.55	94.56	92.8
11		91.86	94.69	101.87	104.47	104.18	102.55	94.62	92.8
12		91.88	94.69	101.87	104.49	104.18	102.55	94.62	92.8
13		91.97	94.75	101.85	104.49	104.33	102.68	93.48	91.77
14		91.97	94.75	101.85	104.49	104.33	102.68	94.84	93.02
15		92.01	94.75	101.85	104.49	104.33	102.68	94.84	93.02
16		92.01	94.75	101.82	104.38	104.22	102.59	94.93	93.17
17		92.01	94.75	101.82	104.38	104.22	102.59	94.93	93.17
18		92.01	94.71	101.8	104.36	104.22	102.35	94.93	93.17
19		91.97	94.69	101.78	104.31	104.22	102.35	94.8	93.11
20		91.97	94.69	101.78	104.31	104.22	102.35	94.8	93.07
21		91.95	94.64	101.76	104	103.92	102.04	94.8	93.07
22		91.92	94.56	101.67	104	103.72	102.04	94.8	92.98
23		91.92	94.56	101.67	104	103.72	102.04	94.78	92.71
24		91.73	94.53	101.65	104	103.72	101.98	94.78	92.71
25		91.55	94.32	101.49	104	103.45	101.43	93.26	91.03
26		91.55	94.32	101.49	104	103.45	101.43	93.26	91.03
27		91.46	94.23	101.49	103.34	103.19	101.43	93.26	91.03
28		91.46	94.23	101.49	103.34	103.19	101.43	94.01	91.88
29		91.25	93.96	101.34	103.34	103.19	101.62	94.01	91.88
30		91.07	93.85	101.21	103.56	103.19	101.62	94.01	91.88
31		91.07	93.85	101.21	103.56	103.19	101.62	92.74	90.39
32		90.96	93.83	101.21	103.56	103.01	101.29	92.74	90.39
33		90.87	93.64	101.05	103.43	103.01	101.29	92.74	90.39
34		90.87	93.64	101.05	103.43	103.01	101.29	93.85	91.73
35		90.85	93.55	101.05	103.39	103.19	101.45	93.85	91.73
36		90.83	93.55	101.07	103.39	103.19	101.67	93.85	91.73
37		90.83	93.55	101.07	103.39	103.19	101.67	92.76	90.5
38		90.85	93.55	101.12	103.5	103.5	101.69	92.76	90.5
39		90.85	93.55	101.21	103.72	103.5	101.87	92.76	90.5
40		90.85	93.55	101.21	103.72	103.5	101.87	93.09	90.89
41		90.98	93.61	101.36	103.85	103.67	101.89	94.27	92.01
42		91.07	93.72	101.38	103.85	103.72	101.89	94.27	92.01
43		91.07	93.72	101.38	103.85	103.72	101.89	94.42	92.5
44		91.14	93.83	101.43	103.85	103.76	101.96	94.49	92.54
45		91.18	93.92	101.54	103.87	103.83	101.96	94.49	92.54
46		91.18	93.92	101.54	103.87	103.83	101.96	94.42	92.54
47		91.38	94.01	101.69	104.11	104.14	102.13	93.33	91.66
48		91.6	94.29	101.87	104.22	104.16	102.37	93.33	91.66
49		91.6	94.29	101.87	104.22	104.16	102.37	93.33	91.66
50		91.68	94.45	101.93	104.36	104.25	102.37	93.5	91.92
51		91.79	94.53	102	104.33	104.25	102.37	93.5	91.92

Wall Temperature Measurements Along Heater Assembly

Stainless Steel Particles- 2.5 mm dia - 250 g loading

Re = 45602 q" = 83.916 kW/m2 T_W = 97.99263

Measure-ment no. (N)		Probe 1 T_1 (°C)	Probe 2 T_2 (°C)	Probe 3 T_3 (°C)	Probe 4 T_4 (°C)	Probe 5 T_5 (°C)	Probe 6 T_6 (oC)	Probe 7 T_7 (oC)	Probe 8 T_8 (oC)
52		91.79	94.53	102	104.33	104.25	102.37	94.89	93.26
53		91.84	94.53	102	104.33	104.18	102.44	94.89	93.42
54		91.84	94.53	102	104.33	104.18	102.44	94.89	93.42
55		91.84	94.58	101.96	104.25	104	102.18	95.08	93.44
56		91.84	94.58	101.93	104.16	104.05	102.33	95.08	93.42
57		91.84	94.58	101.93	104.16	104.05	102.33	95.08	93.42
58		91.92	94.67	101.96	104.25	104.05	102.33	94.97	93.28
59		91.95	94.71	102.04	104.51	104.38	102.44	94.97	93.28
60		91.95	94.71	102.04	104.51	104.38	102.44	93.72	92.01
61		91.92	94.69	102.22	104.86	104.62	102.7	93.72	91.9
62		92.06	95.1	102.46	104.86	104.64	102.88	93.72	91.9
63		92.06	95.1	102.46	104.86	104.64	102.88	93.57	91.77
64		92.43	95.06	102.46	104.97	105.08	103.06	93.57	91.77
65		92.43	95.06	102.46	105.06	105.08	103.06	93.57	91.77
66		92.43	95.06	102.46	105.06	105.08	103.06	94.38	92.43
67		92.39	95	102.46	105.08	104.95	102.92	94.38	92.43
68		92.17	94.8	102.29	104.88	104.29	102.26	94.38	92.43
69		92.17	94.8	102.29	104.88	104.29	102.26	94.34	92.06
70		92.14	94.73	102.02	104.49	104.29	102.26	94.34	91.9
71		91.92	94.53	102.02	104.49	104.29	102.26	94.34	91.9
72		91.92	94.53	102.02	104.49	104.29	102.26	93.24	90.67
73		91.07	93.9	101.49	104.16	104.05	101.89	94.01	91.68
74		90.94	93.77	101.49	104.07	103.7	101.74	94.01	91.68
75		90.94	93.77	101.49	104.07	103.7	101.74	92.91	90.46
76		90.78	93.7	101.43	104	103.7	101.76	94.01	91.68
77		90.78	93.7	101.43	104	103.7	101.76	94.01	91.68
78		90.78	93.7	101.43	103.87	103.63	101.76	92.78	90.57
79		90.92	93.72	101.43	103.81	103.61	101.67	92.91	90.76
80		90.92	93.72	101.43	103.81	103.61	101.67	92.91	90.76
81		90.92	93.77	101.47	103.81	103.37	101.67	92.91	90.76
82		90.92	93.77	101.47	103.89	103.37	101.74	94.29	92.21
83		90.92	93.77	101.47	103.89	103.37	101.74	94.29	92.21
84		91.07	93.88	101.56	103.89	103.61	101.91	94.29	92.21
85		91.07	93.9	101.6	103.89	103.61	101.91	94.29	92.25
86		91.07	93.9	101.6	103.89	103.61	101.91	94.29	92.25
87		91.14	93.92	101.65	103.89	103.7	101.85	93.28	91.35
88		91.29	94.1	101.69	104.11	103.56	101.85	93.28	91.35
89		91.29	94.1	101.69	104.11	103.56	101.85	94.62	92.63
90		91.38	94.16	101.67	104.09	103.59	102.24	94.62	92.89
91		91.44	94.16	101.65	103.98	103.59	102.31	94.62	92.89
92		91.44	94.16	101.65	103.98	103.59	102.31	94.78	92.91
93		91.51	94.23	101.65	103.98	103.67	102.24	94.78	92.91
94		91.73	94.38	101.85	104.22	103.67	101.91	94.78	92.91
95		91.73	94.38	101.85	104.22	103.67	101.91	94.78	92.91
96		91.73	94.42	101.85	104.22	103.63	101.91	94.86	93.09
97		91.73	94.42	101.82	104.22	103.63	101.91	94.86	93.09
98		91.73	94.42	101.82	104.22	103.63	101.91	94.86	93.09
99		91.68	94.42	101.78	104.22	103.74	102.02	94.8	92.89
100		91.73	94.42	101.82	104.2	104.09	102.18	94.8	92.89

Wall Temperature Measurements Along Heater Assembly

Stainless Steel Particles- 2.5 mm dia - 250 g loading

Re = 45602 q" = 111.888 kW/m2 T_W = 99.94768

Measure-ment no. (N)	T* =	92.3392 Probe 1 T_1 (°C)	95.8833 Probe 2 T_2 (°C)	104.0943 Probe 3 T_3 (°C)	106.7102 Probe 4 T_4 (°C)	106.8346 Probe 5 T_5 (°C)	104.9011 Probe 6 T_6 (oC)	95.3029 Probe 7 T_7 (oC)	93.5158 Probe 8 T_8 (oC)
1		92.01	95.7	103.92	106.65	106.89	104.91	95.54	93.42
2		92.01	95.7	103.92	106.65	106.89	104.91	95.46	93.33
3		91.99	95.61	103.83	106.54	106.82	104.71	94.21	92.08
4		91.99	95.61	103.83	106.54	106.82	104.71	94.21	92.08
5		91.77	95.5	103.78	106.47	106.67	104.71	94.21	92.08
6		91.6	95.3	103.78	106.47	106.49	104.69	95.26	93.11
7		91.6	95.3	103.78	106.47	106.49	104.69	95.26	93.11
8		91.55	95.26	103.72	106.45	106.47	104.66	95.35	93.24
9		91.6	95.26	103.72	106.43	106.49	104.69	95.39	93.39
10		91.6	95.26	103.72	106.43	106.49	104.69	95.39	93.39
11		91.62	95.24	103.7	106.34	106.51	104.47	95.35	93.39
12		91.62	95.24	103.7	106.34	106.51	104.47	95.35	93.39
13		91.64	95.24	103.7	106.34	106.51	104.47	94.29	92.45
14		91.82	95.43	103.83	106.4	106.51	104.47	94.32	92.47
15		91.82	95.43	103.83	106.4	106.51	104.47	94.32	92.47
16		91.9	95.48	103.96	106.51	106.8	104.66	95.63	94.03
17		92.08	95.63	104	106.69	106.87	104.8	95.67	94.14
18		92.08	95.63	104	106.69	106.87	104.8	95.67	94.14
19		92.17	95.72	104.03	106.74	106.93	104.93	95.7	94.32
20		92.25	95.74	104.2	106.74	106.93	104.93	95.7	94.32
21		92.25	95.74	104.2	106.74	106.93	104.93	95.7	94.32
22		92.41	95.89	104.2	106.54	106.67	104.55	95.87	94.56
23		92.5	95.94	104.25	106.56	106.69	104.58	95.87	94.56
24		92.5	95.94	104.25	106.56	106.69	104.58	94.56	93.28
25		92.76	96.05	104.27	106.74	107.07	104.95	94.56	93.26
26		92.82	96.16	104.4	107	107.07	105.08	94.56	93.26
27		92.82	96.16	104.4	107	107.07	105.08	94.56	93.26
28		92.91	96.27	104.49	107.07	107.18	105.28	95.92	94.56
29		92.91	96.27	104.49	107.07	107.18	105.28	95.92	94.56
30		92.89	96.31	104.6	107.15	107.35	105.59	95.89	94.53
31		92.98	96.42	104.6	107.15	107.53	105.83	95.85	94.27
32		92.98	96.42	104.6	107.15	107.53	105.83	95.85	94.27
33		93	96.42	104.6	107.15	107.62	105.83	95.87	94.29
34		93	96.42	104.55	107.18	107.53	105.83	95.87	94.32
35		93	96.42	104.55	107.18	107.53	105.83	95.87	94.32
36		93	96.42	104.55	107.18	107.18	105.44	95.87	94.32
37		92.89	96.35	104.33	106.93	107.15	105.28	95.83	94.16
38		92.89	96.35	104.33	106.93	107.15	105.28	95.83	94.16
39		92.69	96.27	104.36	106.91	107.18	105.3	95.81	93.94
40		92.6	96.16	104.27	106.91	107.18	105.08	95.67	93.94
41		92.6	96.16	104.27	106.91	107.18	105.08	95.67	93.94
42		92.56	96.05	104.25	106.78	106.69	104.88	95.65	93.48
43		92.36	95.89	104.07	106.65	106.69	104.88	95.59	93.26
44		92.36	95.89	104.07	106.65	106.69	104.88	95.59	93.26
45		92.21	95.81	104.07	106.62	106.96	105.02	95.65	93.26
46		92.01	95.7	103.98	106.6	106.98	105.02	95.59	93.11
47		92.01	95.7	103.98	106.6	106.98	105.02	95.59	93.11
48		91.97	95.61	103.92	106.6	106.98	105	95.43	93.13
49		91.97	95.61	103.92	106.6	106.98	105	94.07	91.88
50		91.92	95.59	103.92	106.67	107	105	94.07	91.88
51		91.92	95.59	103.92	106.78	107.07	104.88	94.01	91.86

Wall Temperature Measurements Along Heater Assembly

Stainless Steel Particles- 2.5 mm dia - 250 g loading

Re = 45602 q" = 111.888 kW/m2 T_W = 99.94768

Measure-ment no. (N)		Probe 1 T_1 (°C)	Probe 2 T_2 (°C)	Probe 3 T_3 (°C)	Probe 4 T_4 (°C)	Probe 5 T_5 (°C)	Probe 6 T_6 (oC)	Probe 7 T_7 (oC)	Probe 8 T_8 (oC)
52		91.92	95.59	103.92	106.78	107.07	104.88	94.01	91.86
53		91.92	95.59	103.96	106.78	107.07	104.97	94.05	91.88
54		91.92	95.63	104	106.78	107.07	104.97	95.57	93.37
55		91.92	95.63	104	106.78	107.07	104.97	95.57	93.37
56		92.01	95.7	103.98	106.71	107.07	105.06	95.59	93.57
57		92.03	95.7	104.05	106.8	106.96	105.06	95.63	93.7
58		92.03	95.7	104.05	106.8	106.96	105.06	95.63	93.7
59		92.14	95.72	104.11	106.87	106.78	104.8	95.74	94.05
60		92.3	95.87	104.09	106.85	106.58	104.58	95.85	94.16
61		92.3	95.87	104.09	106.85	106.58	104.58	95.85	94.16
62		92.45	95.89	104	106.4	106.56	104.6	95.85	94.18
63		92.45	95.87	103.98	106.38	106.54	104.58	95.85	94.18
64		92.45	95.87	103.98	106.38	106.54	104.58	95.85	94.18
65		92.54	95.85	104.09	106.67	106.47	104.64	95.76	94.29
66		92.52	95.87	104.16	106.67	106.45	104.66	94.47	92.96
67		92.52	95.87	104.16	106.67	106.45	104.66	94.47	92.96
68		92.69	96.14	104.25	106.85	106.65	104.69	95.74	94.4
69		92.69	96.14	104.25	106.85	106.65	104.69	94.58	93.17
70		92.82	96.27	104.25	106.82	106.8	104.69	94.58	93.17
71		92.87	96.35	104.29	106.91	106.8	104.8	95.74	94.49
72		92.87	96.35	104.29	106.91	106.8	104.8	94.58	93.2
73		93.04	96.49	104.33	106.91	107.07	105.19	94.58	93.2
74		93.04	96.49	104.33	106.93	107.09	105.19	95.89	94.45
75		93.04	96.49	104.33	106.93	107.09	105.19	95.89	94.4
76		92.96	96.42	104.31	106.93	107.22	105.08	95.89	94.4
77		92.91	96.42	104.25	106.89	107.09	104.97	95.89	94.45
78		92.91	96.42	104.25	106.89	107.09	104.97	95.89	94.45
79		92.91	96.42	104.25	106.82	106.62	104.97	95.83	94.4
80		92.87	96.4	104.25	106.78	106.6	104.97	95.7	94.12
81		92.87	96.4	104.25	106.78	106.6	104.97	95.7	94.12
82		92.6	96.18	104.11	106.74	106.6	104.97	95.83	93.9
83		92.6	96.18	104.11	106.74	106.6	104.97	95.67	93.88
84		92.5	96.09	104.09	106.69	106.6	104.69	95.67	93.88
85		92.5	96.09	104.05	106.6	106.43	104.27	95.67	93.75
86		92.5	96.09	104.05	106.6	106.43	104.27	94.42	92.65
87		92.5	95.85	103.89	106.21	106.27	104.14	94.42	92.65
88		92.12	95.76	103.78	106.21	106.27	104.14	94.16	92.03
89		92.12	95.76	103.78	106.21	106.27	104.14	94.16	92.03
90		91.92	95.63	103.78	106.36	106.54	104.86	94.16	92.03
91		91.9	95.54	103.83	106.56	106.65	104.91	94.03	91.95
92		91.9	95.54	103.83	106.56	106.65	104.91	94.03	91.95
93		91.9	95.52	103.94	106.56	106.69	105.15	95.43	93.37
94		91.92	95.52	103.96	106.6	106.82	105.15	95.48	93.37
95		91.92	95.52	103.96	106.6	106.82	105.15	95.48	93.37
96		92.03	95.59	103.98	106.65	107.02	105.04	95.59	93.61
97		92.1	95.59	104.05	106.8	106.85	105	95.76	93.85
98		92.1	95.59	104.05	106.8	106.85	105	95.76	93.85
99		92.19	95.78	104.05	106.8	106.78	104.8	95.76	93.85
100		92.28	95.83	104.03	106.51	106.78	104.8	95.67	93.96

Wall Temperature Measurements Along Heater Assembly

Stainless Steel Particles- 2.5 mm dia - 250 g loading

Re = 45602 q" = 139.860 kW/m2 T_W = 101.7084

Measure-ment no. (N)	T* =	93.5347 Probe 1 T_1 (°C)	97.1771 Probe 2 T_2 (°C)	106.1958 Probe 3 T_3 (°C)	109.0552 Probe 4 T_4 (°C)	109.3105 Probe 5 T_5 (°C)	107.3686 Probe 6 T_6 (oC)	96.8468 Probe 7 T_7 (oC)	94.1781 Probe 8 T_8 (oC)
1		93.59	97.12	106.16	108.81	108.87	106.91	97.41	94.6
2		93.59	97.12	106.16	108.81	108.87	106.91	97.41	94.49
3		93.33	96.99	106.16	108.98	109.11	107	97.14	94.49
4		93.33	96.99	106.16	108.98	109.11	107	97.14	94.49
5		93.07	96.9	106.16	109.18	109.4	107.15	97.14	94.4
6		93.07	96.82	106.14	109.18	109.4	107.15	97.12	94.4
7		93	96.79	106.1	108.89	108.94	106.91	97.12	94.4
8		93	96.79	106.1	108.89	108.94	106.91	97.19	94.4
9		93.07	96.82	106.1	108.85	108.74	106.87	95.85	93.33
10		93.04	96.84	106.1	108.65	108.83	106.78	95.85	93.33
11		93.04	96.84	106.1	108.65	108.83	106.78	96.05	93.33
12		93.13	96.86	106.14	108.65	108.48	106.87	96.05	93.33
13		93.13	96.86	106.14	108.65	108.48	106.87	96.05	93.33
14		93.26	96.88	106.14	108.65	108.83	106.87	96.05	93.33
15		93.26	96.95	106.16	108.87	109.2	107.4	97.34	94.58
16		93.26	96.95	106.16	108.87	109.2	107.4	97.34	94.58
17		93.42	97.03	106.18	108.87	109.25	107.42	96.16	93.68
18		93.53	97.14	106.29	109.16	109.38	107.7	96.16	93.68
19		93.53	97.14	106.29	109.16	109.38	107.7	96.4	93.68
20		93.66	97.25	106.32	109.18	109.4	107.73	96.4	93.68
21		93.85	97.43	106.32	109.14	109.22	107.4	96.4	93.68
22		93.85	97.43	106.32	109.14	109.22	107.4	97.76	95
23		93.9	97.45	106.32	109.14	109.22	107.22	97.78	95
24		93.94	97.45	106.38	109.14	109.29	107.22	97.78	95
25		93.94	97.45	106.38	109.14	109.29	107.22	97.78	94.89
26		94.03	97.47	106.4	109.25	109.53	107.73	97.67	94.89
27		94.07	97.52	106.43	109.25	109.75	107.88	97.67	94.89
28		94.07	97.52	106.43	109.25	109.75	107.88	97.67	94.93
29		94.1	97.56	106.49	109.4	109.91	108.08	97.82	95.04
30		94.25	97.69	106.49	109.4	109.91	108.08	97.82	95.04
31		94.25	97.69	106.49	109.4	109.91	108.08	97.82	94.95
32		94.25	97.69	106.49	109.53	109.8	107.75	97.82	94.95
33		94.1	97.65	106.47	109.31	109.66	107.77	97.82	94.95
34		94.1	97.65	106.47	109.31	109.66	107.77	97.56	94.67
35		94.1	97.6	106.45	109.49	109.66	107.86	96.25	93.57
36		94.1	97.56	106.4	109.33	109.75	107.86	96.25	93.57
37		94.1	97.56	106.4	109.33	109.75	107.86	95.92	93.24
38		93.99	97.5	106.34	109.33	109.86	107.84	95.94	93.26
39		93.72	97.39	106.32	109.33	109.86	107.7	95.94	93.26
40		93.72	97.39	106.32	109.33	109.86	107.7	97.23	94.6
41		93.59	97.25	106.18	109.2	109.86	107.59	97.21	94.58
42		93.55	97.23	106.18	109.2	109.6	107.51	97.21	94.58
43		93.55	97.23	106.18	109.2	109.6	107.51	97.08	94.58
44		93.28	97.03	106.18	109.16	109.55	107.37	97.01	94.32
45		93.28	96.97	106.21	109.14	109.47	107.37	97.01	94.32
46		93.28	96.97	106.21	109.14	109.47	107.37	95.65	93.13
47		93.2	96.97	106.18	109.07	109.38	107.44	97.01	94.32
48		93.2	96.97	106.18	109.07	109.38	107.44	97.01	94.32
49		93.15	96.9	106.21	109.09	109.27	107.44	97.03	94.53
50		93.13	96.92	106.16	109.05	109	106.87	97.03	94.53
51		93.13	96.92	106.16	109.05	109	106.87	97.03	94.53

Wall Temperature Measurements Along Heater Assembly

Stainless Steel Particles- 2.5 mm dia - 250 g loading

Re = 45602 q" = 139.860 kW/m2 T_W = 101.7084

Measure-ment no. (N)		Probe 1 T_1 (°C)	Probe 2 T_2 (°C)	Probe 3 T_3 (°C)	Probe 4 T_4 (°C)	Probe 5 T_5 (°C)	Probe 6 T_6 (oC)	Probe 7 T_7 (oC)	Probe 8 T_8 (oC)
52		93.15	96.92	106.21	108.98	108.92	106.87	97.06	94.64
53		93.24	96.92	106.21	108.98	108.92	106.87	95.94	93.55
54		93.24	96.92	106.21	108.98	108.92	106.87	95.94	93.55
55		93.33	96.99	106.25	109.03	108.98	107.24	95.94	93.55
56		93.39	97.1	106.29	109.27	109.44	107.46	95.94	93.35
57		93.39	97.1	106.29	109.27	109.44	107.46	95.94	93.35
58		93.61	97.17	106.34	109.38	109.82	107.97	95.94	93.35
59		93.7	97.39	106.38	109.44	110	108.17	97.34	94.69
60		93.7	97.39	106.38	109.44	110	108.17	97.34	94.69
61		93.9	97.43	106.43	109.44	110.11	108.19	97.54	94.86
62		94.12	97.6	106.45	109.42	110.11	108.19	97.56	94.93
63		94.12	97.6	106.45	109.42	110.11	108.19	97.56	94.93
64		94.12	97.6	106.45	109.42	109.86	108.12	97.63	95
65		93.61	97.58	106.45	109.42	109.8	107.92	97.63	94.95
66		93.61	97.58	106.45	109.42	109.8	107.92	97.63	94.95
67		93.61	97.32	106.1	109.07	109.66	107.59	96.18	93.59
68		93.68	97.28	106.01	109.07	109.51	107.59	96.16	93.57
69		93.68	97.28	106.01	109.07	109.51	107.59	96.16	93.57
70		93.72	97.3	106.01	109.07	109.51	107.64	97.45	94.82
71		93.68	97.28	106.01	109.11	109.66	107.66	97.47	94.84
72		93.68	97.28	106.01	109.11	109.66	107.66	97.47	94.84
73		93.7	97.3	106.01	109.14	109.66	107.64	97.5	94.84
74		93.7	97.3	106.01	109.14	109.66	107.64	97.5	94.84
75		93.68	97.23	106.01	109.14	109.62	107.62	95.92	93.46
76		93.55	97.19	106.25	109.22	109.36	107.44	95.92	93.44
77		93.55	97.19	106.25	109.22	109.36	107.44	95.92	93.44
78		93.24	97.03	105.79	108.74	109.11	106.98	95.92	93.44
79		93.11	96.99	105.92	108.87	108.94	106.76	95.89	93.15
80		93.11	96.99	105.92	108.87	108.94	106.76	95.89	93.15
81		93.02	96.84	105.79	108.72	108.61	106.43	95.85	93.15
82		93.02	96.84	105.92	108.87	108.61	106.43	95.85	93.15
83		93.02	96.84	105.92	108.87	108.61	106.43	95.85	93.15
84		92.87	96.73	105.72	108.54	108.85	106.76	97.1	94.45
85		92.87	96.73	105.74	108.54	109	107	97.1	94.45
86		92.87	96.73	105.74	108.54	109	107	97.1	94.45
87		92.93	96.77	105.74	108.54	109	107.02	97.1	94.56
88		93.39	97.03	106.18	108.89	109.18	107.02	95.89	93.22
89		93.39	97.03	106.18	108.89	109.18	107.02	95.89	93.22
90		93.39	97.03	106.18	108.94	109.18	107.42	97.19	94.53
91		93.39	97.03	106.16	108.89	109.18	107.42	97.45	94.75
92		93.39	97.03	106.16	108.89	109.18	107.42	97.45	94.75
93		93.59	97.12	106.16	108.94	108.96	107.26	97.45	94.75
94		93.64	97.12	106.21	108.96	108.87	107.13	97.45	94.75
95		93.64	97.12	106.21	108.96	108.87	107.13	97.45	94.75
96		93.66	97.19	106.21	108.96	108.81	106.98	96.44	93.7
97		93.66	97.19	106.21	108.96	108.81	106.98	96.44	93.7
98		93.85	97.32	106.14	108.41	108.56	106.98	97.8	94.95
99		93.94	97.34	106.03	108.41	108.56	107	96.6	93.7
100		93.94	97.34	106.03	108.41	108.56	107	96.6	93.7

Wall Temperature Measurements Along Heater Assembly

Stainless Steel Particles- 2.5 mm dia - 250 g loading

Re = 45602 q" = 167.832 kW/m2 T_W = 102.9804

Measure-ment no. (N)	T* =	93.9552 Probe 1 T_1 (°C)	97.9609 Probe 2 T_2 (°C)	107.4871 Probe 3 T_3 (°C)	110.6261 Probe 4 T_4 (°C)	111.1553 Probe 5 T_5 (°C)	109.1386 Probe 6 T_6 (oC)	99.0938 Probe 7 T_7 (oC)	94.4265 Probe 8 T_8 (oC)
1		94.03	98	107.51	110.68	111.47	109.42	99.6	95.02
2		94.03	98	107.51	110.68	111.47	109.42	99.6	95.02
3		94.34	98.26	107.55	110.68	111.47	109.42	99.6	95.02
4		94.36	98.33	107.62	110.68	111.39	109.42	99.73	95.04
5		94.36	98.33	107.62	110.68	111.39	109.42	99.73	95.04
6		94.53	98.42	107.62	110.68	111.39	109.42	98.35	93.75
7		94.69	98.53	107.62	110.64	111.28	109.64	98.35	93.81
8		94.69	98.53	107.62	110.64	111.28	109.64	98.35	93.81
9		94.53	98.53	107.62	110.68	111.39	109.64	98.37	93.83
10		94.53	98.53	107.62	110.68	111.39	109.64	98.35	93.81
11		94.53	98.53	107.64	110.75	111.28	109.36	98.35	93.81
12		94.53	98.48	107.66	110.75	111.28	109.05	99.91	95.06
13		94.53	98.48	107.66	110.75	111.28	109.05	98.42	93.7
14		94.53	98.46	107.66	110.72	111.14	108.98	98.42	93.7
15		94.36	98.37	107.64	110.72	111.14	108.98	99.56	94.53
16		94.36	98.37	107.64	110.72	111.14	108.98	99.45	94.51
17		94.29	98.35	107.64	110.72	111.32	109.16	99.45	94.51
18		94.03	98.11	107.62	110.77	111.32	109.31	99.45	94.51
19		94.03	98.11	107.62	110.77	111.32	109.31	99.38	94.51
20		93.96	98.02	107.57	110.72	111.32	109.31	99.38	94.51
21		93.88	98.02	107.59	110.75	110.99	109.07	99.21	94.53
22		93.88	98.02	107.59	110.75	110.99	109.07	99.21	94.53
23		93.85	97.76	107.48	110.68	110.97	109.05	99.21	94.53
24		93.64	97.67	107.42	110.59	111.19	109.18	98.96	94.49
25		93.64	97.67	107.42	110.59	111.19	109.18	98.94	94.47
26		93.48	97.67	107.37	110.55	111.21	109.18	98.94	94.47
27		93.44	97.65	107.42	110.59	111.3	109.27	97.91	93.39
28		93.44	97.65	107.42	110.59	111.3	109.27	97.91	93.39
29		93.46	97.67	107.42	110.68	111.36	109.29	97.91	93.15
30		93.46	97.71	107.42	110.68	111.47	109.42	97.91	93.15
31		93.46	97.71	107.42	110.68	111.47	109.42	97.91	93.15
32		93.72	97.82	107.37	110.64	111.47	109.42	99.29	94.75
33		93.72	97.82	107.37	110.64	111.47	109.42	99.34	94.89
34		93.77	97.91	107.37	110.64	111.25	109.03	99.34	94.89
35		93.92	98	107.48	110.55	111.21	109.03	99.58	94.95
36		93.92	98	107.48	110.55	111.21	109.03	99.58	94.95
37		93.99	98	107.51	110.64	111.21	109.42	99.58	94.95
38		93.96	98	107.46	110.59	111.45	109.4	98.13	93.57
39		93.96	98	107.46	110.59	111.45	109.4	98.13	93.57
40		94.16	98.07	107.48	110.7	111.45	109.2	98.13	93.57
41		94.21	98.13	107.46	110.61	111.43	109.22	99.78	95.15
42		94.21	98.13	107.46	110.61	111.43	109.22	100.02	95.15
43		94.32	98.17	107.4	110.44	110.83	109.18	100.02	95.15
44		94.34	98.2	107.42	110.46	110.79	108.83	100.02	94.97
45		94.34	98.2	107.42	110.46	110.79	108.83	98.44	93.5
46		94.21	98.09	107.4	110.41	110.77	108.81	98.44	93.5
47		94.21	98.02	107.42	110.46	111.08	108.87	98.33	93.48
48		94.21	98.02	107.42	110.46	111.08	108.87	98.33	93.48
49		94.07	98	107.42	110.57	111.12	108.92	98.33	93.48
50		94.05	97.93	107.42	110.57	111.12	108.89	99.42	94.75
51		94.05	97.93	107.42	110.57	111.12	108.89	99.53	94.75

Wall Temperature Measurements Along Heater Assembly

Stainless Steel Particles- 2.5 mm dia - 250 g loading

Re = 45602 q" = 167.832 kW/m2 T_W = 102.9804

Measure-ment no. (N)		Probe 1 T_1 (°C)	Probe 2 T_2 (°C)	Probe 3 T_3 (°C)	Probe 4 T_4 (°C)	Probe 5 T_5 (°C)	Probe 6 T_6 (oC)	Probe 7 T_7 (oC)	Probe 8 T_8 (oC)
52		93.88	97.8	107.37	110.5	110.9	108.89	99.53	94.75
53		93.72	97.71	107.31	110.48	110.88	108.87	99.53	94.62
54		93.72	97.71	107.31	110.48	110.88	108.87	99.12	94.56
55		93.59	97.67	107.26	110.57	111.25	109.16	99.12	94.56
56		93.59	97.67	107.26	110.57	111.25	109.16	97.82	93.15
57		93.53	97.65	107.24	110.55	111.23	109.14	97.67	93.11
58		93.48	97.65	107.29	110.64	111.21	109.2	97.67	93.11
59		93.48	97.65	107.29	110.64	111.21	109.2	97.67	93.11
60		93.39	97.54	107.35	110.55	111.08	109.16	97.67	93.22
61		93.39	97.54	107.35	110.55	110.99	109.05	97.67	93.22
62		93.39	97.54	107.35	110.55	110.99	109.05	99.21	94.71
63		93.46	97.52	107.31	110.55	110.99	109.05	99.27	94.75
64		93.57	97.58	107.31	110.55	110.88	108.81	99.27	94.75
65		93.57	97.58	107.31	110.55	110.88	108.81	99.62	94.78
66		93.57	97.65	107.31	110.55	110.88	108.76	99.62	94.91
67		93.57	97.65	107.26	110.22	110.55	108.76	99.62	94.91
68		93.57	97.65	107.26	110.22	110.55	108.76	99.62	94.93
69		93.61	97.65	107.26	110.22	110.48	108.67	99.62	94.93
70		93.81	97.69	107.37	110.35	110.55	108.87	99.71	95.06
71		93.81	97.69	107.37	110.35	110.55	108.87	99.78	95.17
72		93.92	97.71	107.48	110.59	110.92	109.11	99.78	95.17
73		93.92	97.71	107.48	110.59	110.92	109.11	99.84	95.17
74		93.96	97.78	107.48	110.61	111.1	109.25	99.93	95.19
75		94.07	97.96	107.46	110.61	111.28	109.33	99.93	95.19
76		94.07	97.96	107.46	110.61	111.28	109.33	99.91	95.21
77		94.18	98.02	107.46	110.61	111.43	109.38	100.06	95.28
78		94.25	98.07	107.51	110.68	111.43	109.38	100.06	95.28
79		94.25	98.07	107.51	110.68	111.43	109.38	100.04	95.26
80		94.36	98.17	107.64	110.79	111.21	109.31	100.06	95.19
81		94.36	98.17	107.57	110.86	111.21	109.31	100.06	95.19
82		94.36	98.17	107.57	110.86	111.21	109.31	99.95	95.13
83		94.32	98.17	107.57	110.86	111.21	109.31	99.93	95.1
84		94.27	98.17	107.55	110.68	110.92	109.05	99.93	95.1
85		94.27	98.17	107.55	110.68	110.92	109.05	99.86	95.1
86		94.21	98.17	107.53	110.59	110.92	108.78	99.86	94.89
87		94.1	98.07	107.53	110.59	110.92	108.78	99.86	94.89
88		94.1	98.07	107.53	110.59	110.92	108.78	99.18	94.67
89		93.9	97.93	107.64	110.77	111.43	109.38	97.93	93.39
90		93.81	97.89	107.64	110.86	111.43	109.38	97.93	93.39
91		93.81	97.89	107.64	110.86	111.43	109.38	97.63	93.33
92		93.64	97.8	107.64	110.77	111.3	109.33	97.63	93.33
93		93.64	97.78	107.68	110.86	111.3	109.07	97.63	93.33
94		93.64	97.78	107.68	110.86	111.3	109.07	99.01	94.71
95		93.59	97.8	107.64	110.77	111.3	108.96	99.34	94.91
96		93.59	97.8	107.64	110.77	111.3	108.96	99.34	94.91
97		93.59	97.91	107.64	110.75	110.94	108.96	99.34	94.91
98		93.81	97.91	107.64	110.66	110.94	108.87	99.62	94.95
99		93.81	97.91	107.64	110.66	110.94	108.87	99.62	94.95
100		93.81	97.91	107.7	110.5	110.88	108.72	99.73	95.02

Wall Temperature Measurements Along Heater Assembly

Stainless Steel Particles- 2.5 mm dia - 250 g loading

Re = 45602 q" = 195.804 kW/m2 T_W = 104.3012

Measure-ment no. (N)	T* =	94.9002 Probe 1 T_1 (°C)	98.9892 Probe 2 T_2 (°C)	109.1944 Probe 3 T_3 (°C)	112.4051 Probe 4 T_4 (°C)	112.9794 Probe 5 T_5 (°C)	110.8822 Probe 6 T_6 (oC)	100.6122 Probe 7 T_7 (oC)	94.4469 Probe 8 T_8 (oC)
1		95.15	99.16	109.33	112.58	113.09	111.14	100.72	94.75
2		94.86	99.03	109.4	112.49	113.11	111.14	99.23	93.44
3		94.86	99.03	109.4	112.49	113.11	111.14	100.72	94.78
4		94.73	99.03	109.4	112.47	113.11	111.1	100.72	94.78
5		94.64	98.94	109.29	112.4	112.8	110.48	101.01	94.56
6		94.64	98.94	109.29	112.4	112.8	110.48	101.01	94.64
7		94.62	98.94	109.25	112.4	112.8	110.48	101.01	94.64
8		94.56	98.83	109.29	112.4	112.82	110.57	100.85	94.56
9		94.56	98.83	109.29	112.4	112.82	110.57	100.85	94.56
10		94.51	98.83	109.22	112.47	112.89	110.59	100.83	94.64
11		94.56	98.85	109.22	112.51	113	110.68	100.77	94.53
12		94.56	98.85	109.22	112.51	113	110.68	100.77	94.53
13		94.56	98.83	109.18	112.45	112.98	110.57	99.69	93.66
14		94.73	98.88	109.2	112.47	113.04	110.97	99.69	93.66
15		94.73	98.88	109.2	112.47	113.04	110.97	99.69	93.66
16		94.71	98.85	109.2	112.45	113.02	110.94	100.92	95
17		94.73	98.88	109.25	112.49	113.06	111.19	100.92	95
18		94.73	98.88	109.25	112.49	113.06	111.19	100.92	95
19		94.86	98.96	109.22	112.47	113.04	111.16	100.92	94.89
20		94.86	98.96	109.22	112.47	113.04	111.16	101.25	94.89
21		95.17	99.23	109.27	112.47	113.02	111.01	101.25	94.89
22		95.21	99.23	109.29	112.47	113.02	110.97	101.25	94.93
23		95.21	99.23	109.29	112.47	113.02	110.97	101.23	94.93
24		95.43	99.34	109.31	112.45	113.02	111.01	101.23	94.93
25		95.43	99.34	109.31	112.4	113.04	111.19	101.23	94.91
26		95.43	99.34	109.31	112.4	113.04	111.19	100.06	93.64
27		95.52	99.25	109.31	112.4	113.11	111.19	100.06	93.64
28		95.46	99.27	109.33	112.53	113.26	111.3	101.25	94.67
29		95.46	99.27	109.33	112.53	113.26	111.3	100.08	93.66
30		95.43	99.23	109.33	112.51	113.24	111.3	100.08	93.66
31		95.24	99.18	109.33	112.49	113.17	111.3	100.94	94.67
32		95.24	99.18	109.33	112.49	113.17	111.3	99.56	93.39
33		95.15	99.16	109.27	112.47	113.13	111.25	99.56	93.39
34		95.13	99.14	109.25	112.47	113.11	111.23	99.38	93.39
35		95.13	99.14	109.25	112.47	113.11	111.23	99.32	93.26
36		94.93	99.01	109.22	112.42	112.75	110.7	99.32	93.26
37		94.75	98.81	109.11	112.42	112.75	110.7	99.32	93.26
38		94.75	98.81	109.11	112.42	112.75	110.7	100.61	94.62
39		94.71	98.81	109.11	112.45	113.13	110.88	100.61	94.62
40		94.71	98.81	109.11	112.45	113.13	110.88	100.61	94.62
41		94.64	98.85	109.16	112.45	113.13	110.88	100.61	94.62
42		94.58	98.83	109.14	112.45	113.09	110.97	100.59	94.67
43		94.58	98.83	109.14	112.45	113.09	110.97	100.83	94.69
44		94.62	98.83	109.09	112.42	112.84	110.83	100.83	94.69
45		94.62	98.77	109.07	112.38	112.84	110.57	100.81	94.67
46		94.62	98.77	109.07	112.38	112.84	110.57	101.07	94.67
47		94.69	98.83	109.07	112.38	112.56	110.44	101.07	94.67
48		94.73	98.88	109.07	112.38	112.56	110.44	99.75	93.72
49		94.73	98.88	109.07	112.38	112.56	110.44	99.93	93.72
50		94.86	98.9	109.07	112.36	112.75	110.57	99.93	93.72
51		94.91	98.96	109.16	112.36	112.8	110.68	99.95	93.75

Wall Temperature Measurements Along Heater Assembly

Stainless Steel Particles- 2.5 mm dia - 250 g loading

Re = 45602 q" = 195.804 kW/m2 T_W = 104.3012

Measure-ment no. (N)		Probe 1 T_1 (°C)	Probe 2 T_2 (°C)	Probe 3 T_3 (°C)	Probe 4 T_4 (°C)	Probe 5 T_5 (°C)	Probe 6 T_6 (oC)	Probe 7 T_7 (oC)	Probe 8 T_8 (oC)
52		94.91	98.96	109.16	112.36	112.8	110.68	101.29	95.13
53		94.91	99.01	109.18	112.36	112.8	110.77	101.29	95.13
54		95.21	99.12	109.22	112.45	112.91	110.77	101.32	95.15
55		95.21	99.12	109.22	112.45	112.91	110.77	101.45	95.15
56		95.24	99.16	109.18	112.2	112.78	110.77	101.45	95.15
57		95.43	99.29	109.14	112.25	112.8	110.64	100	93.7
58		95.43	99.29	109.14	112.25	112.8	110.64	101.32	95.02
59		95.43	99.29	109.14	112.25	112.8	110.64	101.32	95.02
60		95.43	99.29	109.14	112.25	112.8	110.64	100	93.64
61		95.26	99.1	109.22	112.4	112.95	110.83	101.32	94.93
62		95.26	99.1	109.22	112.47	112.95	110.83	101.32	94.93
63		95.26	99.1	109.22	112.47	112.95	110.83	99.84	93.5
64		95.26	99.1	109.22	112.47	112.95	110.92	100.94	94.78
65		95.13	99.07	109.22	112.47	112.95	110.92	100.94	94.78
66		95.13	99.07	109.22	112.47	112.95	110.92	99.58	93.42
67		94.86	98.96	109.25	112.58	113.02	111.23	100.96	94.67
68		94.8	98.9	109.25	112.58	113.02	111.23	100.96	94.67
69		94.8	98.9	109.25	112.58	113.02	111.23	99.42	93.46
70		94.75	98.85	109.18	112.45	112.93	110.94	100.92	94.67
71		94.47	98.79	109.09	112.38	112.84	110.81	100.92	94.67
72		94.47	98.79	109.09	112.38	112.84	110.81	99.42	93.46
73		94.4	98.72	109.11	112.29	112.93	110.81	100.74	94.75
74		94.29	98.7	109.11	112.29	112.98	110.81	100.74	94.75
75		94.29	98.7	109.11	112.29	112.98	110.81	99.4	93.37
76		94.29	98.7	109.11	112.31	113.11	110.7	100.74	94.73
77		94.38	98.7	109.11	112.33	113.11	110.59	100.74	94.73
78		94.38	98.7	109.11	112.33	113.11	110.59	99.4	93.46
79		94.38	98.7	109.11	112.38	112.98	110.59	99.62	93.57
80		94.38	98.7	109.09	112.38	112.91	110.59	99.62	93.57
81		94.38	98.7	109.09	112.38	112.91	110.59	99.62	93.53
82		94.53	98.77	109	112.16	112.91	110.61	99.62	93.57
83		94.53	98.77	109	112.16	112.91	110.61	99.62	93.57
84		94.53	98.79	109	112.16	112.93	110.7	100.99	95
85		94.53	98.81	109.09	112.16	112.93	110.77	101.23	95.08
86		94.53	98.81	109.09	112.16	112.93	110.77	101.23	95.08
87		94.78	98.83	109.14	112.25	113.02	110.9	101.23	95.08
88		94.86	98.96	109.18	112.25	112.95	110.9	101.36	95.15
89		94.86	98.96	109.18	112.25	112.95	110.9	101.36	95.15
90		95.15	99.07	109.18	112.29	113.2	111.03	101.34	95.13
91		95.19	99.12	109.2	112.31	113.22	111.05	101.34	95.13
92		95.19	99.12	109.2	112.31	113.22	111.05	101.25	95.15
93		95.17	99.1	109.22	112.42	113.28	111.19	101.23	95.13
94		95.21	99.12	109.22	112.51	113.28	111.19	101.23	95.13
95		95.21	99.12	109.22	112.51	113.28	111.19	101.23	95.13
96		95.41	99.34	109.22	112.51	113.04	111.08	101.23	95.02
97		95.41	99.34	109.2	112.42	112.98	111.01	101.23	95.02
98		95.41	99.34	109.2	112.42	112.98	111.01	101.03	94.86
99		95.3	99.32	109.2	112.42	112.98	111.08	101.03	94.86
100		95.17	99.16	109.2	112.49	113.24	111.12	101.03	94.86

Wall Temperature Measurements Along Heater Assembly

Stainless Steel Particles- 2.5 mm dia - 250 g loading

Re = 45602 q" = 223.776 kW/m2 T_W = 105.1924

Measure-ment no.	T* =	95.4946	99.6177	110.3715	113.5658	114.025	111.9615	101.8189	94.684
		Probe 1	Probe 2	Probe 3	Probe 4	Probe 5	Probe 6	Probe 7	Probe 8
(N)		T_1 (°C)	T_2 (°C)	T_3 (°C)	T_4 (°C)	T_5 (°C)	T_6 (oC)	T_7 (oC)	T_8 (oC)
1		95.08	99.42	110.33	113.62	114.03	111.85	102.04	94.84
2		95.08	99.42	110.33	113.62	114.03	111.85	102.04	94.84
3		95.1	99.42	110.33	113.62	114.03	111.85	102.04	94.84
4		95.15	99.42	110.35	113.62	114.03	111.98	102.04	94.84
5		95.15	99.42	110.35	113.62	114.03	111.98	102.04	94.84
6		95.57	99.53	110.37	113.64	113.86	111.98	101.23	94.01
7		95.63	99.71	110.35	113.62	113.86	111.98	101.23	94.01
8		95.63	99.71	110.35	113.62	113.86	111.98	101.1	93.99
9		95.83	99.84	110.35	113.62	113.9	111.98	101.23	94.01
10		96	99.86	110.37	113.64	114.03	112.07	101.23	94.01
11		96	99.86	110.37	113.64	114.03	112.07	102.46	95.21
12		96	99.86	110.37	113.7	114.3	112.33	102.51	95.24
13		96	99.86	110.5	113.75	114.3	112.33	102.51	95.24
14		96	99.86	110.5	113.75	114.3	112.33	102.48	95.08
15		95.92	99.86	110.5	113.75	114.1	112.14	100.9	93.88
16		95.92	99.86	110.5	113.75	114.1	112.14	100.9	93.88
17		95.92	99.89	110.44	113.66	114.1	112.09	100.9	93.88
18		95.83	99.84	110.44	113.66	114.1	112.09	102.13	94.91
19		95.83	99.84	110.44	113.66	114.1	112.09	102.13	94.91
20		95.76	99.69	110.48	113.73	114.23	112.22	102.15	94.91
21		95.67	99.69	110.48	113.79	114.28	112.22	102.15	94.91
22		95.67	99.69	110.48	113.79	114.28	112.22	102.15	94.91
23		95.63	99.69	110.48	113.79	114.23	112.03	102.18	95.02
24		95.59	99.64	110.41	113.62	114.03	111.67	102.18	95.02
25		95.59	99.64	110.41	113.62	114.03	111.67	102.18	95.02
26		95.46	99.56	110.37	113.55	114.03	111.67	102.02	94.69
27		95	99.25	110.33	113.55	114.03	111.89	101.8	94.69
28		95	99.25	110.33	113.55	114.03	111.89	101.8	94.69
29		94.86	99.25	110.37	113.66	114.17	112.05	101.74	94.6
30		94.86	99.34	110.39	113.75	114.32	112.16	101.74	94.6
31		94.86	99.34	110.39	113.75	114.32	112.16	101.67	94.6
32		94.93	99.4	110.39	113.75	114.32	112.16	101.67	94.6
33		94.93	99.4	110.39	113.75	114.32	112.16	101.67	94.6
34		94.93	99.4	110.35	113.57	113.97	111.78	101.78	94.82
35		94.91	99.27	110.3	113.57	113.95	111.72	101.91	94.82
36		94.91	99.27	110.3	113.57	113.95	111.72	101.91	94.82
37		94.91	99.23	110.3	113.66	113.97	111.72	101.91	94.82
38		94.91	99.27	110.35	113.66	114.1	111.98	102.13	94.82
39		94.91	99.27	110.35	113.66	114.1	111.98	102.13	94.82
40		95.06	99.32	110.35	113.64	114.1	112.05	102.15	94.89
41		95.1	99.42	110.37	113.62	114.1	111.98	102.15	95.15
42		95.1	99.42	110.37	113.62	114.1	111.98	102.15	95.15
43		95.28	99.53	110.41	113.64	114.12	112.07	102.29	95.15
44		95.28	99.53	110.41	113.64	114.12	112.07	102.29	95.15
45		95.52	99.6	110.41	113.64	113.95	111.85	102.29	95.15
46		95.67	99.71	110.37	113.53	114.08	112.07	102.26	95.15
47		95.67	99.71	110.37	113.53	114.08	112.07	102.26	95.15
48		95.81	99.78	110.37	113.53	114.08	112.07	101.98	95.08
49		95.83	99.8	110.39	113.62	114.19	112.09	101.8	95.24
50		95.83	99.8	110.39	113.62	114.19	112.09	101.8	95.24
51		95.92	99.8	110.39	113.64	114.23	112.27	101.8	95.24

Wall Temperature Measurements Along Heater Assembly

Stainless Steel Particles- 2.5 mm dia - 250 g loading

Re = 45602 q" = 223.776 kW/m2 T_W = 105.1924

Measure-ment no. (N)		Probe 1 T_1 (°C)	Probe 2 T_2 (°C)	Probe 3 T_3 (°C)	Probe 4 T_4 (°C)	Probe 5 T_5 (°C)	Probe 6 T_6 (oC)	Probe 7 T_7 (oC)	Probe 8 T_8 (oC)
52		96	99.91	110.48	113.66	114.19	112.09	102.18	95.26
53		96	99.91	110.48	113.66	114.19	112.09	102.18	95.26
54		95.92	99.93	110.48	113.66	114.23	112.22	102.42	95.26
55		96.09	99.95	110.46	113.66	114.26	112.22	102.42	94.97
56		96.09	99.95	110.46	113.66	114.26	112.22	102.42	94.97
57		96.05	99.95	110.44	113.7	114.3	112.36	102.22	94.97
58		96.05	99.91	110.39	113.73	114.37	112.45	102.11	94.97
59		96.05	99.91	110.39	113.73	114.37	112.45	102.11	94.97
60		95.83	99.84	110.39	113.73	114.37	112.45	100.55	93.44
61		95.7	99.73	110.41	113.75	114.45	112.45	100.46	93.2
62		95.7	99.73	110.41	113.75	114.45	112.45	100.46	93.2
63		95.61	99.71	110.46	113.79	114.45	112.49	100.28	93.2
64		95.61	99.71	110.46	113.79	114.45	112.49	100.28	93.37
65		95.41	99.56	110.48	113.77	114.43	112.45	100.28	93.37
66		95.24	99.53	110.46	113.75	114.32	111.96	101.8	94.84
67		95.24	99.53	110.46	113.75	114.32	111.96	101.8	94.84
68		95.21	99.53	110.35	113.75	114.17	111.96	101.8	94.84
69		94.91	99.42	110.35	113.57	114.01	111.87	101.78	94.73
70		94.91	99.42	110.35	113.57	114.01	111.87	101.78	94.73
71		94.91	99.42	110.3	113.57	114.01	111.87	101.78	94.73
72		95.21	99.45	110.24	113.33	113.44	111.52	102.07	94.8
73		95.21	99.45	110.24	113.33	113.44	111.52	102.07	94.8
74		95.21	99.45	110.24	113.33	113.44	111.52	102.07	94.95
75		95.24	99.47	110.37	113.46	113.81	111.65	102.07	95.06
76		95.24	99.47	110.37	113.46	113.81	111.65	102.07	95.06
77		95.26	99.56	110.37	113.44	113.84	111.76	102.15	95.06
78		95.35	99.58	110.39	113.46	113.92	112.05	102.2	95.1
79		95.35	99.58	110.39	113.46	113.92	112.05	102.2	95.1
80		95.43	99.58	110.39	113.48	113.95	112.05	102.22	95.1
81		95.63	99.73	110.35	113.46	113.92	112.03	102.22	95.1
82		95.63	99.73	110.35	113.46	113.92	112.03	102.22	95.1
83		95.65	99.75	110.28	113.44	113.95	112.05	102.35	95.26
84		95.65	99.75	110.28	113.44	113.95	112.05	101.07	93.92
85		95.94	99.89	110.28	113.31	113.95	111.85	101.07	93.92
86		95.92	99.82	110.28	113.42	113.95	111.85	101.07	93.9
87		95.92	99.82	110.28	113.42	113.95	111.85	101.01	93.85
88		95.98	99.84	110.26	113.31	113.7	111.65	101.01	93.85
89		95.92	99.82	110.33	113.22	113.55	111.54	100.99	93.72
90		95.92	99.82	110.33	113.22	113.55	111.54	101.01	93.75
91		95.85	99.75	110.33	113.22	113.57	111.58	101.01	93.75
92		95.67	99.62	110.33	113.26	113.55	111.52	102.33	94.93
93		95.67	99.62	110.33	113.26	113.55	111.52	102.33	94.93
94		95.61	99.62	110.33	113.26	113.57	111.52	102.33	94.93
95		95.43	99.6	110.3	113.26	113.55	111.23	102.26	94.95
96		95.43	99.6	110.3	113.26	113.55	111.23	102.11	94.95
97		95.39	99.45	110.24	113.06	113.57	111.45	102.11	94.95
98		95.1	99.32	110.24	113.06	113.57	111.45	102.11	94.95
99		95.1	99.32	110.24	113.06	113.57	111.45	101.91	94.78
100		95.02	99.32	110.24	113.26	113.79	111.78	101.91	94.78

Wall Temperature Measurements Along Heater Assembly

Stainless Steel Particles- 2.5 mm dia - 250 g loading

Re = 45602 q" = 251.748 kW/m2 T_W = 105.8611

Measure-ment no. (N)	T* =	95.8307 Probe 1 T_1 (°C)	99.9555 Probe 2 T_2 (°C)	111.4238 Probe 3 T_3 (°C)	114.4017 Probe 4 T_4 (°C)	114.7286 Probe 5 T_5 (°C)	112.7758 Probe 6 T_6 (oC)	103.1174 Probe 7 T_7 (oC)	94.6556 Probe 8 T_8 (oC)
1		95.92	100.08	111.52	114.5	114.67	112.67	103.37	94.71
2		95.92	100.08	111.52	114.5	114.67	112.67	103.37	94.71
3		95.76	100.02	111.56	114.52	114.81	112.69	103.14	94.71
4		95.72	100.02	111.63	114.54	114.85	112.73	103.12	94.73
5		95.72	100.02	111.63	114.54	114.85	112.73	103.12	94.73
6		95.57	100	111.63	114.54	114.85	112.73	103.08	94.73
7		95.57	100	111.63	114.54	114.85	112.73	103.08	94.73
8		95.57	100	111.54	114.43	114.7	112.6	101.87	93.37
9		95.28	99.67	111.52	114.43	114.7	112.6	101.87	93.37
10		95.28	99.67	111.52	114.43	114.7	112.6	101.87	93.37
11		95.28	99.67	111.52	114.59	114.7	112.6	101.69	93.35
12		95.28	99.67	111.54	114.61	114.94	112.84	101.6	93.53
13		95.28	99.67	111.54	114.61	114.94	112.84	101.6	93.53
14		95.28	99.71	111.58	114.59	114.94	112.93	101.6	93.53
15		95.35	99.73	111.58	114.61	114.94	112.93	103.23	94.8
16		95.35	99.73	111.58	114.61	114.94	112.93	103.23	94.8
17		95.74	99.93	111.61	114.54	114.85	112.8	103.32	95.13
18		95.76	100.02	111.63	114.56	114.7	112.75	103.34	95.39
19		95.76	100.02	111.63	114.56	114.7	112.75	103.34	95.39
20		95.89	100.04	111.63	114.39	114.65	112.75	103.56	95.39
21		96.03	100.08	111.36	114.28	114.61	112.73	103.56	95.37
22		96.03	100.08	111.36	114.28	114.61	112.73	103.56	95.37
23		96.05	100.08	111.34	114.28	114.61	112.73	102.09	93.99
24		96.05	100.08	111.36	114.28	114.61	112.73	102.09	93.99
25		96.05	100.08	111.36	114.28	114.61	112.73	102.09	93.99
26		96.22	100.11	111.45	114.28	114.67	112.8	103.89	95.19
27		96.22	100.11	111.45	114.28	114.67	112.8	103.89	95.19
28		96.2	100.08	111.43	114.23	114.56	112.73	103.89	95.19
29		96.03	100.06	111.43	114.23	114.65	112.78	103.67	95.17
30		96.03	100.06	111.43	114.23	114.65	112.78	103.67	95.17
31		95.96	100.04	111.43	114.45	114.59	112.75	103.63	95.02
32		95.96	100.04	111.43	114.45	114.81	112.84	103.59	95
33		95.96	100.04	111.43	114.45	114.81	112.84	103.59	95
34		95.96	100.04	111.54	114.56	114.65	112.75	103.59	94.84
35		95.96	100.04	111.54	114.59	114.81	112.89	103.59	94.84
36		95.96	100.04	111.54	114.59	114.81	112.89	103.59	94.84
37		95.89	100.04	111.56	114.63	114.81	112.75	103.37	94.84
38		95.76	100.04	111.63	114.65	114.85	112.84	103.25	94.71
39		95.76	100.04	111.63	114.65	114.85	112.84	103.25	94.71
40		95.65	100.02	111.63	114.65	114.81	112.75	103.3	94.73
41		95.59	100	111.61	114.65	114.85	112.84	103.17	94.73
42		95.59	100	111.61	114.65	114.85	112.84	103.17	94.73
43		95.59	100	111.58	114.63	114.76	112.71	103.17	94.73
44		95.57	99.84	111.52	114.45	114.76	112.8	102.2	93.79
45		95.57	99.84	111.52	114.45	114.76	112.8	102.2	93.79
46		95.78	100.02	111.5	114.43	114.63	112.8	102.2	93.79
47		95.83	99.84	111.45	114.26	114.61	112.91	103.56	94.97
48		95.83	99.84	111.45	114.26	114.61	112.91	103.56	94.97
49		95.89	99.91	111.39	114.26	114.59	112.91	103.63	94.97
50		96	99.89	111.28	114.17	114.56	112.73	103.56	94.97
51		96	99.89	111.28	114.17	114.56	112.73	103.81	95.26

Wall Temperature Measurements Along Heater Assembly

Stainless Steel Particles- 2.5 mm dia - 250 g loading

Re = 45602 q" = 251.748 kW/m2 T_W = 105.8611

Measure-ment no. (N)		Probe 1 T_1 (°C)	Probe 2 T_2 (°C)	Probe 3 T_3 (°C)	Probe 4 T_4 (°C)	Probe 5 T_5 (°C)	Probe 6 T_6 (oC)	Probe 7 T_7 (oC)	Probe 8 T_8 (oC)
52		96.14	100	111.28	114.19	114.56	112.67	103.81	95.26
53		96.14	100	111.28	114.19	114.56	112.67	103.72	95.19
54		96.14	100	111.21	114.19	114.56	112.67	103.72	95.19
55		96.14	100	111.21	114.21	114.74	112.93	103.72	95.19
56		96.14	100	111.21	114.21	114.74	112.93	103.59	95.15
57		96.16	100.04	111.41	114.52	114.98	113.13	103.59	95.15
58		96.31	100.22	111.43	114.52	114.98	113.13	103.59	95.15
59		96.31	100.22	111.43	114.52	114.98	113.13	103.61	95.13
60		96.35	100.22	111.43	114.5	114.94	113	103.61	95.13
61		96.35	100.22	111.41	114.3	114.74	112.8	103.61	95.13
62		96.35	100.22	111.41	114.3	114.74	112.8	103.61	95.13
63		96.35	100.17	111.39	114.28	114.43	112.47	103.61	95.13
64		96.29	100.17	111.25	114.19	114.43	112.47	103.72	95.08
65		96.29	100.17	111.25	114.19	114.43	112.47	103.72	95.08
66		96.09	100.04	111.23	114.19	114.43	112.47	103.72	95.08
67		95.78	99.89	111.25	114.39	114.92	112.82	103.5	94.93
68		95.78	99.89	111.25	114.39	114.92	112.82	103.37	94.93
69		95.76	99.86	111.36	114.41	115.01	112.93	103.37	94.93
70		95.54	99.78	111.41	114.45	115.01	112.93	103.25	94.73
71		95.54	99.78	111.41	114.45	115.01	112.93	101.91	93.46
72		95.5	99.78	111.36	114.41	114.83	112.67	101.91	93.46
73		95.43	99.73	111.3	114.39	114.83	112.67	101.71	93.35
74		95.43	99.73	111.3	114.39	114.83	112.67	101.71	93.35
75		95.26	99.64	111.3	114.39	114.83	112.82	101.71	93.35
76		95.26	99.64	111.3	114.39	114.83	112.82	103.21	94.78
77		95.26	99.64	111.41	114.59	114.83	112.82	103.21	94.78
78		95.39	99.82	111.41	114.59	114.79	112.86	103.21	94.78
79		95.39	99.82	111.41	114.59	114.79	112.86	101.93	93.5
80		95.57	99.84	111.39	114.61	114.79	112.89	101.93	93.5
81		95.57	99.84	111.39	114.59	114.74	112.89	101.93	93.5
82		95.57	99.84	111.39	114.59	114.74	112.89	103.61	95.13
83		95.59	99.84	111.39	114.48	114.92	112.91	103.61	95.13
84		95.78	99.86	111.36	114.48	114.76	112.69	103.61	95.13
85		95.78	99.86	111.36	114.48	114.76	112.69	102.11	93.88
86		95.83	99.8	111.34	114.34	114.61	112.82	102.11	93.88
87		95.92	99.91	111.32	114.19	114.61	112.82	102.11	93.88
88		95.92	99.91	111.32	114.19	114.61	112.82	102.31	93.9
89		95.87	99.93	111.32	114.34	114.61	112.82	103.83	95.13
90		96.05	99.93	111.34	114.3	114.52	112.82	103.83	95.13
91		96.05	99.93	111.34	114.3	114.52	112.82	103.83	95.3
92		96.14	100.04	111.34	114.3	114.5	112.69	103.87	95.32
93		96.14	100.04	111.34	114.3	114.5	112.69	103.87	95.32
94		96.14	100.04	111.21	114.06	114.5	112.58	103.87	95.32
95		96.11	100.13	111.23	114.08	114.52	112.6	103.83	95.1
96		96.11	100.13	111.23	114.08	114.52	112.6	103.83	95.1
97		96	99.97	111.32	114.08	114.54	112.53	103.61	95.02
98		96	100	111.34	114.15	114.74	112.64	103.61	95.02
99		96	100	111.34	114.15	114.74	112.64	103.61	95.02
100		95.81	100	111.41	114.41	114.9	112.84	102.09	93.5

Wall Temperature Measurements Along Heater Assembly

Stainless Steel Particles- 2.5 mm dia - 250 g loading

Re = 45602 q" = 279.720 kW/m2 T_W = 107.1645

Measure-ment no. (N)	T* =	97.1568 Probe 1 T_1 (°C)	100.6795 Probe 2 T_2 (°C)	112.1011 Probe 3 T_3 (°C)	115.2482 Probe 4 T_4 (°C)	115.5708 Probe 5 T_5 (°C)	113.7998 Probe 6 T_6 (oC)	105.0144 Probe 7 T_7 (oC)	97.7455 Probe 8 T_8 (oC)
1		96.9	100.5	111.94	115.09	115.4	113.55	105.57	97.82
2		96.9	100.5	111.94	115.09	115.4	113.55	105.5	98
3		96.92	100.5	111.94	115.09	115.45	113.57	105.48	98
4		96.95	100.57	111.98	115.14	115.54	113.68	105.48	98
5		96.95	100.57	111.98	115.14	115.54	113.68	103.85	96.66
6		96.95	100.57	111.98	115.14	115.54	113.68	103.87	96.68
7		97.12	100.63	111.98	115.14	115.54	113.68	103.87	96.68
8		97.12	100.63	111.98	115.14	115.54	113.68	104.14	96.84
9		97.17	100.66	111.98	115.14	115.47	113.64	104.14	96.84
10		97.14	100.63	112.03	115.16	115.47	113.64	105.46	98.31
11		97.14	100.63	112.03	115.16	115.47	113.64	105.46	97.98
12		97.03	100.61	112.03	115.14	115.47	113.64	105.46	97.98
13		97.03	100.61	112.03	115.14	115.47	113.64	105.46	97.98
14		97.03	100.59	112.03	115.12	115.47	113.64	105.46	97.98
15		97.03	100.59	112.03	115.12	115.47	113.64	105.57	97.98
16		97.03	100.59	112.05	115.12	115.45	113.64	103.85	96.6
17		97.06	100.59	112.05	115.09	115.38	113.64	103.85	96.6
18		97.06	100.59	112.05	115.09	115.38	113.64	105.24	98.07
19		97.01	100.61	112.07	115.16	115.45	113.73	103.85	96.84
20		97.08	100.63	112.07	115.12	115.4	113.64	103.85	96.84
21		97.08	100.63	112.07	115.12	115.4	113.64	105.24	98.07
22		97.17	100.66	112.11	115.16	115.51	113.75	105.41	98.2
23		97.17	100.66	112.11	115.16	115.58	113.75	105.41	98.2
24		97.17	100.66	112.11	115.16	115.58	113.75	105.41	98.28
25		97.17	100.66	112.14	115.16	115.58	113.79	105.41	98.35
26		97.14	100.68	112.18	115.29	115.54	113.81	105.41	98.35
27		97.14	100.68	112.18	115.29	115.54	113.81	105.37	98.35
28		97.14	100.68	112.16	115.2	115.51	113.7	105.37	98.35
29		97.14	100.68	112.16	115.2	115.51	113.7	104.05	96.95
30		97.21	100.72	112.14	115.2	115.51	113.7	104.05	96.95
31		97.25	100.77	112.14	115.18	115.56	113.86	104.05	96.95
32		97.25	100.77	112.14	115.18	115.56	113.86	104.07	96.79
33		97.21	100.72	112.14	115.18	115.58	113.88	104.07	96.79
34		97.25	100.77	112.14	115.18	115.58	113.86	105.39	98.37
35		97.25	100.77	112.14	115.18	115.58	113.86	103.96	96.86
36		97.19	100.72	112.07	115.18	115.62	113.99	103.96	96.86
37		97.19	100.72	112.07	115.18	115.62	113.99	105.48	98.44
38		97.25	100.72	112.07	115.32	115.6	113.99	103.81	96.92
39		97.12	100.66	112.07	115.32	115.65	114.1	103.81	96.92
40		97.12	100.66	112.07	115.32	115.65	114.1	105.48	98.26
41		97.36	100.68	112.07	115.32	115.62	114.1	105.59	98.28
42		97.17	100.66	112.07	115.29	115.62	114.01	105.59	98.28
43		97.17	100.66	112.07	115.29	115.62	114.01	105.59	98.28
44		97.21	100.66	112.07	115.23	115.56	113.86	105.61	98.09
45		97.19	100.66	112.07	115.2	115.51	113.81	105.61	98.09
46		97.19	100.66	112.07	115.2	115.51	113.81	105.61	98.09
47		97.21	100.68	112.07	115.25	115.58	113.84	105.61	98.28
48		97.21	100.66	112.07	115.23	115.54	113.73	105.61	98.28
49		97.21	100.66	112.07	115.23	115.54	113.73	105.61	98.28
50		97.21	100.66	112.05	115.16	115.58	113.77	105.61	98.28
51		97.23	100.66	112.05	115.16	115.6	113.77	105.37	98.28

Wall Temperature Measurements Along Heater Assembly

Stainless Steel Particles- 2.5 mm dia - 250 g loading

Re = 45602 q" = 279.720 kW/m2 T_W = 107.1645

Measure-ment no. (N)		Probe 1 T_1 (°C)	Probe 2 T_2 (°C)	Probe 3 T_3 (°C)	Probe 4 T_4 (°C)	Probe 5 T_5 (°C)	Probe 6 T_6 (oC)	Probe 7 T_7 (oC)	Probe 8 T_8 (oC)
52		97.23	100.66	112.05	115.16	115.6	113.77	105.37	98.22
53		97.23	100.74	112.09	115.23	115.6	113.86	105.37	98.22
54		97.23	100.74	112.09	115.23	115.6	113.86	105.37	98.22
55		97.23	100.72	112.09	115.23	115.65	113.86	103.89	96.73
56		97.3	100.77	112.09	115.23	115.65	113.86	103.89	96.73
57		97.3	100.77	112.09	115.23	115.65	113.86	103.89	96.73
58		97.3	100.72	112.11	115.27	115.76	114.06	103.87	96.71
59		97.32	100.72	112.14	115.29	115.78	114.08	103.87	96.71
60		97.32	100.72	112.14	115.29	115.78	114.08	105.41	98.15
61		97.25	100.72	112.14	115.2	115.6	113.92	105.41	98.15
62		97.25	100.72	112.14	115.2	115.6	113.92	103.92	96.92
63		97.14	100.68	112.11	115.18	115.56	113.84	105.57	98.26
64		97.14	100.7	112.11	115.18	115.56	113.68	105.57	98.26
65		97.14	100.7	112.11	115.18	115.56	113.68	105.57	98.48
66		97.12	100.68	112.09	115.18	115.56	113.68	105.68	98.48
67		97.1	100.7	112.07	115.18	115.51	113.68	105.68	98.48
68		97.1	100.7	112.07	115.18	115.51	113.68	105.68	98.44
69		97.1	100.79	112.07	115.25	115.51	113.68	104.14	96.92
70		97.12	100.79	112.07	115.25	115.47	113.68	104.14	96.92
71		97.12	100.79	112.07	115.25	115.47	113.68	104.14	96.92
72		97.12	100.68	112.07	115.25	115.54	113.68	104.14	96.92
73		97.12	100.68	112.07	115.25	115.54	113.68	105.77	98.33
74		97.12	100.61	112.05	115.23	115.47	113.68	105.77	98.33
75		97.03	100.59	112.03	115.25	115.54	113.66	105.77	98.33
76		97.03	100.59	112.03	115.25	115.54	113.66	104.2	97.1
77		97.1	100.61	112.03	115.29	115.51	113.66	104.2	97.1
78		97.08	100.61	112.07	115.32	115.51	113.68	104.2	97.1
79		97.08	100.61	112.07	115.32	115.51	113.68	105.72	98.28
80		97.1	100.63	112.14	115.32	115.51	113.68	105.72	98.28
81		97.12	100.63	112.16	115.36	115.6	113.84	105.72	98.28
82		97.12	100.63	112.16	115.36	115.6	113.84	105.66	98.28
83		97.12	100.63	112.18	115.43	115.67	113.84	104	96.77
84		97.12	100.66	112.2	115.45	115.76	113.99	104	96.77
85		97.12	100.66	112.2	115.45	115.76	113.99	105.61	98.26
86		97.17	100.66	112.22	115.45	115.76	113.99	105.61	98.26
87		97.34	100.81	112.25	115.43	115.71	114.03	105.61	98.26
88		97.34	100.81	112.25	115.43	115.71	114.03	105.61	98.26
89		97.34	100.81	112.25	115.43	115.69	114.01	105.72	98.26
90		97.34	100.81	112.25	115.43	115.69	114.01	105.72	98.26
91		97.19	100.77	112.2	115.45	115.69	113.95	105.7	98.09
92		97.19	100.77	112.22	115.45	115.67	113.86	105.7	98.09
93		97.19	100.77	112.22	115.45	115.67	113.86	105.72	98.11
94		97.23	100.77	112.22	115.43	115.67	113.84	105.63	98.11
95		97.23	100.77	112.22	115.43	115.67	113.84	105.63	98.11
96		97.23	100.77	112.22	115.43	115.67	113.84	105.5	98.22
97		97.21	100.77	112.22	115.43	115.65	113.9	105.5	98.22
98		97.21	100.74	112.22	115.49	115.65	113.9	105.5	98.22
99		97.21	100.74	112.22	115.49	115.65	113.9	105.5	98.22
100		97.25	100.74	112.22	115.43	115.65	113.88	103.85	96.68

Stainless Steel. 2.5 mm diameter. 250g loading

Subcooled Temperature = 90 ^{0}C **Liquid Flowrate = 14 LPM**

Data for Boiling Curve and Heat Transfer Coefficient Plots

q (W)	A (m^2)	q" (W/m^2)	T_W (°C)	Tf_i (°C)	Tf_o (°C)	Tf* (°C)	T_W-Tf* (K)	α ($W/m^2.K$)
0	7.15E-03	0				0	0	
200	7.15E-03	27972.03	91.99323	87	92.19	89.595	2.39823	11663.61
400	7.15E-03	55944.06	94.70918	87.2	92.61	89.905	4.80418	11644.87
600	7.15E-03	83916.08	97.99263	89	92.67	90.835	7.15763	11724.00
800	7.15E-03	111888.1	99.94768	89.16	92.89	91.025	8.92268	12539.74
1000	7.15E-03	139860.1	101.7084	89.21	93.54	91.375	10.3334	13534.76
1200	7.15E-03	167832.2	102.9804	89.29	93.42	91.355	11.6254	14436.68
1400	7.15E-03	195804.2	104.3012	90.94	93.35	92.145	12.1562	16107.35
1600	7.15E-03	223776.2	105.1924	90.2	93.67	91.935	13.2574	16879.34
1800	7.15E-03	251748.3	105.8611	90.12	93.83	91.975	13.8861	18129.51
2000	7.15E-03	279720.3	107.1645	91.16	93.89	92.525	14.6395	19107.23

Nomenclature	
q	Power (W)
A	Cross-sectional area of riser column (m2)
q"	Heat Flux (W/m2)
α	Heat transfer coefficient (W/m2.K)
Tf_i	Temperature of fluid into flow channel (°C)
Tf_o	Temperature of fluid out of flow channel (°C)
T_W	Measured wall temperature (°C)
Tf*	Mean fluid Temperature (°C)

Appendix A.2/2

Stainless Steel. 2.5 mm diameter. 250g loading

Subcooled Temperature = 90 ^{0}C **Liquid Flowrate = 16 LPM**

Data for Boiling Curve and Heat Transfer Coefficient Plots

q (W)	A (m^2)	q" (W/m^2)	T_W (°C)	Tf_i (°C)	Tf_o (°C)	Tf* (°C)	T_W-Tf* (K)	α ($W/m^2.K$)
0	7.15E-03	0				0	0	
200	7.15E-03	27972.03	91.5275	87.91	91	89.455	2.0725	13496.76
400	7.15E-03	55944.06	93.94574	88.06	91.55	89.805	4.14074	13510.64
600	7.15E-03	83916.08	96.02631	88.07	91.69	89.88	6.14631	13653.08
800	7.15E-03	111888.1	98.25088	88.1	92.87	90.485	7.76588	14407.65
1000	7.15E-03	139860.1	100.3249	89.28	92.5	90.89	9.4349	14823.70
1200	7.15E-03	167832.2	102.022	89.13	93.02	91.075	10.947	15331.34
1400	7.15E-03	195804.2	102.9982	89.69	92.8	91.245	11.7532	16659.65
1600	7.15E-03	223776.2	104.2668	89.19	93.75	91.47	12.7968	17486.89
1800	7.15E-03	251748.3	105.4052	90.34	93.56	91.95	13.4552	18710.11
2000	7.15E-03	279720.3	106.6489	90.32	94.33	92.325	14.3239	19528.22

Nomenclature	
q	Power (W)
A	Cross-sectional area of riser column (m2)
q"	Heat Flux (W/m2)
α	Heat transfer coefficient (W/m2.K)
Tf_i	Temperature of fluid into flow channel (°C)
Tf_o	Temperature of fluid out of flow channel (°C)
T_W	Measured wall temperature (°C)
Tf*	Mean fluid Temperature (°C)

Appendix A.2/3

Stainless Steel. 2.5 mm diameter. 250g loading

Subcooled Temperature = 90 ^{0}C **Liquid Flowrate = 18 LPM**

Data for Boiling Curve and Heat Transfer Coefficient Plots

q (W)	A (m^2)	q" (W/m^2)	T_W (°C)	Tf_i (°C)	Tf_o (°C)	Tf* (°C)	T_W-Tf* (K)	α ($W/m^2.K$)
0	7.15E-03	0				0	0	
200	7.15E-03	27972.03	91.07175	87	91.43	89.215	1.85675	15065.05
400	7.15E-03	55944.06	93.6805	87.8	92.09	89.945	3.7355	14976.32
600	7.15E-03	83916.08	95.91501	88.25	92.42	90.335	5.58001	15038.70
800	7.15E-03	111888.1	98.0642	89.04	92.71	90.875	7.1892	15563.36
1000	7.15E-03	139860.1	100.5016	89.77	93.84	91.805	8.6966	16082.16
1200	7.15E-03	167832.2	101.9257	89.76	93.87	91.815	10.1107	16599.46
1400	7.15E-03	195804.2	103.1982	89.98	93.67	91.825	11.3732	17216.28
1600	7.15E-03	223776.2	104.4817	90.02	93.68	91.85	12.6317	17715.45
1800	7.15E-03	251748.3	105.6538	90.74	93.46	92.1	13.5538	18574.00
2000	7.15E-03	279720.3	106.9239	90.89	94.24	92.565	14.3589	19480.62

Nomenclature	
q	Power (W)
A	Cross-sectional area of riser column (m2)
q"	Heat Flux (W/m2)
α	Heat transfer coefficient (W/m2.K)
Tf_i	Temperature of fluid into flow channel (°C)
Tf_o	Temperature of fluid out of flow channel (°C)
T_W	Measured wall temperature (°C)
Tf*	Mean fluid Temperature (°C)

Stainless Steel. 2.5 mm diameter. 250g loading

Subcooled Temperature = 90 ^{0}C **Liquid Flowrate = 20 LPM**

Data for Boiling Curve and Heat Transfer Coefficient Plots

q (W)	A (m^2)	q" (W/m^2)	T_W (°C)	Tf_i (°C)	Tf_o (°C)	Tf* (°C)	T_W-Tf* (K)	α ($W/m^2.K$)
0	7.15E-03	0				0	0	
200	7.15E-03	27972.03	91.1345	87	91.91	89.455	1.6795	16654.97
400	7.15E-03	55944.06	93.13785	87.07	92.45	89.76	3.37785	16562.03
600	7.15E-03	83916.08	95.49515	88.02	92.92	90.47	5.02515	16699.22
800	7.15E-03	111888.1	97.81828	89.3	93.16	91.23	6.58828	16982.90
1000	7.15E-03	139860.1	99.93381	90.16	93.43	91.795	8.13881	17184.35
1200	7.15E-03	167832.2	101.5477	90.39	93.49	91.94	9.6077	17468.51
1400	7.15E-03	195804.2	102.8795	90.52	93.57	92.045	10.8345	18072.29
1600	7.15E-03	223776.2	104.2067	90.84	93.46	92.15	12.0567	18560.32
1800	7.15E-03	251748.3	105.5087	90.65	93.91	92.28	13.2287	19030.46
2000	7.15E-03	279720.3	106.8761	91.14	94.33	92.735	14.1411	19780.66

Nomenclature	
q	Power (W)
A	Cross-sectional area of riser column (m2)
q"	Heat Flux (W/m2)
α	Heat transfer coefficient (W/m2.K)
Tf_i	Temperature of fluid into flow channel (°C)
Tf_o	Temperature of fluid out of flow channel (°C)
T_W	Measured wall temperature (°C)
Tf*	Mean fluid Temperature (°C)

Stainless Steel. 2.5 mm diameter. 250g loading

Subcooled Temperature = 90 ^{0}C **Liquid Flowrate = 22 LPM**

Data for Boiling Curve and Heat Transfer Coefficient Plots

q (W)	A (m^2)	q" (W/m^2)	T_W (°C)	Tf_i (°C)	Tf_o (°C)	Tf* (°C)	T_W-Tf* (K)	α ($W/m^2.K$)
0	7.15E-03	0				0	0	
200	7.15E-03	27972.03	91.05434	86.45	92.3	89.375	1.67934	16656.56
400	7.15E-03	55944.06	93.33049	87.25	92.7	89.975	3.35549	16672.40
600	7.15E-03	83916.08	95.47385	88.03	92.88	90.455	5.01885	16720.18
800	7.15E-03	111888.1	97.7673	89.17	93.16	91.165	6.6023	16946.84
1000	7.15E-03	139860.1	99.90078	89.93	93.55	91.74	8.16078	17138.08
1200	7.15E-03	167832.2	101.4431	90.12	93.54	91.83	9.6131	17458.69
1400	7.15E-03	195804.2	102.6239	90.01	93.63	91.82	10.8039	18123.47
1600	7.15E-03	223776.2	103.7122	90.17	93.24	91.705	12.0072	18636.84
1800	7.15E-03	251748.3	105.2967	90.35	93.88	92.115	13.1817	19098.31
2000	7.15E-03	279720.3	106.1698	90.23	93.87	92.05	14.1198	19810.50

Nomenclature	
q	Power (W)
A	Cross-sectional area of riser column (m2)
q"	Heat Flux (W/m2)
α	Heat transfer coefficient (W/m2.K)
Tf_i	Temperature of fluid into flow channel (°C)
Tf_o	Temperature of fluid out of flow channel (°C)
T_W	Measured wall temperature (°C)
Tf*	Mean fluid Temperature (°C)

Stainless Steel. 2.5 mm diameter. 250g loading

Subcooled Temperature = 90 ^{0}C **Liquid Flowrate = 24 LPM**

Data for Boiling Curve and Heat Transfer Coefficient Plots

q (W)	A (m^2)	q" (W/m^2)	T_W (°C)	Tf_i (°C)	Tf_o (°C)	Tf* (°C)	T_W-Tf* (K)	α ($W/m^2.K$)
0	7.15E-03	0				0	0	
200	7.15E-03	27972.03	91.71904	87.55	92.29	89.92	1.79904	15548.31
400	7.15E-03	55944.06	94.10769	88.39	92.56	90.475	3.63269	15400.17
600	7.15E-03	83916.08	96.30319	88.79	93	90.895	5.40819	15516.48
800	7.15E-03	111888.1	98.47769	89.41	93.4	91.405	7.07269	15819.74
1000	7.15E-03	139860.1	100.3488	89.65	93.75	91.7	8.6488	16171.05
1200	7.15E-03	167832.2	101.5334	89.53	93.89	91.71	9.8234	17084.94
1400	7.15E-03	195804.2	102.7903	89.8	93.59	91.695	11.0953	17647.49
1600	7.15E-03	223776.2	103.8058	90.26	93.16	91.71	12.0958	18500.32
1800	7.15E-03	251748.3	105.3055	90.29	93.75	92.02	13.2855	18949.10
2000	7.15E-03	279720.3	106.5023	90.34	93.64	91.99	14.5123	19274.70

Nomenclature	
q	Power (W)
A	Cross-sectional area of riser column (m2)
q"	Heat Flux (W/m2)
α	Heat transfer coefficient (W/m2.K)
Tf_i	Temperature of fluid into flow channel (°C)
Tf_o	Temperature of fluid out of flow channel (°C)
T_W	Measured wall temperature (°C)
Tf*	Mean fluid Temperature (°C)

Stainless Steel. 2.5 mm diameter. 250g loading

Subcooled Temperature = 90 ^{0}C **Liquid Flowrate = 26 LPM**

Data for Boiling Curve and Heat Transfer Coefficient Plots

q (W)	A (m^2)	q" (W/m^2)	T_W (°C)	Tf_i (°C)	Tf_o (°C)	Tf* (°C)	T_W-Tf* (K)	α ($W/m^2.K$)
0	7.15E-03	0				0	0	
200	7.15E-03	27972.03	91.99624	88.05	92.29	90.17	1.82624	15316.73
400	7.15E-03	55944.06	94.4205	88.97	92.56	90.765	3.6555	15304.08
600	7.15E-03	83916.08	96.78145	89.59	93	91.295	5.48645	15295.15
800	7.15E-03	111888.1	98.78329	90.29	93	91.645	7.13829	15674.36
1000	7.15E-03	139860.1	100.5803	90.72	93.11	91.915	8.6653	16140.25
1200	7.15E-03	167832.2	102.2498	91.48	93.11	92.295	9.9548	16859.42
1400	7.15E-03	195804.2	104.2302	92	93.95	92.975	11.2552	17396.78
1600	7.15E-03	223776.2	105.7778	93.1	93.96	93.53	12.2478	18270.73
1800	7.15E-03	251748.3	106.9439	93.3	93.81	93.555	13.3889	18802.76
2000	7.15E-03	279720.3	108.1214	93.27	93.68	93.475	14.6464	19098.23

Nomenclature	
q	Power (W)
A	Cross-sectional area of riser column (m2)
q"	Heat Flux (W/m2)
α	Heat transfer coefficient (W/m2.K)
Tf_i	Temperature of fluid into flow channel (°C)
Tf_o	Temperature of fluid out of flow channel (°C)
T_W	Measured wall temperature (°C)
Tf*	Mean fluid Temperature (°C)

Wall Temperature Measurements Along Heater Assembly

Stainless Steel Particles- 2 mm dia - 250 g loading

Re = 71614 q" = 27.972 kW/m2 T_W = 92.52015

Measure-ment no. (N)	T* =	91.8821 Probe 1 T_1 (°C)	92.2593 Probe 2 T_2 (°C)	94.1211 Probe 3 T_3 (°C)	94.887 Probe 4 T_4 (°C)	95.0799 Probe 5 T_5 (°C)	94.7843 Probe 6 T_6 (oC)	88.906 Probe 7 T_7 (oC)	88.2415 Probe 8 T_8 (oC)
1		92.1	92.5	94.29	95.17	95.28	95	89.54	88.84
2		92.1	92.5	94.29	95.17	95.28	95	89.47	88.7
3		92.01	92.45	94.23	95.06	95.24	94.93	89.47	88.7
4		91.95	92.34	94.18	94.97	95.15	94.84	89.47	88.7
5		91.95	92.34	94.18	94.97	95.15	94.84	88.11	87.43
6		91.95	92.3	94.16	94.95	95.15	94.82	88.11	87.43
7		91.88	92.28	94.12	94.95	95.1	94.78	88.05	87.41
8		91.88	92.28	94.12	94.95	95.1	94.78	88.03	87.39
9		91.82	92.28	94.12	94.91	95.06	94.75	88.03	87.39
10		91.79	92.23	94.05	94.86	95.04	94.75	88.03	87.39
11		91.79	92.23	94.05	94.86	95.04	94.75	88	87.39
12		91.79	92.21	94.03	94.84	95	94.71	88	87.39
13		91.79	92.19	94.03	94.84	95	94.67	87.98	87.3
14		91.79	92.19	94.03	94.84	95	94.67	87.98	87.3
15		91.75	92.19	94.03	94.8	95	94.64	87.98	87.3
16		91.75	92.19	94.03	94.8	95	94.64	87.98	87.33
17		91.75	92.17	93.99	94.8	94.97	94.64	87.96	87.33
18		91.77	92.17	94.01	94.82	94.95	94.67	87.96	87.33
19		91.77	92.17	94.01	94.82	94.95	94.67	87.96	87.33
20		91.77	92.14	94.01	94.78	94.95	94.67	87.96	87.33
21		91.77	92.14	93.99	94.78	94.95	94.67	87.96	87.33
22		91.77	92.14	93.99	94.78	94.95	94.67	89.23	88.53
23		91.77	92.14	93.99	94.8	94.97	94.67	89.23	88.53
24		91.77	92.12	93.99	94.8	94.97	94.67	89.23	88.55
25		91.77	92.12	93.99	94.8	94.97	94.67	89.25	88.55
26		91.77	92.12	93.99	94.78	94.93	94.64	89.25	88.55
27		91.77	92.12	93.99	94.78	94.93	94.67	89.23	88.55
28		91.77	92.12	93.99	94.78	94.93	94.67	89.25	88.53
29		91.75	92.14	93.99	94.78	94.93	94.64	89.25	88.53
30		91.75	92.14	93.99	94.75	94.93	94.6	89.21	88.51
31		91.75	92.14	93.99	94.75	94.93	94.6	89.21	88.51
32		91.73	92.06	93.94	94.71	94.86	94.58	89.21	88.51
33		91.73	92.06	93.92	94.71	94.86	94.6	87.98	87.24
34		91.73	92.06	93.92	94.71	94.86	94.6	87.94	87.24
35		91.71	92.08	93.96	94.71	94.86	94.6	87.94	87.24
36		91.71	92.08	93.96	94.71	94.86	94.6	87.94	87.24
37		91.71	92.06	93.94	94.71	94.86	94.6	88.09	87.24
38		91.68	92.06	93.94	94.69	94.86	94.6	88.09	87.24
39		91.68	92.06	93.94	94.69	94.86	94.6	88.09	87.22
40		91.68	92.06	93.94	94.67	94.84	94.6	89.12	88.44
41		91.68	92.03	93.9	94.67	94.84	94.58	89.12	88.44
42		91.68	92.03	93.9	94.67	94.84	94.58	87.89	87.22
43		91.6	91.99	93.85	94.62	94.8	94.56	89.1	88.38
44		91.57	91.95	93.85	94.6	94.78	94.56	89.1	88.38
45		91.57	91.95	93.85	94.6	94.78	94.56	89.1	88.35
46		91.57	91.92	93.83	94.6	94.78	94.56	89.12	88.4
47		91.55	91.9	93.81	94.58	94.73	94.51	89.12	88.4
48		91.55	91.9	93.81	94.58	94.73	94.51	89.1	88.4
49		91.55	91.9	93.81	94.51	94.73	94.45	89.1	88.4
50		91.46	91.9	93.81	94.51	94.71	94.45	89.1	88.4
51		91.46	91.9	93.81	94.51	94.71	94.45	89.08	88.35

Wall Temperature Measurements Along Heater Assembly

Stainless Steel Particles- 2 mm dia - 250 g loading

Re = 71614 q" = 27.972 kW/m2 T_W = 92.52015

Measure-ment no. (N)		Probe 1 T_1 (°C)	Probe 2 T_2 (°C)	Probe 3 T_3 (°C)	Probe 4 T_4 (°C)	Probe 5 T_5 (°C)	Probe 6 T_6 (oC)	Probe 7 T_7 (oC)	Probe 8 T_8 (oC)
52		91.49	91.92	93.83	94.56	94.73	94.47	89.05	88.38
53		91.51	91.92	93.85	94.6	94.8	94.51	89.05	88.38
54		91.51	91.92	93.85	94.6	94.8	94.51	87.89	87.19
55		91.53	91.95	93.85	94.6	94.8	94.51	87.89	87.19
56		91.53	91.95	93.85	94.6	94.8	94.51	87.89	87.19
57		91.64	92.03	93.9	94.67	94.86	94.6	87.96	87.33
58		91.73	92.1	94.03	94.75	94.95	94.69	87.96	87.33
59		91.73	92.1	94.03	94.75	94.95	94.69	88.18	87.61
60		91.86	92.23	94.12	94.91	95.13	94.84	89.32	88.75
61		92.06	92.36	94.23	95.02	95.26	95	89.32	88.75
62		92.06	92.36	94.23	95.02	95.26	95	89.58	89.08
63		92.21	92.52	94.4	95.19	95.43	95.19	89.58	89.08
64		92.43	92.69	94.6	95.35	95.61	95.28	89.58	89.08
65		92.43	92.69	94.6	95.35	95.61	95.28	89.71	89.19
66		92.54	92.89	94.71	95.48	95.7	95.35	90	89.4
67		92.71	92.96	94.78	95.52	95.78	95.46	90	89.4
68		92.71	92.96	94.78	95.52	95.78	95.46	90	89.4
69		92.71	93.02	94.8	95.57	95.78	95.48	89.93	89.4
70		92.71	93.02	94.8	95.57	95.7	95.46	89.93	89.4
71		92.71	93.02	94.8	95.57	95.7	95.46	88.7	88.16
72		92.69	92.96	94.73	95.52	95.7	95.41	89.84	89.25
73		92.6	92.93	94.67	95.46	95.61	95.37	89.84	89.25
74		92.6	92.93	94.67	95.46	95.61	95.37	88.66	88.03
75		92.45	92.87	94.62	95.35	95.54	95.28	88.66	88.03
76		92.45	92.87	94.62	95.35	95.54	95.28	89.67	89.08
77		92.43	92.76	94.58	95.3	95.52	95.24	89.6	88.92
78		92.32	92.69	94.47	95.24	95.43	95.13	89.6	88.92
79		92.32	92.69	94.47	95.24	95.43	95.13	89.6	88.92
80		92.21	92.58	94.38	95.15	95.37	95.02	89.51	88.92
81		92.1	92.47	94.32	95.06	95.32	94.95	89.51	88.92
82		92.1	92.47	94.32	95.06	95.32	94.95	89.43	88.79
83		91.99	92.43	94.25	94.97	95.26	94.86	89.38	88.73
84		91.9	92.32	94.18	94.91	95.17	94.86	89.38	88.73
85		91.9	92.32	94.18	94.91	95.17	94.86	89.32	88.66
86		91.84	92.23	94.12	94.89	95.13	94.75	89.23	88.55
87		91.82	92.19	94.1	94.82	95.04	94.67	89.23	88.55
88		91.82	92.19	94.1	94.82	95.04	94.67	89.19	88.49
89		91.75	92.12	94.05	94.71	95	94.64	89.19	88.49
90		91.66	92.1	93.99	94.71	94.97	94.62	89.19	88.49
91		91.66	92.1	93.99	94.71	94.97	94.62	89.14	88.46
92		91.62	92.06	93.99	94.69	94.93	94.56	89.1	88.46
93		91.57	92.03	93.94	94.67	94.91	94.56	89.1	88.46
94		91.57	92.03	93.94	94.67	94.91	94.56	89.1	88.4
95		91.57	92.01	93.92	94.64	94.89	94.56	89.1	88.4
96		91.62	92.01	93.92	94.67	94.89	94.58	89.1	88.4
97		91.62	92.01	93.92	94.67	94.89	94.58	89.1	88.4
98		91.64	92.01	93.99	94.75	94.97	94.64	89.19	88.53
99		91.71	92.1	94.05	94.8	95.04	94.71	89.19	88.53
100		91.71	92.1	94.05	94.8	95.04	94.71	89.23	88.59

Wall Temperature Measurements Along Heater Assembly

Appendix A.3/2:1

Stainless Steel Particles- 2 mm dia - 250 g loading

Re = 71614 q" = 55.944 kW/m2 T_W = 95.07715

Measure-ment no. (N)	T* =	92.477 Probe 1 T_1 (°C)	93.3285 Probe 2 T_2 (°C)	97.0229 Probe 3 T_3 (°C)	98.3658 Probe 4 T_4 (°C)	98.7706 Probe 5 T_5 (°C)	99.2022 Probe 6 T_6 (oC)	91.399 Probe 7 T_7 (oC)	90.0512 Probe 8 T_8 (oC)
1		91.49	92.36	96.16	97.69	97.98	99.18	91.05	89.8
2		91.49	92.36	96.16	97.69	97.98	99.18	91.25	90.02
3		91.51	92.58	96.18	97.71	98.28	99.21	91.25	90.02
4		91.51	92.58	96.18	97.71	98.28	99.21	91.25	90.02
5		91.66	92.6	96.4	97.78	98.28	99.05	89.95	88.92
6		91.64	92.6	96.42	97.85	98.31	98.83	89.97	88.94
7		91.64	92.6	96.42	97.85	98.31	98.83	89.97	88.94
8		91.66	92.87	96.71	98.02	98.46	98.79	90.15	89.05
9		92.28	93.22	96.97	98.04	98.55	98.79	90.52	89.45
10		92.28	93.22	96.97	98.04	98.55	98.79	90.52	89.45
11		92.36	93.26	97.06	98.42	98.88	99.29	91.66	90.54
12		92.39	93.72	97.45	98.83	99.23	99.38	91.66	90.54
13		92.39	93.72	97.45	98.83	99.23	99.38	90.78	89.67
14		93.11	93.85	97.54	98.96	99.32	99.42	91.99	90.92
15		93.2	93.94	97.6	98.99	99.36	99.8	91.99	90.92
16		93.2	93.94	97.6	98.99	99.36	99.8	92.21	91.03
17		93.2	93.94	97.63	98.99	99.36	99.8	92.28	91.03
18		93.2	93.96	97.63	98.92	99.34	99.45	92.28	91.03
19		93.2	93.96	97.63	98.92	99.34	99.45	92.3	91
20		93.11	93.92	97.58	98.9	99.25	99.29	92.06	90.83
21		93.11	93.92	97.58	98.9	99.25	99.29	92.06	90.83
22		93.07	93.83	97.52	98.77	99.14	99.18	90.85	89.62
23		92.93	93.77	97.43	98.72	99.05	99.18	90.65	89.38
24		92.93	93.77	97.43	98.72	99.05	99.18	90.65	89.38
25		92.85	93.66	97.36	98.68	98.96	99.14	90.65	89.38
26		92.76	93.57	97.3	98.55	98.9	99.03	91.79	90.41
27		92.76	93.57	97.3	98.55	98.9	99.03	91.79	90.41
28		92.69	93.53	97.21	98.46	98.79	98.96	91.79	90.41
29		92.56	93.42	97.14	98.42	98.72	98.96	91.73	90.35
30		92.56	93.42	97.14	98.42	98.72	98.96	91.73	90.35
31		92.52	93.35	97.12	98.37	98.72	98.96	91.66	90.3
32		92.47	93.28	97.01	98.31	98.66	98.99	91.64	90.21
33		92.47	93.28	97.01	98.31	98.66	98.99	91.64	90.21
34		92.36	93.26	97.01	98.28	98.64	99.01	91.53	90.06
35		92.34	93.2	96.95	98.24	98.61	99.18	90.24	88.86
36		92.34	93.2	96.95	98.24	98.61	99.18	90.24	88.86
37		92.32	93.13	96.88	98.17	98.55	99.18	90.15	88.73
38		92.28	93.11	96.84	98.13	98.53	99.16	90.15	88.73
39		92.28	93.11	96.84	98.13	98.53	99.16	90.15	88.73
40		92.21	93.07	96.79	98.11	98.5	99.16	90.13	88.7
41		92.21	93.02	96.79	98.09	98.5	99.21	91.4	89.95
42		92.21	93.02	96.79	98.09	98.5	99.21	91.4	89.95
43		92.23	93.02	96.79	98.09	98.53	99.21	91.46	90.02
44		92.23	93.02	96.79	98.09	98.53	99.21	91.46	90.02
45		92.3	93.11	96.86	98.17	98.64	99.21	91.46	90.02
46		92.34	93.2	96.95	98.31	98.75	99.42	91.51	90.13
47		92.34	93.2	96.95	98.31	98.75	99.42	91.77	90.43
48		92.45	93.31	97.03	98.42	98.81	99.42	91.77	90.43
49		92.67	93.44	97.19	98.5	98.96	99.42	91.77	90.43
50		92.67	93.44	97.19	98.5	98.96	99.42	91.97	90.57
51		92.67	93.44	97.36	98.72	99.18	99.58	91.97	90.57

Wall Temperature Measurements Along Heater Assembly

Appendix
A.3/2:2

Stainless Steel Particles- 2 mm dia - 250 g loading

Re = 71614 q" = 55.944 kW/m2 T_W = 95.07715

Measure-ment no. (N)		Probe 1 T_1 (°C)	Probe 2 T_2 (°C)	Probe 3 T_3 (°C)	Probe 4 T_4 (°C)	Probe 5 T_5 (°C)	Probe 6 T_6 (oC)	Probe 7 T_7 (oC)	Probe 8 T_8 (oC)
52		92.89	93.59	97.36	98.72	99.18	99.58	92.3	90.98
53		92.89	93.59	97.36	98.72	99.18	99.58	92.52	91
54		93.26	93.72	97.01	98.81	99.32	99.58	92.52	91
55		93.31	94.01	97.01	98.81	99.38	99.64	92.52	91
56		93.31	94.01	97.01	98.81	99.38	99.64	92.58	91.14
57		93.37	94.1	97.76	99.05	99.38	99.64	92.58	91.14
58		93.37	94.1	97.76	99.05	99.38	99.67	92.56	91.14
59		93.37	94.1	97.76	99.05	99.38	99.67	92.56	91.14
60		93.33	94.1	97.69	99.01	99.36	99.8	92.56	91.14
61		93.33	94.1	97.69	99.01	99.36	99.8	92.45	90.98
62		93.28	94.05	97.67	98.99	99.32	99.8	92.3	90.92
63		93.2	94.01	97.65	98.96	99.29	99.34	92.3	90.92
64		93.2	94.01	97.65	98.96	99.29	99.34	92.3	90.92
65		93.2	93.99	97.56	98.88	99.25	99.21	92.3	90.92
66		93.09	93.85	97.47	98.79	99.1	99.12	90.85	89.47
67		93.09	93.85	97.47	98.79	99.1	99.12	90.85	89.47
68		92.98	93.77	97.36	98.64	99.01	99.1	91.95	90.57
69		92.87	93.66	97.28	98.57	99.01	99.62	91.95	90.57
70		92.87	93.66	97.28	98.57	99.01	99.62	91.95	90.57
71		92.71	93.55	97.25	98.5	98.9	99.62	91.95	90.57
72		92.65	93.48	97.21	98.5	98.88	99.05	91.75	90.52
73		92.65	93.48	97.21	98.5	98.88	99.05	90.52	89.21
74		92.65	93.44	97.17	98.5	98.81	99.05	90.52	89.21
75		92.6	93.35	97.08	98.44	98.75	99.05	91.62	90.3
76		92.6	93.35	97.08	98.44	98.75	99.05	90.35	89.08
77		92.5	93.33	97.03	98.37	98.7	99.1	90.35	89.08
78		92.47	93.26	96.97	98.33	98.7	99.23	91.55	90.24
79		92.47	93.26	96.97	98.33	98.7	99.23	91.57	90.24
80		92.43	93.26	96.97	98.26	98.68	99.23	91.57	90.24
81		92.43	93.26	96.97	98.26	98.68	99.23	91.57	90.24
82		92.41	93.2	96.9	98.24	98.66	99.12	90.24	88.88
83		92.41	93.2	96.86	98.24	98.59	99.12	90.24	88.88
84		92.41	93.2	96.86	98.24	98.59	99.12	90.24	88.88
85		92.36	93.17	96.82	98.17	98.59	99.16	90.21	88.86
86		91.97	93.13	96.82	98.15	98.59	99.16	90.21	88.86
87		91.97	93.13	96.82	98.15	98.59	99.16	90.21	88.86
88		91.82	92.65	96.82	97.67	98.07	98.75	91.55	90.06
89		91.71	92.67	96.33	97.67	98.07	98.75	91.55	90.06
90		91.71	92.67	96.33	97.67	98.07	98.75	90.24	88.79
91		91.6	92.58	96.27	97.65	98.15	98.77	91.57	90.06
92		91.66	92.58	96.29	97.65	98.15	98.77	91.57	90.06
93		91.66	92.58	96.29	97.65	98.15	98.77	91.55	90.04
94		91.66	92.58	96.27	97.69	98.2	98.77	91.55	90.04
95		91.66	92.58	96.27	97.69	98.2	98.79	91.55	90.04
96		91.66	92.58	96.27	97.69	98.2	98.79	91.55	90.04
97		91.55	92.58	96.27	97.71	98.22	98.81	91.6	90.06
98		91.55	92.58	96.27	97.71	98.22	98.81	91.6	90.06
99		91.51	92.56	96.29	97.71	98.22	98.81	91.6	90.06
100		91.4	92.47	96.29	97.71	98.17	98.75	91.6	90.06

Wall Temperature Measurements Along Heater Assembly

Stainless Steel Particles- 2 mm dia - 250 g loading

Re = 71614 q" = 83.916 kW/m2 T_W = 96.82979

Measure-ment no. (N)	T* =	92.2196 Probe 1 T_1 (°C)	93.8129 Probe 2 T_2 (°C)	99.2573 Probe 3 T_3 (°C)	101.3107 Probe 4 T_4 (°C)	101.8998 Probe 5 T_5 (°C)	101.3001 Probe 6 T_6 (oC)	93.2552 Probe 7 T_7 (oC)	91.5827 Probe 8 T_8 (oC)
1		92.76	94.42	99.71	101.76	102.24	101.69	94.21	92.78
2		92.76	94.42	99.71	101.76	102.24	101.69	92.71	91.27
3		92.76	94.4	99.58	101.67	102.13	101.56	92.71	91.27
4		92.58	94.23	99.56	101.54	102.09	101.51	92.71	91.27
5		92.58	94.23	99.56	101.54	102.09	101.51	92.71	91.2
6		92.47	94.21	99.49	101.54	102.13	101.51	93.96	92.19
7		92.47	94.12	99.47	101.47	102.07	101.49	93.96	92.19
8		92.47	94.12	99.47	101.47	102.07	101.49	93.85	92.08
9		92.34	94.03	99.4	101.45	102	101.47	93.85	92.08
10		92.34	94.03	99.4	101.45	102	101.47	93.85	92.08
11		92.34	93.94	99.38	101.43	102	101.4	93.83	92.01
12		92.28	93.92	99.29	101.4	101.96	101.4	93.79	91.99
13		92.28	93.92	99.29	101.4	101.96	101.4	93.79	91.99
14		92.23	93.81	99.27	101.36	101.96	101.4	92.5	90.78
15		92.12	93.77	99.21	101.36	101.93	101.38	93.77	91.97
16		92.12	93.77	99.21	101.36	101.93	101.38	93.77	91.97
17		92.06	93.72	99.18	101.32	101.85	101.34	92.41	90.65
18		92.03	93.66	99.18	101.32	101.85	101.34	92.41	90.54
19		92.03	93.66	99.18	101.32	101.85	101.34	92.41	90.54
20		91.99	93.68	99.16	101.27	101.85	101.32	92.41	90.54
21		91.95	93.61	99.16	101.21	101.87	101.29	93.66	91.75
22		91.95	93.61	99.16	101.21	101.87	101.29	93.66	91.75
23		91.92	93.59	99.14	101.12	101.8	101.16	93.66	91.75
24		91.99	93.59	99.16	101.12	101.82	101.16	92.36	90.48
25		91.99	93.59	99.16	101.12	101.82	101.16	92.36	90.48
26		92.01	93.66	99.18	101.14	101.82	101.25	92.34	90.48
27		92.14	93.64	99.21	101.32	101.85	101.25	92.34	90.48
28		92.14	93.64	99.21	101.32	101.85	101.25	92.34	90.5
29		92.14	93.68	99.21	101.34	101.89	101.25	92.32	90.52
30		92.12	93.68	99.18	101.34	101.89	101.32	92.32	90.52
31		92.12	93.68	99.18	101.34	101.89	101.32	93.64	91.82
32		92.12	93.68	99.18	101.34	101.91	101.32	92.36	90.57
33		92.12	93.7	99.18	101.34	101.91	101.34	92.36	90.57
34		92.12	93.7	99.18	101.34	101.91	101.34	93.64	91.84
35		92.12	93.66	99.18	101.34	101.89	101.27	93.64	91.88
36		92.12	93.66	99.18	101.34	101.89	101.27	93.64	91.88
37		92.1	93.7	99.21	101.34	101.89	101.34	93.64	91.88
38		92.14	93.7	99.27	101.32	101.93	101.25	93.64	91.84
39		92.14	93.7	99.27	101.32	101.93	101.25	93.64	91.84
40		92.17	93.72	99.32	101.36	101.96	101.36	93.64	91.84
41		92.21	93.72	99.32	101.34	101.96	101.27	93.64	91.92
42		92.21	93.72	99.32	101.34	101.96	101.27	93.64	91.92
43		92.17	93.7	99.32	101.32	101.96	101.27	93.64	91.92
44		92.06	93.64	99.14	101.16	101.82	101.16	93.61	91.88
45		92.06	93.64	99.14	101.16	101.82	101.16	93.61	91.88
46		91.99	93.57	99.12	101.16	101.82	101.14	92.34	90.57
47		92.03	93.57	99.14	101.25	101.85	101.14	93.64	91.86
48		92.03	93.57	99.14	101.25	101.85	101.14	93.64	91.86
49		92.03	93.57	99.12	101.25	101.85	101.16	93.61	91.84
50		92.03	93.59	99.12	101.21	101.85	101.16	93.61	91.86
51		92.03	93.59	99.12	101.21	101.85	101.16	93.61	91.86

Wall Temperature Measurements Along Heater Assembly

Stainless Steel Particles- 2 mm dia - 250 g loading

Re = 71614 q" = 83.916 kW/m2 T_W = 96.82979

Measure-ment no. (N)		Probe 1 T_1 (°C)	Probe 2 T_2 (°C)	Probe 3 T_3 (°C)	Probe 4 T_4 (°C)	Probe 5 T_5 (°C)	Probe 6 T_6 (oC)	Probe 7 T_7 (oC)	Probe 8 T_8 (oC)
52		91.97	93.59	99.07	101.18	101.78	101.16	93.61	91.86
53		91.97	93.59	99.07	101.18	101.78	101.16	93.61	91.9
54		91.97	93.59	99.07	101.18	101.78	101.16	93.61	91.9
55		91.95	93.59	99.03	101.16	101.76	101.18	93.59	91.92
56		91.95	93.59	99.03	101.16	101.76	101.18	93.61	91.92
57		91.95	93.59	99.03	101.16	101.74	101.18	93.61	91.92
58		91.95	93.59	99.03	101.16	101.74	101.16	93.59	91.88
59		91.95	93.59	99.03	101.16	101.74	101.16	92.28	90.59
60		91.95	93.59	99.03	101.16	101.69	101.16	92.28	90.59
61		91.9	93.59	99.01	101.16	101.67	101.16	92.23	90.54
62		91.9	93.59	99.01	101.16	101.67	101.16	92.19	90.52
63		91.95	93.57	99.01	101.14	101.67	101.12	92.19	90.52
64		91.9	93.57	98.96	101.03	101.67	101.12	92.19	90.52
65		91.9	93.57	98.96	101.03	101.67	101.12	92.19	90.52
66		91.88	93.57	98.96	101.03	101.69	101.18	92.19	90.52
67		91.88	93.57	98.99	101.03	101.71	101.18	93.53	91.82
68		91.88	93.57	98.99	101.03	101.71	101.18	93.53	91.82
69		91.88	93.48	98.99	101.1	101.71	101.14	93.5	91.75
70		91.88	93.48	98.99	101.1	101.71	101.05	93.5	91.79
71		91.88	93.48	98.99	101.1	101.71	101.05	93.5	91.79
72		91.88	93.48	98.9	100.96	101.58	101.01	93.5	91.75
73		91.84	93.5	98.85	100.96	101.56	100.94	93.5	91.75
74		91.84	93.5	98.85	100.96	101.56	100.94	93.5	91.75
75		91.84	93.48	98.85	100.94	101.56	100.94	93.53	91.75
76		91.84	93.5	98.92	100.96	101.58	100.94	92.25	90.61
77		91.84	93.5	98.92	100.96	101.58	100.94	92.25	90.61
78		91.84	93.57	98.92	100.99	101.65	100.99	93.64	91.84
79		91.84	93.57	98.99	101.03	101.65	101.07	92.36	90.74
80		91.84	93.57	98.99	101.03	101.65	101.07	92.36	90.74
81		92.03	93.59	99.03	101.21	101.78	101.1	92.41	90.85
82		92.23	93.75	99.21	101.23	101.82	101.29	92.41	90.85
83		92.23	93.75	99.21	101.23	101.82	101.29	92.41	90.85
84		92.41	93.83	99.27	101.36	102.07	101.29	93.92	92.43
85		92.5	94.14	99.49	101.58	102.07	101.51	93.92	92.43
86		92.5	94.14	99.49	101.58	102.07	101.51	93.92	92.43
87		92.78	94.14	99.67	101.65	102.24	101.58	92.87	91.6
88		92.78	94.14	99.67	101.65	102.24	101.58	92.87	91.6
89		92.87	94.36	99.8	101.76	102.24	101.69	92.87	91.6
90		93	94.42	99.84	101.76	102.35	101.78	94.16	92.98
91		93	94.42	99.84	101.76	102.35	101.78	94.21	92.98
92		93.07	94.56	99.89	101.76	102.37	101.8	94.21	92.98
93		93.13	94.58	99.89	101.74	102.37	101.8	94.18	92.93
94		93.13	94.58	99.89	101.74	102.37	101.8	94.18	92.82
95		93.13	94.58	99.8	101.62	102.26	101.62	94.18	92.82
96		93.02	94.49	99.78	101.62	102.15	101.47	94.01	92.6
97		93.02	94.49	99.78	101.62	102.15	101.47	94.01	92.54
98		92.91	94.42	99.78	101.56	102.15	101.43	94.01	92.54
99		92.85	94.38	99.67	101.49	102	101.43	94.01	92.54
100		92.85	94.38	99.67	101.49	102	101.43	93.94	92.34

Wall Temperature Measurements Along Heater Assembly

Stainless Steel Particles- 2 mm dia - 250 g loading

Re = 71614 q" = 111.888 kW/m2 T_W = 98.83104

Measure-ment no. (N)	T* =	92.7722 Probe 1 T_1 (°C)	94.9616 Probe 2 T_2 (°C)	101.8388 Probe 3 T_3 (°C)	103.9336 Probe 4 T_4 (°C)	104.4232 Probe 5 T_5 (°C)	103.6466 Probe 6 T_6 (oC)	95.7571 Probe 7 T_7 (oC)	93.3152 Probe 8 T_8 (oC)
1		92.89	94.95	101.96	104.27	104.93	104.09	96.05	93.66
2		93.09	95.13	102.09	104.33	104.95	104.14	95	93.28
3		93.2	95.41	102.22	104.53	105.02	104.18	95	93.28
4		93.2	95.41	102.22	104.53	105.02	104.18	96.27	94.34
5		93.53	95.57	102.33	104.62	105.11	104.33	95.02	93.28
6		93.55	95.72	102.42	104.66	105.19	104.4	95.02	93.28
7		93.55	95.72	102.42	104.66	105.19	104.4	96.49	94.42
8		93.57	95.76	102.42	104.66	105.11	104.36	96.44	94.42
9		93.59	95.76	102.42	104.62	105.13	104.36	96.44	94.42
10		93.59	95.76	102.42	104.62	105.13	104.36	96.49	94.42
11		93.59	95.67	102.42	104.6	105.11	104.33	96.44	94.36
12		93.59	95.67	102.42	104.6	105.11	104.33	96.44	94.36
13		93.5	95.61	102.35	104.55	105	104.2	96.42	94.34
14		93.39	95.61	102.31	104.44	104.88	104.18	96.42	93.96
15		93.39	95.61	102.31	104.44	104.88	104.18	96.42	93.96
16		93.33	95.46	102.29	104.33	104.88	104.09	96.35	93.92
17		93.22	95.39	102.2	104.29	104.77	103.98	96.38	93.9
18		93.22	95.39	102.2	104.29	104.77	103.98	96.38	93.9
19		93.17	95.39	102.11	104.27	104.75	103.96	96.33	93.85
20		93.09	95.26	102.04	104.22	104.69	103.94	96.22	93.7
21		93.09	95.26	102.04	104.22	104.69	103.94	96.22	93.7
22		92.93	95.21	102.04	104.2	104.69	103.87	96.22	93.7
23		92.91	95.1	102.04	104.14	104.66	103.87	96.22	93.7
24		92.91	95.1	102.04	104.14	104.66	103.87	96.27	93.7
25		92.85	95.1	102.02	104.14	104.64	103.87	96.27	93.7
26		92.82	95.04	102	104.05	104.58	103.81	96.27	93.7
27		92.82	95.04	102	104.05	104.58	103.81	96.25	93.61
28		92.74	95	101.98	103.96	104.53	103.67	96.25	93.61
29		92.74	95	101.98	103.96	104.53	103.67	96.25	93.61
30		92.74	94.93	101.96	103.92	104.36	103.59	96.27	93.66
31		92.74	94.89	101.89	103.92	104.36	103.5	96.27	93.66
32		92.74	94.89	101.89	103.92	104.36	103.5	96.27	93.66
33		92.65	94.84	101.76	103.85	104.33	103.48	96.22	93.57
34		92.58	94.89	101.76	103.85	104.31	103.45	96.07	93.44
35		92.58	94.89	101.76	103.85	104.31	103.45	96.07	93.44
36		92.65	94.89	101.78	103.83	104.29	103.45	96.07	93.44
37		92.6	94.95	101.8	103.85	104.29	103.48	96.18	93.75
38		92.6	94.95	101.8	103.85	104.29	103.48	96.18	93.75
39		92.65	94.95	101.78	103.83	104.27	103.48	96.18	93.75
40		92.65	94.89	101.78	103.78	104.22	103.48	96	93.48
41		92.65	94.89	101.78	103.78	104.22	103.48	96	93.48
42		92.65	94.89	101.78	103.78	104.22	103.48	94.51	91.97
43		92.65	94.91	101.8	103.83	104.25	103.5	94.51	91.97
44		92.65	94.91	101.8	103.83	104.25	103.5	94.51	91.97
45		92.65	94.93	101.82	103.87	104.38	103.52	94.75	92.45
46		92.67	94.97	101.89	103.85	104.36	103.52	94.8	92.45
47		92.67	94.97	101.89	103.85	104.36	103.52	94.8	92.45
48		92.78	95.02	101.91	103.96	104.42	103.54	94.75	92.34
49		92.78	95.02	101.91	103.96	104.42	103.54	94.6	92.03
50		92.8	95.04	101.93	103.98	104.36	103.54	94.6	92.03
51		92.58	94.89	101.78	103.81	104.25	103.48	94.6	92.03

Wall Temperature Measurements Along Heater Assembly

Stainless Steel Particles- 2 mm dia - 250 g loading

Re = 71614 q" = 111.888 kW/m2 T_W = 98.83104

Measure-ment no. (N)		Probe 1 T_1 (°C)	Probe 2 T_2 (°C)	Probe 3 T_3 (°C)	Probe 4 T_4 (°C)	Probe 5 T_5 (°C)	Probe 6 T_6 (oC)	Probe 7 T_7 (oC)	Probe 8 T_8 (oC)
52		92.58	94.89	101.78	103.81	104.25	103.48	96.07	93.48
53		92.58	94.86	101.69	103.81	104.25	103.48	96.07	93.48
54		92.58	94.89	101.74	103.83	104.25	103.48	96.07	93.48
55		92.58	94.89	101.74	103.83	104.25	103.48	96.09	93.72
56		92.6	94.86	101.74	103.83	104.25	103.43	96.09	93.72
57		92.56	94.84	101.74	103.78	104.22	103.41	94.8	92.54
58		92.56	94.84	101.74	103.78	104.22	103.41	95.87	93.35
59		92.6	94.84	101.74	103.78	104.22	103.41	95.87	93.35
60		92.58	94.89	101.69	103.81	104.22	103.45	94.64	92.06
61		92.58	94.89	101.69	103.81	104.22	103.45	95.89	93.37
62		92.56	94.86	101.71	103.78	104.2	103.43	95.89	93.37
63		92.58	94.8	101.69	103.72	104.22	103.41	94.71	92.43
64		92.58	94.8	101.69	103.72	104.22	103.41	94.71	92.43
65		92.58	94.73	101.67	103.7	104.14	103.39	94.71	92.43
66		92.6	94.75	101.65	103.7	104.18	103.37	94.71	92.43
67		92.6	94.75	101.65	103.7	104.18	103.37	94.71	92.43
68		92.6	94.73	101.62	103.72	104.18	103.37	96.14	93.53
69		92.67	94.69	101.62	103.67	104.18	103.43	96.14	93.53
70		92.67	94.69	101.62	103.67	104.18	103.43	96.14	93.53
71		92.67	94.73	101.6	103.7	104.18	103.43	94.8	92.39
72		92.67	94.73	101.6	103.7	104.18	103.43	94.8	92.23
73		92.6	94.71	101.62	103.67	104.18	103.43	94.86	92.23
74		92.58	94.73	101.58	103.7	104.16	103.43	94.86	92.23
75		92.58	94.73	101.58	103.7	104.16	103.43	96.09	93.39
76		92.47	94.71	101.58	103.67	104.16	103.43	96.09	93.39
77		92.47	94.73	101.58	103.7	104.25	103.43	96.11	93.66
78		92.47	94.73	101.58	103.7	104.25	103.43	96.11	93.66
79		92.58	94.73	101.74	103.78	104.36	103.54	96.11	93.66
80		92.58	94.73	101.74	103.78	104.36	103.54	96.09	93.59
81		92.58	94.73	101.74	103.78	104.36	103.54	95.89	93.28
82		92.58	94.73	101.65	103.76	104.25	103.54	95.89	93.28
83		92.58	94.67	101.6	103.72	104.25	103.48	95.89	93.28
84		92.58	94.67	101.6	103.72	104.25	103.48	96.11	93.66
85		92.56	94.67	101.6	103.72	104.25	103.48	96.11	93.66
86		92.58	94.69	101.62	103.74	104.25	103.48	96.11	93.66
87		92.58	94.69	101.62	103.74	104.25	103.48	95.67	93.04
88		92.52	94.69	101.58	103.63	104.16	103.45	95.67	93.04
89		92.52	94.69	101.58	103.63	104.16	103.45	95.67	93.04
90		92.47	94.62	101.58	103.59	104.16	103.48	95.81	93.22
91		92.47	94.6	101.49	103.63	104.11	103.45	95.81	93.22
92		92.47	94.6	101.49	103.63	104.11	103.45	96.07	93.64
93		92.47	94.58	101.49	103.61	104.09	103.43	96.07	93.64
94		92.47	94.58	101.49	103.61	104.11	103.43	96.07	93.64
95		92.47	94.58	101.49	103.61	104.11	103.43	95.94	93.31
96		92.52	94.58	101.49	103.61	104.14	103.43	94.62	92.19
97		92.52	94.58	101.6	103.65	104.16	103.5	94.62	92.19
98		92.52	94.58	101.6	103.65	104.16	103.5	95.94	93.31
99		92.54	94.69	101.6	103.72	104.33	103.61	96.03	93.64
100		92.54	94.69	101.6	103.72	104.33	103.65	96.03	93.64

Wall Temperature Measurements Along Heater Assembly

Stainless Steel Particles- 2 mm dia - 250 g loading

Re = 71614 q" = 139.860 kW/m2 T_W = 101.1343

Measure-ment no. (N)	T* =	94.0162 Probe 1 T_1 (°C)	96.7157 Probe 2 T_2 (°C)	104.5898 Probe 3 T_3 (°C)	106.9472 Probe 4 T_4 (°C)	107.5658 Probe 5 T_5 (°C)	106.695 Probe 6 T_6 (oC)	97.7486 Probe 7 T_7 (oC)	94.7959 Probe 8 T_8 (oC)
1		94.18	96.84	104.8	107.02	107.59	106.69	98.04	95.13
2		94.1	96.84	104.66	106.96	107.59	106.67	98.07	95.13
3		94.1	96.84	104.66	106.96	107.59	106.67	98.07	95.13
4		94.1	96.84	104.58	106.93	107.59	106.65	98.09	95.13
5		94.1	96.75	104.58	106.96	107.59	106.67	98.07	95.1
6		94.1	96.75	104.58	106.96	107.59	106.67	98.07	95.1
7		94.07	96.75	104.64	107	107.59	106.67	98.11	95.02
8		94.05	96.77	104.64	107.04	107.59	106.67	98.11	95.02
9		94.05	96.77	104.64	107.04	107.59	106.67	98.11	95.02
10		94.07	96.77	104.64	107	107.59	106.69	98.11	95.02
11		94.07	96.77	104.64	107	107.59	106.69	98.11	95.06
12		94.07	96.77	104.73	107.02	107.59	106.69	98.11	95.06
13		94.07	96.86	104.73	107.02	107.57	106.69	98.11	95.06
14		94.07	96.86	104.73	107.02	107.57	106.69	98.07	95.06
15		94.05	96.86	104.69	107.02	107.53	106.67	98.07	95.06
16		94.05	96.86	104.69	107.02	107.57	106.67	98.07	95.06
17		94.05	96.86	104.69	107.02	107.57	106.67	98.07	95.08
18		94.05	96.9	104.71	107.04	107.57	106.65	98.07	95.08
19		94.1	96.9	104.71	107.04	107.57	106.65	98.07	95.08
20		94.1	96.9	104.71	107.04	107.57	106.65	98.07	95.08
21		94.18	96.82	104.66	107	107.59	106.65	98.09	95.1
22		94.21	96.82	104.66	106.98	107.59	106.71	98.09	95.1
23		94.21	96.82	104.66	106.98	107.59	106.71	98.09	95.1
24		94.18	96.79	104.62	106.91	107.59	106.71	98.09	95.1
25		94.18	96.77	104.71	106.98	107.57	106.71	98	95.04
26		94.18	96.77	104.71	106.98	107.57	106.71	98	95.04
27		94.14	96.77	104.64	107	107.57	106.76	98.02	95.04
28		94.14	96.77	104.64	107	107.57	106.76	98	95.04
29		94.14	96.82	104.71	107.02	107.62	106.76	98	95.04
30		94.14	96.82	104.71	107	107.64	106.74	98.07	95.08
31		94.14	96.82	104.71	107	107.64	106.74	98	95.08
32		94.21	96.84	104.73	107.07	107.66	106.76	98	95.08
33		94.21	96.84	104.71	107.02	107.64	106.76	96.64	93.68
34		94.21	96.84	104.71	107.02	107.64	106.76	96.64	93.68
35		94.21	96.84	104.66	107.02	107.64	106.74	96.64	93.68
36		94.21	96.82	104.66	106.96	107.57	106.71	97.98	95.02
37		94.21	96.82	104.66	106.96	107.57	106.71	98.04	95.04
38		94.12	96.82	104.64	106.96	107.57	106.71	98.04	95.04
39		94.12	96.79	104.62	106.96	107.57	106.69	98.07	95.06
40		94.12	96.79	104.62	106.96	107.57	106.69	98.04	95.04
41		94.1	96.79	104.62	106.96	107.62	106.74	98.04	95.04
42		94.1	96.79	104.62	107	107.64	106.78	98.04	95
43		94.1	96.79	104.62	107	107.64	106.78	98.04	94.95
44		94.1	96.82	104.62	107	107.62	106.78	98.04	94.95
45		94.1	96.82	104.62	107	107.62	106.78	96.55	93.66
46		94.1	96.79	104.64	107	107.62	106.74	96.55	93.66
47		94.05	96.77	104.6	106.91	107.53	106.71	96.53	93.66
48		94.05	96.77	104.6	106.91	107.53	106.71	96.53	93.66
49		94.03	96.75	104.64	106.93	107.62	106.74	96.53	93.66
50		94.01	96.75	104.6	106.98	107.66	106.78	98	95
51		94.01	96.75	104.6	106.98	107.66	106.78	98.02	95.02

Wall Temperature Measurements Along Heater Assembly

Stainless Steel Particles- 2 mm dia - 250 g loading

Re = 71614 q" = 139.860 kW/m2 T_W = 101.1343

Measure-ment no. (N)		Probe 1 T_1 (°C)	Probe 2 T_2 (°C)	Probe 3 T_3 (°C)	Probe 4 T_4 (°C)	Probe 5 T_5 (°C)	Probe 6 T_6 (oC)	Probe 7 T_7 (oC)	Probe 8 T_8 (oC)
52		94.03	96.77	104.64	106.98	107.66	106.78	98.02	95.02
53		94.01	96.75	104.6	106.96	107.64	106.74	98.02	95.04
54		94.01	96.75	104.6	106.96	107.64	106.74	98.02	95.04
55		94.01	96.75	104.62	106.96	107.59	106.69	98.02	95.04
56		93.99	96.77	104.62	106.98	107.62	106.71	98.02	95.04
57		93.99	96.77	104.62	106.98	107.62	106.71	97.93	95.04
58		93.99	96.77	104.6	106.96	107.55	106.74	97.93	95.04
59		93.96	96.66	104.55	106.93	107.53	106.71	98.02	95.06
60		93.96	96.66	104.55	106.93	107.53	106.71	98.02	95.06
61		93.96	96.66	104.55	106.91	107.53	106.69	98.02	95.06
62		93.94	96.68	104.55	106.93	107.55	106.71	98.02	95.06
63		93.94	96.68	104.55	106.93	107.55	106.71	97.96	95.06
64		93.92	96.68	104.55	106.93	107.51	106.67	97.96	95.06
65		93.92	96.66	104.55	106.93	107.66	106.71	97.96	95.06
66		93.92	96.66	104.55	106.93	107.66	106.71	96.62	93.77
67		93.99	96.66	104.55	106.98	107.59	106.71	96.62	93.77
68		93.99	96.66	104.55	106.98	107.59	106.74	96.53	93.72
69		93.99	96.66	104.55	106.98	107.59	106.74	96.53	93.72
70		94.01	96.71	104.6	106.98	107.59	106.74	96.53	93.72
71		94.01	96.71	104.6	106.98	107.59	106.74	97.93	95
72		93.99	96.73	104.58	106.98	107.55	106.74	97.93	95
73		93.99	96.71	104.58	106.96	107.51	106.69	97.93	95
74		93.99	96.71	104.58	106.96	107.51	106.69	97.91	95.02
75		93.99	96.68	104.53	106.96	107.51	106.62	97.91	95.02
76		93.99	96.64	104.51	106.91	107.48	106.6	97.91	95.04
77		93.99	96.64	104.51	106.91	107.48	106.6	97.89	95.04
78		93.99	96.62	104.51	106.85	107.46	106.58	97.89	95.04
79		93.94	96.62	104.49	106.85	107.46	106.6	97.93	95.06
80		93.94	96.62	104.49	106.85	107.46	106.6	98	95.04
81		93.9	96.57	104.47	106.82	107.44	106.6	98	95.04
82		93.88	96.57	104.42	106.87	107.44	106.65	98	95.04
83		93.88	96.57	104.42	106.87	107.44	106.65	98	95.04
84		93.85	96.53	104.42	106.82	107.44	106.65	98	95.04
85		93.85	96.53	104.42	106.82	107.44	106.65	96.53	93.66
86		93.83	96.53	104.4	106.8	107.44	106.65	96.51	93.66
87		93.85	96.53	104.42	106.82	107.53	106.69	96.51	93.66
88		93.85	96.53	104.42	106.82	107.53	106.69	96.53	93.66
89		93.85	96.49	104.42	106.85	107.53	106.71	97.91	94.91
90		93.81	96.53	104.47	106.93	107.53	106.78	97.91	94.91
91		93.81	96.53	104.47	106.93	107.53	106.78	97.93	95.02
92		93.85	96.49	104.49	106.87	107.53	106.71	97.96	95.02
93		93.81	96.51	104.47	106.87	107.53	106.62	97.96	95.02
94		93.81	96.51	104.47	106.87	107.53	106.62	97.96	95.02
95		93.81	96.51	104.51	106.87	107.53	106.62	97.96	95
96		93.79	96.49	104.47	106.8	107.51	106.6	97.96	95
97		93.79	96.49	104.47	106.8	107.51	106.6	96.46	93.64
98		93.7	96.46	104.47	106.8	107.51	106.62	97.91	94.93
99		93.77	96.46	104.44	106.8	107.55	106.62	97.91	94.93
100		93.77	96.46	104.44	106.8	107.55	106.62	97.89	94.93

Wall Temperature Measurements Along Heater Assembly

Stainless Steel Particles- 2 mm dia - 250 g loading

Re = 71614 q" = 167.832 kW/m2 T_W = 103.3311

Measure-ment no. (N)	T* =	96.2388 Probe 1 T_1 (°C)	98.8087 Probe 2 T_2 (°C)	107.3101 Probe 3 T_3 (°C)	109.7084 Probe 4 T_4 (°C)	110.4286 Probe 5 T_5 (°C)	109.3599 Probe 6 T_6 (oC)	99.7086 Probe 7 T_7 (oC)	95.0857 Probe 8 T_8 (oC)
1		96.4	98.92	107.4	109.82	110.46	109.38	100.39	95.7
2		96.35	98.92	107.37	109.77	110.46	109.38	98.92	94.38
3		96.35	98.92	107.37	109.77	110.46	109.38	98.92	94.38
4		96.35	98.92	107.37	109.77	110.55	109.42	98.94	94.34
5		96.35	98.92	107.37	109.77	110.55	109.42	98.94	94.34
6		96.35	98.9	107.42	109.86	110.55	109.42	98.88	94.32
7		96.35	98.92	107.42	109.86	110.52	109.42	98.94	94.34
8		96.35	98.92	107.42	109.86	110.52	109.42	98.94	94.34
9		96.35	98.92	107.42	109.86	110.52	109.44	98.9	94.34
10		96.38	98.94	107.42	109.86	110.55	109.44	100.35	95.67
11		96.38	98.94	107.42	109.86	110.55	109.44	100.35	95.67
12		96.38	98.96	107.42	109.86	110.55	109.44	100.35	95.7
13		96.38	98.99	107.42	109.82	110.52	109.4	100.35	95.7
14		96.38	98.99	107.42	109.82	110.52	109.4	100.35	95.7
15		96.35	98.96	107.37	109.77	110.48	109.38	100.35	95.7
16		96.35	98.96	107.37	109.77	110.46	109.38	98.79	94.25
17		96.35	98.96	107.37	109.77	110.46	109.38	98.79	94.25
18		96.33	98.92	107.35	109.73	110.46	109.38	100.35	95.67
19		96.33	98.92	107.35	109.73	110.46	109.4	100.35	95.67
20		96.33	98.92	107.35	109.73	110.46	109.4	100.35	95.67
21		96.35	98.9	107.33	109.71	110.41	109.38	100.35	95.67
22		96.35	98.9	107.33	109.71	110.41	109.38	100.35	95.65
23		96.38	98.85	107.37	109.73	110.5	109.44	100.35	95.65
24		96.35	98.85	107.37	109.77	110.52	109.47	98.92	94.29
25		96.35	98.85	107.37	109.77	110.52	109.47	100.33	95.65
26		96.35	98.88	107.4	109.8	110.57	109.49	100.33	95.65
27		96.35	98.88	107.46	109.82	110.57	109.47	98.88	94.29
28		96.35	98.88	107.46	109.82	110.57	109.47	100.3	95.65
29		96.35	98.92	107.46	109.82	110.57	109.47	100.3	95.65
30		96.33	98.9	107.46	109.82	110.52	109.44	100.33	95.7
31		96.33	98.9	107.46	109.82	110.52	109.44	100.33	95.7
32		96.33	98.9	107.37	109.8	110.44	109.4	100.33	95.7
33		96.38	98.9	107.37	109.75	110.44	109.4	100.26	95.7
34		96.38	98.9	107.37	109.75	110.44	109.4	98.79	94.32
35		96.38	98.9	107.37	109.73	110.46	109.38	98.79	94.32
36		96.35	98.88	107.37	109.73	110.46	109.38	98.79	94.32
37		96.35	98.88	107.37	109.73	110.46	109.38	98.79	94.32
38		96.35	98.88	107.37	109.73	110.46	109.38	98.83	94.29
39		96.33	98.88	107.35	109.73	110.48	109.4	98.88	94.27
40		96.33	98.88	107.35	109.73	110.48	109.4	98.88	94.27
41		96.33	98.88	107.37	109.77	110.48	109.4	98.85	94.25
42		96.33	98.88	107.37	109.77	110.48	109.4	98.88	94.27
43		96.33	98.85	107.35	109.73	110.44	109.4	98.88	94.27
44		96.27	98.81	107.29	109.64	110.41	109.31	100.3	95.65
45		96.27	98.81	107.29	109.64	110.41	109.31	98.83	94.27
46		96.27	98.81	107.24	109.64	110.39	109.31	98.83	94.27
47		96.27	98.79	107.24	109.62	110.39	109.31	98.85	94.25
48		96.27	98.79	107.24	109.62	110.39	109.31	98.85	94.25
49		96.2	98.79	107.24	109.62	110.35	109.31	98.85	94.25
50		96.2	98.79	107.26	109.64	110.35	109.31	98.85	94.25
51		96.2	98.79	107.26	109.64	110.35	109.31	100.3	95.61

Wall Temperature Measurements Along Heater Assembly

Stainless Steel Particles- 2 mm dia - 250 g loading

Re = 71614 q" = 167.832 kW/m2 T_W = 103.3311

Measure-ment no. (N)		Probe 1 T_1 (°C)	Probe 2 T_2 (°C)	Probe 3 T_3 (°C)	Probe 4 T_4 (°C)	Probe 5 T_5 (°C)	Probe 6 T_6 (oC)	Probe 7 T_7 (oC)	Probe 8 T_8 (oC)
52		96.2	98.77	107.26	109.69	110.35	109.31	100.3	95.61
53		96.2	98.77	107.26	109.69	110.35	109.31	100.28	95.61
54		96.2	98.77	107.26	109.69	110.35	109.31	100.3	95.67
55		96.18	98.75	107.24	109.66	110.33	109.29	100.3	95.67
56		96.18	98.75	107.24	109.66	110.35	109.31	100.3	95.67
57		96.18	98.75	107.24	109.66	110.35	109.31	100.3	95.61
58		96.18	98.7	107.26	109.64	110.37	109.29	100.3	95.61
59		96.18	98.7	107.26	109.64	110.37	109.29	98.83	94.21
60		96.18	98.7	107.24	109.64	110.37	109.29	98.81	94.21
61		96.18	98.72	107.24	109.64	110.37	109.29	98.81	94.21
62		96.18	98.72	107.24	109.64	110.37	109.29	98.83	94.27
63		96.18	98.72	107.24	109.62	110.35	109.29	98.79	94.29
64		96.16	98.75	107.24	109.64	110.37	109.31	98.79	94.29
65		96.16	98.75	107.24	109.64	110.37	109.31	100.28	95.65
66		96.16	98.75	107.24	109.64	110.37	109.31	100.28	95.63
67		96.16	98.75	107.29	109.71	110.41	109.38	100.28	95.63
68		96.16	98.75	107.29	109.71	110.41	109.38	100.33	95.65
69		96.16	98.77	107.33	109.71	110.41	109.38	100.33	95.63
70		96.18	98.77	107.33	109.71	110.46	109.4	100.33	95.63
71		96.18	98.77	107.33	109.71	110.46	109.4	98.85	94.25
72		96.18	98.75	107.29	109.71	110.44	109.4	98.85	94.25
73		96.16	98.72	107.29	109.66	110.44	109.4	98.85	94.25
74		96.16	98.72	107.29	109.66	110.44	109.4	100.28	95.61
75		96.14	98.72	107.26	109.66	110.44	109.36	100.28	95.61
76		96.16	98.75	107.29	109.69	110.46	109.38	100.28	95.61
77		96.16	98.75	107.29	109.69	110.46	109.38	100.35	95.61
78		96.16	98.72	107.24	109.69	110.44	109.36	100.35	95.61
79		96.16	98.72	107.26	109.69	110.44	109.38	100.33	95.63
80		96.16	98.72	107.26	109.69	110.44	109.38	100.33	95.63
81		96.11	98.72	107.24	109.69	110.44	109.38	100.33	95.63
82		96.11	98.72	107.24	109.69	110.44	109.38	100.28	95.63
83		96.11	98.72	107.26	109.64	110.35	109.31	100.24	95.61
84		96.09	98.7	107.22	109.58	110.3	109.25	100.24	95.61
85		96.09	98.7	107.22	109.58	110.3	109.25	98.75	94.27
86		96.11	98.7	107.2	109.58	110.3	109.25	100.24	95.61
87		96.11	98.68	107.18	109.58	110.3	109.25	100.24	95.61
88		96.11	98.68	107.18	109.58	110.3	109.25	100.33	95.63
89		96.09	98.68	107.18	109.62	110.3	109.25	100.33	95.63
90		96.09	98.7	107.22	109.62	110.37	109.25	100.33	95.63
91		96.09	98.7	107.22	109.62	110.37	109.25	100.24	95.59
92		96.09	98.72	107.26	109.66	110.37	109.29	98.77	94.25
93		96.07	98.7	107.26	109.66	110.37	109.31	98.77	94.25
94		96.07	98.7	107.26	109.66	110.37	109.31	98.77	94.25
95		96.07	98.7	107.26	109.66	110.33	109.31	100.26	95.63
96		96.07	98.7	107.22	109.62	110.33	109.31	100.26	95.63
97		96.07	98.7	107.22	109.62	110.33	109.31	100.26	95.63
98		96.09	98.7	107.24	109.69	110.39	109.31	100.28	95.63
99		96.09	98.7	107.24	109.69	110.39	109.31	100.28	95.63
100		96.07	98.68	107.22	109.66	110.37	109.33	100.26	95.63

Wall Temperature Measurements Along Heater Assembly

Stainless Steel Particles- 2 mm dia - 250 g loading

Re = 71614 q" = 195.804 kW/m2 T_W = 104.3131

Measure-ment no. (N)	T* =	96.4568 Probe 1 T_1 (°C)	99.3725 Probe 2 T_2 (°C)	108.4209 Probe 3 T_3 (°C)	111.0513 Probe 4 T_4 (°C)	111.7389 Probe 5 T_5 (°C)	110.4875 Probe 6 T_6 (oC)	101.2424 Probe 7 T_7 (oC)	95.7343 Probe 8 T_8 (oC)
1		96.42	99.29	108.34	110.99	111.69	110.64	101.71	96.09
2		96.42	99.29	108.34	110.99	111.74	110.5	101.67	96.09
3		96.4	99.25	108.34	110.99	111.78	110.5	101.67	96.09
4		96.4	99.25	108.34	110.99	111.78	110.5	100.26	94.69
5		96.4	99.25	108.37	111.01	111.78	110.48	100.06	94.69
6		96.4	99.27	108.37	111.01	111.76	110.5	100.06	94.69
7		96.4	99.27	108.37	111.01	111.76	110.5	100.06	94.69
8		96.33	99.27	108.3	110.99	111.74	110.46	100.11	94.75
9		96.33	99.27	108.3	110.99	111.74	110.46	100.11	94.75
10		96.33	99.27	108.3	110.99	111.74	110.46	101.6	96.09
11		96.33	99.34	108.32	110.97	111.76	110.46	101.65	96.14
12		96.4	99.36	108.43	111.01	111.78	110.48	101.65	96.14
13		96.4	99.36	108.43	111.01	111.78	110.48	101.67	96.14
14		96.4	99.4	108.43	111.03	111.83	110.52	101.71	96.14
15		96.4	99.36	108.48	111.03	111.83	110.48	101.71	96.14
16		96.4	99.36	108.48	111.03	111.83	110.48	101.71	96.14
17		96.4	99.34	108.48	111.08	111.78	110.48	101.58	96.16
18		96.42	99.36	108.48	111.1	111.81	110.5	101.58	96.16
19		96.42	99.36	108.48	111.1	111.81	110.5	101.58	96.16
20		96.49	99.36	108.48	111.1	111.81	110.55	101.65	96.16
21		96.49	99.4	108.48	111.16	111.81	110.59	101.65	96.16
22		96.49	99.4	108.48	111.16	111.81	110.59	101.69	96.14
23		96.46	99.4	108.52	111.16	111.78	110.55	101.69	96.11
24		96.46	99.4	108.52	111.16	111.78	110.55	101.69	96.11
25		96.46	99.4	108.52	111.16	111.83	110.55	101.69	96.11
26		96.46	99.4	108.5	111.16	111.83	110.55	101.6	96.11
27		96.46	99.4	108.5	111.16	111.83	110.55	101.6	96.11
28		96.46	99.45	108.5	111.21	111.83	110.59	101.6	96.07
29		96.49	99.45	108.5	111.21	111.78	110.59	101.71	96.07
30		96.49	99.45	108.5	111.21	111.78	110.59	101.71	96.07
31		96.55	99.47	108.54	111.23	111.78	110.59	101.71	96.07
32		96.55	99.42	108.54	111.14	111.92	110.68	101.71	96.07
33		96.55	99.42	108.54	111.14	111.92	110.68	100.17	94.71
34		96.51	99.4	108.5	111.08	111.92	110.68	100.17	94.71
35		96.51	99.4	108.5	111.08	111.92	110.68	100.17	94.71
36		96.4	99.38	108.5	111.05	111.78	110.55	101.65	96.09
37		96.4	99.38	108.5	111.1	111.78	110.5	101.67	96.14
38		96.4	99.38	108.5	111.1	111.78	110.5	101.67	96.14
39		96.4	99.38	108.52	111.12	111.78	110.5	101.67	96.14
40		96.46	99.38	108.5	111.12	111.78	110.48	101.69	96.16
41		96.46	99.38	108.5	111.12	111.78	110.48	101.69	96.16
42		96.46	99.38	108.5	111.12	111.78	110.5	101.71	96.2
43		96.44	99.38	108.48	111.1	111.67	110.46	101.71	96.2
44		96.44	99.38	108.48	111.1	111.67	110.46	101.71	96.2
45		96.44	99.4	108.5	111.1	111.67	110.44	101.69	96.14
46		96.44	99.4	108.45	111.1	111.67	110.44	101.76	96.14
47		96.44	99.4	108.45	111.1	111.67	110.44	101.76	96.14
48		96.44	99.42	108.45	111.08	111.67	110.44	101.74	96.05
49		96.44	99.4	108.43	111.08	111.69	110.46	101.58	96.07
50		96.44	99.4	108.43	111.08	111.69	110.46	101.58	96.07
51		96.42	99.4	108.43	111.05	111.74	110.39	101.56	96.09

Wall Temperature Measurements Along Heater Assembly

Appendix A.3/7:2

Stainless Steel Particles- 2 mm dia - 250 g loading

Re = 71614 q" = 195.804 kW/m2 T_W = 104.3131

Measure-ment no. (N)		Probe 1 T_1 (°C)	Probe 2 T_2 (°C)	Probe 3 T_3 (°C)	Probe 4 T_4 (°C)	Probe 5 T_5 (°C)	Probe 6 T_6 (oC)	Probe 7 T_7 (oC)	Probe 8 T_8 (oC)
52		96.42	99.4	108.41	111.05	111.74	110.39	101.56	96.09
53		96.42	99.4	108.41	111.05	111.74	110.39	101.56	96.09
54		96.42	99.42	108.43	111.08	111.78	110.39	101.58	96.11
55		96.42	99.42	108.43	111.08	111.78	110.39	101.74	96.16
56		96.46	99.45	108.41	111.1	111.74	110.44	101.74	96.16
57		96.46	99.45	108.43	111.1	111.74	110.46	101.74	96.16
58		96.46	99.45	108.43	111.1	111.74	110.46	101.6	96.14
59		96.4	99.45	108.39	111.05	111.72	110.46	101.6	96.14
60		96.4	99.45	108.43	111.03	111.69	110.46	101.56	96.14
61		96.4	99.45	108.43	111.03	111.69	110.46	101.6	96.14
62		96.4	99.45	108.43	111.03	111.69	110.48	101.6	96.14
63		96.42	99.45	108.48	111.05	111.69	110.46	101.6	96.11
64		96.42	99.45	108.48	111.05	111.69	110.46	101.6	96.11
65		96.46	99.4	108.48	111.03	111.69	110.39	101.65	96.11
66		96.53	99.38	108.39	110.97	111.69	110.39	101.67	96.11
67		96.53	99.38	108.39	110.97	111.69	110.39	101.67	96.11
68		96.53	99.38	108.39	110.97	111.69	110.41	101.71	96.11
69		96.53	99.38	108.41	111.03	111.69	110.5	101.71	96.09
70		96.53	99.38	108.41	111.03	111.69	110.5	101.71	96.09
71		96.55	99.38	108.41	111.03	111.69	110.5	101.6	96.11
72		96.55	99.38	108.41	111.01	111.69	110.46	101.58	96.11
73		96.55	99.38	108.41	111.01	111.69	110.46	101.58	96.11
74		96.55	99.36	108.41	110.99	111.72	110.46	101.58	96.11
75		96.55	99.36	108.41	110.99	111.72	110.46	100.11	94.71
76		96.53	99.36	108.34	110.97	111.69	110.46	100.11	94.71
77		96.53	99.4	108.43	110.99	111.72	110.46	100.11	94.69
78		96.53	99.4	108.43	110.99	111.72	110.46	100.11	94.69
79		96.53	99.51	108.56	111.23	111.85	110.66	100.11	94.69
80		96.82	99.53	108.63	111.23	111.92	110.7	100.15	94.69
81		96.82	99.53	108.63	111.23	111.92	110.7	100.15	94.69
82		96.82	99.53	108.63	111.23	111.92	110.7	100.15	94.69
83		96.51	99.29	108.3	110.92	111.61	110.44	100.13	94.69
84		96.51	99.29	108.3	110.92	111.61	110.44	100.13	94.69
85		96.44	99.29	108.28	110.92	111.61	110.35	100.13	94.69
86		96.44	99.29	108.28	110.92	111.61	110.35	101.62	96.07
87		96.44	99.29	108.28	110.92	111.61	110.35	101.69	96.09
88		96.44	99.29	108.28	110.94	111.63	110.35	101.69	96.09
89		96.4	99.29	108.28	110.94	111.65	110.44	101.69	96.09
90		96.4	99.29	108.28	110.94	111.65	110.44	101.78	96.09
91		96.4	99.29	108.28	110.94	111.65	110.41	101.78	96.09
92		96.35	99.29	108.32	110.94	111.65	110.44	100.17	94.71
93		96.35	99.29	108.32	110.94	111.65	110.44	101.6	96.11
94		96.46	99.29	108.37	111.03	111.67	110.44	101.6	96.11
95		96.38	99.34	108.32	111.03	111.65	110.44	100.08	94.69
96		96.38	99.34	108.32	111.03	111.65	110.44	100.06	94.67
97		96.44	99.34	108.25	110.94	111.63	110.48	100.06	94.67
98		96.44	99.34	108.25	110.94	111.63	110.48	100.06	94.67
99		96.38	99.29	108.25	110.92	111.63	110.41	100.06	94.67
100		96.38	99.23	108.25	110.94	111.63	110.41	100.17	94.67

Wall Temperature Measurements Along Heater Assembly

Appendix A.3/8:1

Stainless Steel Particles- 2 mm dia - 250 g loading

Re = 71614 q" = 223.776 kW/m2 T_W = 105.6601

Measure-ment no. (N)	T* =	97.321 Probe 1 T_1 (°C)	100.2206 Probe 2 T_2 (°C)	110.0589 Probe 3 T_3 (°C)	112.931 Probe 4 T_4 (°C)	113.6189 Probe 5 T_5 (°C)	112.1665 Probe 6 T_6 (oC)	102.5797 Probe 7 T_7 (oC)	96.3845 Probe 8 T_8 (oC)
1		97.3	100.15	109.95	112.84	113.57	112.16	101.43	95.39
2		97.28	100.15	109.95	112.86	113.55	112.11	101.43	95.39
3		97.3	100.17	110.02	112.86	113.59	112.18	101.38	95.37
4		97.3	100.17	110.02	112.86	113.59	112.18	101.36	95.39
5		97.28	100.22	110.02	112.86	113.53	112.11	101.36	95.39
6		97.28	100.22	110.02	112.86	113.53	112.16	101.38	95.39
7		97.28	100.22	110.02	112.86	113.53	112.16	102.92	96.77
8		97.28	100.22	110.02	112.86	113.53	112.16	102.92	96.77
9		97.28	100.17	109.97	112.86	113.57	112.16	102.92	96.79
10		97.28	100.17	109.97	112.86	113.57	112.16	102.95	96.77
11		97.25	100.17	110	112.82	113.57	112.14	102.95	96.77
12		97.25	100.17	110	112.82	113.57	112.14	102.95	96.79
13		97.25	100.17	109.97	112.82	113.55	112.14	102.95	96.75
14		97.3	100.19	110	112.84	113.55	112.16	102.95	96.75
15		97.3	100.19	110	112.84	113.55	112.16	101.38	95.32
16		97.32	100.22	110	112.89	113.59	112.16	101.38	95.32
17		97.32	100.22	110.04	112.89	113.62	112.16	101.38	95.32
18		97.32	100.22	110.04	112.89	113.62	112.16	102.95	96.73
19		97.28	100.19	110.06	112.89	113.59	112.16	102.95	96.73
20		97.28	100.19	110.08	112.93	113.64	112.2	102.95	96.73
21		97.28	100.19	110.08	112.93	113.64	112.2	102.95	96.73
22		97.3	100.22	110.08	112.89	113.59	112.2	101.43	95.35
23		97.32	100.22	110	112.89	113.57	112.2	101.43	95.35
24		97.32	100.22	110	112.89	113.57	112.2	101.43	95.3
25		97.32	100.19	110	112.91	113.59	112.18	101.43	95.3
26		97.32	100.19	110	112.91	113.59	112.16	101.43	95.3
27		97.32	100.19	110	112.91	113.59	112.16	102.95	96.66
28		97.3	100.19	110	112.91	113.57	112.16	102.95	96.66
29		97.28	100.15	110.02	112.91	113.57	112.16	102.95	96.66
30		97.28	100.15	110.02	112.91	113.57	112.16	102.88	96.66
31		97.25	100.13	110.02	112.93	113.62	112.16	102.88	96.66
32		97.25	100.13	110.02	112.93	113.62	112.16	102.88	96.73
33		97.25	100.13	110.04	112.93	113.62	112.18	102.88	96.73
34		97.25	100.13	110.02	112.93	113.59	112.18	102.88	96.73
35		97.25	100.13	110.02	112.93	113.59	112.18	102.88	96.73
36		97.25	100.15	110.04	112.91	113.59	112.18	102.9	96.73
37		97.25	100.15	110.04	112.91	113.59	112.16	102.9	96.73
38		97.25	100.15	110.04	112.91	113.59	112.16	102.9	96.75
39		97.25	100.15	110.04	112.91	113.64	112.2	102.9	96.73
40		97.28	100.22	110.04	112.95	113.64	112.16	102.9	96.73
41		97.28	100.22	110.04	112.95	113.64	112.16	102.9	96.71
42		97.32	100.22	110.04	112.91	113.64	112.18	102.95	96.71
43		97.28	100.22	110.08	112.95	113.64	112.18	102.95	96.71
44		97.28	100.22	110.08	112.95	113.64	112.18	102.95	96.71
45		97.3	100.22	110.06	112.98	113.66	112.2	102.99	96.66
46		97.3	100.22	110.06	112.98	113.66	112.2	102.99	96.66
47		97.3	100.22	110.08	112.98	113.57	112.18	101.43	95.28
48		97.3	100.22	110.04	112.98	113.57	112.18	102.86	96.66
49		97.3	100.22	110.04	112.98	113.57	112.18	102.86	96.66
50		97.3	100.22	110.06	112.98	113.64	112.2	101.38	95.28
51		97.3	100.24	110.06	112.95	113.66	112.22	102.86	96.66

Wall Temperature Measurements Along Heater Assembly

Stainless Steel Particles- 2 mm dia - 250 g loading

Re = 71614 q" = 223.776 kW/m2 T_W = 105.6601

Measure-ment no. (N)		Probe 1 T_1 (°C)	Probe 2 T_2 (°C)	Probe 3 T_3 (°C)	Probe 4 T_4 (°C)	Probe 5 T_5 (°C)	Probe 6 T_6 (oC)	Probe 7 T_7 (oC)	Probe 8 T_8 (oC)
52		97.3	100.24	110.06	112.95	113.66	112.22	102.86	96.66
53		97.3	100.24	110.08	112.95	113.68	112.22	101.38	95.28
54		97.34	100.26	110.17	113	113.7	112.27	102.92	96.66
55		97.34	100.26	110.17	113	113.7	112.27	102.92	96.66
56		97.34	100.24	110.15	113	113.68	112.2	101.4	95.48
57		97.34	100.24	110.15	112.98	113.66	112.22	102.95	96.73
58		97.34	100.24	110.15	112.98	113.66	112.22	102.95	96.73
59		97.36	100.24	110.13	112.98	113.66	112.18	102.99	96.73
60		97.36	100.26	110.13	112.98	113.66	112.2	102.99	96.73
61		97.36	100.26	110.13	112.98	113.66	112.2	102.99	96.73
62		97.36	100.26	110.08	112.95	113.62	112.16	102.99	96.71
63		97.34	100.26	110.06	112.95	113.66	112.2	102.99	96.71
64		97.34	100.26	110.06	112.95	113.66	112.2	102.99	96.71
65		97.34	100.26	110.06	112.95	113.66	112.16	102.95	96.68
66		97.34	100.22	110.06	112.95	113.66	112.14	102.95	96.71
67		97.34	100.22	110.06	112.95	113.66	112.14	102.95	96.71
68		97.36	100.19	110.06	112.93	113.62	112.11	102.92	96.73
69		97.36	100.19	110.06	112.93	113.62	112.11	102.92	96.73
70		97.34	100.19	110.06	112.93	113.62	112.11	102.92	96.73
71		97.36	100.22	110.06	112.93	113.64	112.11	102.92	96.71
72		97.36	100.22	110.06	112.93	113.64	112.11	102.92	96.71
73		97.36	100.24	110.08	112.95	113.68	112.2	101.36	95.26
74		97.36	100.24	110.11	112.95	113.68	112.11	102.92	96.66
75		97.36	100.24	110.11	112.95	113.68	112.11	102.92	96.66
76		97.39	100.24	110.11	112.95	113.66	112.2	102.92	96.66
77		97.34	100.24	110.08	112.93	113.62	112.16	102.92	96.66
78		97.34	100.24	110.08	112.93	113.62	112.16	102.92	96.66
79		97.34	100.24	110.06	112.93	113.62	112.16	102.88	96.66
80		97.34	100.26	110.13	112.98	113.62	112.16	102.88	96.66
81		97.34	100.26	110.13	112.98	113.62	112.16	102.88	96.66
82		97.34	100.26	110.11	113	113.62	112.16	101.38	95.26
83		97.39	100.26	110.11	113	113.66	112.16	101.38	95.24
84		97.39	100.26	110.11	113	113.66	112.16	101.38	95.24
85		97.36	100.26	110.11	113	113.66	112.16	101.38	95.24
86		97.36	100.26	110.11	113	113.66	112.16	102.92	96.68
87		97.39	100.28	110.11	112.98	113.66	112.18	102.92	96.68
88		97.39	100.3	110.11	112.98	113.66	112.16	102.97	96.68
89		97.39	100.3	110.11	112.98	113.66	112.16	102.99	96.68
90		97.39	100.3	110.08	112.98	113.66	112.18	102.99	96.68
91		97.39	100.28	110.06	112.95	113.66	112.16	102.99	96.66
92		97.39	100.28	110.06	112.95	113.66	112.16	102.99	96.66
93		97.39	100.28	110.06	112.98	113.66	112.14	102.97	96.64
94		97.39	100.28	110.11	112.95	113.64	112.14	102.97	96.64
95		97.39	100.28	110.11	112.95	113.64	112.14	102.97	96.64
96		97.36	100.28	110.11	112.95	113.59	112.11	102.97	96.68
97		97.36	100.28	110.06	112.93	113.59	112.11	102.97	96.71
98		97.36	100.28	110.06	112.93	113.59	112.11	102.97	96.71
99		97.36	100.28	110.04	112.86	113.57	112.11	102.9	96.68
100		97.36	100.28	110.06	112.93	113.57	112.14	102.9	96.73

Wall Temperature Measurements Along Heater Assembly

Stainless Steel Particles- 2 mm dia - 250 g loading

Re = 71614 q" = 251.748 kW/m2 T_W = 106.6277

Measure-ment no. (N)	T* =	97.2715 Probe 1 T_1 (°C)	100.4207 Probe 2 T_2 (°C)	111.0933 Probe 3 T_3 (°C)	114.1919 Probe 4 T_4 (°C)	114.8167 Probe 5 T_5 (°C)	113.2982 Probe 6 T_6 (oC)	103.3168 Probe 7 T_7 (oC)	98.6121 Probe 8 T_8 (oC)
1		97.12	100.3	110.99	114.1	114.74	113.2	103.85	99.14
2		97.12	100.3	110.99	114.1	114.74	113.2	103.85	99.14
3		97.12	100.3	110.99	114.1	114.72	113.22	102.33	97.78
4		97.12	100.3	111.01	114.12	114.74	113.2	102.33	97.78
5		97.12	100.3	111.01	114.12	114.74	113.2	102.33	97.78
6		97.12	100.3	111.01	114.12	114.74	113.2	102.29	97.74
7		97.12	100.3	111.01	114.12	114.74	113.2	102.29	97.74
8		97.12	100.3	111.01	114.12	114.74	113.2	102.29	97.74
9		97.14	100.3	111.01	114.12	114.74	113.2	102.35	97.69
10		97.14	100.37	111.03	114.12	114.74	113.22	103.89	99.23
11		97.14	100.37	111.03	114.12	114.74	113.22	103.89	99.23
12		97.19	100.37	111.05	114.17	114.79	113.22	103.87	99.14
13		97.19	100.37	111.05	114.17	114.79	113.22	103.94	99.25
14		97.19	100.33	111.08	114.17	114.79	113.22	103.94	99.25
15		97.17	100.33	111.05	114.17	114.79	113.22	103.89	99.21
16		97.17	100.33	111.05	114.17	114.79	113.22	103.89	99.21
17		97.14	100.33	111.08	114.17	114.74	113.17	103.89	99.21
18		97.14	100.33	111.05	114.17	114.76	113.22	103.89	99.18
19		97.14	100.33	111.05	114.17	114.76	113.22	103.89	99.18
20		97.14	100.35	111.08	114.17	114.76	113.22	103.89	99.18
21		97.14	100.35	111.03	114.15	114.76	113.22	103.89	99.18
22		97.14	100.35	111.03	114.15	114.76	113.22	103.89	99.18
23		97.17	100.35	111.03	114.15	114.7	113.2	102.57	97.87
24		97.17	100.35	111.03	114.12	114.7	113.2	102.57	97.87
25		97.17	100.35	111.03	114.12	114.7	113.2	102.57	97.87
26		97.19	100.39	111.05	114.12	114.79	113.22	102.29	97.67
27		97.21	100.41	111.08	114.19	114.79	113.28	102.29	97.67
28		97.21	100.41	111.08	114.19	114.79	113.28	102.29	97.67
29		97.23	100.46	111.1	114.21	114.81	113.26	102.29	97.65
30		97.23	100.44	111.1	114.19	114.81	113.26	102.29	97.63
31		97.23	100.44	111.1	114.19	114.81	113.26	102.29	97.63
32		97.21	100.44	111.05	114.15	114.74	113.24	102.29	97.63
33		97.21	100.44	111.05	114.15	114.74	113.24	103.89	99.07
34		97.21	100.44	111.05	114.15	114.74	113.24	103.89	99.07
35		97.25	100.41	111.08	114.15	114.79	113.24	103.92	99.12
36		97.25	100.41	111.08	114.15	114.79	113.24	103.89	99.14
37		97.3	100.41	111.08	114.15	114.81	113.31	103.89	99.14
38		97.25	100.41	111.08	114.15	114.81	113.31	103.92	99.16
39		97.25	100.41	111.08	114.15	114.81	113.31	103.92	99.16
40		97.32	100.41	111.05	114.15	114.79	113.28	103.92	99.16
41		97.3	100.41	111.01	114.12	114.79	113.26	102.33	97.71
42		97.3	100.41	111.01	114.12	114.79	113.26	102.33	97.71
43		97.32	100.41	111.01	114.1	114.76	113.26	102.33	97.71
44		97.32	100.44	111.05	114.12	114.81	113.28	103.87	99.23
45		97.32	100.44	111.05	114.12	114.81	113.28	103.87	99.21
46		97.32	100.44	111.05	114.1	114.81	113.28	103.87	99.21
47		97.28	100.41	111.05	114.1	114.81	113.28	103.94	99.16
48		97.28	100.41	111.05	114.1	114.81	113.28	103.92	99.14
49		97.28	100.39	111.05	114.12	114.74	113.28	103.92	99.14
50		97.28	100.39	111.12	114.19	114.74	113.28	103.89	99.14
51		97.28	100.39	111.12	114.19	114.74	113.28	103.87	99.14

Wall Temperature Measurements Along Heater Assembly

Stainless Steel Particles- 2 mm dia - 250 g loading

Re = 71614 q" = 251.748 kW/m2 T_W = 106.6277

Measure-ment no. (N)		Probe 1 T_1 (°C)	Probe 2 T_2 (°C)	Probe 3 T_3 (°C)	Probe 4 T_4 (°C)	Probe 5 T_5 (°C)	Probe 6 T_6 (oC)	Probe 7 T_7 (oC)	Probe 8 T_8 (oC)
52		97.32	100.46	111.12	114.19	114.76	113.28	103.87	99.14
53		97.32	100.46	111.12	114.19	114.76	113.28	103.87	99.14
54		97.32	100.46	111.1	114.17	114.79	113.28	103.89	99.16
55		97.28	100.41	111.08	114.17	114.79	113.28	103.89	99.16
56		97.28	100.41	111.08	114.17	114.79	113.28	103.92	99.16
57		97.3	100.44	111.1	114.19	114.85	113.33	103.92	99.18
58		97.3	100.44	111.1	114.21	114.85	113.33	103.92	99.18
59		97.3	100.44	111.1	114.21	114.85	113.33	103.89	99.12
60		97.3	100.44	111.1	114.23	114.85	113.33	102.33	97.69
61		97.28	100.41	111.08	114.21	114.83	113.31	102.33	97.69
62		97.28	100.41	111.08	114.21	114.83	113.31	102.33	97.67
63		97.3	100.41	111.1	114.23	114.85	113.35	102.33	97.67
64		97.32	100.46	111.14	114.23	114.85	113.33	102.4	97.67
65		97.32	100.46	111.14	114.23	114.85	113.33	103.94	99.14
66		97.32	100.46	111.1	114.23	114.87	113.35	103.94	99.14
67		97.3	100.41	111.12	114.21	114.85	113.37	103.94	99.21
68		97.3	100.41	111.12	114.21	114.85	113.37	103.92	99.21
69		97.3	100.41	111.12	114.21	114.85	113.37	103.92	99.21
70		97.3	100.41	111.12	114.23	114.83	113.37	103.89	99.14
71		97.3	100.41	111.12	114.23	114.83	113.37	103.89	99.14
72		97.3	100.44	111.12	114.19	114.83	113.37	103.89	99.14
73		97.3	100.44	111.12	114.19	114.83	113.37	102.31	97.69
74		97.3	100.44	111.1	114.21	114.83	113.37	102.33	97.69
75		97.32	100.44	111.1	114.21	114.83	113.37	102.33	97.69
76		97.32	100.44	111.1	114.21	114.83	113.37	102.35	97.71
77		97.34	100.48	111.16	114.23	114.87	113.37	103.89	99.23
78		97.34	100.48	111.16	114.23	114.87	113.37	103.89	99.23
79		97.34	100.48	111.16	114.23	114.87	113.37	103.89	99.23
80		97.34	100.5	111.14	114.26	114.9	113.37	103.92	99.23
81		97.34	100.5	111.14	114.26	114.9	113.37	103.92	99.23
82		97.34	100.5	111.14	114.26	114.9	113.37	103.89	99.18
83		97.34	100.52	111.19	114.28	114.92	113.39	102.55	97.69
84		97.36	100.5	111.19	114.28	114.92	113.39	102.55	97.69
85		97.36	100.5	111.19	114.28	114.92	113.39	102.53	97.67
86		97.36	100.48	111.16	114.3	114.92	113.39	103.94	99.05
87		97.36	100.48	111.14	114.3	114.9	113.37	103.94	99.05
88		97.36	100.48	111.14	114.3	114.9	113.37	103.98	99.12
89		97.39	100.52	111.14	114.3	114.92	113.37	103.96	99.14
90		97.39	100.52	111.14	114.3	114.92	113.37	103.96	99.14
91		97.41	100.55	111.16	114.32	114.92	113.37	103.96	99.21
92		97.41	100.5	111.16	114.23	114.9	113.37	103.92	99.21
93		97.41	100.5	111.16	114.23	114.9	113.37	103.92	99.21
94		97.39	100.5	111.16	114.23	114.87	113.37	103.89	99.18
95		97.41	100.5	111.21	114.28	114.9	113.37	102.35	97.67
96		97.41	100.5	111.21	114.28	114.9	113.37	102.35	97.67
97		97.41	100.52	111.23	114.32	114.9	113.42	102.31	97.65
98		97.43	100.52	111.23	114.34	114.96	113.44	102.31	97.65
99		97.43	100.52	111.23	114.34	114.96	113.44	102.31	97.65
100		97.43	100.57	111.25	114.34	114.96	113.42	102.33	97.65

Wall Temperature Measurements Along Heater Assembly

Stainless Steel Particles- 2 mm dia - 250 g loading

Re = 71614 q" = 279.720 kW/m2 T_W = 107.4116

Measure-ment no. (N)	T* =	96.8383 Probe 1 T_1 (°C)	100.282 Probe 2 T_2 (°C)	111.9639 Probe 3 T_3 (°C)	115.3353 Probe 4 T_4 (°C)	115.9156 Probe 5 T_5 (°C)	114.3617 Probe 6 T_6 (oC)	104.6164 Probe 7 T_7 (oC)	99.9797 Probe 8 T_8 (oC)
1		96.68	100.15	111.89	115.25	115.87	114.23	104.86	100.19
2		96.71	100.15	111.87	115.25	115.87	114.23	104.86	100.19
3		96.71	100.15	111.87	115.25	115.89	114.28	104.93	100.19
4		96.71	100.15	111.87	115.25	115.89	114.28	103.3	98.7
5		96.71	100.17	111.87	115.27	115.89	114.32	103.3	98.7
6		96.68	100.19	111.92	115.32	115.89	114.32	103.32	98.68
7		96.68	100.19	111.92	115.32	115.89	114.32	103.28	98.68
8		96.68	100.19	111.92	115.32	115.89	114.3	103.28	98.68
9		96.68	100.17	111.89	115.29	115.89	114.3	103.32	98.68
10		96.68	100.17	111.89	115.29	115.89	114.3	103.34	98.72
11		96.68	100.13	111.89	115.27	115.87	114.28	103.34	98.72
12		96.68	100.13	111.89	115.23	115.91	114.32	103.32	98.7
13		96.68	100.13	111.89	115.23	115.91	114.32	103.32	98.7
14		96.71	100.13	111.89	115.27	115.87	114.3	104.93	100.15
15		96.75	100.19	111.94	115.27	115.91	114.32	104.93	100.15
16		96.75	100.19	111.94	115.27	115.91	114.32	104.93	100.15
17		96.79	100.24	111.96	115.34	115.96	114.34	104.93	100.22
18		96.79	100.24	111.96	115.34	115.96	114.34	104.91	100.22
19		96.77	100.22	111.96	115.32	115.93	114.34	104.91	100.22
20		96.77	100.24	111.96	115.34	115.91	114.34	104.91	100.17
21		96.77	100.24	111.96	115.34	115.91	114.34	104.91	100.17
22		96.77	100.24	111.94	115.34	115.91	114.34	104.91	100.17
23		96.75	100.24	111.94	115.29	115.96	114.34	104.91	100.17
24		96.75	100.24	111.94	115.29	115.96	114.34	104.86	100.22
25		96.77	100.24	111.94	115.29	115.96	114.34	104.86	100.22
26		96.77	100.26	111.96	115.32	115.91	114.37	104.84	100.19
27		96.77	100.26	111.96	115.32	115.91	114.37	104.88	100.24
28		96.77	100.26	111.96	115.32	115.91	114.41	104.88	100.24
29		96.77	100.26	111.98	115.36	115.98	114.43	104.86	100.28
30		96.77	100.26	111.98	115.36	115.98	114.43	104.91	100.24
31		96.79	100.28	112	115.36	115.98	114.43	104.91	100.24
32		96.79	100.28	112	115.34	115.93	114.39	104.88	100.22
33		96.79	100.28	112	115.34	115.93	114.39	104.86	100.24
34		96.82	100.26	111.98	115.29	115.91	114.37	104.86	100.24
35		96.84	100.26	111.89	115.27	115.89	114.37	104.84	100.22
36		96.84	100.26	111.89	115.27	115.89	114.37	104.84	100.22
37		96.82	100.22	111.87	115.25	115.89	114.32	104.84	100.22
38		96.82	100.22	111.87	115.25	115.89	114.32	103.23	98.7
39		96.84	100.22	111.87	115.27	115.89	114.34	103.23	98.7
40		96.84	100.24	111.89	115.32	115.93	114.37	103.23	98.7
41		96.84	100.24	111.89	115.32	115.93	114.37	104.91	100.17
42		96.84	100.26	111.98	115.38	115.93	114.41	104.91	100.17
43		96.82	100.24	111.96	115.36	115.89	114.39	104.91	100.17
44		96.82	100.24	111.96	115.36	115.89	114.39	104.91	100.26
45		96.79	100.24	111.98	115.36	115.87	114.39	104.91	100.26
46		96.79	100.28	111.98	115.36	115.87	114.45	104.91	100.26
47		96.79	100.28	111.98	115.36	115.87	114.45	104.95	100.26
48		96.77	100.28	111.98	115.36	115.93	114.45	104.86	100.26
49		96.86	100.28	112.03	115.36	115.93	114.43	104.86	100.26
50		96.86	100.28	112.03	115.36	115.93	114.43	104.95	100.26
51		96.79	100.3	112.03	115.4	115.93	114.43	104.86	100.26

Wall Temperature Measurements Along Heater Assembly

Stainless Steel Particles- 2 mm dia - 250 g loading

Re = 71614 q" = 279.720 kW/m2 T_W = 107.4116

Measure-ment no. (N)		Probe 1 T_1 (°C)	Probe 2 T_2 (°C)	Probe 3 T_3 (°C)	Probe 4 T_4 (°C)	Probe 5 T_5 (°C)	Probe 6 T_6 (oC)	Probe 7 T_7 (oC)	Probe 8 T_8 (oC)
52		96.86	100.3	111.98	115.4	115.89	114.43	104.86	100.26
53		96.86	100.3	111.98	115.4	115.89	114.43	104.86	100.28
54		96.84	100.28	111.96	115.36	115.89	114.39	104.86	100.26
55		96.88	100.28	111.94	115.29	115.87	114.37	104.86	100.26
56		96.88	100.28	111.94	115.29	115.87	114.37	104.84	100.26
57		96.84	100.28	111.94	115.29	115.87	114.39	104.88	100.24
58		96.82	100.28	112	115.36	115.93	114.43	104.88	100.24
59		96.82	100.28	112	115.36	115.93	114.43	104.91	100.24
60		96.82	100.28	112	115.36	115.93	114.43	104.91	100.24
61		96.82	100.28	112	115.36	115.93	114.43	104.93	100.24
62		96.82	100.3	111.98	115.36	115.89	114.32	104.91	100.26
63		96.82	100.3	111.98	115.36	115.89	114.32	104.91	100.26
64		96.84	100.28	111.98	115.36	115.84	114.28	104.91	100.22
65		96.84	100.28	111.98	115.36	115.84	114.32	104.86	100.24
66		96.84	100.28	111.98	115.36	115.84	114.32	104.86	100.24
67		96.86	100.3	112.03	115.38	115.93	114.34	104.91	100.24
68		96.86	100.3	112.03	115.38	115.93	114.39	104.86	100.24
69		96.86	100.3	112.03	115.38	115.93	114.39	104.86	100.24
70		96.88	100.35	112	115.36	115.93	114.34	104.93	100.3
71		96.88	100.35	112	115.34	115.91	114.32	103.32	98.81
72		96.88	100.35	112	115.34	115.91	114.32	103.32	98.81
73		96.92	100.35	112	115.34	115.89	114.32	104.91	100.33
74		96.92	100.33	112	115.34	115.89	114.32	104.91	100.3
75		96.92	100.33	112	115.34	115.89	114.32	104.91	100.3
76		96.92	100.33	111.98	115.36	115.89	114.39	104.91	100.33
77		96.92	100.33	111.98	115.36	115.96	114.37	104.95	100.35
78		96.92	100.33	111.98	115.36	115.96	114.37	104.95	100.35
79		96.9	100.37	112.03	115.43	115.96	114.37	104.95	100.35
80		96.9	100.37	112.03	115.43	115.96	114.37	104.93	100.3
81		96.92	100.37	112.05	115.43	115.96	114.37	104.93	100.3
82		96.9	100.37	112.03	115.43	115.96	114.37	104.91	100.3
83		96.9	100.37	112.03	115.43	115.96	114.37	104.88	100.3
84		96.9	100.37	111.96	115.38	115.91	114.37	104.88	100.3
85		96.9	100.37	111.96	115.38	115.96	114.37	104.91	100.3
86		96.9	100.37	111.96	115.38	115.96	114.37	104.95	100.33
87		96.9	100.37	112.05	115.38	115.96	114.43	104.95	100.33
88		96.95	100.37	112.07	115.4	116	114.41	104.95	100.35
89		96.95	100.37	112.07	115.4	116	114.41	104.95	100.35
90		97.03	100.44	112.05	115.38	116	114.41	104.95	100.35
91		97.06	100.44	112	115.36	115.93	114.39	104.95	100.28
92		97.06	100.44	112	115.36	115.93	114.39	104.95	100.28
93		97.06	100.39	111.96	115.29	115.89	114.34	103.34	98.83
94		97.06	100.37	111.94	115.29	115.89	114.32	103.34	98.83
95		97.06	100.37	111.94	115.29	115.89	114.32	103.34	98.83
96		97.03	100.37	111.96	115.29	115.89	114.34	105	100.28
97		97.03	100.37	111.96	115.29	115.89	114.34	105	100.3
98		96.99	100.37	111.94	115.34	115.89	114.37	105	100.3
99		96.99	100.44	111.96	115.38	115.98	114.41	104.95	100.3
100		96.99	100.44	111.96	115.38	115.98	114.41	104.95	100.3

Stainless Steel. 2 mm diameter. 250g loading

Subcooled Temperature = 90 ^{0}C **Liquid Flowrate = 14 LPM**

Data for Boiling Curve and Heat Transfer Coefficient Plots

q (W)	A (m^2)	q" (W/m^2)	T_W (°C)	Tf_i (°C)	Tf_o (°C)	Tf* (°C)	T_W-Tf* (K)	α ($W/m^2.K$)
0	7.15E-03	0				0	0	
200	7.15E-03	27972.03	92.33714	88	91.1	89.55	2.78714	10036.10
400	7.15E-03	55944.06	94.4604	87.1	90.72	88.91	5.5504	10079.28
600	7.15E-03	83916.08	97.31241	87.05	91	89.025	8.28741	10125.73
800	7.15E-03	111888.1	99.50848	87.38	91.54	89.46	10.04848	11134.83
1000	7.15E-03	139860.1	101.0358	87.55	91.67	89.61	11.4258	12240.73
1200	7.15E-03	167832.2	101.987	88.04	91.77	89.905	12.082	13891.09
1400	7.15E-03	195804.2	103.1779	88.88	91.63	90.255	12.9229	15151.72
1600	7.15E-03	223776.2	103.9587	89.25	91.6	90.425	13.5337	16534.74
1800	7.15E-03	251748.3	104.9459	89.93	91.78	90.855	14.0909	17866.02
2000	7.15E-03	279720.3	105.8096	89.94	92.19	91.065	14.7446	18971.03

Nomenclature	
q	Power (W)
A	Cross-sectional area of riser column (m2)
q"	Heat Flux (W/m2)
α	Heat transfer coefficient (W/m2.K)
Tf_i	Temperature of fluid into flow channel (°C)
Tf_o	Temperature of fluid out of flow channel (°C)
T_W	Measured wall temperature (°C)
Tf*	Mean fluid Temperature (°C)

Appendix A.4/2

Stainless Steel. 2 mm diameter. 250g loading

Subcooled Temperature = 90 ^{0}C **Liquid Flowrate = 16 LPM**

Data for Boiling Curve and Heat Transfer Coefficient Plots

q (W)	A (m^2)	q" (W/m^2)	T_W (°C)	Tf_i (°C)	Tf_o (°C)	Tf* (°C)	T_W-Tf* (K)	α ($W/m^2.K$)
0	7.15E-03	0				0	0	
200	7.15E-03	27972.03	92.31824	89.39	90.34	89.865	2.45324	11402.08
400	7.15E-03	55944.06	94.45424	88.37	90.8	89.585	4.86924	11489.28
600	7.15E-03	83916.08	98.10873	88.94	92.44	90.69	7.41873	11311.38
800	7.15E-03	111888.1	100.1353	89.4	92.06	90.73	9.4053	11896.28
1000	7.15E-03	139860.1	101.3981	89	92.03	90.515	10.8831	12851.13
1200	7.15E-03	167832.2	102.6091	89.44	92.28	90.86	11.7491	14284.68
1400	7.15E-03	195804.2	103.6269	89.83	92.17	91	12.6269	15506.91
1600	7.15E-03	223776.2	104.3017	90.51	91.69	91.1	13.2017	16950.56
1800	7.15E-03	251748.3	105.405	91.1	91.71	91.405	14	17982.02
2000	7.15E-03	279720.3	106.3286	90.89	92.57	91.73	14.5986	19160.76

Nomenclature	
q	Power (W)
A	Cross-sectional area of riser column (m2)
q"	Heat Flux (W/m2)
α	Heat transfer coefficient (W/m2.K)
Tf_i	Temperature of fluid into flow channel (°C)
Tf_o	Temperature of fluid out of flow channel (°C)
T_W	Measured wall temperature (°C)
Tf*	Mean fluid Temperature (°C)

Stainless Steel. 2 mm diameter. 250g loading

Subcooled Temperature = 90 ^{0}C **Liquid Flowrate = 18 LPM**

Data for Boiling Curve and Heat Transfer Coefficient Plots

q (W)	A (m^2)	q" (W/m^2)	T_W (°C)	Tf_i (°C)	Tf_o (°C)	Tf* (°C)	T_W-Tf* (K)	α ($W/m^2.K$)
0	7.15E-03	0				0	0	
200	7.15E-03	27972.03	92.12703	88.56	91.32	89.94	2.18703	12789.96
400	7.15E-03	55944.06	94.75718	89.11	91.59	90.35	4.40718	12693.84
600	7.15E-03	83916.08	97.69805	89.19	93	91.095	6.60305	12708.69
800	7.15E-03	111888.1	99.91518	89.23	93.45	91.34	8.57518	13047.90
1000	7.15E-03	139860.1	102.2778	90.39	93.88	92.135	10.1428	13789.11
1200	7.15E-03	167832.2	104.0459	91.78	93.95	92.865	11.1809	15010.61
1400	7.15E-03	195804.2	105.1981	91.75	93.84	92.795	12.4031	15786.71
1600	7.15E-03	223776.2	106.0291	91.85	93.91	92.88	13.1491	17018.37
1800	7.15E-03	251748.3	106.7246	92.11	93.85	92.98	13.7446	18316.16
2000	7.15E-03	279720.3	107.3726	92.12	93.53	92.825	14.5476	19227.93

Nomenclature	
q	Power (W)
A	Cross-sectional area of riser column (m2)
q"	Heat Flux (W/m2)
α	Heat transfer coefficient (W/m2.K)
Tf_i	Temperature of fluid into flow channel (°C)
Tf_o	Temperature of fluid out of flow channel (°C)
T_W	Measured wall temperature (°C)
Tf*	Mean fluid Temperature (°C)

Stainless Steel. 2 mm diameter. 250g loading

Subcooled Temperature = 90 ^{0}C **Liquid Flowrate = 20 LPM**

Data for Boiling Curve and Heat Transfer Coefficient Plots

q (W)	A (m^2)	q" (W/m^2)	T_W (°C)	Tf_i (°C)	Tf_o (°C)	Tf* (°C)	T_W-Tf* (K)	α ($W/m^2.K$)
0	7.15E-03	0				0	0	
200	7.15E-03	27972.03	92.5469	89.1	92.2	90.65	1.8969	14746.18
400	7.15E-03	55944.06	95.14003	90.01	92.67	91.34	3.80003	14722.00
600	7.15E-03	83916.08	97.6785	90.6	93.43	92.015	5.6635	14817.00
800	7.15E-03	111888.1	99.3312	90.15	93.54	91.845	7.4862	14945.92
1000	7.15E-03	139860.1	101.8044	91.88	93.97	92.925	8.8794	15751.08
1200	7.15E-03	167832.2	103.5012	92.77	93.93	93.35	10.1512	16533.23
1400	7.15E-03	195804.2	104.5702	92.46	93.94	93.2	11.3702	17220.82
1600	7.15E-03	223776.2	105.6067	92.79	93.87	93.33	12.2767	18227.72
1800	7.15E-03	251748.3	106.8306	92.98	93.97	93.475	13.3556	18849.64
2000	7.15E-03	279720.3	107.4701	92.88	93.81	93.345	14.1251	19803.07

Nomenclature	
q	Power (W)
A	Cross-sectional area of riser column (m2)
q"	Heat Flux (W/m2)
α	Heat transfer coefficient (W/m2.K)
Tf_i	Temperature of fluid into flow channel (°C)
Tf_o	Temperature of fluid out of flow channel (°C)
T_W	Measured wall temperature (°C)
Tf*	Mean fluid Temperature (°C)

Stainless Steel. 2 mm diameter. 250g loading

Subcooled Temperature = 90 ^{0}C **Liquid Flowrate = 22 LPM**

Data for Boiling Curve and Heat Transfer Coefficient Plots

q (W)	A (m^2)	q" (W/m^2)	T_W (°C)	Tf_i (°C)	Tf_o (°C)	Tf* (°C)	T_W-Tf* (K)	α ($W/m^2.K$)
0	7.15E-03	0				0	0	
200	7.15E-03	27972.03	92.52015	88.87	92.12	90.495	2.02515	13812.32
400	7.15E-03	55944.06	95.07715	89.53	92.53	91.03	4.04715	13823.07
600	7.15E-03	83916.08	96.82979	89.19	92.33	90.76	6.06979	13825.20
800	7.15E-03	111888.1	98.83104	89.69	92.16	90.925	7.90604	14152.23
1000	7.15E-03	139860.1	101.1343	90.69	92.87	91.78	9.3543	14951.43
1200	7.15E-03	167832.2	103.3311	92.79	93	92.895	10.4361	16081.89
1400	7.15E-03	195804.2	104.3131	92	93.34	92.67	11.6431	16817.19
1600	7.15E-03	223776.2	105.6601	92.96	93.48	93.22	12.4401	17988.30
1800	7.15E-03	251748.3	106.6277	92.86	93.24	93.05	13.5777	18541.30
2000	7.15E-03	279720.3	107.4116	92.66	93.67	93.165	14.2466	19634.18

Nomenclature	
q	Power (W)
A	Cross-sectional area of riser column (m2)
q"	Heat Flux (W/m2)
α	Heat transfer coefficient (W/m2.K)
Tf_i	Temperature of fluid into flow channel (°C)
Tf_o	Temperature of fluid out of flow channel (°C)
T_W	Measured wall temperature (°C)
Tf*	Mean fluid Temperature (°C)

APPENDIX B

Calculating the uncertainty in the result α (kW/m^{2}K)

for the case of two-phase (vapour-liquid) flow boiling at

a liquid delivery rate of 10 litres/min (i.e. *Re* 32342)

where 95% confidence uncertainty, U_α, is given by: $U_\alpha = (P^2_\alpha + B^2_\alpha)^{1/2}$

Appendix	Description	Numbering
B.O	**Terms and Expressions**	**B.0:1 to B.0:3**
B.1	**Sample calculations for q "= 83.92 kW/m^2** B.1/1: Estimating the Precision limit, P_α B.1/2: Estimating the Bias limit, B_α	**B.1/1:1 to B.1/2**
B.2	**Sample calculations for q "= 195.80 kW/m^2** B.2/1: Estimating the Precision limit, P_α B.2/2: Estimating the Bias limit, B_α	**B.2/1:1 to B.2/2**
B.3	**Sample calculations for q "= 279.72 kW/m^2** B.3/1: Estimating the Precision limit, P_α B.3/2: Estimating the Bias limit, B_α	**B.3/1:1 to B.3/2**
B.4	**Summary table presenting the calculated uncertainty, U_α, for q "= 83.92 → 279.72 kW/m^2**	**B.4**

Appendix B.0

Terms and Expressions for Calcuating the

Uncertainty In Result of Heat Transfer Coefficient, α (kW/m^2.K).

where

95% confidence uncertainty, U_α, is given by: $U_\alpha = (P^2_\alpha + B^2_\alpha)^{1/2}$

Table 1: Recalling equations for determining the result of heat transfer coefficient, α

Description	Symbol	Expression (where applicable)
Heat Transfer Coefficient, kW/m^2.K (investigated)	α	$q" / Tw - Tf^*$
Heat Flux, kW/m^2 (imposed)	$q"$	q / A
Power, kW (imposed)	q	
Heat transfer surface arfea, m^2	A	
Measured wall temperature, °C	Tw	$({}^K\Sigma_{j=1}\, T^*_j) / K$
The total number of thermocouple probes	K	8
Mean local wall temperature, °C measured by probe number j	T^*	$({}^N\Sigma_{i=1}\, T_i) / N$
Individual local wall temperature measurement sampled by probe j, °C	T	
Number of repeated measurements (per second basis) in a sample	N	100
Mean bulk fluid temperature, °C	Tf^*	$(Tf.i + Tf.o) / 2$
Inlet fluid temperature, °C	$Tf.i$	
Outlet fluid temperature, °C	$Tf.o$	
Temperature driving force, °C (or K)	ΔT	$Tw - Tf^*$

Table 2: Related equations for calculating the precision limit of the result, α

Description	Symbol	Expression (where applicable)
95% confidence uncertainty of result α, kW/m^2.K or %	U_α	$(P^2{}_\alpha + B^2{}_\alpha)^{1/2}$
Precision limit of result α, kW/m^2.K or %	P_α	$[(\Theta_{Tw}.P_{Tw})^2 + (\Theta_{Tf*}.P_{Tf*})^2]^{1/2}$
Sensitivity coefficient of measured wall temperature, kW/m^2.K	Θ_{Tw}	$\partial\alpha / \partial T_w = -[q" / (\Delta T)^2]$
Sensitivity coefficient of mean bulk fluid temperature, kW/m^2.K	Θ_{Tf*}	$\partial\alpha / \partial T_w = q" / (\Delta T)^2$
Precision limit of measured wall temperature, °C	P_{Tw}	$[{}^K\Sigma_{j=1} (P^2{}_{T*})_j]^{1/2.}$
Precision error of mean local wall temperature, °C	P_{T*}	$2.S_M$
Sampling error for a set of observations (i.e several random samples) for the estimation of the mean local wall temperature, °C	S_M	$S_T / (N)^{1/2}$
Precision index for a sample (size N) of local wall temperature readings, °C	S_T	$[\{\Sigma(T_i - T^*)^2\} / N - 1]^{1/2}$
Precision limit of bulk fluid temperature, °C	P_{Tf*}	$[P^2{}_{Tf.i} + P^2{}_{Tf.o}]^{1/2}$
Precision error of inlet fluid temperature, °C	$P_{Tf.i}$	-
Precision error of outlet fluid temperature, °C	$P_{Tf.o}$	-

Table 3: Related equations for calculating the bias limit of the result, α

Description	Symbol	Expression (where applicable)
95% confidence uncertainty of result α, kW/m^2.K or %	U_α	$(P^2{}_\alpha + B^2{}_\alpha)^{1/2}$
Bias limit of result α, kW/m^2.K or %	B_α	$[(\Theta_{Tw}.B_{Tw})^2 + (\Theta_{Tf*}.B_{Tf*})^2]^{1/2}$
Sensitivity coefficient of measured wall temperature, kW/m^2.K	Θ_{Tw}	$\partial\alpha / \partial T_w = -[q'' / (\Delta T)^2]$
Sensitivity coefficient of mean bulk fluid temperature, kW/m^2.K	Θ_{Tf*}	$\partial\alpha / \partial T_w = q'' / (\Delta T)^2$
Bias limit of measured wall temperature, °C	B_{Tw}	$[{}^K\Sigma_{j=1} (B^2{}_T)_j]^{1/2.}$
Local wall temperature, point measured by probe number j, °C	T	
Bias error of point measured local wall temperature, °C	B_T	$[B e^2_T + B c^2_T]^{1/2}$
Elemental bias contribution, supplied by probe(s) manufacturer, °C	$B e_T$	0.4
Conceptual bias contribution established by *in-situ* calibration testing	$B c_T$	-
Bias limit of bulk fluid temperature, °C	B_{Tf*}	$[B^2_{Tf.i} + B^2_{Tf.o}]^{1/2}$
Bias error of point measured inlet fluid temperature, °C	$B_{Tf.i}$	$[B e^2_{Tf.i} + B c^2_{Tf.i}]^{1/2}$
Elemental bias contribution to inlet fluid temperature, supplied by probe(s) manufacturer, °C	$B e_{Tf.i}$	0.4
Conceptual bias contribution to inlet fluid temperature, established by calibration testing, °C	$B c_{Tf.i}$	-
Bias error of point measured outlet fluid temperature, °C	$B_{Tf.o}$	$[B e^2_{Tf.o} + B c^2_{Tf.o}]^{1/2}$
Elemental bias contribution to outlet fluid temperature, supplied by probe(s) manufacturer, °C	$B e_{Tf.o}$	0.4
Conceptual bias contribution to outlet fluid temperature, established by calibration testing °C	$B c_{Tf.o}$	-

"Appendix B.1/1: Calculating the Precision limit (i.e. P_α) of the result α, kW/m^2.K"

where $P_\alpha = [(\theta_{Tw}.P_{Tw})^2 + (\theta_{Tf}.P_{Tf})^2]^{1/2}$

Test Conditions: SERIES A - 2 Phase Flow Boiling, Distilled H_2O	
Reynolds Number = 32342	**Subcooled Temperature = 90°C**
Heat Flux (q/A) = 83.916 kW/m^2	**System Pressure ~ Atmospheric**

Estimating precision error (i.e. P_{Tw}) of measured wall temperature T_w

where P_{Tw} is given by: $[^K\Sigma_{j=1}(P^2{}_{T^*})_j]^{1/2}$.

Table A (i): N-numbers 1 to 50 Probes 1 to 6

N measurements, taken on per second basis

N-number	Probe 1		Probe 2		Probe 3		Probe 4		Probe 5		Probe 6	
	T_i (°C)	$(T_i - T^*)^2$ (°C)	T_i (°C)	$(T_i - T^*)^2$ (°C)	T_i (°C)	$(T_i - T^*)^2$ (°C)	T_i (°C)	$(T_i - T^*)^2$ (°C)	T_i (°C)	$(T_i - T^*)^2$ (°C)	T_i (°C)	$(T_i - T^*)^2$ (°C)
1	97.34	0.4855302	98.61	0.058274	101.56	0.148225	103.7	0.0731162	103.76	0.131044	102.64	0.4137062
2	97.19	0.2989902	98.59	0.049018	101.54	0.133225	103.67	0.0577922	103.74	0.116964	102.62	0.3883782
3	97.19	0.2989902	98.59	0.049018	101.54	0.133225	103.67	0.0577922	103.74	0.116964	102.62	0.3883782
4	97.19	0.2989902	98.68	0.09697	101.47	0.087025	103.67	0.0577922	103.67	0.073984	102.57	0.3285582
5	97.19	0.2989902	98.68	0.09697	101.47	0.087025	103.67	0.0577922	103.67	0.073984	102.57	0.3285582
6	97.06	0.1737222	98.68	0.09697	101.43	0.065025	103.54	0.0121882	103.65	0.063504	102.51	0.2633742
7	96.97	0.1067982	98.57	0.040562	101.38	0.042025	103.52	0.0081722	103.63	0.053824	102.46	0.2145542
8	96.97	0.1067982	98.57	0.040562	101.38	0.042025	103.52	0.0081722	103.63	0.053824	102.46	0.2145542
9	96.92	0.0766182	98.55	0.032906	101.38	0.042025	103.5	0.0049562	103.61	0.044944	102.46	0.2145542
10	96.84	0.0387302	98.48	0.01241	101.34	0.027225	103.48	0.0025402	103.54	0.020164	102.37	0.1392782
11	96.84	0.0387302	98.48	0.01241	101.34	0.027225	103.48	0.0025402	103.54	0.020164	102.37	0.1392782
12	96.84	0.0387302	98.46	0.008354	101.32	0.021025	103.48	0.0025402	103.52	0.014884	102.42	0.1790982
13	96.82	0.0312582	98.42	0.002642	101.27	0.009025	103.43	1.6E-07	103.5	0.010404	102.42	0.1790982
14	96.82	0.0312582	98.42	0.002642	101.27	0.009025	103.43	1.6E-07	103.5	0.010404	102.42	0.1790982
15	96.79	0.0215502	98.39	0.000458	101.27	0.009025	103.39	0.0015682	103.37	0.000784	102.48	0.2334822
16	96.66	0.0002822	98.37	1.96E-06	101.27	0.009025	103.39	0.0015682	103.37	0.000784	102.48	0.2334822
17	96.66	0.0002822	98.37	1.96E-06	101.27	0.009025	103.39	0.0015682	103.37	0.000784	102.48	0.2334822
18	96.6	0.0018662	98.35	0.000346	101.32	0.021025	103.34	0.0080282	103.34	0.003364	102.35	0.1247502
19	96.53	0.0128142	98.31	0.003434	101.27	0.009025	103.3	0.0167962	103.34	0.003364	102.33	0.1110222
20	96.53	0.0128142	98.31	0.003434	101.27	0.009025	103.3	0.0167962	103.34	0.003364	102.33	0.1110222
21	96.57	0.0053582	98.31	0.003434	101.27	0.009025	103.3	0.0167962	103.32	0.006084	102.18	0.0335622
22	96.57	0.0053582	98.31	0.003434	101.27	0.009025	103.3	0.0167962	103.32	0.006084	102.18	0.0335622
23	96.51	0.0177422	98.28	0.00785	101.23	0.003025	103.3	0.0167962	103.32	0.006084	102.04	0.0018662
24	96.51	0.0177422	98.28	0.00785	101.23	0.003025	103.23	0.0398402	103.23	0.028224	102	1.024E-05
25	96.51	0.0177422	98.28	0.00785	101.23	0.003025	103.23	0.0398402	103.23	0.028224	102	1.024E-05
26	96.49	0.0234702	98.31	0.003434	101.23	0.003025	103.19	0.0574082	103.19	0.043264	101.98	0.0002822
27	96.44	0.0412902	98.31	0.003434	101.18	2.5E-05	103.12	0.0958522	103.25	0.021904	101.85	0.0215502
28	96.44	0.0412902	98.31	0.003434	101.18	2.5E-05	103.12	0.0958522	103.25	0.021904	101.85	0.0215502
29	96.31	0.1110222	98.31	0.003434	101.03	0.021025	103.12	0.0958522	103.17	0.051984	101.49	0.2568462
30	96.27	0.1392782	98.22	0.022082	100.94	0.055225	103.17	0.0673922	103.06	0.114244	101.29	0.4995662
31	96.27	0.1392782	98.22	0.022082	100.94	0.055225	103.17	0.0673922	103.06	0.114244	101.29	0.4995662
32	96.27	0.1392782	98.15	0.047786	100.85	0.105625	103.21	0.0482242	102.97	0.183184	100.9	1.2029702
33	96.2	0.1964262	98.15	0.047786	100.83	0.119025	103.21	0.0482242	102.97	0.183184	100.88	1.2472422
34	96.2	0.1964262	98.15	0.047786	100.83	0.119025	103.21	0.0482242	102.97	0.183184	100.88	1.2472422
35	96.2	0.1964262	98.2	0.028426	100.83	0.119025	103.21	0.0482242	102.95	0.200704	100.85	1.3151502
36	96.2	0.1964262	98.2	0.028426	100.83	0.119025	103.23	0.0398402	102.9	0.248004	100.85	1.3151502
37	96.2	0.1964262	98.2	0.028426	100.83	0.119025	103.23	0.0398402	102.9	0.248004	100.85	1.3151502
38	96.16	0.2334822	98.11	0.066874	100.77	0.164025	103.19	0.0574082	102.84	0.311364	100.77	1.5050382
39	96.18	0.2145542	98.13	0.05693	100.79	0.148225	103.14	0.0838682	102.86	0.289444	100.79	1.4563662
40	96.18	0.2145542	98.13	0.05693	100.79	0.148225	103.14	0.0838682	102.86	0.289444	100.79	1.4563662
41	96.18	0.2145542	98.2	0.028426	100.79	0.148225	103.08	0.1222202	102.46	0.879844	100.7	1.6816902
42	96.38	0.0692742	98.26	0.011794	100.9	0.075625	103.14	0.0838682	102.48	0.842724	100.66	1.7870342
43	96.38	0.0692742	98.26	0.011794	100.9	0.075625	103.14	0.0838682	102.48	0.842724	100.66	1.7870342
44	96.35	0.0859662	98.24	0.016538	100.88	0.087025	103.28	0.0223802	102.81	0.345744	100.7	1.6816902
45	96.44	0.0412902	98.26	0.011794	100.9	0.075625	103.3	0.0167962	102.86	0.289444	100.88	1.2472422
46	96.44	0.0412902	98.26	0.011794	100.9	0.075625	103.3	0.0167962	102.86	0.289444	100.88	1.2472422
47	96.46	0.0335622	98.35	0.000346	101.01	0.027225	103.37	0.0035522	103.1	0.088804	101.01	0.9737742
48	96.6	0.0018662	98.35	0.000346	101.12	0.003025	103.54	0.0121882	103.23	0.028224	101.58	0.1737222
49	96.6	0.0018662	98.35	0.000346	101.12	0.003025	103.54	0.0121882	103.23	0.028224	101.58	0.1737222
50	96.71	0.0044622	98.48	0.01241	101.12	0.003025	103.65	0.0485762	103.37	0.000784	101.91	0.0075342

Test Conditions: SERIES A - 2 Phase Flow Boiling, Distilled H_2O	
Reynolds Number = 32342	**Subcooled Temperature = 90°C**
Heat Flux (q/A) = 83.916 kW/m²	**System Pressure ~ Atmospheric**

Estimating precision error (i.e. P_{Tw}) of measured wall temperature T_w ...continued

where P_{Tw} is given by: $[^{K}\Sigma_{j=1}(P^{2}_{T^*})_j]^{1/2}$.

K is the total number of thermocouple probes = 8

P_{T^*} is the precision error of the mean local wall temperature.

T^* is the mean local wall temperature, measured by probe number j.

Table A (i.i): *N*- numbers 51 to 100 Probes 1 to 6 $N = 100$

N - number	Probe 1		Probe 2		Probe 3		Probe 4		Probe 5		Probe 6	
	T_i (°C)	$(T_i - T^*)^2$ (°C)	T_i (°C)	$(T_i - T^*)^2$ (°C)	T_i (°C)	$(T_i - T^*)^2$ (°C)	T_i (°C)	$(T_i - T^*)^2$ (°C)	T_i (°C)	$(T_i - T^*)^2$ (°C)	T_i (°C)	$(T_i - T^*)^2$ (°C)
51	96.86	0.0470022	98.53	0.02605	101.27	0.009025	103.7	0.0731162	103.48	0.006724	102.33	0.1110222
52	96.86	0.0470022	98.53	0.02605	101.27	0.009025	103.7	0.0731162	103.48	0.006724	102.33	0.1110222
53	96.95	0.0941262	98.59	0.049018	101.32	0.021025	103.85	0.1767362	103.63	0.053824	102.57	0.3285582
54	96.95	0.0941262	98.59	0.049018	101.32	0.021025	103.85	0.1767362	103.63	0.053824	102.57	0.3285582
55	97.1	0.2086662	98.7	0.109826	101.4	0.050625	103.92	0.2404922	103.72	0.103684	102.57	0.3285582
56	97.12	0.2273382	98.72	0.123482	101.51	0.112225	103.92	0.2404922	103.74	0.116964	102.77	0.5978382
57	97.12	0.2273382	98.72	0.123482	101.51	0.112225	103.92	0.2404922	103.74	0.116964	102.77	0.5978382
58	97.14	0.2468102	98.75	0.145466	101.54	0.133225	103.92	0.2404922	103.76	0.131044	102.77	0.5978382
59	97.25	0.3682062	98.75	0.145466	101.54	0.133225	103.92	0.2404922	103.81	0.169744	102.77	0.5978382
60	97.25	0.3682062	98.75	0.145466	101.54	0.133225	103.92	0.2404922	103.81	0.169744	102.77	0.5978382
61	97.28	0.4055142	98.7	0.109826	101.56	0.148225	103.87	0.1939522	103.89	0.242064	102.81	0.6612942
62	97.23	0.3443342	98.64	0.073658	101.58	0.164025	103.87	0.1939522	103.89	0.242064	102.81	0.6612942
63	97.23	0.3443342	98.64	0.073658	101.58	0.164025	103.87	0.1939522	103.89	0.242064	102.81	0.6612942
64	97.19	0.2989902	98.61	0.058274	101.58	0.164025	103.76	0.1091642	103.89	0.242064	102.79	0.6291662
65	97.12	0.2273382	98.61	0.058274	101.58	0.164025	103.85	0.1767362	103.89	0.242064	102.77	0.5978382
66	97.12	0.2273382	98.61	0.058274	101.58	0.164025	103.85	0.1767362	103.89	0.242064	102.77	0.5978382
67	96.99	0.1202702	98.53	0.02605	101.56	0.148225	103.74	0.0963482	103.89	0.242064	102.77	0.5978382
68	96.92	0.0766182	98.53	0.02605	101.49	0.099225	103.7	0.0731162	103.85	0.204304	102.73	0.5375822
69	96.92	0.0766182	98.53	0.02605	101.49	0.099225	103.7	0.0731162	103.85	0.204304	102.73	0.5375822
70	96.92	0.0766182	98.5	0.017266	101.4	0.050625	103.63	0.0401602	103.81	0.169744	102.62	0.3883782
71	96.9	0.0659462	98.48	0.01241	101.38	0.042025	103.63	0.0401602	103.81	0.169744	102.62	0.3883782
72	96.9	0.0659462	98.48	0.01241	101.38	0.042025	103.63	0.0401602	103.81	0.169744	102.62	0.3883782
73	96.86	0.0470022	98.48	0.01241	101.38	0.042025	103.63	0.0401602	103.81	0.169744	102.62	0.3883782
74	96.68	0.0013542	98.39	0.000458	101.32	0.021025	103.59	0.0257282	103.81	0.169744	102.62	0.3883782
75	96.68	0.0013542	98.39	0.000458	101.32	0.021025	103.59	0.0257282	103.81	0.169744	102.62	0.3883782
76	96.68	0.0013542	98.35	0.000346	101.32	0.021025	103.5	0.0049562	103.63	0.053824	102.73	0.5375822
77	96.73	0.0075342	98.33	0.00149	101.25	0.005625	103.45	0.0004162	103.56	0.026244	102.7	0.4944902
78	96.73	0.0075342	98.33	0.00149	101.25	0.005625	103.45	0.0004162	103.56	0.026244	102.7	0.4944902
79	96.73	0.0075342	98.28	0.00785	101.16	0.000225	103.43	1.6E-07	103.56	0.026244	102.62	0.3883782
80	96.73	0.0075342	98.28	0.00785	101.16	0.000225	103.43	1.6E-07	103.56	0.026244	102.62	0.3883782
81	96.57	0.0053582	98.2	0.028426	101.1	0.005625	103.37	0.0035522	103.54	0.020164	102.46	0.2145542
82	96.51	0.0177422	98.2	0.028426	101.1	0.005625	103.34	0.0080282	103.52	0.014884	102.29	0.0859662
83	96.51	0.0177422	98.2	0.028426	101.1	0.005625	103.34	0.0080282	103.52	0.014884	102.29	0.0859662
84	96.44	0.0412902	98.22	0.022082	101.1	0.005625	103.34	0.0080282	103.52	0.014884	102.18	0.0335622
85	96.42	0.0498182	98.24	0.016538	100.96	0.046225	103.37	0.0035522	103.32	0.006084	102	1.024E-05
86	96.42	0.0498182	98.24	0.016538	100.96	0.046225	103.37	0.0035522	103.32	0.006084	102	1.024E-05
87	96.4	0.0591462	98.22	0.022082	100.94	0.055225	103.37	0.0035522	103.23	0.028224	101.65	0.1202702
88	96.31	0.1110222	98.24	0.016538	100.94	0.055225	103.37	0.0035522	103.23	0.028224	101.54	0.2086662
89	96.31	0.1110222	98.24	0.016538	100.94	0.055225	103.37	0.0035522	103.23	0.028224	101.54	0.2086662
90	96.31	0.1110222	98.22	0.022082	100.83	0.119025	103.19	0.0574082	103.25	0.021904	101.47	0.2775182
91	96.29	0.1247502	98.22	0.022082	100.83	0.119025	103.1	0.1086362	103.25	0.021904	101.34	0.4313862
92	96.29	0.1247502	98.22	0.022082	100.83	0.119025	103.1	0.1086362	103.25	0.021904	101.34	0.4313862
93	96.25	0.1546062	98.07	0.089162	100.83	0.119025	103.08	0.1222202	103.28	0.013924	101.32	0.4580582
94	96.14	0.2532102	98.07	0.089162	100.83	0.119025	103.08	0.1222202	103.28	0.013924	101.27	0.5282382
95	96.14	0.2532102	98.07	0.089162	100.83	0.119025	103.08	0.1222202	103.28	0.013924	101.27	0.5282382
96	96.14	0.2532102	98.07	0.089162	100.79	0.148225	103.08	0.1222202	103.28	0.013924	101.23	0.5879822
97	96.14	0.2532102	98.07	0.089162	100.79	0.148225	103.08	0.1222202	103.28	0.013924	101.23	0.5879822
98	96.14	0.2532102	98.04	0.107978	100.74	0.189225	103.01	0.1760642	103.19	0.043264	101.23	0.5879822
99	96.14	0.2532102	98.02	0.121522	100.72	0.207025	102.95	0.2300162	103.12	0.077284	101.05	0.8964302
100	96.14	0.2532102	98.02	0.121522	100.72	0.207025	102.95	0.2300162	103.12	0.077284	101.05	0.8964302
SUM =	9664.32	12.371176	9836.86	3.797204	10117.5	7.0323	10342.96	6.936584	10339.8	11.7366	10199.68	50.288976
Mean T* (°C) =	96.6432		98.3686		101.175		103.4296		103.398		101.9968	

Test Conditions: SERIES A - 2 Phase Flow Boiling, Distilled H_2O	
Reynolds Number = 32342	**Subcooled Temperature = 90°C**
Heat Flux (q/A) = 83.916 kW/m^2	**System Pressure ~ Atmospheric**

Estimating precision error (i.e. P_{Tw}) of measured wall temperature T_w ...continued

where P_{Tw} is given by: $[^K\Sigma_{j=1}(P^2{}_{T^*})_j]^{1/2}$ K is the total number of thermocouple probes = 8

T* is the mean local wall temperature, measured by probe number j.

Table A (i.i.i): N-numbers 1 to 50 Probes 7 and 8

N measurements, taken on per second basis

N-number	Probe 7		Probe 8	
	T_i (°C)	$(T_i - T^*)^2$ (°C)	T_i (°C)	$(T_i - T^*)^2$ (°C)
1	95.02	0.3521236	94.21	0.833569
2	95.02	0.3521236	94.21	0.833569
3	95.02	0.3521236	94.21	0.833569
4	95.02	0.3521236	94.1	0.644809
5	95.02	0.3521236	94.1	0.644809
6	93.39	1.0745396	92.52	0.603729
7	94.93	0.2534116	93.94	0.413449
8	94.93	0.2534116	93.94	0.413449
9	94.86	0.1878356	93.9	0.363609
10	94.86	0.1878356	93.9	0.363609
11	94.86	0.1878356	93.9	0.363609
12	94.8	0.1394276	93.7	0.162409
13	93.26	1.3609556	92.25	1.096209
14	93.26	1.3609556	92.25	1.096209
15	93.28	1.3146916	92.28	1.034289
16	94.73	0.0920516	93.57	0.074529
17	94.73	0.0920516	93.57	0.074529
18	94.73	0.0920516	93.57	0.074529
19	94.73	0.0920516	93.57	0.074529
20	94.71	0.0803156	93.55	0.064009
21	94.71	0.0803156	93.42	0.015129
22	94.71	0.0803156	93.42	0.015129
23	94.71	0.0803156	93.39	0.008649
24	94.71	0.0803156	93.39	0.008649
25	94.71	0.0803156	93.39	0.008649
26	94.71	0.0803156	93.37	0.005329
27	94.69	0.0693796	93.26	0.001369
28	94.69	0.0693796	93.26	0.001369
29	94.69	0.0693796	93.26	0.001369
30	94.67	0.0592436	93.22	0.005929
31	94.67	0.0592436	93.22	0.005929
32	94.64	0.0455396	93.22	0.005929
33	94.64	0.0455396	93.22	0.005929
34	94.64	0.0455396	93.22	0.005929
35	94.62	0.0374036	93.2	0.009409
36	94.6	0.0300676	93.13	0.027889
37	94.6	0.0300676	93.13	0.027889
38	94.6	0.0300676	93.13	0.027889
39	94.6	0.0300676	93.13	0.027889
40	94.6	0.0300676	93.13	0.027889
41	94.6	0.0300676	93.15	0.021609
42	94.6	0.0300676	93.15	0.021609
43	94.69	0.0693796	93.33	0.001089
44	94.71	0.0803156	93.44	0.020449
45	94.71	0.0803156	93.44	0.020449
46	94.69	0.0693796	93.44	0.020449
47	93.31	1.2467956	92.36	0.877969
48	93.31	1.2467956	92.36	0.877969
49	93.31	1.2467956	92.36	0.877969
50	93.33	1.2025316	92.56	0.543169

Test Conditions: SERIES A - 2 Phase Flow Boiling, Distilled H_2O	
Reynolds Number = 32342	**Subcooled Temperature = 90°C**
Heat Flux (q/A) = 83.916 kW/m^2	**System Pressure ~ Atmospheric**

Estimating precision error (i.e. P_{Tw}) of measured wall temperature T_w ...continued

where P_{Tw} is given by: $[^K\Sigma_{j=1}(P^2{}_{T^*})_j]^{1/2.}$ K is the total number of thermocouple probes = 8

T* is the mean local wall temperature, measured by probe number j.

Table A (i.v): N-numbers 51 to 100 Probes 7 and 8 N = 100

N-number	Probe 7		Probe 8	
	T_i (°C)	$(T_i - T^*)^2$ (°C)	T_i (°C)	$(T_i - T^*)^2$ (°C)
51	93.33	1.2025316	92.56	0.543169
52	93.35	1.1590676	92.65	0.418609
53	93.46	0.9343156	92.71	0.344569
54	93.46	0.9343156	92.71	0.344569
55	93.46	0.9343156	92.71	0.344569
56	93.48	0.8960516	92.85	0.199809
57	93.48	0.8960516	92.85	0.199809
58	95	0.3287876	94.27	0.946729
59	93.48	0.8960516	92.85	0.199809
60	93.48	0.8960516	92.85	0.199809
61	93.48	0.8960516	92.8	0.247009
62	93.48	0.8960516	92.8	0.247009
63	93.5	0.8585876	92.82	0.227529
64	94.93	0.2534116	94.05	0.567009
65	94.93	0.2534116	94.05	0.567009
66	94.97	0.2952836	94.05	0.567009
67	94.91	0.2336756	94.03	0.537289
68	94.91	0.2336756	94.03	0.537289
69	93.37	1.1164036	92.45	0.717409
70	93.39	1.0745396	92.47	0.683929
71	93.39	1.0745396	92.47	0.683929
72	94.82	0.1547636	93.81	0.263169
73	94.84	0.1708996	93.83	0.284089
74	94.84	0.1708996	93.83	0.284089
75	94.75	0.1045876	93.77	0.223729
76	94.75	0.1045876	93.61	0.097969
77	94.75	0.1045876	93.61	0.097969
78	94.71	0.0803156	93.53	0.054289
79	94.75	0.1045876	93.55	0.064009
80	94.75	0.1045876	93.55	0.064009
81	94.73	0.0920516	93.53	0.054289
82	94.73	0.0920516	93.5	0.041209
83	94.73	0.0920516	93.5	0.041209
84	94.71	0.0803156	93.46	0.026569
85	94.67	0.0592436	93.35	0.002809
86	94.67	0.0592436	93.35	0.002809
87	94.67	0.0592436	93.28	0.000289
88	94.67	0.0592436	93.28	0.000289
89	94.67	0.0592436	93.28	0.000289
90	94.67	0.0592436	93.26	0.001369
91	94.67	0.0592436	93.26	0.001369
92	94.58	0.0235316	93.26	0.001369
93	94.58	0.0235316	93.22	0.005929
94	94.58	0.0235316	93.22	0.005929
95	94.58	0.0235316	93.22	0.005929
96	94.58	0.0235316	93.17	0.016129
97	94.58	0.0235316	93.17	0.016129
98	94.58	0.0235316	93.11	0.034969
99	94.58	0.0235316	93.11	0.034969
100	94.6	0.0300676	93.11	0.034969
SUM =	9442.66	33.317844	9329.7	24.6759
Mean T* (°C) =	94.4266		93.297	

Test Conditions: SERIES A - 2 Phase Flow Boiling, Distilled H_2O	
Reynolds Number = 32342	**Subcooled Temperature = 90°C**
Heat Flux (q/A) = 83.916 kW/m^2	**System Pressure ~ Atmospheric**

Estimating precision error (i.e. P_{Tw}) of measured wall temperature T_w ...continued

where P_{Tw} is given by: $[{}^{K}\Sigma_{j=1}(P^2{}_{T^*})_j]^{1/2}$ K is the total number of thermocouple probes = 8

T* is the mean local wall temperature, measured by probe number j.

Table B

Probe No. j	S_T, (°C) $[\{\Sigma(T_j-T^*)^2\}/N-1]^{1/2}$	S_M, (°C) $S_T/(N)^{1/2}$	P_{T^*}, (°C) $2.S_M$	$P^2{}_{T^*}$, (°C) $(2.S_M)^2$	P_{Tw}, (°C) $[{}^{K}\Sigma_{j=1}(P_{T^*})_j^2]^{1/2}$
1	1.24334997	0.124334997	0.248669994	0.061836766	
2	0.381633361	0.038163336	0.076326672	0.005825761	
3	0.706772743	0.070677274	0.141354549	0.019981108	
4	0.697152923	0.069715292	0.139430585	0.019440888	
5	1.179572682	0.117957268	0.235914536	0.055655669	
6	5.054232257	0.505423226	1.010846451	1.021810548	1.370798168
7	3.348569314	0.334856931	0.669713863	0.448516658	
8	2.480021263	0.248002126	0.496004253	0.246020219	

N = 100

"Appendix B.1/2: Calculating the Bias limit (i.e. B_α) of the result α, kW/m^2.K"

where $B_\alpha = [\,(\theta_{Tw}.B_{Tw})^2 + (\theta_{Tf\bullet}.B_{Tf\bullet})^2\,]^{1/2}$

Test Conditions: SERIES A - 2 Phase Flow Boiling, Distilled H_2O	
Reynolds Number = 32342	**Subcooled Temperature = 90°C**
Heat Flux (q/A) = 83.916 kW/m^2	**System Pressure ~ Atmospheric**

Estimating bias error (i.e. B_{Tw}) of measured wall temperature T_w

where B_{Tw} is given by: $[\,^K\Sigma_{j=1}(B^2_T)_j\,]^{1/2}$

K is the total number of thermocouple probes = 8

T is the local wall temperature, point measured by probe number j.

for each probe the bias error of point measured T B_T, is given by: $[B e^2_T + B c^2_T]^{1/2}$

$B e_T$ is the elemental bias contibution = 0.4°C

$B e_C$ is the conceptual bias contribution established via calibration testing

Probe No. j	$B e_T$ (°C)	$B e^2_T$ (°C)	$B c_T$ (°C)	$B c^2_T$ (°C)	B_T (°C)	B^2_T (°C)	B_{Tw} (°C)
1	0.4	0.16	0	0	0.4	0.16	
2	0.4	0.16	0	0	0.4	0.16	
3	0.4	0.16	0	0	0.4	0.16	
4	0.4	0.16	0	0	0.4	0.16	
5	0.4	0.16	0	0	0.4	0.16	
6	0.4	0.16	0	0	0.4	0.16	1.1313708
7	0.4	0.16	0	0	0.4	0.16	
8	0.4	0.16	0	0	0.4	0.16	

Estimating bias error (i.e. $B_{Tf\bullet}$) of mean fluid temperature $T_{f\bullet}$

where $B_{Tf\bullet}$ is given by: $[B^2_{Tf.i} + B^2_{Tf.o}]^{1/2}$

$B_{Tf.i}$ is the fixed error of point measured inlet fluid temperature Tf.i

$B_{Tf.o}$ is the fixed error of point measured outlet fluid temperature Tf.o

further, $B_{Tf.i}$ is given by: $[B e^2_{Tf.i} + B c^2_{Tf.i}]^{1/2}$

$B_{Tf.o}$ is given by: $[B e^2_{Tf.o} + B c^2_{Tf.o}]^{1/2}$

$B e_{Tf.i}$ and $B e_{Tf.o}$ are elemental bias contributions = 0.4°C respectively

$B c_{Tf.i}$ and $B c_{Tf.o}$ are conceptual bias contributions

Probe A - inlet fluid temperature						Probe B - outlet fluid temperature					
$B e_{Tf.i}$ (°C)	$B e^2_{Tf.i}$ (°C)	$B c_{Tf.i}$ (°C)	$B c^2_{Tf.i}$ (°C)	$B_{Tf.i}$ (°C)	$B^2_{Tf.i}$ (°C)	$B e_{Tf.o}$ (°C)	$B e^2_{Tf.o}$ (°C)	$B c_{Tf.o}$ (°C)	$B c^2_{Tf.o}$ (°C)	$B_{Tf.o}$ (°C)	$B^2_{Tf.o}$ (°C)
0.4	0.16	0	0	0.4	0.16	0.4	0.16	0	0	0.4	0.16

$B_{Tf\bullet}$ - bias error of bulk fluid temperature, °C = 0.5656854

Appendix B.2

"Appendix B.2/1: Calculating the Precision limit (i.e. P_α) of the result α, kW/m^2.K"

where $P_\alpha = [(\theta_{Tw}.P_{Tw})^2 + (\theta_{Tf^*}.P_{Tf^*})^2]^{1/2}$

Test Conditions: SERIES A - 2 Phase Flow Boiling, Distilled H_2O	
Reynolds Number = 32342	**Subcooled Temperature = 90°C**
Heat Flux (q/A) = 195.80 kW/m^2	**System Pressure ~ Atmospheric**

Estimating precision error (i.e. P_{Tw}) of measured wall temperature T_w

where P_{Tw} is given by: $[^K\Sigma_{j=1}(P^2_{T^*})_j]^{1/2}$

Table A (i): N-numbers 1 to 50 Probes 1 to 6 — N measurements, taken on per second basis

N-number	Probe 1		Probe 2		Probe 3		Probe 4		Probe 5		Probe 6	
	T_i (°C)	$(T_i - T^*)^2$ (°C)	T_i (°C)	$(T_i - T^*)^2$ (°C)	T_i (°C)	$(T_i - T^*)^2$ (°C)	T_i (°C)	$(T_i - T^*)^2$ (°C)	T_i (°C)	$(T_i - T^*)^2$ (°C)	T_i (°C)	$(T_i - T^*)^2$ (°C)
1	97.28	0.052441	99.05	0.0170303	106.18	0.009293	109.14	9.409E-05	108.14	0.0425597	107.64	0.0258566
2	97.25	0.067081	99.03	0.0122103	106.18	0.009293	109.14	9.409E-05	108.1	0.0606637	107.64	0.0258566
3	97.28	0.052441	98.96	0.0016403	106.18	0.009293	109.05	0.0064481	108.14	0.0425597	107.66	0.0198246
4	97.28	0.052441	98.96	0.0016403	106.18	0.009293	109.05	0.0064481	108.14	0.0425597	107.66	0.0198246
5	97.43	0.006241	98.85	0.0048302	106.23	0.002153	108.98	0.0225901	108.17	0.0310817	107.7	0.0101606
6	97.43	0.006241	98.85	0.0048302	106.23	0.002153	108.98	0.0225901	108.17	0.0310817	107.7	0.0101606
7	97.58	0.005041	98.83	0.0080102	106.25	0.000697	109.03	0.0100601	108.17	0.0310817	107.7	0.0101606
8	97.58	0.005041	98.83	0.0080102	106.25	0.000697	109.03	0.0100601	108.17	0.0310817	107.7	0.0101606
9	97.58	0.005041	98.94	0.0004203	106.25	0.000697	109.03	0.0100601	108.21	0.0185777	107.66	0.0198246
10	97.58	0.005041	98.94	0.0004203	106.25	0.000697	109.03	0.0100601	108.21	0.0185777	107.66	0.0198246
11	97.58	0.005041	98.94	0.0004203	106.29	0.000185	109.05	0.0064481	108.23	0.0135257	107.64	0.0258566
12	97.65	0.019881	98.94	0.0004203	106.32	0.001901	109.05	0.0064481	108.28	0.0043957	107.64	0.0258566
13	97.65	0.019881	98.94	0.0004203	106.32	0.001901	109.05	0.0064481	108.28	0.0043957	107.64	0.0258566
14	97.76	0.063001	99.01	0.0081903	106.32	0.001901	109.07	0.0036361	108.32	0.0006917	107.75	0.0025806
15	97.76	0.063001	99.01	0.0081903	106.32	0.001901	109.07	0.0036361	108.32	0.0006917	107.75	0.0025806
16	97.78	0.073441	99.05	0.0170303	106.32	0.001901	109.11	0.0004121	108.45	0.0107537	107.77	0.0009486
17	97.8	0.084681	99.07	0.0226503	106.32	0.001901	109.11	0.0004121	108.5	0.0236237	107.75	0.0025806
18	97.8	0.084681	99.07	0.0226503	106.32	0.001901	109.11	0.0004121	108.5	0.0236237	107.75	0.0025806
19	97.8	0.084681	99.07	0.0226503	106.32	0.001901	109.16	0.0008821	108.52	0.0301717	107.77	0.0009486
20	97.69	0.032761	99.07	0.0226503	106.29	0.000185	109.16	0.0008821	108.52	0.0301717	107.73	0.0050126
21	97.69	0.032761	99.07	0.0226503	106.29	0.000185	109.16	0.0008821	108.52	0.0301717	107.73	0.0050126
22	97.69	0.032761	99.03	0.0122103	106.29	0.000185	109.16	0.0008821	108.52	0.0301717	107.79	0.0001166
23	97.78	0.073441	99.05	0.0170303	106.29	0.000185	109.18	0.0024701	108.52	0.0301717	107.75	0.0025806
24	97.78	0.073441	99.05	0.0170303	106.29	0.000185	109.18	0.0024701	108.52	0.0301717	107.75	0.0025806
25	97.78	0.073441	99.05	0.0170303	106.29	0.000185	109.25	0.0143281	108.59	0.0593897	107.79	0.0001166
26	97.8	0.084681	99.07	0.0226503	106.29	0.000185	109.27	0.0195161	108.59	0.0593897	107.77	0.0009486
27	97.8	0.084681	99.07	0.0226503	106.29	0.000185	109.27	0.0195161	108.59	0.0593897	107.77	0.0009486
28	97.85	0.116281	99.14	0.0486203	106.51	0.054569	109.27	0.0195161	108.61	0.0695377	107.77	0.0009486
29	97.87	0.130321	99.14	0.0486203	106.51	0.054569	109.22	0.0080461	108.54	0.0375197	107.77	0.0009486
30	97.87	0.130321	99.14	0.0486203	106.51	0.054569	109.22	0.0080461	108.54	0.0375197	107.77	0.0009486
31	97.87	0.130321	99.14	0.0486203	106.4	0.015277	109.22	0.0080461	108.52	0.0301717	107.73	0.0050126
32	97.87	0.130321	99.16	0.0578403	106.38	0.010733	109.16	0.0008821	108.43	0.0070057	107.73	0.0050126
33	97.87	0.130321	99.16	0.0578403	106.38	0.010733	109.16	0.0008821	108.43	0.0070057	107.73	0.0050126
34	97.87	0.130321	99.16	0.0578403	106.38	0.010733	109.16	0.0008821	108.43	0.0070057	107.75	0.0025806
35	97.78	0.073441	99.1	0.0325803	106.43	0.023593	109.16	0.0008821	108.39	0.0019097	107.79	0.0001166
36	97.78	0.073441	99.1	0.0325803	106.43	0.023593	109.16	0.0008821	108.39	0.0019097	107.79	0.0001166
37	97.78	0.073441	99.03	0.0122103	106.43	0.023593	109.14	9.409E-05	108.39	0.0019097	107.75	0.0025806
38	97.78	0.073441	99.03	0.0122103	106.43	0.023593	109.14	9.409E-05	108.39	0.0019097	107.75	0.0025806
39	97.71	0.040401	98.99	0.0049703	106.4	0.015277	109.14	9.409E-05	108.39	0.0019097	107.73	0.0050126
40	97.71	0.040401	98.99	0.0049703	106.4	0.015277	109.09	0.0016241	108.37	0.0005617	107.73	0.0050126
41	97.71	0.040401	98.99	0.0049703	106.4	0.015277	109.09	0.0016241	108.37	0.0005617	107.73	0.0050126
42	97.74	0.053361	98.99	0.0049703	106.4	0.015277	109.07	0.0036361	108.37	0.0005617	107.77	0.0009486
43	97.71	0.040401	98.92	2.5E-07	106.34	0.004045	109.05	0.0064481	108.28	0.0043957	107.75	0.0025806
44	97.71	0.040401	98.92	2.5E-07	106.34	0.004045	109.05	0.0064481	108.28	0.0043957	107.75	0.0025806
45	97.63	0.014641	98.92	2.5E-07	106.34	0.004045	109.05	0.0064481	108.28	0.0043957	107.68	0.0145926
46	97.5	8.1E-05	98.92	2.5E-07	106.29	0.000185	109.11	0.0004121	108.32	0.0006917	107.68	0.0145926
47	97.5	8.1E-05	98.92	2.5E-07	106.29	0.000185	109.11	0.0004121	108.32	0.0006917	107.68	0.0145926
48	97.5	8.1E-05	98.99	0.0049703	106.18	0.009293	109.11	0.0004121	108.37	0.0005617	107.77	0.0009486
49	97.45	0.003481	98.99	0.0049703	106.18	0.009293	109.07	0.0036361	108.37	0.0005617	107.77	0.0009486
50	97.45	0.003481	98.99	0.0049703	106.18	0.009293	109.07	0.0036361	108.37	0.0005617	107.77	0.0009486

Test Conditions:	
SERIES A - 2 Phase Flow Boiling, Distilled H_2O	
Reynolds Number = 32342	**Subcooled Temperature = 90°C**
Heat Flux (q/A) = 195.80 kW/m^2	**System Pressure ~ Atmospheric**

Estimating precision error (i.e. P_{Tw}) of measured wall temperature T_w

where P_{Tw} is given by: $[^K\Sigma_{j=1}(P^2{}_{T^*})_j]^{1/2}$.

K is the total number of thermocouple probes = 8

P_{T^*} is the precision error of the mean local wall temperature.

T^* is the mean local wall temperature, measured by probe number j.

Table A (i.i): *N*- numbers 51 to 100 Probes 1 to 6 N = 100

N -	Probe 1		Probe 2		Probe 3		Probe 4		Probe 5		Probe 6	
number	T_i (°C)	$(T_i - T^*)^2$ (°C)	T_i (°C)	$(T_i - T^*)^2$ (°C)	T_i (°C)	$(T_i - T^*)^2$ (°C)	T_i (°C)	$(T_i - T^*)^2$ (°C)	T_i (°C)	$(T_i - T^*)^2$ (°C)	T_i (°C)	$(T_i - T^*)^2$ (°C)
51	97.39	0.014161	98.94	0.0004203	106.21	0.004409	109.07	0.0036361	108.39	0.0019097	107.79	0.0001166
52	97.39	0.014161	98.92	2.5E-07	106.21	0.004409	108.98	0.0225901	108.3	0.0021437	107.73	0.0050126
53	97.39	0.014161	98.92	2.5E-07	106.21	0.004409	108.98	0.0225901	108.3	0.0021437	107.73	0.0050126
54	97.39	0.014161	98.94	0.0004203	106.21	0.004409	109.11	0.0004121	108.3	0.0021437	107.77	0.0009486
55	97.39	0.014161	98.94	0.0004203	106.21	0.004409	109.11	0.0004121	108.3	0.0021437	107.77	0.0009486
56	97.39	0.014161	98.92	2.5E-07	106.16	0.013549	109.03	0.0100601	108.25	0.0092737	107.77	0.0009486
57	97.39	0.014161	98.96	0.0016403	106.21	0.004409	109.03	0.0100601	108.25	0.0092737	107.77	0.0009486
58	97.39	0.014161	98.96	0.0016403	106.21	0.004409	109.03	0.0100601	108.25	0.0092737	107.77	0.0009486
59	97.34	0.028561	98.92	2.5E-07	106.16	0.013549	109.03	0.0100601	108.25	0.0092737	107.77	0.0009486
60	97.36	0.022201	98.94	0.0004203	106.18	0.009293	109.05	0.0064481	108.28	0.0043957	107.79	0.0001166
61	97.36	0.022201	98.94	0.0004203	106.18	0.009293	109.05	0.0064481	108.28	0.0043957	107.79	0.0001166
62	97.36	0.022201	98.92	2.5E-07	106.18	0.009293	109.05	0.0064481	108.28	0.0043957	107.79	0.0001166
63	97.36	0.022201	98.9	0.0003802	106.18	0.009293	109.03	0.0100601	108.28	0.0043957	107.77	0.0009486
64	97.36	0.022201	98.9	0.0003802	106.18	0.009293	109.03	0.0100601	108.28	0.0043957	107.77	0.0009486
65	97.32	0.035721	98.88	0.0015602	106.21	0.004409	109.03	0.0100601	108.28	0.0043957	107.77	0.0009486
66	97.23	0.077841	98.68	0.0573602	106.18	0.009293	109.07	0.0036361	108.23	0.0135257	107.81	8.464E-05
67	97.23	0.077841	98.68	0.0573602	106.18	0.009293	109.07	0.0036361	108.23	0.0135257	107.81	8.464E-05
68	97.23	0.077841	98.68	0.0573602	106.18	0.009293	109.09	0.0016241	108.23	0.0135257	107.95	0.0222606
69	97.23	0.077841	98.7	0.0481802	106.18	0.009293	109.11	0.0004121	108.23	0.0135257	107.99	0.0357966
70	97.23	0.077841	98.7	0.0481802	106.18	0.009293	109.11	0.0004121	108.23	0.0135257	107.99	0.0357966
71	97.23	0.077841	98.72	0.0398002	106.21	0.004409	109.14	9.409E-05	108.25	0.0092737	108.01	0.0437646
72	97.32	0.035721	98.75	0.0287302	106.29	0.000185	109.14	9.409E-05	108.32	0.0006917	107.99	0.0357966
73	97.32	0.035721	98.75	0.0287302	106.29	0.000185	109.14	9.409E-05	108.32	0.0006917	107.99	0.0357966
74	97.25	0.067081	98.75	0.0287302	106.32	0.001901	109.18	0.0024701	108.32	0.0006917	107.95	0.0222606
75	97.25	0.067081	98.75	0.0287302	106.32	0.001901	109.18	0.0024701	108.32	0.0006917	107.95	0.0222606
76	97.32	0.035721	98.79	0.0167702	106.29	0.000185	109.2	0.0048581	108.32	0.0006917	107.92	0.0142086
77	97.32	0.035721	98.72	0.0398002	106.18	0.009293	109.2	0.0048581	108.32	0.0006917	107.88	0.0062726
78	97.32	0.035721	98.72	0.0398002	106.18	0.009293	109.2	0.0048581	108.32	0.0006917	107.88	0.0062726
79	97.32	0.035721	98.75	0.0287302	106.18	0.009293	109.11	0.0004121	108.32	0.0006917	107.88	0.0062726
80	97.28	0.052441	98.75	0.0287302	106.18	0.009293	109.11	0.0004121	108.34	3.969E-05	107.88	0.0062726
81	97.28	0.052441	98.75	0.0287302	106.18	0.009293	109.11	0.0004121	108.34	3.969E-05	107.88	0.0062726
82	97.28	0.052441	98.75	0.0287302	106.18	0.009293	109.11	0.0004121	108.28	0.0043957	107.81	8.464E-05
83	97.32	0.035721	98.75	0.0287302	106.14	0.018605	109.16	0.0008821	108.25	0.0092737	107.75	0.0025806
84	97.32	0.035721	98.75	0.0287302	106.14	0.018605	109.16	0.0008821	108.25	0.0092737	107.75	0.0025806
85	97.34	0.028561	98.81	0.0119902	106.14	0.018605	109.16	0.0008821	108.25	0.0092737	107.75	0.0025806
86	97.39	0.014161	98.81	0.0119902	106.27	4.096E-05	109.16	0.0008821	108.3	0.0021437	107.86	0.0035046
87	97.39	0.014161	98.81	0.0119902	106.27	4.096E-05	109.16	0.0008821	108.3	0.0021437	107.86	0.0035046
88	97.41	0.009801	98.79	0.0167702	106.29	0.000185	109.18	0.0024701	108.37	0.0005617	107.92	0.0142086
89	97.3	0.043681	98.77	0.0223502	106.16	0.013549	109.11	0.0004121	108.3	0.0021437	107.9	0.0098406
90	97.3	0.043681	98.77	0.0223502	106.16	0.013549	109.11	0.0004121	108.3	0.0021437	107.9	0.0098406
91	97.28	0.052441	98.79	0.0167702	106.18	0.009293	109.18	0.0024701	108.32	0.0006917	107.79	0.0001166
92	97.28	0.052441	98.79	0.0167702	106.18	0.009293	109.18	0.0024701	108.32	0.0006917	107.79	0.0001166
93	97.32	0.035721	98.85	0.0048302	106.21	0.004409	109.2	0.0048581	108.32	0.0006917	107.79	0.0001166
94	97.54	0.000961	98.88	0.0015602	106.45	0.030137	109.38	0.0623501	108.56	0.0456677	108.03	0.0525326
95	97.54	0.000961	98.88	0.0015602	106.45	0.030137	109.38	0.0623501	108.56	0.0456677	108.03	0.0525326
96	97.54	0.000961	98.9	0.0003802	106.45	0.030137	109.38	0.0623501	108.56	0.0456677	108.08	0.0779526
97	97.5	8.1E-05	98.9	0.0003802	106.43	0.023593	109.36	0.0527621	108.56	0.0456677	108.08	0.0779526
98	97.5	8.1E-05	98.9	0.0003802	106.43	0.023593	109.36	0.0527621	108.56	0.0456677	108.08	0.0779526
99	97.5	8.1E-05	98.94	0.0004203	106.43	0.023593	109.33	0.0398801	108.41	0.0040577	108.1	0.0895206
100	97.54	0.000961	98.94	0.0004203	106.38	0.010733	109.31	0.0322921	108.41	0.0040577	108.1	0.0895206
SUM =	9750.9	4.3441	9891.95	1.648475	10627.64	0.966104	10913.03	0.824091	10834.63	1.450331	10780.08	1.257936
Mean T* (°C) =	97.509		98.9195		106.2764		109.1303		108.3463		107.8008	

Test Conditions: SERIES A - 2 Phase Flow Boiling, Distilled H_2O	
Reynolds Number = 32342	**Subcooled Temperature = 90°C**
Heat Flux (q/A) = 195.80 kW/m^2	**System Pressure ~ Atmospheric**

Estimating precision error (i.e. P_{Tw}) of measured wall temperature T_w ...continued

where P_{Tw} is given by: $[^{K}\Sigma_{j=1}(P^2_{T^*})_j]^{1/2}$ K is the total number of thermocouple probes = 8

T^* is the mean local wall temperature, measured by probe number j.

Table A (i.i.i): N-numbers 1 to 50 Probes 7 and 8

N measurements, taken on per second basis

N - number	Probe 7		Probe 8	
	T_i (°C)	$(T_i - T^*)^2$ (°C)	T_i (°C)	$(T_i - T^*)^2$ (°C)
1	100.41	0.0069556	93.83	0.0377136
2	100.24	0.0074996	93.94	0.0925376
3	100.24	0.0074996	93.94	0.0925376
4	100.24	0.0074996	93.94	0.0925376
5	100.24	0.0074996	93.94	0.0925376
6	100.33	1.156E-05	94.07	0.1885296
7	100.33	1.156E-05	94.07	0.1885296
8	100.63	0.0920516	94.07	0.1885296
9	100.68	0.1248916	94.07	0.1885296
10	100.68	0.1248916	94.07	0.1885296
11	100.79	0.2147396	94.25	0.3772416
12	100.81	0.2336756	94.25	0.3772416
13	100.81	0.2336756	94.25	0.3772416
14	100.96	0.4011956	94.34	0.4958976
15	101.03	0.4947716	94.42	0.6149696
16	101.03	0.4947716	94.42	0.6149696
17	101.16	0.6945556	94.45	0.6629216
18	101.23	0.8161316	94.47	0.6958896
19	101.23	0.8161316	94.47	0.6958896
20	101.16	0.6945556	94.51	0.7642256
21	101.18	0.7282916	94.53	0.7995936
22	101.18	0.7282916	94.53	0.7995936
23	101.01	0.4670356	94.51	0.7642256
24	99.58	0.5574116	93.07	0.3201296
25	99.58	0.5574116	93.07	0.3201296
26	99.58	0.5574116	93.07	0.3201296
27	101.25	0.8526676	94.51	0.7642256
28	101.25	0.8526676	94.51	0.7642256
29	101.27	0.8900036	94.49	0.7296576
30	101.27	0.8900036	94.49	0.7296576
31	101.27	0.8900036	94.4	0.5840016
32	101.27	0.8900036	94.4	0.5840016
33	101.27	0.8900036	94.4	0.5840016
34	101.27	0.8900036	94.4	0.5840016
35	101.27	0.8900036	94.34	0.4958976
36	101.27	0.8900036	94.34	0.4958976
37	101.25	0.8526676	94.21	0.3297056
38	99.71	0.3801956	92.74	0.8024576
39	99.71	0.3801956	92.74	0.8024576
40	99.47	0.7337636	92.71	0.8571056
41	99.47	0.7337636	92.71	0.8571056
42	99.47	0.7337636	92.71	0.8571056
43	101.01	0.4670356	94.18	0.2961536
44	101.01	0.4670356	94.18	0.2961536
45	101.01	0.4670356	94.18	0.2961536
46	99.42	0.8219236	92.58	1.1147136
47	99.42	0.8219236	92.58	1.1147136
48	99.42	0.8219236	92.58	1.1147136
49	101.05	0.5233076	94.03	0.1553936
50	101.05	0.5233076	94.03	0.1553936

Test Conditions: SERIES A - 2 Phase Flow Boiling, Distilled H_2O	
Reynolds Number = 32342	**Subcooled Temperature = 90°C**
Heat Flux (q/A) = 195.80 kW/m^2	**System Pressure ~ Atmospheric**

Estimating precision error (i.e. P_{Tw}) of measured wall temperature T_w ...continued

where P_{Tw} is given by: $[^K\Sigma_{j=1}(P^2{}_{T*})_j]^{1/2.}$ K is the total number of thermocouple probes = 8

T* is the mean local wall temperature, measured by probe number j.

Table A (i.v): N-numbers 51 to 100 Probes 7 and 8 **N = 100**

N-number	Probe 7		Probe 8	
	T_i (°C)	$(T_i - T^*)^2$ (°C)	T_i (°C)	$(T_i - T^*)^2$ (°C)
51	101.05	0.5233076	94.03	0.1553936
52	100.9	0.3287876	94.03	0.1553936
53	100.88	0.3062516	93.99	0.1254576
54	100.88	0.3062516	93.99	0.1254576
55	100.57	0.0592436	93.88	0.0596336
56	100.57	0.0592436	93.88	0.0596336
57	100.57	0.0592436	93.88	0.0596336
58	100.59	0.0693796	93.9	0.0698016
59	100.63	0.0920516	93.83	0.0377136
60	100.63	0.0920516	93.83	0.0377136
61	99.16	1.3609556	92.6	1.0728816
62	100.52	0.0374036	93.83	0.0377136
63	100.52	0.0374036	93.83	0.0377136
64	100.52	0.0374036	93.88	0.0596336
65	100.52	0.0374036	93.88	0.0596336
66	100.52	0.0374036	93.88	0.0596336
67	100.59	0.0693796	93.88	0.0596336
68	100.68	0.1248916	94.01	0.1400256
69	100.68	0.1248916	94.01	0.1400256
70	100.88	0.3062516	94.01	0.1400256
71	100.88	0.3062516	94.01	0.1400256
72	100.88	0.3062516	94.01	0.1400256
73	100.83	0.2534116	93.92	0.0807696
74	100.83	0.2534116	93.92	0.0807696
75	99.25	1.1590676	92.52	1.2450096
76	99.25	1.1590676	92.52	1.2450096
77	99.25	1.1590676	92.52	1.2450096
78	99.38	0.8960516	92.54	1.2007776
79	100.79	0.2147396	93.85	0.0458816
80	100.79	0.2147396	93.85	0.0458816
81	100.83	0.2534116	93.85	0.0458816
82	100.83	0.2534116	93.85	0.0458816
83	100.83	0.2534116	93.85	0.0458816
84	98.83	2.2398116	92.58	1.1147136
85	98.83	2.2398116	92.58	1.1147136
86	98.83	2.2398116	92.58	1.1147136
87	98.81	2.3000756	92.6	1.0728816
88	98.81	2.3000756	92.6	1.0728816
89	98.83	2.2398116	92.63	1.0116336
90	98.81	2.3000756	92.45	1.4061216
91	98.81	2.3000756	92.45	1.4061216
92	98.85	2.1803476	92.45	1.4061216
93	98.85	2.1803476	92.43	1.4539536
94	98.85	2.1803476	92.43	1.4539536
95	99.34	0.9733796	92.5	1.2900416
96	99.34	0.9733796	92.5	1.2900416
97	99.34	0.9733796	92.5	1.2900416
98	99.34	0.9733796	92.5	1.2900416
99	99.34	0.9733796	92.5	1.2900416
100	100.9	0.3287876	94.05	0.1715616
SUM =	10032.66	67.269844	9363.58	54.264836
Mean T* (°C) =	100.3266		93.6358	

Test Conditions: SERIES A - 2 Phase Flow Boiling, Distilled H_2O	
Reynolds Number = 32342	**Subcooled Temperature = 90°C**
Heat Flux (q/A) = 195.80 kW/m^2	**System Pressure ~ Atmospheric**

Estimating precision error (i.e. P_{Tw}) of measured wall temperature T_w ...continued

where P_{Tw} is given by: $[^K\Sigma_{j=1}(P^2{}_{T^*})_j\ ]^{1/2.}$ K is the total number of thermocouple probes = 8

T^* is the mean local wall temperature, measured by probe number j.

Table B

Probe No. j	S_T, (°C) $[\ \{\ \Sigma(T_i-T^*)^2\ \}\ /N-1\ ]^{1/2}$	S_M, (°C) $S_T/(N)^{1/2}$	P_{T^*}, (°C) $2.S_M$	$P^2{}_{T^*}$, (°C) $(\ 2.S_M\ )^2$	P_{Tw}, (°C) $[\ ^K\Sigma_{j=1}\ (P_{T^*})_j^2\ ]^{1/2}$
1	0.436598477	0.043659848	0.087319695	0.007624729	
2	0.165677971	0.016567797	0.033135594	0.001097968	
3	0.097097105	0.009709711	0.019419421	0.000377114	
4	0.082824262	0.008282426	0.016564852	0.000274394	
5	0.14576375	0.014576375	0.02915275	0.000849883	
6	0.126427325	0.012642732	0.025285465	0.000639355	1.740404151
7	6.760873705	0.67608737	1.352174741	1.82837653	
8	5.453821222	0.545382122	1.090764244	1.189766637	

N = 100

"Appendix B.2/2: Calculating the Bias limit (i.e. B_α) of the result α, kW/m^2.K"

where $B_\alpha = [(\theta_{Tw}.B_{Tw})^2 + (\theta_{Tf^*}.B_{Tf^*})^2]^{1/2}$

Test Conditions: SERIES A - 2 Phase Flow Boiling, Distilled H_2O	
Reynolds Number = 32342	**Subcooled Temperature = 90°C**
Heat Flux (q/A) = 195.80 kW/m^2	**System Pressure ~ Atmospheric**

Estimating bias error (i.e. B_{Tw}) of measured wall temperature T_w

where B_{Tw} is given by: $[^K\Sigma_{j=1}(B^2_T)_j]^{1/2.}$

K is the total number of thermocouple probes = 8

T is the local wall temperature, point measured by probe number j.

for each probe the bias error of point measured Tβ_T, is given by: $[B\,e^2_T + B\,c^2_T]^{1/2}$

$B\,e_T$ is the elemental bias contibution = 0.4°C

$B\,e_C$ is the conceptual bias contribution established via calibration testing

Probe No. j	$B\,e_T$ (°C)	$B\,e^2_T$ (°C)	$B\,c_T$ (°C)	$B\,c^2_T$ (°C)	B_T (°C)	B^2_T (°C)	B_{Tw} (°C)
1	0.4	0.16	0	0	0.4	0.16	
2	0.4	0.16	0	0	0.4	0.16	
3	0.4	0.16	0	0	0.4	0.16	
4	0.4	0.16	0	0	0.4	0.16	
5	0.4	0.16	0	0	0.4	0.16	
6	0.4	0.16	0	0	0.4	0.16	1.1313708
7	0.4	0.16	0	0	0.4	0.16	
8	0.4	0.16	0	0	0.4	0.16	

Estimating bias error (i.e. B_{Tf^*}) of mean fluid temperature, T_f

where B_{Tf^*} is given by: $[B^2_{Tf.i} + B^2_{Tf.o}]^{1/2}$

$B_{Tf.i}$ is the fixed error of point measured inlet fluid temperature Tf.i

$B_{Tf.o}$ is the fixed error of point measured outlet fluid temperature Tf.o

further, $B_{Tf.i}$ is given by: $[B\,e^2_{Tf.i} + B\,c^2_{Tf.i}]^{1/2}$

$B_{Tf.o}$ is given by: $[B\,e^2_{Tf.o} + B\,c^2_{Tf.o}]^{1/2}$

$B\,e_{Tf.i}$ and $B\,e_{Tf.o}$ are elemental bias contributions = 0.4°C respectively

$B\,c_{Tf.i}$ and $B\,c_{Tf.o}$ are conceptual bias contributions

Probe A - inlet fluid temperature						Probe B - outlet fluid temperature					
$B\,e_{Tf.i}$ (°C)	$B\,e^2_{Tf.i}$ (°C)	$B\,c_{Tf.i}$ (°C)	$B\,c^2_{Tf.i}$ (°C)	$B_{Tf.i}$ (°C)	$B^2_{Tf.i}$ (°C)	$B\,e_{Tf.o}$ (°C)	$B\,e^2_{Tf.o}$ (°C)	$B\,c_{Tf.o}$ (°C)	$B\,c^2_{Tf.o}$ (°C)	$B_{Tf.o}$ (°C)	$B^2_{Tf.o}$ (°C)
0.4	0.16	0	0	0.4	0.16	0.4	0.16	0	0	0.4	0.16

B_{Tf^*} - bias error of bulk fluid temperature, °C = 0.5656854

"Appendix B.3/1: Calculating the Precision limit (i.e. P_a) of the result a, kW/m^2.K"

where $P_a = [(\theta_{Tw}.P_{Tw})^2 + (\theta_{Tf^*}.P_{Tf^*})^2]^{1/2}$

Test Conditions: SERIES A - 2 Phase Flow Boiling, Distilled H_2O	
Reynolds Number = 32342	**Subcooled Temperature = 90°C**
Heat Flux (q/A) = 279.720 kW/m^2	**System Pressure ~ Atmospheric**

Estimating precision error (i.e. P_{Tw}) of measured wall temperature T_w

where P_{Tw} is given by: $[^K\Sigma_{j=1}(P^2_{T^*})_j]^{1/2.}$

Table A (i): N-numbers 1 to 50 Probes 1 to 6 — N measurements, taken on per second basis

N-number	Probe 1		Probe 2		Probe 3		Probe 4		Probe 5		Probe 6	
	T_i (°C)	$(T_i - T^*)^2$ (°C)	T_i (°C)	$(T_i - T^*)^2$ (°C)	T_i (°C)	$(T_i - T^*)^2$ (°C)	T_i (°C)	$(T_i - T^*)^2$ (°C)	T_i (°C)	$(T_i - T^*)^2$ (°C)	T_i (°C)	$(T_i - T^*)^2$ (°C)
1	97.41	0.0026936	99.05	0.0001613	108.98	0.030976	112.45	0.0238702	112.38	0.0104244	110.48	0.0106502
2	97.39	0.0051696	98.96	0.0059753	108.89	0.070756	112.4	0.0418202	112.33	0.0231344	110.46	0.0151782
3	97.39	0.0051696	98.96	0.0059753	108.89	0.070756	112.4	0.0418202	112.33	0.0231344	110.46	0.0151782
4	97.34	0.0148596	98.96	0.0059753	108.89	0.070756	112.4	0.0418202	112.33	0.0231344	110.44	0.0205062
5	97.36	0.0103836	99.01	0.0007453	108.94	0.046656	112.45	0.0238702	112.36	0.0149084	110.46	0.0151782
6	97.36	0.0103836	99.01	0.0007453	108.94	0.046656	112.45	0.0238702	112.36	0.0149084	110.46	0.0151782
7	97.36	0.0103836	99.01	0.0007453	108.98	0.030976	112.45	0.0238702	112.45	0.0010304	110.66	0.0058982
8	97.45	0.0001416	98.99	0.0022373	109.03	0.015876	112.49	0.0131103	112.47	0.0001464	110.77	0.0348942
9	97.45	0.0001416	98.99	0.0022373	109.03	0.015876	112.49	0.0131103	112.47	0.0001464	110.77	0.0348942
10	97.45	0.0001416	98.96	0.0059753	109.09	0.004356	112.47	0.0180903	112.45	0.0010304	110.77	0.0348942
11	97.45	0.0001416	98.96	0.0059753	109.09	0.004356	112.47	0.0180903	112.45	0.0010304	110.77	0.0348942
12	97.58	0.0139476	98.99	0.0022373	109.09	0.004356	112.53	0.0055503	112.42	0.0038564	110.77	0.0348942
13	97.58	0.0139476	98.99	0.0022373	109.09	0.004356	112.53	0.0055503	112.42	0.0038564	110.77	0.0348942
14	97.6	0.0190716	99.07	0.0010693	109.09	0.004356	112.53	0.0055503	112.45	0.0010304	110.75	0.0278222
15	97.58	0.0139476	99.07	0.0010693	109.09	0.004356	112.56	0.0019802	112.49	6.241E-05	110.68	0.0093702
16	97.58	0.0139476	99.07	0.0010693	109.09	0.004356	112.56	0.0019802	112.49	6.241E-05	110.68	0.0093702
17	97.52	0.0033756	98.99	0.0022373	109.11	0.002116	112.58	0.0006003	112.64	0.0249324	110.64	0.0032262
18	97.5	0.0014516	98.96	0.0059753	109.16	1.6E-05	112.6	2.025E-05	112.67	0.0353064	110.59	4.624E-05
19	97.5	0.0014516	98.96	0.0059753	109.16	1.6E-05	112.6	2.025E-05	112.67	0.0353064	110.59	4.624E-05
20	97.45	0.0001416	98.96	0.0059753	109.16	1.6E-05	112.56	0.0019802	112.62	0.0190164	110.66	0.0058982
21	97.45	0.0001416	98.96	0.0059753	109.16	1.6E-05	112.56	0.0019802	112.49	6.241E-05	110.81	0.0514382
22	97.45	0.0001416	98.96	0.0059753	109.16	1.6E-05	112.56	0.0019802	112.49	6.241E-05	110.81	0.0514382
23	97.5	0.0014516	99.03	5.329E-05	109.14	0.000256	112.49	0.0131103	112.53	0.0022944	110.81	0.0514382
24	97.5	0.0014516	99.03	5.329E-05	109.14	0.000256	112.49	0.0131103	112.53	0.0022944	110.81	0.0514382
25	97.5	0.0014516	99.03	5.329E-05	109.14	0.000256	112.53	0.0055503	112.49	6.241E-05	110.64	0.0032262
26	97.39	0.0051696	99.01	0.0007453	109.11	0.002116	112.51	0.0089302	112.51	0.0007784	110.61	0.0007182
27	97.39	0.0051696	99.01	0.0007453	109.11	0.002116	112.51	0.0089302	112.51	0.0007784	110.61	0.0007182
28	97.39	0.0051696	98.99	0.0022373	109.14	0.000256	112.56	0.0019802	112.56	0.0060684	110.61	0.0007182
29	97.43	0.0010176	99.01	0.0007453	109.14	0.000256	112.62	0.0002403	112.56	0.0060684	110.61	0.0007182
30	97.43	0.0010176	99.01	0.0007453	109.14	0.000256	112.62	0.0002403	112.56	0.0060684	110.61	0.0007182
31	97.47	6.561E-05	99.01	0.0007453	109.16	1.6E-05	112.71	0.0111302	112.45	0.0010304	110.57	0.0001742
32	97.43	0.0010176	99.01	0.0007453	109.14	0.000256	112.73	0.0157503	112.45	0.0010304	110.52	0.0039942
33	97.43	0.0010176	99.01	0.0007453	109.14	0.000256	112.73	0.0157503	112.45	0.0010304	110.52	0.0039942
34	97.47	6.561E-05	99.01	0.0007453	109.2	0.001936	112.75	0.0211702	112.56	0.0060684	110.52	0.0039942
35	97.39	0.0051696	98.99	0.0022373	109.11	0.002116	112.73	0.0157503	112.53	0.0022944	110.5	0.0069222
36	97.39	0.0051696	98.99	0.0022373	109.11	0.002116	112.73	0.0157503	112.53	0.0022944	110.5	0.0069222
37	97.43	0.0010176	99.01	0.0007453	109.18	0.000576	112.73	0.0157503	112.56	0.0060684	110.55	0.0011022
38	97.41	0.0026936	98.96	0.0059753	109.11	0.002116	112.71	0.0111302	112.49	6.241E-05	110.52	0.0039942
39	97.41	0.0026936	98.96	0.0059753	109.11	0.002116	112.71	0.0111302	112.49	6.241E-05	110.52	0.0039942
40	97.43	0.0010176	98.99	0.0022373	109.18	0.000576	112.69	0.0073102	112.6	0.0139004	110.55	0.0011022
41	97.43	0.0010176	98.99	0.0022373	109.18	0.000576	112.69	0.0073102	112.6	0.0139004	110.55	0.0011022
42	97.41	0.0026936	98.99	0.0022373	109.14	0.000256	112.69	0.0073102	112.51	0.0007784	110.57	0.0001742
43	97.41	0.0026936	99.03	5.329E-05	109.18	0.000576	112.78	0.0308002	112.49	6.241E-05	110.59	4.624E-05
44	97.47	6.561E-05	99.07	0.0010693	109.18	0.000576	112.78	0.0308002	112.49	6.241E-05	110.59	4.624E-05
45	97.47	6.561E-05	99.07	0.0010693	109.18	0.000576	112.78	0.0308002	112.49	6.241E-05	110.59	4.624E-05
46	97.47	6.561E-05	99.1	0.0039313	109.2	0.001936	112.75	0.0211702	112.49	6.241E-05	110.68	0.0093702
47	97.47	6.561E-05	99.1	0.0039313	109.2	0.001936	112.75	0.0211702	112.49	6.241E-05	110.68	0.0093702
48	97.47	6.561E-05	99.1	0.0039313	109.2	0.001936	112.75	0.0211702	112.49	6.241E-05	110.68	0.0093702
49	97.47	6.561E-05	99.12	0.0068393	109.16	1.6E-05	112.75	0.0211702	112.45	0.0010304	110.59	4.624E-05
50	97.47	6.561E-05	99.12	0.0068393	109.16	1.6E-05	112.75	0.0211702	112.45	0.0010304	110.59	4.624E-05

Test Conditions:	
SERIES A - 2 Phase Flow Boiling, Distilled H_2O	
Reynolds Number = 32342	**Subcooled Temperature = 90°C**
Heat Flux (q/A) = 279.720 kW/m^2	**System Pressure ~ Atmospheric**

Estimating precision error (i.e. P_{Tw}) of measured wall temperature T_w

where P_{Tw} is given by: $[^K\Sigma_{j=1}(P^2_{T^*})_j]^{1/2.}$

K is the total number of thermocouple probes = 8

P_{T^*} is the precision error of the mean local wall temperature.

T^* is the mean local wall temperature, measured by probe number j.

Table A (i.i): *N*- numbers 51 to 100 Probes 1 to 6 N = 100

N - number	Probe 1		Probe 2		Probe 3		Probe 4		Probe 5		Probe 6	
	T_i (°C)	$(T_i - T^*)^2$ (°C)	T_i (°C)	$(T_i - T^*)^2$ (°C)	T_i (°C)	$(T_i - T^*)^2$ (°C)	T_i (°C)	$(T_i - T^*)^2$ (°C)	T_i (°C)	$(T_i - T^*)^2$ (°C)	T_i (°C)	$(T_i - T^*)^2$ (°C)
51	97.41	0.0026936	99.14	0.0105473	109.16	1.6E-05	112.69	0.0073102	112.45	0.0010304	110.59	4.624E-05
52	97.41	0.0026936	99.12	0.0068393	109.16	1.6E-05	112.69	0.0073102	112.45	0.0010304	110.59	4.624E-05
53	97.41	0.0026936	99.12	0.0068393	109.16	1.6E-05	112.69	0.0073102	112.45	0.0010304	110.59	4.624E-05
54	97.47	6.561E-05	99.05	0.0001613	109.29	0.017956	112.67	0.0042903	112.51	0.0007784	110.61	0.0007182
55	97.47	6.561E-05	99.05	0.0001613	109.29	0.017956	112.67	0.0042903	112.51	0.0007784	110.61	0.0007182
56	97.47	6.561E-05	99.05	0.0001613	109.29	0.017956	112.67	0.0042903	112.51	0.0007784	110.61	0.0007182
57	97.47	6.561E-05	99.05	0.0001613	109.29	0.017956	112.67	0.0042903	112.53	0.0022944	110.61	0.0007182
58	97.47	6.561E-05	99.05	0.0001613	109.11	0.002116	112.71	0.0111302	112.47	0.0001464	110.57	0.0001742
59	97.47	6.561E-05	99.05	0.0001613	109.11	0.002116	112.71	0.0111302	112.47	0.0001464	110.57	0.0001742
60	97.45	0.0001416	99.01	0.0007453	109.11	0.002116	112.75	0.0211702	112.47	0.0001464	110.57	0.0001742
61	97.45	0.0001416	98.99	0.0022373	109.11	0.002116	112.75	0.0211702	112.47	0.0001464	110.59	4.624E-05
62	97.45	0.0001416	98.99	0.0022373	109.11	0.002116	112.75	0.0211702	112.47	0.0001464	110.59	4.624E-05
63	97.45	0.0001416	98.99	0.0022373	109.11	0.002116	112.75	0.0211702	112.47	0.0001464	110.64	0.0032262
64	97.45	0.0001416	98.99	0.0022373	109.11	0.002116	112.75	0.0211702	112.47	0.0001464	110.64	0.0032262
65	97.47	6.561E-05	99.03	5.329E-05	109.11	0.002116	112.73	0.0157503	112.47	0.0001464	110.64	0.0032262
66	97.47	6.561E-05	99.1	0.0039313	109.14	0.000256	112.71	0.0111302	112.47	0.0001464	110.64	0.0032262
67	97.47	6.561E-05	99.1	0.0039313	109.14	0.000256	112.71	0.0111302	112.47	0.0001464	110.64	0.0032262
68	97.47	6.561E-05	99.03	5.329E-05	109.36	0.041616	112.56	0.0019802	112.47	0.0001464	110.55	0.0011022
69	97.47	6.561E-05	99.12	0.0068393	109.36	0.041616	112.53	0.0055503	112.47	0.0001464	110.61	0.0007182
70	97.47	6.561E-05	99.12	0.0068393	109.36	0.041616	112.53	0.0055503	112.47	0.0001464	110.61	0.0007182
71	97.47	6.561E-05	99.12	0.0068393	109.36	0.041616	112.53	0.0055503	112.53	0.0022944	110.55	0.0011022
72	97.45	0.0001416	99.12	0.0068393	109.31	0.023716	112.58	0.0006003	112.53	0.0022944	110.61	0.0007182
73	97.45	0.0001416	99.12	0.0068393	109.31	0.023716	112.58	0.0006003	112.53	0.0022944	110.61	0.0007182
74	97.47	6.561E-05	99.1	0.0039313	109.22	0.004096	112.67	0.0042903	112.51	0.0007784	110.64	0.0032262
75	97.47	6.561E-05	99.1	0.0039313	109.22	0.004096	112.67	0.0042903	112.45	0.0010304	110.64	0.0032262
76	97.47	6.561E-05	99.1	0.0039313	109.22	0.004096	112.67	0.0042903	112.45	0.0010304	110.64	0.0032262
77	97.47	6.561E-05	99.1	0.0039313	109.22	0.004096	112.56	0.0019802	112.45	0.0010304	110.57	0.0001742
78	97.5	0.0014516	99.1	0.0039313	109.22	0.004096	112.56	0.0019802	112.45	0.0010304	110.57	0.0001742
79	97.5	0.0014516	99.1	0.0039313	109.22	0.004096	112.56	0.0019802	112.45	0.0010304	110.57	0.0001742
80	97.47	6.561E-05	99.03	5.329E-05	109.14	0.000256	112.53	0.0055503	112.47	0.0001464	110.44	0.0205062
81	97.47	6.561E-05	99.03	5.329E-05	109.14	0.000256	112.53	0.0055503	112.47	0.0001464	110.44	0.0205062
82	97.5	0.0014516	99.01	0.0007453	109.16	1.6E-05	112.56	0.0019802	112.47	0.0001464	110.44	0.0205062
83	97.45	0.0001416	99.01	0.0007453	109.14	0.000256	112.51	0.0089302	112.45	0.0010304	110.44	0.0205062
84	97.45	0.0001416	99.01	0.0007453	109.14	0.000256	112.51	0.0089302	112.45	0.0010304	110.44	0.0205062
85	97.54	0.0060996	99.05	0.0001613	109.16	1.6E-05	112.53	0.0055503	112.36	0.0149084	110.46	0.0151782
86	97.45	0.0001416	99.07	0.0010693	109.16	1.6E-05	112.53	0.0055503	112.36	0.0149084	110.46	0.0151782
87	97.45	0.0001416	99.07	0.0010693	109.16	1.6E-05	112.53	0.0055503	112.36	0.0149084	110.46	0.0151782
88	97.54	0.0060996	99.07	0.0010693	109.16	1.6E-05	112.58	0.0006003	112.51	0.0007784	110.46	0.0151782
89	97.45	0.0001416	99.07	0.0010693	109.22	0.004096	112.58	0.0006003	112.51	0.0007784	110.46	0.0151782
90	97.45	0.0001416	99.07	0.0010693	109.22	0.004096	112.58	0.0006003	112.51	0.0007784	110.46	0.0151782
91	97.54	0.0060996	99.07	0.0010693	109.22	0.004096	112.51	0.0089302	112.47	0.0001464	110.46	0.0151782
92	97.5	0.0014516	99.07	0.0010693	109.22	0.004096	112.51	0.0089302	112.47	0.0001464	110.48	0.0106502
93	97.5	0.0014516	99.07	0.0010693	109.22	0.004096	112.51	0.0089302	112.47	0.0001464	110.48	0.0106502
94	97.5	0.0014516	99.05	0.0001613	109.18	0.000576	112.53	0.0055503	112.51	0.0007784	110.48	0.0106502
95	97.52	0.0033756	99.07	0.0010693	109.2	0.001936	112.56	0.0019802	112.53	0.0022944	110.48	0.0106502
96	97.52	0.0033756	99.07	0.0010693	109.2	0.001936	112.56	0.0019802	112.53	0.0022944	110.48	0.0106502
97	97.52	0.0033756	99.01	0.0007453	109.2	0.001936	112.53	0.0055503	112.51	0.0007784	110.48	0.0106502
98	97.52	0.0033756	99.05	0.0001613	109.25	0.008836	112.53	0.0055503	112.47	0.0001464	110.5	0.0069222
99	97.52	0.0033756	99.05	0.0001613	109.25	0.008836	112.53	0.0055503	112.47	0.0001464	110.5	0.0069222
100	97.43	0.0010176	99.03	5.329E-05	109.29	0.017956	112.53	0.0055503	112.45	0.0010304	110.61	0.0007182
SUM =	9746.19	0.245939	9903.73	0.251571	10915.6	0.8496	11260.45	1.067875	11248.21	0.391859	11058.32	0.963576
Mean T* (°C) =	97.4619		99.0373		109.156		112.6045		112.4821		110.5832	

Test Conditions: SERIES A - 2 Phase Flow Boiling, Distilled H_2O	
Reynolds Number = 32342	**Subcooled Temperature = 90°C**
Heat Flux (q/A) = 279.720 kW/m^2	**System Pressure ~ Atmospheric**

Estimating precision error (i.e. P_{Tw}) of measured wall temperature T_w ...continued

where P_{Tw} is given by: $[^K\Sigma_{j=1}(P^2{}_{T^*})_j]^{1/2.}$ K is the total number of thermocouple probes = 8

T* is the mean local wall temperature, measured by probe number j.

Table A (i.i.i): N-numbers 1 to 50 Probes 7 and 8

N measurements, taken on per second basis

N-number	Probe 7		Probe 8	
	T_i (°C)	$(T_i - T^*)^2$ (°C)	T_i (°C)	$(T_i - T^*)^2$ (°C)
1	105.02	0.1743063	95.04	0.1485332
2	103.5	1.2155062	93.59	1.1333732
3	103.5	1.2155062	93.5	1.3331012
4	103.5	1.2155062	93.5	1.3331012
5	103.52	1.1718062	93.5	1.3331012
6	105.28	0.4590063	95.28	0.3911252
7	105.28	0.4590063	95.28	0.3911252
8	105.28	0.4590063	95.28	0.3911252
9	103.39	1.4701562	93.72	0.8734772
10	103.39	1.4701562	93.72	0.8734772
11	103.39	1.4701562	93.72	0.8734772
12	103.39	1.4701562	93.72	0.8734772
13	105.04	0.1914063	95.06	0.1643492
14	105.15	0.2997563	95.26	0.3665092
15	105.15	0.2997563	95.26	0.3665092
16	105.04	0.1914063	95.26	0.3665092
17	105.22	0.3813063	95.24	0.3426932
18	105.22	0.3813063	95.24	0.3426932
19	105.22	0.3813063	95.24	0.3426932
20	105.22	0.3813063	95.24	0.3426932
21	105.24	0.4064063	95.24	0.3426932
22	105.24	0.4064063	95.24	0.3426932
23	105.24	0.4064063	95.17	0.2656372
24	105.24	0.4064063	95.17	0.2656372
25	105.15	0.2997563	95.21	0.3084692
26	105.15	0.2997563	95.21	0.3084692
27	105.24	0.4064063	95.21	0.3084692
28	105.22	0.3813063	95.21	0.3084692
29	105.22	0.3813063	95.21	0.3084692
30	105.22	0.3813063	95.19	0.2866532
31	105.15	0.2997563	95.1	0.1983812
32	105.15	0.2997563	95.1	0.1983812
33	105.15	0.2997563	95.08	0.1809652
34	105.17	0.3220563	95.06	0.1643492
35	105.17	0.3220563	95.06	0.1643492
36	103.41	1.4220562	93.66	0.9892292
37	103.54	1.1289062	93.68	0.9498452
38	103.54	1.1289062	93.68	0.9498452
39	103.56	1.0868062	93.7	0.9112612
40	105.26	0.4323063	95.06	0.1643492
41	105.26	0.4323063	95.06	0.1643492
42	105.26	0.4323063	95.15	0.2454212
43	105.24	0.4064063	95.15	0.2454212
44	105.24	0.4064063	95.15	0.2454212
45	105.15	0.2997563	95.19	0.2866532
46	103.5	1.2155062	93.68	0.9498452
47	103.5	1.2155062	93.68	0.9498452
48	105.04	0.1914063	95.08	0.1809652
49	105.04	0.1914063	95.02	0.1335172
50	105.04	0.1914063	95.02	0.1335172

Test Conditions: SERIES A - 2 Phase Flow Boiling, Distilled H_2O	
Reynolds Number = 32342	**Subcooled Temperature = 90°C**
Heat Flux (q/A) = 279.720 kW/m^2	**System Pressure ~ Atmospheric**

Estimating precision error (i.e. P_{Tw}) of measured wall temperature T_w ...continued

where P_{Tw} is given by: $[^K\Sigma_{j=1}(P^2{}_{T^*})_j]^{1/2.}$ K is the total number of thermocouple probes = 8

T* is the mean local wall temperature, measured by probe number j.

Table A (i.v): N-numbers 51 to 100 Probes 7 and 8 N = 100

N-number	Probe 7		Probe 8	
	T_i (°C)	$(T_i - T^*)^2$ (°C)	T_i (°C)	$(T_i - T^*)^2$ (°C)
51	105.04	0.1914063	95.02	0.1335172
52	103.5	1.2155062	93.64	1.0294132
53	103.5	1.2155062	93.64	1.0294132
54	103.5	1.2155062	93.64	1.0294132
55	105.04	0.1914063	95.04	0.1485332
56	105.04	0.1914063	95.04	0.1485332
57	105.04	0.1914063	95.04	0.1485332
58	105.04	0.1914063	95.04	0.1485332
59	103.37	1.5190562	93.61	1.0911892
60	103.37	1.5190562	93.61	1.0911892
61	103.37	1.5190562	93.61	1.0911892
62	105.13	0.2782563	95.06	0.1643492
63	105.15	0.2997563	95.06	0.1643492
64	105.15	0.2997563	95.06	0.1643492
65	105.15	0.2997563	95.02	0.1335172
66	103.34	1.5939062	93.55	1.2201412
67	103.34	1.5939062	93.55	1.2201412
68	103.34	1.5939062	93.55	1.2201412
69	103.32	1.6448062	93.55	1.2201412
70	103.32	1.6448062	93.55	1.2201412
71	105.04	0.1914063	95.06	0.1643492
72	105.04	0.1914063	95.06	0.1643492
73	105.04	0.1914063	95.06	0.1643492
74	105.04	0.1914063	95.06	0.1643492
75	105.02	0.1743063	95.02	0.1335172
76	105.02	0.1743063	95.02	0.1335172
77	104.93	0.1072563	94.82	0.0273572
78	104.71	0.0115563	94.73	0.0056852
79	104.71	0.0115563	94.73	0.0056852
80	104.71	0.0115563	94.73	0.0056852
81	104.71	0.0115563	94.73	0.0056852
82	104.73	0.0162563	94.75	0.0091012
83	104.73	0.0162563	94.75	0.0091012
84	104.73	0.0162563	94.75	0.0091012
85	104.64	0.0014063	94.71	0.0030692
86	104.58	0.0005062	94.71	0.0030692
87	104.58	0.0005062	94.71	0.0030692
88	104.53	0.0052562	94.69	0.0012532
89	104.53	0.0052562	94.71	0.0030692
90	104.53	0.0052562	94.71	0.0030692
91	104.69	0.0076563	94.71	0.0030692
92	104.69	0.0076563	94.71	0.0030692
93	104.69	0.0076563	94.71	0.0030692
94	104.64	0.0014063	94.71	0.0030692
95	104.66	0.0033063	94.73	0.0056852
96	104.66	0.0033063	94.73	0.0056852
97	104.64	0.0014063	94.71	0.0030692
98	104.64	0.0014063	94.71	0.0030692
99	104.64	0.0014063	94.64	0.0002132
100	104.47	0.0175562	94.64	0.0002132
SUM =	10460.25	50.055075	9465.46	38.900084
Mean T* (°C) =	104.6025		94.6546	

Test Conditions: SERIES A - 2 Phase Flow Boiling, Distilled H_2O	
Reynolds Number = 32342	**Subcooled Temperature = 90°C**
Heat Flux (q/A) = 279.720 kW/m^2	**System Pressure ~ Atmospheric**

Estimating precision error (i.e. P_{Tw}) of measured wall temperature T_w ...continued

where P_{Tw} is given by: $[{}^{K}\Sigma_{j=1}(P^2{}_{T*})_j]^{1/2}$ K is the total number of thermocouple probes = 8

T* is the mean local wall temperature, measured by probe number j.

Table B

Probe No. j	S_T, (°C) $[\{\Sigma(T_i-T^*)^2\}/N-1]^{1/2}$	S_M, (°C) $S_T/(N)^{1/2}$	P_{T*}, (°C) $2.S_M$	$P^2{}_{T*}$, (°C) $(2.S_M)^2$	P_{Tw}, (°C) $[{}^{K}\Sigma_{j=1}(P_{T*})_j^2]^{1/2}$
1	0.0247178	0.00247178	0.00494356	2.44388E-05	
2	0.025283837	0.002528384	0.005056767	2.55709E-05	
3	0.085388013	0.008538801	0.017077603	0.000291645	
4	0.107325476	0.010732548	0.021465095	0.00046075	
5	0.039383311	0.003938331	0.007876662	6.20418E-05	
6	0.096843032	0.009684303	0.019368606	0.000375143	1.274742208
7	5.030724322	0.503072432	1.006144864	1.012327488	
8	3.909605544	0.390960554	0.781921109	0.61140062	

N = 100

"Appendix B.3/2: Calculating the Bias limit (i.e. B_α) of the result α, kW/m^2.K"

where $B_\alpha = [(\theta_{Tw}.B_{Tw})^2 + (\theta_{Tf^*}.B_{Tf^*})^2]^{1/2}$

Test Conditions: SERIES A - 2 Phase Flow Boiling, Distilled H_2O	
Reynolds Number = 32342	**Subcooled Temperature = 90°C**
Heat Flux (q/A) = 279.720 kW/m^2	**System Pressure ~ Atmospheric**

Estimating bias error (i.e. B_{Tw}) of measured wall temperature T_w

where B_{Tw} is given by: $[^K\Sigma_{j=1}(B^2_T)_j]^{1/2}$

K is the total number of thermocouple probes = 8

T is the local wall temperature, point measured by probe number j.

for each probe the bias error of point measured T B_T, is given by: $[B e^2_T + B c^2_T]^{1/2}$

$B e_T$ is the elemental bias contibution = 0.4°C

$B e_C$ is the conceptual bias contribution established via calibration testing

Probe No. j	$B e_T$ (°C)	$B e^2_T$ (°C)	$B c_T$ (°C)	$B c^2_T$ (°C)	B_T (°C)	B^2_T (°C)	B_{Tw} (°C)
1	0.4	0.16	0	0	0.4	0.16	
2	0.4	0.16	0	0	0.4	0.16	
3	0.4	0.16	0	0	0.4	0.16	
4	0.4	0.16	0	0	0.4	0.16	
5	0.4	0.16	0	0	0.4	0.16	
6	0.4	0.16	0	0	0.4	0.16	1.1313708
7	0.4	0.16	0	0	0.4	0.16	
8	0.4	0.16	0	0	0.4	0.16	

Estimating bias error (i.e. B_{Tf^*}) of mean fluid temperature, T_{f^*}

where B_{Tf^*} is given by: $[B^2_{Tf.i} + B^2_{Tf.o}]^{1/2}$

$B_{Tf.i}$ is the fixed error of point measured inlet fluid temperature Tf.i

$B_{Tf.o}$ is the fixed error of point measured outlet fluid temperature Tf.o

further, $B_{Tf.i}$ is given by: $[B e^2_{Tf.i} + B c^2_{Tf.i}]^{1/2}$

$B_{Tf.o}$ is given by: $[B e^2_{Tf.o} + B c^2_{Tf.o}]^{1/2}$

$B e_{Tf.i}$ and $B e_{Tf.o}$ are elemental bias contributions = 0.4°C respectively

$B c_{Tf.i}$ and $B c_{Tf.o}$ are conceptual bias contributions

Probe A - inlet fluid temperature						Probe B - outlet fluid temperature					
$B e_{Tf.i}$ (°C)	$B e^2_{Tf.i}$ (°C)	$B c_{Tf.i}$ (°C)	$B c^2_{Tf.i}$ (°C)	$B_{Tf.i}$ (°C)	$B^2_{Tf.i}$ (°C)	$B e_{Tf.o}$ (°C)	$B e^2_{Tf.o}$ (°C)	$B c_{Tf.o}$ (°C)	$B c^2_{Tf.o}$ (°C)	$B_{Tf.o}$ (°C)	$B^2_{Tf.o}$ (°C)
0.4	0.16	0	0	0.4	0.16	0.4	0.16	0	0	0.4	0.16
B_{Tf^*} - bias error of bulk fluid temperature, °C =						0.5656854					

Appendix B.4

Presenting the calculated uncertainties in the heat transfer coefficient (α) values

measured over the specfied boiling range

Test Conditions: SERIES A - 2 Phase Flow Boiling, Distilled H_2O	
Reynolds Number = 32342	**Subcooled Temperature = 90°C**
Heat Flux Range = 83.916 → 279.72 kW/m²	**System Pressure ~ Atmospheric**

q'' kW/m²	ΔT K	α kW/m².K	P_{Tw} °C	P_{Tf^*} °C	B_{Tw} °C	B_{Tf^*} °C	$\partial\alpha / \partial T_w$ kW/m²K	$\partial\alpha / \partial Tf^*$ kW/m²K	P_α kW/m²K	B_α kW/m²K	$U\alpha$ kW/m²K	$U\alpha$ %
83.916	11.95685	7.02	1.370798168	0	1.13137085	0.565685425	-0.586963658	0.586963658	0.804608706	0.742456825	1.094822957	15.59968763
111.888	12.1257	9.23	1.71680847	0	1.13137085	0.565685425	-0.760974094	0.760974094	1.306446771	0.962564551	1.622754966	17.58637199
139.86	12.9765	10.78	0.876894957	0	1.13137085	0.565685425	-0.830574095	0.830574095	0.728326235	1.050602363	1.278367877	11.8609615
167.832	14.7267	11.40	1.53670832	0	1.13137085	0.565685425	-0.773862657	0.773862657	1.189201184	0.978867437	1.540253523	13.51521257
195.804	15.0781	12.99	1.740404151	0	1.13137085	0.565685425	-0.861248188	0.861248188	1.498919921	1.089402361	1.852986356	14.26912299
223.776	15.0108	14.91	1.091985828	0	1.13137085	0.565685425	-0.993129379	0.993129379	1.084483207	1.256220339	2.622394382	17.59091126
251.748	16.3946	15.36	1.732172183	0	1.13137085	0.565685425	-0.936622052	0.936622052	1.622390665	1.184743597	2.008922313	13.08271675
279.72	17.0428	16.41	1.274742208	0	1.13137085	0.565685425	-0.96303401	0.96303401	1.2276201	1.218152374	1.729435259	10.53711541

APPENDIX C

Correlating heat transfer in three-phase flow boiling

where

$$\alpha_{TFB} = \left[(\alpha_{NB})^{t_R} + (\alpha_{CB})^{t_R} \right]^{1/t_R}$$

$$\alpha_{TFB} = \left[\left\{ \left(\alpha_{npb,p} . F_{NB}\right)^{b_E} \right\}^{t_R} + \left\{ \alpha_{LS} . F_{CB} . f(U) \right\}^{t_R} \right]^{1/t_R}$$

Appendix	Description	Numbering
C.1	**Comparing theoretical convective heat transfer with results obtained during forced convective boiling** C.1/0: Equations and useful values C.1/1: Evaluation for d_p = 2 mm C.1/2: Evaluation for d_p = 2.5 mm	**C.1/0** **to** **C.1/2**
C.2	**Comparing theoretical 3-phase heat transfer coefficient with results obtained during nucleate boiling** C.2/0: Equations and useful values C.2/1: Evaluation for d_p = 2 mm C.2/1/1: q'' = 111.89 kW/m^2 C.2/1/2: q'' = 167.83 kW/m^2 C.2/1/3: q'' = 223.78 kW/m^2 C.2/1/4: q'' = 279.72 kW/m^2	**C.2/0** **to** **C.2/1/4:2**

Appendix C.1

Comparing Theoretical Convective H.t.c Contribution, α_{CB}, with Experimental

Heat Transfer Results, α_{tfb}, obtained in Forced Convective (l-s) Region of 3-phase CFB

where, $\alpha_{TFB} \approx \alpha_{CB} = \{\alpha_{LS}.F_{CB}.f(U)\}$

Equations

For all relevant equations, please refer to main body of thesis

Useful Values

Liquid Properties [Read at 115 °C]				
Thermal Cond. (W/mK)	Density (kg/m^3)	Sp. Heat Capacity (J/kgK)	Dynamic Viscosity (kg/m.s)	Kinematic Viscosity (m^2/s)
λ_L	ρ_L	$C_{p,L}$	μ_L	ν_L
0.686	946.66	4239	2.42E-04	2.56E-07

Liquid Properties [Read at 90 °C Subcooled Bulk Temperature]						
Thermal Cond. (W/mK)	Density (kg/m^3)	Sp. Heat Capacity (J/kgK)	Latent Heat of Vap. (J/kg)	Thermal Diff.Coeff. (m^2/s)	Kinematic Viscosity (m^2/s)	Surface Tension (N/m)
λ_L	ρ_L	$C_{p,L}$	Δh_v	Ω	ν_L	σ_L
0.679	965	4205	2.28E+06	1.67E-07	3.16E-07	0.06082

Solid Properties				Vapour Properties		
Thermal Cond. (W/mK)	Density (kg/m^3)	Sp. Heat Capacity (J/kgK)	Solid Size (mm)	Liquid-Sat Temp. (K)	Density at 90 °C (kg/m^3)	Vapor Fraction
λ_p	ρ_p	$C_{p,p}$	d_p	T_{sat}	ρ_V	x
48.85	7850	460.5	2	373	0.424	0.1

Comparing Theoretical Convective H.t.c Contribution, α_{CB}, with Experimental Heat Transfer Results, α_{tfb}, obtained in Forced Convective (l-s) Region of 3-phase CFB

where, $$\alpha_{TFB} \approx \alpha_{CB} = \{\alpha_{LS}.F_{CB}.f(U)\}$$

Calculation Procedure

S.Steel Particles, 2 mm (d_p) **q" = 27.972, 55.944, and 83.916 kW/m^2**

Step 1 : Estimating static bed voidage, ε_{SB}, and solid fraction, ε_p

Particle Diameter (m)	Particle Density (kg/m^3)	Mass Added (kg)	Particle Vol. added (m^3)	Bed equiv. Diameter (m)	Length of bed (m)	Total Bed Volume (m^3)	Solid Fraction	Static Bed Voidage
d_p	ρ_p	m_p	V_p	D_e	L	V_T	ε_p	ε_{SB}
0.002	7850	0.25	3.1847E-05	0.01455385	1.2	0.0001996	0.1595305	0.4038971

Step 2 : Averaging α_{tfb} across forced convective region, where α_{tfb} is independent of q"

Liquid Flow rate		Liquid Velocity	Liquid Re No.	Solid T.vel (wall effect)	q" (W/m^2)	q" (W/m^2)	q" (W/m^2)	α^*_{tfb}
					27972	55944	83916	{averaged}
Q (l/m)	Q(m^3/s)	U (m/s)	Re	U_t (m/s)	α_{tfb}	α_{tfb}	α_{tfb}	(W/m^{2}K)
14	0.00023333	0.9870068	45602.2111	4.2329293	10036.10	10079.28	10125.73	10080.37
16	0.00026667	1.1280077	52116.8127	4.2329293	11402.08	11489.28	11311.38	11400.913
18	0.0003	1.2690087	58631.4143	4.2329293	12789.96	12693.84	12708.69	12730.83
20	0.00033333	1.4089964	65099.2027	4.2329293	14746.18	14722	14817	14761.727
22	0.00036667	1.5500075	71614.2691	4.2329293	13812.32	13823.07	13825.2	13820.197
24	0.0004	1.6909923	78128.125	4.2329293	13777.02	13766.17	13844.32	13795.837
26	0.00043333	1.8320051	84643.275	4.2329293	13228.61	13201.55	13179.62	13203.26

Step 3 : Calculation of convective contribution to theoretical 3-Phase H.t.c [i.e.α_{CB}]

Liquid Velocity	Archime-des No.	Particle Reynolds Number $\mathrm{Log}_{10} Re_{p\infty}$			Solid Ter. velocity	Solid T.vel (wall effect)	Fluidisa-tion index	Bed Voidage
U(m/s)	Ar	P[I]	R[I]	$Re_{p\infty}$	U_∞ (m/s)	U_t (m/s)	Z	ε
0.9870068	5605193.03	3.636247	1.00247454	4338.30757	5.8084698	4.2329293	0.6555712	0.4685796
1.1280077	5605193.03	3.636247	1.00247454	4338.30757	5.8084698	4.2329293	0.6555712	0.4831923
1.2690087	5605193.03	3.636247	1.00247454	4338.30757	5.8084698	4.2329293	0.6555712	0.4987989
1.4089964	5605193.03	3.636247	1.00247454	4338.30757	5.8084698	4.2329293	0.6555712	0.515223
1.5500075	5605193.03	3.636247	1.00247454	4338.30757	5.8084698	4.2329293	0.6555712	0.5326579
1.6909923	5605193.03	3.636247	1.00247454	4338.30757	5.8084698	4.2329293	0.6555712	0.5509438
1.8320051	5605193.03	3.636247	1.00247454	4338.30757	5.8084698	4.2329293	0.6555712	0.5700531

Collision Frequency	Friction Factor	Calc. liquid only h.t.c	Calc. solids area h.t.c	Calc. htc in L-S flow	Convective factor	$\alpha_{LS}.F_{CB}$	Convective Adj. Factor	α_{CB}
f	fi	α_c(W/m^{2}K)	α_p(W/m^{2}K)	α_{LS}(W/m^{2}K)	F_{CB}	(W/m^{2}K)	f(U)	(W/m^{2}K)
137.19163	0.02137813	8116.1314	24883.0758	32999.2071	9.8435	324827.7	0.0340933	11074.458
155.31554	0.02073328	9056.4347	26475.7162	35532.1508	9.8435	349760.73	0.0340933	11924.508
171.39669	0.0201884	9975.8806	27812.5924	37788.473	9.8435	371970.83	0.0340933	12681.725
185.04019	0.01972212	10871.003	28898.3666	39769.3699	9.8435	391469.79	0.0381879	14949.403
196.19804	0.01931104	11757.085	29756.8936	41513.9788	9.8435	408642.85	0.0350799	14335.15
204.56685	0.01894696	12629.163	30384.9053	43014.0682	9.8435	423408.98	0.0324645	13745.781
210.009	0.01862101	13489.029	30786.4219	44275.4509	9.8435	435825.4	0.0302309	13175.381

Comparing Theoretical Convective H.t.c Contribution, α_{CB}, with Experimental Heat Transfer Results, α_{tfb}, obtained in Forced Convective (l-s) Region of 3-phase CFB

where, $$\alpha_{TFB} \approx \alpha_{CB} = \{\alpha_{LS}.F_{CB}.f(U)\}$$

Calculation Procedure

S.Steel Particles, 2.5 mm (d_p) **q'' = 27.972, 55.944, and 83.916 kW/m^2**

Step 1 : Estimating static bed voidage, ε_{SB}, and solid fraction, ε_p

Particle Diameter (m)	Particle Density (kg/m^3)	Mass Added (kg)	Particle Vol. added (m^3)	Bed equiv. Diameter (m)	Length of bed (m)	Total Bed Volume (m^3)	Solid Fraction	Static Bed Voidage
d_p	ρ_p	m_p	V_p	D_e	L	V_T	ε_p	ε_{SB}
0.0025	7850	0.25	3.1847E-05	0.01455385	1.2	0.0001996	0.1595305	0.4111104

Step 2 : Averaging α_{tfb} across forced convective region, where α_{tfb} is independent of q"

Liquid Flow rate		Liquid Velocity	Liquid Re No.	Solid T.vel (wall effect)	q" (W/m^2)	q" (W/m^2)	q" (W/m^2)	α^{*}_{tfb} {averaged}
Q (l/m)	Q (m^3/s)	U (m/s)	Re	U_t (m/s)	α_{tfb}	α_{tfb}	α_{tfb}	(W/m^{2}K)
14	0.00023333	0.9870068	45602.2111	5.16136213	11663.61	11644.87	11724.00	11677.493
16	0.00026667	1.1280077	52116.8127	5.16136213	13496.76	13510.64	13653.08	13553.493
18	0.0003	1.2690087	58631.4143	5.16136213	15065.05	14976.32	15038.7	15026.69
20	0.00033333	1.4089964	65099.2027	5.16136213	16654.97	16562.03	16699.22	16638.74
22	0.00036667	1.5500075	71614.2691	5.16136213	16656.56	16672.4	16720.18	16683.047
24	0.0004	1.6909923	78128.125	5.16136213	15548.31	15400.17	15516.48	15488.32
26	0.00043333	1.8320051	84643.275	5.16136213	15316.73	15304.08	15295.15	15305.32

Step 3 : Calculation of convective contribution to theoretical 3-Phase H.t.c [i.e. α_{CB}]

Liquid Velocity	Archime-des No.	Particle Reynolds Number $\mathrm{Log}_{10} Re_{p\infty}$			Solid Ter. velocity	Solid T.vel (wall effect)	Fluidisa-tion index	Bed Voidage
U(m/s)	Ar	P[I]	R[I]	$Re_{p\infty}$	U_∞ (m/s)	U_t (m/s)	Z	ε
0.9870068	10947642.6	3.7802198	1.00264586	6044.59653	7.6654954	5.1613621	0.6544982	0.4581357
1.1280077	10947642.6	3.7802198	1.00264586	6044.59653	7.6654954	5.1613621	0.6544982	0.4687786
1.2690087	10947642.6	3.7802198	1.00264586	6044.59653	7.6654954	5.1613621	0.6544982	0.480149
1.4089964	10947642.6	3.7802198	1.00264586	6044.59653	7.6654954	5.1613621	0.6544982	0.4921183
1.5500075	10947642.6	3.7802198	1.00264586	6044.59653	7.6654954	5.1613621	0.6544982	0.5048274
1.6909923	10947642.6	3.7802198	1.00264586	6044.59653	7.6654954	5.1613621	0.6544982	0.5181599
1.8320051	10947642.6	3.7802198	1.00264586	6044.59653	7.6654954	5.1613621	0.6544982	0.5320956

Collision Frequency	Friction Factor	Calc. liquid only h.t.c	Calc. solids area h.t.c	Calc. htc in L-S flow	Convective factor	$\alpha_{LS}.F_{CB}$	Convective Adj. Factor	α_{CB}
f	fi	α_c (W/m^{2}K)	α_p (W/m^{2}K)	α_{LS} (W/m^{2}K)	F_{CB}	(W/m^{2}K)	f(U)	(W/m^{2}K)
106.64504	0.02137813	8116.1314	23396.4219	31512.5532	9.8435	310193.82	0.0426167	13219.425
122.50297	0.02073328	9056.4347	25075.6628	34132.0975	9.8435	335979.3	0.0426167	14318.317
137.40933	0.0201884	9975.8806	26557.5023	36533.3829	9.8435	359616.35	0.0426167	15325.649
151.05644	0.01972212	10871.003	27845.0967	38716.1	9.8435	381101.93	0.0465774	17750.748
163.45966	0.01931104	11757.085	28965.7253	40722.8106	9.8435	400854.99	0.0427866	17151.241
174.35528	0.01894696	12629.163	29915.5274	42544.6903	9.8435	418788.66	0.0395967	16582.66
183.61459	0.01862101	13489.029	30699.5998	44188.6289	9.8435	434970.77	0.0368723	16038.385

Appendix C.2

Comparing Calculated 3-phase Heat Transfer Coefficient, α_{TFB}, with Experimental Results, α_{tfb}, obtained in Nucleate Boiling Region of (v-l-s) Fluidised Bed

Equations

For all relevant equations, please refer to main body of thesis

Useful Values

Liquid Properties [Read at 115 °C]				
Thermal Cond. (W/mK)	Density (kg/m^3)	Sp. Heat Capacity (J/kgK)	Dynamic Viscosity (kg/m.s)	Kinematic Viscosity (m^2/s)
λ_L	ρ_L	$C_{p,L}$	μ_L	ν_L
0.686	946.66	4239	2.42E-04	2.56E-07

Liquid Properties [Read at 90 °C Subcooled Bulk Temperature]						
Thermal Cond. (W/mK)	Density (kg/m^3)	Sp. Heat Capacity (J/kgK)	Latent Heat of Vap. (J/kg)	Thermal Diff.Coeff. (m^2/s)	Kinematic Viscosity (m^2/s)	Surface Tension (N/m)
λ_L	ρ_L	$C_{p,L}$	Δh_v	Ω	ν_L	σ_L
0.679	965	4205	2.28E+06	1.67E-07	3.16E-07	0.06082

Solid Properties				Vapour Properties		
Thermal Cond. (W/mK)	Density (kg/m^3)	Sp. Heat Capacity (J/kgK)	Solid Size (mm)	Liquid-Sat Temp. (K)	Density at 90 °C (kg/m^3)	Vapor Fraction
λ_p	ρ_p	$C_{p,p}$	d_p	T_{sat}	ρ_V	x
48.85	7850	460.5	2	373	0.424	0.1

Correction Factors and Exponents						
Correction Function (dim.less)	Roughnes Cor. Factor (dim.less)	Diameter Cor. Factor (dim.less)	Fluid Molecular Weight Cor. Factor (dimensionless)			Transition exponent (dim.less)
			method a	method b	method c	
$f(m,x)$	$F(Ra)$	$F(d)$	$F_1(M)$	$F_2(M)$	$F_3(M)$	t_R
1	1	0.8595257	0.7856445	0.952184	0.72	3

Comparing Calculated 3-phase Heat Transfer Coefficient, α_{TFB}, with Experimental Results, α_{tfb}, obtained in Nucleate Boiling Region of (v-l-s) Fluidised Bed

note $$\alpha_{TFB} = \left[(\alpha_{NB})^{t_R} + (\alpha_{CB})^{t_R} \right]^{1/t_R} = \left[\left\{ (\alpha_{npbp} . F_{NB})^{b_E} \right\}^{t_R} + \left\{ \alpha_{LS} . F_{CB} . f(U) \right\}^{t_R} \right]^{1/t_R}$$

Calculation Procedure

S.Steel Particles, 2 mm (d_p) $q'' = 111.888$ kW/m^2

Step 1 : Recall calculation of convective contribution to theoretical 3-Phase H.t.c [i.e.α_{CB}]

Liquid Velocity	Liquid Re No.	Particle Reynolds Number $\mathrm{Log}_{10} Re_{p\infty}$			Solid Ter. velocity	Solid T.vel (wall effect)	Fluidisation index	Bed Voidage
U (m/s)	Re	P [I]	R [I]	$Re_{p\infty}$	U_∞ (m/s)	U_t (m/s)	Z	ε
0.9870068	45602.211	3.63624699	1.00247454	4338.307572	5.808469778	4.2329293	0.6555712	0.4685796
1.1280077	52116.813	3.63624699	1.00247454	4338.307572	5.808469778	4.2329293	0.6555712	0.4831923
1.2690087	58631.414	3.63624699	1.00247454	4338.307572	5.808469778	4.2329293	0.6555712	0.4987989
1.4089964	65099.203	3.63624699	1.00247454	4338.307572	5.808469778	4.2329293	0.6555712	0.515223
1.5500075	71614.269	3.63624699	1.00247454	4338.307572	5.808469778	4.2329293	0.6555712	0.5326579
1.6909923	78128.125	3.63624699	1.00247454	4338.307572	5.808469778	4.2329293	0.6555712	0.5509438
1.8320051	84643.275	3.63624699	1.00247454	4338.307572	5.808469778	4.2329293	0.6555712	0.5700531

Collision Frequency	Friction Factor	Calc. liquid only h.t.c	Calc. solids area h.t.c	Calc. htc in L-S flow	Convective factor	$\alpha_{LS}.F_{CB}$	Convective Adj. Factor	α_{CB}
f	fi	α_c (W/m^{2}K)	α_p (W/m^{2}K)	α_{LS} (W/m^{2}K)	F_{CB}	(W/m^{2}K)	f(U)	(W/m^{2}K)
137.19163	0.0213781	8116.13136	24883.0758	32999.20711	9.8435	324827.7	0.0340933	11074.458
155.31554	0.0207333	9056.43467	26475.7162	35532.15084	9.8435	349760.73	0.0340933	11924.508
171.39669	0.0201884	9975.8806	27812.5924	37788.47304	9.8435	371970.83	0.0340933	12681.725
185.04019	0.0197221	10871.0033	28898.3666	39769.36986	9.8435	391469.79	0.0381879	14949.403
196.19804	0.019311	11757.0852	29756.8936	41513.97882	9.8435	408642.85	0.0350799	14335.15
204.56685	0.018947	12629.1629	30384.9053	43014.06815	9.8435	423408.98	0.0324645	13745.781
210.009	0.018621	13489.0291	30786.4219	44275.45094	9.8435	435825.4	0.0302309	13175.381

Step 2 : Computation of nucleate boiling correction factor,F_{NB}, based on $F_{1\ to\ 3}(M)$

Liquid Velocity	Liquid Reynolds no.	Fluid Molecular Weight Cor. Factor (dimensionless)			Pressure Cor. Factor (dim.less)	Reduced Pressure (bar)	Exponent of nucleate flow boiling	Normalised Heat Flux (W/m^2)
		method a	method b	method c				
U (m/s)	Re	$F_1(M)$	$F_2(M)$	$F_3(M)$	F_{pr}	P_R^*	r	q''_o
0.9870068	45602.211	0.7856445	0.95218398	0.72	0.248298878	0.0045323	0.6992037	150000
1.1280077	52116.813	0.7856445	0.95218398	0.72	0.248298878	0.0045323	0.6992037	150000
1.2690087	58631.414	0.7856445	0.95218398	0.72	0.248298878	0.0045323	0.6992037	150000
1.4089964	65099.203	0.7856445	0.95218398	0.72	0.248298878	0.0045323	0.6992037	150000
1.5500075	71614.269	0.7856445	0.95218398	0.72	0.248298878	0.0045323	0.6992037	150000
1.6909923	78128.125	0.7856445	0.95218398	0.72	0.248298878	0.0045323	0.6992037	150000
1.8320051	84643.275	0.7856445	0.95218398	0.72	0.248298878	0.0045323	0.6992037	150000

Heat Flux (W/m^2)	Diameter Cor. Fact. (dim.less)	Critical Pressure (bar)	System Pressure (bar)	Nucleate Boiling Correction Factor (dimensionless)		
				method a	method b	method c
q''	$F(d)$	P_{CR}^*	P^*	$F_{NB,1}$	$F_{NB,2}$	$F_{NB,3}$
111888	0.8595257	220.64	1	0.13659841	0.165554289	0.1251849
111888	0.8595257	220.64	1	0.13659841	0.165554289	0.1251849
111888	0.8595257	220.64	1	0.13659841	0.165554289	0.1251849
111888	0.8595257	220.64	1	0.13659841	0.165554289	0.1251849
111888	0.8595257	220.64	1	0.13659841	0.165554289	0.1251849
111888	0.8595257	220.64	1	0.13659841	0.165554289	0.1251849
111888	0.8595257	220.64	1	0.13659841	0.165554289	0.1251849

Comparing Calculated 3-phase Heat Transfer Coefficient, α_{TFB}, with Experimental Results, α_{tfb}, obtained in Nucleate Boiling Region of (v-l-s) Fluidised Bed

note $$\alpha_{TFB} = \left[(\alpha_{NB})^{t_R} + (\alpha_{CB})^{t_R} \right]^{1/t_R} = \left[\left\{ (\alpha_{npbp} . F_{NB})^{b_E} \right\}^{t_R} + \left\{ \alpha_{LS} . F_{CB} . f(U) \right\}^{t_R} \right]^{1/t_R}$$

Calculation Procedure

S.Steel Particles, 2 mm (d_p) $q'' = 111.888$ kW/m^2

Step 3 : Determining nucleate boiling contribution to theoretical 3-Phase H.t.c [α_{NB}]

Liquid Velocity (m/s)	Liquid Reynolds no.	Solid Fraction	$\left(\frac{\lambda_M}{\lambda_L}\right)^{1.7} = [(1-2J)/(1+J)]^{1.7} = Y'' = \frac{\alpha_{npb,p}}{\alpha_{npb}}$		Heat Flux (W/m^2)	Bubble Diameter (m)
U	Re	ε_p	J	Y''	q''	d_b
0.9870068	45602.211	0.16801561	-0.161199011	2.168181013	111888	0.0023556
1.1280077	52116.813	0.16801561	-0.161199011	2.168181013	111888	0.0023556
1.2690087	58631.414	0.16801561	-0.161199011	2.168181013	111888	0.0023556
1.4089964	65099.203	0.16801561	-0.161199011	2.168181013	111888	0.0023556
1.5500075	71614.269	0.16801561	-0.161199011	2.168181013	111888	0.0023556
1.6909923	78128.125	0.16801561	-0.161199011	2.168181013	111888	0.0023556
1.8320051	84643.275	0.16801561	-0.161199011	2.168181013	111888	0.0023556

Thermal Diffu.Coef. (m^2/s)	Htc in pure liquid pool (W/m^{2}K)	Htc in pool of particles (W/m^{2}K)	Nucleate Boiling Correction Factor (dimensionless)			Nucleate Boiling Contibution (W/m^{2}K)		
			method a	method b	method c	method a	method b	method c
Ω	α_{npb}	$\alpha_{npb,p}$	$F_{NB,1}$	$F_{NB,2}$	$F_{NB,3}$	$\alpha_{NB,1}$	$\alpha_{NB,2}$	$\alpha_{NB,3}$
1.673E-07	9709.4123	21051.7635	0.13659841	0.165554289	0.125184934	2875.6374	3485.2097	2635.3636
1.673E-07	9709.4123	21051.7635	0.13659841	0.165554289	0.125184934	2875.6374	3485.2097	2635.3636
1.673E-07	9709.4123	21051.7635	0.13659841	0.165554289	0.125184934	2875.6374	3485.2097	2635.3636
1.673E-07	9709.4123	21051.7635	0.13659841	0.165554289	0.125184934	2875.6374	3485.2097	2635.3636
1.673E-07	9709.4123	21051.7635	0.13659841	0.165554289	0.125184934	2875.6374	3485.2097	2635.3636
1.673E-07	9709.4123	21051.7635	0.13659841	0.165554289	0.125184934	2875.6374	3485.2097	2635.3636
1.673E-07	9709.4123	21051.7635	0.13659841	0.165554289	0.125184934	2875.6374	3485.2097	2635.3636

Step 4 : Predicted (v-l-s) H.t.c, [α_{TFB}], versus measured data, [α_{tfb}]

Liquid Velocity (m/s)	Liquid Reynolds no.	Boiling Enhancement Exponent	Theoretical 3-Phase Htc (W/m^{2}K)			Experimental 3-Phase Heat Transfer Coefficient (W/m^2.K)
			method a	method b	method c	
U	Re	b_E	$\alpha_{TFB,1}$	$\alpha_{TFB,2}$	$\alpha_{TFB,3}$	α_{tfb}
0.9870068	45602.211	1.05	11283.8976	11452.478	11234.27723	11134.83
1.1280077	52116.813	1.05	12105.8188	12252.69481	12062.74389	11896.28
1.2690087	58631.414	1.05	12842.4345	12973.19852	12804.1814	13047.90
1.4089964	65099.203	1.05	15065.6208	15161.00507	15037.85607	14945.92
1.5500075	71614.269	1.05	14461.4104	14564.84685	14431.26985	14152.23
1.6909923	78128.125	1.05	13882.9407	13995.0732	13850.22713	14358.60
1.8320051	84643.275	1.05	13324.4753	13446.07705	13288.95102	13995.30

Comparing Calculated 3-phase Heat Transfer Coefficient, α_{TFB}, with Experimental Results, α_{tfb}, obtained in Nucleate Boiling Region of (v-l-s) Fluidised Bed

note $\alpha_{TFB} = \left[(\alpha_{NB})^{t_R} + (\alpha_{CB})^{t_R} \right]^{1/t_R} = \left[\left\{ (\alpha_{npbp}.F_{NB})^{b_E} \right\}^{t_R} + \left\{ \alpha_{LS}.F_{CB}.f(U) \right\}^{t_R} \right]^{1/t_R}$

Calculation Procedure

S.Steel Particles, 2 mm (d_p) $q'' = 167.832$ kW/m^2

Step 1 : Recall calculation of convective contribution to theoretical 3-Phase H.t.c [i.e.α_{CB}]

Liquid Velocity	Liquid Re No.	Particle Reynolds Number $\mathrm{Log}_{10} Re_{p\infty}$			Solid Ter. velocity	Solid T.vel (wall effect)	Fluidisation index	Bed Voidage
U(m/s)	Re	P[I]	R[I]	$Re_{p\infty}$	U_∞ (m/s)	U_t (m/s)	Z	ε
0.987	45602.211	3.636247	1.0024745	4338.3076	5.8084698	4.2329293	0.6555712	0.4685796
1.128	52116.813	3.636247	1.0024745	4338.3076	5.8084698	4.2329293	0.6555712	0.4831923
1.269	58631.414	3.636247	1.0024745	4338.3076	5.8084698	4.2329293	0.6555712	0.4987989
1.409	65099.203	3.636247	1.0024745	4338.3076	5.8084698	4.2329293	0.6555712	0.515223
1.55	71614.269	3.636247	1.0024745	4338.3076	5.8084698	4.2329293	0.6555712	0.5326579
1.691	78128.125	3.636247	1.0024745	4338.3076	5.8084698	4.2329293	0.6555712	0.5509438
1.832	84643.275	3.636247	1.0024745	4338.3076	5.8084698	4.2329293	0.6555712	0.5700531

Collision Frequency	Friction Factor	Calc. liquid only h.t.c	Calc. solids area h.t.c	Calc. htc in L-S flow	Convective factor	$\alpha_{LS}.F_{CB}$	Convective Adj. Factor	α_{CB}
f	fi	α_c (W/m^{2}K)	α_p (W/m^{2}K)	α_{LS} (W/m^{2}K)	F_{CB}	(W/m^{2}K)	f(U)	(W/m^{2}K)
137.19	0.0213781	8116.1314	24883.076	32999.207	9.8435	324827.7	0.0340933	11074.458
155.32	0.0207333	9056.4347	26475.716	35532.151	9.8435	349760.73	0.0340933	11924.508
171.4	0.0201884	9975.8806	27812.592	37788.473	9.8435	371970.83	0.0340933	12681.725
185.04	0.0197221	10871.003	28898.367	39769.37	9.8435	391469.79	0.0381879	14949.403
196.2	0.019311	11757.085	29756.894	41513.979	9.8435	408642.85	0.0350799	14335.15
204.57	0.018947	12629.163	30384.905	43014.068	9.8435	423408.98	0.0324645	13745.781
210.01	0.018621	13489.029	30786.422	44275.451	9.8435	435825.4	0.0302309	13175.381

Step 2 : Computation of nucleate boiling correction factor,F_{NB}, based on $F_{1\ to\ 3}(M)$

Liquid Velocity	Liquid Reynolds no.	Fluid Molecular Weight Cor. Factor (dimensionless)			Pressure Cor. Factor (dim.less)	Reduced Pressure (bar)	Exponent of nucleate flow boiling	Normalised Heat Flux (W/m^2)
		method a	method b	method c				
U(m/s)	Re	$F_1(M)$	$F_2(M)$	$F_3(M)$	F_{pr}	P_R^*	r	q''_o
0.987	45602.211	0.7856445	0.952184	0.72	0.2482989	0.0045323	0.6992037	150000
1.128	52116.813	0.7856445	0.952184	0.72	0.2482989	0.0045323	0.6992037	150000
1.269	58631.414	0.7856445	0.952184	0.72	0.2482989	0.0045323	0.6992037	150000
1.409	65099.203	0.7856445	0.952184	0.72	0.2482989	0.0045323	0.6992037	150000
1.55	71614.269	0.7856445	0.952184	0.72	0.2482989	0.0045323	0.6992037	150000
1.691	78128.125	0.7856445	0.952184	0.72	0.2482989	0.0045323	0.6992037	150000
1.832	84643.275	0.7856445	0.952184	0.72	0.2482989	0.0045323	0.6992037	150000

Heat Flux (W/m^2)	Diameter Cor. Fact. (dim.less)	Critical Pressure (bar)	System Pressure (bar)	Nucleate Boiling Correction Factor (dimensionless)		
				method a	method b	method c
q''	$F(d)$	P_{CR}^*	P^*	$F_{NB,1}$	$F_{NB,2}$	$F_{NB,3}$
167832	0.8595257	220.64	1	0.1813716	0.2198184	0.1662171
167832	0.8595257	220.64	1	0.1813716	0.2198184	0.1662171
167832	0.8595257	220.64	1	0.1813716	0.2198184	0.1662171
167832	0.8595257	220.64	1	0.1813716	0.2198184	0.1662171
167832	0.8595257	220.64	1	0.1813716	0.2198184	0.1662171
167832	0.8595257	220.64	1	0.1813716	0.2198184	0.1662171
167832	0.8595257	220.64	1	0.1813716	0.2198184	0.1662171

Comparing Calculated 3-phase Heat Transfer Coefficient, α_{TFB}, with Experimental Results, α_{tfb}, obtained in Nucleate Boiling Region of (v-l-s) Fluidised Bed

note $$\alpha_{TFB} = \left[(\alpha_{NB})^{t_R} + (\alpha_{CB})^{t_R} \right]^{1/t_R} = \left[\left\{ (\alpha_{npbp} . F_{NB})^{b_E} \right\}^{t_R} + \{ \alpha_{LS} . F_{CB} . f(U) \}^{t_R} \right]^{1/t_R}$$

Calculation Procedure

S.Steel Particles, 2 mm (d_p) $q'' = 167.832$ kW/m^2

Step 3 : Determining nucleate boiling contribution to theoretical 3-Phase H.t.c [α_{NB}]

Liquid Velocity (m/s)	Liquid Reynolds no.	Solid Fraction	$\left(\frac{\lambda_M}{\lambda_L}\right)^{1.7} = [(1-2J)/(1+J)]^{1.7} = Y'' = \frac{\alpha_{npb,p}}{\alpha_{npb}}$		Heat Flux	Bubble Diameter
U	Re	ε_p	J	Y''	q'' (W/m^2)	d_b (m)
0.987	45602.211	0.1680156	-0.161199011	2.168181013	167832	0.0023556
1.128	52116.813	0.1680156	-0.161199011	2.168181013	167832	0.0023556
1.269	58631.414	0.1680156	-0.161199011	2.168181013	167832	0.0023556
1.409	65099.203	0.1680156	-0.161199011	2.168181013	167832	0.0023556
1.55	71614.269	0.1680156	-0.161199011	2.168181013	167832	0.0023556
1.691	78128.125	0.1680156	-0.161199011	2.168181013	167832	0.0023556
1.832	84643.275	0.1680156	-0.161199011	2.168181013	167832	0.0023556

Thermal Diffu.Coe (m^2/s)	Htc in pure liquid pool (W/m^{2}K)	Htc in pool of particles (W/m^{2}K)	Nucleate Boiling Correction Factor (dimensionless)			Nucleate Boiling Contibution (W/m^{2}K)		
			method a	method b	method c	method a	method b	method c
Ω	α_{npb}	$\alpha_{npb,p}$	$F_{NB,1}$	$F_{NB,2}$	$F_{NB,3}$	$\alpha_{NB,1}$	$\alpha_{NB,2}$	$\alpha_{NB,3}$
2E-07	12760.816	27667.759	0.1813716	0.2198184	0.1662171	5018.146	6081.8834	4598.855
2E-07	12760.816	27667.759	0.1813716	0.2198184	0.1662171	5018.146	6081.8834	4598.855
2E-07	12760.816	27667.759	0.1813716	0.2198184	0.1662171	5018.146	6081.8834	4598.855
2E-07	12760.816	27667.759	0.1813716	0.2198184	0.1662171	5018.146	6081.8834	4598.855
2E-07	12760.816	27667.759	0.1813716	0.2198184	0.1662171	5018.146	6081.8834	4598.855
2E-07	12760.816	27667.759	0.1813716	0.2198184	0.1662171	5018.146	6081.8834	4598.855
2E-07	12760.816	27667.759	0.1813716	0.2198184	0.1662171	5018.146	6081.8834	4598.855

Step 4 : Predicted (v-l-s) H.t.c, [α_{TFB}], versus measured data, [α_{tfb}]

Liquid Velocity (m/s)	Liquid Reynolds no.	Boiling Enhancemen Exponent	Theoretical 3-Phase Htc (W/m^{2}K)			Experimental 3-Phase Heat Transfer Coefficient (W/m^2.K)
			method a	method b	method c	
U	Re	b_E	$\alpha_{TFB,1}$	$\alpha_{TFB,2}$	$\alpha_{TFB,3}$	α_{tfb}
0.987	45602.211	1.05	12191.043	12985.07	11941.466	13891.09
1.128	52116.813	1.05	12905.092	13620.449	12683.101	14284.68
1.269	58631.414	1.05	13559.759	14212.375	13359.172	15010.61
1.409	65099.203	1.05	15597.515	16098.597	15446.695	16533.23
1.55	71614.269	1.05	15036.155	15573.43	14873.677	16081.89
1.691	78128.125	1.05	14503.538	15078.763	14328.689	15777.41
1.832	84643.275	1.05	13994.493	14609.712	13806.432	15689.35

Comparing Calculated 3-phase Heat Transfer Coefficient, α_{TFB}, with Experimental Results, α_{tfb}, obtained in Nucleate Boiling Region of (v-l-s) Fluidised Bed

note $$\alpha_{TFB} = \left[(\alpha_{NB})^{t_R} + (\alpha_{CB})^{t_R} \right]^{1/t_R} = \left[\left\{ (\alpha_{npbp}.F_{NB})^{b_E} \right\}^{t_R} + \left\{ \alpha_{LS}.F_{CB}.f(U) \right\}^{t_R} \right]^{1/t_R}$$

Calculation Procedure

S.Steel Particles, 2 mm (d_p) $q'' = 223.776$ kW/m^2

Step 1 : Recall calculation of convective contribution to theoretical 3-Phase H.t.c [i.e.α_{CB}]

Liquid Velocity	Liquid Re No.	Particle Reynolds Number $\mathrm{Log}_{10} Re_{p\infty}$			Solid Ter. velocity	Solid T.vel (wall effect)	Fluidisation index	Bed Voidage
U(m/s)	Re	P[I]	R[I]	$Re_{p\infty}$	U_∞ (m/s)	U_t (m/s)	Z	ε
0.9870068	45602.211	3.636247	1.0024745	4338.3076	5.8084698	4.2329293	0.6555712	0.4685796
1.1280077	52116.813	3.636247	1.0024745	4338.3076	5.8084698	4.2329293	0.6555712	0.4831923
1.2690087	58631.414	3.636247	1.0024745	4338.3076	5.8084698	4.2329293	0.6555712	0.4987989
1.4089964	65099.203	3.636247	1.0024745	4338.3076	5.8084698	4.2329293	0.6555712	0.515223
1.5500075	71614.269	3.636247	1.0024745	4338.3076	5.8084698	4.2329293	0.6555712	0.5326579
1.6909923	78128.125	3.636247	1.0024745	4338.3076	5.8084698	4.2329293	0.6555712	0.5509438
1.8320051	84643.275	3.636247	1.0024745	4338.3076	5.8084698	4.2329293	0.6555712	0.5700531

Collision Frequency	Friction Factor	Calc. liquid only h.t.c	Calc. solids area h.t.c	Calc. htc in L-S flow	Convective factor	$\alpha_{LS}.F_{CB}$	Convective Adj. Factor	α_{CB}
f	fi	α_c(W/m^{2}K)	α_p(W/m^{2}K)	α_{LS}(W/m^{2}K)	F_{CB}	(W/m^{2}K)	f(U)	(W/m^{2}K)
137.19163	0.0213781	8116.1314	24883.076	32999.207	9.8435	324827.7	0.0340933	11074.458
155.31554	0.0207333	9056.4347	26475.716	35532.151	9.8435	349760.73	0.0340933	11924.508
171.39669	0.0201884	9975.8806	27812.592	37788.473	9.8435	371970.83	0.0340933	12681.725
185.04019	0.0197221	10871.003	28898.367	39769.37	9.8435	391469.79	0.0381879	14949.403
196.19804	0.019311	11757.085	29756.894	41513.979	9.8435	408642.85	0.0350799	14335.15
204.56685	0.018947	12629.163	30384.905	43014.068	9.8435	423408.98	0.0324645	13745.781
210.009	0.018621	13489.029	30786.422	44275.451	9.8435	435825.4	0.0302309	13175.381

Step 2 : Computation of nucleate boiling correction factor,F_{NB}, based on $F_{1\ to\ 3}(M)$

Liquid Velocity	Liquid Reynolds no.	Fluid Molecular Weight Cor. Factor (dimensionless)			Pressure Cor. Factor (dim.less)	Reduced Pressure (bar)	Exponent of nucleate flow boiling	Normalised Heat Flux (W/m^2)
		method a	method b	method c				
U(m/s)	Re	$F_1(M)$	$F_2(M)$	$F_3(M)$	F_{pr}	P_R^*	r	q''_o
0.9870068	45602.211	0.7856445	0.952184	0.72	0.2482989	0.0045323	0.6992037	150000
1.1280077	52116.813	0.7856445	0.952184	0.72	0.2482989	0.0045323	0.6992037	150000
1.2690087	58631.414	0.7856445	0.952184	0.72	0.2482989	0.0045323	0.6992037	150000
1.4089964	65099.203	0.7856445	0.952184	0.72	0.2482989	0.0045323	0.6992037	150000
1.5500075	71614.269	0.7856445	0.952184	0.72	0.2482989	0.0045323	0.6992037	150000
1.6909923	78128.125	0.7856445	0.952184	0.72	0.2482989	0.0045323	0.6992037	150000
1.8320051	84643.275	0.7856445	0.952184	0.72	0.2482989	0.0045323	0.6992037	150000

Heat Flux	Diameter Cor. Fact.	Critical Pressure	System Pressure	Nucleate Boiling Correction Factor (dimensionless)		
(W/m^2)	(dim.less)	(bar)	(bar)	method a	method b	method c
q''	$F(d)$	P_{CR}^*	P^*	$F_{NB,1}$	$F_{NB,2}$	$F_{NB,3}$
223776	0.8595257	220.64	1	0.2217823	0.2687953	0.2032513
223776	0.8595257	220.64	1	0.2217823	0.2687953	0.2032513
223776	0.8595257	220.64	1	0.2217823	0.2687953	0.2032513
223776	0.8595257	220.64	1	0.2217823	0.2687953	0.2032513
223776	0.8595257	220.64	1	0.2217823	0.2687953	0.2032513
223776	0.8595257	220.64	1	0.2217823	0.2687953	0.2032513
223776	0.8595257	220.64	1	0.2217823	0.2687953	0.2032513

Comparing Calculated 3-phase Heat Transfer Coefficient, α_{TFB}, with Experimental Results, α_{tfb}, obtained in Nucleate Boiling Region of (v-l-s) Fluidised Bed

note $$\alpha_{TFB} = \left[(\alpha_{NB})^{t_R} + (\alpha_{CB})^{t_R} \right]^{1/t_R} = \left[\left\{ (\alpha_{npbp} . F_{NB})^{b_E} \right\}^{t_R} + \left\{ \alpha_{LS} . F_{CB} . f(U) \right\}^{t_R} \right]^{1/t_R}$$

Calculation Procedure

S.Steel Particles, 2 mm (d_p) $q'' = 223.776$ kW/m^2

Step 3 : Determining nucleate boiling contribution to theoretical 3-Phase H.t.c [α_{NB}]

Liquid Velocity (m/s)	Liquid Reynolds no.	Solid Fraction	$\left(\frac{\lambda_M}{\lambda_L}\right)^{1.7} = [(1-2J)/(1+J)]^{1.7} = Y'' = \frac{\alpha_{npb,p}}{\alpha_{npb}}$		Heat Flux	Bubble Diameter
U	Re	ε_p	J	Y''	(W/m^2) q''	(m) d_b
0.9870068	45602.211	0.1680156	-0.161199011	2.168181013	223776	0.0023556
1.1280077	52116.813	0.1680156	-0.161199011	2.168181013	223776	0.0023556
1.2690087	58631.414	0.1680156	-0.161199011	2.168181013	223776	0.0023556
1.4089964	65099.203	0.1680156	-0.161199011	2.168181013	223776	0.0023556
1.5500075	71614.269	0.1680156	-0.161199011	2.168181013	223776	0.0023556
1.6909923	78128.125	0.1680156	-0.161199011	2.168181013	223776	0.0023556
1.8320051	84643.275	0.1680156	-0.161199011	2.168181013	223776	0.0023556

Thermal Diffu.Coef. (m^2/s)	Htc in pure liquid pool (W/m^2K)	Htc in pool of particles (W/m^2K)	Nucleate Boiling Correction Factor (dimensionless)			Nucleate Boiling Contibution (W/m^2K)		
			method a	method b	method c	method a	method b	method c
Ω	α_{npb}	$\alpha_{npb,p}$	$F_{NB,1}$	$F_{NB,2}$	$F_{NB,3}$	$\alpha_{NB,1}$	$\alpha_{NB,2}$	$\alpha_{NB,3}$
1.673E-07	15491.275	33587.888	0.2217823	0.2687953	0.2032513	7449.1999	9028.2676	6826.7822
1.673E-07	15491.275	33587.888	0.2217823	0.2687953	0.2032513	7449.1999	9028.2676	6826.7822
1.673E-07	15491.275	33587.888	0.2217823	0.2687953	0.2032513	7449.1999	9028.2676	6826.7822
1.673E-07	15491.275	33587.888	0.2217823	0.2687953	0.2032513	7449.1999	9028.2676	6826.7822
1.673E-07	15491.275	33587.888	0.2217823	0.2687953	0.2032513	7449.1999	9028.2676	6826.7822
1.673E-07	15491.275	33587.888	0.2217823	0.2687953	0.2032513	7449.1999	9028.2676	6826.7822
1.673E-07	15491.275	33587.888	0.2217823	0.2687953	0.2032513	7449.1999	9028.2676	6826.7822

Step 4 : Predicted (v-l-s) H.t.c, [α_{TFB}], versus measured data, [α_{tfb}]

Liquid Velocity (m/s)	Liquid Reynolds no.	Boiling Enhancemen Exponent	Theoretical 3-Phase Htc (W/m^2K)			Experimental 3-Phase Heat Transfer Coefficient ($W/m^2.K$)
			method a	method b	method c	
U	Re	b_E	$\alpha_{TFB,1}$	$\alpha_{TFB,2}$	$\alpha_{TFB,3}$	α_{tfb}
0.9870068	45602.211	1.05	14313.865	16189.499	13669.732	16534.74
1.1280077	52116.813	1.05	14842.957	16607.678	14246.86	16950.56
1.2690087	58631.414	1.05	15346.119	17013.377	14790.706	17018.37
1.4089964	65099.203	1.05	17002.851	18396.565	16554.881	18227.72
1.5500075	71614.269	1.05	16534.465	17998.845	16059.621	17988.30
1.6909923	78128.125	1.05	16098.001	17632.755	15595.804	17633.64
1.8320051	84643.275	1.05	15688.822	17293.828	15158.699	17590.12

Comparing Calculated 3-phase Heat Transfer Coefficient, α_{TFB}, with Experimental Results, α_{tfb}, obtained in Nucleate Boiling Region of (v-l-s) Fluidised Bed

note $$\alpha_{TFB} = \left[(\alpha_{NB})^{t_R} + (\alpha_{CB})^{t_R} \right]^{1/t_R} = \left[\left\{ (\alpha_{npbp}.F_{NB})^{b_E} \right\}^{t_R} + \{\alpha_{LS}.F_{CB}.f(U)\}^{t_R} \right]^{1/t_R}$$

Calculation Procedure

S.Steel Particles, 2 mm (d_p) $q'' = 279.720$ kW/m^2

Step 1 : Recall calculation of convective contribution to theoretical 3-Phase H.t.c [i.e.α_{CB}]

Liquid Velocity	Liquid Re No.	Particle Reynolds Number $\mathrm{Log}_{10} Re_{p\infty}$			Solid Ter. velocity	Solid T.vel (wall effect)	Fluidisation index	Bed Voidage
U (m/s)	Re	P[I]	R[I]	$Re_{p\infty}$	U_∞ (m/s)	U_t (m/s)	Z	ε
0.9870068	45602.211	3.636247	1.0024745	4338.3076	5.8084698	4.2329293	0.6555712	0.4685796
1.1280077	52116.813	3.636247	1.0024745	4338.3076	5.8084698	4.2329293	0.6555712	0.4831923
1.2690087	58631.414	3.636247	1.0024745	4338.3076	5.8084698	4.2329293	0.6555712	0.4987989
1.4089964	65099.203	3.636247	1.0024745	4338.3076	5.8084698	4.2329293	0.6555712	0.515223
1.5500075	71614.269	3.636247	1.0024745	4338.3076	5.8084698	4.2329293	0.6555712	0.5326579
1.6909923	78128.125	3.636247	1.0024745	4338.3076	5.8084698	4.2329293	0.6555712	0.5509438
1.8320051	84643.275	3.636247	1.0024745	4338.3076	5.8084698	4.2329293	0.6555712	0.5700531

Collision Frequency	Friction Factor	Calc. liquid only h.t.c	Calc. solids area h.t.c	Calc. htc in L-S flow	Convective factor	$\alpha_{LS}.F_{CB}$	Convective Adj. Factor	α_{CB}
f	fi	α_c (W/m^{2}K)	α_p (W/m^{2}K)	α_{LS} (W/m^{2}K	F_{CB}	(W/m^{2}K)	f(U)	(W/m^{2}K)
137.19163	0.0213781	8116.1314	24883.076	32999.207	9.8435	324827.7	0.0340933	11074.458
155.31554	0.0207333	9056.4347	26475.716	35532.151	9.8435	349760.73	0.0340933	11924.508
171.39669	0.0201884	9975.8806	27812.592	37788.473	9.8435	371970.83	0.0340933	12681.725
185.04019	0.0197221	10871.003	28898.367	39769.37	9.8435	391469.79	0.0381879	14949.403
196.19804	0.019311	11757.085	29756.894	41513.979	9.8435	408642.85	0.0350799	14335.15
204.56685	0.018947	12629.163	30384.905	43014.068	9.8435	423408.98	0.0324645	13745.781
210.009	0.018621	13489.029	30786.422	44275.451	9.8435	435825.4	0.0302309	13175.381

Step 2 : Computation of nucleate boiling correction factor,F_{NB}, based on $F_{1\ to\ 3}(M)$

Liquid Velocity	Liquid Reynolds no.	Fluid Molecular Weight Cor. Factor (dimensionless)			Pressure Cor. Factor (dim.less)	Reduced Pressure (bar)	Exponent of nucleate flow boiling	Normalised Heat Flux (W/m^2)
		method a	method b	method c				
U (m/s)	Re	$F_1(M)$	$F_2(M)$	$F_3(M)$	F_{pr}	P_R^*	r	q''_o
0.9870068	45602.211	0.7856445	0.952184	0.72	0.2482989	0.0045323	0.6992037	150000
1.1280077	52116.813	0.7856445	0.952184	0.72	0.2482989	0.0045323	0.6992037	150000
1.2690087	58631.414	0.7856445	0.952184	0.72	0.2482989	0.0045323	0.6992037	150000
1.4089964	65099.203	0.7856445	0.952184	0.72	0.2482989	0.0045323	0.6992037	150000
1.5500075	71614.269	0.7856445	0.952184	0.72	0.2482989	0.0045323	0.6992037	150000
1.6909923	78128.125	0.7856445	0.952184	0.72	0.2482989	0.0045323	0.6992037	150000
1.8320051	84643.275	0.7856445	0.952184	0.72	0.2482989	0.0045323	0.6992037	150000

Heat Flux	Diameter Cor. Fact.	Critical Pressure	System Pressure	Nucleate Boiling Correction Factor (dimensionless)		
(W/m^2)	(dim.less)	(bar)	(bar)	method a	method b	method c
q''	$F(d)$	P_{CR}^*	P^*	$F_{NB,1}$	$F_{NB,2}$	$F_{NB,3}$
279720	0.8595257	220.64	1	0.2592309	0.3141822	0.2375709
279720	0.8595257	220.64	1	0.2592309	0.3141822	0.2375709
279720	0.8595257	220.64	1	0.2592309	0.3141822	0.2375709
279720	0.8595257	220.64	1	0.2592309	0.3141822	0.2375709
279720	0.8595257	220.64	1	0.2592309	0.3141822	0.2375709
279720	0.8595257	220.64	1	0.2592309	0.3141822	0.2375709
279720	0.8595257	220.64	1	0.2592309	0.3141822	0.2375709

Comparing Calculated 3-phase Heat Transfer Coefficient, α_{TFB}, with Experimental Results, α_{tfb}, obtained in Nucleate Boiling Region of (v-l-s) Fluidised Bed

note $$\alpha_{TFB} = \left[(\alpha_{NB})^{t_R} + (\alpha_{CB})^{t_R} \right]^{1/t_R} = \left[\left\{ (\alpha_{npbp}.F_{NB})^{b_E} \right\}^{t_R} + \left\{ \alpha_{LS}.F_{CB}.f(U) \right\}^{t_R} \right]^{1/t_R}$$

Calculation Procedure

S.Steel Particles, 2 mm (d_p) $q'' = 279.720\ kW/m^2$

Step 3 : Determining nucleate boiling contribution to theoretical 3-Phase H.t.c [α_{NB}]

Liquid Velocity (m/s)	Liquid Reynolds no.	Solid Fraction	$\left(\frac{\lambda_M}{\lambda_L}\right)^{1.7} = [(1-2J)/(1+J)]^{1.7} = Y'' = \frac{\alpha_{npb,p}}{\alpha_{npb}}$		Heat Flux (W/m^2)	Bubble Diameter (m)
U	Re	ε_p	J	Y''	q''	d_b
0.9870068	45602.211	0.1680156	-0.161199011	2.168181013	279720	0.0023556
1.1280077	52116.813	0.1680156	-0.161199011	2.168181013	279720	0.0023556
1.2690087	58631.414	0.1680156	-0.161199011	2.168181013	279720	0.0023556
1.4089964	65099.203	0.1680156	-0.161199011	2.168181013	279720	0.0023556
1.5500075	71614.269	0.1680156	-0.161199011	2.168181013	279720	0.0023556
1.6909923	78128.125	0.1680156	-0.161199011	2.168181013	279720	0.0023556
1.8320051	84643.275	0.1680156	-0.161199011	2.168181013	279720	0.0023556

Thermal Diffu.Coef. (m^2/s)	Htc in pure liquid pool (W/m^2K)	Htc in pool of particles (W/m^2K)	Nucleate Boiling Correction Factor (dimensionless)			Nucleate Boiling Contibution (W/m^2K)		
			method a	method b	method c	method a	method b	method c
Ω	α_{npb}	$\alpha_{npb,p}$	$F_{NB,1}$	$F_{NB,2}$	$F_{NB,3}$	$\alpha_{NB,1}$	$\alpha_{NB,2}$	$\alpha_{NB,3}$
1.673E-07	18005.472	39039.123	0.2592309	0.3141822	0.2375709	10120.147	12265.397	9274.5583
1.673E-07	18005.472	39039.123	0.2592309	0.3141822	0.2375709	10120.147	12265.397	9274.5583
1.673E-07	18005.472	39039.123	0.2592309	0.3141822	0.2375709	10120.147	12265.397	9274.5583
1.673E-07	18005.472	39039.123	0.2592309	0.3141822	0.2375709	10120.147	12265.397	9274.5583
1.673E-07	18005.472	39039.123	0.2592309	0.3141822	0.2375709	10120.147	12265.397	9274.5583
1.673E-07	18005.472	39039.123	0.2592309	0.3141822	0.2375709	10120.147	12265.397	9274.5583
1.673E-07	18005.472	39039.123	0.2592309	0.3141822	0.2375709	10120.147	12265.397	9274.5583

Step 4 : Predicted (v-l-s) H.t.c, [α_{TFB}], versus measured data, [α_{tfb}]

Liquid Velocity (m/s)	Liquid Reynolds no.	Boiling Enhancemen Exponent	Theoretical 3-Phase Htc (W/m^2K)			Experimental 3-Phase Heat Transfer Coefficient ($W/m^2.K$)
			method a	method b	method c	
U	Re	b_E	$\alpha_{TFB,1}$	$\alpha_{TFB,2}$	$\alpha_{TFB,3}$	α_{tfb}
0.9870068	45602.211	1.05	17643.08	20748.776	16507.838	18971.03
1.1280077	52116.813	1.05	17997.209	21006.779	16910.616	19160.76
1.2690087	58631.414	1.05	18344.445	21263.448	17302.399	19227.93
1.4089964	65099.203	1.05	19552.266	22182.6	18644.623	19803.07
1.5500075	71614.269	1.05	19201.475	21911.631	18257.754	19634.18
1.6909923	78128.125	1.05	18880.985	21666.88	17902.285	19510.79
1.8320051	84643.275	1.05	18586.465	21444.423	17573.775	19216.04

APPENDIX D

Technical Drawings

In chronological order

D.1	**Water pipe construction**
D.2	**Strike plate section (Outlet chamber)**
D.3	**Housing Block Left hand Side (Aluminum Frame)**
D.4	**Housing Block Right hand Side (Aluminum Frame)**
D.5	**Heater Housing Block**
D.6	**Copper Heating Block**

REVISION HISTORY			
REV	DESCRIPTION	DATE	APPROVED

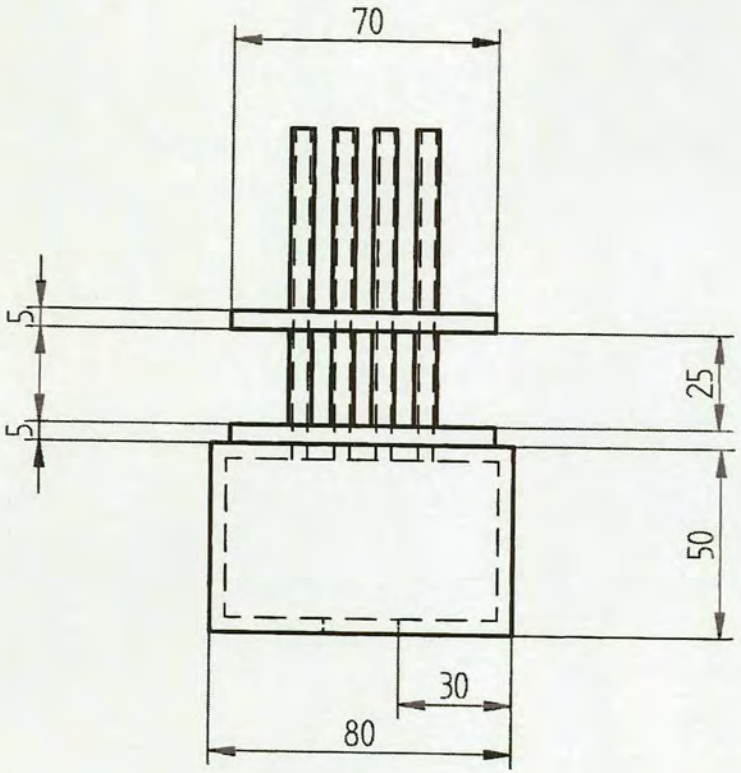

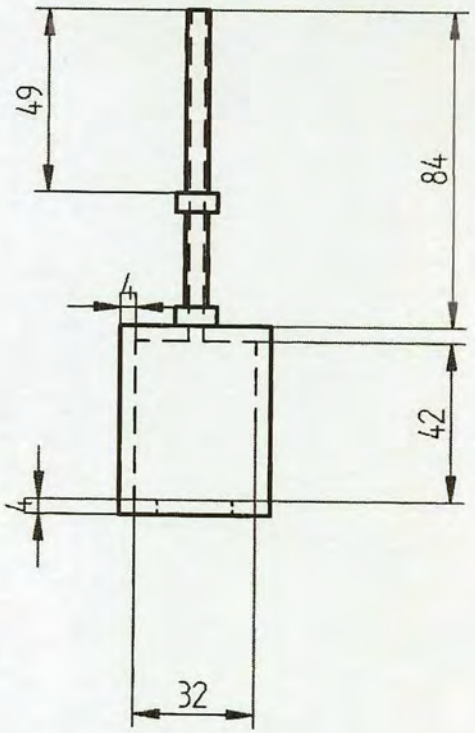

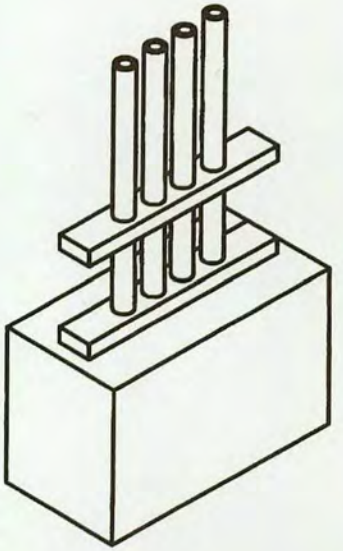

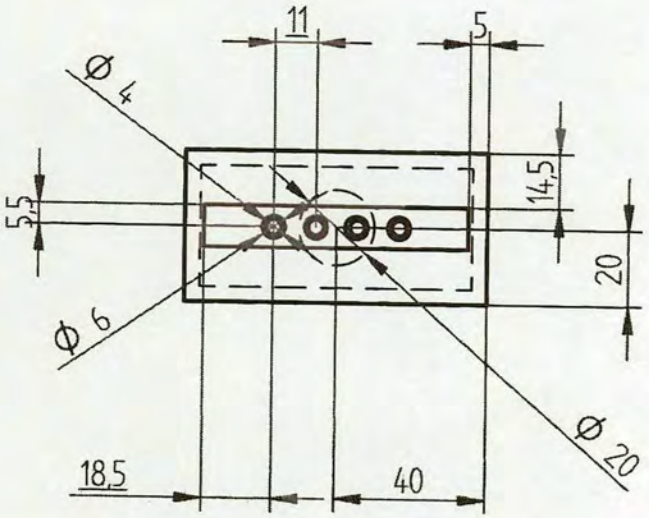

Scale 1 : 2

	NAME	DATE
DRAWN	ALASTAIR MOLDAW	16/05
CHECKED		
ENG APPR		
MGR APPR		

UNLESS OTHERWISE SPECIFIED
DIMENSIONS ARE IN MILLIMETERS
ANGLES ±X.X°
2 PL ±X.XX 3 PL ±X.XXX

SOLID EDGE
EDS-PLM SOLUTIONS

TITLE
Water pipe construct

SIZE	DWG NO	REV
A4		

FILE NAME: water box.dft

SCALE:	WEIGHT:	SHEET 1 OF 1

REVISION HISTORY			
REV	DESCRIPTION	DATE	APPROVED

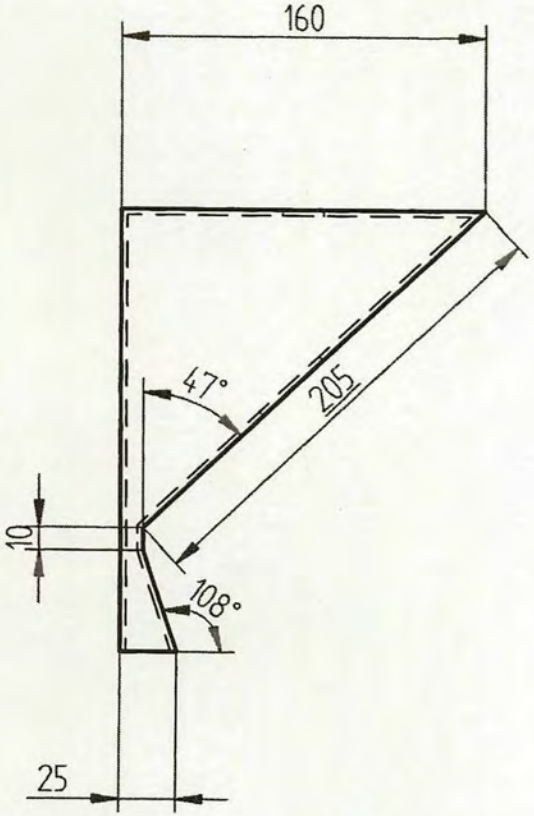

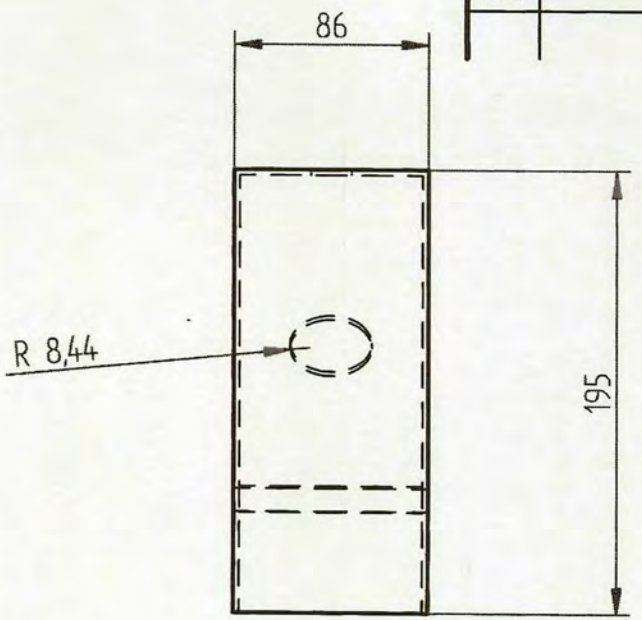

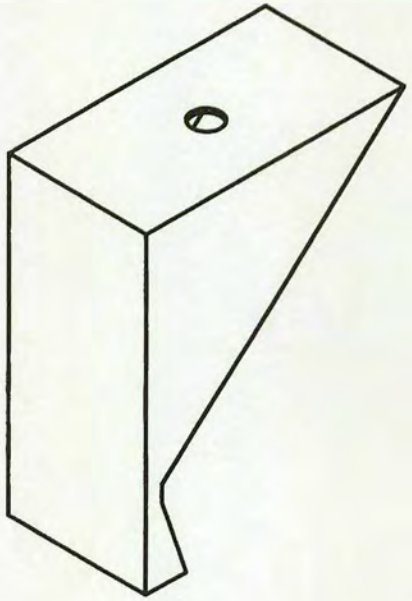

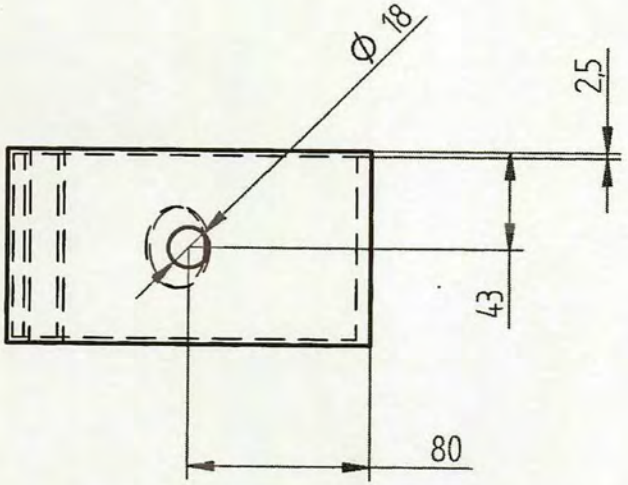

	NAME	DATE
DRAWN	Alastair	02/14/06
CHECKED		
ENG APPR		
MGR APPR		

UNLESS OTHERWISE SPECIFIED
DIMENSIONS ARE IN MILLIMETERS
ANGLES ±X.X°
2 PL ±X.XX 3 PL ±X.XXX

SOLID EDGE
EDS-PLM SOLUTIONS

TITLE
Strike plate section

SIZE	DWG NO	REV
A4		

FILE NAME: strike plate.dft

SCALE:	WEIGHT:	SHEET 1 OF 1

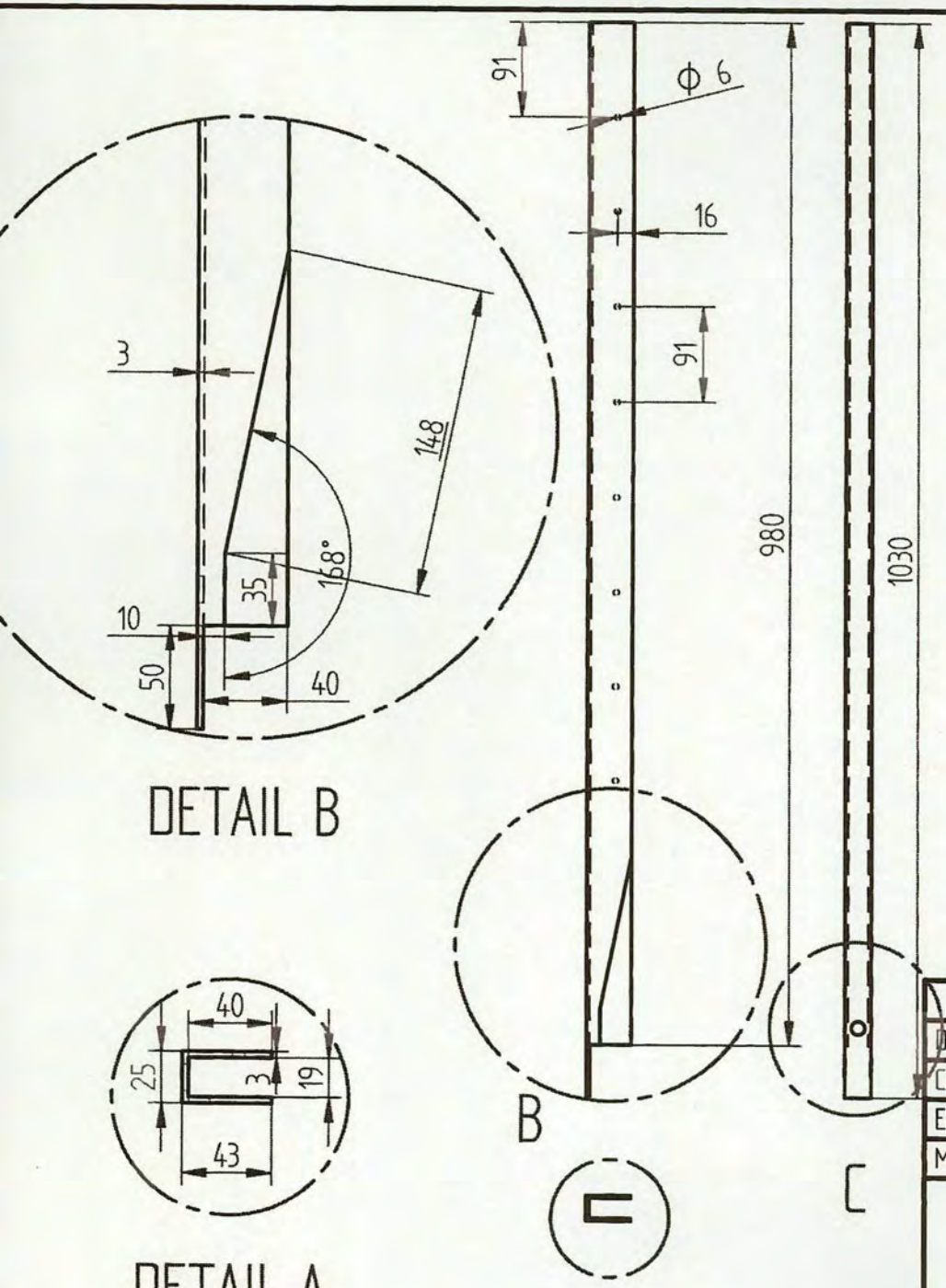

DETAIL B

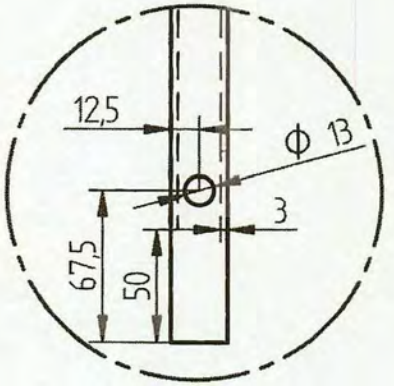

DETAIL C

DETAIL A

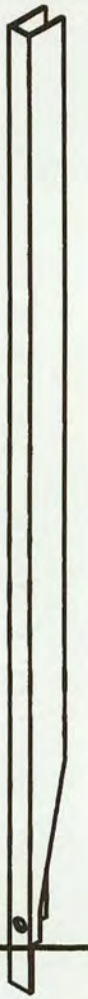

REVISION HISTORY

REV	DESCRIPTION	DATE	APPROVED

	NAME	DATE
DRAWN	Alastair	02/14/06
CHECKED		
ENG APPR		
MGR APPR		

UNLESS OTHERWISE SPECIFIED
DIMENSIONS ARE IN MILLIMETERS
ANGLES ±X.X°
2 PL ±X.XX 3 PL ±X.XXX

SOLID EDGE
EDS-PLM SOLUTIONS

TITLE
Housing Block left hand side

SIZE	DWG NO	REV
A4		

FILE NAME: left hand housing block.dft

SCALE:	WEIGHT:	SHEET 1 OF 1

REVISION HISTORY			
REV	DESCRIPTION	DATE	APPROVED

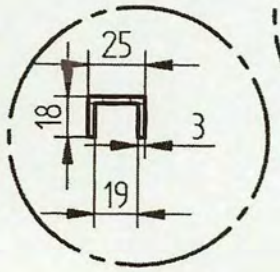

DETAIL A

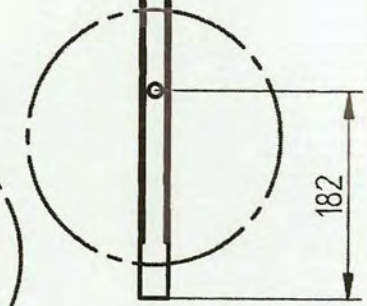

B

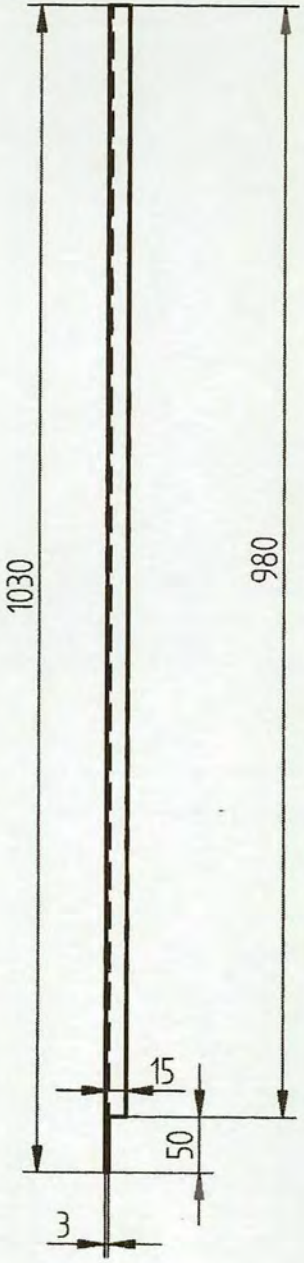

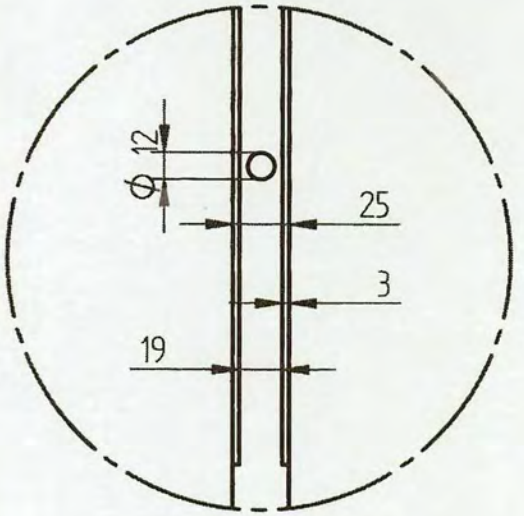

DETAIL B

	NAME	DATE
DRAWN	Alastair	02/27/06
CHECKED		
ENG APPR		
MGR APPR		

UNLESS OTHERWISE SPECIFIED
DIMENSIONS ARE IN MILLIMETERS
ANGLES ±X.X°
2 PL ±X.XX 3 PL ±X.XXX

SOLID EDGE
EDS-PLM SOLUTIONS

TITLE
Housing Block right hand side

SIZE	DWG NO	REV
A4		

FILE NAME: right hand wall.dft

SCALE:	WEIGHT:	SHEET 1 OF 1

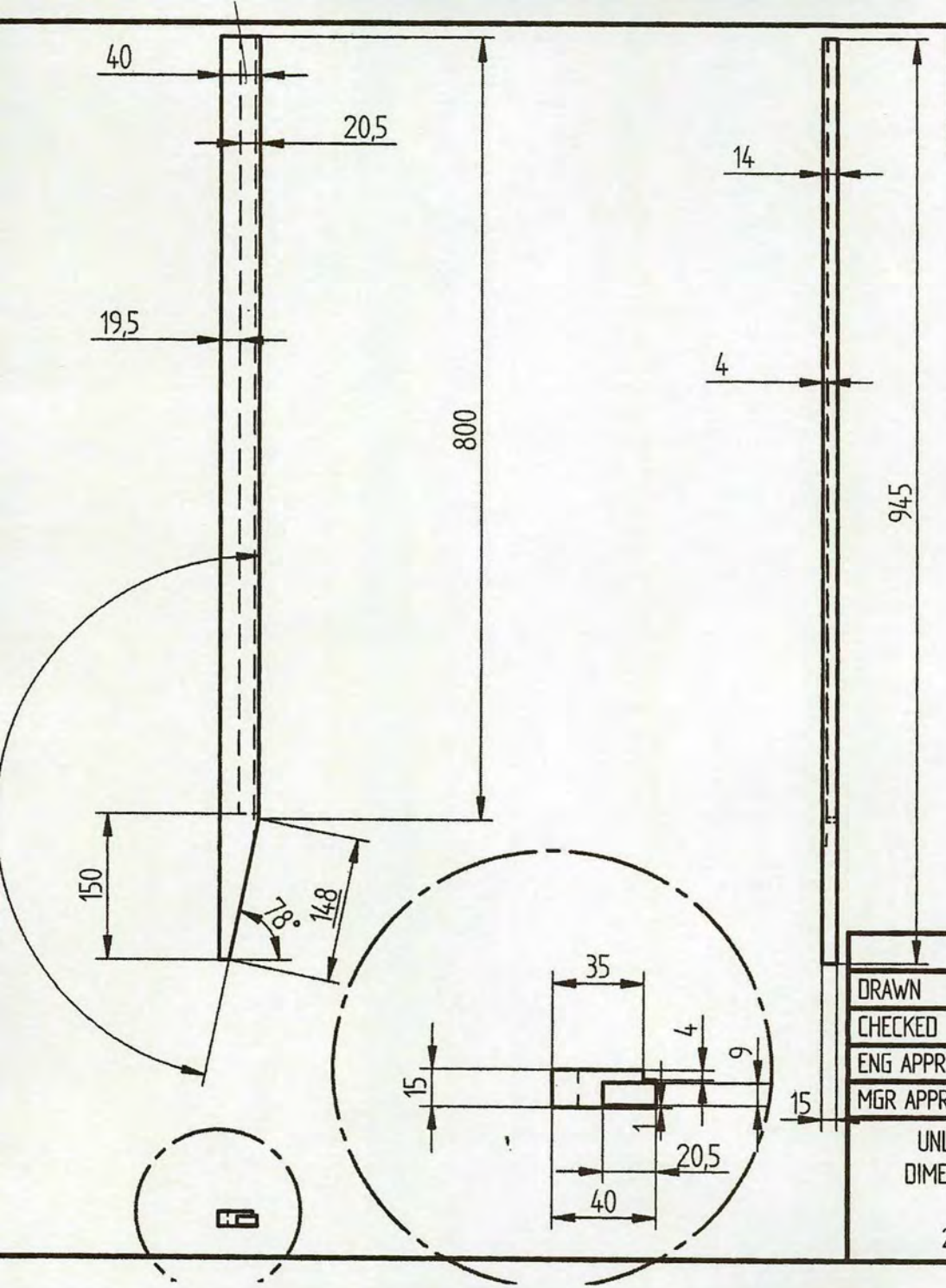

REVISION HISTORY			
REV	DESCRIPTION	DATE	APPROVED

	NAME	DATE
DRAWN	Alastair	08/15/05
CHECKED		
ENG APPR		
MGR APPR		

UNLESS OTHERWISE SPECIFIED
DIMENSIONS ARE IN MILLIMETERS
ANGLES ±X.X°
2 PL ±X.XX 3 PL ±X.XXX

SOLID EDGE
EDS-PLM SOLUTIONS

TITLE
Heater Housing block

SIZE	DWG NO	REV
A4		

FILE NAME: housing heater block.dft

SCALE:	WEIGHT:	SHEET 1 OF 1

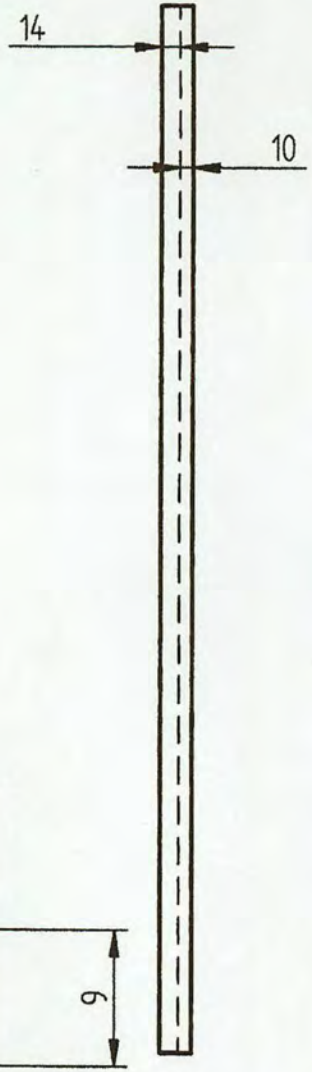

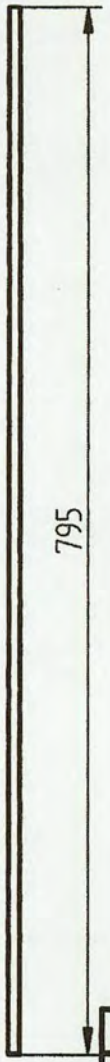

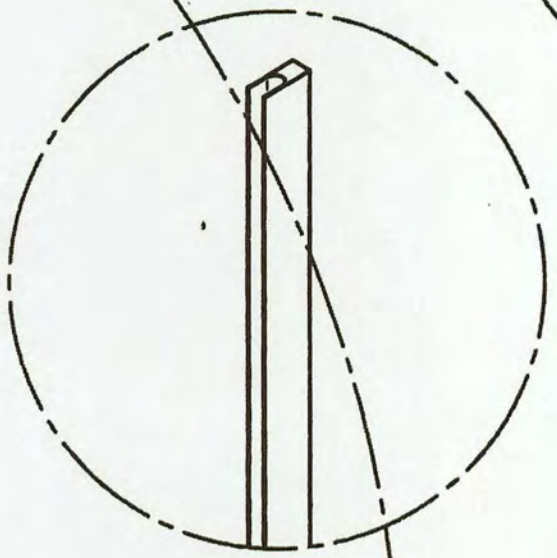

DETAIL B

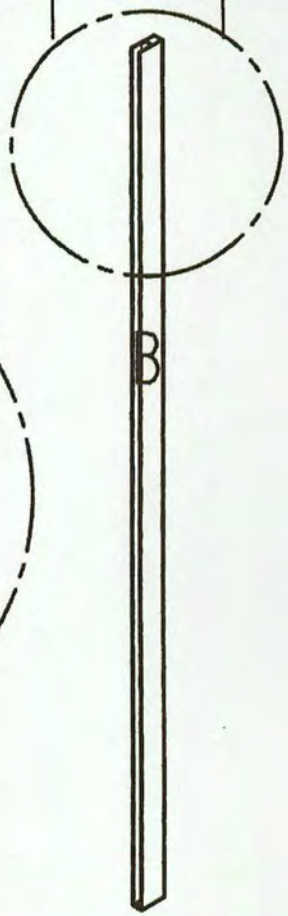

DETAIL A

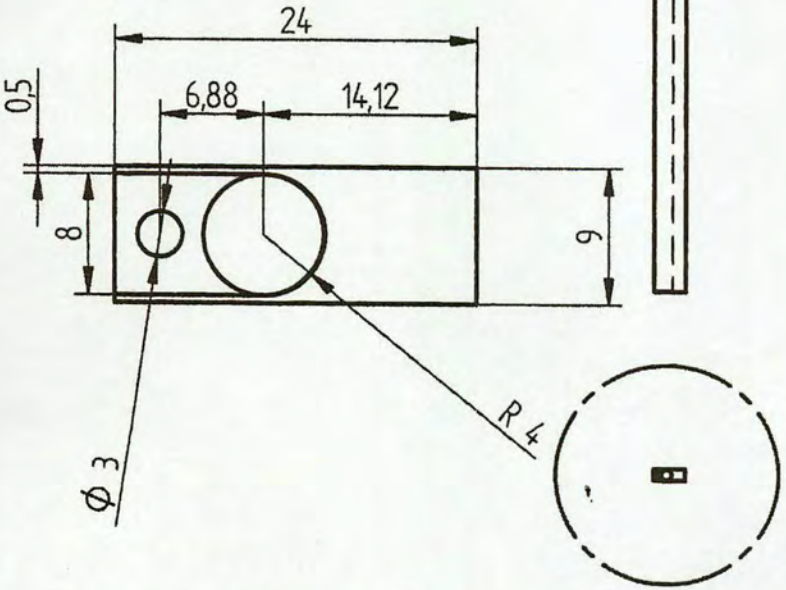

REVISION HISTORY

REV	DESCRIPTION	DATE	APPROVED

	NAME	DATE
DRAWN	Alastair	02/14/06
CHECKED		
ENG APPR		
MGR APPR		

UNLESS OTHERWISE SPECIFIED
DIMENSIONS ARE IN MILLIMETERS
ANGLES ±X.X°
2 PL ±X.XX 3 PL ±X.XXX

SOLID EDGE
EDS-PLM SOLUTIONS

TITLE: Copper Heating Block

SIZE	DWG NO	REV
A4		

FILE NAME: copper block.dft

SCALE:	WEIGHT:	SHEET 1 OF 1